The oldest carbonate minerals on Earth: insights into the early history of the Solar System

Mahmood Sofe
M.Sc. University of Manchester

Thesis Submitted for Degree of Doctor of Philosophy (Ph.D.)

School of Geographical and Earth Sciences
College of Science and Engineering
University of Glasgow

October 2012

Abstract

CM carbonaceous chondrites display a range of alteration (aqueous alteration) from slightly altered (CM2.5) to most altered (CM2.0). They are of particular interest in understanding early solar system evolution because they are made of a mixture of mineral grains that formed at high temperatures in the solar nebula with secondary minerals including phyllosilicates and carbonates whose origin is controversial. Previous studies suggest that these secondary minerals were produced by low temperature water-mediated alteration of anhydrous minerals within the asteroidal parent body of carbonaceous chondrites. Others have suggested that phyllosilicates and other secondary minerals may have formed from a nebula gas or within an earlier-formed asteroid. This study has focused on answering these questions by the study of carbonates. Results from this study are consistent with an origin of all the secondary minerals by parent body aqueous alteration.

In addition to aragonite, calcite and dolomite, CM chondrites contain breunnerite and Ca-poor dolomite. This study has found a very complex sequence of mineralisation in CM chondrites, which was: aragonite ≥ (i.e. formed before or at the same time) calcite free of rims > calcite rimmed with tochilinite and/or Fe-sulphide > phyllosilicate pseudomorphs after calcite ≥ calcite replacing Mg-rich olivine > calcite veins > dolomite > calcite replacing dolomite > dolomite veins > breunnerite > Ca-poor dolomite > calcite cement.

Aragonite grains record a period relatively early in the aqueous alteration history of the parent body of CM chondrites. This initial parent body water crystallized aragonite with high oxygen isotope values (average $\delta^{18}O$ of 39.9 ± 0.57 ‰ and $\delta^{17}O$ of 20.4 ± 1.1‰), these values falling as the water obtained oxygen from reaction with anhydrous silicates. Aragonite was probably present in all CM chondrites, but was dissolved or replaced by calcite in some moderately and highly altered CM chondrites as aqueous alteration progressed. Aragonite in less altered CM chondrites crystallized from fluids with higher concentrations of Fe than those from which the aragonite grains in the moderately altered chondrites crystallized, and whether aragonite or calcite formed was determined by the fluid Mg/Ca ratio. The majority of aragonite grains in CM chondrites have a preferred orientation, which is most likely to be the result of compression in the parent body during crystallisation. Calcite free of rims and inclusions is comparable in texture and petrographic appearance to most aragonite grains, but it exhibits more complex CL

patterns, which suggests that this calcite precipitated from fluids that were less compositionally stable than those from which aragonite crystallized.

Calcite grains rimmed with tochilinite and/or Fe-sulphide are present in all CM chondrites studied, and are more abundant than aragonite and calcite free of rims and inclusions. CL patterns of this calcite are more complex than those of the other carbonate generations. The most complicated CL patterns have been found in grains from less altered CM chondrites, and CL characteristics become simpler towards the highly altered CM chondrites. Rimmed calcite has lower $\delta^{18}O$ values (average $\delta^{18}O$ of 37.5 ± 0.65‰ and $\delta^{17}O$ of 20.9 ± 1.3‰) than aragonite grains, and so probably formed after aragonite. It was partially replaced by phyllosilicates to leave serpentine-tochilinite rimmed pseudomorphs, which in some cases comprise 3.15 vol% of a meteorite. Tochilinite-serpentine pseudomorphs after calcite are present only in moderately altered CM chondrites, whereas Mg-rich serpentine pseudomorphs after calcite occur in the moderately and highly altered CM chondrites, indicating that solutions at later stages in the alteration sequence were richer Mg than Fe, a result of the dissolution of Mg-rich silicates; consequently new minerals rich in Mg were formed.

Calcite replacing Mg-rich olivine is found in all the studied CM chondrites, but it is more abundant and coarser grained with increasing degree of alteration. Results of this study suggest that calcite after Mg-rich olivine, and Mg-rich serpentine or serpentine-tochilinite intergrowth with calcite, probably formed at the same time or immediately after each other. Fe, Mg and Si were released from Mg-rich olivine, and were used for the replacement of calcite by Mg-rich serpentine.

Calcite veins in CM chondrites formed in late stages of aqueous alteration as a result of dissolution and recrystallisation of earlier formed Ca-carbonate grains. A large calcite vein (millimetres in size) in the Antarctic CM chondrite LON 94101 has average $\delta^{18}O$ of 18.4 ± 0.3‰ and $\delta^{17}O$ of 9.0 ± 0.5‰, and low concentrations of Fe in comparison with other calcite and aragonite grains. Petrographic observations show that shock post dated the crystallization of rimmed calcite grains and the LON 94101 vein, suggesting this calcite vein was formed by water in the parent body rather than by Antarctic weathering.

Dolomite is found mainly in the highly altered CM chondrites. These rocks also contain calcite intergrown with dolomite and inclusions of dolomite within calcite. Dolomite has probably been completely replaced by calcite in the most altered CM chondrites. In

common with calcite veins, dolomite veins in highly altered CM chondrites have very low concentrations of Fe and Mn, and more Mg than dolomite grains in the meteorite matrix, and may have been sourced from dissolution of earlier dolomite grains. The Antarctic CM chondrite QUE 93005 contains complex carbonate minerals consisting of bimineralic grains (i.e. dolomite-breunnerite) and polymineralic grains (i.e. breunnerite-(Ca-poor-dolomite)-calcite cement). The presence of breunnerite in this meteorite suggests an evolutionary link between CM and CI chondrites (CI chondrites are more aqueously altered than CM chondrites).

Based on the results of this study, CM chondrites were probably derived from the same parent body, but from different regions that vary in ice content, porosity and permeability, and source of heating (^{26}Al with a half-life 717,000 years).

Table of contents

1- LINDGREN, P., LEE, M. R., SOFE, M. & BURCHELL, M. J. 2011. Microstructure of calcite in the CM2 carbonaceous chondrite LON 94101: Implications for deformation history during and/or after aqueous alteration. *Earth and Planetary Science Letters,* 306, 289-298.

2- LEE, M., LINDGREN, P., SOFE, M., ALEXANDER, C. & WANG, J. 2012. Extended chronologies of aqueous alteration in the CM2 carbonaceous chondrites: evidence from carbonates in Queen Alexandra Range 93005. *Geochimica et Cosmochimica Acta,* 92, 148-169.

List of tables

List of figures

Acknowledgement

The first thank goes to **ALLAH** for the blessing, inspiration and patience to complete this research.

This research was funded by Higher Education Ministry of Libya and also supported by grants from the UK STFC for which I am very grateful.

My sincere and special thanks go to my first supervisor – Prof. Martin Lee for the help and guidance he has given me throughout this project at the University of Glasgow. He was always there to encourage, advise and inspire me whenever I had difficulties. I want to thank him for all his help, and for being so patient with me while reading and correcting this thesis.

Many thanks go to my second supervisor Dr. Caroline Smith at the Natural History Museum, London, for her great discussions and recommendations throughout this study, and valuable assistance in providing thin sections of meteorites that were required for this study.

I am deeply grateful to Dr. Paula Lindgren for many great discussions over the past three years. Special thanks to Dr Tim Tomkinson for his help in oxygen isotope analyses.

I must not forget to convey my special thanks to NASA and the Natural History Museum, London, who provided the samples used in this study. I would like to acknowledge the Hunterian Museum and Art Gallery, University of Glasgow, who provided natural aragonite sample that used as a standard for oxygen isotope analyses. Thanks for the Scottish Universities Environmental Research Centre, who determined oxygen isotopic composition of this aragonite sample.

I am especially grateful to Peter Chung for all his assistance with SEM, EBSD, CL and Raman spectroscopy. I must thank Dr. Chris Hayward (University of Edinburgh) for many hours of help with EPMA. I should express my thanks to Dr. Paul Edwards (Department of Physics, Strathclyde University) who was able to help with CL spectroscopy. I would like to thank Billy Smith and Colin How (School of Physics and Astronomy, University of

Glasgow) for their assistance with FIB and TEM respectively. I am also grateful to Dr. Ian Franchi and Dr. Natalie Starkey (Planetary & Space Sciences Research Institute, Open University), who welcomed me in Milton Keynes and helped me with NanoSIMS, and also provided the valuable information needed for interpretation of oxygen isotope analyses.

A special big thank you goes to the past and present PhD students who shared some time of their lives in the room 418, Gregory Building over the last four years. In particular, I would like to thank Joanne, Clare, Laura, Heidi, Susan, Ram, Heather, Emma, Rebecca, Callum, and Jill for being on hand to answer random questions. I most sincerely thank Heidi Burdett for her constant help with compile and format the thesis.

Finally, my biggest thanks go to my family (mother, wife, sons, sisters and brothers) for their unwavering love and enthusiastic moral support at all times.

Declaration

The material presented in this thesis is the result of four years independent research carried out at the School of Geographical & Earth Sciences at the University of Glasgow and the Department of Earth Sciences at the Natural History Museum (London). The research was supervised by Prof. Martin Lee and Dr. Caroline Smith. This thesis represents my own research and any published or unpublished work by other authors has been given full acknowledgement in the text.

……

Mahmood Sofe

Abbreviations

AOAs: Amoboid Olivine Aggregates

AU: Astronomical Unit

BSE: Backscattered Electron

CAIs: Calcium and Aluminium-rich Inclusions

CI: Confidence Index

CL: Cathodoluminescence

EBSD: Electron Backscatter Diffraction

EDS: Energy Dispersive X-Ray Spectroscopy

EPMA: Electron Probe Micro-Analysis

FEG: Field Emission Gun

FIB: Focused Ion Beam

IPF: Inverse Pole Figure

IQ: Image Quality

MAI: Mineralogic Alteration Index

ND: Normal Direction

OIM: Orientation Imaging Microscope

PCP: Poorly Characterized Phase

PSD-XRD: Position Sensitive Detector X-ray Diffraction

RD: Rolling Direction

RI: Refractive Index

RIs: Refractory Inclusions

RL: Reflected Light

SAED: Selected Area Electron Diffraction

SE: Secondary Electron

SEM: Scanning Electron Microscope

SEM-CL: Scanning Electron Microscope-Cathodoluminescence

TEM: Transmission Electron Microscope

SIMS: Secondary Ion Mass Spectrometry

STEM: Scanning Transmission Electron Microscopes

TD: Transverse Direction

TL: Transmitted Light

TSL: TexSEM Laboratory

WDS: Wave Dispersive X-Ray Spectroscopy

List of Publications

LEE, M. R., SOFE, M. & LINDGREN, P. 2011. Evolution of Carbonate Mineralization in the CM2 Carbonaceous Chondrites. *42nd Lunar and Planetary Science Conference***,** 1710.

LEE, M.R., SOFE, M.R. & LINDGREN, P. 2012. Evolution of Carbonate Mineralogy Through the CM2-CM1 Series. *75th Annual Meeting of the Meteoritical Society*, 5246.

LEE, M., LINDGREN, P., SOFE, M., ALEXANDER, C. & WANG, J. 2012. Extended chronologies of aqueous alteration in the CM2 carbonaceous chondrites: evidence from carbonates in Queen Alexandra Range 93005. *Geochimica et Cosmochimica Acta,* 92**,** 148-169.

LINDGREN, P., LEE, M. R. & SOFE, M. 2012. Evidence for multiple fluid pulses in the CM1 carbonaceous chondrite parent body. *43rd Lunar and Planetary Science Conference,* (abstract 1949).

LINDGREN, P., LEE, M. R., SOFE, M. & BURCHELL, M. 2010. Microstructures of a calcite vein in LON 94101: Evidence for asteroidal fluid flow? *Meteoritics & Planetary Science,* 45**,** A119.

LINDGREN, P., LEE, M. R., SOFE, M. & BURCHELL, M. J. 2011. Microstructure of calcite in the CM2 carbonaceous chondrite LON 94101: Implications for deformation history during and/or after aqueous alteration. *Earth and Planetary Science Letters,* 306**,** 289-298.

LINDGREN, P., LEE, M. R., SOFE, M. & ZOLENSKY, M. E. 2011. Xenoliths in the CM2 carbonaceous chondrite LON 94101: implications for complex mixing on the asteroidal parent body. *42nd Lunar and Planetary Science Conference*, 1608, p.1349.

SOFE, M., LEE, M. R., LINDGREN, P. & SMITH, C. L. 2011. CL zoning of calcite in CM carbonaceous chondrites and its relationship to degree of aqueous alteration. *Meteoritics & Planetary Science*, 46, A218.

SOFE, M., LINDGREN, P. & LEE, M. 2010. Do calcite veins in Antarctic CM2 carbonaceous chondrites indicate asteroidal fluid flow?, *Abstract IMA 2010 Conference, Budapest*.

SOFE, M. R., LEE, M. R. & LINDGREN, P. 2011. Aragonite in the CM carbonaceous chondrites: a proxy for the magnitude of aqueous alteration. *Meteoritics & Planetary Science,* 46, A217.

SOFE, M. R., LEE, M. R. & SMITH, C. L. 2010. Mg-phyllosilicate pseudomorphs after calcite in the pollen (CM2) carbonaceous chondrite: new insights into aqueous alteration. *Meteoritics & Planetary Science,* 45, A193.

1

Introduction

1.1 The significance of CM carbonaceous chondrites studies

Carbonaceous chondrite meteorites are the oldest rocks available for study, and record processes that occurred during the birth and early evolution of the solar system ~4.5 billion years ago (Scott and Krot, 2007). Carbonaceous chondrites span the range from unaltered (pristine) rocks made mainly of solar system condensate, to rocks completely altered by water. Thus, these meteorites record processes that took place prior to and during the early history of the solar system (McSween, 1979).

CM carbonaceous chondrites are of particular interest in understanding early solar system evolution because they are made of a mixture of mineral grains (i.e. chondrules and chondrule fragments that contain olivine and pyroxene) that formed at high temperatures in the solar nebula, with secondary minerals including phyllosilicates and carbonates whose origin is controversial. Although most workers (e.g. Kerridge and Bunch, 1979; Bunch and Chang, 1980; Barber, 1981; McSween, 1987) believe that these secondary minerals were produced by low temperature water-mediated alteration of anhydrous minerals within the asteroidal parent body of carbonaceous chondrites, others have suggested that phyllosilicates and other secondary minerals (e.g. carbonates, sulphates, oxides, and sulphides) may have formed from a nebula gas or within an earlier-formed asteroid (e.g. Arrhenius and Alfven, 1971; Metzler et al., 1992; Howard et al., 2011).

Results from this study are consistent with an origin of all secondary minerals by parent body aqueous alteration. CM carbonaceous chondrites display a range alteration from slightly altered to highly altered (Rubin et. al., 2007). They were only subjected to aqueous

processes, not to thermal metamorphism (Brearly and Jones, 1998), thus making CM chondrites extremely important for understanding the enigmatic and complex history of the solar system, and to reconstruct the evolution of asteroidal parents of the carbonaceous chondrites.

1.2 Formation of the solar system

A coherent picture of planet formation can be obtained from astronomical observations and cosmochemical studies (Chambers, 2007). The solar system was created before ~ 4.6Ga from the solar nebula, which was a flattened and rotating disk of gas and dust; the solar nebula itself was formed by the gravitational collapse of a massive molecular cloud core (Boss, 2007).

1.2.1 Molecular cloud to accretion disc

Observations of pre-collapse molecular clouds indicate that they consist mainly of molecular helium, hydrogen, and carbon monoxide (Boss, 2007). The processes that drove accretion within the disc to make planetary bodies are still poorly understood; however, the accretion disks were probably turbulent (Chambers, 2007). Kokubo and Ida (2000) reported that several young stars have a gas disk. These provide an opportunity to understand the starting point of planet formation. The limited lifetime of protoplanetary disks indicate that mass progressively disappears over time, and the disk extends to conserve angular momentum (Chambers, 2007). The rotating magnetic field of a disk in its internal part interacts with gas (Chambers, 2007). The starting point of planet formation was probably when the cloud of molecular gas became gravitationally unstable (e.g. Cameron & Truran, 1977; Boss, 1995). Prior to collapse, the clouds have complex shapes and most lower-mass clouds are likely to be closer to oblate than prolate (Jones et al., 2001); on a larger scale the prolate shape appears to correspond more to oblate spheroids (Boss, 2007).

Theories of solar system formation suggest that the solar nebula had the same composition as the Sun (Weidenschilling, 1977). About 0.5% of total mass in the hot internal part of the nebula was composed of solid metal grains, sulphides and silicates, but the initial mass consisted of about 2% of solids in areas far from the Sun where temperatures became low enough for volatile ices to condense (Chambers, 2007).

1.2.2 Accretion processes formation of asteroids and planets

Raymond (2010) classified planet growth into three dynamic stages (Figure1.1); from dust to planetesimals, from planetesimals to planetary embryos, and from planetary embryos to terrestrial planets. The first stage is an initial phase in which gas dominates, followed by gravity dominated growth stages, leading eventually to the formation of the smallest rocky bodies (planetesimals), which are thought to have a size of about 1 km (Raymond, 2010). The theory of planetesimal growth suggests that aggregates were formed within the nebula by collisions and accumulation of dust grains, and these processes continued until the planet-like objects arose (Chambers, 2004).

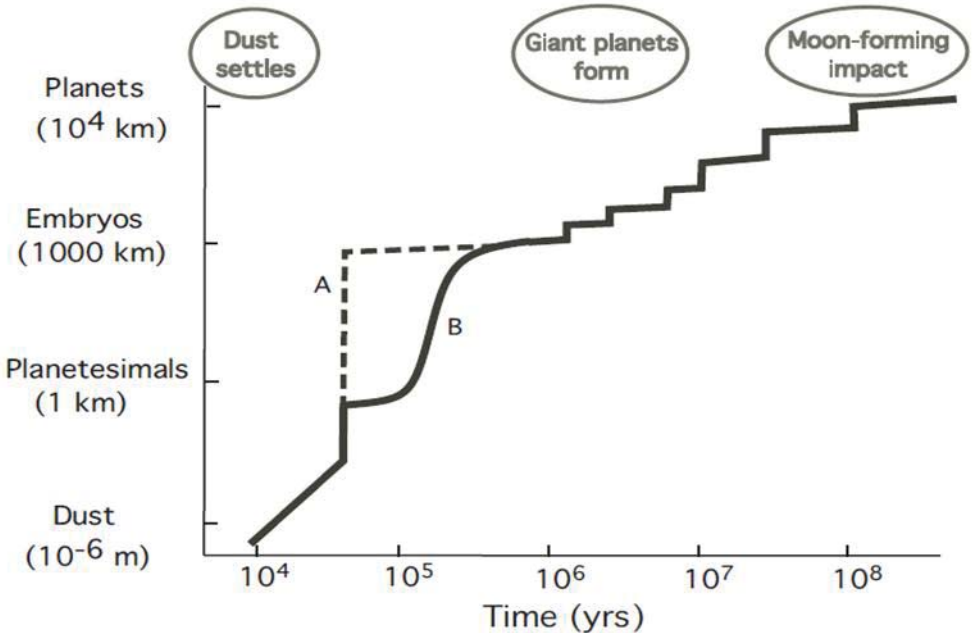

Figure 1.1- Schematic of the stages of planet growth from dust grains to planets.
Curve A displays stages when fragments in sizes of cm or m were adequate to concentrate and form planetary embryos, whereas the curve B covers stage of runaway growth (large planetesimals grow more quickly than small planetesimals (Kokubo and Ida, 1996)) during which time embryos grew from km-sized planetesimals, Raymond (2010).

The planetary embryo stage began when solid material accreted to form planetesimals a few kilometers in diameter (Chambers, 2004). Planetary embryos are likely to have been created by planetesimal collision (e.g., Kokubo and Ida, 2000). Probably at the stage of oligarchic growth a few hundred embryos appeared in the interior of the solar system (Raymond, 2010). Some of these embryos were feeding the terrestrial planets (e.g., Wetherill, 1996; Chambers, 2004). The stage from planetary embryos to terrestrial planets is the last stage in planetary accretion, and the final phase of terrestrial planet growth, (Wetherill, 1996; Chambers and Wetherill, 1998). Over time, areas where planets were

growing became empty, and the width of the feeding zone increased and moved outward (Raymond et al., 2006). The late stage of terrestrial planet accretion was strongly controlled by the giant planets (Raymond, 2010). The era of the final stage of accretion was also controlled by the presence of nebula gas, where still available (Chambers, 2004). It is possible that the Earth formed in 5 million years (Hayashi et al., 1985), but numerical simulations indicate that, with the absence of considerable volumes of gas, the Earth may have taken about 100 million years to form (Chambers, 2001; Agnor et al., 1999). The beginning of the formation of Jupiter may have slowed down the growth of large asteroids in the asteroid belt. The relative velocities of planetesimals, in particular those of different sizes, may have been increased by gravitational perturbations from Jupiter (Chambers, 2004).

The main events that took place during the early stages of the solar system are summarised in Figure 1.2, after Chambers (2007). He reported that the oldest materials that crystallized and survived in the solar nebula are refractory inclusions.

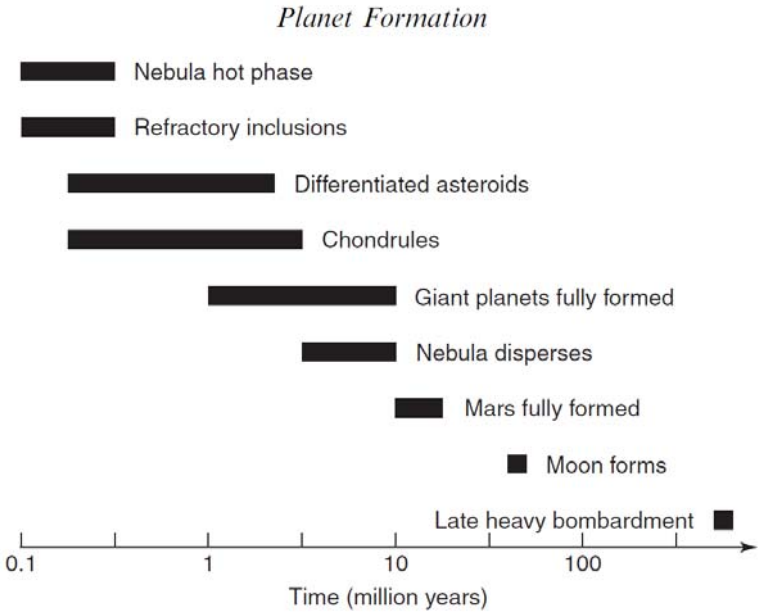

Figure 1.2- Timescale of events during the early stages of the solar system with an approximate time scale, taken from Chambers (2007).

1.2.3 First solar system solids- chondrules and refractory inclusions

Refractory inclusions (RIs) include calcium and aluminium-rich inclusions (CAIs) and amoboid olivine aggregates (AOAs). RIs and chondrules are objects that formed in the solar nebula by melting and cooling of fine grained dust balls over a short time period

(Jones et al., 2000). CAIs are some of the oldest materials in the solar system (Brearley and Jones, 1998) and preserve important information on the timing of planet formation. The modal (Pb/Pb) ages for CAIs in Allende (CV3 chondrite) were calculated to be close to 4.56 Ga; consequently the age of the solar system is 4.559±0.04 Ga (Chen and Wasserburg, 1981).

Chondrules are rounded, composed mainly of Mg-Fe silicates, and their texture indicates that they formed rapidly by cooling of melt silicates, during the early stage of the solar system. They are major constituents of most primitive meteorites (Jones et al., 2000). Differences between ratios of Mg to Si were recorded in a variety of primitive meteorites (Drake and Righter, 2002), and are likely to be related to chemical reactions between gas around chondrules, and chondrules while they were still hot (Chambers, 2007). Many chondrules are enclosed by thick rims of fine grained dust, as a consequence of their movement through regions of dust after their formation in solar nebula (Chambers, 2007).

In contrast, CAIs in most types of chondrites are numerically more abundant than chondrules and are composed mainly of Ca-Al silicates and oxides (Jones et al., 2000). Isotope dating shows that RIs (CAIs and AOAs) are the first solids to have formed in the solar nebula. They contain high proportions of ^{16}O, whereas chondrules are richer in the heavy oxygen isotopes (Chambers, 2007). Ages of RIs suggest that these materials were combined in to their parent bodies after a million years of existence in the solar nebula (Chambers, 2007), and formed within an interval of a few hundred thousand years (about 0.3 million years) (Wadhwa and Russell, 2000) before about 4.56 Ga (Almelin et al., 2002).

Interpretation of ^{26}Al data for CAIs showed that they are the oldest materials formed in the solar system. Chondrules were formed within 2 million years after most CAIs. There is a problem with absolute dating of CAIs and chondrules, as the most events took place during the early stages of the solar system (0.01 Gyr of 4.5 Gyr), and the only system that has been used for successful age dating of CAIs and chondrules is $^{235}U/^{207}Pb$ (Jones et al., 2000). High precision lead-lead (^{207}Pb-^{206}Pb) dating for CAIs showed that their age is 4559 million years (Chen and Wasserburg, 1981), 4566 Ma (Allègre et al., 1995), and 4568.2 Ma (Bouvier and Wadhwa, 2010).

Radiogenic fractions of four CAIs from Allende CV3 chondrite determined by Allègre et al. (1995) show Pb-Pb modal ages of 4,566±2 Ma. Bouvier and Wadhwa (2010) also found

the modal age of ^{26}Al-^{27}Mg for CAIs consistent with their absolute lead-lead age. Lead – lead ages (^{207}Pb-^{206}Pb) of chondrules in CB carbonaceous chondrites (described in section 1.4.3) are 4,562.7±0.5 million years for Hammadah al Hamara 237 and 4,562.8±0.9 million years for Gujba (Krot et al., 2005), so CAIs are ~5 million years older than chondrules (McKeegan and Davis, 2007).

1.2.4 Post-accretion processes: heating, melting, differentiation and aqueous alteration

Isotopic analyses of meteorites indicate that asteroids formed within a few million years of the first solar system solids (Chambers, 2004). Using thermal modeling, Bizzarro et al. (2005) reported that asteroids underwent melting and differentiation within two million years of solar system formation. This implies that the heat required to provide melting was supplied by short-lived radioactive isotopes (Chambers, 2007). Asteroids that formed later experienced lower temperatures that prevented them from melting (Chambers, 2007), which may be an explanation of why CM carbonaceous chondrite parent bodies did not melt (Fujiya et al., 2012). Reflectance spectra of asteroids can reveal some information on their mineral composition (Chambers, 2007). The composition and textures of primitive meteorites also indicate that their components were exposed to thermal conditions, or aqueous alteration, or both (Grossman et al., 2000). McKeegan and Davis (2007) reported that planetary scale melting started a few million years after CAI formation, but it is still unclear whether the formation of chondrules continued during aqueous alteration.

The early differentiation of planetesimals can be calibrated using an absolute timescale; angrites (i.e. an unusual group of basaltic meteorites) contain large fractionation of Mn relative to Cr and can be utilised for precise dating by the ^{53}Mn/^{55}Mn system (McKeegan and Davis, 2007). Angrites were used in determination of the high precision of lead-lead ages for Lewis Cliff 86010 (LEW) and Angra dos Reis (ADOR) by Lugmair and Galer (1992). Results showed that the absolute ages of crystallization in these meteorites are 4,557.84±0.52 and 4557±0.52 Ma respectively. The lead-lead age for SAH99555 angrite is 4,566.2±0.0001 Ma (Baker et al., 2005), and this implies that basalt crystallization on the surface of parent body of angrite meteorite was 1 Ma after CAI formation (McKeegan and Davis, 2007).

Phosphate minerals, including merrillite and apatite, are secondary phases formed by metamorphic processes as a consequence of oxidation of phosphorus that was initially

available in metal grains (McKeegan and Davis, 2007). These minerals were separated and obtained from seven ordinary chondrites that show different degrees of metamorphism (see petrographic classification of chondrites below) for accurate model dating by Pb-Pb. Model ages of Pb-Pb for all meteorite types are not correlated with metamorphic grade, but the Pb-Pb model ages of H chondrites range from 4,610 Ma for H4 Forest Vale to 4520 Ma for H6 Guareña, which are consistently correlated with metamorphic grade (Göpel et al., 1994).

It is still poorly understood whether water existed in a solid or gas phase during the formation of planetesimals in the internal part of the solar system. Nevertheless, the dry composition of primitive meteorites derived from the internal part of the asteroid belt indicates that little water ice was available during the formation of planetesimals in the regions of terrestrial planets. It is possible therefore that bodies rich in water such as carbonaceous chondrites and comets could have provided the Earth with its water (Chambers, 2007). Comets contain an abundance of volatile elements (Chambers, 2007), but it is thought the Earth acquired only 10% of its water from comets as they have very little opportunity to fall to Earth (Levison et al., 2000; Chambers, 2007).

One of the most complex processes that have modified chondritic meteorites is aqueous alteration (Brearly, 2003). Aqueous alteration is identified by the occurrence of secondary minerals such as phyllosilicates, carbonates, sulphates, oxides (i.e. magnetite), and secondary sulphides (Brearly, 2003). As stated in Brearley (2003), there are several possibilities for the location and conditions involved in producing these materials: (i) high temperature phases (e.g. olivine and pyroxene) reacted with water vapor within the solar nebula as a result of temperatures falling to about 375 K (e.g. Grossman and Larimer, 1974); (ii) anhydrous dust in the solar nebula experienced hydration as a consequence of shock wave passage (Ciesla et al., 2003); (iii) during the pre-accretionary phase, aqueous alteration took place within short-lived small parent bodies (~ten metres in diameter) which were later broken apart, and ultimately altered contents and unaltered materials were mixed in the final asteroidal parent bodies (Metzler et al., 1992; Bischoff, 1998); (iv) aqueous alteration took place within asteroids (Kerridge and Bunch, 1979; Zolensky and McSween, 1988).

The timescale of aqueous alteration on the asteroidal parent bodies of carbonaceous chondrites has been discussed by several authors. Using Rb-Sr techniques, Macdougall et al. (1984) estimated the time of aqueous alteration process within CI chondrites (described

in section 1.4.3), as about 50 Ma after accretion, but Endress et al. (1996) and Hutcheon and Phinney (1996) used the Mn-Cr isotope system and found the aqueous alteration of CI chondrites started less than 20 Ma after CAI formation. Macdougall et al. (1984) reported that carbonate minerals in CI chondrites are possibly secondary products of aqueous alteration that formed during or shortly after the formation of their parent bodies within 100 million years. McKeegan and Davis (2007) argued that initial values of $^{53}Mn/^{55}Mn$ from carbonate in CM chondrites and unique chondrites are contemporaneous with values of chondrules, and the formation of carbonates in some carbonaceous chondrites occurred at an early stage whilst in their parent bodies about 4,567 million years.

Mn-Cr systematics was also used for the dating of carbonates in CM chondrites by De Leuw et al. (2009) and Fujiya et al. (2012). De Leuw et al. (2009) reported that the age of carbonate formation correlates somewhat with the aqueous alteration degree of CM chondrites, and the aqueous alteration on the CM chondrites parent body/ies synchronously began with the formation of CAIs, or shortly after and lasted at least 4 million years (Figure 1.3a). However, Fujiya et al. (2012) found that the age of carbonate in four CM chondrites (Murchison, Y791198, ALH 83100 and Sayama) is identical, which is 4,563.4+0.4/-0.5 Ma, and about 4.8 Ma after the formation of CAIs. They combined these results with models of thermal histories of the parent body, and concluded that the accretion of the parent body/ies performed within 3 million years after CAIs formation (Figure 1.3b).

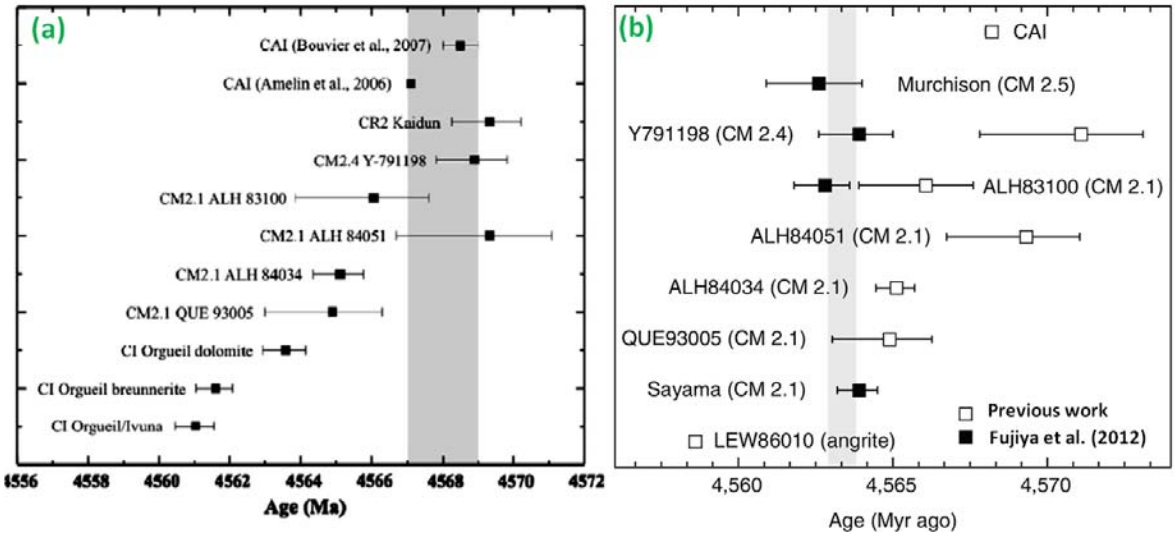

Figure 1.3- Formation age of carbonates in CI and CM chondrites relative to the absolute ages of CAIs and LEW 86010 angrite as reported by De Leuw et al. (2009) and Fujiya et al. (2012).
(a) Comparison of Mn-Cr ages of carbonates in QUE 93005 and ALH 83100 calculated by De Leuw et al. (2009) and carbonate ages of other CM and CI chondrites reported by other researchers (e.g. Endress et al., 1996; Brearley and Hutcheon, 2002; Hutcheon et al., 1999; Tyra et al., 2009) (summarized by De Leuw et el. (2009)). Note the age of carbonates is correlated with aqueous alteration degree. CAIs ages are labeled in gray band for reference. (b) Comparison between the formation age of carbonates in CM chondrites determined by Fujiiya et al. (2012) (plotted in gray) and formation age of carbonates in the other CM and CI chondrites as shown in (a). Note the age data by Fujiiya et al. (2012) suggests an identical age of carbonate formation in CM chondrites, whereas results by De Leuw et al. (2009) show wider range of formation age of carbonates in CM chondrites (QUE 93005 and ALH 83100).

1.3 Samples of primitive bodies meteorites

Meteorites are rocks that are derived from asteroids by cratering collisions, eventually crossing Earth′s orbit to land on the Earth's surface (Greenberg and Chapman, 1983). The orbital relationships between chondrites and asteroids suggest that the interior of the asteroid belt is characterised by parent bodies with an abundance of chondrules. Chondritic materials were also most likely used to form the terrestrial planets (Scott and Krot, 2007).

Most asteroids orbit the sun between Mars and Jupiter at about 1.8 to 5.2 AU (Astronomical Unit) (Shearer et al., 1998). On the basis of differences in composition, the constituents of the asteroid belt can be classified into primitive asteroids, metamorphic asteroids and igneous asteroids (Figure 1.4). Igneous (differentiated) asteroids are characterised by moderate-high albedo (i.e. the proportion of reflected light to incident light by surface (McSween, 1999)) and occur at about 2.7 AU. They are comprised of spectral classes A, E, M, R, S, and V (see Table 1.1 for more details) (Shearer et al., 1998). These asteroids are probably the parent bodies of basaltic achondrites, enstatite chondrites, pallasites and iron meteorites (Bell et al., 1989). Metamorphic asteroids include C-type asteroids, whose surface appearance has been affected by heating and the presence of

liquid water; they orbit between 2.8 and 3.8 AU and have a moderate to low albedo (Shearer et al., 1998). Primitive asteroids have low albedo, include types P and D, and cover all asteroids occurring out to 4.0 AU. They are characterised by the presence of water ice and the absence of hydrous minerals (Shearer et al., 1998). Highly altered carbonaceous chondrites are most likely related to T-type asteroids (see Table 1.1 for more details) (Bell et al., 1989).

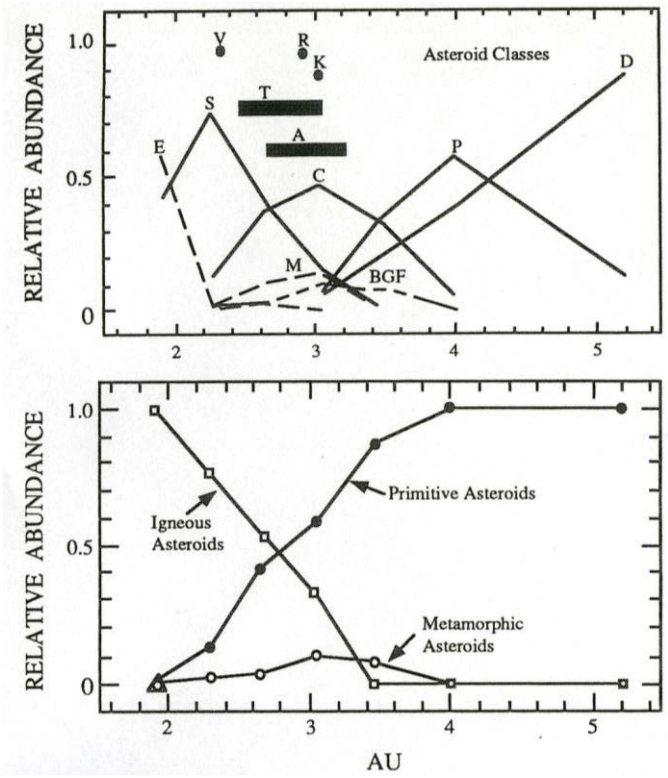

Figure 1.4- Upper graph shows taxonomic classes and distributions of asteroids. The bottom plot displays the distribution of three major groups in the asteroid belt. Figures from Shearer et al. (1998), modified after Bell et al (1989).

Undifferentiated and differentiated meteorites have been linked to their parent bodies by Lipschutz et al. (1989), Bell et al. (1989) and Shearer et al. (1998) (Table 1.1) using asteroidal spectral taxonomy and surface mineralogy.

In Table 1.1 the possible parent bodies for CI and CM meteorites are listed, which are C-type and its related classes B, F and G. Shearer et al. (1998) reported the largest asteroid, 1 Ceres (C class), as probably the parent body of CI and CM chondrites, based on the interpretation of its spectral features that reveal the presence of hydrous silicates on the surface. 1 Ceres is located at 2.77 AU from the Sun (Shearer et al., 1998). McSween (1999) showed a spectrum for 1 Ceres with a deep absorption band in the infrared region at 3 μm wavelength, which is consistent with the presence of hydrated silicate minerals (water bound in their structures). He observed that the presence of iron in phyllosilicates,

and probably organic materials in C-type asteroids could have produced other spectral features with weak absorptions. These mineral compositions and spectral features have similarities with CI and CM chondrites that have been affected by aqueous alteration.

Type	No.	Surface Mineralogy	Suggested Meteorite Analogues
A	3	olivine, olivine+metal	Olivine achondirtes, pallasites
B C F G	6 41 10 5	hydrated silicates and carbon/organics /opaques	CI-CM assemblages with some additional alteration or metamorphism
D	19	carbon/organic rich	Organic-rich cosmic dust grains?
P	23	silicates (?)+carbon-rich	CI-CM assemblages plus organics (?)
E	8	iron-free enstatite, forsterite	Enstatite achondrites
M	21	metal, metal+enstatite	Irons
Q	1	olivine,pyroxene, metal	Ordinary chondrites
R	1	pyroxene+olivine+metal	Olivine-rich achondrites
S	73	metal+olivine+pyroxene	Pallasites or olivine-rich stony-iron
V	1	pyroxene, feldspar	Basaltic achondrites
T	1	hydrate silicates and carbon/ organics/opaques but more highly altered than BCFG	Highly altered CI-CM assemblages

Table 1.1- The link between asteroid classes and meteorite classification.
Taken from Shearer et al. (1998) who has modified it after Lipschutz et al. (1989) and Bell et al. (1989). No. is number of asteroids.

1.3.1 Meteorite Orbits:

The heliocentric orbit of the Neuschwanstein meteorite (enstatite chondrite) was precisely computed by Spurný et al. (2003) using three properties of its journey, namely the accurate time of the fireball, its initial velocity, and radiant position. As the fall of the

Neuschwanstein meteorite was recorded by camera networks, its atmospheric trajectory and pre-atmospheric orbit could be determined. The journey of this meteorite prior to its collision with Earth was described by movement around the Sun in an elliptical low-inclination orbit with its aphelion (i.e. at its greatest distance from the Sun) in the asteroid belt. This fireball followed the same orbit of the Příbram H5 ordinary chondrite that landed in 1959. This new discovery indicates that the Earth orbit is cut by a stream of meteoritic materials (Spurný et al., 2003). The fall location and orbit of the meteorite Bunburra Rockhole (BR) was also determined using triangulated observations of fireballs, orbit features and isotopic analyses in the Nullarbor desert of Australia. Observations indicate that BR was derived from a distinctive parent body, likely to be a V-type asteroid (Bland et al., 2009b). This meteorite fragmented into two pieces at an elevation of 29.59 km before landing on Earth. It is an igneous achondrite (eucrite) and is composed of several clasts (Bland et al., 2009b). Eucrites are classified under the large clan of achondrites (HEDs), and linked to 4 Vesta (Binzel, 1993), the largest asteroid in the main belt (Bland et al., 2009b). BR however has a different oxygen isotope composition to meteorites associated with 4 Vesta, suggesting that BR was derived from another source of basaltic achondrites. The orbit of BR (Figure 1.5) has been determined and can be used to track its orbital history. It arrived from Aten asteroids that are near-Earth objects (NEOs).

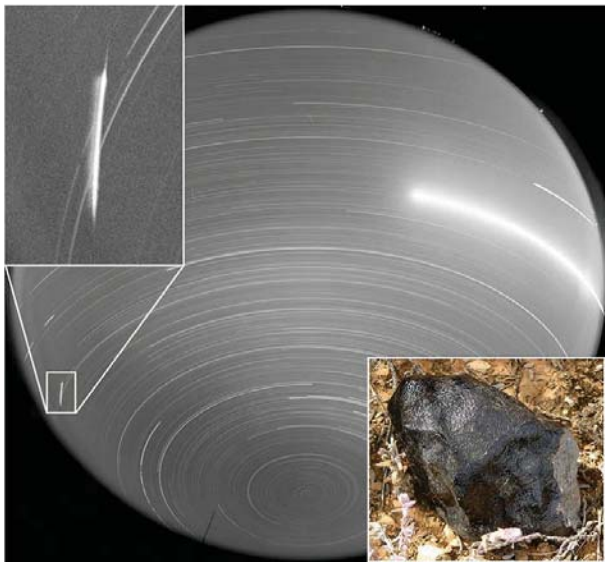

Figure 1.5- Image of all-sky displays the trace of fireball in left side, near to horizon, and Bunburra Rockhole (BR) on Earth.
This image was taken by Desert Fireball Network (Bland et al., 2009b).

1.4 Meteorite classification

The classification of meteorites is based on their mineralogy, chemical and isotopic composition, and petrographic features (Weisberg et al., 2006). Processes such as shock metamorphism, and terrestrial weathering are used to sub-classify them. A variety of schemes have been proposed to divide the various meteorites into classes and groups. In the most popular of these classifications, originally developed by Rose-Tschermak-Brezina (RTB) (1904), texture and mineralogy are used. RTB distinguished 31 different chondrites in the final stage of their classification (Hutchison, 2004).

In order to reduce the complexity of the RTB classification, in 1916 Prior used the similarity of mineralogy and chemical composition (Norton, 2002). He utilized variations of iron-nickel metal and iron in olivine and pyroxene to subdivide chondrites. These chemical and mineral relationships are called Prior's rules. In this scheme the lower the concentration of iron-nickel metal in a chondrite, the richer the metallic iron is in nickel and the less iron-nickel metal in a chondrite, the richer in iron are the magnesium silicates. The final phase of this classification (Table.1.2) defines five groups of meteorites including chondrites, achondrites (calcium poor), achondrites (calcium rich), stony irons and irons (Norton, 2002).

1.4.1 Chondrite classification

The term 'chondrite' was proposed by Gustav Rose (1863) for stony meteorites that contain chondrules (Norton, 2002). In most of the current classifications, these meteorites are essentially divided into "differentiated" and "undifferentiated" (Figure 1.6) according to their mineralogy and mineral chemistry. One category is defined under undifferentiated: chondrites, and three very broad categories are recognized under differentiated: achondrites, stony-iron meteorites and iron meteorites. There are also various sub-categories within each category called classes, and well defined groups are listed under each class (e.g. Bischoff, 2001; Weisberg et al., 2006).

Group	Class	Major minerals
Chondrites	Enstatite	Enstatite, iron–nickel
	Olivine–bronzite	Olivine, bronzite, iron–nickel
	Olivine–hypersthene	Olivine, hypersthene, iron–nickel
	Olivine–pigeonite	Olivine, pigeonite
	Carbonaceous	Serpentine
Achondrites (Ca-poor)	Aubrites	Enstatite
	Diogenites	Hypersthene
	Chassignites	Olivine
	Ureilites	Olivine, pigeonite, iron–nickel
Achondrites (Ca-rich)	Angrite	Augite
	Nakhlites	Olivine, diopside
	Eucrites	Pigeonite, plagioclase
	Howardites	Hypersthene, plagioclase
Stony-irons	Pallasites	Olivine, iron–nickel
	Siderophyre	Bronzite, iron–nickel
	Lodranites	Bronzite, olivine, iron–nickel
	Mesosiderites	Pyroxene, plagioclase, iron–nickel
Irons	Hexahedrites	Iron–nickel alloy (kamacite)
	Octahedrites	Iron–nickel alloy (kamacite, taenite)
	Ataxites	Iron–nickel alloy (nickel-rich taenite)

Table 1.2- The Prior meteorite classification.
This classification shows five groups of meteorites including chondrites, related to amounts of iron-nickel in meteorites. Mineralogy was used to name achondrites, primary silicate to classify stony irons, and nickel concentrations and internal structure to name irons. Taken from Norton (2002)

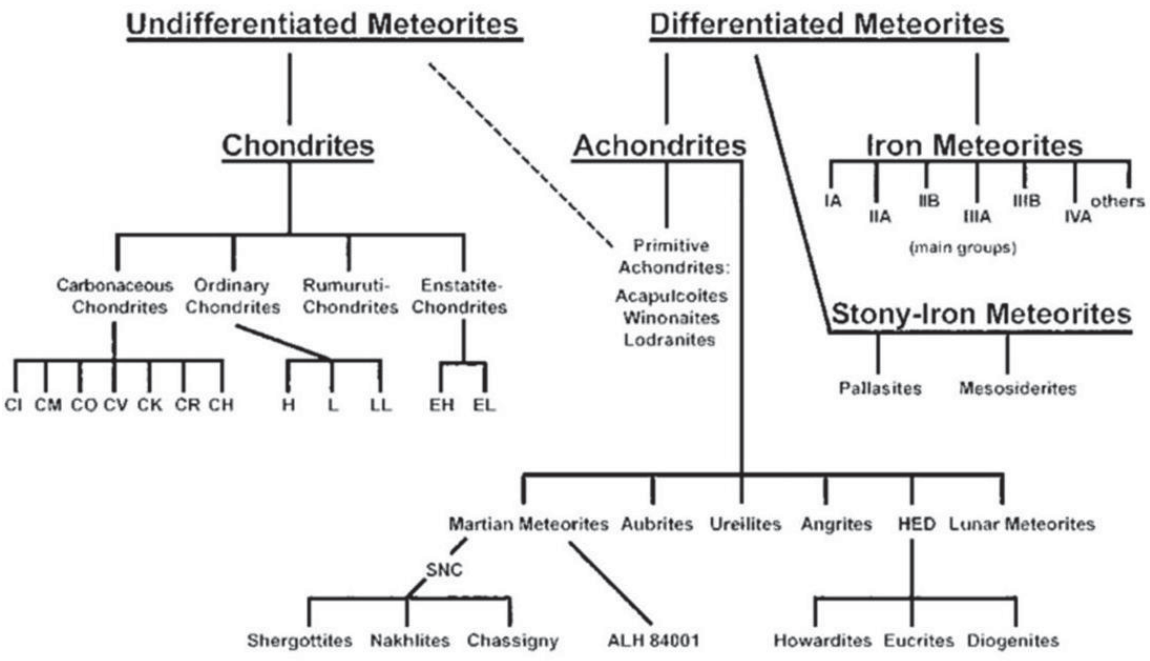

Figure 1.6- Classification of meteorites.
Meteorites are divided into two main categories including differentiated and undifferentiated. From Bischoff (2001)

1.4.2 Weathering classification

Generally, meteorites are described as 'finds' or as observed meteorites (falls). 'Finds' are meteorites that fell to the Earth's surface during the last 2.5 million years (Hutchison, 2004), so have been exposed for terrestrial weathering, forming weathering products within these meteorites (e.g. Jull et al., 1988; Hutchison, 2004; Tyra et al., 2007). Antarctic meteorites have been classified into three types (A, B and C) by Jull et al. (1988). Their classification is mainly based on the amounts of visible rust. A indicates minor amounts of rust, B refers to moderate amounts of rust and C indicates severe amounts of rust. Alternatively, Wlotzka (1993) has provided a weathering scale that classifies the weathering effects into seven weathering grades (W0-W6). These stages have been identified by optical observations on polished sections. These stages described by them are as follows:

W0: no visible oxidation in metal or sulphide.

W1: minor oxide rims are present around metal and sulphide, minor oxide veins are also present.

W2: oxidation has affected ~20-60% of metal.

W3: oxidation in this level is heavy, 60-95% of metal and sulphide are altered.

W4: oxidation of metal and sulphide is complete (>95%), however silicates are preserved.

W5: slight alteration in mafic silicates.

W6: clay minerals and oxides have replaced silicates.

1.4.3 Petrographic classification of chondrites

Krot et al. (2007) showed that bulk composition and texture can also be used to classify meteorites into chondrites and nonchondritic meteorites. They then sub-divided chondrites and nonchondritic meteorites (Figure 1.7) into groups based on their oxygen isotopes, chemistry, mineralogy and petrography. They also included primitive achondrites and differentiated rocks (formed by igneous processes) with the non-chondritic meteorites. The chondrites consist of carbonaceous, ordinary and enstatite classes. In order to provide more specific classification, labels of classes were added for meteorites that are probably derived from the same parent bodies. In this classification, the groups subdivided into subgroups and petrographic types (1-6) were also included. The taxonomic terms were used to recognise 14 chondrite groups; a number of other chondrites are known as ungrouped, due to their difference in mineral composition and chemistry from any known group. This scheme was used to classify meteorites that were obtained for the present research project.

On the basis of texture and mineralogy, the petrologic type scheme was introduced by Van Schmus and Wood (1967), and this classification has been modified by Krot et al. (2007), Norton (2002), Hutchison (2004), Weisberg et al. (2006) and Krot et al. (2007),. In this classification, alteration by thermal and aqueous processes was used to divide the chondrites into six types. Types (1-2) experienced aqueous alteration at low temperatures. Types (4-6) were subjected to thermal metamorphism. Type (1) displays higher degree of aqueous alteration than type (2), Type (6) represent higher grades of metamorphism compared to type (4). Type (3) is the midpoint (pristine chondrites) (e.g. Krot, et al., 2007; Hutchison, 2004; Weisberg et al., 2006) (Figure 1.8 d). Types (4-6) chondrites (Figure 1.8 a-c) represent progressively higher degrees of alteration by thermal metamorphism; these types are known as equilibrated, in which the mineral chemical compositions become progressively more homogeneous (Krot et al., 2007). Type (3) chondrites (Figure 1.8d) contain silicate minerals such as olivine and pyroxene that are inhomogeneous, and are characterised by absences of matrix intergrowth with chondrules (Hutchison, 2004). Types (1-2) (Figure 1.8 e-f) represent all chondrites that are partly or completely composed of secondary minerals that were formed by aqueous alteration (Krot et al., 2007).

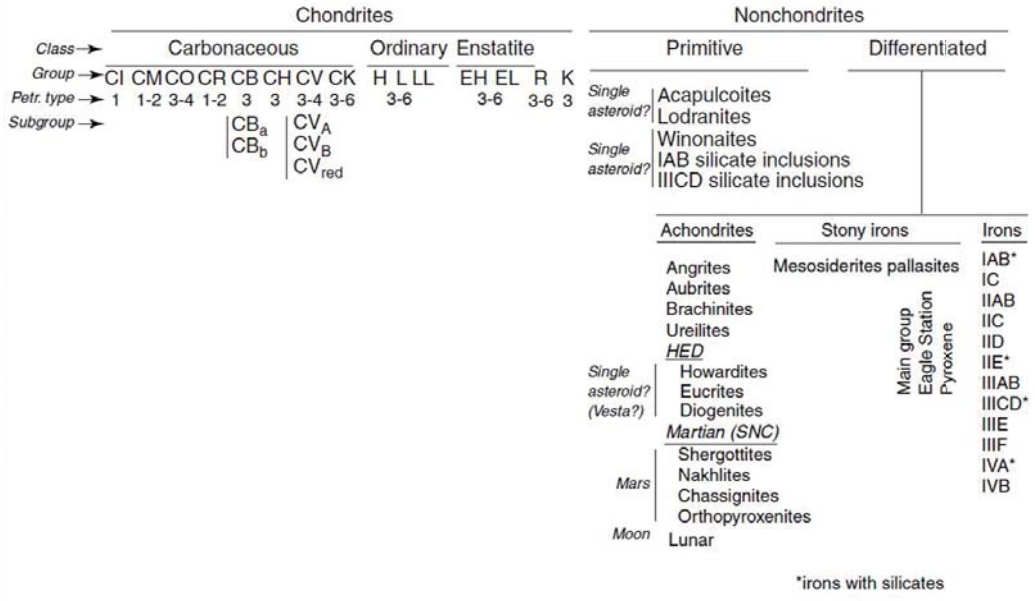

Figure 1.7- Classification of meteorites.
Groups of chondrites are subdivided into subgroups and petrographic types of chondrites are included. From Krot et al. (2007).

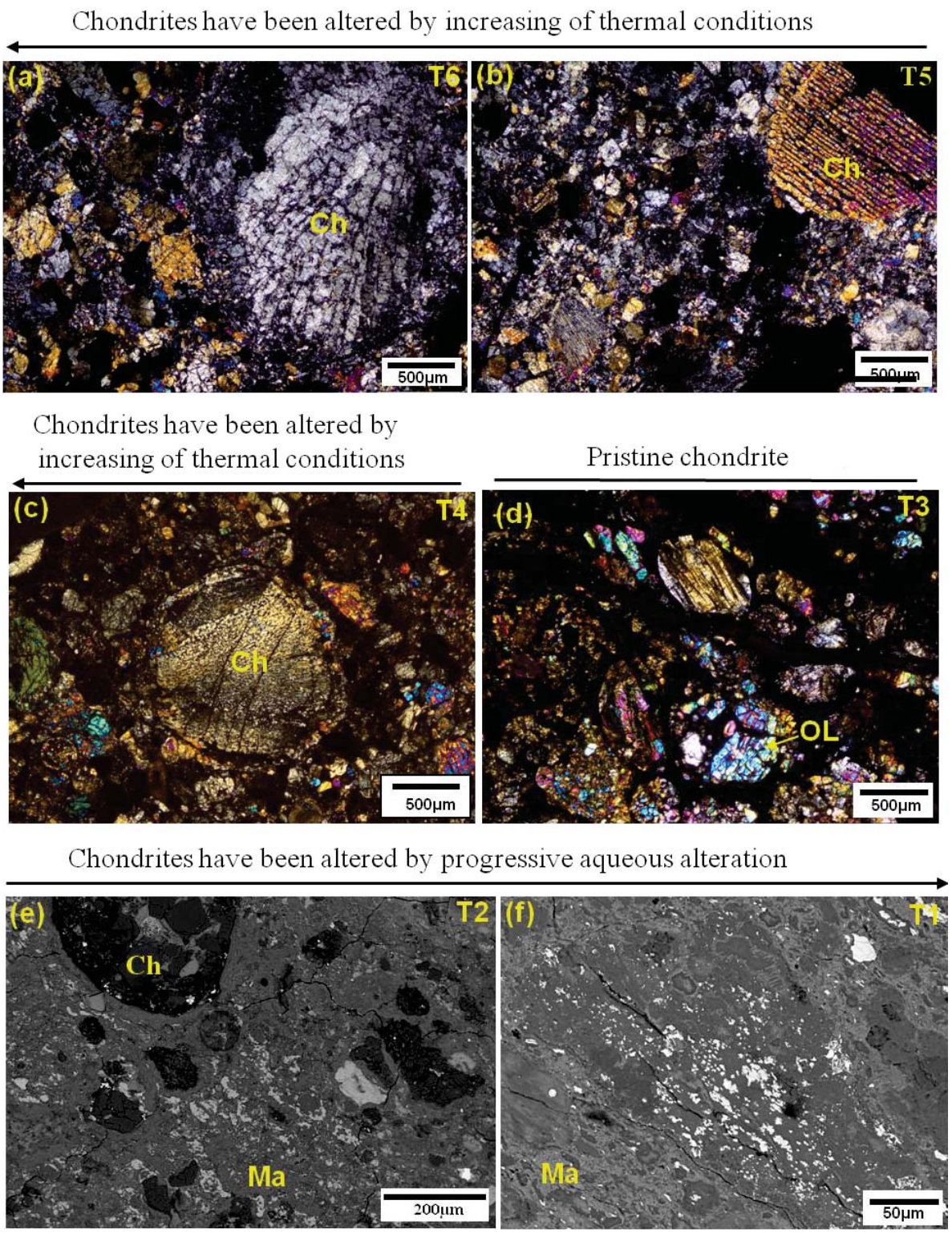

Figure 1.8- Images of chondrites types (1-2) that experienced aqueous alteration at low temperatures and types (4-6) that were subjected to thermal metamorphism.
a-d Ordinary chondrites viewed between crossed polarised (a) Type 6 chondrite, Ch is chondrule. (b) Crumlin chondrite type 5. (c) Type 4 Tennasilm chondrite, Ch is chondrule. (d) Type 3 chondrite, OL is olivine. e-f BSE images of CM carbonaceous chondrites. (e) BSE of Pollen CM2 partly altered, Ch is preserved chondrule and Ma is phyllosilicate matrix. (f) BSE image of SCO 06043 CM1 which is highly altered, note the absence of chondrules.

Carbonaceous chondrites are considerably richer in carbon than non-carbonaceous chondrites. They are subdivided into eight groups (CI, CM, CO, CR, CH, CB, CV, and CK) that vary in petrographic properties and texture features (see Table 1.3). The terms of these chondrites refer to typical chondrites, which are Ivuna-like (CI), Mighei-like (CM), Ornans-like (CO), Renazzo-like (CR), ALH85085-like (CH), Bencubbin-like (CB), Vigarano-like (CV), Karoonda-like (CK) (Krot and Scott, 2007).

	CI	CM	CO	CR	CH	CB	CV	CK
Petrologic type	1	1-2	3-4	3-4	3-6	1-2	3	3
Chondrule size (mm)	-	0.3	0.15	0.7	0.02	0.1-20	1	0.7
Matrix (vol%)	>99	70	34	30-50	5	<5	40	75
Chondrule (vol%)	<<1	20	48	50-60	~70	30-40	45	15
CAIs and AOA (vol%)	<<1	5	13	0.5	0.1	<0.1	10	4
Metal (Vol%)	0	0.1	1-5	5-8	20	60-70	0-5	<0.01

Table 1.3- Classification of carbonaceous chondrites.
Carbonaceous chondrites are subdivided into eight groups that vary in their components and petrographic types, modified after Krot and Scott (2007)

1.5 What is a chondrite?

Chondrites are stony meteorites and comprise up to 86% of all meteorites that fall to Earth (Figure 1.9). The majority of chondrites are characterized by the presence of chondrules.

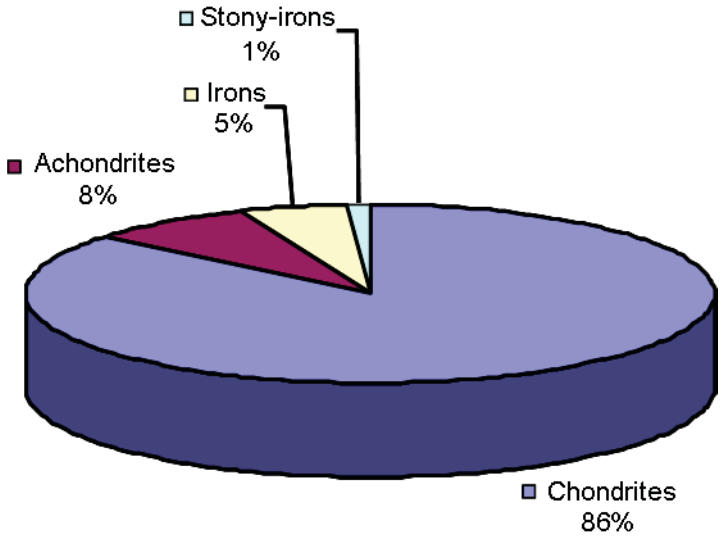

Figure 1.9- Pie chart illustrates the relative abundance of meteorite types that have fallen to the Earth 86% of these meteorites are chondrites and 8% achondrites.
From McSween (1999).

1.5.1 Components of chondrites

The main constituents of chondrites are chondrules, iron nickel metal, refractory inclusions including calcium-aluminum rich (CAIs) and amoeboid olivine aggregates (AOAs), and fine grained matrices (<1μm) (Krot et al., 2007). These constituents are present in chondrites in various percentages: 0.01-10 vol. % refractory inclusions, <0.1-70 vol. % metallic Fe-Ni, 1-80 vol. % matrix material, and <5-80 vol% chondrules.

1.5.1.1 Chondrules

Chondrules are spherical to sub-spherical 'droplets' or fragments within a size range of 1μm to 5cm, composed mainly of the ferromagnesian minerals pyroxene and/or olivine (e.g. Hutchison, 2004). They formed by partial to complete melting of precursors of silicates (Norton, 2002), and Hutchison (2004) noted that "chondrules are objects that were totally or partly molten before or during the accretion period which led to the formation of chondrites". In some cases, chondrules are composed of ferromagnesian silicates and surrounded with fine grains that are similar to its mineral composition (Norton, 2002). Scott and Krot (2007) pointed out that chondrules can be enclosed by two different types of rims (Figure 1.10): fine-grained rims (<1μm) (phyllosilicates) and coarse grain igneous rims; these rims are absent from CB and CH chondrites. Chondrules display a variety of textures based on their mineral composition and conditions of melting and cooling (Norton, 2002). These include porphyritic and non porphyritic chondrules.

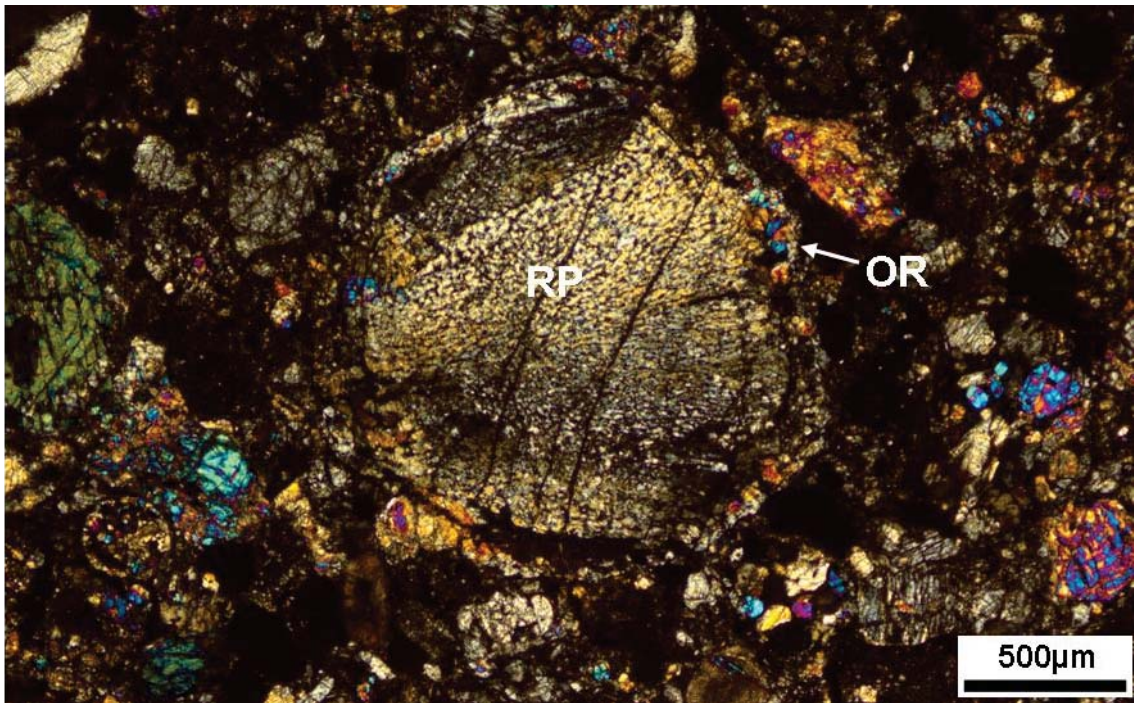

**Figure 1.10- Photomicrograph of a thin section of the Tennasilm, ordinary chondrite (54635) L4.
A radial pyroxene (RP) chondrule viewed between crossed polarisers showing a fan-shaped array of pyroxene crystals radiating from a point on the chondrule surface. Note presence of rims of large (~50 µm) olivine (OR) and pyroxene crystals that surround the chondrule.**

1.5.1.1.1 Porphyritic chondrules

Porphyritic chondrules include the types porphyritic olivine (PO), porphyritic pyroxene (PP) and porhyritic olivine-pyroxene (POP) (Norton, 2002). Porphyritic olivine chondrules (Figure 1.11) contain well formed crystals of olivine with euhedral to anhedral shapes. Porphyritic pyroxene chondrules (Figure 1.12) are composed of low Ca-pyroxene or clinoenstatite, and are characterised by their low order birefringence colours (gray shades) and multiple parallel twinning (Norton, 2002). Porphyritic olivine pyroxene (POP) represents 48% of porphyritic chondrules and consists of a mixture of clinoenstatite and olivine. The textures of these chondrules often show small olivine grains rimmed with large pyroxene crystals (Norton, 2002). Granular olivine (GOP) chondrules contain a mixture of small olivine and anhedral grains of pyroxene (Norton, 2002); they are sometimes classified as nonporphyritic chondrules (e.g. Hutchison, 2004).

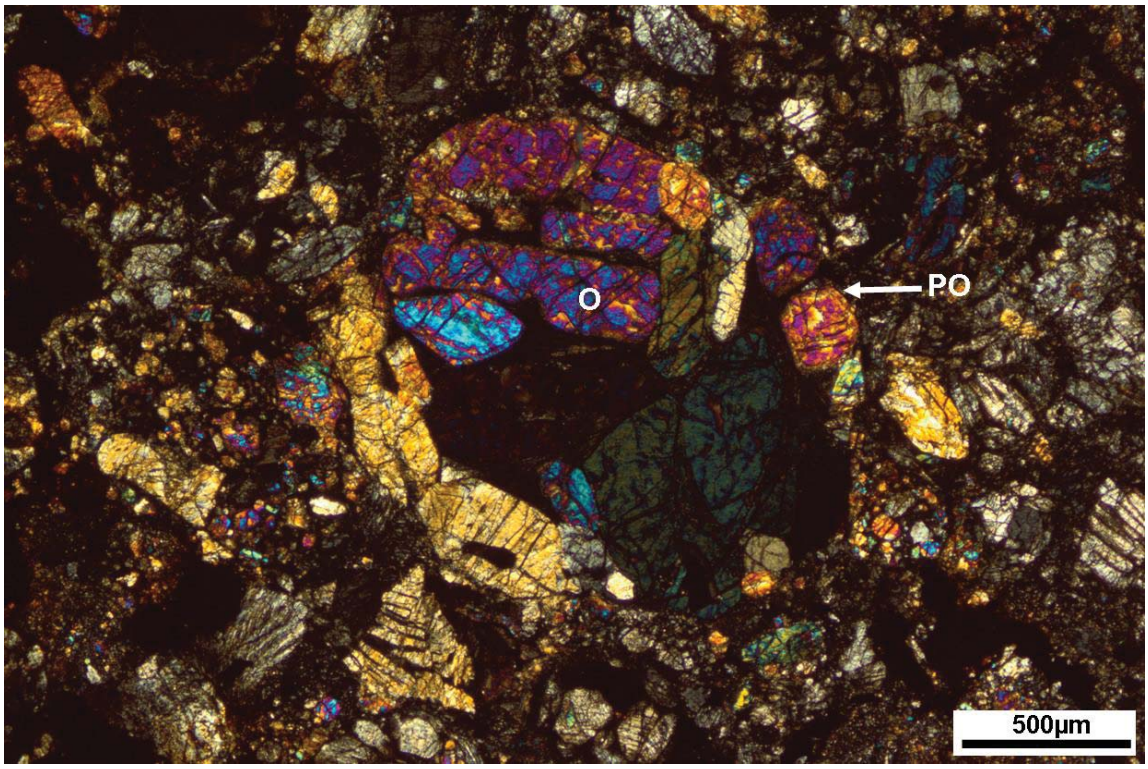

**Figure 1.11- A porphyritic olivine (PO) chondrule between crossed polarizers showing euhedral and subhedral olivine crystals with sharp edges.
Thin section of the Tennasilm L4 ordinary chondrite.**

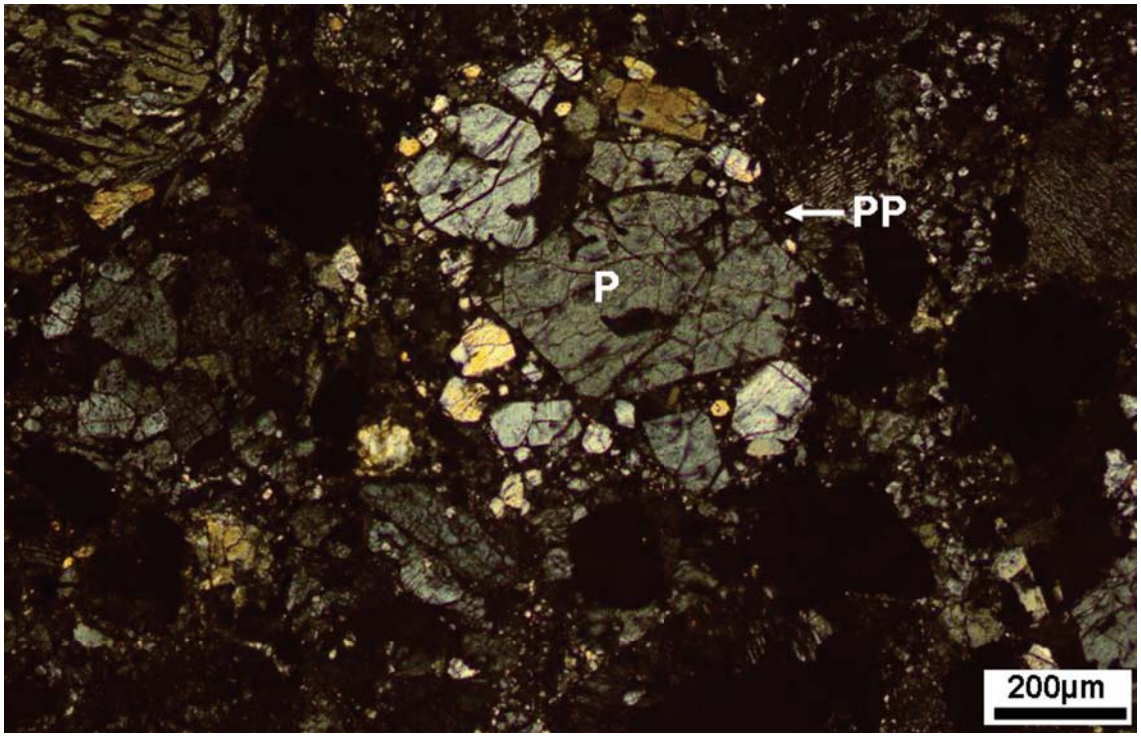

Figure 1.12- Porphyritic pyroxene (PP) chondrule between crossed polarisers showing a large (~250 µm) pyroxene crystal (P) surrounded by small and medium sized pyroxene crystals (~30 µm), with a poor cleavage.
Thin section of the Tennasilm L4 ordinary chondrite.

1.5.1.1.2 Non-porphyritic chondrules

Non porphyritic chondrules are spherical chondrules that crystallized from melts. They are also called droplet chondrules as they contain droplets of sulphide or/and metal (Norton, 2002). On the basis of FeO concentrations, non porphyritic chondrules can be subdivided into types I and II (Hutchison, 2004). Nonporphyritic chondrules are texturally divided into radial pyroxene (RP), barried olivine (BO), and cryptocrystalline (C) (Norton, 2002). Radial pyroxene chondrules (RP) (Figure 1.13) comprise 44% of nonporphyritic chondrules and show radial textures that consist of narrow fibers of low Ca-poor pyroxene or bronzite.

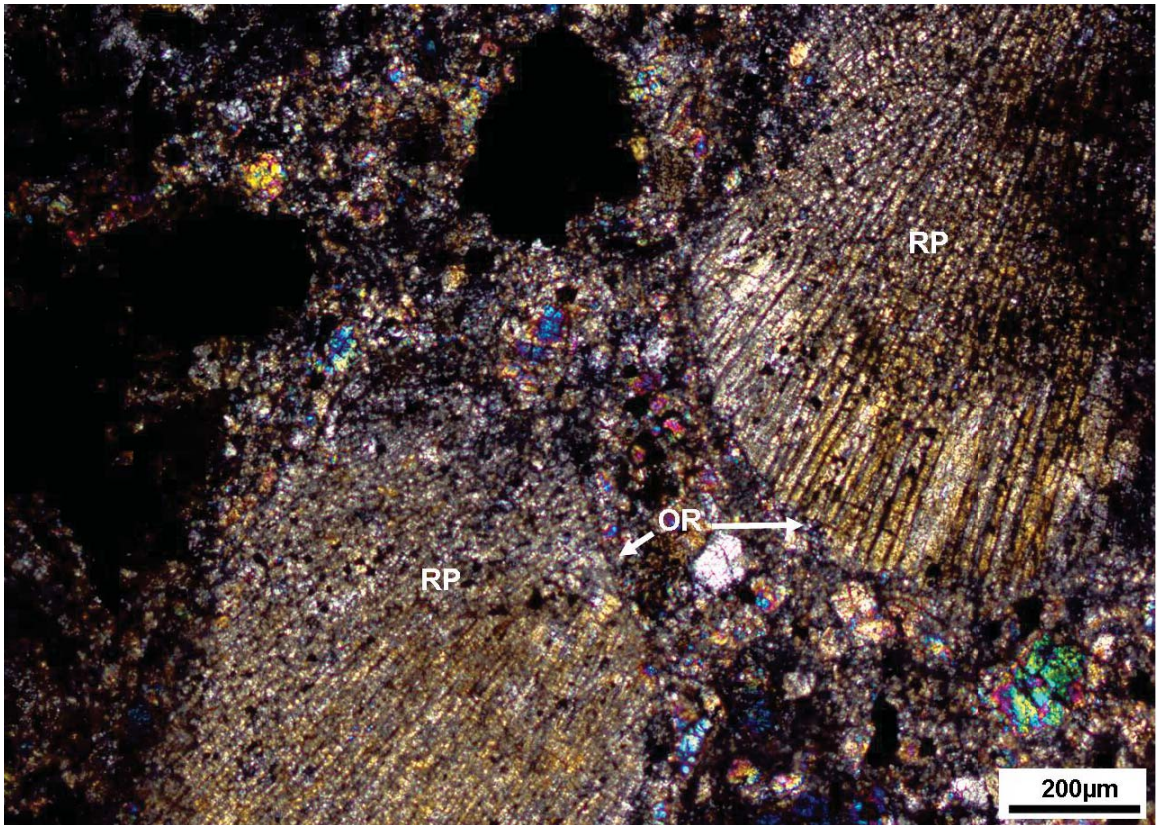

Figure 1.13- Radial pyroxene chondrules (RP) viewed between crossed polarisers, from the Crumlin L5 ordinary chondrite.
The texture of two large chondrules (~600 µm), their olivine rims (OR) and other constituents, have been degraded due to thermal metamorphism.

Cryptocrystalline (C) chondrules are microcrystalline in texture and are hard to recognise using the polarising microscope. They consist of orthopyroxene crystals. The barred olivine (BO) type represents 25% of non-porphyritic chondrules and exhibit layered textures of olivine that can readily be resolved with the polarising light microscope (Figure 1.14) (Norton, 2002). Glassy chondrules are also classified under the nonporphyritic chondrules. They are uncommon, and mainly composed of Na-rich feldspathic glass (Norton, 2002).

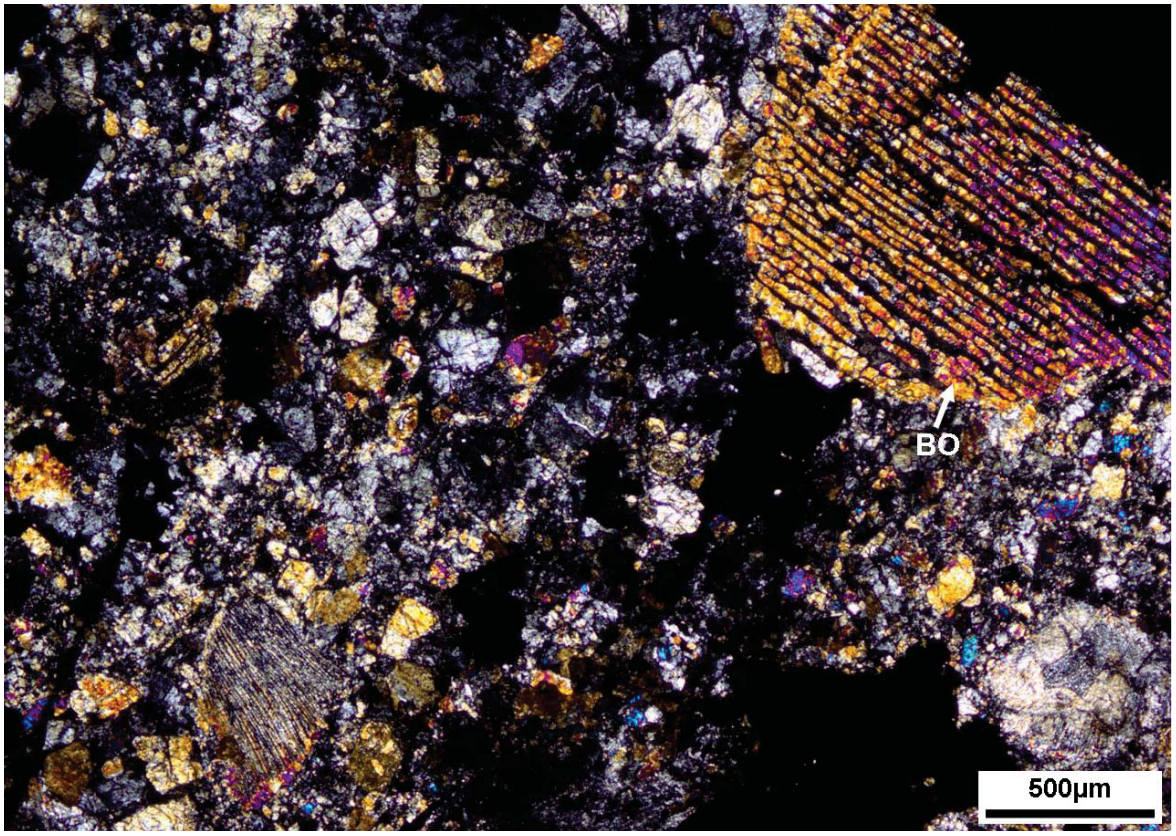

Figure 1.14- Barred olivine (BO) chondrule with parallel bars of olivine viewed between crossed polarisers.
Thin section of the Crumlin L5 ordinary chondrite.

1.5.1.2 Iron nickel metal and sulphide

Chondrites contain two types of metal, namely grains consisting of the refractory elements molybdenum (Mo), tungsten (W), rhenium (Ru), osmium (Os), iridium (Ir) and ruthenium (Ru), and grains that mainly consist of nickel, iron and cobalt (Campbell et al., 2005). The majority of the grains of metallic Fe-Ni and troilite (Fe-sulphides) in the groundmass of chondrites may have crystallised during the melting of chondrules (Scott and Krot, 2007).

CM chondrites contain Fe-Ni metal and sulphides. Most of the metals in CM chondrites are similar in texture and compositional range to those in CH and CR chondrites and Acfer 094 (unclassified carbonaceous chondrites). However, they show differences to the compositional distribution and texture of metals in un-equilibrated ordinary and CO chondrites (Kimura et al., 2011). Compositions of metal and sulphide textures were used to classify CM chondrites into three categories (A, B and C) that are linked to the degree of secondary heating. Category (A) contains Fe-Ni metal that is kamacite to martensite. Fe-Ni metal in category (B) contains lamellae or blebs of pentlandite; category (C) represents CM chondrites that contain aggregates of Ni-Co rich metal, kamacite and pyrrhotite

(Kimura et al., 2011). CM chondrites in category (C) were exposed to intense secondary heating, but CMs in category (B) were subjected to mild secondary heating and un-heated CM chondrites are classified in category (A) (Kimura et al., 2011).

1.5.1.3 Refractory inclusions

1.5.1.3.1 Calcium-aluminium rich inclusions (CAIs)

CAIs are complex objects and clasts in chondrites, ranging from sub-millimetre to centimetres in size. These are the oldest objects in the solar system, and contain unusual isotopic constituents that indicate a pre-solar dust component (Scott et al. 2007). Since the development of the ion microprobe in 1988, which allowed the microanalysis of oxygen isotopes in a petrographic thin section, a combination of isotopic analysis (oxygen and beryllium-boron) and theoretical modelling has indicated that the formation of CAIs was closely linked to the birth of the sun, and then they were scattered into the accretion regions of chondrites (MacPherson, 2007). CAIs contain minerals that can be classified as primary and secondary phases. The primary minerals formed during the early stages by processes such as solid-state recrystallization, direct condensation or melt solidification. The secondary phase refers to minerals formed by replacement of an earlier phase. CAIs are also commonly surrounded with thin layers of fine-grained materials (<1μm) of variable mineral composition (MacPherson, 2007).

1.5.1.3.2 Amoeboid olivine aggregates (AOAs)

Amoeboid olivine aggregates (AOAs) are refractory inclusions of nebular-gas-solid condensates and common in carbonaceous chondrites including CM, CR, CH, CV, CO and some ungrouped carbonaceous chondrites. They were originally observed in the CV chondrite Allende in 1976 by Grossman and Steele (Krot et al., 2004). AOAs are a possible link between chondrules and CAIs as they are chemically closer to magnesian chondrules than other refractory inclusions (Krot et al., 2004). They preserve distinctive information on condensation from the solar nebula gas, which includes its temperature, pressure, oxygen fugacity and isotopic composition (e.g. Krot et al., 2002; Krot et al., 2004). AOAs contain forsterite, Fe-Ni metal, and ~ 10% of amboeboid olivine aggregates comprise forsterite that has been replaced by low Ca-pyroxene. Amoeboid olivine aggregates in chondrites such as CR, CM, CO and CV contain secondary minerals that are similar to the mineral constituents of chondrules, matrix and CAIs (Krot et al., 2004).

The main types of refractory inclusions that are found in CM chondrites are AOAs (Krot et al., 2004). Detailed studies on AOAs in Murchison were carried out by MacPherson et al. (1988); study of CAIs in Cold Bokkeveld has also been reported by Greenwood et al. (1994). AOAs in CM chondrites are composed of forsterite and a refractory constituent comprising of spinel, Al-diopside and anorthite or secondary materials such as phyllosilicates and carbonate minerals (Krot et al., 2004).

1.5.1.3.3 Matrix Material

The matrix materials of chondrites have been previously interpreted as the secondary products of their parent bodies (Nagy et al., 1963), but now the matrix materials in the majority of chondrites are understood to be a mixture of complex phases of presolar materials and nebular condensation which were combined with silicate fragments (chondrule fragments) and eventually subjected to aqueous alteration and thermal metamorphism (Scott et al., 1988).

Matrices occur in all carbonaceous chondrites in proportions that range from 34 to 99 vol%. They rarely occur in ordinary chondrites and are absent from enstatite chondrites (Brearley and Jones, 1998). Matrix grains range in size from 10nm to 5μm and are opaque under the polarizing light microscope as these materials are mainly composed of the phyllosilicate minerals. Matrix grains include sulphides, Fe-Ni metal, oxides and silicates, in addition to phyllosilicates and carbonate minerals, which are particularly common within the matrix of type II chondrites (Scott and Krot, 2007). Carbonaceous chondrites (type I and II) underwent aqueous alteration to produce matrix material consisting of phyllosilicates and other complex phases (McSween JR., 1987). Many authors (e.g. Zolensky et al, 1993; Scott and Krot, 2007; Brearley and Jones, 1998) suggest that the matrices of the carbonaceous chondrites can be subdivided into matrix and fine-grained chondrule rims (<1μm) (Figure 1.15). Chondrule rims are absent in some chondrites such as CH, CB and CK (Scott and Krot, 2007), and are also absent from CI chondrites that lack chondrules (Zolensky et al., 1993). The fine-grained rims (<1μm) are likely to be formed from dust in the nebula (e.g., Morfill et al., 1998; Cuzzi, 2004) but some authors suggest that the rims formed in asteroidal regoliths (e.g., Tomeoka and Tanimura, 2000; Trigo-Rodriguez et al., 2006).

The mineralogy and composition of the matrix and fine grained (<1μm) chondrule rims in carbonaceous chondrites has been studied by Zolensky et al. (1993). They reported the fine

grained (<1μm) matrix to be made up of saponite, tochilinite, intergrowths of tochilinite with serpentine, olivine, pyroxene, pyrrhotite, pentlandite, Fe-Mg oxides, carbonate minerals, Ca-phosphates, Fe-Ni metal, and ferromagnesian and feldspathic material. They also showed that electron probe chemical analyses of the matrix and fine grained rims (<1μm) in all carbonaceous chondrites have some degree of heterogeneity within a sample.

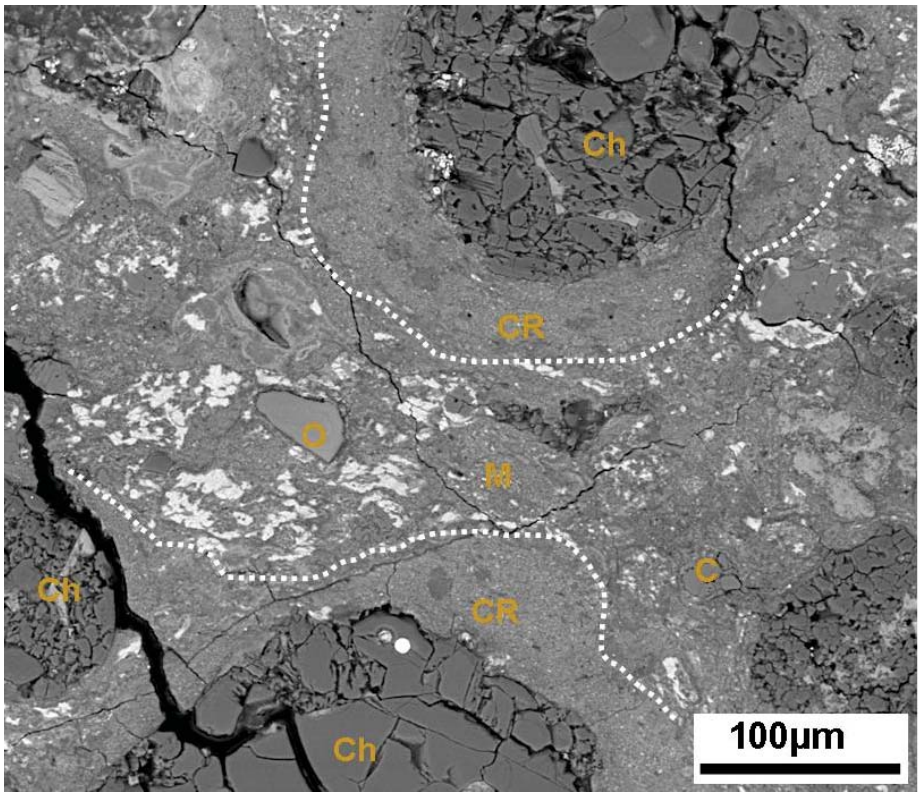

Figure 1.15- BSE image shows two different types of the matrices in Murray.
The matrices are fine grained (<1μm) chondrule rims (CR) surrounding chondrules (Ch) and matrix (M) that slightly coarser and contains other components like Fe-rich olivine fragments (O), Fe-Ni metal (bright areas), tochilinite and carbonate grains (C).

Phyllosilicates are the dominant constituents of the matrices of CM chondrites (Brearley, 1998; Scott and Krot, 2007; Zolensky et al., 1993). The mineralogy of the matrix and chondrule rims of CM chondrites were summarised by Zolensky et al. (1993), who found that the mineral compositions of fine grained (<1μm) rims and matrix are very similar in CM chondrites. They also concluded that matrix and chondrule rims consist mainly of serpentine and, occasionally, other phyllosilicates including saponite and clinochlore.

1.6 Previous work on carbonates in CM carbonaceous chondrites

Previous studies indicate that carbonate minerals have infilled pore spaces within phyllosilicates matrices, and can fill fractures to make veins (e.g. Barber, 1981). They

occur as isolated grains (Riciputi et al., 1993; Benedix et al., 2003) and as intergrowths within sulphides in the fine-grained matrix (<1μm).

Many researchers have discussed the carbonate minerals in terms of petrographic occurrence, mineralogy, and chemical and isotopic composition. The early petrographic observations were carried out by Fuchs et al. (1973), Kerridge and Bunch (1979), Bunch and Chang (1980), Barber (1981) and Armstrong et al. (1982). Later studies were performed by other authors (e.g. Grady et al., 1988; Johnson and Prinz, 1994; Kojima and Yanai, 1993; Riciputi et al., 1994; Browning et al., 1996; Brearley, 1998; Brearley et al., 1999; Brearley et al., 2001; Benedix et al., 2003; Rubin et al., 2007; Tyra et al., 2007; Lee and Ellen, 2008; De Leuw et al., 2006; 2009; 2010). All work to date on carbonate minerals in CM chondrites is summarized below:

Author, year, CM chondrites studied	Techniques used	The main results
Fuchs et al. (1973). Murchison	Optical examination and X-ray diffraction	Calcite grains of a relatively large size (20-50 μm) were found in the matrix.
Müller et al. (1979). Cochabamba	TEM	An aragonite grain was found in the matrix of the Cochabamba meteorite.
Bunch and Chang (1980). Murchison, Murray, and Nogoya	EPMA, SEM, TEM and X-ray diffraction.	Carbonates formed by aqueous alteration in the parent bodies. Calcite is present within the matrix and referred to as an alteration product. Calcite in chondrules of Murray and Nogoya formed by replacement. Electron probe and SEM analyses imply the calcite is free of any cations apart for calcium.
Barber (1981). Murchison, Cold Bokkeveld, Nawapali and Cochabamba	TEM, HRTEM, HVEM, SEM and X-ray analysis	Petrographic observations show intergrowths of carbonates with sulphides and phyllosilicates. Carbonates in Murchison and Cold Bokkeveld postdate the matrix. Calcite in Cold Bokkeveld formed prior to aragonite.
Clayton and Mayeda (1984) Murchison and other	Oxygen isotopic analyses were acquired from whole rock, carbonates,	Murchison contains about 1% of calcite that shows compositions of 35.14‰ for $\delta^{18}O$ and 16.67‰ for $\delta^{17}O$, and matrix with

carbonaceous chondrites.	spinel, matrix, and density-separated silicates.	$\delta^{18}O$ = 12.61‰ and $\delta^{17}O$ = 4.69‰. Consequently, the alteration occurred at ≥ 25°C.
Grady et al. (1988) Y 82042, ALHA 77306, ALHA 81002, ALHA 82100, ALHA 83100, Banten, Belgica 7904, Bells, Boriskino, Cold Bokkeveld, EET 83226, EET 83250, Erakort, Essebi, Kivesvaara, Mighei, Murchison, Murray, Nogoya, Pollen, Y 790003, Y 790032, Y 791198, Y 791824 and Y 793321.	CO_2 was liberated from carbonates in CM chondrites and other carbonaceous chondrites by exposure of powders of whole meteoritic samples to orthophosphoric acid (100%) for 18 hours at 25ºC.	Ratios of $^{13}C/^{12}C$ and $^{18}O/^{16}O$ for carbonaceous chondrites (CI, CM, and CR) and ordinary chondrites were measured. Carbonates in CM conhdrites have $\delta^{13}C$ ranges between +40 to +50‰, and $\delta^{18}O$ ranges between +18.6 to +45.5‰. The occurrences of carbonates with diverse isotopic signatures caused dissimilarity in isotopic composition of oxygen and carbon in CM2 chondrites.
Johnson and Prinz (1993) Bells, Boriskino, Cold Bokkeveld, Erakto, Essebi, Haripura, Mighei, Murchison, Nogoya, ALH83100-172, GRO85202-18, LEW87148-12 and MAC88100-14	EPMA was utilized to obtain chemical analyses of carbonate minerals.	In this study dolomite in CM chondrites was identified and analysed for the first time. They reported that Fe contents in dolomite are uniformly distributed in CM and CI chondrites, but dolomite Mn contents are heterogeneously distributed.
Kojima and Yanai (1993) Yamato-74662, Yamato-791198	EPMA was used to analyze the composition of carbonate minerals.	They divided carbonate minerals into two types. The chemical analyses of this study indicate that type I is pure calcite. Type II including ankerite, dolomite and impure calcite occurred in highly altered CM chondrites and calcium contents in these carbonates decline with increasing degree of alteration.

Riciputi et al. (1994) Boriskino, Murchison, Nogoya, ALH83100 and Orgueil (CI).	Ion microprobe analyses of calcites and dolomites in CM chondrites and dolomites in CI chondrites were acquired for elements including: Fe, Mg, Mn, Sr, Na, Ba and B.	Dolomite in CI and CM chondrites crystallized from brines that were similar in chemical composition. Calcite formed from saline solutions with low concentrations of Mg, Fe and Mn, but with increasing degree of alteration in parent bodies these fluids became more like dolomite fluids. During the final stages of aqueous alteration of carbonaceous chondrites veins were filled by calcite then dolomite and later with sulphates.
Brearley (1998) Murchison	SEM equipped with Oxford CL detector was used to obtain CL images of 20 grains of calcite.	Calcite in CM chondrites occurs in two different phases associated with PCP and surrounded by matrix. CL properties of calcite grains imply that they crystallized from fluids under complex conditions.
Brearley et al. (1999) Murchison	SEM was utilized to acquire BSE and CL images. Ion microprobe was used to determine oxygen isotope compositions of calcite crystals.	Two different occurrences of calcite were observed. The first was associated with PCP and the second occurred as isolated grain in the fine grained matrix (<1μm). Grains associated with PCP show four different kinds of CL properties. Grains that occur within the fine-grained matrix display diverse patterns of CL zoning. They concluded that only calcite is present in Murchison and $\delta^{18}O$ values of calcite lie in the range of 27.4 to 37.2‰
Brearley et al. (2001) Y791198	They used SEM to acquire BSE and CL images, EPMA for chemical analyses, and SIMS for ^{53}Mn-^{53}Cr dating.	Complex zoning of carbonates was observed. On the basis of CL characteristics Ca-carbonate was divided into several types: asymmetric zoning was observed in individual grains and seldom found in aggregate grains. Another zoning type occurred in two aggregate grains that display complex variations of low CL intensity. Low CL intensity areas of calcite grains contain about or less than 0.4% of MgO, MnO and FeO. Increasing CL

		intensity in rims of some grains are coincident with elevated MnO contents. SIMS results demonstrated large variations in Mn/Cr in each calcite grain. Data from Y791198 carbonates indicate that formation of secondary products is likely to have occurred in asteroidal environments.
Benedix et al. (2003) Murchison, Murray, Nogoya, Cold Bokkeveld and Mighei	Elemental X-ray maps were acquired using EPMA. BSE images were obtained by SEM. Splits from carbonates of each chondrite were analyzed for $\delta^{18}O$ and $\delta^{17}O$ and the results related to mineralogic alteration index (MAI).	Oxygen isotopic compositions of carbonates minerals were obtained. They discussed petrographic observations of carbonates and hypothesized fluid compositions during alteration of CM chondrites. Values of carbonate $\Delta^{17}O$ are linked MAI; $\Delta^{17}O$ becomes more negative with increasing of MAI. Fluid compositional evolution within the parent bodies of CM chondrites indicates that values of $\Delta^{17}O$ fell from higher to lower with increasing of degree of alteration. Calcite and dolomite from the same split and meteorite shows similar $\Delta^{17}O$ values and imply that dolomite and calcite in each formed from an isolated fluid reservoir.
Rubin et al. (2007) QUE97990, Murchison, Kivesvaara, Murray, Y791198, QUE99355, Nogoya, Cold Bokkeveld, QUE93005, LAP02277 and MET01070.	Microscopy with transmitted and reflected light, SEM and EPMA were used to determine the petrologic properties of 11 CM chondrites.	Using various petrologic properties, they proposed a numerical alteration sequence for CM chondrites and classified 11 CM chondrites into petrologic subtypes (± 0.1). They correlated the changes in carbonate mineralogy with the degree of alteration. Chemically simple carbonates were observed in less altered chondrites (CM2.6 to CM2.3). No complex carbonate was found in CM2.2 (Cold Bokkeveld) whereas nearly pure calcite is present in highly altered CM2.1 (QUE 93005). Mn contents in carbonates increase with the increasing degree of aqueous alteration. Ca-carbonates formed prior to more complex carbonates.

Tyra et al. (2007) Antarctic CM chondrites: EET96006, EET96016, EET96017 and EET96019	This study aimed to investigate how terrestrial weathering impacts C and O isotopes of carbonates in CM chondrites. SIMS was used to measure oxygen and carbon isotopes in carbonates. EPMA was also used for X-ray elemental mapping and chemical analyses.	Based on morphology, calcite was classified into two types, clean and mottled. Mottled grains range in size from 50 to 250 μm. The results showed that some carbonates formed from atmospheric CO_2 as a consequence of silicate weathering, and another type of carbonate either formed earlier or from non atmospheric sources.
Lee and Ellen (2008) Murray	SEM was used to acquire BSE, and CL images, EBSD maps and X-ray microanalyses (EDX). EPMA to obtain CL emission spectra and quantitative chemical analysis.	Petrography, microstructure and composition of aragonite grains in Murray were addressed. Aragonite formed during the last stage of aqueous alteration in its parent body. Aragonite grains formed in isolated clusters and within a weak compactional fabric of the matrix that may have controlled the orientation of aragonites. Results of this study indicate that aragonite formed after calcite in CM chondrites.
De Leuw et al. (2009) QUE 93005, ALH 83100	Secondary ion mass spectrometry (SIMS) was used to obtain isotopic measurements of Mn-Cr of carbonates in CM2 chondrites in order to resolve the alteration times and to correlate the degree of alteration with timing and duration of alteration.	It was concluded that aqueous alteration in parent body/ies of CM chondrites occurred during the earliest stages in development of the solar system and shortly after the formation of refractory inclusions. The results also show that carbonate crystallization age corresponds with degree of alteration of CM chondrites. In addition, the low values of $^{53}Mn/^{55}Mn$ are recorded from highly altered CM chondrites
De Leuw et al. (2010) Y-791198, LaPaz Icefield 04796, Cold Bokkeveld, Nogoya, Queen Alexandra	Elemental X-ray maps and EPMA were used to investigate the carbonate composition and to compare results with	Results of this study indicate the carbonates in CM chondrites are more complex than previously thought and show differences in composition to those in CI chondrites. Carbonates in CM chondrites crystallized

Range 93005, Allan Hills 83100, and Meteorite Hills 01070.	previous work of carbonates in CI chondrites.	in an asteroidal environment that progressively produced ions of Ca^{2+} and Mg^{2+}, and consequently a metastable phase of calcian dolomite was formed. Dolomites are absent in highly altered CM2.0 chondrites as a result of the instability of calcian dolomite with progressive aqueous alteration. Calcite in less altered CM chondrites contains higher $FeCO_3$ concentrations than in highly altered samples.
Fujiya et al. (2010) Murchison CM (2.5) and ALH 83100 CM (2.1).	SEM was used to obtain BSE and CL images, and SIMS for ^{53}Mn-^{53}Cr dating.	Results show that Murchison contains zoned calcite grains from its CL features and ion images obtained by NanoSIMS. It was reported that Mn concentrations in the bright areas of CL images reach up to ~0.68 wt%. In contrast the lower CL intensity cores contain less Mn and are insufficient for Mn-Cr dating. It was concluded that carbonate formed within about 4-5 Myr of CAIs, and the age difference between calcite in the least (CM2.1) and most highly (CM2.5) altered CM chondrites is about 2 Ma.
Sofe et al. (2010b) Pollen	SEM was used to obtain BSE and CL images.	It was reported that Pollen contains 2.02 vol% aragonite and calcite, present as individual and aggregate grains. They also identified three generations of calcite in Pollen including: (i) zoned calcite grains that are rimmed with serpentine-tochilinite and contain inclusions of Fe-sulphides, (ii) calcite replaced forsteritic olivine and pyroxene, (iii) calcite free of rims and inclusions.
Sofe et al. (2010a) LON 94101	Polarizing light microscopy and SEM were used for imaging.	New observations about the presence of a large (~1.2 mm) twinned calcite vein in LON 94101.

Sofe et al. (2011a) Murchison, Murray, Pollen, Mighei and Nogoya.	SEM was used to obtain BSE and CL images. EPMA was used for chemical analyses and CL spectroscopy. Laser Raman spectroscopy was use for mineral identification.	They related CL characteristics of Ca-carbonates to the alteration degree of the sample studied and to their petrographic features. The least altered meteorites (Murchison, Murray, Pollen and Mighei) contain 1.3 to 2.0 vol%. of Ca-carbonate (aragonite and calcite) that have a variety of CL characteristics, whereas Ca-carbonate grains in Nogoya, the more highly aqueously altered CM2, show no CL variation and a low emission intensity.
Lee et al. (2011) QUE 93005, LON 94101, Mighei, Murchison, Murray, Nogoya.	X-ray mapping and quantitative chemical analyses. Laser Raman spectroscopy for mineral identifications. Quanta SEM for CL imaging.	It was concluded that CM2.5 to CM2.2 chondrites contains aragonite and calcite, and the calcite most likely to have formed first. QUE 93005 contains four phases of carbonate minerals including: breunnerite, calcite, dolomite, breunnerite, and calcian breunnerite a composition between dolomite and breunnerite.
Sofe et al. (2011b) Pollen, Murray, Mighei, LON 94101, Nogoya, QUE 93005, CM1 SCO 06043	SEM imaging, X-ray microanalysis, and Raman spectroscopy were used for the study.	Results show that aragonite and calcite are present in less and moderately alerted CM chondrites (CM2.5-CM2.3), but aragonite is absent in highly altered chondrites (CM2.1-CM2.0). Calcite and dolomite are present in highly altered CM chondrites. Nogoya (CM2.2) contains aragonite, calcite and dolomite. This suggested that crystallization of aragonite rather than calcite is favoured in solutions with Mg/Ca >~1, and that significantly higher Mg/Ca ratio will yield dolomite.
Lindgren et al. (2011a) LON 94101	EBSD and quantitative elemental ED X-ray analyses.	Results suggest that two generations of calcite have formed during aqueous alteration. Crystallographic orientations of calcite indicate at least three phases of calcite deformation have taken place in the parent body of LON 94101. These results also show that the calcite vein in LON

		94101 has been affected by at least two deformation events.
Tyra et al. (2012) EET 96006, EET 96016, EET 96017, and EET 96019.	FEG SEM was used for BSE imaging and X-ray mapping. SIMS was used to determine the oxygen isotope compositions of calcite.	They identified two types of calcite that vary isotopically and morphologically. One type is small matrix calcite grains with a mean $\delta^{18}O$ of 33.7 ± 2.3‰, whereas the second type (calcite aggregates) has a mean $\delta^{18}O$ of 19.4 ± 1.5‰.
Lindgren et al. (2012) MET 01070, SCO 06043.	SEM was used for BSE imaging and X-ray point analyses and mapping. EPMA was used for chemical analyses.	They concluded that MET 01070 and SCO 06043 (both CM2.0) exhibit evidence for multiple pulses of fluids in the parent body/ies of these meteorites. This was inferred by observations about dolomite veins, formation of sulphide lens, and dissolution and re-crystallization of calcite in the sample studied.
Lee et al. (2012) QUE 93005	NanoSIMS 50L was used to determine the formation age of carbonates.	The crystallization of dolomite was at 3.93±0.23 Ma after the formation of the oldest solids in the solar system at 4568 Ma (i.e. ~ 4564 Ma).
Fujiya et al. (2012) Murchison, Y791198, ALH 83100, Sayama.	NanoSIMS 50 was used to determine the age of carbonates.	The age of carbonate is 4,563.4+0.4/-0.5 Ma, about 4.8 Ma after the formation of CAI.

The most important previous studies on carbonate minerals in carbonaceous chondrites are defined as follows: **Riciputi et al. (1994)** who reported that dolomite in CI and CM chondrites crystallized from brines that were similar in chemical composition, and that calcite formed from saline solutions with low concentrations of Mg, Fe and Mn. However, with an increasing degree of alteration in parent bodies, these fluids became saturated in dolomite. **Lee and Ellen (2008)** who concluded that aragonite in Murray (CM chondrite) formed during the last stage of aqueous alteration in its parent body. **De Leuw et al. (2010)** who reported that calcite in less altered CM chondrites contains higher $FeCO_3$ concentrations than in highly altered samples. **Lee et al. (2012)** who reported that

breunnerite is present in QUE 93005 (CM chondrite). **Tyra et al. (2012)** who identified two types of calcite in CM chondrites that vary isotopically and morphologically.

1.7 Aims of this study

This research has a special focus on the carbonate minerals in CM carbonaceous chondrites. An important motivation for studying carbonates is to understand the action of water and its chemical composition during and after the alteration of primitive materials (e.g. olivine and pyroxene). Carbonate minerals in CM carbonaceous chondrites can be used as powerful tools to provide new insights into the mechanism of the aqueous alteration of the CMs, and a better understanding of the timing and location of the alteration of primitive materials (see Brearley et al., 1999). These carbonates are relatively large (5-50 μm), and so more readily analysed by micro-electron beam tecniques than the phyllosilicate matrix (Johnson and Prinz, 1993).

This work aims to construct a consistent model of how carbonate crystals in CM chondrites formed under diverse and complex conditions, and seeks in particular to resolve the debate on the formation location (see section 1.2.4) of carbonate minerals in CM chondrites (e.g. Kerridge and Bunch, 1979; Brearley et al., 1999; Hua et al., 1999; Brearley et al., 2001; Gounelle and Zolensky, 2001; Tyra et al., 2007; Lee and Ellen, 2008). The results of this work, in combination with the published literature, will be used to understand how carbonates were distributed and later modified in the parent body/ies of CM chondrites. This model will also be related to the degree of alteration of the CM chondrites in order to provide a better understanding of their parent body/ies.

This work will be carried out using state of the art microscopy techniques to characterise the petrography, chemical composition and microstructure of these minerals, and to assess the petrographic relationships of the carbonates to phyllosilicate matrices. The petrography, microstructure and formation of carbonate minerals in the CM carbonaceous can be utilised to evaluate temperature and chemistry of solutions, and the structure of the meteorite matrix during crystal growth (Lee and Ellen, 2008). Information about variable conditions such as temperature, pressure and fluctuation of water volume that led to further modifications of the carbonate crystals play an important role in understanding the significant evolution of the parent bodies of CM chondrites.

Specifically, the precise origins and formational conditions of carbonate minerals in the CMs chondrites remain poorly understood and need to be addressed. The timing of

precipitation of carbonate minerals relative to each other and to the matrix is still poorly-understood. An additional question is whether the Ca-carbonate and other carbonates formed all at once, or over several generations. There are also several topics that need to be examined in order to achieve the main goal of this research (i.e. to construct a model of carbonates formation in parent body/ies of CM chondrites), which are:

- Only three carbonate minerals (aragonite, calcite and dolomite) have been found by previous work, but this study seeks to explore if there are any other phases of carbonates in CM chondrites (i.e. breunnerite and siderite) as have been observed in CI chondrites (e.g. Endress and Bischoff, 1996). The main aim of identifying other carbonate minerals such as breunnerite and siderite is to clarify any evolutionary links between CM and CI chondrites.
- Aragonite has received less attention than calcite as it is rarely reported in CM chondrites, but tracing aragonite in CM chondrites can help to provide new insights into the scale connectivity of the aqueous alteration, given its much greater solubility than calcite.
- No previous work has been done in detail on post crystallization deformation (e.g. dissolution, replacement, recrystallization, shock events) of carbonate minerals in CM chondrites. Therefore a detailed study of these features can also help to discover the environmental conditions of the parent body during the late stages of aqueous alteration.

1.8 Thesis Structure

In addition to the introduction, this thesis contains a methodology chapter, four data chapters and a final discussion and conclusions chapter.

Chapter two outlines the theoretical background and discusses the working conditions, standardisation and calibration of each technique involved in this study. A full description of carbonates and their associated minerals in CM chondrites was obtained using a FEI Quanta 200F field-mission SEM to acquire backscattered electron (BSE) images (revealing petrographic features and post crystallization deformation), cathodoluminsecence (CL) images (to identify trace element zoning), X-ray chemical analysis and maps (for identification of minerals and determination of their chemical variations), Raman Spectroscopy (to distinguish aragonite from calcite), electron probe microanalysis (EPMA) (for quantitative chemical analysis), electron backscatter diffraction (EBSD) maps (for mineral identification, determination of their crystallographic orientations and

identifications of twins and subcrystals), and CL spectroscopy (for identification of CL activators including Mn^{2+}). Destructive techniques such as transmission electron microscopy (TEM) and secondary ion mass spectrometry (NanoSIMS) were used in the final phase of this study. Carbonate grains and associated minerals were studied at higher resolution by imaging, electron diffraction and chemical analysis using a FEI Tecnai T20 TEM, to provide a better understanding of the sequence of events in the early stages of the solar system. NanoSIMS 50L was used to determine oxygen isotopic compositions from different generations of Ca-carbonates that can also provide clues to the genesis and origin of the fluids from which they crystallized.

Chapter three provides a background and detailed petrographic description of the CM chondrites used in this study. CM chondrites have been altered to different degrees and show a range of internal structures, and so they have been subdivided into subtypes using these variations (i.e. Rubin et al.'s classification (2007)). Samples used in this study that were unclassified have been also assigned into subtypes using their petrographic features including the abundance of Fe-Ni metal, and the proportion of alteration products within chondrules and chondrule fragments. Chapter three also explores the changing chemical composition of the phyllosilicate matrix and shows how this chemical composition is different from meteorite to meteorite. It also outlines the relationship between the abundance of secondary products (formed by aqueous alteration) in CM chondrites studied and their aqueous alteration degree.

The work then concentrates on carbonates and associated minerals in CM chondrites. Chapters four, five and six provide a coherent picture of how these minerals vary from meteorite to meteorite as a result of changing aqueous alteration conditions and environments

Chapter four discusses the carbonate minerals that are found in less and moderately CM chondrites. It provides the first report of aragonite in CM2 chondrites since the EBSD work of aragonite in Murray by Lee and Ellen (2008). Results from aragonite and calcite are used in chapter four to provide important new insights into the sequence of events during the evolution of the parent body. It discusses the first oxygen isotopic analyses of aragonite in carbonaceous chondrites and how these analyses were used with those of calcite grains to discover the time formation of aragonite relative to the calcite and the chemical history of fluids from which these minerals precipitated. Petrographic observations and EBSD maps of the aragonite-calcite intergrowth were also used in chapter four to infer the relative timing of these minerals. Quantitative chemical analyses

and SEM-CL imaging of aragonite and calcite were used as a chemical fingerprint to track the alteration degree of CM chondrites studied. Chapter four provides evidence for the location of formation of a large (~1.2 mm) calcite vein observed in the LON 94101 CM2 chondrite, and that has been used as guidance for water flow in a stage of aqueous alteration.

Chapter five discusses carbonate minerals that are present in highly altered CM2 chondrites. It provides new observations of the presence of aggregates of complex carbonates in CM chondrites. Previous work (e.g. Zolensky et al., 1997; Rubin et al., 2007; De Leuw et al., 2010) suggested that the less altered CM2 chondrites contains Ca-carbonate, whereas complex carbonates are present in highly aqueously altered CM2 chondrites. However, the identification and origin of these minerals remain unknown. Description of complex carbonates (Mg and Fe-rich carbonates) in highly altered CM2 chondrites can also be used to investigate how the mineralogy and composition of meteoritic carbonates gradually developed during aqueous alteration. Study of carbonate minerals in these chondrites also helps to investigate how aragonite disappeared with increasing aqueous alteration, and how the precipitation of dolomite commenced in the middle stage of alteration and increased with progressive aqueous alteration.

Chapter six describes carbonates that are present in the most altered in CM chondrites. It describes the relationship between calcite and dolomite in the final stage of aqueous alteration in the parent body/ies of CM chondrites. Chapter six also provides a snapshot of the final phase of aqueous alteration processes by which carbonates have been transformed into phyllosilicates and recrystallized as carbonate veins.

Chapter seven and chapter eight (discussion and conclusion) bring together the results of this study in an improved model and greater understanding of carbonate formation within the parent body/ies of CM chondrites.

2

Methods and Techniques

2.1 Introduction

A suite of analytical instruments were utilized to build up a coherent picture of how carbonate minerals formed within the parent bodies of CM chondrites. Surrounding materials such as Fe,Mg silicates and matrices were also investigated to define their relationships with the carbonate minerals. These techniques include: polarising light microscopy, scanning electron microscopy (SEM), SEM cathodoluminescence (SEM-CL), laser Raman spectroscopy and transmission electron microscopy (TEM) (all at the University of Glasgow); electron probe microanalysis (EPMA) (at the University of Edinburgh and Strathclyde University). This chapter describes applications, theory of operation and the outcomes of each of these techniques. It also introduces sample preparation, and the working conditions, standardization and calibration of each technique.

2.2 Light Microscopy

Traditional petrographic techniques such as polarizing light microscopy do not have sufficient resolution to study the fine-grained (<1μm) matrix of CMs carbonaceous chondrites, which are also opaque in transmitted light (Benedix et al., 2003). Nevertheless, prior to carbon coating all thin sections were studied in transmitted and reflected light using an Olympus BX41 petrological microscope equipped with objectives ranging from x5 to x40. This microscope also allows digital images to be obtained using an Olympus DP25 digital camera operated through cell^B software. For polarising light microscopy a polariser is positioned in the light microscope between a sample and light source and an

analyzer is placed between the sample and eyepieces. In contrast to transmitted light, incident light can also be strongly reflected by the surface of some materials - such as sulphides and metal - and can be collected by the objectives by specular reflection.

Reflected light was used to characterise the abundance and distribution of Fe-Ni metal and sulphides within the samples (see Figure 2.1). The light microscope in transmitted light was also used to illustrate the presence of coarse grains of high temperature phases (Fe,Mg silicates), and to correlate their abundance with the those of low temperature phases (e.g. phyllosilicates) that are very finely crystalline, and so opaque in transmitted light. The light microscope was also a useful tool to observe the occurrence of coarse veins of carbonate minerals within the phyllosilicate matrix (see Figure 2.2).

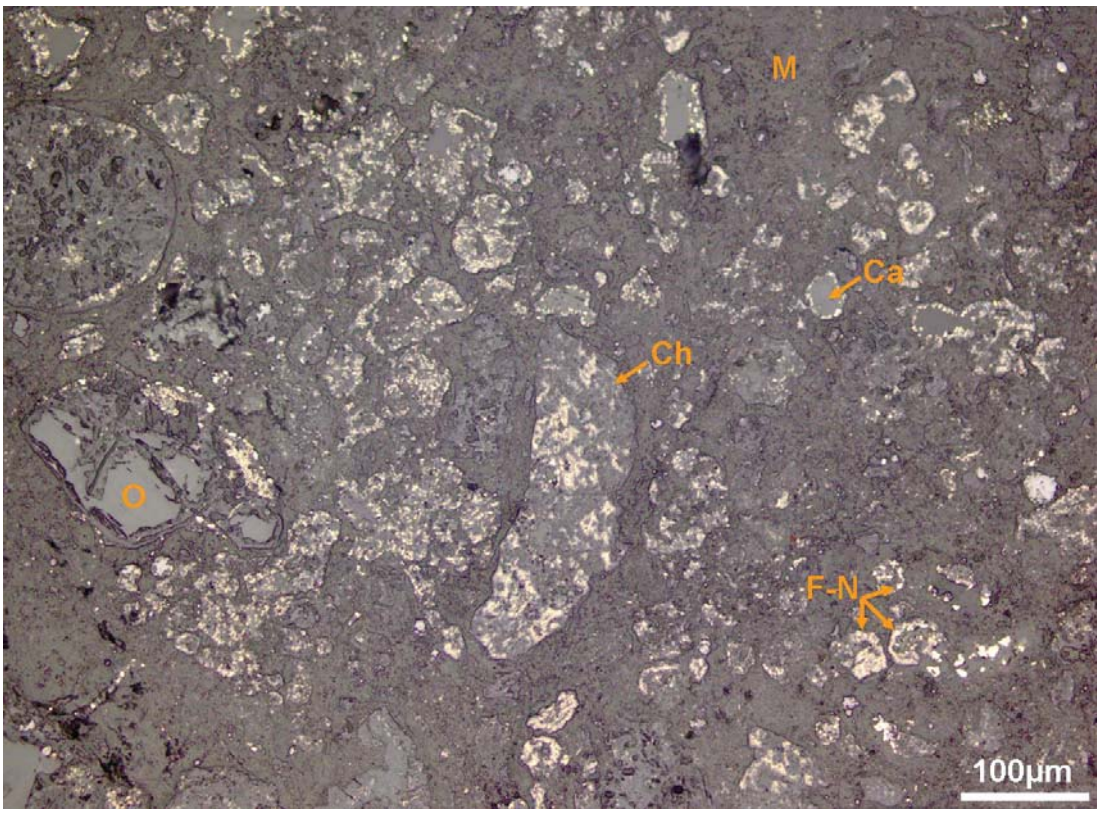

Figure 2.1- Photomicrograph of a thin section in reflected light (QUE 93005, CM2).
It shows the occurrence of Fe-Ni metal (F-N) (bright grains) around carbonate grains (Ca) and within chondrules (Ch). O is olivine and M is phyllosilicates within matrix and chondrule rims.

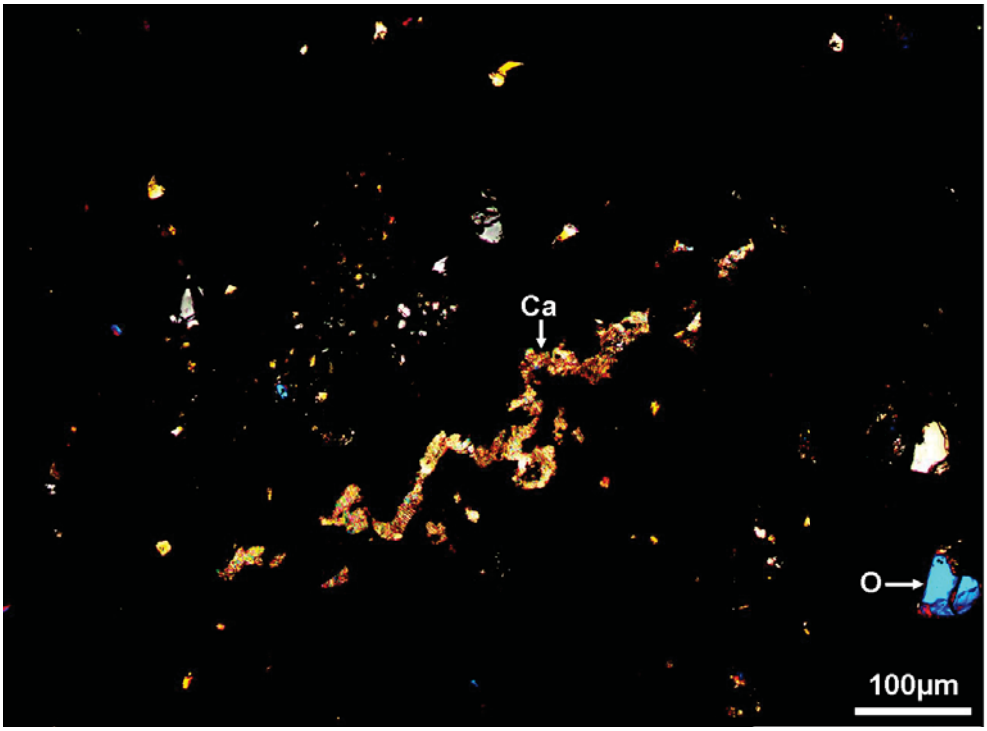

Figure 2.2- Photomicrograph of thin section under transmitted light and between crossed polarisers (LON94101, CM2).
This image displays a vein of calcite (Ca) within phyllosilicate matrix (dark areas). O is Mg-rich olivine.

2.3 Scanning electron microscope

Due to limitations of the polarizing light microscope when studying carbonaceous chondrites, the scanning electron microscope (SEM) was the instrument of choice for detailed petrographic study. This instrument magnifies objects up to x300,000. High resolution images down to a few tens of nanometres can be acquired. It was also used to describe the surface topography of a sample, to examine crystal structure, microfabric and chemical composition of minerals, and to characterise textures and microstructures of crystals.

Detailed petrographic study, chemical analysis and crystallographic orientation analysis were carried out using a FEI Quanta 200F field-emission environmental SEM and a Zeiss Sigma field emission SEM. This work was undertaken in high vacuum mode (0.00373 Pa) and low vacuum mode (~69.327 Pa). High vacuum work required the samples to be coated with thin (5-15nm) layer of carbon. Work in low vacuum mode was carried out without carbon coat to obtain backscattered electron (BSE) images of the most altered CM chondrites in which the phyllosilicate minerals are dominant. Removal of the carbon coat from a sample requires polishing over methanol and/or polishing over 0.3µm colloidal

silica for at least 5 minutes. This may pluck out friable materials such as phyllosilicates from the sample; hence the highly altered CM chondrites were coated with carbon for later stages of laboratory work, such as electron probe microanalysis and Focused Ion Beam (FIB) milling. The main drawback with low vacuum work is charging that accumulates on the sample surface (i.e. increase contrast over some areas of the sample). Charge on a sample surface is related to interaction between the sample and water vapour in the specimen chamber, when there is an electric field below and above the sample (Thiel et al., 2004). Each thin section was placed in the SEM chamber in a specific orientation that was used in all stages of SEM work (imaging, mapping, SEM point counting etc.).

2.3.1 How does the SEM work?

2.3.1.1 Electron gun

The SEM emits a stream of electrons from its gun. The electrons are accelerated by an electric potential of 2-30 kV. The point source of electron beam is a tiny area of the filament (cathode=negative electrode) (Figure 2.3) that uses a sharpened tungsten tip. Electrons are emitted from the tip when it is heated to temperatures of 2000 to 2700K. The second part of the electron gun is the grid cap (Whenelt cap) in which the electron emissions spread out and are attracted towards a small diameter aperture in the anode plate (positive electrode) that is the third part of electron gun. The beam is focused within the anode aperture and allowed to move down the column into lenses.

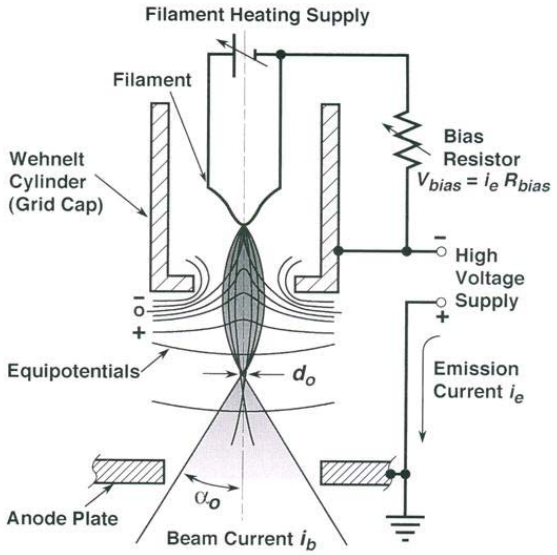

Figure 2.3- Schematic diagram showing three parts of the electron gun.
Electrons are accelerated using a voltage, d_0 is crossover diameter and α_0 is divergence angle between anode and grid cap. From Goldstein et al. (2003).

2.3.1.2 Electron lenses

In the SEM an electromagnetic field is created within three magnetic lenses between the electron gun and a sample surface. Magnetic electron lenses are used to focus the electron beam emitted from the electron gun (e.g. ~50μm) to a small spot size on the sample surface (e.g. ~10nm). These lenses consist of a coil of copper wire within a case of iron to generate a magnetic field within the lens hole. The first lenses in the SEM are the condenser lenses (the number varies from one to three); the first condenser lens is designed to control the focusing of the electron beam. In microscopes with two condenser lenses, both lenses contain apertures that help to reduce the spot size. The final lens is the objective lens, which is stronger than the first two condenser lenses and controls the final demagnification of the electron beam. The most common type of objective lens is the pinhole lens, where the sample is located outside the lens and further from the magnetic field. The pinhole lens has an aperture with a very small diameter to retain the magnetic field inside the lens.

2.3.2 Electron beam-sample interaction

Collision of an electron beam with a solid surface causes interactions between these accelerated electrons and atoms in the solid materials. It produces secondary electrons, backscattered electrons, X-rays and visible light (i.e.CL) (Figure 2.4). Some accelerated electrons can pass through the sample without interaction with atoms and/or are diffracted inside the sample (this is used in Electron Backscatter Diffraction (EBSD)). Interaction between the electron beam and positively charged atoms causes deflection of the electron beam without loss, or with low loss, of kinetic energy (i.e. elastic scattering) and eventually leaves the sample as backscattered electrons. In inelastic scattering the electron beam intercepts the electrons in shells around atoms, causing loss of their high kinetic energy, and they are directed back out of the sample as secondary electrons. In this respect Auger electrons are also involved. They are ejected by transformation of energy of the incident electrons to an electron in the core shell structure of an atom. Then an electron is emitted from the core level of the atom, and an electron in the outer level of this atom falls to the vacant core level. This causes transfer of energy to another electron that is ejected as an Auger electron.

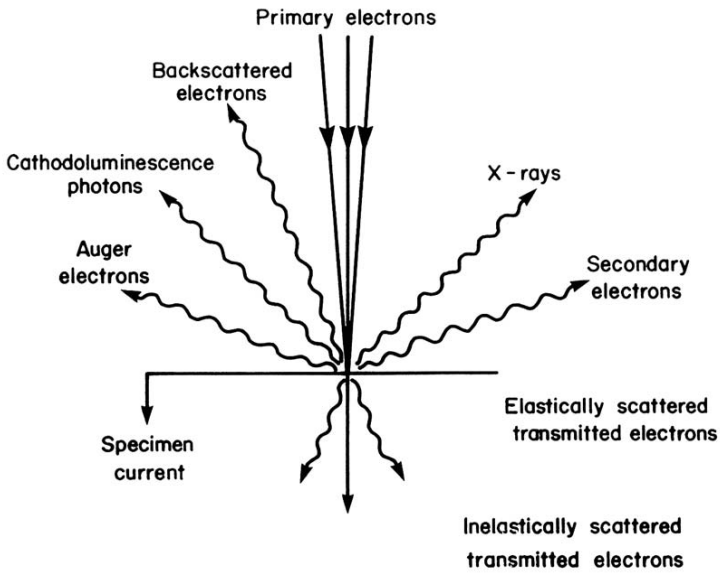

Figure 2.4- Schematic diagram showing electron beam interactions with the surface of a specimen and the different signals that are produced.
From Krinsley et al. (1998).

2.3.3 Backscattered Electron Imaging

Backscattered electron (BSE) images were obtained using the Quanta SEM with a solid-state backscattered electron detector. At least 1000 high resolution BSE images were obtained from each polished thin section, and were used to characterise textures and microstructures of matrices and individual crystals.

BSE imaging is particularly useful for polished samples. It can be employed to image features and microstructures of crystals at scales down to a few tens of nanometres. The resolution of BSE imaging is controlled by conditions including: (i) working distance between the backscatter detector and sample surface, (ii) beam current; and (iii) accelerating voltage (Figure 2.5). BSE imaging is strongly dependent on the mean atomic number of the sample; the most efficient emission of backscattered electrons is from minerals with the highest mean atomic number. Materials with a higher mean atomic number scatter most of the incident electrons close to the surface of the sample (>90º). This can be related to the low depth penetration of the electron beam in high atomic number materials, whereas it penetrates more deeply in low atomic number materials (Figure 2.5) (Krinsley et al., 1998).

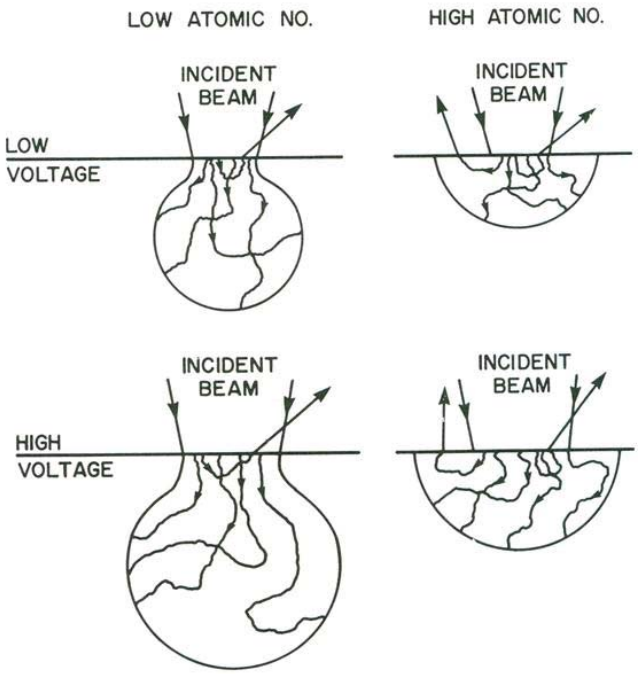

Figure 2.5- Diagram showing the relationships between the penetration dimensions of incident beam within solid surface and accelerating voltage and atomic number of the examined materials. From Krinsley et al. (1998).

2.3.4 Secondary electron images

Secondary electron (SE) imaging is typically used to characterise specimen topography. SE provides high resolution images of rough surfaces because an area with slopes increases SE emission. SE imaging of polished thin sections was carried out using the Quanta SEM in conjunction with SEM cathodoluminescence (SEM-CL) or electron backscatter diffraction (EBSD) to localise target areas for CL imaging or EBSD mapping. The SE detector was used to locate grains in these cases, because the BSE detector is not capable of operating together with the CL detector or EBSD camera inserted in the Quanta SEM. SE emission differs from BSE by its very low energy (less than 50 eV, Krinsley et al., 1998). Secondary electrons are emitted from areas close to the sample surface, whereas backscatter electrons are ejected from greater depth (Figure 2.6).

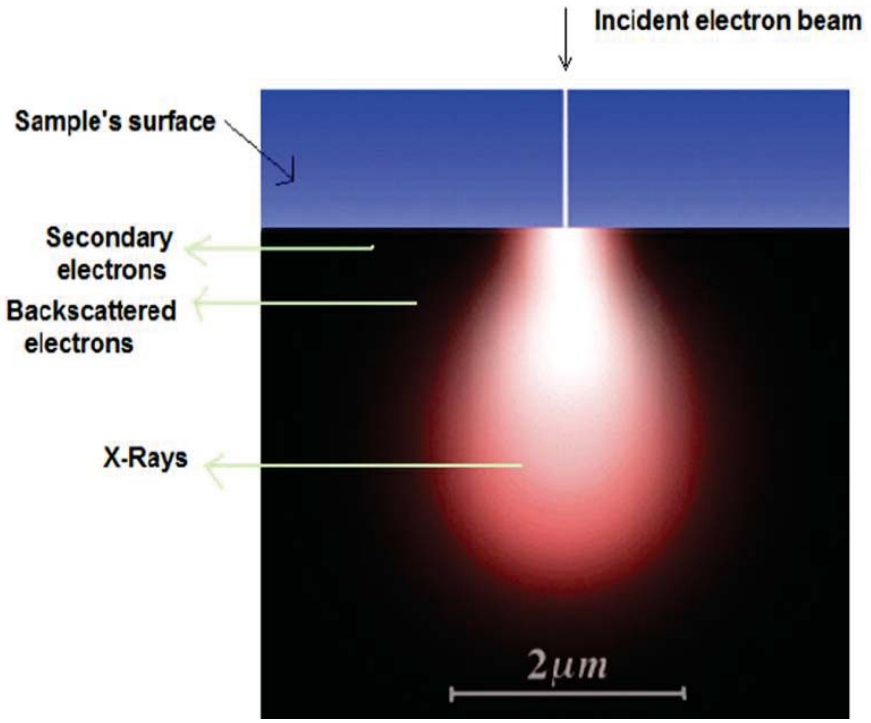

Figure 2.6- Schematic diagram showing interaction of incident beam with surface and interior of a specimen.
Note the variation in volumes of electron emission beneath sample surface with different electron types. From: www.mansic.eu/documents/PAM1/Giannakopoulos1.pdf.

2.3.5 Energy Dispersive X-ray Spectroscopy

It was important to initially identify minerals prior to further and more detailed chemical analyses. This was done by Energy Dispersive X-Ray Spectroscopy (EDS). EDS is an extremely useful technique that operates in conjunction with the electron detectors to obtain quantitative and qualitative chemical analyses of a sample or particular area within it.

2.3.5.1 Qualitative spot analysis and elemental mapping

Spot analysis and elemental mapping was undertaken using an Oxford Instruments EDS system attached to the Sigma SEM, and running INCA software. The Quanta 200F FEG-SEM was also used, and is equipped with an EDAX Pegasus 2000 X-Ray detector system and EDAX Genesis hardware and software.

Qualitative analysis provides a very quick determination of elements that are present in specimens in the form of X-ray spectra or X-ray elemental maps**.** X-rays are generated when an electron beam interacts with the sample (Figure 2.4). As previously mentioned with respect to Auger electrons, interaction between incident electrons and atomic nuclei causes them to emit an electron from their inner shell, then an electron in the outer shell

drops down to fill the 'hole' left by the emitted electron (Figure 2.7). This process causes a change of energetic states from high to low, the amount of which reflects the difference in energy levels. The energy difference in electron levels is emitted in the form of X-rays whose energy/wavelength characterises a specific element, so can be used to obtain local chemical information. When an electron is emitted from the inner atomic level (K), the X-ray emission is assigned as K_α radiation and represented by emission line energies or wavelengths of that specific element. Outer atomic shells yield L_α and M_α radiation. Analyses are acquired by accumulation of X-ray measurements over a time period, and eventually a spectrum is created (Figure 2.8).

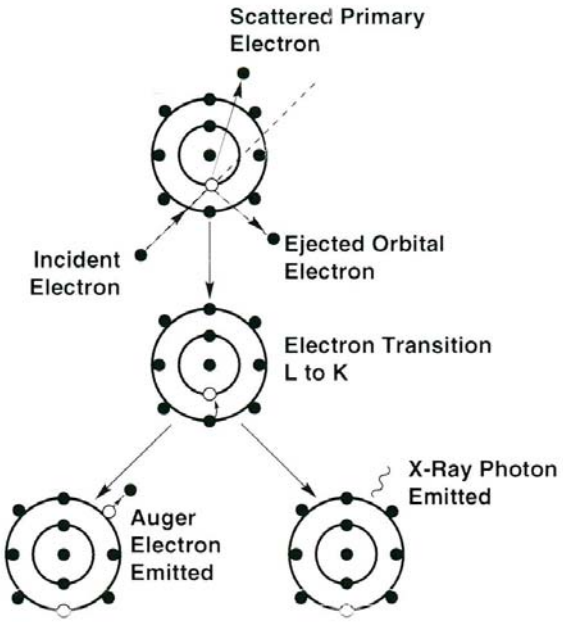

Figure 2.7- Schematic diagram showing X-ray and Auger electron emission.
They formed by removal of an electron from the inner K level and a X-ray photon or Auger electron is emitted. From Goldstein et al. (2003).

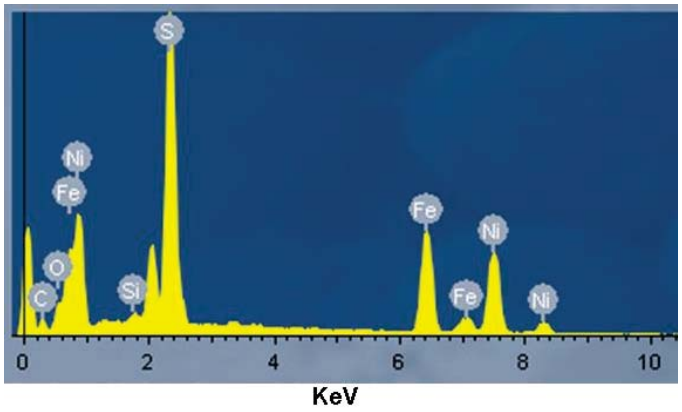

Figure 2.8- Typical EDS X-ray spectrum displaying peaks of six elements.
These peaks are automatically identified by the INCA software and are labelled with element symbols. The vertical scale is number of counts. KeV is element type energy.

EDX also enables elemental mapping for the whole sample or a small area (Figure 2.9a). Elemental mapping is an especially useful tool to locate specific mineral grains for further analysis (Figure 2.10). For this purpose, concentrations of elements over a particular area are counted and output as gray scale images by software that controls the ED spectrometer. It is possible to replace gray levels with primary colours. Images for individual elements can be assigned into primary colours, then three elements can be overlaid in one element map with three primary colours (blue, green and red). The intensity of each colour in these maps reflects the concentration of a particular element present in the mapped area. Mixed colours produce combined colour and so represent the presence of different elements. Assuming that an area of the element map is a mixture of red and green then the colour appears in yellow, cyan colour means green and blue are mixed, and magenta is produced when red and blue are present in the same area (Figure 2.9a) (Goldstein et al., 2003). X-ray counts along a line between two points of an element map can be presented to illustrate the variation of element concentration (Figure 2.9b). X-ray maps can be also combined with an electron montage to identify the distribution and concentration of a particular element in the examined sample. This was useful to locate Ca-carbonate, that usually occurs as isolated grains of a very small size within the fine grained (<1µm) matrix of CM chondrites (Figure 2.10).

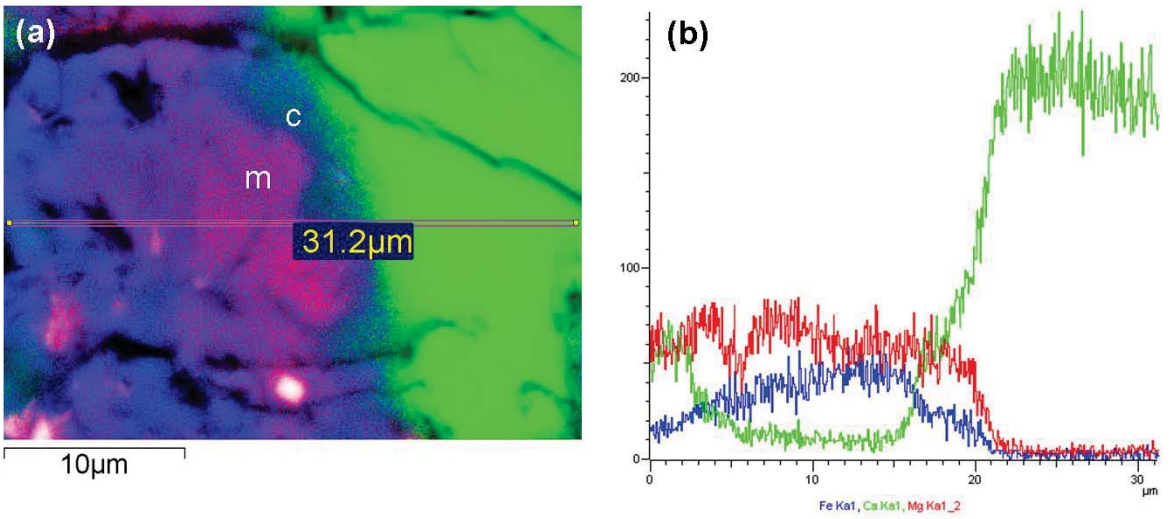

Figure 2.9- X-ray map of carbonate minerals in the QUE 93005 CM2 chondrite.
(a) Element map of the carbonate growth zones contain calcite (green), dolomite (m is magenta=blue plus red) and breunnerite (blue). c is cyan in which blue and green are mixed. (b) Plot of Ca, Mg and Fe concentrations across the grain in (a) obtained using INCA software. The Y-axis is counts and X-axis is distance (31.2µm). Analytical conditions that used to acquire elements maps are shown in Table 2.3.

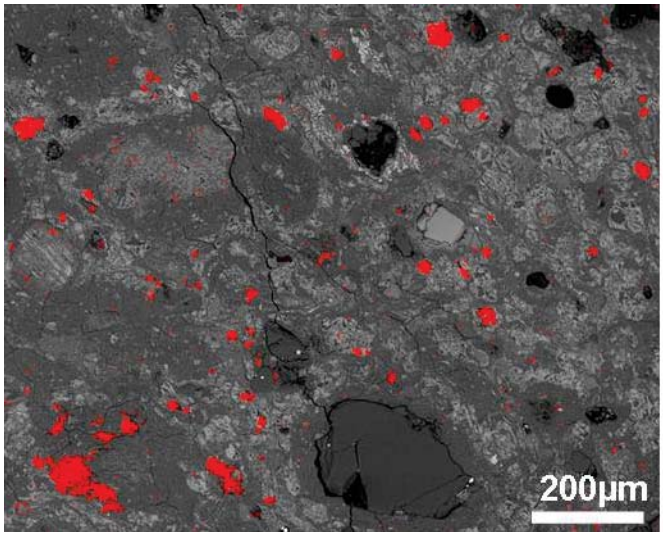

Figure 2.10- A combination of a calcium X-ray map and BSE image.
The composite image shows calcium distributions within fine grained (<1µm) matrix of the Pollen CM2 chondrite. High concentrations of calcium are in red and highlight grains of calcite and aragonite.

2.4 Quantitative chemical analysis

Qualitative chemical analysis was used to identify the elements that are present in a specimen, whereas quantitative analysis was used to determine the concentrations of those elements.

2.4.1 Electron probe microanalysis (EPMA)

Quantitative chemical analysis provides small volume analysis with high precision and accuracy, and can be carried out by electron probe microanalysis (EPMA). EPMA was performed by wavelength dispersive X-ray spectroscopy using a Cameca SX100 electron microprobe at the Grant Institute of Earth Science, University of Edinburgh. This technique was used to analyse carbonate minerals, meteorite matrices and phyllosilicate pseudomorphs after carbonate grains.

2.4.1.1 Wavelength-dispersive spectroscopy

The wavelength dispersive (WD) spectrometer was used for quantitative chemical analysis as it can cope very well with chemically complex minerals and intergrowths of fine grained (<1µm) phyllosilicate matrices of CM carbonaceous chondrites. The WD spectrometers analyse X-rays by wavelength using the Bragg reflection (explained below). The spectra resolution of WD spectrometers is high in comparison with EDS which distinguishes X-

rays by their energy (Reed, 2005). WD has excellent detection limits that in general are 0.02-0.05 wt.% oxide, whereas EDS detection limits range from 0.2 to 0.5 wt% oxide.

2.4.1.2 Operating conditions, calibration standards and data output

EPMA work was undertaken at high vacuum on polished thin sections, coated with about 20nm carbon. It used 15kV accelerating voltage, a spot size of 5μm and a 3 nA beam current. The most appropriate natural mineral standards were used for calibration. These standards are well characterised and homogenous, with a range of elements that are expected to be found in examined crystals. Carbonate minerals were analysed for Ca, Mg, Fe, Mn, Sr and Na. Phyllosilicate pseudomorphs after carbonates, phyllosilicate matrices (fine grained (<1μm) matrix and chondrule rims), tochilinite-serpentine intergrowths and tochilinite rims to pseudomorphs were all analyzed for: Mg, Al, Si, P, S, K, Ca, Ti, Cr, Mn, Fe and Ni. This work used standards that are listed in Table 2.1. Standard analyses were undertaken every session before and after the sample analyses, to verify the stability of the electron beam and the calibrations. The conditions that were used for quantitative chemical analyses of carbonate and phyllosilicates, as well as the detection limits are listed in Table 2.2. The raw data output from the Cameca SX-100 represents the number of X-ray counts collected during the counting time at a particular spectrometer position. These can be loaded directly into a spreadsheet as wt% elements, wt% element oxide, atom proportions in a molecule, etc. Oxygen was not analysed for silicates, but was added. Also, O and C were added for carbonates. For example, O was added for Si to obtain SiO_2 using the following calculations: SiO_2 = (Si wt% / atomic weight of Si (28.0855)) * (atomic weight of Si + (2 * atomic number of O))

Element and X-ray line	Standard
Na K_α 1	Jadeite
Mg K_α 1	Spinel
Al K_α 1	Spinel
Fe K_α 1	Fayalite
Ca K_α1	Wollastonite
Si K_α 1	Wollastonite
Mn K_α 1	Mn metal
K K_α 1	Orthoclase
Ti K_α1	Rutile
S K_α 1	Barite
Cr K_α 1	Cr metal
Ni K_α 1	Ni metal
Sr L_α 1	Celestite

Table 2.1- EPMA quantitative analysis detection and calibration standards.

Conditions of EPMA			
Carbonate		Phyllosilicates	
Current	3 nA and 20 nA	Current	3 nA and 20 nA
Beam spot size (μm)	5	Beam spot size (μm)	5
Accelerating voltage	15 KeV	Accelerating voltage	15 KeV
Total counting time	5 min	Total counting time	10 min
Typical detection limits in wt%			
Carbonate		Phyllosilicates	
Na	0.04	Na	0.09
Ca	0.17	Mg	0.05
Mg	0.01	Al	0.07
Fe	0.04	Fe	0.18
Mn	0.05	Ca	0.06
Sr	0.04	Si	0.11
		Mn	0.14
		K	0.03
		P	0.02
		Ti	0.02
		S	0.02
		Cr	0.04
		Ni	0.05

Table 2.2- Analytical conditions and detection limits for chemical analyses of carbonate and phyllosilicates by EPMA.

The detection limit data in ppm were converted into wt% and average calculated for each analysis run. The analyses of each element in wt% which are below the average of its detection limit have been assumed to be zero. The chemical analyses in element wt% of carbonate minerals have also been converted into mole% to determine molar proportions of elements in these minerals.

2.4.2 Quantitative chemical analyses using the Zeiss Sigma field-emission SEM

Quantitative elemental ED X-ray analyses of carbonate minerals and phyllosilicates in some of the samples studied were acquired using the Zeiss Sigma field-emission SEM. For these analyses the samples and the standards were coated with carbon. For accuracy, the stability of the beam was continuously checked, using the Faraday cup. Quantitative analyses by this instrument required calibration before analysis of each sample (carbonate or phyllosilicates), and details of operating conditions and calibrations are listed in Tables 2.3 and 2.4.

Conditions		Typical detection limit in wt%			
Aperture	60 µm	Na	0.09	Ti	0.20
Probe current	2 nA	Mg and Ni	0.05	Mn	0.40
Accelerating voltage	15 KeV	Al, P, S and CI	0.10	Fe	0.30
Total counting time	60 seconds	Si	0.09	Sr	0.14
Analytical working distance	10 mm	K	0.13		
Raster area	~ 5 μm^2	Ca	0.15		

Table 2.3- Analytical conditions and detection limits for the chemical analyses of carbonate and phyllosilicates by the Zeiss Sigma SEM (EDX).

Element	Standard for calibration
Na and Al	Jadeite
Si and Mn	Rhodonite
Fe and S	Pyrite
Ca	Calcite
Ni	Ni metal
Mg	Periclase
Sr	Celestite

Table 2.4- Calibration standards for quantitative EDX analysis.

Due to the small sizes of carbonate grains in CM chondrites, BSE images of these grains were acquired before and after chemical analyses, to ensure that the analyses had been obtained from the correct place. The electron beam leaves a hole on the surface of the grain which relates approximately to the beam size during analysis (Figure 2.11).

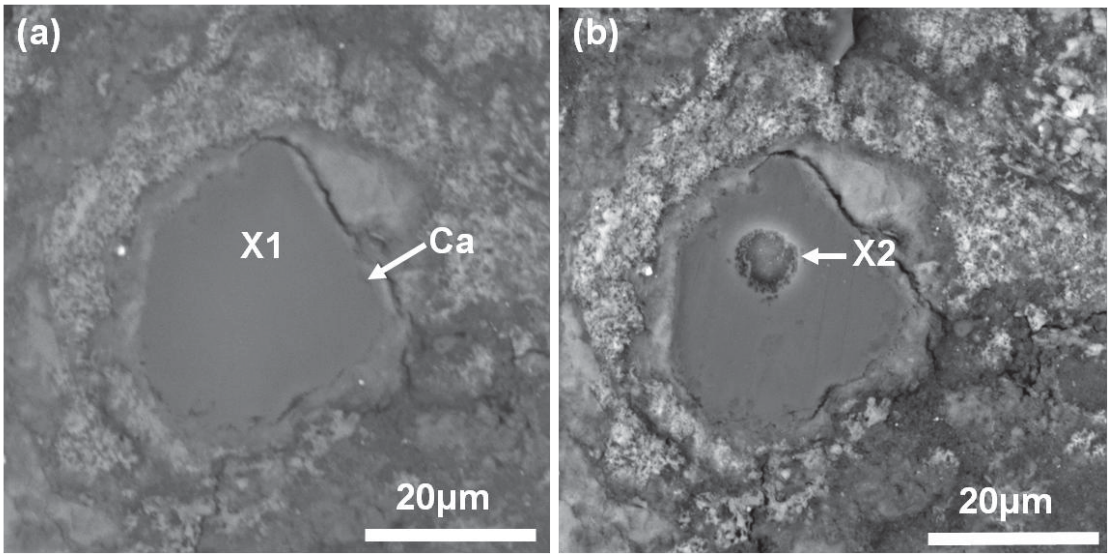

Figure 2.11- BSE images of a calcite grain before and after chemical analysis.
(a) BSE image of calcite grain (Ca) in Murchison (CM2) taken prior to electron probe analysis. X1 area was chosen for quantitative analysis. (b) BSE image of the grain in (a) after chemical analysis (using EPMA). X2 is the hole was 'drilled' by the electron beam during the analysis that approximately reflects the diameter of electron beam (5µm). This image was taken to ensure that the chemical analysis has been obtained sufficiently far from the surrounding materials (matrix).

BSE images and X-ray spectra were used to describe the petrographic composition of the samples studied. Based on the petrographic features of the matrix and carbonate minerals in the samples studied, areas of these materials were selected for detailed study (i.e. chemical analyses and oxygen isotopic analyses). For instance, Pollen (CM chondrite) contains two different phases of phyllosilicate-rich matrix; phase I and chondrule rims are composed of phyllosilicate that are almost free of Fe-sulphide; phase II contains phyllosilicate matrix; that includes Fe-sulphide; and tochilinite clumps, and is slightly coarser grained (see Figure 3.12 and Figure 3.13). Pollen also contains CI-like clasts that consist of very fine phyllosilicates. Therefore the generation of data was representative, as the quantitative chemical analyses of these materials were determined (using EPMA and the Zeiss Sigma field-emission SEM), and compared with those that occur in other CM chondrites (e.g. chemical composition of chondrule rims in Pollen CM chondrite were compared with those in Murray CM chondrite). Furthermore, Cathodoluminescence was used to identify the variations of CL intensity within carbonate minerals (aragonite, calcite and dolomite), and low and high CL intensity of the scanned crystals were selected to obtain individual CL emission spectra and quantitative analyses, using EPMA and CL spectroscopy respectively (e.g. Figure 4.63 and Table 4.16). Chemical analyses were obtained from areas of carbonate minerals and pseudomorphs after carbonate minerals that were free of inclusions and sufficiently far from the fine grained (<1μm) matrix.

2.5 SEM cathodoluminescence (SEM-CL) imaging and CL spectroscopy

In this work panchromatic CL imaging was used since, as described by Edwards and Martin (2011), is the simplest mode of CL imaging. Another technique was used whereby CL spectra are acquired while the electron beam is slowly scanned over the sample, this is termed CL spectrum imaging, CL wavelength imaging (CLWI) or CL hyperspectral mapping (Edwards and Martin, 2011). SEM-CL imaging and CL spectroscopy were used separately in this work to investigate the compositional variations within carbonates in CM chondrites. The Quanta SEM with a KE Developments Centaurus panchromatic CL detector attached was used for SEM-CL imaging, a Cameca SX100 equipped with wavelength-dispersive spectrometers (WD) and a photomultiplier was used for the CL spectroscopy.

2.5.1 SEM Cathodoluminescence (SEM-CL) imaging

The FEI Quanta 200F SEM equipped with a CL detector was used to obtain CL images from calcite, aragonite and dolomite crystals. The SEM was operated at 20 kV, using a high beam current, and all thin sections were coated with ~15 nm carbon. The EDS detector was used in conjunction with the SEM-CL detector to help locate grains for CL imaging. The technique of SEM-CL provides images with a higher spatial resolution and sensitivity than optical-CL, and produces good results from calcite crystals (Lee et al., 2005). This CL detector provides gray scale images of variations in the intensity of visible light. It uses a 10 mm multi-alkali photomultiplier (PM), and is positioned ~2 mm above the thin section in the SEM sample chamber (Figure 2.12).

The CL detector collects the light (luminescence) by a parabolic mirror when the electron beam scans across a crystal, then the output of a photomultiplier produces the CL images. Lee (2000) reported that sharp images of zoned calcite grains were obtained using long dwell times, owing to phosphorescence (i.e. continuing CL emission after the electron beam has moved to the next spot). This finding is consistent with this work, as the images with high quality and resolution were acquired using a very slow scan (about 16 minutes). Specific conditions used to obtain the CL images are listed in Table 2.5.

CL imaging conditions	
Dwell time	1024*884=1000 µs/pixel
Frame time	946.75 s
Line time	1.06 s

Table 2.5- The conditions that were used to optimize CL images.

The emission of light when electrons interact with minerals (Figure 2.13a) may be activated by trace elements or defects in the crystal structure (Reed, 2005).

The luminescence (Figure 2.13b) of calcite is known to be controlled by the Mn^{2+} concentration in the crystal whereas the quenching of the crystal is due to ferrous iron (Fe^{2+}) (Marshall, 1988; Habermann et al., 1998). Thus, the luminescence intensity of calcite broadly relates to the ratio of iron to manganese. However, Calderon et al. (1984) reported that the intrinsic CL in calcite at ~420 nm (activation in blue) is probably due to electron recombination of Ca^{2+} and CO_3^- (see Figure 2.14)

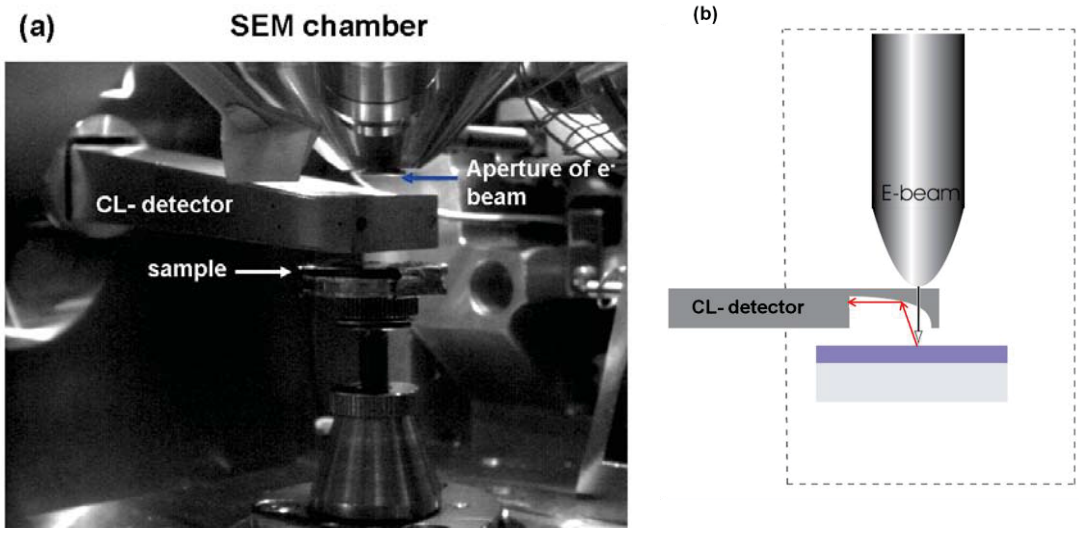

Figure 2.12- Infra-red image of the sample chamber in the FEI Quanta SEM.
(a) CL detector placed between the sample and aperture of electron beam. (b) Internal structure of CL detector showing how luminescence is reflected by a mirror and collected by the detector. Modified (b) after Wijngaarden (2005)

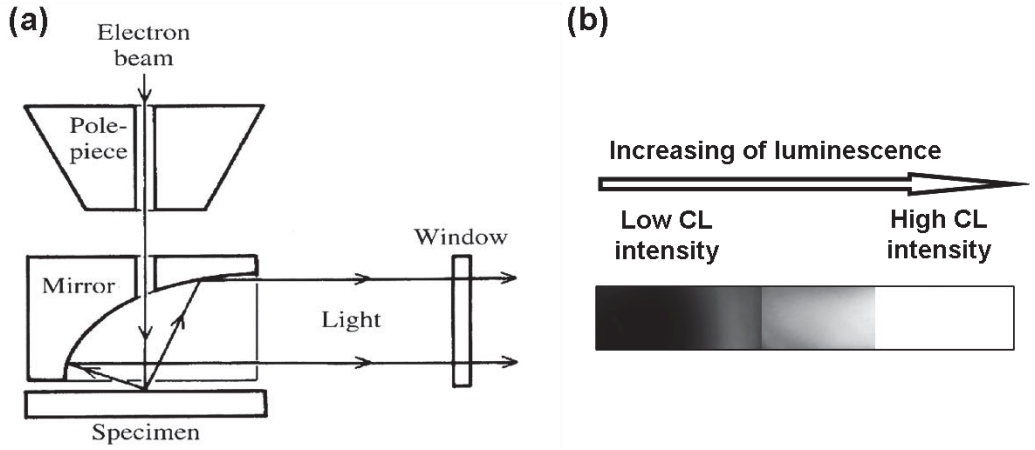

Figure 2.13- The output of a CL photomultiplier.

(a) Schematic diagram showing light (luminescence) collected by a parabolic mirror (from Reed, 2005). (b) Scale of CL intensity ranging from low to high seen on the microscope monitor.

2.6 CL spectroscopy

CL spectroscopy is a technique for collection of CL spectra from a small section of a crystal. It has high sensitivity to distinguish variations of chemical composition within crystals. It is mainly used to track the presence of trace elements (less than 1 wt%) within a particular area of the sample. In this study CL spectroscopy has been integrated with CL imaging and chemical analysis (qualitative and quantitative analyses) to localise the occurrence of trace elements and relate it to the variation of CL intensity as well as conditions during crystal growth.

Zoned aragonite and calcite grains in CM chondrites that show variations of SEM-CL intensity were selected to obtain individual CL emission spectra. For this purpose, a Cameca SX100 EPMA at the University of Strathclyde was used. It is equipped with WDX and a silicon CCD spectrograph that produces spectra from 336-852 nm with a resolution of 0.5 nm. The emission spectra were acquired over 5 seconds with EPMA operated at conditions listed in Table 2.6. The focused electron beam interacts with the sample and the raw data presented by the software as CL intensity (counts) against wavelength (i.e. 336-852 nm). These raw data can be easily plotted as CL emission spectra (Figure 2.14).

Operating condition	
Beam current	10 nA
Spot size (μm)	5
Accelerating voltage	20 KeV
Counting time	5 seconds

Table 2.6- Operating conditions for CL spectroscopy by EPMA.

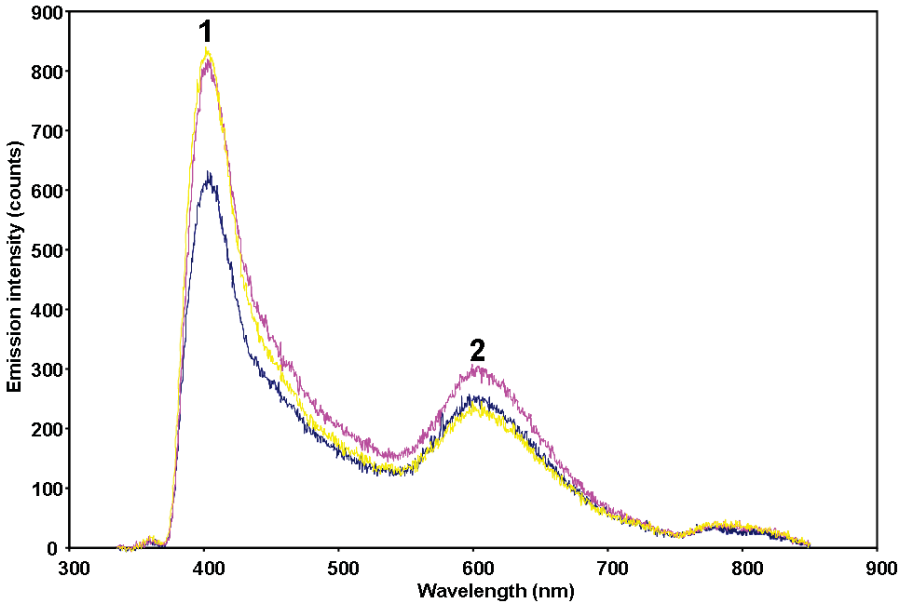

Figure 2.14- Emission spectra from calcite.
Bands with the strongest CL intensity yield blue CL (1) and are probably defect related. Peak (2) is due to Mn^{2+} activation.

2.7 Electron Backscatter Diffraction (EBSD)

The earliest observations of EBSD were by Kikuchi (1928) who showed remarkable lines diffraction patterns obtained from the crystals by transmission electron microscopy (TEM) (Dingley, 2000). Kikuchi lines were also formed in the TEM by Alam (1954). The technique of EBSD has gradually become more important in comparison to electron diffraction in the TEM (Reed, 2005). In 1969 a diffraction technique was developed using

SACP (selected area electron channelling pattern) at Oxford University. The first true EBSD was explained by Venables (1973) (Dingley, 2000) and is an SEM technique. It is designed to obtain fast and reliable data on crystallographic orientations. It is also used for characterisation of crystal boundaries and grain size, and to enable mineral identification.

2.7.1 How it works-EBSD

EBSD uses a polished (flat) sample tilted to 70º relative to the horizontal and towards the detector, which is a backscatter diffraction camera of a phosphor screen. A CCD camera works in conjunction with this detector to record Kikuchi patterns. The EBSD detector is usually inserted in a perpendicular plane to form an angle of 90º to the pole piece (Figure 2.15).

When the electron beam intercepts the sample surface, it interacts with the crystal lattice in the specimen so that electrons are diffracted from atomic planes and produce Kikuchi patterns. The loss of energy of the backscattered electrons is estimated to be very small (Reed, 2005). Diffraction of the incident electron is described by Bragg's law which relates the wavelength of incident electron beam (λ) to the atomic plane spacing (d) and the Bragg angle (θ) in the following equation: $\boldsymbol{n\lambda = 2dsin\theta}$ where n is integer order (1,2, etc.).

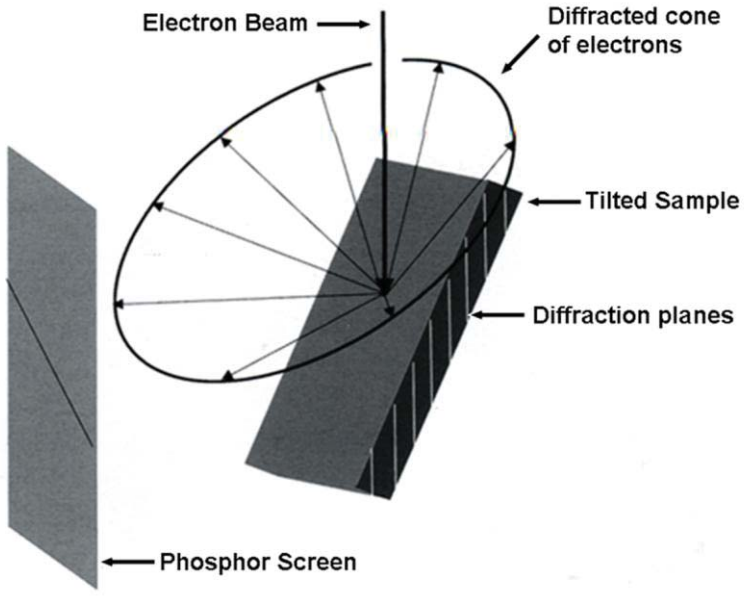

Figure 2.15- Schematic representation of the detection of diffracted electrons with the EBSD phosphor screen.
From Goldstein et al. (2003).

For mapping, Kikuchi patterns are recorded from each point as the polished surface is scanned by the electron beam. The Kikuchi patterns are processed by specialised computer

software to identify the Kikuchi lines. In this respect a Hough transform of the Kikuchi patterns is also used to detect bands (Maitland and Sitzman, 2006). The patterns are then indexed to determine crystallographic orientations.

2.7.2 Parameters and conditions of EBSD mapping

Meteorites are very complicated rocks to study, since the samples are small and fragile. The EBSD technique was used to analyze carbonates that are embedded within a fine grained (<1μm) matrix; EBSD work was carried out either in high vacuum or in low vacuum modes to minimize the effects of charging, and to obtain high quality patterns. In high vacuum mode the samples were coated with a thin layer of carbon (about 10nm).

2.7.2.1 Conditions of EBSD

EBSD work on terrestrial calcite was undertaken prior to EBSD analysis of the studied samples. It was performed several times by setting up binning corrected image of the camera in 2 x 2 (320 x 240 pixel) with an exposure time of 50 ms, 4 x 4 (160 x 120 pixel) with exposure time of 15 ms, 8 x 8 (80 x 60 pixel) and exposure time of 4 ms. 4 x 4 showed better resolution and was also relatively fast. Hence, the binning operation of 4 x 4 was chosen to acquire the EBSD patterns from Ca-carbonate grains in studied samples. Also, all samples were polished down for about 4 minutes, using 0.3μm colloidal silica to optimise the Kikuchi patterns quality by removal of the damaged crystal surface. The conditions that were used for EBSD mapping are listed in Table 2.7.

EBSD conditions	
Tilt	70º
Accelerating voltage	20 kV
Pressure	70 Pa
Spot size	4
Working Distance (WD)	14±3 mm
Coating	Uncoated or 10nm carbon
Binning	4*4 (160*120 pixels)
Exposure time	4 ms
Aragonite phase	*a* axis=4.99 and *c* axis= 17.062
Calcite phase	*a* axis=4.961, *b* axis=7.967 and *c* axis= 17.062

Table 2.7- Conditions that were used for EBSD mapping.

2.7.2.2 Parameters of EBSD

EBSD work used specific parameters (Table 2.8) to optimise the Hough transform to index of the strongest Kikuchi bands (brightest peaks) in Hough space. The matching lines of all

peaks on the original diffraction pattern help to evaluate the result prior to acquisition of an EBSD map (Figure 2.16).

Hough page parameters	
Pattern size	120
Maximum peak count	15
Minimum peak count	6
Minimum peak distance	6
Peak symmetry	0.67
Step size	1-2 microns

Table 2.8- Parameters that were used in Hough page to identify the best Hough peaks prior to an EBSD scan.

The Hough transform is also used to distinguish the Kikuchi patterns from the indexed pattern (Figure 2.17).

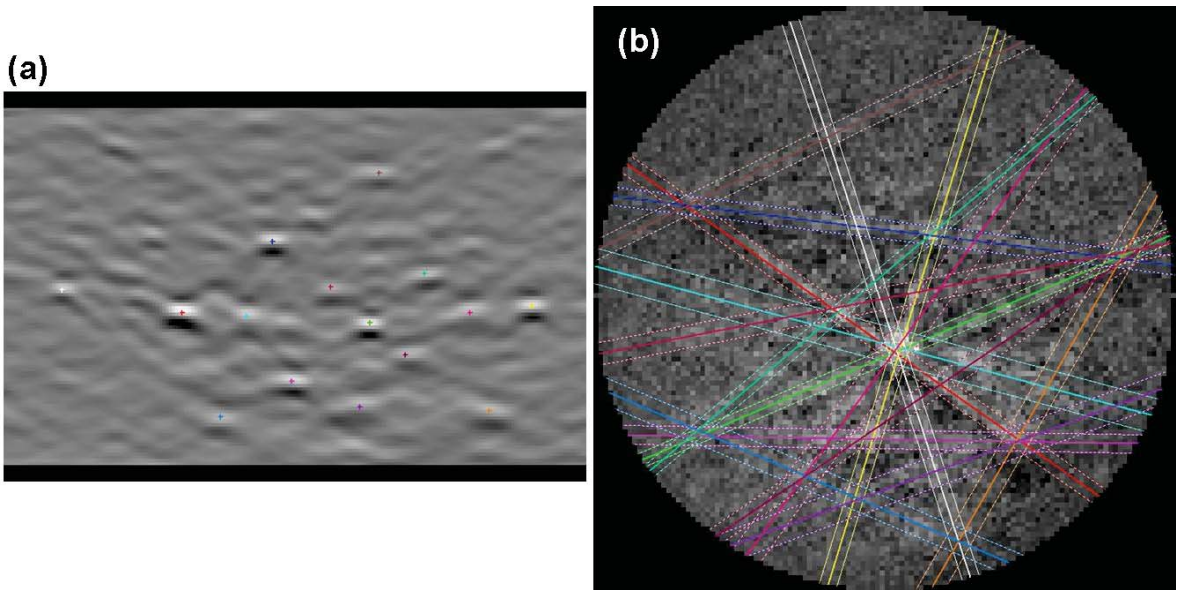

Figure 2.16- Kikuchi patterns.
(a) The locations of the brightest peaks (indicated by a cross) in Hough space of calcite. These peaks are distinguished from false peaks and identify the crystal structure of calcite. (b) Image showing the corresponding lines of the brightest peaks (in a) that are overlaid on the Kikuchi patterns. These diffraction patterns were obtained using the conditions and parameters in Table 2.1 and Table 2.2 respectively.

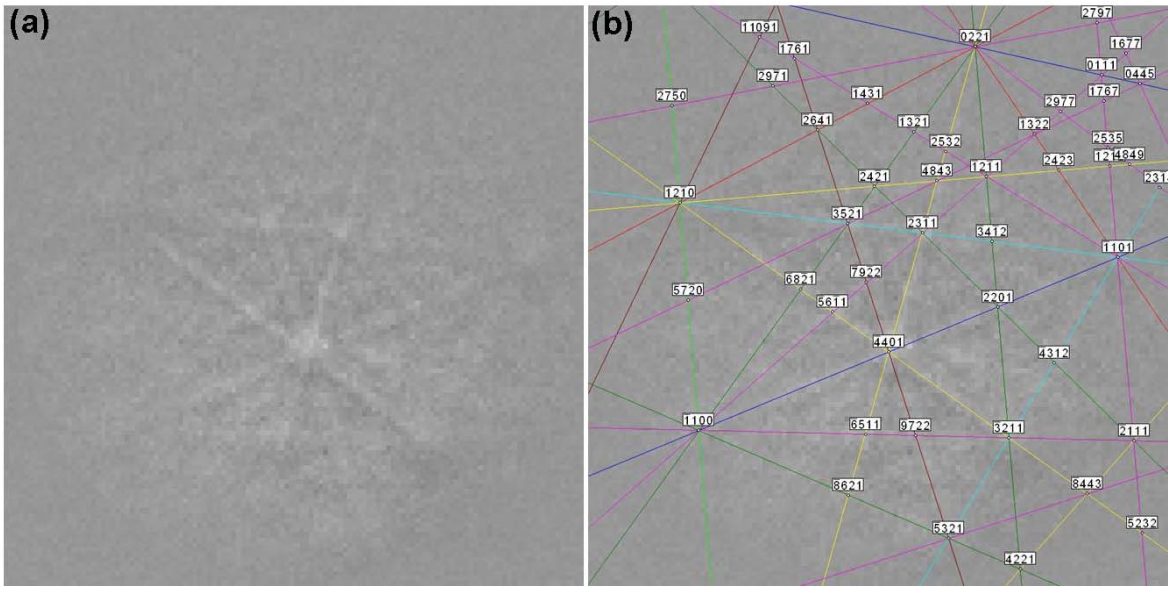

Figure 2.17- Automated indexing of Kikuchi patterns.
(a) Diffraction pattern of same calcite sample in Figure 2.16. (b) Overlaid indexing solution proposed by the TSL OIM 5.2 software. Here the planes of (hkil) in the calcite crystal corresponded to the numbers in (b).

2.7.3 Post processing of EBSD Data

EBSD analyses were performed using the FEI Quanta 200F SEM equipped with a TSL (TexSEM Laboratory) EBSD system running TSL OIM 5.2 software

The OIM 5.2 software was used to analyse crystallographic orientations, and to produce phase maps of the scanned area or crystal. It is also used to clean up data by removing points with a low confidence index. The Hough transform with a 3º tolerance was utilised to optimise the Kikuchi bands from the diffraction patterns. The first EBSD work on Ca-carbonates in CM chondrites was performed by Lee and Ellen (2008). In their study, the low confidence index (CI) of data points was related to the meteorite matrix. Low CI also can be a consequence of open pores on the sample surface. The OIM 5.2 software provides a clean-up method that is useful to remove errors in data. All data sets in this study were individually cleaned after each scan using the neighbouring CI correlation method. In this procedure a new partition was created for each scan from the original data by adjustment of the mean CIs according to reliable data, defined as the minimum value of CI; essentially the most reliable data points are displayed in the final dataset (Figure 2.18).

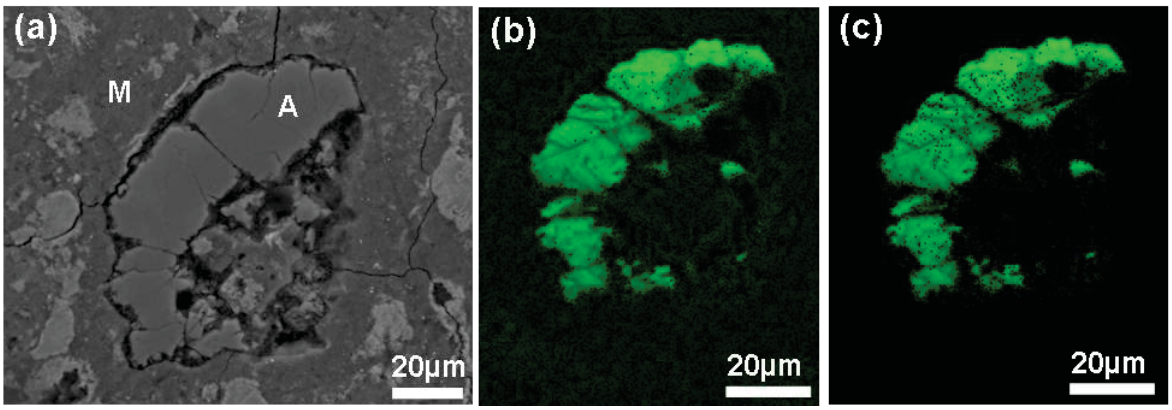

Figure 2.18- Typical EBSD results from aragonite.
(a) BSE image of aragonite grain (A) within matrix (M) of the Cold Bokkeveld CM2 chondrite. (b) EBSD phase map of grain (A) before cleaning data that represent matrix (green spots in black region). Note the absence of this noisy data in (c) after cleaning process using neighbour CI correlation method. Reliable data only are now present.

EBSD mapping also provides image quality (IQ) maps that characterise the quality of EBSD pattern. Image quality was defined by Tao and Eades (2002) as the total of peaks that are detected on the Hough transform. It appears in gray scale in the mapped area. Image quality can be overlaid with colours to identify known minerals; this enables identifications of mineral locations and their polymorphism such as aragonite and calcite.

EBSD maps show orientation data by plots of the inverse pole figure (IPF) with RGB colouring scheme. In the IPF plot a colour is assigned to a specific crystallographic orientation relative to the sample coordinate (Figure 2.19). For example, if the scanned grain has an orthorhombic crystal structure, then a crystal oriented with the pole to (001) normal to the sample surface is coloured in red, (100) appears green and blue represents (010). Large numbers of orientation measurements are displayed in IPF with respect to the normal direction of the sample (Figure 2.20), and every point indicates a particular measurement.

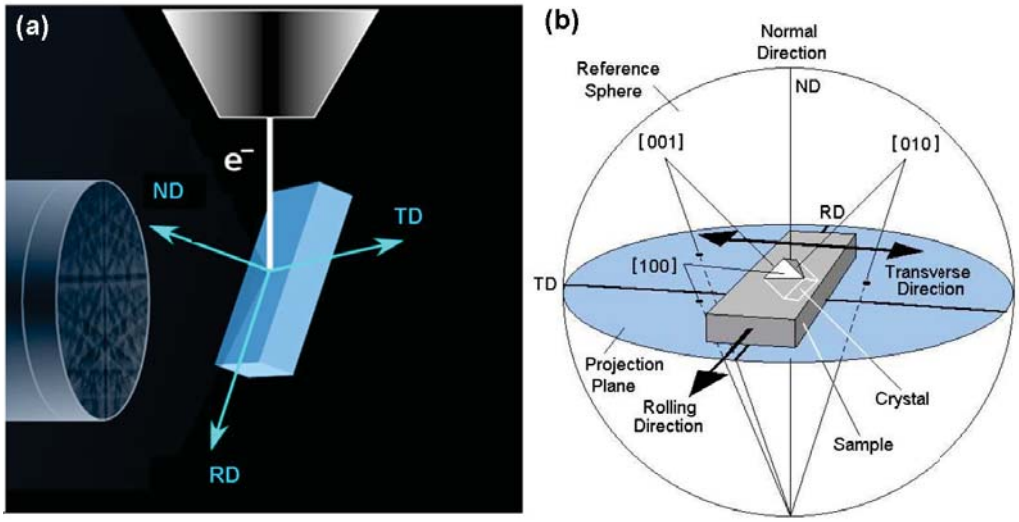

Figure 2.19- Reference coordinates (ND, RD and TD) of EBSD mapping.
(a) Reference coordinates (ND, RD and TD) of EBSD mapping relative to tilted thin section and incident beam. Figure modified after manual user of OIM software. (b) Schematic showing poles for planes in the sample. It also displays reference directions of EBSD. Only ND was used in this study.From: http://www.krist.uni-freiburg.de/studium/Praktikum/EDX_EBSD_MSc_engl.pdf

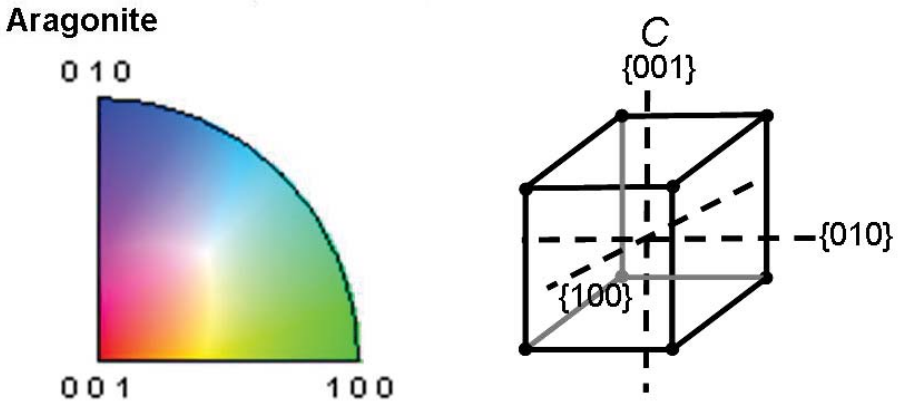

Figure 2.20- Colour key of crystallographic orientations for a pole figure made from an EBSD map of a grain of aragonite (orthorhombic system).
In this scale red refers to the pole to the (001) plane that parallel to normal direction (ND).

In this study, the pole figures used are compass directions (N, S, E, W). Crystallographic orientation maps were constructed from each scanned area or polycrystalline grain. Orientations of particular planes were plotted as stereographic pole figures in the upper hemisphere (positive hemisphere) to determine any preferred orientation of Ca-carbonate grains in each sample. Determination of preferred crystallographic orientation may provide more information about the processes of the formation of carbonate minerals in CM chondrites (e.g. Lee and Ellen 2008; Lindgren et al. 2010).

2.8 SEM point counting

The Quanta 200F FEG-SEM equipped with an EDAX Pegasus 2000 EDS and EDAX Genesis hardware and software, was employed to determine the abundance of constituents in the samples examined. Backscattered imaging, together with EDS, was used to point count carbonates, silicates (olivine, pyroxene etc.), matrix (serpentine, tochilinite etc.) and chondrules in the studied CM chondrites. The combination of BSE imaging and EDS is a very quick way to identify an unknown grain within the sample. Prior to point counting, specific conditions were set for the SEM; these conditions are listed in Table 2.9. The sample constituents were manually counted using a grid of about 30 horizontal and vertical lines, yielding 900 points (intersection points of lines). However the number of lines is mainly based on the area in mm^2 of the sample examined. The total number of each constituent (e.g. calcite) was converted to a percentage that represents percent of total volume of a sample.

Conditions of SEM point counting	
Vacuum mode	High
Spot size (μm)	4
Accelerating voltage	20 KeV
Working distance	13 mm
Magnification	1000X
Sample	Polished thin section coated with carbon
Brightness and contrast	Similar in all sessions

Table 2.9- Conditions used for SEM point counting.

2.9 Raman Spectroscopy

The first discovery of Raman scattering was by Raman and Krishnan (1928) who used sunlight focused by telescope objectives to record light scattered from six different liquids. Today Raman spectroscopy uses a micrometer sized focused laser beam and analyses the Raman scattered light to determine material composition and structure. This is a powerful tool that can be used to identify minerals and other compounds and to characterise their bonding. Raman spectra were obtained using a Renishaw in a Via Raman microscope with a 514 nm laser. Calibration was made relative to the wave number of a Si standard. The spectra were acquired in 30 increments with a measuring time of 2 s each. The Raman signal is detected by a charged coupled device (CCD) camera with an array of 2048 X 512 pixels. The uncoated sample was positioned on the stage of a petrographic microscope equipped with objectives of 5X-100X. 10 mW of laser power was focused on the sample

surface to obtain a single spectrum with an average of 20 accumulations. Wire 3.2 software associated with a Raman spectroscopy library was used to process the Raman data.

This technique uses micrometer sized incident beam of monochromatic light that is of a single frequency. The vast majority of scattered light (photons) from the examined material remain as the frequency of incident light (elastic scattering) (Roberts and Beattie, 1995) (Figure 2.21). Nevertheless, a very small amount of light has minor changes of colour due to its new frequencies (inelastic scattering), which is known as Raman scattering or the Raman effect (Figure 2.21) (Roberts and Beattie, 1995).

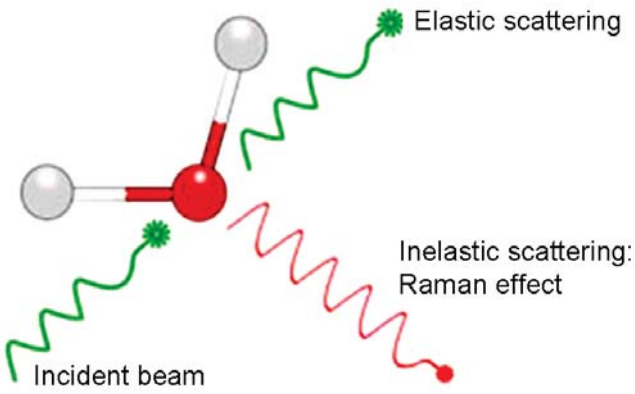

Figure 2.21- Schematic diagram showing a laser beam hitting a molecule and undergoing elastic and inelastic scattering.
Modified from HORIBA scientific. Website: http://www.horiba.com/fr/scientific/products/raman-spectroscopy/tutorial-faqs/raman-faqs/what-is-raman-spectroscopy/

Raman scattering results when an electromagnetic field interacts with a molecule or penetrates the crystal lattice and is presented with shifts in energy of which the examined crystal is characterised. Raman Spectroscopy uses a CCD camera identical to infrared spectroscopy to observe the vibration in molecules (Renishaw plc, 2006).

The wavelength position and intensity of the Raman effect is expressed by peaks in the Raman spectrum, with each peak related to a particular vibration of a molecular bond, e.g. C=C, N-O, C-H, N-O, etc (HORIBA, 1996). For example, three modes of vibration are observed for H_2O and CO_2 molecules including deformation (bending) mode, symmetrical stretch and asymmetrical stretch (Smith and Dent, 2005). General comments about intensities of Raman spectra have been summarised by Nishimura et al. (1978) as following: deformational vibration is expected to be less intense than stretching vibrations. Multiple chemical bonds, for example C=C, provide more intense vibration than a vibration of C-C. In addition, a rise in stretching vibrations is likely to be produced from

atomic bonds of large atomic mass. The vibrational Raman spectrum is a feature of the examined sample, and indicates the specific molecular bonds (Roberts and Beattie, 1995).

Here Raman spectroscopy was used to distinguish aragonite from calcite. Both aragonite and calcite have Raman shifts at 1086 Δcm^{-1} as a consequence of CO_3 vibration (symmetrical stretch). Raman shift is also present at 155 Δcm^{-1} by lattice mode. Some other locations of small Raman shifts of these minerals differ from each other, as they have different crystal structures. Small Raman shifts of calcite occur at 282 and 713 Δcm^{-1}, whereas aragonite produces small bands at 207, 704 and 713 Δcm^{-1} (Figure 2.22) (White, 2009).

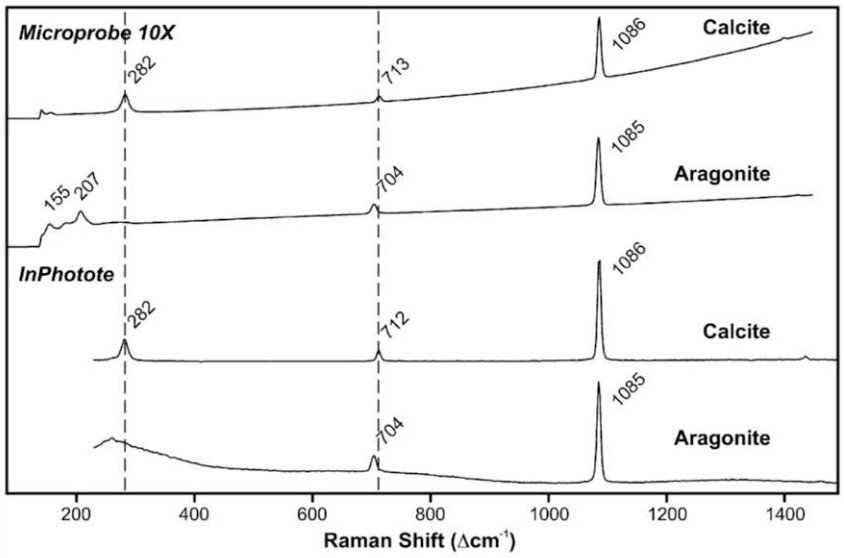

Figure 2.22- Spectra of terrestrial aragonite and calcite showing the difference between minor Raman bands from both minerals.
The spectra in the upper part were acquired using a microprobe equipped with X10 objective and using green excitation, whereas the spectra in lower part acquired by InPhotote (control software is used to obtain single accumulations) with red excitation. These spectra are taken from White (2009).

2.10 Transmission Electron Microscopy

Transmission Electron Microscopy (TEM) was used to study the microstructure of fine grained (<1μm) rims around the carbonates and pseudomorph after carbonates in CM chondrites, in an effort to describe the sequence of events after crystallisation of the carbonate minerals.

TEM was developed as a consequence of the imaging limitations of optical light microscopy. Early explanations of TEM by Thomson (1927) highlighted diffraction from

electrons that have been transmitted through thin solid materials. It was expected that an image with a high spatial resolution could be obtained if the transmitted electrons were focused and given the very short wavelength (i.e. 0.037 Å, Champness, 1977) (Egerton, 2005), since the wavelength is linked to its electron energy (Williams and Carter, 2009). Electron lenses were developed as an alternative to the light microscope to reveal the interior structure of a sample by Ernst Ruska in 1931, who had also produced the first transmission image (Egerton, 2005). In 1970s ion beam milling became available for the preparation of high quality thin sections of solid materials, which made the TEM a powerful tool for geology (Lee, 2010).

TEM is typically used to magnify objects down to a resolution of micrometers to sub-nanometers. TEM provides electron diffraction patterns, microstructural and crystallographic information (e.g Lee 2010; Egerton, 2005). It is capable of displaying details smaller than the atomic scale (Williams and Carter, 2009). The TEM has an electron optical system (Figure 2.23) which comprises an electron gun and several electromagnetic lenses (5 or more) placed vertically to form the electron column of the TEM, and working in a vacuum.

The electron column can be divided into three parts including: illumination system, specimen stage and imaging system. The illumination system is composed of an electron gun (the source of electrons beam) and set of condenser lenses (2 or more). Electrons are accelerated to high kinetic energy (ranging from 20-1000 keV) and focused by condenser lenses to go through the thin sample. The common type of electrons source is thermionic gun, in which the filament contains tungsten wire heated to ~2700 K to produce electrons in a vacuum field (thermionic emission). The illumination system operates in two different modes, including the convergent-beam/probe mode in which the beam is converged to sub nanometer size. This mode is utilised for imaging of scanning transmission electron microscopes (STEM)); and parallel beam TEM mode which is used for SAED (selected area electron diffraction) and TEM imaging (Lee, 2010).

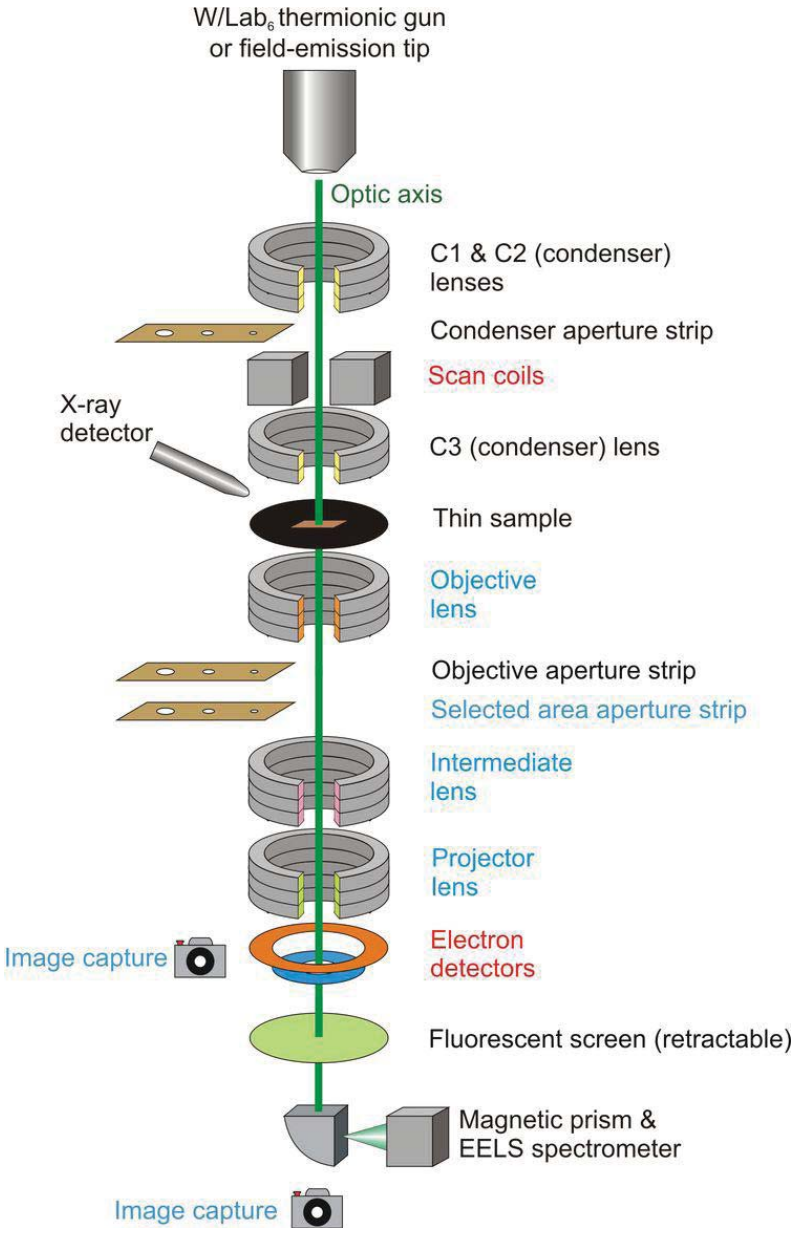

Figure 2.23- Schematic diagram showing the main components of the instrument that operates in the mechanisms of TEM and STEM.
The components are labelled in black used for both, the components are labelled in blue only used for TEM and blue ones are used for STEM, from Lee (2010).

The specimen stage/holder is the centre of the TEM, where the thin sample interacts with incident electrons. Elastic scattered electrons are formed by the interaction of the electron beam with the atomic nucleus of the specimen (Lee, 2010), whereas inelastic scattering is the consequence of interaction between incident electrons and atomic electrons (Egerton, 2005). Both mechanisms generate the contrast in TEM and STEM images (Lee, 2010).

TEM results are presented in two different modes, bright-field images (e.g. Figure 2.24 a) and dark-field images. These images are also produced in direct beam and scattered electrons respectively. Diffraction patterns are also produced by TEM mode and using its objective aperture (Lee, 2010) (e.g. Figure 2.24 b).

TEM work here used a FEI Tecnai T20 TEM at the Kelvin Nanocharacterization Centre, School of Physics and Astronomy, University of Glasgow. This instrument contains a SIS Megaview III CCD camera to acquire diffraction patterns and a Gatan Image Filter, GIF 2000 for low magnification imaging of microstructures.

The spacing of spots or rings in a diffraction patterns is equal to the spacing of lattice planes in a crystal. The two are related by TEM camera factor, which is the magnification of the diffraction pattern.

The spacing of a lattice plane (d spacing) is presented in the following equation:

$$d = cf/s$$

where ***cf*** is the camera factor, ***s*** is spot or ring spacing and ***d*** is d-spacing .

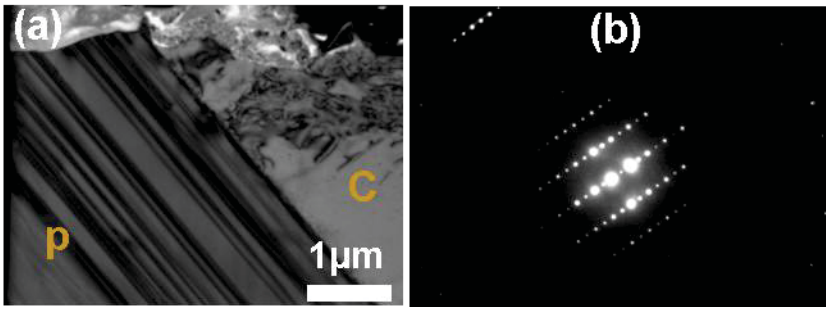

Figure 2.24- Representation of TEM results.
(a) Bright field image of calcite (C) and pyroxene (P) in Pollen. Note the presence of parallel exsolution lamellae in pyroxene. (b) Diffraction pattern of the pyroxene.

2.10.1 Sample preparation for TEM

The Focused Ion Beam (FIB) is principally used for TEM sample preparation. FIB is a very useful tool that can be employed to understand the mineralogy of the Earth and planetary materials (Lee et al., 2003). Foils from carbonate and phyllosilicates of Nogoya and Pollen (CM2 chondrites) were prepared for this study. They was carried out using a FEI Nova 200 Dualbeam focused ion beam (FIB) system at the Kelvin Nanocharacterisation Centre, University of Glasgow. The method uses a polished thin section coated with carbon. Very thin sections (foils) (less than about 100nm) are required, which are electron transparent (see Lee et al., 2003). FIB uses Ga^+ ions accelerated to 30 KV (Heaney et al., 2001). The momentum of these ions is about 350 times an equivalent electron beam, and electrostatic lenses are used in this instrument to focus the ion beam (Heaney et al., 2001). FIB milling of the Lafayette Martain meteorite by Vicenzi and Heaney (1999) showed that some materials are altered when they are bombarded with high energy Ga^+ ions. However, Lee et al. (2007) conquered the problem by coating the samples

with a thick layer (>85 nm) of gold. In this study, a platinum (Pt) protection strap (~1µm) was deposited over the area of interest, and an ion beam was used to mill trenches on either side of the region of interest, to form a section with a thickness of about 1µm. The needle of an Omniprobe 100 micromanipulator was then brought into contact with the section and Pt was used to weld the section to this needle. The section was cut from the trench and the bulk sample moved to a holder for milling to 100nm thickness (Figure 2.25).

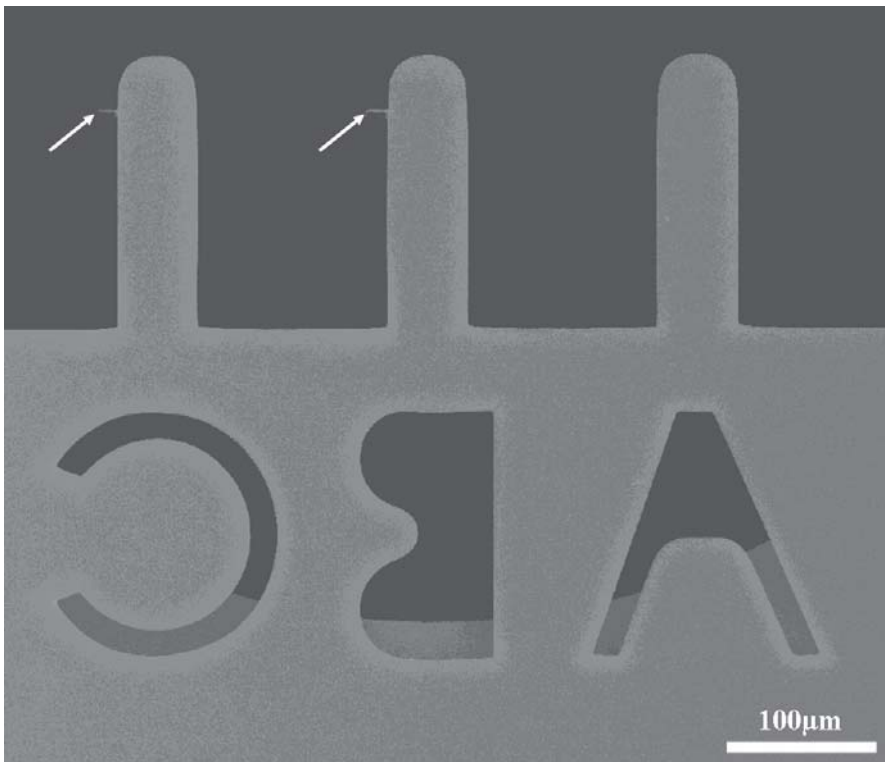

Figure 2.25- SE image showing two foils (arrowed) that have been lifted out in-situ. They have been welded to the needles of a holder using a FEI Nova 200 Dualbeam focused ion beam.

2.11 Secondary Ion mass Spectrometry (SIMS)

The Cameca NanoSIMS 50L at the Open University was used for oxygen isotopic analyses of Ca-carbonates (both aragonite and calcite) in the LON 94101 CM2 chondrite. SIMS uses primary ion bombardment to sputter a few atomic layers from the sample surface and atomic clusters and atoms are ejected. Some are secondary ions that represent the composition of the analysed area (Figure 2.26). These secondary ions are separated based on their mass.

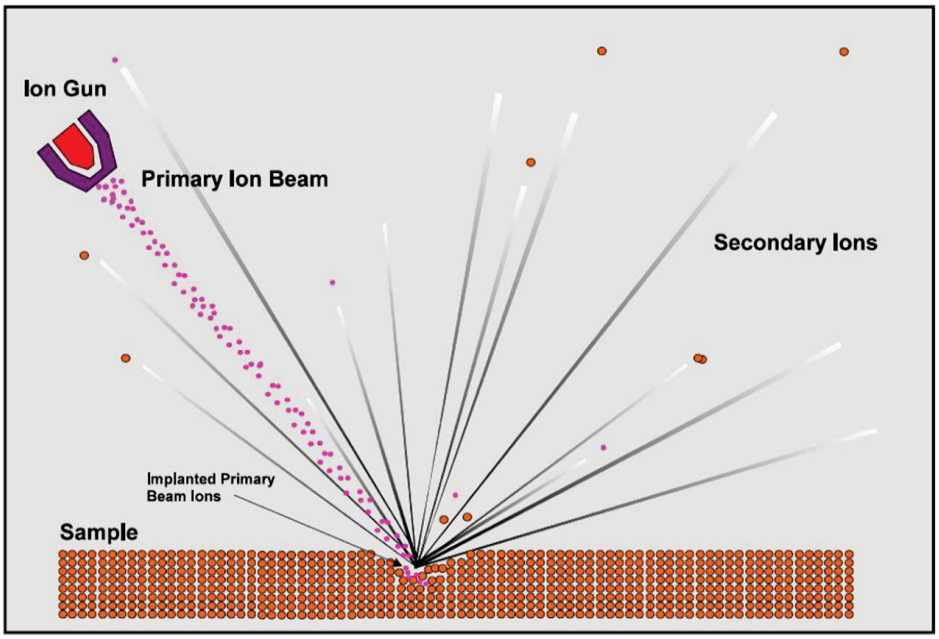

Figure 2.26- Schematic diagram of secondary Ion sputter-erosion.
The image shows primary ion beam impacting on the sample surface, and freeing secondary ions from the area. Note that in the Cameca NanoSIMS 50L the primary beam is perpendicular to the sample surface. From: JAC C:\IP\DOC\SIMS4.DOC

NanoSIMS uses O_2^+, O^-, Cs^+, Ar^+, Ga^+ or neutrals as the primary ion beam. The NanoSIMS has a beam of Cs^+ or O^- primary ions can produce spot sizes on the sample of about 50 nm. The secondary ions are extracted by the magnetic sector mass analyzer in order to be mass filtered. NanoSIMS has the ability to record at the same time up to seven mass selected images of different isotopes or species. An electron sensitive multiplier(s) is used to detect the secondary ion signals. The NanoSIMS 50L at the Open University is equipped with seven movable/adjustable electron multipliers and three Faraday cups (a Faraday cup was used for this study), and an optical microscope with CCD camera. The electron multiplier differentiates between the energy of the ion and its type in comparison to the Faraday Cup. The NanoSIMS 50L has co-axial optics through which the primary and secondary ions are focused, which are oriented normal to the sample surface (e.g. Figure 2.27).

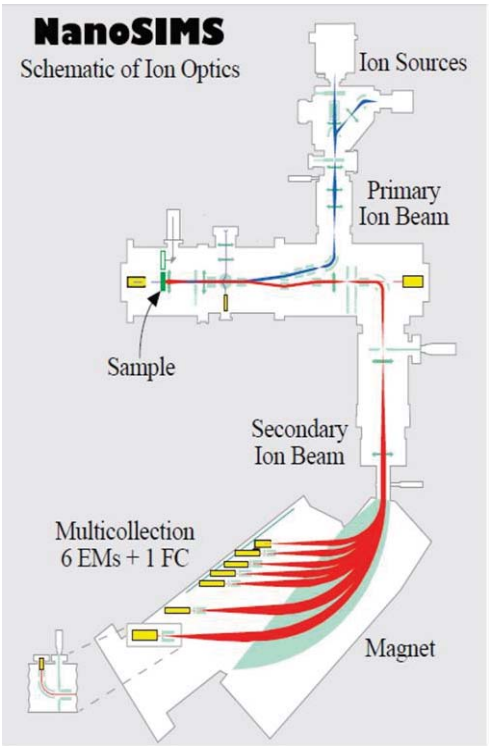

Figure 2.27- Schematic diagram showing NanoSIMS ion optics.
The diagram shows that primary and secondary ion beams are focused co-axially. Note also the parallel 6 multipliers (6EMs) and one Faraday cup (1FC) for multicollections. From Stadermann et al. (1999).

The sample used for NanoSIMS work is a polished thin section 25,400 μm in diameter with a thickness of about 0.3 μm. As CM chondrites are extremely fragile, cleaning of the sample was performed without ultra-sonication, just by rinse and blow dry with a gentle nitrogen supply. BSE images of grains of interest were obtained before and after the SIMS analyses to verify the position of the analyses.

Oxygen isotope analyses were undertaken using conditions listed below:

1. Primary ion beam was Cs^+
2. 60pA probe current with electron gun for charge compensation
3. Pre-sputter area was 7x7 μm for 3 minutes.
4. Analysis area was 5x5 μm with analysis time of 6 minutes.
5. Mass resolving power was >10,000 for oxygen (Cameca definition). ^{16}O was measured on a Faraday Cup, ^{17}O and ^{18}O were measured using electron multipliers.

6. Counts of MgO, CaO and FeO were monitored at the same time as the oxygen isotope measurements

7. All data are reported referenced to Standard Mean Ocean Water (SMOW).

In nature, the three stable isotopes of oxygen are ^{16}O: 99.76%, ^{17}O: 0.039% and ^{18}O: 0.202%. In the respect of isotopic ratios, the differences in abundances or concentrations of the isotopes are generally referred to SMOW, as following:

$$\delta^{18}O = \left(\frac{(^{18}O/^{16}O)_{sample}}{(^{18}O/^{16}O)_{SMOW}} - 1 \right) x10^3 \qquad \text{(Clayton, 2003)}$$

$$\delta^{17}O = \left(\frac{(^{17}O/^{16}O)_{sample}}{(^{17}O/^{16}O)_{SMOW}} - 1 \right) x10^3 \qquad \text{(Clayton, 2003)}$$

Oxygen isotope analyses of calcite and aragonite were performed in two different sessions, as the standards of these minerals used to calibrate the NanoSIMS are different. Standard analyses of each mineral were performed before and after the analysis of the sample. Additional analyses of aragonite standard were also carried out during the session of aragonite analyses. Representatives of oxygen isotope analysis of the aragonite and calcite standards are listed in Table 2.10.

This work used as a standard natural aragonite provided by the Hunterian Museum and Art Gallery, University of Glasgow. The sample was collected from cavities in basalt flows in Kyogle, New South Wales, Australia. Three separate locations for analyses of this aragonite 'in house' standard sample were prepared to check that the sample was homogenous in $\delta^{18}O$ composition. The powdered samples were reacted with anhydrous H_3PO_4 at 70 ± 0.1 °C for 24 hours to produce CO_2. An AP2003 continuous-flow mass spectrometer was used (at the Scottish Universities Environmental Research Centre, SUERC) to obtain $\delta^{18}O_{VSMOW}$ for the aragonite standard. Triplicate ~1 mg powered sub-samples of the three aragonite samples were run, interspaced with international standards NBS18, NBS19 and internal laboratory standards for calibration and corrections. The carbon and oxygen isotope analyses of the powdered samples are listed in Table 2.11.

Standard	$\delta^{17}O$ (‰)	2σ (‰)	$\delta^{18}O$ (‰)	2σ (‰)	$\Delta^{17}O$ (‰)	2σ (‰)
Calcite	7.66	2.58	15.33	1.37	-0.31	2.92
Calcite	6.01	2.58	15.18	1.37	-1.88	2.92
Calcite	5.71	2.58	14.46	1.37	-1.81	2.92
Calcite	7.18	2.58	14.07	1.37	-0.14	2.92
Calcite	7.82	2.58	15.37	1.37	-0.18	2.92
Calcite	8.98	2.58	15.47	1.37	0.94	2.92
Calcite	7.84	2.58	15.18	1.37	-0.05	2.92
Calcite	8.25	2.58	15.52	1.37	0.18	2.92
Calcite	7.97	2.58	16.24	1.37	-0.48	2.92
Calcite	9.69	2.58	15.61	1.37	1.57	2.92
Standard	**$\delta^{17}O$ (‰)**	**2σ (‰)**	**$\delta^{18}O$ (‰)**	**2σ (‰)**	**$\Delta^{17}O$ (‰)**	**2σ (‰)**
Aragonite	15.72	1.45	27.68	1.16	1.33	1.85
Aragonite	15.70	1.45	28.17	1.16	1.05	1.85
Aragonite	15.04	1.45	28.02	1.16	0.47	1.85
Aragonite	15.75	1.45	27.73	1.16	1.33	1.85
Aragonite	14.46	1.45	27.68	1.16	0.06	1.85
Aragonite	14.15	1.45	26.72	1.16	0.26	1.85
Aragonite	13.77	1.45	27.54	1.16	-0.55	1.85
Aragonite	15.32	1.45	27.68	1.16	0.92	1.85
Aragonite	14.15	1.45	27.63	1.16	-0.22	1.85
Aragonite	14.96	1.45	27.15	1.16	0.85	1.85

Table 2.10- Oxygen isotope analyses of the aragonite and calcite standards.

Name	$\delta^{13}C$ VPDB	$\delta^{18}O$ VPDB	$\delta^{18}O$ VSMOW
Aragonite A	-13.13	-3.52	27.28
Aragonite A	-13.15	-3.33	27.48
Aragonite B	-14.52	-3.29	27.52
Aragonite B	-14.67	-3.11	27.70
Aragonite C	-13.73	-3.44	27.36
Aragonite C	-13.64	-3.20	27.61
Average	-13.81	-3.32	27.49

Table 2.11- Carbon and oxygen isotope compositions of three separate locations of the aragonite sample that were determined by An AP2003 continuous-flow mass spectrometer.

2.11.1 Statistical analysis

Statistical analysis of the isotopic data was carried out using Minitab 15 statistical software. The ANOVA (ANalysis Of Variance) test was used to compare variability between three types of Ca-carbonate. It was used to determine the significance of Ca-carbonate variability in $\delta^{18}O$ values. In the statistical hypothesis testing, there is null hypothesis (H_0) and alternative hypothesis (H_1). Null hypothesis refers to no statistical variation between three sets of data of the sample examined. Alternative hypothesis refers

to a significant statistical difference between three sets of data of the sample examined. In statistics a probability for something to occur of < 0.05 (i.e = 5%) is conservatively considered. The p-value assigns to measure of the null hypothesis credibility. The null hypothesis (H_0) is usable in less than 5% of cases, may be rejected, and the alternative hypothesis (H_1) is valid where p = less than 0.05.

3

Petrologic subtypes of CM carbonaceous chondrites inferred from petrographic observations and literature review

3.1 Introduction and definitions

The CM carbonaceous chondrites can divided into two main types, namely CM2 and CM1, based on their degree of aqueous alteration (Zolensky et al., 1997). Several researchers have used the mineralogy and abundance of the matrices of CM carbonaceous chondrites to identify different degrees of alteration, and so to divide these chondrites into subtypes (e.g. Browning et al., 1996; Rubin et al., 2007; Howard et al., 2011). Samples used in this study that were unclassified were assigned into subtypes using petrographic observations including the abundance of Fe-Ni metal, and the proportion of alteration products within chondrules and chondrule fragments.

Some terms are used throughout this study, which are defined as following:

High temperature phase refers to minerals (e.g. olivine, pyroxene) that formed in the solar nebula at high temperatures.

Low temperature phase is assigned to secondary minerals (e.g. phyllosilicates and carbonates) that formed as a result of aqueous alteration on the parent body/ies of CM chondrites.

Fine grained matrix refers to optically opaque (grain size <1μm) phyllosilicate-rich matrix.

Chondrule rims applies to very fine-grained (<1μm) phyllosilicate rims to chondrules.

Poorly characterized phase (PCP) was introduced by Fuchs et al. (1973) for Fe-S-O phases in Murchison. Tomeoka and Buseck (1985) reported that PCP is present in different proportions of Fe-Ni-S-O and cronstedtite in the matrix of CM chondrites. Currently, the term PCP refers to serpentine-tochilinite intergrowths (e.g. Rubin et al., 2007).

The most significant secondary minerals that occur in CM chondrites (Brearley, 2006) are as follows:

Silicates: *Fe-Mg serpentines* - $Mg_3Si_2O_5(OH)_4$

cronstedtite - $Fe^{2+}{}_2Fe^{3+}{}_2SiO_5(OH)_4$

chlorite - $(Mg,Fe)_3(Si,Al)_4O_{10}(OH)_2 \cdot (Mg,Fe)_3(OH)_6$

saponite - $(Mg,Fe)_3(Si,Al)_4O_{10}(OH)_2(0.5Ca,Na)_{0.3}\,4(H_2O)$

vermiculite - $Mg_{1.8}Fe^{2+}{}_{0.9}Al_{4.3}SiO_{10}(OH)_2 \bullet 4(H_2O)$

Tochilinite: *tochilinite* - $FeS(Mg,Fe)(OH)_2$

Carbonates: *breunnerite* – $(Mg,Fe)CO_3$

calcite - $CaCO_3$

dolomite - $CaMg(CO_3)_2$

aragonite - $CaCO_3$

Sulphates: *gypsum* - $CaSO_4 \cdot 2H_2O$

hemihydrate - $CaSO_4 \cdot \sim 0.5H_2O$

anhydrite - $CaSO_4$

thenardite - Na_2SO_4

***Oxides*:** *magnetite* - $\cdot Fe_3O_4$

Hydroxides: *brucite* - $Mg(OH)_2$

Sulphides: *pyrrhotite* - $Fe_{(1-x)}S$ (x = 0 to 0.2)

Pentlandite - $(Fe,Ni)_9S_8$

Halides: *halite* - NaCl

sylvite - KCl

3.2 Previous studies on progressive aqueous alteration of the matrices CM chondrites

Many studies have indicated that carbonaceous chondrites contain a fine-grained (<1μm) matrix and fine grained rims (<1μm) around chondrules (e.g. Zolensky et al., 1993), but the chondrule rims are absent in CI chondrites (Zolensky et al., 1993). Most CM chondrites are described as regolith breccias and principally contain partially to completely altered chondrules, a phyllosilicate matrix, carbonaceous matter, carbonates and poorly characterized phase (PCP) (or serpentine-tochilinite intergrowths) (Bunch and Chang, 1978). They were subjected to aqueous alteration in their parent bodies after brecciation (Browning and Keil, 1997).

McSween (1979) reported that the components of matrix (defined by him as the meteorite contents that are not optically identifiable as one of the other components (e.g. chondrules) or pores) can be utilized to measure qualitatively the alteration degree of each meteorite. He suggested a scale of alteration for CM chondrites, and found that the matrix abundance in CM chondrites ranges from 57 to 85 vol%, with the greatest proportion for highly altered chondrites. The ratio of Fe/Si in matrices decreases with increasing alteration as a result of crystallization of phyllosilicates with higher Mg/Fe ratios. He placed the CM chondrites in a relative scale: Crescent, Murray, Mighei and Murchison (partly altered), Cold Bokkeveld, Santa Cruz, Boriskino, Erkot, Essebi, Pollen, Allan Hills 77306 and Bells (altered chondrites), Nogoya (highly altered).

Tomeoka and Buseck (1985) found that Mighei, Murchison and Murray are slightly altered and contain the Fe-Ni-S-O phase (i.e. tochilinite) and cronstedtite in abundance, but in highly altered CM chondrites the Fe-Ni-S-O phase had been replaced by cronstedtite, magnetite and sulphides. They also noted that CM matrix became richer in Mg with increasing alteration. They concluded that the poorly characterized phase (PCP) in highly altered CM chondrites was mixed with Mg-rich phyllosilicates.

The least altered CM chondrites including Murray, Mighei, Murchison and Pollen that contain the Fe-Ni-S-O mineral in abundance are characterized by the presence of small amounts of metal, and very little or no magnetite. Bells, Nogoya, Santa Cruz, Essebi, and Haripura have magnetite and very little metal; and Cold Bokkeveld and Crescent have both

magnetite and metal (McSween and Richardson, 1977). Abundant alteration products were observed in Cold Bokkeveld and Nogoya, with more than 95% for Nogoya (Bunch and Chang, 1980). These meteorites are classified as altered and highly altered respectively (Bunch and Chang, 1980).

McSween (1987) noted that the non-Antarctic and Antarctic CM chondrites differ slightly in their matrix compositions. The ratio of PCP/(PCP+Serpentine) within individual CM chondrite matrices differs from 0.16 to 0.58; and there is a wide range in relative percentages of Mg-rich serpentines and Fe-rich serpentines. The progressive aqueous alteration of the matrix of CM chondrites is likely to have occurred by the crystallization of tochilinite, the subsequent formation of cronstedtite and Mg-rich serpentine, and, ultimately formation of Fe-rich serpentine and sulphides (McSween, 1987). The progressive Fe-depletion of matrix that was reported by McSween (1987), was also explained in Tomeoka and Buseck´s model (1985). Tomeoka and Buseck´s model for progressive aqueous alteration of the matrix of CM chondrites was summarized by McSween (1987) as follows: formation of tochilinite by alteration of chondrules with metal, Mg-rich serpentine formation as matrix olivine reacts, cronstedtite formation from reaction of tochilinite with silicon, then other alteration processes formed sulphides, magnetite, and Fe-rich serpentine.

3.2.1 Mineralogic alteration index (MAI)

3.2.1.1 Overview

The mineralogic alteration index was proposed by Browning et al. (1996) to quantify the relative progressive alteration of CM chondrites. It describes the alteration of cronstedtite to Mg-serpentine, which increases with progressive aqueous alteration. MAI values were allocated using electron microprobe data, and by estimating the average of phyllosilicate matrix composition in individual CM chondrites. CM matrix was defined in this scheme as the sum of the volumes of fine grained phases. Another two parameters were used: (i) the vol% of silicate minerals, which decreases with increasing aqueous alteration, and (ii) the vol% of chondrule alteration, which shows the progression of chondrule phyllosilicate production and increases with progressive alteration. Based on MAI values the CM chondrites are ranked by them (Browning et al., 1996) in the following sequence: Murchison ≤ Bells < Pollen ≤ Murray < Mighei < Nogoya < Cold Bokkeveld.

3.2.1.2 MAI determinations

Browning et al. (1996) suggested that progressive alteration of CM chondrites can be quantified by calculating the progress of Si and Fe^{3+} substitutions that allow and follow the transition from cronstedtite to serpentine. In these substitutions ferric Fe substitutes one tetrahedral ion of silicon and takes the octahedral site in the endmember cronstedtite structure. In order to describe the compositions of individual matrix of phyllosilicates, the general formula of stoichiometric phyllosilicate was employed as follows: (Fe^{2+}, Mg, Mn, Ca …)$_{3-x}$ (Al, Fe^{3+})$_x$ (Si_{2-x}(Al,Fe^{3+})$_x O_5(OH)_4$ and the total range of serpentine composition in the matrices of CM chondrite also shown by the formulae in Table 3.1. They also found that the mineral composition of phyllosilicates changes throughout the alteration process as a result of gradual replacement of cronstedtite ($Fe^{2+}{}_2Fe^{3+}(Si,Fe^{3+})_2O_5(OH)_4$) by Mg-rich serpentine ($Mg_3Si_2O_5(OH)_4$).

Mg-Bearing Members	Chrysotile Lizardite Antigorite	$Mg_3Si_2O_5(OH)_4$
Fe-Bearing Members	Cronstedtite	$Fe^{2+}{}_2Fe^{+3}(SiFe^{+3})O_5(OH)_4$
	Greenalite	$(Fe^{+2},Fe^{+3})_{2-3}Si_2O_5(OH)_4$
	Ferroan Antigorite	$(Mg,Fe,Mn)_3(Si,Al)_2O_5(OH)_4$
Intermediate Members	Amesite	$Mg_2Al(SiAl)O_5(OH)_4$
	Berthierine	$(Fe^{2+},Fe^{3+},Mg)_{2-3}(Si,Al)_2O_5(OH)_4$

Table 3.1 Serpentine formulae, after Zolensky and Mcsween (1988), taken from Browning et al. (1996)

As mentioned above, the relative percentage of isolated anhydrous silicates (olivine and pyroxene) in the matrices of CM chondrites was also used Browning et al. (1996) to estimate the progress of alteration. Their petrographic observations indicate that some areas of olivine grains have been etched during aqueous alteration and the phyllosilicate matrix was a secondary product of this process. As this kind of alteration is common in the matrices of CM chondrites, it is possible to use the modal proportion of anhydrous silicates in matrices, as measured using point counting, to estimate the relative degree of alteration. The correlation between the vol% of altered chondrules and the modal proportion of isolated matrix silicates shows consumption of anhydrous silicate and production of phyllosilicates during progressive alteration of CM chondrites. During the alteration process, further anhydrous phases are altered and new phyllosilicates are formed (Browning et al., 1996).

Browning et al. (1996) used oxygen isotope data from Nogoya and other meteorites that was published by Clayton (1993), Clayton and Mayeda (1984) and Rowe et al. (1994) respectively. Browning et al. (1996) compared the relative order of increasing CM alteration to the order of increasing $\delta^{18}O$ in CM samples, and this showed that Bells and Murchison, the least altered CM chondrites, contain the lowest values of bulk $\delta^{18}O$, whereas Cold Bokkeveld is a highly altered chondrite with the highest value of $\delta^{18}O$.

3.2.2 Numerical alteration sequence for CM chondrites (Rubin et al., 2007)

Rubin et al. (2007) proposed a numerical alteration sequence to rank CM chondrites into petrologic subtypes ranging from 2.6 (least altered) to 2.0 (most altered). The 2.0 subtype has been previously classified as a CM1 chondrite. In this scheme the main mineralogical and texture features of CM chondrites which vary with progressive alteration are correlated with petrologic subtypes. 11 CM chondrites with different degrees of alteration were examined by transmitted and reflected light microscopy and SEM. This scheme was designed to avoid the complicated algorithm applied to electron microprobe data to calculate MAI. Measurement numerical alteration sequence used a reflected light microscope to determine the abundance of metallic Fe-Ni, sulphide and silicates. It also utilized BSE imaging to approximate the abundance of PCP clumps, X-ray mapping to identify abundance of carbonate, electron probe to calculate the composition of PCP, and neutron-activation analysis (INAA) to analyze the trace element compositions of the least altered chondrites Murchison and QUE 97990, and highly altered chondrites QUE 93005 and MET 01070. The criteria used to develop this scheme were based on the presence of PCP clumps and alteration of glassy chondrule mesostases. A hypothetical meteorite with unaltered glassy chondrule mesostases and no PCP clumps would be classified as CM 3.0 (Rubin et al., 2007).

Rubin et al. (2007) found that the least altered CM2 chondrite examined is ***QUE 97990*** (CM2.6), which has 1 vol% Fe-Ni in chondrules and matrix. Glassy mesostases within chondrules are altered to hydrated phases, and mafic phenocrysts in areas near to the chondrules remain unaltered. It also contains 1-2 vol% of carbonates, 1.4 vol% of sulphides and 30 vol% serpentine-tochilinite intergrowths. ***Murchison*** is classified as CM2.5 and has contents of metallic Fe-Ni at 0.11 vol% within chondrules, mafic silicate phenocrysts remain unaltered, and glassy mesostases have been altered into hydrated

phases. It also contains 1-2 vol% Ca-carbonate, 0.55 vol% sulphide and a high abundance of PCP clumps. *Kivesvaara* is also assigned as a 2.5 CM chondrite and has 0.09 vol% metal within porphyritic chondrules and matrix, 0.54 vol% sulphide and about 25 vol% PCP. ***Murray*** is classified as a 2.4/2.5 chondrite and contains 0.16 vol% metallic Fe-Ni within porphyritic chondrules, 0.36 vol% sulphide; PCP and carbonates are also present. The ratio of FeO/SiO_2 in PCP in Murray is 3.3, which is greater than the ratio of FeO/SiO_2 in PCP of the least altered chondrites. Phenocrysts of mafic silicate within chondrules remain unaltered. Murray contains mesotases within chondrules that have been altered to hydrous materials. ***Y 791198*** is classified as a CM2.4 and contains metallic Fe-Ni at 0.27 vol% within chondrules and matrix, 12-15 vol% of Ca-carbonate, 1.4 vol% of pyrrhotite, and 30-40 vol% PCP. Mesostases within porphyritic olivine chondrules have been totally replaced by fine grained (<1μm) phyllosilicates. ***QUE 99355*** is not brecciated, and classified as CM2.3. It contains 0.34 vol% sulphide, carbonate and an abundance of PCP, and about 10-15% of phenocrysts of mafic silicate within chondrules that have been altered to hydrated materials. It contains also a very small amount of metal grains that remain unaltered. The ratio of FeO/SiO_2 in PCP is 1.8. ***Nogoya*** is CM2.2 has 0.09 vol% metal within prophyritic chondrules, 1.2% vol% sulphide and about 30 vol% PCP. It also has in some areas about 60% of PCP clumps, and some of the mafic silicate phenocrysts have been replaced by hydrous minerals. The ratio of FeO/SiO_2 in PCP is 1.7. ***Cold Bokkeveld*** is breccia. It has 0.24 vol% metal in porphyritic chondrules, and more than 90% of chondrules are free of metal. It contains Ca-carbonate, 0.64% of sulphide, and 30-40% vol% of PCP with a 1.2 ratio of FeO/SiO_2 ratio. About 15-20% of mafic silicates within chondrules have been replaced by hydrous minerals. ***QUE 93005*** is described as a highly altered CM2 chondrite and assigned to CM2.1. It is not breccia, and contains very little metallic Fe-Ni, less than 0.01 vol%. About 95-98% of mafic silicates within chondrules have been altered to hydrous minerals. Most of the chondrules are composed mainly of phyllosilicate and sulphide, however, some have small cores of olivine. This chondrite contains about 8 vol% of carbonate and 1.2 vol% of sulphide. The ratio of FeO/SiO_2 in PCP is 1.2, which is similar to the ratio of FeO/SiO_2 in PCP in Cold Bokkeveld. ***LAP 02277*** is not breccia, is classified as CM2.1, and all mafic silicate grains within it have been altered. It contains 2.4 vol% of sulphide, and metallic Fe-Ni is less than 0.01 vol%. Chondrule pseudomorphs are composed mainly of sulphides, phyllosilicates and opaque oxides. The ratio of FeO/SiO_2 in PCP is 1.2, and is equivalent QUE 93005 and Cold Bokkeveld. ***MET 01070*** is described as CM 2.0. It is not breccia and has no mafic silicate. This meteorite contains less than 0.01 vol% of metallic Fe-Ni, 2.8 vol% of sulphide, and about 3 vol% PCP (Rubin et al., 2007).

Chemical analyses by Rubin et al. (2007) reveal that PCP in highly altered chondrites (CM2.2-CM2.0) has higher concentrations of SiO_2, Cr_2O_3, TiO_2, MnO and CaO than in the least altered chondrites (CM2.6-CM2.3). Also Ca-carbonate minerals occur in the least altered CM chondrites CM2.6-CM2.3, and no complex carbonate minerals are found in Cold Bokkeveld CM2.2, but chemically complex carbonate minerals are present in QUE 93005 CM2.

Thus in summary, Rubin et al. (2007) found that CM chondrites record several changes with increasing aqueous alteration; during the intermediate stages of alteration changes occurred in matrix hydration, phyllosilicate formation, primary igneous glass within chondrules and PCP clump production (Rubin et al., 2007). Processes active during the alteration sequence caused metallic Fe-Ni oxidation, changes in mineralogy of carbonate, PCP composition and chondrule phenocrysts alteration. On the basis of this information, Rubin et al. (2007) subdivided CM chondrites into sub-types as shown in the following sequence: QUE 97990, CM2.6; Murchison, CM2.5; Kivesvaara, CM2.5; Murray, CM2.4/2.5; Y 791198, CM2.4; QUE 99355, CM2.3; Nogoya, CM2.2; Cold Bokkeveld, CM2.2; QUE 93005, CM2.1; LAP 02277, CM2.0; MET 01070, CM2.

3.2.3 Modal mineralogy of CM chondrites by X-ray diffraction (PSD-XRD) (Howard et al. 2009 and 2011)

Position Sensitive Detector X-ray Diffraction (PSD-XRD) has also been used to classify CM chondrites. 0.2 g samples were powdered for modal mineralogy. PSD-XRD was used to quantify phyllosilicate production by aqueous alteration of anhydrous Fe, Mg silicates. Howard et al. (2011) included the Antarctic CM finds for a whole petrographic range, from the least altered CM2 to highly altered CM1 that are equivalent to petrographic subtypes 2.6-2.0 proposed by Rubin et al. (2007). Howard et al. (2009, 2011) showed that CM2 chondrites have 13 to 31% olivine and pyroxene, and 67% to 82% phyllosilicates; whereas CM1 chondrites have 6 to 10% olivine plus pyroxene and 86 to 88% phyllosilicates.

As the secondary minerals have formed by alteration of minerals that had crystallized at high temperature (olivine and pyroxene), the ratio of total phyllosilicate to total high temperature phase (Fe, Mg silicates) represents the degree of hydration (Howard et al., 2009; Howard et al., 2011). Results of these modal mineralogy determinations revealed a sequence of CM chondrites in order of increasing of hydration as follows: QUE 97990 < Y

791198 < Murchison < Murray < Mighei < ALHA 81002 < Nogoya ≤ Cold Bokkeveld ≤ Essebi < QUE 93005 < ALH 83100 < MET 01070 < SCO 06043 (Table 3.2).

		Total anhydrous Fe, Mg silicate (%)	Total phyllosilicates (%)	Phyllosilicate/ anhydrous
QUE 97990	CM2	30.6	67	2.19
Y 791198	CM2	26.9	70.9	2.64
Murchison	CM2	23.4	72.5	3.1
Murray	CM2	22.8	74	3.24
Mighei (average)	CM2	20	74.6	3.74
ALHA 81002	CM2	19.7	77.6	3.94
Nogoya (average)	CM2	18.5	75.8	4.09
Essebi	CM2/C2 ung	16.5	74.5	4.52
Cold Bokkeveld (average)	CM2	16.4	77.4	4.87
QUE 93005	CM2	12.6	82.1	6.54
ALH 83100	CM2/1	9.4	86.7	9.23
MET 01070	CM1	7.6	87.5	11.48
MET 01070 (2)	CM1	7.6	87.5	11.4
SCO 06043	CM1	6.3	87.6	13.85

Table 3.2- Alteration degree and ratio of total phyllosilicate to high temperature Fe, Mg silicate (olivine plus pyroxene) (Howard et al., 2011)

Modal mineralogy also indicates that the minor contents of CM2 chondrites are 0.62-2.4% magnetite, 0-1.9% calcite and 0.6-3.65% sulphide. The modal mineralogy of CM1/2 and CM1 chondrites shows that they consist of 6-10% anhydrous Fe, Mg silicate, 86% - 88% phyllosilicates of which 61-66% is Mg-rich serpentine. Minor contents of CM1 chondrites are magnetite (1.6-1.8%), calcite (1.2-1.9%) and sulphide (1-2.7%).

In their alteration modal, Howard et al. (2011) concluded that Fe-rich-cronstedtite and tochilinite intergrowths (i.e. PCP) formed during early stages of aqueous activity as a result of rapid alteration of metal, iron-rich olivine and probably also amorphous iron-rich silicate. In early stages glassy mesostasis was altered to saponite. Chlorite grew as layers on serpentine because of mesostasis dissolution. Over time, iron-rich minerals were consumed, and so the formation of iron-cronstedtite stopped and a variety of Mg-rich components were altered to form phyllosilicate, and then iron-rich cronstedtite recrystallized to Mg-rich serpentine. During the middle stages of aqueous alteration tochilinite is consumed, and this can account for the absence of tochilinite in some CM1/2 and CM1 chondrites. Then, minute amounts of saponite crystallized with Mg-rich serpentine, since fluids were dominated by Mg, and were very fine-grained, amorphous and/or poor crystalline phyllosilicate formed during the late stages of aqueous alteration.

3.3 Kimura et al. ′s model (2011)

Kimura et al. (2011) used the abundance of Fe-Ni metal and alteration of silicates within chondrules to classify CM chondrites into three general alteration degrees. BSE imaging and microprobe analyses were mainly used to construct their model. They reported that the highly altered chondrites contain weakly altered volumes of metal with common alteration of mafic silicates in chondrules (e.g. Cold Bokkeveld; Nogoya); low abundances of metal and minor alteration of mafic silicates in chondrules are only recorded in the moderately altered CM chondrites (petrographic subtypes: 2.3-2.5), e.g. Murchison, Murray and QUE 99355. The least altered chondrites (petrographic subtypes 2.6) contain a moderate abundance of metal and preserved mafic silicates within chondrules (e.g. QUE 97990).

3.4 Petrologic subtypes of the CM chondrites studied

All samples studied (thin sections of Murchison, Murray, Pollen, Mighei, EET 96029, LON 94101, Nogoya, Cold Bokkeveld, QUE 93005, LAP 031166, SCO 06043 and ALH 88045) here have been compared against the previous classifications using petrographic observations and SEM point counting.

The abundance of Fe-Ni metal (Figure 3.1a) primary anhydrous Fe, Mg silicates and alteration products within chondrules (Figure 3.1b), and chondrule fragments were determined by SEM point counting to assess the degree of alteration of all samples studied that were unclassified previously. These samples are Mighei, LON 94101, EET 96029, LAP 031166 and ALH 88045. The criteria are based upon the fact that the Fe-rich silicates in CM chondrites are progressively lost with increasing of aqueous alteration (e.g. Howard et al., 2011). This fundamental trend was used also to track the affects of aqueous alteration on Fe-Ni metal and Mg-rich silicates. CM chondrites contain Fe-Ni metal within chondrule interiors or on their surfaces, and grains are also present isolated in phyllosilicate matrices. Some of these materials remain unaltered in spite of aqueous processes by which the CM chondrites have been altered, and this can be related to protection by enclosing silicates (Kimura et al., 2011).

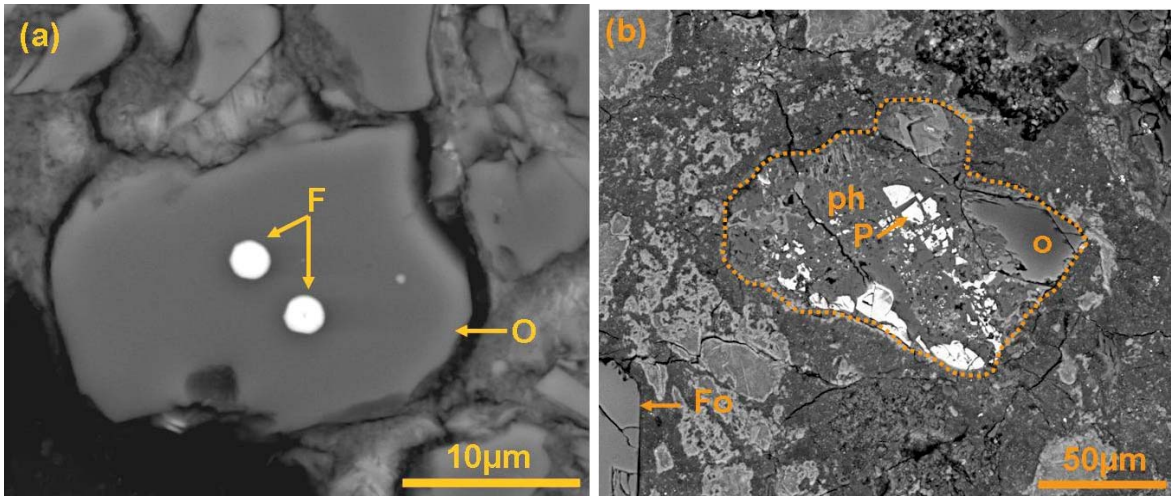

Figure 3.1- BSE images of Fe-Ni metal in CM chondrites.
(a) BSE image of Nogoya (CM2) illustrates the occurrence of Fe-Ni metal (F) within Mg-rich olivine (O) The location of this area in the sample studied is shown in appendix D7. (b) BSE image of LON 94101. The middle part shows large chondrule (150 µm) that has been nearly completely replaced by phyllosilicate (ph) and pentlandite (p); a small part of olivine (O) is unaltered. The left lower corner shows preserved Fe-rich olivine in the matrix (FO). The location of this area in the sample studied is shown in appendix D6. The degree of alteration of previously unclassified samples was determined using such petrographic observations.

Petrographic observations of the current study indicate that Fe-Ni metal occurs mainly inside Mg-rich olivine and as isolated grains within phyllosilicate matrix; Fe,Mg silicates within chondrules and chondrule fragments have been subjected to aqueous processes that have produced phyllosilicates. The abundance of these materials differs from chondrite to chondrite, and even from chondrule to chondrule within the individual meteorites.

The petrologic subtypes of all studied CM chondrites are shown in Table 3.3. This table was constructed from results of previous studies (i.e. Browning et al., 1996; Rubin et al., 2007; Howard et al., 2011) and petrographic observations and SEM point counting results of the current work.

	MAI Browning et al. (1996)**	Phyllosilicate /anhydrous Howard et al. (2011)**	Rubin et al. (2007)** and this work*	Fe,Ni metal*	Mafic phenocryst alteration*
Murchison	0.43	3.10	2.5**	<0.2%	Partly preserved
Murray	0.57	3.24	2.4/2.5**	<0.2%	Partly preserved
Pollen	0.53	-----	Low 2.4*	<0.2%	Very minor alteration of crystal edges
Mighei	0.77	3.74	2.3*	<0.2%	Slight
EET 96029	-----	-----	2.3*	<0.2%	Very minor alteration of crystal edges, nearly similar to Pollen
LON 94101	-----	-----	2.3*	<0.2%	Slight, more than Mighei
Nogoya	0.97	4.09	2.2/2.3*	<0.2% in 2.3 lithology	Part 1: the vast majority is altered Part 2: partly altered
Cold Bokkeveld	1.03	4.87	2.2**	<0.2%	The vast majority are replaced
QUE 93005	-----	6.54	2.1**	<0.2%	The vast majority are altered
LAP 031166	-----	-----	2.1/2.0*	<0.2%	Near complete altered to altered
SCO 06043	-----	13.85	2.0*	<0.2%	Very rare
ALH 88045	-----	-----	2.0*	<0.2%	Completely altered

Table 3.3- Alteration degree of studied CM chondrites.
It was inferred from previous studies (**) and petrographic observations of this work (*). All studied CM chondrites are assigned into petrologic subtypes (±0.1).

The petrographic observation and abundance of the components of each sample are described below in detail. In the following petrographic descriptions of CM chondrites studied, the term 'fine-grained matrix' is used for optically opaque phyllosilicate-rich matrix (<1 μm), and 'chondrule rims' is used for the fine-grained phyllosilicate rims to chondrules (<1 μm).

3.5 Murchison CM2.5

Murchison fell in Victoria, Australia (36° 37′ S., 145º 12′ E.) in 1969, September 28, 1045-1100 hours (Graham et al., 1985). The total mass of this meteorite is 100kg and the weight of largest stone is 7kg (Graham et al., 1985). Murchison is the biggest fall of the carbonaceous chondrites. This study used one thin section (P11449) of Murchison with

area of about 6mm^2, however this sample is representative as it contains carbonate grains (0.9 vol%) that are sufficient for this study. This thin section was obtained from the Natural History Museum (London). An image of a fragment of the Murchison is shown in Figure 3.2. The first study of this meteorite was carried out by Fuchs et al. (1973), showing it to be a breccia that contains xenolithic fragments as inclusions (Fuchs et al., 1973).

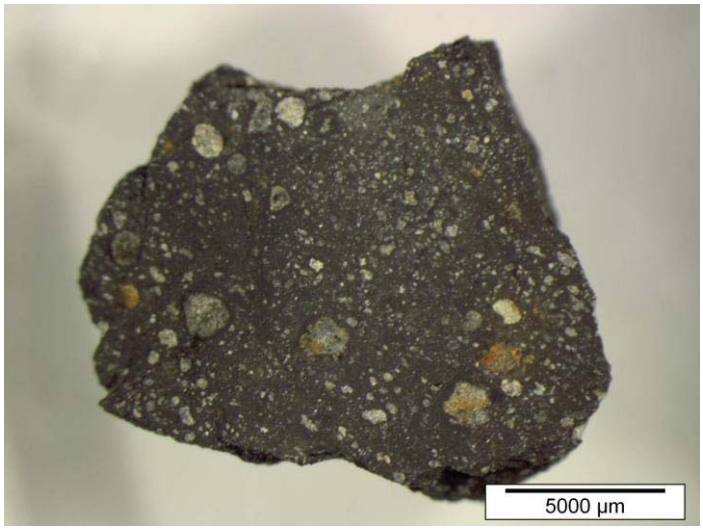

Figure 3.2- Image of a fragment of Murchison. Photograph of the sample was generously provided by Prof Martin Lee (personal collection).

3.5.1 Composition and mineralogy of Murchison

Petrographic observations show that Murchison consists of a fine grained (<1µm) matrix (Figure 3.3) within which phyllosilicate and tochilinite-cronstedtite intergrowths are dominant. It contains large Fe, Mg olivine grains (up to 150 µm); most of these grains are unaltered, but very rare Fe-rich olivine chondrules have been partially replaced by phyllosilicates. Some chondrules have fine grained (<1µm) rims that are free of tochilinite and Fe-sulphide. A little of the tochilinite is found as isolated assemblages in the fine-grained (<1µm) matrix. The Murchison matrix also contains scarce pyroxene. Fe-Ni metal is rare within Mg-rich-olivine chondrules and chondrule fragments, and in fine grained phyllosilicate matrix (<1µm). Rubin et al. (2007) reported that Murchison contains between 0.09-0.14 vol% of Fe-Ni metal. The chemical compositions in element wt% of Fe-Ni metal in chondrules and isolated grains in the matrix of Murchison was determined by Kimura et al. (2011) (Table 3.4). Their analyses showed that Fe-Ni metal inside chondrules has more Ni (+10 wt%) than in the fine-grained matrix (<1µm). Fe sulphide is commonly present within the fine grained matrix and encloses most of the Ca-carbonate grains and grains of Mg-rich serpentine. Carbonate minerals in Murchison are calcite and aragonite.

The abundance of high temperature phases (Mg, Fe silicates) and low temperature phases (secondary products) in Murchison was determined by SEM point counting (Table 3.5).

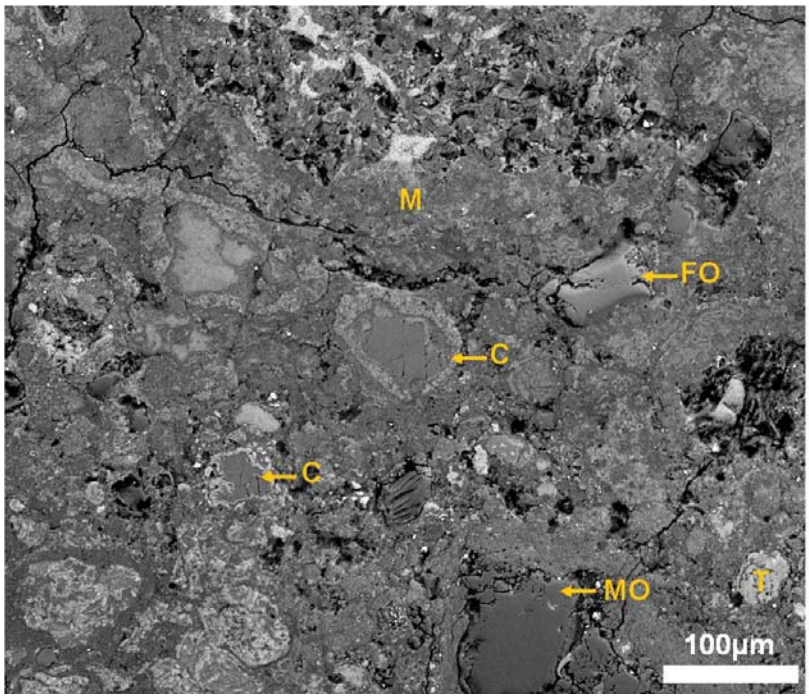

Figure 3.3- BSE image of Murchison matrix.
The image shows of very well preserved Fe-rich-olivine (FO) and Mg-rich-olivine (MO) fragments, phyllosilicate matrix (M), calcite grains (C) and tochilinite grains (T). The location of this area in the sample studied is shown in appendix D1.

	Occurrence	
Element wt%	**Isolated grains**	**Inside chondrule**
Si	b.d.	0.05
P	0.46	0.18
Cr	0.27	0.53
Fe	93.77	83.62
Co	0.27	0.21
Ni	5.03	15.21
Sum	99.79	99.80

Table 3.4- Occurrence and chemical composition in element wt% of Fe-Ni metal in Murchison, From Kimura et al. (2011).

Components		vol%
Fine-grained (<1μm) matrix		75.4
	Fe-sulphide	4.7
	Tochilinite	2.6
	Mg-rich serpentine grains rimmed with Fe-sulphides	2.2
	Mg-rich-olivine fragments	1.3
	Fe-rich-olivine fragments	1.3
	Pyroxene	1.3
	Ca-carbonate	0.9
Partly altered chondrules		5.2
Mg-rich-olivine chondrule		3.9
Chondrule rims		0.7
CI-like-clast		0.4

Table 3.5- Abundance in vol% of Murchison constituents as quantified by SEM point counting. Only 232 points were counted as the thin section of this sample is quite small.

3.5.2 Alteration degree of Murchison

Murchison was classified as a CM 2.5 by Rubin et al. (2007). It contains mafic silicate phenocrysts that remain unaltered and glassy mesostases that have been altered to hydrous phases (Rubin et al., 2007). Howard et al. (2011) found that Murchison contains 23.4% anhydrous Fe, Mg silicates and 72.5% of hydrous phyllosilicate, which is less than almost all other CMs studied (see Table 3.2). Murchison was described by Browning et al. (1996) as the least altered CM chondrite. Zolensky et al. (1993) found that Murchison contains 72 vol% of matrix and 1 vol% of chondrule rims. The sample used for this study shows the Murchison contains 75.4 vol% fine-grained matrix and 0.7 vol% of chondrule rims. Based on these data and the petrographic observations discussed above, Murchison is assigned as the least altered CM chondrite used in this study (CM2.5).

3.5.3 Chemical composition of the Murchison matrix

Zolensky et al. (1993) summarized the chemical composition of the matrix and chondrule rims in Murchison and other CM chondrites, as have McSween and Richardson (1977). Zolensky et al. (1993) found that the average compositions of the matrix (here called fine grained matrix (<1μm)) of carbonaceous chondrites is generally comparable with those published by McSween and Richardson (1977), but their analyses cannot be compared directly with each other, as the analyses of Zolensky et al. (1993) used a focused beam (the excited area was ~10μm) whereas the McSween and Richardson (1977) employed a defocused electron beam (100μm diameter) to acquire the analyses. Microprobe analyses of the Murray matrix (the same thin section) using focused and defocused beam are not

directly comparable, in particular for Fe, Si and Mg (wt%) (Zolensky et al., 1993). The analyses of Zolensky et al. (1993) and McSween and Richardson (1977) were presented as wt% oxides, and so these data were converted to element wt% for comparison with the current work. The average of their chemical analyses of the fine grained matrix (<1μm) and chondrule rims of Murchison, in wt% oxides and elements, are listed in Table 3.6. The analyses of the Murchison matrix show a close correlation, with an exception for Si and S (see Table 3.6). The data presented by McSween and Richardson (1977) display anomalous values of S in Murchison and some other chondrites, possibly related to abundance of Fe-sulphide within the fine grained (<1μm) matrix. The results of Zolensky et al. (1993) show that the composition of the fine grained matrix and chondrule rims in Murchison are similar to one another (±0.2 wt%), and also showed that Fe contents in fine grained (<1μm) matrix and chondrule rims are higher than Mg and Si contents.

	Zolensky et al. (1993)		McSween and Richardson (1977)
Oxides wt%	**Matrix**	**Rims**	**Matrix**
Na_2O	0.36	0.34	0.31
MgO	15.26	17.67	14.00
Al_2O_3	2.97	2.52	3.33
SiO_2	27.24	30.81	22.30
P_2O_5	0.35	0.40	--
S	2.26	2.07	3.42
K_2O	0.1	0.21	0.13
CaO	0.76	0.71	0.85
TiO_2	0.07	0.01	0.04
Cr_2O_3	0.37	0.39	0.31
MnO	0.19	0.22	0.18
FeO	33.43	32.74	33.4
NiO	2.67	1.52	2.05
Total	86.03	89.61	85.43
Elements wt%	**Matrix**	**Rims**	**Matrix**
Na	0.27	0.25	0.23
Mg	9.19	10.64	8.43
Al	1.56	1.33	1.75
Si	12.73	14.40	10.42
P	0.09	0.11	--
S	2.26	2.07	3.42
K	0.08	0.17	0.11
Ca	0.54	0.51	0.61
Ti	0.04	0.01	0.02
Cr	0.25	0.27	0.21
Mn	0.15	0.17	0.14
Fe	25.99	25.45	25.96
Ni	2.10	1.19	1.61
O	30.77	33.04	32.43
n	40	55	20

Table 3.6- Chemical composition of the Murchison matrices in oxides and elements wt% taken from Zolensky et al. (1993), and McSween and Richardson (1977).

The results of Zolensky et al. (1993) in element wt% were used to obtain the synthesized spectrum using INCA software. Mg and Fe peaks of this spectrum (Figure 3.4b) are closely comparable with Mg and Fe peaks in the EDS spectrum of mapped area in the Murchison section that was used for this study (Figure 3.4a). However, the EDS spectra (Figure 3.4 a-b) have higher peaks of Si than those of Mg and Fe, and higher peaks of Mg than peaks of Fe.

The concentration and distribution of Si, Mg, Fe, and Ca of small region (about 1mm^2) of Murchison matrix was qualitatively assessed using multi-element X-ray mapping (e.g. Figure 3.5). The map shows that Ca (green colour) is concentrated within small grains in the fine-grained (<1μm) matrix where the Ca-carbonate grains are present, and it is less uniformly distributed than other elements such as Si, Fe and Mg. The Mg (red colour) locates the Mg-rich olivine and the Fe (blue colour) characterizes the distribution of sulphides and Fe-Ni metal in the sample. The map shows also that elements including Si, Mg and Fe are equally concentrated within fine grained (<1μm) matrix and chondrule rims.

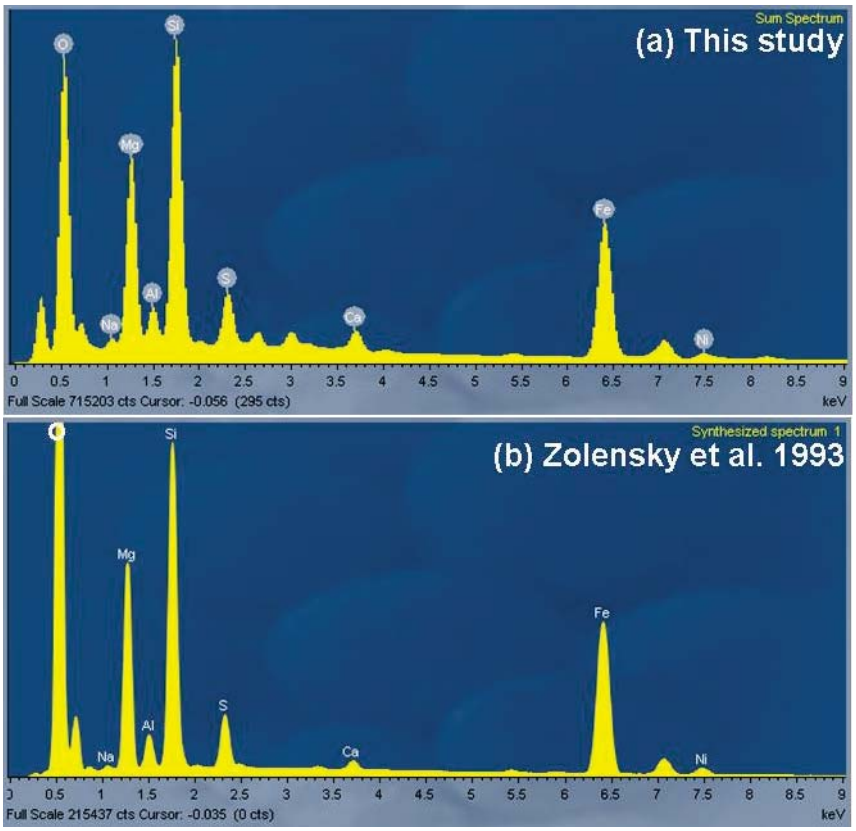

Figure 3.4- EDS spectra of the Murchison matrix.
(a) A spectrum of a small area of the Murchison matrix that has been element mapped, and is shown in Figure 3.5. (b) EDS spectrum constructed from Zolensky et al. (1993) analyses of Murchison matrices (the average of element wt% of chondrule rims and matrix). Note the peaks of Si in both spectra are higher than those of Fe and Mg. Relative peak heights are comparable between the two spectra (apart for O that cannot be reliably synthesised using the INCA software). Unidentified peaks are contaminants.

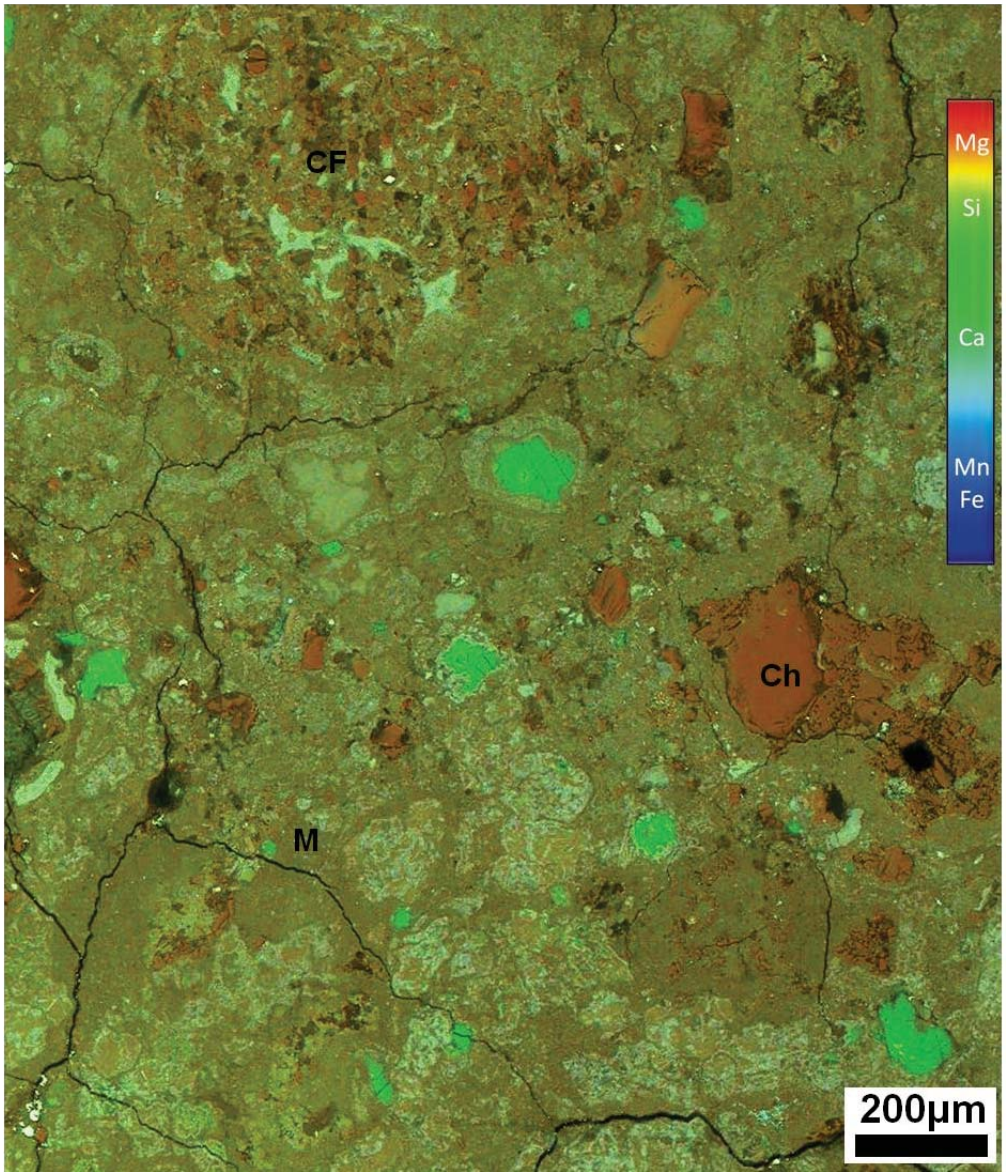

Figure 3.5- Combined elemental map of the matrix of Murchison.
False colour multi-element X-ray map of ~1mm^2 area of Murchison showing the relative concentration and distribution of Si, Fe, Mg and Ca. The colour scale is provided in the upper right part of the map. The high intensity of green colour overlays on Ca-carbonate grains; Mg is red and locates Mg-rich olivine. M is fine grained (<1µm) matrix, Ch is chondrule and CF is chondrule fragment. The location of this map in the sample studied is shown in appendix D1.

3.6 Murray CM2.4/2.5

The CM2 chondrite Murray fell in 1950, Sept. 20, 01:35, in Calloway County, Kentucky, U.S.A. (36° 36′ N., 88° 6′ W). The shower of fragments (e.g. Figure 3.6) landed nine miles east of Murray. The total weight recovered is 7kg, which was collected as several broken

fragments with the biggest piece 3.4kg. Subsequent collection of material yielded a total of 12.6kg (Graham et al., 1985). For this work one polished thin section (P13114) of Murray was obtained from the Natural History Museum (London). The total area of this thin section is approximately 102 mm^2.

Figure 3.6- Image of a fragment of Murray.
Collection No. B156.1 -A of the Murray fragment, its weight 6.944 gram.
From: www.historicmeteorites.com/HistoricMeteorites/M-Murray.html

3.6.1 Composition and mineralogy of Murray

Using PSD-XRD Howard et al. (2009) reported that Murray contains 49 vol% Fe-cronstedtite, 25 vol% Mg-serpentine, 17 vol% olivine, 5.6 vol% pyroxene, 1.8 vol% pyrrhotite and 1.4 vol% magnetite. Lee and Ellen (2008) reported that Murray contains 59.8 vol% fine-grained matrix, 13.2 vol% tochilinite and serpentine; it has also 13 vol% anhydrous silicate, sulphides and metal grains, 11.9 vol% pristine chondrules and 2.3 vol% Ca-carbonate grains.

About 2000 BSE images of the thin section were obtained for petrographic study of carbonates and other constituents. In the middle part of this section are two large rounded porphyritic Mg-rich olivine chondrules. The diameter of each chondrule is about 1mm. Both chondrules are composed of Mg-rich olivine grains and tochilinite, which is present between some of the olivine grains. Olivine within these chondrules contains grains of Fe-Ni ranging from 1-4 μm in size. Another two large chondrules are also present on the edge of the sample; they are elongate, approximately 1mm by 2mm in size. They are porphyritic olivine-pyroxene (POP) and porphyritic Fe-Mg olivine in which Mg and Fe olivine grains are welded to each other. Rare tochilinite was observed between the olivine grains in these chondrules, and it has partially replaced some of internal areas and margins of the Fe-rich olivine crystals. Other Mg-rich olivine chondrules and Mg-rich olivine fragments occur in most areas of the sample, and range in size from a few microns to up to 200 μm (Figure 3.7). Fe-rich olivine chondrules and Fe-rich olivine fragments are rarely present in the fine

grained (<1μm) matrix of this meteorite. The few Mg-rich olivine grains are zoned in their outer parts with high concentrations of Fe.

Murray contains both chondrule rims and a fine-grained matrix. The fine-grained matrix (<1μm) is slightly coarser than the chondrule rims. It mainly consisted of fine-grained phyllosilicates (<1μm) and Fe-sulphide and/or tochilinite-serpentine intergrowths. Fe-sulphides and tochilinite appear as individual clumps within the fine grained-matrix, are also found around calcite grains as partial rims or completely enclosing them, and as the groundmass of calcite aggregates. Fe-sulphides occur as small inclusions within Ca-carbonate grains, and as micro-veins in the phyllosilicate matrix. Murray contains Ca-carbonate including aragonite and calcite which are present (Lee and Ellen, 2008) as individual crystals; very rare pyroxene fragments, apatite grains, and grains and micro-veins of pentlandite also occur.

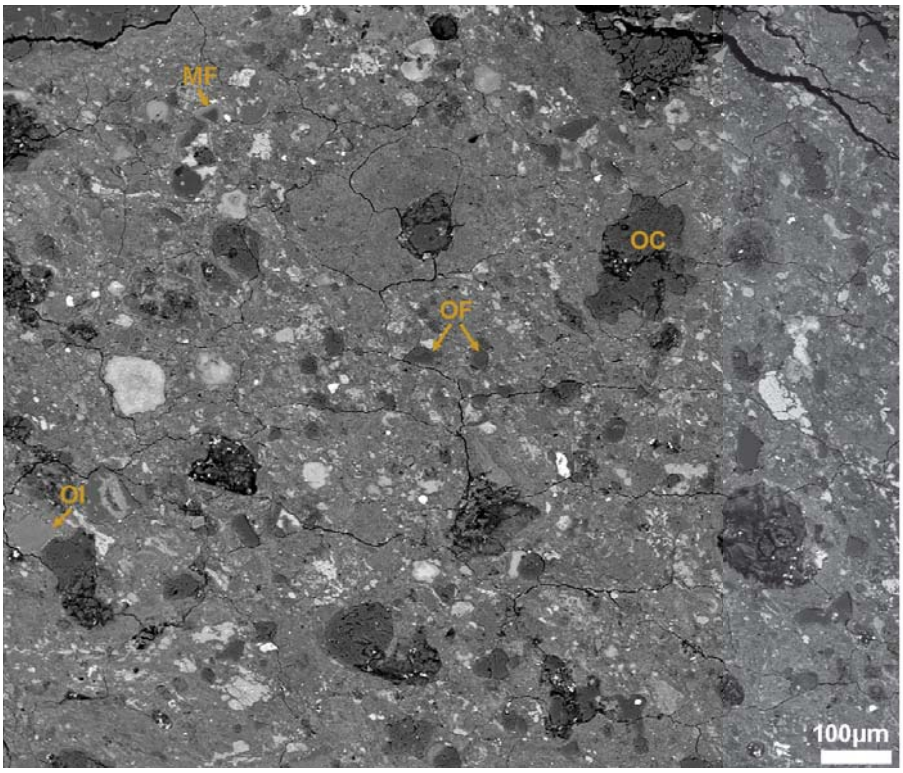

Figure 3.7- BSE image showing the occurrence of the high temperature materials in Murray. The materials including Mg-rich olivine chondrules (OC) and chondrule fragments (OF) within the fine grained (<1μm) matrix. Mg-rich olivine in this region is more abundant than Fe-rich olivine (OI). MF is Mg-olivine grain that is zoned with Fe in its margins. The location of this map in the sample studied is shown in appendix D2.

The chondrule rims in Murray are characterized by a very fine grain size (<~0.5μm) and absence of Fe-sulphides and tochilinite. They are found around most of the chondrule and chondrule fragments, and are also present as individual objects in the fine grained (<1μm)

matrix (Figure 3.8). The abundance of the constituents of Murray was determined by SEM point counting (Table 3.7). The high temperature phases including olivine aggregates, olivine fragments and other mineral grains represent 32.19 vol% of whole meteorite, whereas the low temperature materials including matrices, tochilinite and Ca-carbonate grains have a combined abundance of 61.37 vol%.

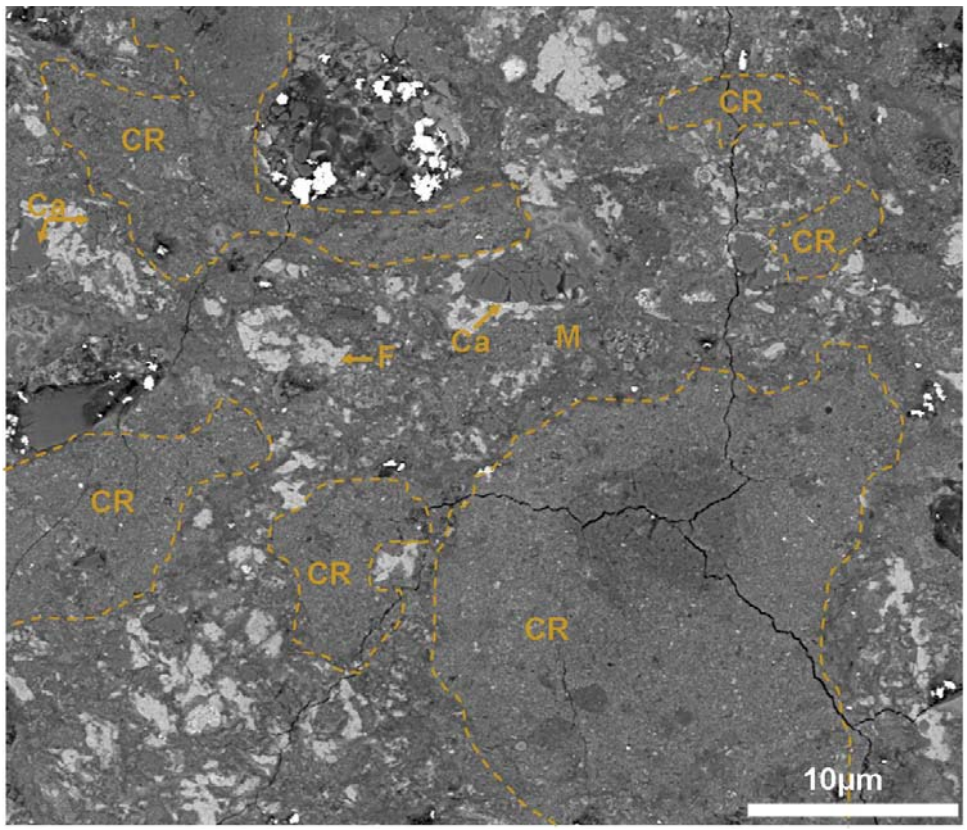

Figure 3.8- BSE image showing the textural difference between the fine grained matrix (M) and the chondrule rims (CR) in Murray.
F is Fe-sulphides, Ca is calcite, and both occur in the fine grained (<1µm) matrix. The location of this map in the sample studied is shown in appendix D2.

Component	Vol%
Fine grained (<1µm) matrix and chondrule rims	46.5
Ca-carbonate grains	1.9
Mg-rich olivine fragment	11.0
Fe-sulphides and Fe-Ni metal	6.4
Tochilinite	13.0
Other mineral grain	5.5
Preserved chondrules	15.7

Table 3.7- Abundance of the Murray components.
Values determined by SEM point counting. The total number of points counted is 420 over all area of the sample..

3.6.2 Alteration degree of Murray

Murray contains 22.8 vol% Fe, Mg silicates, 74.0 vol% phyllosilicates and, therefore, a phyllosilicate/Fe,Mg silicate ratio of 3.24 (Howard et al., 2011). Some early studies were carried out on the matrix of Murray (e.g. Wiik, 1956; Wood, 1967; McSween and Richardson, 1977; McSween, 1979). Murray is texturally a regolith breccia and has CM and C3 like clasts (Bunch and Chang, 1978). The current study shows that Murray contains CI-like clasts, and Lee and Ellen (2008) also reported that CI-like clasts in Murray. Chemical analyses of these CI-like clasts are presented in Table 3.9. Murray and Murchison are very comparable in the matrix characteristics (Bunch and Chang, 1978). Murray was described as partly altered by McSween (1979), Browning et al. (1996), and Howard et al. (2011) and was classified as more altered than Murchison by Browning et al. (1996) and Howard et al. (2011). Hanowski and Brearley (2001) concluded that Murray and Murchison are at the same stage of alteration. Murray was classified as a 2.4/2.5CM chondrite by Rubin et al. (2007).

Petrographic observations of Murray show that the vast majority of Mg-rich olivine chondrules and chondrule fragments are pristine. Very rarely are these materials slightly affected by aqueous alteration processes. Some of the Fe-rich olivine grains within porphyritic chondrules and chondrule fragments have been etched on their margins and their interiors have been replaced by Mg-rich serpentine and tochilinite (Figure 3.9a). Fe-Ni metal is only observed in Mg-rich olivine grains and fine grained (<1μm) matrix; most grains are intact (Figure 3.9b) but some are partly altered (Figure 3.9b). SEM point counting showed that Murray contains <0.2 vol% Fe-Ni metal. Rubin et al. (2007) reported that Murray contains 0.16 vol% metallic Fe-Ni that mainly occurs within mafic Mg silicates. Kimura et al. (2011) pointed out that the Fe-Ni metal in Murray ranges between kamacite and Ni-rich metal, and the contents of Ni in Ni-rich metal range from 3.7 to 6.8 wt%.

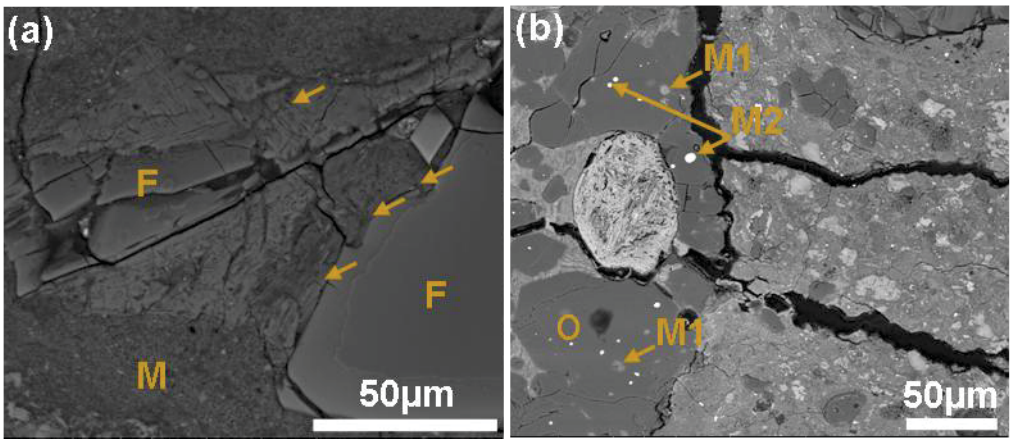

Figure 3.9- BSE images of olivine and Fe-Ni metal in Murray.
(a) BSE image showing Fe-rich olivine fragment (F) that has been partially replaced by Mg-rich serpentine (arrowed areas). (b) A part of large (2 mm) Mg-rich chondrule (O) that contains nodules of Fe-Ni metal that are near completely altered (M1) and intact (M2). The location of these maps in the sample studied is shown in appendix D2.

The degree of alteration of Murray is assigned to be 2.4/2.5 on the basis of these petrographic observations and data published by Rubin et al. (2007) and Kimura et al. (2011).

3.6.3 Chemical composition of Murray matrix

Microprobe analyses of Murray matrix in oxide wt %, were presented by McSween and Richardson (1977), and Zolensky et al. (1993) (Table 3.8). These analyses were converted into element wt% and are listed in Table 3.8. In this study, the Murray matrix was analysed by EPMA for fine grained (<1µm) matrix, and using the Zeiss Sigma SEM for both the fine grained matrix and chondrule rims. The analyses of the fine grained (<1µm) matrix show a very slight difference in elemental compositions from point to point in areas that are away from tochilinite and/or Fe sulphide clumps. The average analyses of the fine grained matrix that were obtained by EPMA show very good agreement with an average of the matrix analyses in Zolensky et al. (1993), with the exception of Fe and S contents that are higher in their analyses. This can be related to the occurrence of Fe-sulphides and/or tochilinite that varies from area to area within the fine grained (<1µm) matrix, and the analyses of the sample used in this work have been taken from areas that are free of these materials. The compositions obtained using the Sigma SEM are nearly identical to those acquired by McSween and Richardson (1977) (Table 3.8). The chemical analyses of Murray matrices indicate that these materials have high concentrations of Fe compared with Si and Mg. All analyses (i.e. Zolensky et al., 1993; McSween and Richardson, 1977; this work by Sigma SEM and EPMA) emphasise that the chemical compositions of the fine

grained (<1μm) matrix and chondrule rims (<1μm) are comparable to one another (± 1-1.5 wt%). These analyses also show that the Murray matrix contains less Mg and Si (about -3.5 wt%) than for Murchison.

	Sigma		EPMA	Zolensky et al. (1993)		McSween and Richardson (1977)
Oxides wt%	**Matrix**	**Rims**	**Matrix**	**Matrix**	**Chondrule rims**	**Matrix**
Na_2O	0.29 ± 0.07	0.25 ± 0.09	0.20 ± 0.08	0.72	0.50	0.24
MgO	12.84 ± 1.47	12.15 ± 1.68	12.13 ± 0.79	13.82	14.47	13.40
Al_2O_3	2.97 ± 0.69	2.97 ± 0.83	2.18 ± 0.13	3.11	3.05	3.88
SiO_2	24.08 ± 1.79	23.81 ± 1.94	25.47 ± 0.77	24.81	25.7	23.00
P_2O_5	0.34 ± 0.26	0.33 ± 0.34	0.13 ± 0.11	0.44	0.30	--
SO_2	3.99 ± 2.51	3.45 ± 1.83	0.47 ± 0.07	S= 3.23	S= 2.26	S= 2.40
K2O	0.08 ± 0.06	0.05 ± 0.03	0.05 ± 0.01	0.08	0.06	0.05
CaO	0.69 ± 0.28	0.75 ± 0.56	0.94 ± 0.67	1.00	0.62	0.75
TiO_2	0.07 ± 0.04	0.08 ± 0.06	0.08 ± 0.00	0.08	0.07	0.07
Cr_2O_3	0.34 ± 0.08	0.45 ± 0.19	0.43 ± 0.03	0.34	0.43	0.3
MnO	0.17 ± 0.05	0.22 ± 0.07	0.19 ± 0.04	0.22	0.23	0.16
FeO	32.39 ± 3.05	32.66 ± 5.57	32.86 ± 0.30	35.79	33.9	30.09
NiO	1.81 ± 0.51	1.98 ± 0.69	2.06 ± 0.05	2.25	2.56	2.04
Sum	80.06	79.16	77.19	85.89	84.16	80.65
n	10	30	2	30	65	20
Element wt%	**Matrix**	**Rims**	**Matrix**	**Matrix**	**Chondrule rims**	**Matrix**
Na	0.21	0.19	0.15	0.53	0.37	0.18
Mg	7.74	7.33	7.31	8.32	8.72	8.07
Al	1.57	1.57	1.15	1.64	1.60	2.04
Si	11.57	11.44	11.91	11.60	12.01	10.75
P	0.15	0.14	0.06	0.12	0.08	0.00
S	1.60	1.38	0.24	3.23	2.26	2.40
K	0.06	0.05	0.04	0.07	0.05	0.04
Ca	0.49	0.54	0.67	0.71	0.44	0.54
Ti	0.04	0.05	0.05	0.05	0.04	0.04
Cr	0.23	0.31	0.30	0.23	0.29	0.21
Mn	0.13	0.17	0.15	0.17	0.18	0.12
Fe	25.18	25.39	25.54	27.82	26.35	23.39
Ni	1.42	1.5	1.62	1.77	2.01	1.60
O	29.67	29.10	28.01	29.63	30.24	31.27
Sum	80.06	79.16	77.19	85.89	84.65	80.65

Table 3.8- The mean of chemical analyses of Murray matrices.
This table shows the comparison between data published by McSween and Richardson (1977), and Zolensky et al. (1993) and the current analyses that were obtained by EPMA and Zeiss Sigma SEM. These values are very similar to each other. Data presented as mean ± SD, error values are calculated to 1σ. The full dataset (analyses of EPMA and Sigma) with standard deviations is listed in appendix A.1.

A combined elemental map was obtained from a small region of Murray in which the constituents of high and low temperature phases are highlighted (Figure 3.10). This map shows high calcium concentrations in isolated areas corresponding to Ca-carbonate grains; calcium also appears in lower concentrations in a few areas where pyroxene fragments are

present. Mg was also used to locate olivine fragments and unaltered chondrules, and is dark red in the map. The map confirms that the fine grained (<1μm) matrix in Murray is dominated by Mg, Fe silicates. Some areas of chondrule rims show high concentrations of Mg in comparison with fine grained (<1μm) matrix. Mg, Si and Fe are uniformly distributed within the fine grained (<1μm) matrix in areas that are free of Fe-sulphide and tochilinite clumps.

An EDS spectrum of the mapped area is shown in Figure 3.10; it has a higher intensity peak for Si than Fe and Mg and confirms that the dominant materials in the Murray matrix are ferro-magnesium silicates. A synthesized spectrum of data in Zolensky et al. (1993) was also obtained from the average of elements wt% of the matrix and chondrule rims using INCA software for comparison with the present study (Figure 3.11). There is also higher peak of Si in the synthesized spectrum (Figure 3.11) than those of Mg and Fe. Apart for O, the two spectra are very similar. However, there are slightly higher peaks of S and Ca in the spectrum of the mapped area in Figure (3.10) than those in synthesized spectrum (Zolensky et al., 1993) as the spectrum was acquired from a small area that contains both phyllosilicates and other secondary products (e.g. calcite, tochilinite).

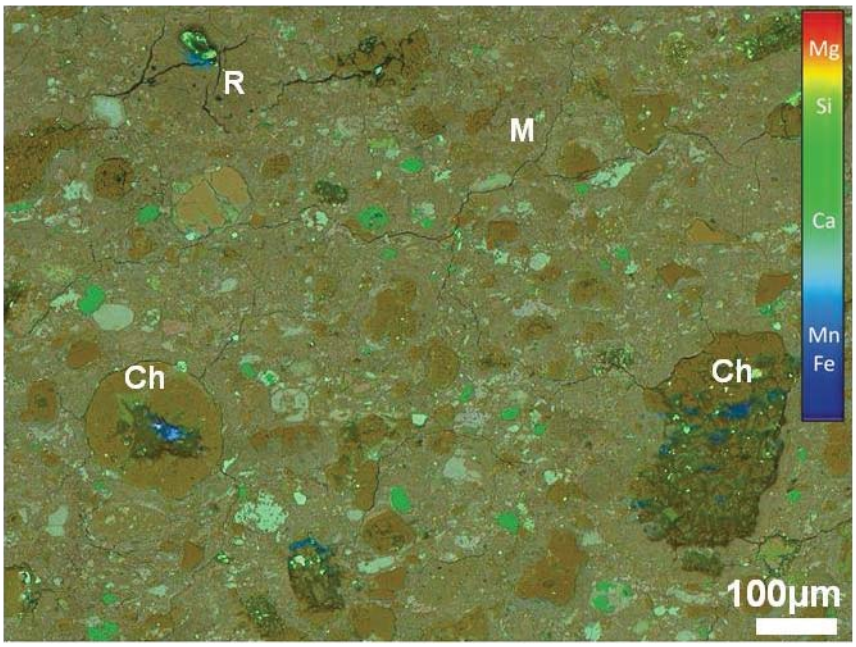

Figure 3.10- Elemental map of the Murray matrix.
Combined elemental map of small region ~1mm^2 of Murray showing the concentration and distribution of Si, Mg, Fe and Ca. In this map Ca (high intensity green colour) locates the Ca-carbonate and Mg (dark red) locates Mg-rich olivine. Note some areas of chondrule rims (R) are enriched in Mg (e.g. upper left part). M is fine grained (<1μm) matrix, Ch is chondrules. The colour scale is provided in the upper right part of the map. The location of this map in the sample studied is shown in appendix D2.

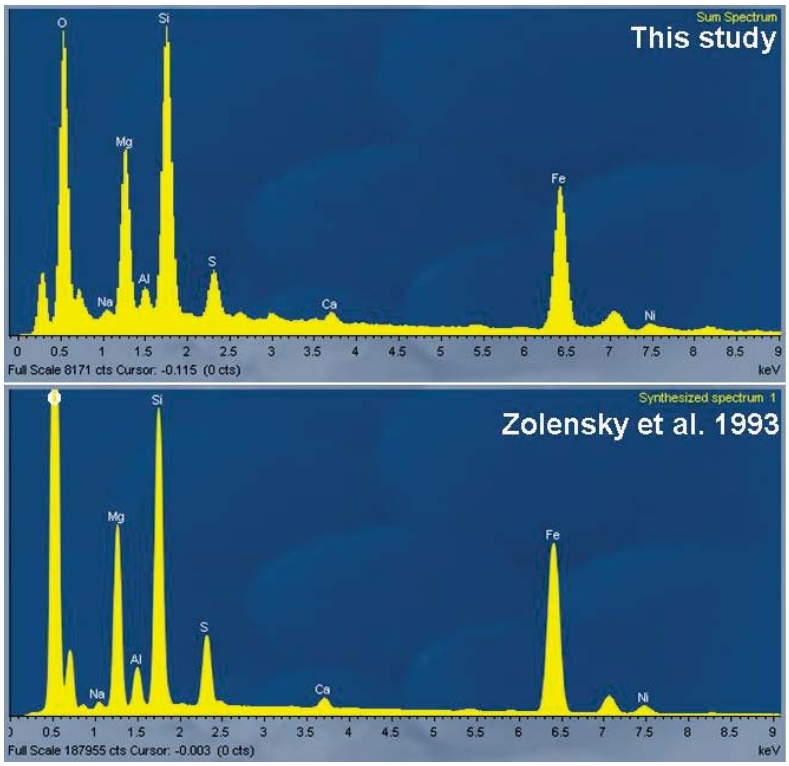

Figure 3.11- EDS spectra of the Murray matrix.
Upper spectrum is representative EDS spectrum from the mapped area in Figure 3.10, the lower spectrum was obtained from data of Zolensky et al. 1993. Relative peak heights are comparable between the two spectra (apart for O). Note Si peak in both spectra is higher than peaks of Fe and Mg.

The Zeiss Sigma SEM was used also to analyse CI-like clasts in Murray (Table 3.9). CI-like clasts contain more Mg and Si (+5 wt%) and less Fe (-5 wt%) than the fine grained (<1μm) matrix and chondrule rims (<1μm). This indicates that Mg increasing with the degree of aqueous alteration since CI chondrites are more highly altered than CMs.

Oxides wt%		Elements wt%	
Na_2O	0.22 ± 0.04	**Na**	0.16
MgO	17.67 ± 2.07	**Mg**	10.66
Al_2O_3	3.05 ± 0.01	**Al**	1.61
SiO_2	29.96 ± 0.79	**Si**	14.39
P_2O_5	0.19 ± 0.04	**P**	0.08
SO_3	5.32 ± 0.03	**S**	2.13
K_2O	0.08 ± 0.00	**K**	0.06
CaO	0.46 ± 0.06	**Ca**	0.33
TiO_2	0.01 ± 0.02	**Ti**	0.01
Cr_2O_3	0.48 ± 0.00	**Cr**	0.33
MnO	0.32 ± 0.05	**Mn**	0.25
FeO	25.10 ± 3.88	**Fe**	19.51
NiO	2.25 ± 0.24	**Ni**	1.77
Total	85.11	**O wt%**	33.82
n	2	2	--

Table 3.9- The average of the chemical analyses of CI-like clasts that are found in Murray.
These analyses were determined by Sigma SEM. Data presented as mean ± SD, error values are calculated to 1σ. The full dataset is listed in appendix A.1.

3.7 Pollen CM2.4

The CM2 chondrite Pollen fell in Norway (66° 20.9′ N., 14° 0.9′ E.), just a half metre from the finder, in 1942, April 6, 1900 hrs. The total mass of Pollen is 253.6g. The largest piece has dimensions of 7.8 cm, 5.3 cm and 5 cm, with a density of 2.574 g/cm^3. The shape of Pollen is multilateral and its boundaries are somewhat rounded It has a fusion crust 1mm in thickness (Wolff, 1963). For this work one polished thin section (P7249) of Pollen was obtained from the Natural History Museum (London), with a surface area of about 45 mm^2.

3.7.1 Composition and mineralogy of Pollen

About 1340 BSE images were acquired and were used to describe the petrographic composition of Pollen. The abundance of the Pollen constituents is listed in Table 3.10. The main component of Pollen is a fine-grained (<1μm) phyllosilicate-rich matrix that has been subdivided into two phases (Figures 3.12-3.13) based on texture and mineral composition. Phase I fine grained (<1μm) matrix contains phyllosilicate that is almost free of Fe-sulphide and tochilinite. Phase II is composed of a fine grained (<1μm) phyllosilicate matrix that includes Fe-sulphide and tochilinite clumps, and is slightly coarser grained. Rare blocky pentlandite is found in phase I and II matrices, and within chondrules. It occurs as individual grains, aggregate grains and veins. Fe-sulphide and tochilinite are intergrown with serpentine in fine grained matrix phase II and occur as rims around some of the calcite grains and all of the Mg-rich phyllosilicate grains. Pollen contains Fe, Mg silicates as fragments and aggregate grains in porphyritic olivine chondrules. All chondrules and some of chondrule fragments are surrounded by very fine-grained phyllosilicate matrix (chondrule rims (<1μm)) (Figure 3.13).

Pollen contains two CI-like clasts, 20 μm and 200 μm in size. They consist of very fine phyllosilicates (<1 μm). The larger clast contains patchy with Fe-sulphide grains and nodules of clay-like minerals, and contains four subhedral calcite grains.

About 700 carbonate grains were located in the Pollen thin section. They are embedded within the phyllosilicate matrix and range in size from 1 μm to 50μm, with most of these grains being in several forms, either subhedral, anhedral or subrounded. Carbonate grains in Pollen are the aragonite and calcite. Mg-rich phyllosilicate has partly or totally replaced many calcite grains and inherited their structural details such as iron sulphide inclusions,

grain outlines and tochilinite rims. The vast majority of these pseudomorph structures are only observed within phase II matrix.

Constituents	(vol%)
Fine grained (<1µm) matrix phase II	52.9
Serpentine-tochilinite intergrowths	6.8
Tochilinite grains and tochilinite rims	6.3
Olivine fragments	4.5
Mg-phyllosilicates pseudomorphism	3.2
Fe-sulphide grains	2.5
Ca-carbonate grains	2.0
Pyroxene fragments	0.5
Fine grained matrix phase I and chondrule rims	17.0
Preserved chondrules	3.7
Chondrule fragments	0.9

Table 3.10- Abundance of the Pollen components.
Values determined by SEM point counting. The total number of points counted was 793 over all area of the sample.

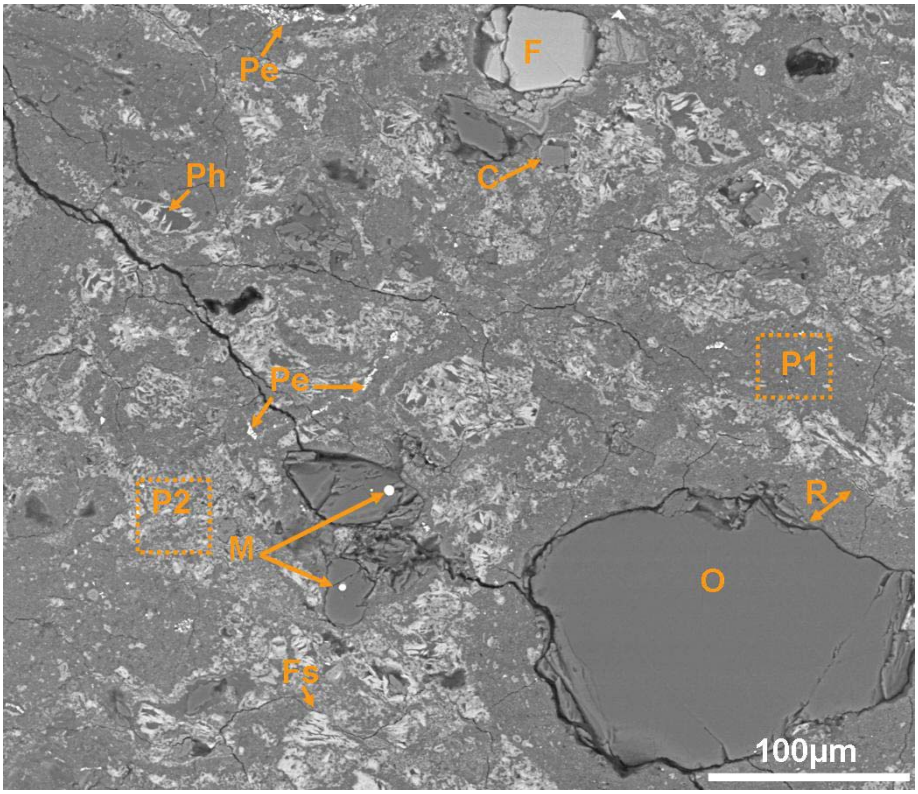

Figure 3.12- BSE image showing the main constituents of Pollen.
The constituents are Mg-rich olivine (O), Fe-rich olivine (F), Fe-Ni metal (M), Fe-sulphides (Fs), pentlandite (Pe), chondrule rims (R), fine grained matrix phase I (P1), fine grained (<1µm) matrix phase II (P2), calcite (c) and Mg-rich phyllosilicate pseudomorphs (Ph). The location of this map in the sample studied is shown in appendix D3.

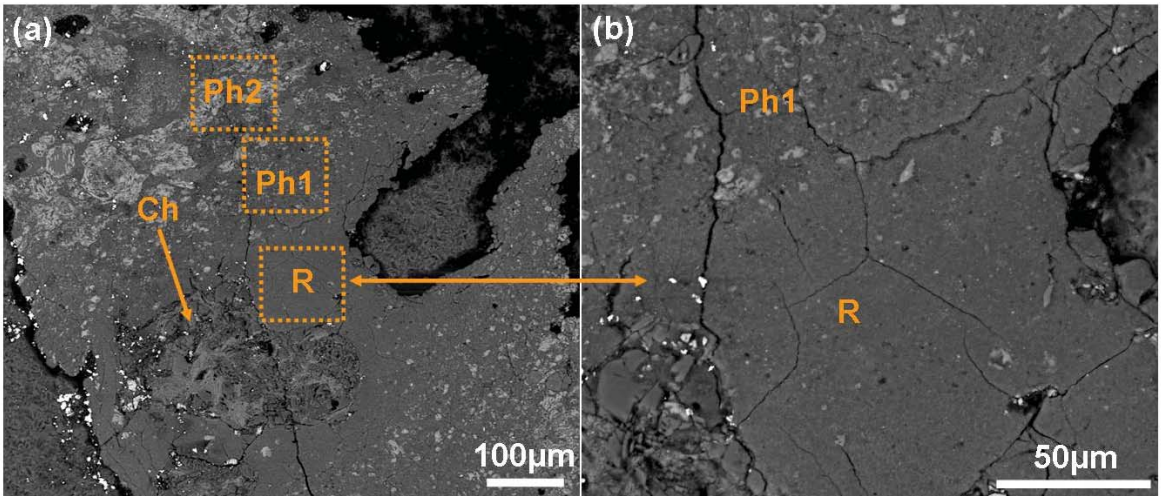

Figure 3.13- BSE images of matrix textures in Pollen.
(a) Displays the variation in texture of Pollen matrix. R is very fine grained (<1µm) matrix (chondrule rims), Ph1 is fine grained (<1µm) matrix (phase I) that contains patches of Fe-sulphide, Ph2 is fine grained matrix phase II that is dominated by iron sulphides (bright areas), Ch is a chondrule that contains inter-chondrule tochilinite (gray areas). (b) BSE image of the small region in image (a) at high magnification showing the difference in texture between the fine grained matrix phase I (Ph1) and chondrule rims (R) that look finer. The location of this map in the sample studied is shown in appendix D3.

3.7.2 Alteration degree of Pollen

Pollen is partially altered (McSween, 1979). Wood (1967) ranked it as less altered than Mighei and more altered than Murray. Using the MAI, Browning et al. (1996) classified Pollen as less altered than Mighei and Murray or similar to Murray, and more altered than Murchison and Bells.

The alteration degree of Pollen was estimated using BSE imaging of several areas of the sample under the same conditions (i.e. working distance, vacuum mode (high), brightness, contrast) to identify the effect of aqueous alteration on Fe, Mg silicates. The abundance of Fe-Ni metal (< 0.2 vol%) inside chondrules and within fine grained (<1µm) matrix was determined by SEM point counting. Fe-Ni metal grains inside some chondrules are etched on their margins (Figure 3.14). The vast majority of mafic phenocryst (Fe, Mg silicates) within chondrules and matrix are preserved; however, some of the isolated Fe-rich olivine grain fragments and grains within chondrules contain small volumes of alteration products, including serpentine and tochilinite (Figure 3.15).

Since Pollen contains rare secondary products within some chondrules and on the margins of Fe, Mg silicate fragments, and also contains <0.2 vol% Fe-Ni metal, its alteration degree is estimated to be slightly less than 2.4 on the scale of Rubin et al. (2007).

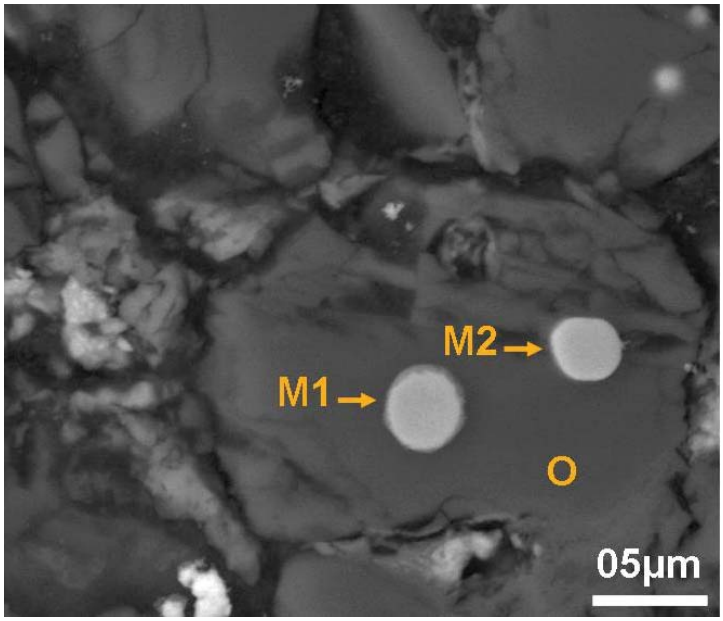

Figure 3.14- BSE image of Fe-Ni metal in Pollen.
The image shows Mg-rich-olivine (O) that contains two grains of unaltered Fe-Ni metal (M2) and (M1) and is rimmed by alteration products. The location of this map in the sample studied is shown in appendix D3.

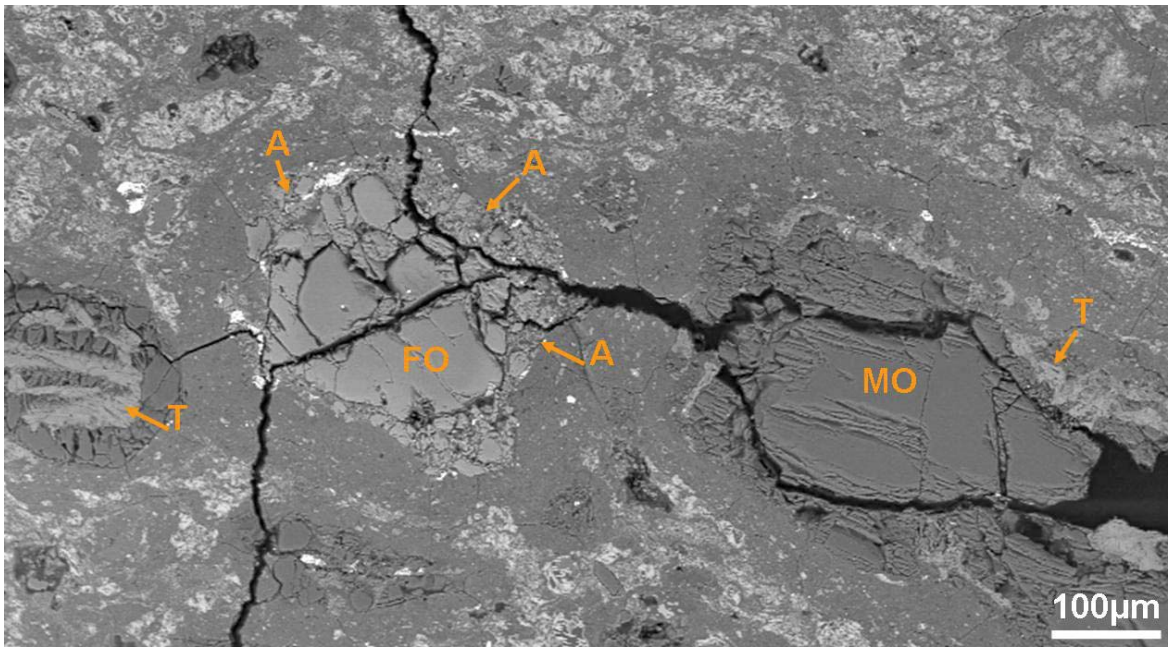

Figure 3.15- BSE image of chondrules in Pollen.
The image shows two large chondrule fragments (250 and 300m), unaltered Mg-olivine (MO) that is surrounded by tochilinite (T), and Fe-olivine (FO) in which the outer part (A) has been partly replaced by phyllosilicate. The location of this map in the sample studied is shown in appendix D3.

3.7.3 Chemical composition of Pollen matrix

Microprobe analyses of Pollen matrix, in oxide wt%, and of the matrices of other carbonaceous chondrites were reported by McSween and Richardson (1977). The means of their chemical analyses are presented in Table 3.11. These results have been converted to element wt% to enable reconstruction of the EDS X-ray spectrum of elements including Si,

Fe, Mg, S, Mn, Na, Ni and Ca, for comparison with this study (Figure 3.17). Their results show that Pollen matrix contains high concentrations of Si compared to Fe and Mg. Chemical analyses of low temperature phases include Phase I and II matrices, and CI-like clasts, were acquired using the Zeiss Sigma SEM and are listed in Table 3.12. These results reveal that fine grained (<1μm) matrix phase II is enriched in Fe, whereas the fine grained matrix phase I and chondrule rims have lower concentrations of Fe. Analyses of fine grained matrix (phase II) using the Zeiss Sigma SEM shows a very good agreement with analyses of Pollen matrix by McSween and Richardson (1977). CI-like clasts in Pollen contain less Fe (-3.47 wt%) than CI-like clasts in Murray (see Table 3.8). EPMA analyses of the fine grained matrix in Murray and Pollen (phase II) indicate that high contents of Fe (~+3.0 wt%) are found in the fine grained matrix phase II of Pollen since it is enriched in Fe-sulphides and tochilinite. The microanalyses using Zeiss Sigma SEM also indicate that the matrix (including chondrule rims and fine-grained matrix) of Pollen has slightly more Mg than Murray matrix.

Oxides wt%		**Elements wt%**	
Na_2O	0.46	**Na**	0.34
MgO	15.50	**Mg**	9.30
Al_2O_3	2.00	**Al**	1.05
SiO_2	24.10	**Si**	11.12
SO_3	6.53	**S**	2.61
K_2O	0.13	**K**	0.10
CaO	0.40	**Ca**	0.28
TiO_2	0.09	**Ti**	0.05
Cr_2O_3	0.30	**Cr**	0.20
MnO	0.19	**Mn**	0.15
FeO	29.80	**Fe**	23.16
NiO	1.97	**Ni**	1.54
Total%	81.47	**O**	28.50
n	**20**		

Table 3.11- Average Microprobe analyses of Pollen matrix (McSween and Richardson, 1977). These chemical analyses (wt% oxides) have been converted to element wt%.

	Sigma			EPMA	
Oxides wt%	**Chondrule rims and fine grained matrix phase I**	**Fine grained matrix phase II**	**CI-Like-clast**	**Chondrule rims and fine grained matrix phase I**	**Fine grained matrix phase II**
Na_2O	0.44 ± 0. 15	0.31 ± 0.14	0.50 ± 0.03	0.35 ± 0.06	0.17
MgO	18.71 ± 1.50	16.01 ± 2.23	21.14 ± 1.72	19.47 ± 1.06	12.40
Al_2O_3	2.13 ± 0.37	2.51 ± 0.30	2.59 ± 0.68	2.16 ± 0.38	2.36
SiO_2	30.45 ± 1.36	27.38 ± 3.28	33.92 ± 2.78	32.26 ± 1.90	25.33
SO_2	4.61 ± 1.22	6.2 ± 3.17	3.93 ± 0.50	0.54 ± 0.34	0.55
K_2O	0.09 ± 0.04	0.07 ± 0.03	0.17 ± 0.09	0.08 ± 0.01	0.05
CaO	0.71 ± 0.39	0.46 ± 0.28	0.33 ± 0.22	0.51 ± 0.15	0.27
TiO_2	0.09 ± 0.04	0.07 ± 0.08	0.06 ± 0.05	0.10 ± 0.01	0.09
Cr_2O_3	0.50 ± 0.10	0.26 ± 0.11	0.38 ± 0.05	0.48 ± 0.04	0.22
MnO	0.25 ± 0.06	0.25 ± 0.04	0.26 ± 0.06	0.24 ± 0.04	0.24
FeO	19. ± 2.09	29.9 ± 6.94	16.3 ± 0.99	20.64 ± 1.95	37.14
NiO	1.89 ± 0.50	1.45 ± 0.45	1.57 ± 0.40	1.33 ± 0.82	0.76
Total%	79.25	84.87	81.14	78.16	79.57
Elements wt%:					
Na	0.33	0.23	0.37	0.26	0.13
Mg	11.27	9.65	12.75	11.74	7.48
Al	1.12	1.32	1.37	1.14	1.25
Si	14.23	12.8	15.86	15.08	11.84
S	1.81	2.48	1.57	0.22	0.22
K	0.08	0.06	0.14	0.06	0.04
Ca	0.51	0.33	0.23	0.36	0.19
Ti	0.05	0.04	0.04	0.059	0.06
Cr	0.34	0.18	0.26	0.32	0.15
Mn	0.19	0.20	0.20	0.18	0.18
Fe	14.88	23.29	12.67	16.04	28.87
Ni	1.49	1.14	1.23	1.04	0.60
O	32.72	33.15	34.45	31.66	28.5
n	55	9	3	4	1

Table 3.12- Average microprobe analyses of Pollen matrices and CI-like clasts.
The analyses were acquired by the Zeiss Sigma SEM and EPMA. Data presented as mean ± SD, error values are calculated to 1σ. The full dataset with standard deviations is listed in appendix A.2.

Elemental mapping of Pollen was carried out to obtain qualitative analyses of its matrix and to image the distribution of elements within it. Every element is assigned to a specific colour and has been combined with the electron image to identify its distribution and concentration throughout the sample or within a particular area. A small region of Pollen which contains both low and high temperature phases was mapped (Figure 3.16). Results of X-ray mapping are consistent with quantitative analyses and petrographic observation that show that the fine grained (<1μm) matrix phase I and chondrule rims have relatively high concentrations of Mg.

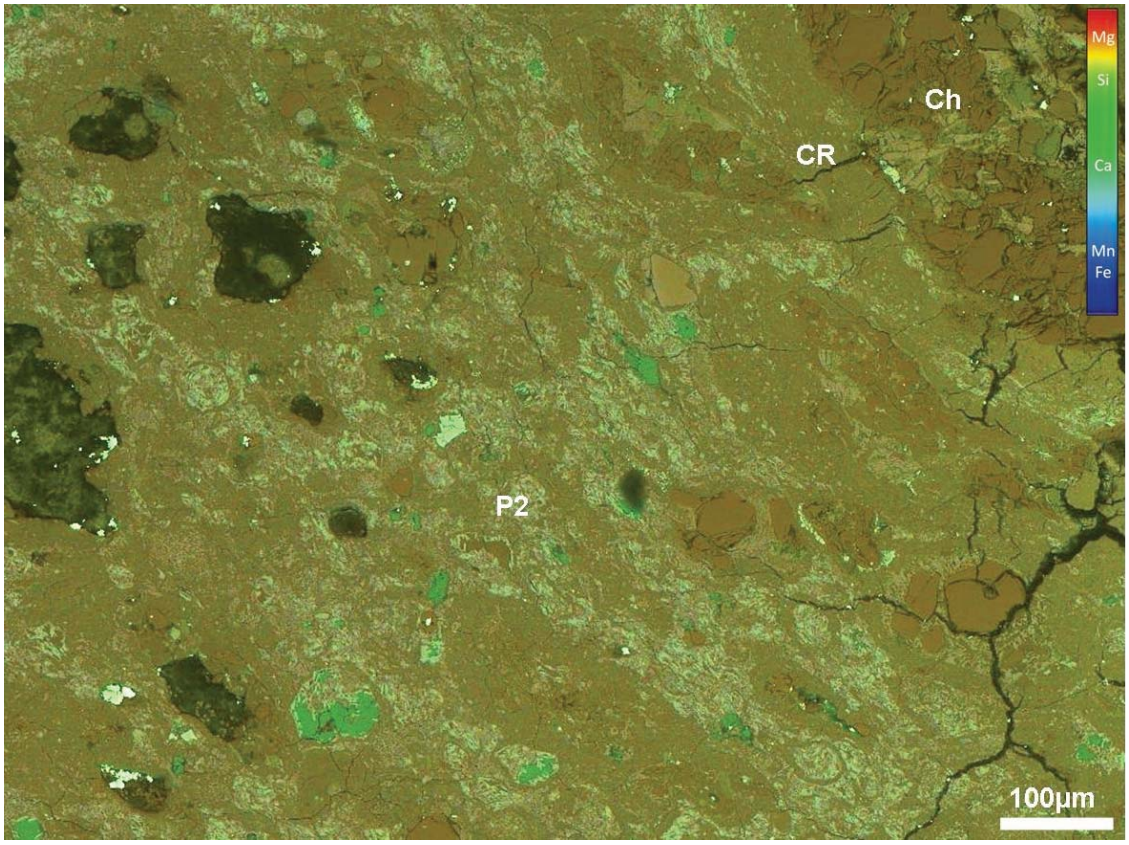

Figure 3.16- False colour multi-element X-ray map with associated colour scale of a small region of Pollen.
The map shows the distribution and concentration of elements including Fe, Si, Mg, Ca and Mg. The high concentration of Mg (dark red areas) overlays on chondrules (Ch) and chondrule fragments as most of these materials contains well preserved Mg, Si silicates. The high intensity green colour locates the Ca-carbonate grains. CR is chondrule rims, P2 is fine grained (<1µm) matrix phase II. Black areas are holes and fractures. The location of this map in the sample studied is shown in appendix D3.

EDS spectra of the mapped area in Figure 3.16 and of data of McSween and Richardson (1977) (synthesized spectrum) of Pollen show a close alignment between Mg peaks, whereas S and Fe peaks of the synthesized spectrum are slightly higher than in the spectrum of mapped area (Figure 3.17). However, both spectra show high peaks of Si relative to the peaks of Mg and Fe. The spectrum of Pollen matrices (this study) was correlated with spectrum of Murray (also this study), and this indicates that the matrix of Pollen contain more Mg and less Fe than the Murray matrix.

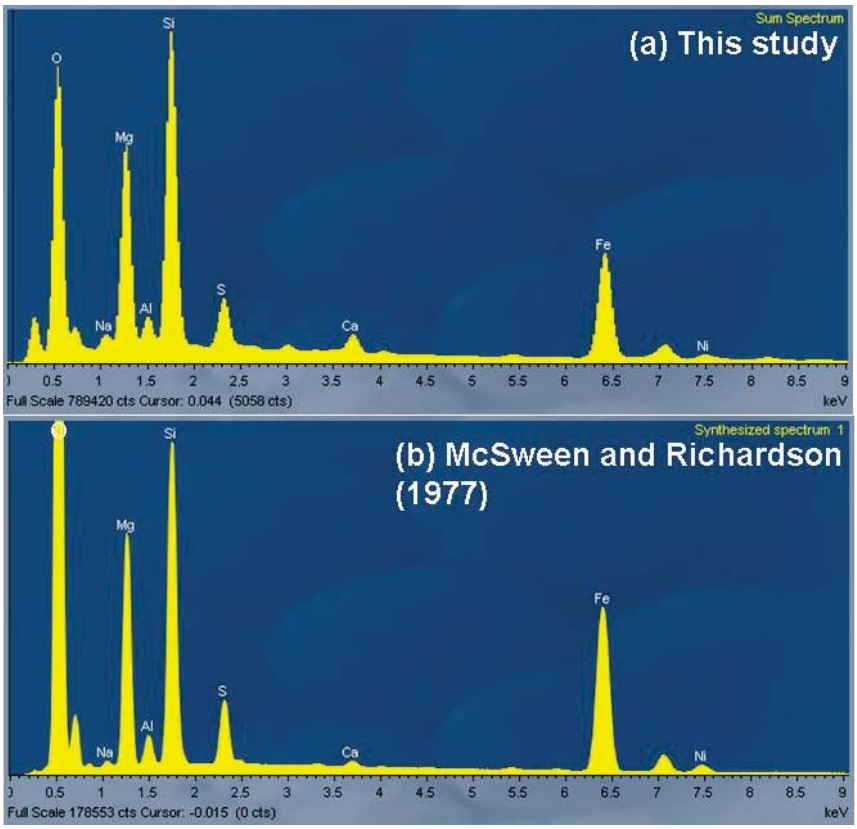

Figure 3.17- EDS X-ray spectra of Pollen matrix.
(a) EDS spectrum of a mapped small region in Pollen (Figure 3.16). (b) Synthesized spectrum of McSween and Richardson´s data (1977) of Pollen matrix, obtained by uploading values of elements wt% into INCA software and then the spectrum was synthesized. Note that Si peaks in the two spectra are higher than those of Mg and Fe. Relative peak heights are comparable between the two spectra (apart for O).

3.8 Mighei CM2.3

Eight kilograms of the CM2 carbonaceous Mighei was observed to fall near to the Mighei village, in Olviopol, Kherson, Ukraine, USSR (48º 4´ N., 30º 58´ E), in 1889, 18th June, 08 hr 30 min (Graham et al., 1985). It fragmented into several pieces shortly after its fall. Currently these fragments are housed in various meteorite collections (Vdovykin, 1973). A piece of Mighei is shown in Figure 3.18. One thin section of Mighei (P7253) was provided by the Natural History Museum in London. The area sectioned is elongate in shape and has an area of about 96 mm^2.

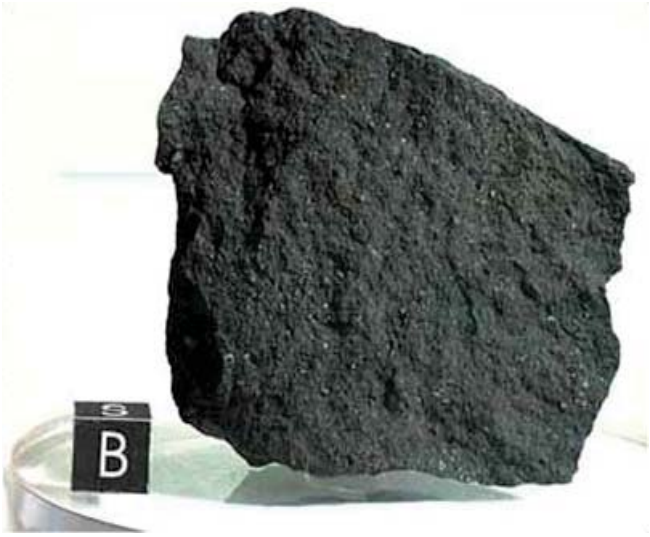

Figure 3.18- Image of Mighei fragment.
The source of the image: http://www.meteorites.ru/menu/description-e/mighei-e.html

3.8.1 Composition and mineralogy of Mighei

Vdovykin (1973) described Mighei as a stony meteorite that has extraterrestrial organic compounds and H_2O combined with Mg silicates. He classified its structure as chondritic and is composed of low and high temperatures phases that are distributed throughout the rock in the same proportions. His petrographic observations showed that the high temperature phases are mainly olivine, pyroxene, Fe-Ni metal, pentlandite, chromite, troilite, magnetite and glass.

Euhedral pyroxene is present within chondrules. Some chondrules are composed mainly of pyroxene, or pyroxene and olivine. The low temperature phases consist of chlorite-serpentine phyllosilicates, carbonates, sulphates and low temperature glass (Vdovykin, 1973).

About 1060 BSE images were acquired to investigate the petrographic relationships of low and high temperatures phases. In common with the least altered CM2 chondrites, the main constituents of Mighei are Fe, Mg silicates and phyllosilicates.

The matrix of Mighei tends to be coarser and more fractured than the matrices of Murchison, Murray and Pollen. Mighei has a fine grained (<1μm) matrix and chondrule rims (<1μm). The fine grained matrix is characterized by abundant of Fe-sulphide (Figure 3.19). Fe-sulphide is present as rims around grains of other minerals such as calcite and olivine, and/or as inclusions within calcite grains. It is also intergrown with tochilinite as fibers and in very rare cases with clay minerals. In this chondrite, some chondrule rims

have two layers that are different in texture and mineralogy. The innermost is mostly comprised of Fe-Ni metal that contains patches of tochilinite, and the second layer is fine grained (<1μm) phyllosilicate (Figure 3.20). Pieces of the chondrule rims are also observed in the fine grained matrix as large fragments (200μm by 400μm). Mighei contains four clasts within the fine grained (<1μm) matrix; two are CI-like clasts (~100μm in size) and two others are highly altered CM2-like clasts (~150μm in size).

The high temperature phases consist of chondrules and chondrule fragments that comprise aggregates of olivine and/or pyroxene. Chondrules are abundant in this section and range in size from hundreds of microns up to 1.5 mm. The majority of these chondrules are porphyritic olivine, and Mg-rich olivine grains are dominant. The abundance of tochilinite differs from chondrule to chondrule, so that some chondrules are free of tochilinite and others contain it in abundance. In some cases grains of Fe-Ni metal are scattered within the porphyritic chondrules, and are mainly contained in Mg-rich olivine. Fe-rich olivine is also present as aggregates in chondrules, and as fragments within the fine grained (<1μm) phyllosilicate matrix. These fragments range in size from a few microns to ~0.5mm. Fe-rich olivine has been more affected by aqueous alteration than Mg-rich olivine. Pyroxene fragments are rare within the phyllosilicate matrix and occur as individual grains and fragments enclosed within tochilinite. Three crystals of spinel were found and are together enclosed by tochilinite. Pentlandite crystals are found within the fine grained matrix in different shapes including euhedral, rounded and elongated, and have a grain size ranging from less than 1 micron to about 100microns. The Ca-carbonates aragonite and calcite are present as isolated grains in the fine grained matrix. The abundance of high and low temperature phases was determined by SEM point counting and is listed in Table 3.13.

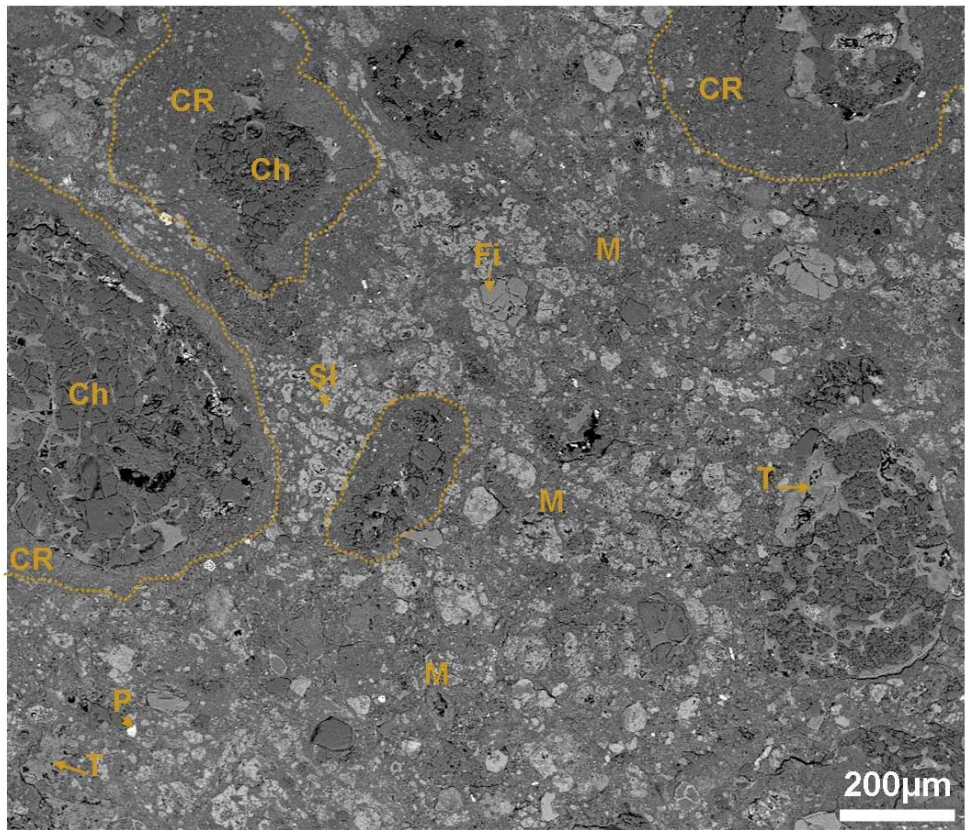

Figure 3.19- BSE image showing the constituents of Mighei.
Ch are porphyritic chondrules containing Mg-rich olivine and/or Fe-rich olivine (Fi) grains and interachondrule tochilinite (T). Note the difference in texture between chondrule rims (CR) and fine grained (<1µm) matrix (M). The fine grained matrix contains abundant of Fe-sulphide (SI) and tochilinite (T) and rare fragments of pentlandite (P). The location of this map in the sample studied is shown in appendix D4.

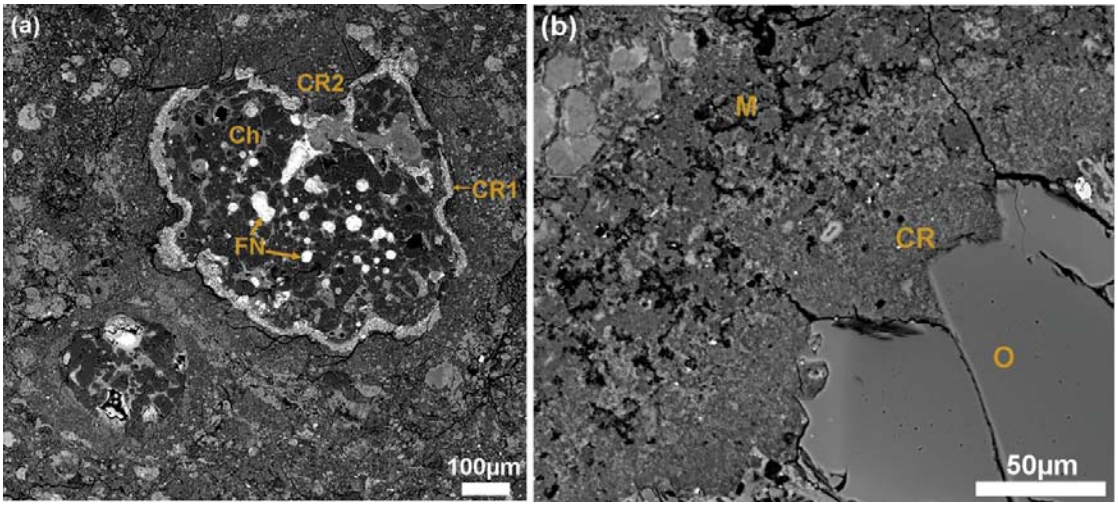

Figure 3.20- BSE images showing the texture of chondrule rim in Mighei.
(a) large (400µm) chondrule (Ch) with two layers of rims. The first layer (CR1) is composed of Fe-Ni metal (using SEM-EDS mineral identification) that has been near completely replaced by tochilinite, and second layer (CR2) is very fine grained (<1µm) phyllosilicate. This chondrule also contains large nodules (30 µm) of Fe-Ni metal (FN) that have partly been replaced by tochilinite. (b) One layer of very fine grained (<1µm) rims (CR) around a large (~130 µm) fragment of Fe-rich olivine. M is fine grained matrix that is coarser than the rim. The locations of these maps in the sample studied are shown in appendix D4.

Components	Vol%
Fine grained (<1µm) matrix	58.9
Tochilinite and Fe-Sulphide	11.3
Mg-rich olivine fragments	4.4
Tochilinite –serpentine	3.6
Ca-carbonate	1.4
Fe-rich olivine fragments	1.0
Pyroxene	0.5
Pristine chondrules	10.6
Chondrule rims	5.3
Chondrule partly or completely altered	2.1
Chondrule fragment	1.0

Table 3.13- Abundance of the Mighei components.
Values determined by SEM point counting. The total number of points counted is 965 over all area of the sample.

3.8.2 Alteration degree of Mighei

Mighei is a partly altered CM2 (e.g. McSween 1979; Tomeoka and Buseck, 1985; Zolensky et al., 1993; Browning et al., 1996). Using the PSD-XRD Howard et al. (2011) reported that the total Fe, Mg silicates and total phyllosilicate in Mighei are 20.0% and 74.6% respectively. Mighei was classified as less altered than Murray and Murchison (Burgess et al.; 1991); less altered than Murray and more altered than Murchison (Zolensky et al., 1993); more altered than Murchison and Murray (Browning et al., 1996).

Petrographic results of this study show that Mighei is brecciated, and in that it contains Fe-Ni metal, mainly within Mg-rich olivine, and has grain sizes from less than 1µm and up to 30 µm, at less than 0.2 vol%. Some of these mineral grains have been partially replaced by tochilinite (Figure 3.21a), and are more affected by aqueous alteration than those in Pollen. As stated above, the vast majority of Mg-rich olivine fragments within matrix and chondrules are intact, but some Fe-rich olivine fragments are etched on their edges (Figure 3.21b). The alteration degree of Mighei in this study is assigned to be CM2.3; based on the petrographic observations of Mighei and the abundance Fe-Ni metal within it, and also using the data in Browning et al. (1996), Howard et al. (2009) and Howard et al. (2011).

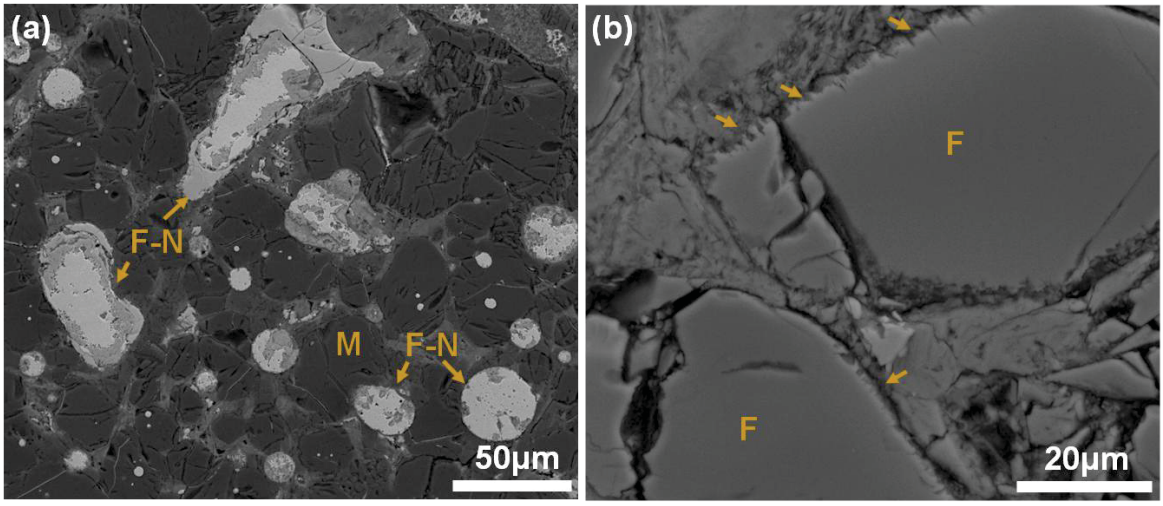

Figure 3.21- BSE images showing the presence of Fe-Ni metal in Mighei.
(a) The occurrence of Fe-Ni metal droplets (F-N) within Mg-rich olivine chondrule (M). The Fe-Ni (white areas) have been partly replaced by tochilinite (gray areas). (b) Fe-rich olivine fragments (F) within chondrule that are etched on their edges (arrowed areas) as consequence of aqueous alteration. The locations of these maps in the sample studied are shown in appendix D4.

3.8.3 Chemical composition of Mighei matrix

Micrprobe analyses (wt% oxides) of the fine grained matrix and chondrule rims of Mighei were presented by Zolensky et al. (1993). The Mighei matrix was also analyzed by McSween and Richardson (1977). Their analyses of the matrix are comparable (±1.5 wt%) with findings of Zolensky et al. (1993), with an exception for values of Si and S that are different (about ± 5wt%) (see Table 3.14).The data from Zolensky et al. (1993) indicates that matrix in Mighei contains more Si, Fe and Mg than the chondrule rims. It also indicates that the chondrule rims in Mighei contains less of Mg (~ -2.5 wt%) than those in Pollen (EPMA analyses), but the fine grained (<1µm) matrix in Mighei has slightly higher concentrations of Mg and Si (~ +1.5 oxides wt%) than the fine grained (<1µm) matrix (phase II) in Pollen (EPMA analyses). However, analyses by McSween and Richardson (1977) reveal more Mg (+1 wt%) in the Pollen matrix.

	Zolensky et al. (1993)		McSween and Richardson (1977)
Oxides in wt%	**Matrix**	**Rims**	**Matrices**
Na_2O	0.56	0.71	0.63
MgO	17.63	15.76	13.20
Al_2O_3	2.04	1.81	1.66
SiO_2	29.62	25.35	20.30
P_2O_5	0.08	0.51	--
S	2.15	2.84	SO3= 7.12
K_2O	0.08	0.08	0.04
CaO	0.15	0.84	0.46
TiO_2	0.07	0.07	0.07
Cr_2O_3	0.50	0.72	0.24
MnO	0.21	0.19	0.15
FeO	27.21	21.30	25.10
NiO	2.87	2.55	1.86
Total	83.19	72.74	70.93
Elements in wt%	**Matrix**	**Rims**	**Matrices**
Na	0.42	0.53	0.47
Mg	10.62	9.49	7.95
Al	1.07	0.95	0.87
Si	13.85	11.85	9.49
P	0.02	0.13	--
S	2.15	2.84	2.92
K	0.07	0.07	0.03
Ca	0.11	0.60	0.33
Ti	0.04	0.04	0.04
Cr	0.34	0.49	0.16
Mn	0.16	0.15	0.12
Fe	21.15	16.56	19.51
Ni	2.26	2.00	1.46
O	30.94	27.04	23.37
Total	83.19	72.74	70.93
n	10	65	20

Table 3.14- Previous analyses of the matrix in Mighei.
Elements and oxides in wt% of Mighei matrices reported by Zolensky et al. (1993) and McSween and Richardson (1977). The data of McSween and Richardson (1977) shows anomalous values of S and Si. The data of Zolensky et al. (1993) indicate that the matrix contains higher contents of Si-Fe-Mg than those in chondrule rims.

The average of the analyses of matrix and chondrule rims of Zolensky et al. (1993) has been presented as a synthesized spectrum (Figure 3.22) using INCA software in an effort to correlate it with the spectrum that was obtained of small mapped region (~1mm^2) in the sample used for this study. Both spectra (Figure 3.22) confirm that the main chemical constituents of Mighei matrices are Fe, Si and Mg, but the two spectra show that they contain more Si than Mg and Fe, and less of Fe than Mg. Comparison between EDS spectra of matrices of Pollen and Mighei (this study) show also that matrices of Mighei contain more Mg and Fe.

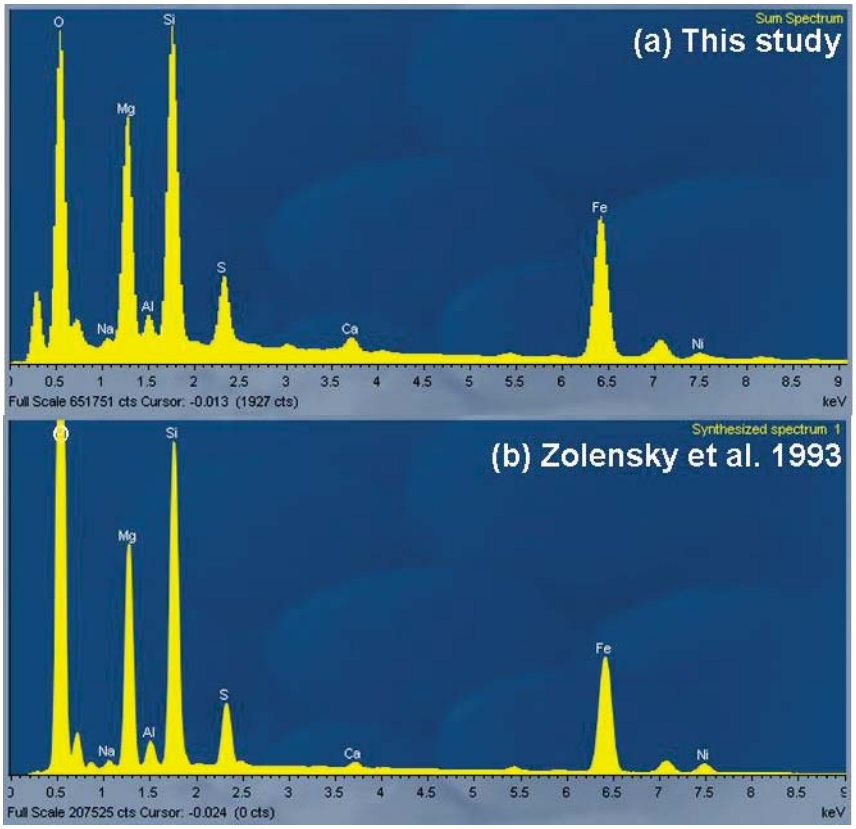

Figure 3.22- Spectra of Mighei matrices.
(a) Spectrum of a small mapped area (Figure 3.23). (b) Synthesized spectrum of average results (both matrix and chondrule rims) of Zolensky et al. (1993). Relative peak heights are fairly comparable between the two spectra (apart for O). However, the upper spectrum was acquired from area contains low and high temperature phases and thus it has slightly higher peaks of Fe, Mg and Ca than those in synthesized spectrum.

A X-ray map (Figure 3.23) was acquired to identify the abundance and concentration of elements within Mighei. This map shows isolated areas of high intensity green colour that overlays on Ca-carbonate grains and dark red areas that locate the Mg-rich olivine grains. This map also reveals a homogeneous distribution of elements including Fe, Mg and Si throughout the fine grained (<1μm) matrix (only areas free of tochilinite and Fe-sulphides) and chondrule rims.

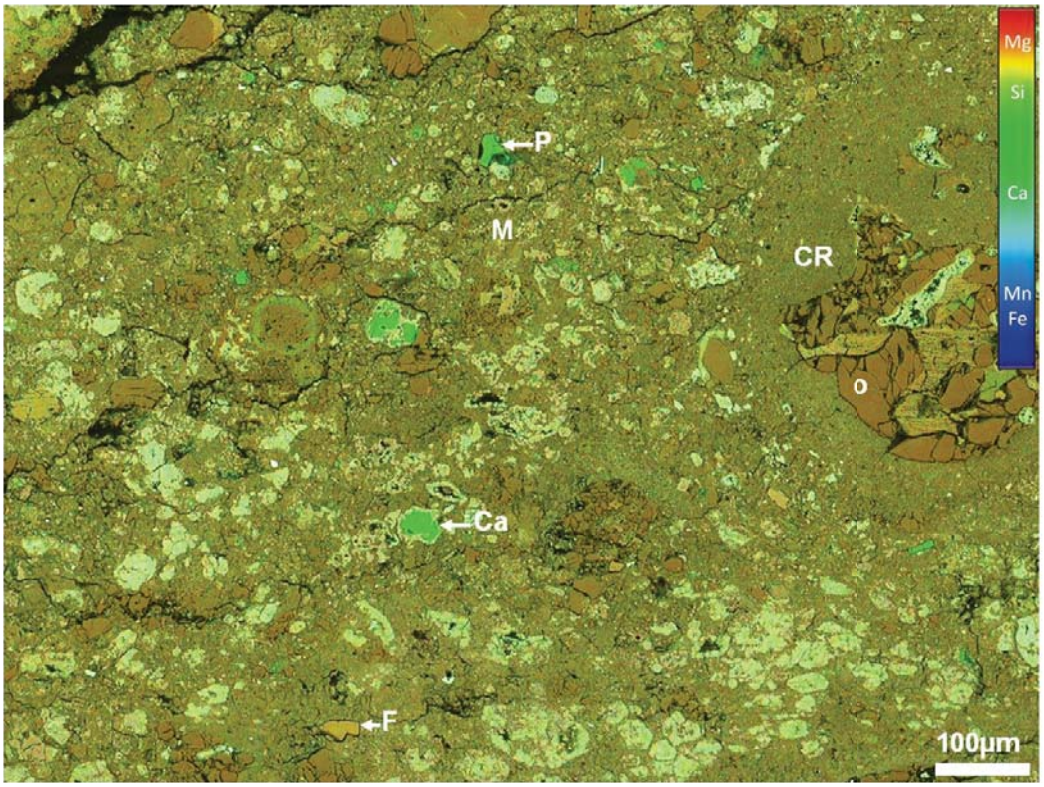

Figure 3.23- Element map combined with BSE image of Mighei.
Combined false colour multielement X-ray map of about 1mm^2 area in which most of the components of Mighei are present. The high concentration of Ca (high intensity green colour) locates the Ca-carbonate (Ca) and pyroxene fragment (P). Elements including Fe, Mg and Si are homogenously distributed within the fine grained (<1µm) matrix (M) and chondrule rims (CR). High concentrations of Mg are dark red (O) and locate Mg-rich olivine fragments and light red colour locates Fe-Mg olivine fragments (F). The location of this map in the sample studied is shown in appendix D4.

3.9 EET 96029 CM2.3

EET 96029 is a CM2 chondrite that was recovered by the Antarctic meteorites collection expedition at Elephant Morraine (76° 11'S, 157° 10'E) in 1996. The total mass of the meteorite is 848.28g and its dimensions are 15 cm by 11 cm by 8.5 cm. The meteorite contains small amounts of dark fusion crust on external surfaces, many cavities and some spots of evaporites (Figure 3.24). The interior is black and has white inclusions. The weathering classification of the meteorite is A/B (AMN, 21(1), 1998). One thin section of EET 96029 (9) was used for this work, which was loaned from the NASA Antarctic meteorite collection at the NASA Johnson Space Center (JSC) in Houston. This thin section is on a round glass slide (1 inch in diameter) and the sample area is approximately 125 mm^2.

Figure 3.24- Photograph of EET 96029.
The sample has a rough surface, is black, and contains some cracks. The source of the image is: http: //www.lpi.usra.edu/meteor/metbull.php?code=9623.

3.9.1 Composition and mineralogy of EET 96029

EET 96029 appears texturally and mineralogy analogous to Mighei. It contains Mg, Fe silicates within a fine grained (<1μm) phyllosilicate matrix. This meteorite has abundant pristine and partly altered chondrules and chondrule fragments in sizes that range from a few microns to about 1.5 mm. The vast majority of these are composed primarily of Mg-rich olivine; more rarely the chondrules consist of Fe-rich and Mg-rich olivine. Fe-rich olivine aggregates are also common in the rock. All the chondrules in this meteorite are porphyritic (described in section 1.5.1.1.1), with exception of only two (~ 0.5mm and 0.2 mm in diameter) that are non porphyritic and texturally are radial pyroxene. Rare pyroxene fragments are also scattered within the fine grained (<1μm) matrix. The chondrules range in shape from rounded to elongated and irregular. Some Mg-rich olivine grains in chondrules and chondrule fragments have a 'spongy' texture. The main inter-chondrule materials are tochilinite, occurring primarily between olivine grains, and, in some cases, as inclusions within them. The most distinct feature is the occurrence of Fe-sulphide and tochilinite, that is less abundant in fine grained matrix in comparison with Mighei and LON 94101 (described below). Tochilinite is generally intergrown with serpentine in the fine grained matrix, and occurs as rims around some other minerals (e.g. calcite). Fe-sulphide occurs as individual grains within the fine grained (<1μm) matrix and some chondrules, and grain sizes range from ~1 μm to ~50 μm. It is also found as thin layers (~10 μm) around chondrule and as a groundmass that encloses other minerals. Metallic Fe-Ni in the form of blebs or circular grains is present inside Mg-rich olivine, and ranges in size from ~1 μm to 25 μm. It is also very rarely found in the fine grained (<1μm) matrix. The vast majority of Fe-rich olivine grains are metal free. Several small CI-like clasts

occur in the matrix of EET 96029, have irregular shapes, and range in size from about 40 to 100 μm. The only carbonate mineral in EET 96029 is calcite.

In terms of texture, chondrule rims are likely to be equivalent to the materials in fine grained (<1μm) matrix in which the tochilinite clumps are absent, but the chondrule rims in areas nearest to chondrules appear finer grained than adjacent areas. Some chondrule rims in EET 96029 are characterized by the presence of empty radial fractures, and these fractures may have formed as consequence of chondrule expansion during aqueous alteration. The abundance of the components of EET 96029 was determined by SEM point counting and is listed in Table 3.15.

Components		Vol%
Fine-grained matrix		66.4
	Mg-olivine	7.1
	Tochilinite grains	2.0
	Fe-olivine	1.9
	Fe-Sulphide	1.1
	Tochilinite-Fe sulphide	0.8
	Pyroxene	0.6
	Refractory inclusions	0.5
	CI-like clast	0.5
	Calcite	0.1
	Fe-Ni metal (inclusions in olivine)	0.1
Partly altered chondrule		9.2
Chondrule rims		5.5
Preserved chondrule (Mg-rich olivine)		3.8
Preserved Chondrule (Fe-rich olivine)		0.4

Table 3.15- Abundance of the EET 96026 components.
Values determined by SEM point counting. The total number of points counted is 1739.

3.9.2 The degree of alteration of EET 96026

The rock appears brecciated. Metallic Fe-Ni is very rare (0.1 vol%; Table 3.12). Some of the Fe-Ni metal blebs inside Mg-rich olivine grains have been completely altered; others are partly altered or well preserved (Figure 3.25). The vast majority (~95%) of Mg-rich olivine grains in chondrules and chondrule fragments are well preserved, whereas some of Fe-rich and Fe-Mg intermediate olivine grains are partly or significantly altered to serpentine and tochilinite (Figure 3.26). A few chondrules are completely altered. The abundance of hydrous materials (phyllosilicates) is 71.94 vol%, whereas the anhydrous materials represent approximately 21 % of the volume of the rock. Based on these observations the alteration degree of EET 96029 is likely to be equivalent to Mighei, which is CM 2.3.

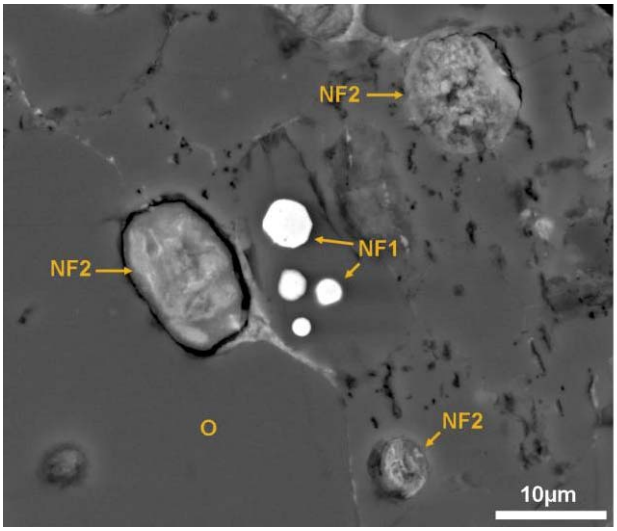

Figure 3.25- BSE image showing the occurrence of Fe-Ni metal inside Mg-rich olivine (O) in EET 96029.
The large (10 µm) altered Fe-Ni granules (NF2) have been replaced by tochilinite. Note small grains that are well preserved (NF1). The location of this map in the sample studied is shown in appendix D5.

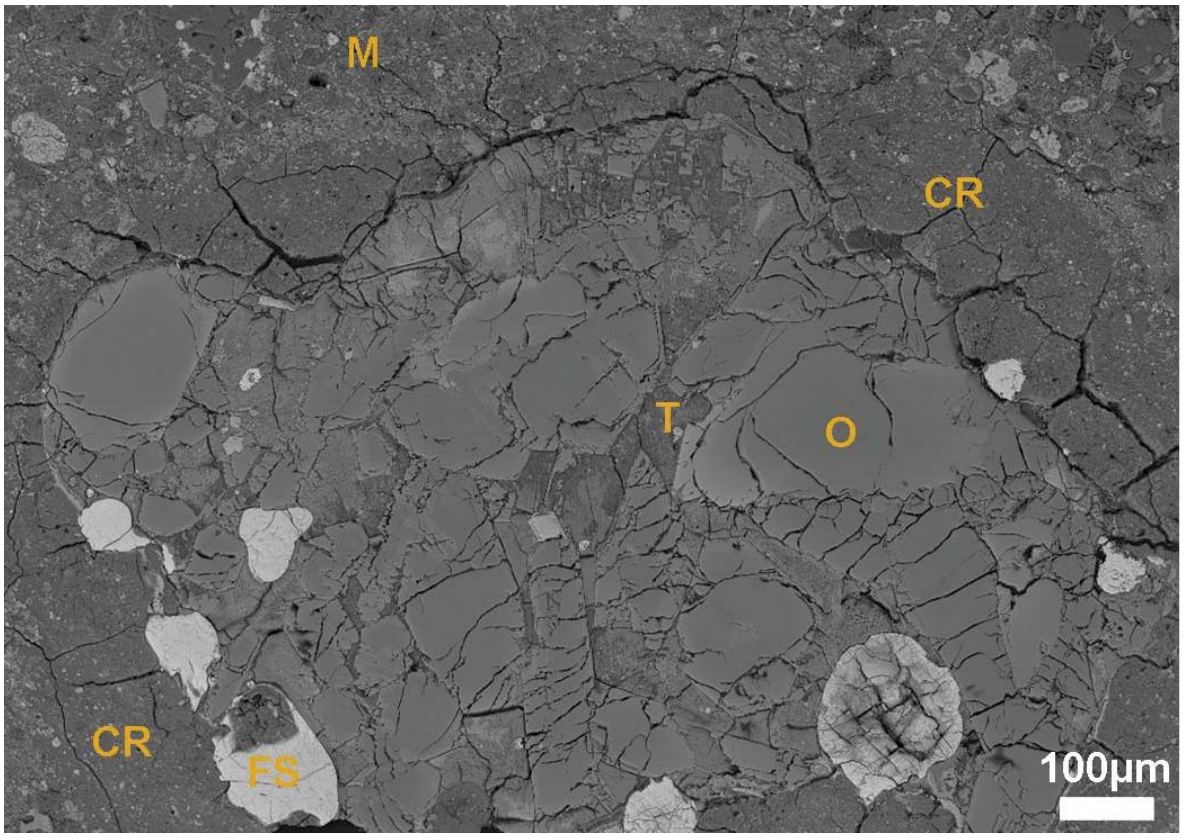

Figure 3.26- BSE image showing a partly altered porphyritic Mg-Fe olivine chondrule in EET 96029. Note that most olivine grains (O) have been slightly etched; some grains have been entirely replaced by tochilinite (T). FS is Fe-sulphide that is partly altered. The rim (CR) around the chondrule is highly fractured relative to fine grained (<1µm) matrix (M). The location of this map in the sample studied is shown in appendix D5.

3.9.3 The chemical composition of EET 96029 matrices

Elemental mapping of the entire thin section and small regions of EET 96026 was undertaken to determine the qualitative chemical composition (e.g. Figure 3.27). Fe, Mg and Si are uniformly distributed within the fine grained (<1μm) matrix. The high concentrations of Mg occur in Mg-rich olivine, and Ca is the best tracer for calcite and Ca-rich pyroxene. The most distinct difference is between the concentrations of Fe in chondrule rims and the fine grained (<1μm) matrix. The Fe map shows that chondrule rims contain less Fe than fine grained matrix; which is consistent with the chemical analyses of Zolensky et al. (1993) that showed the matrix of Mighei contains more Fe than chondrule rims. Elemental mapping of EET 96029 also shows that some areas of chondrule rims have high concentrations of Mg relative to the fine grained (<1μm) matrix.

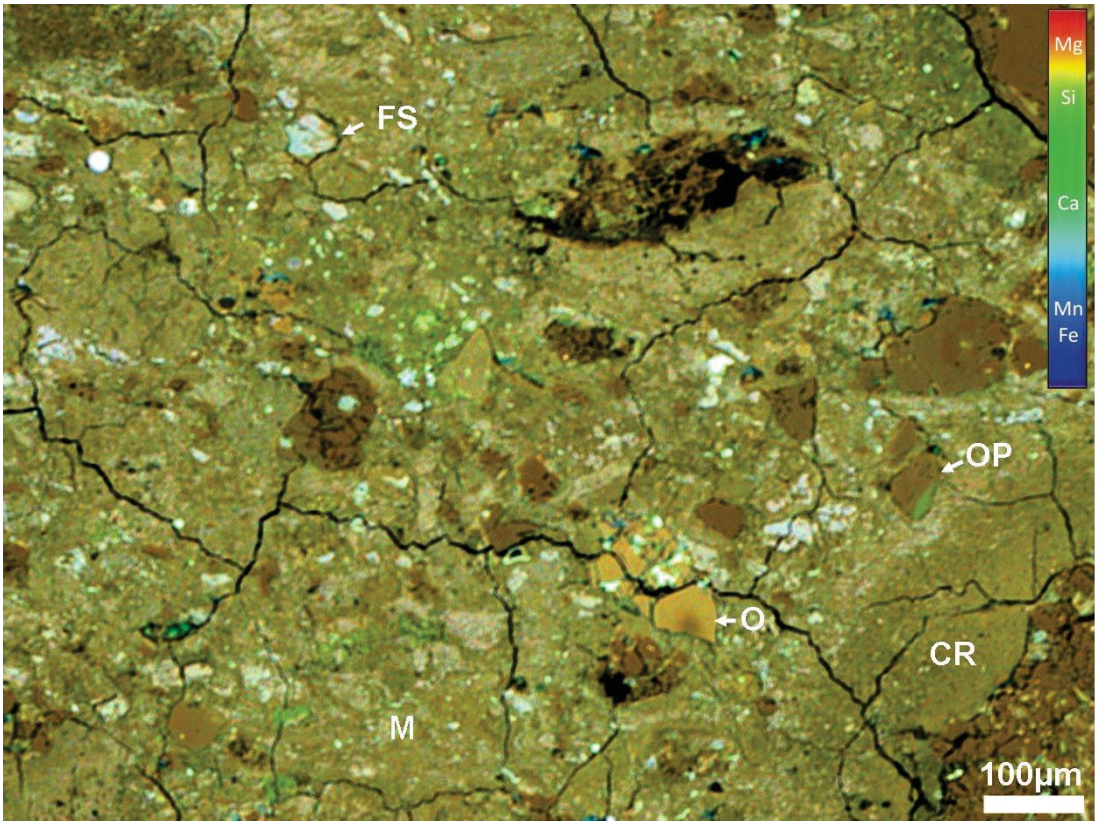

Figure 3.27- Multielement X-ray map associated with colour scale bar (right side) showing that Fe, Mg and Si are homogeneously distributed within the fine grained (<1μm) matrix (M) of EET 96029. Areas of chondrule rims (CR) contain higher concentrations of Mg (reddish in the map) than fine grained (<1μm) matrix (M). Note also the reddish colour marks Mg-Fe olivine (O), greenish colour locates Ca-rich pyroxene fragments (P) and Mg-rich olivine appears in dark red. FS is Fe-sulphide, OP olivine-pyroxene intergrowth. The location of this map in the sample studied is shown in appendix D5.

X-ray spectra from several regions of the EET 96029 matrix illustrate that it contains higher concentrations of Fe in comparison with chondrule rims. Comparison between the

EDS spectrum of the EET 96029 matrix (Figure 3.28) and spectrum of Mighei matrix (Figure 3.22a) indicates that matrix of EET 96029 contains less Mg, Fe and S than Mighei.

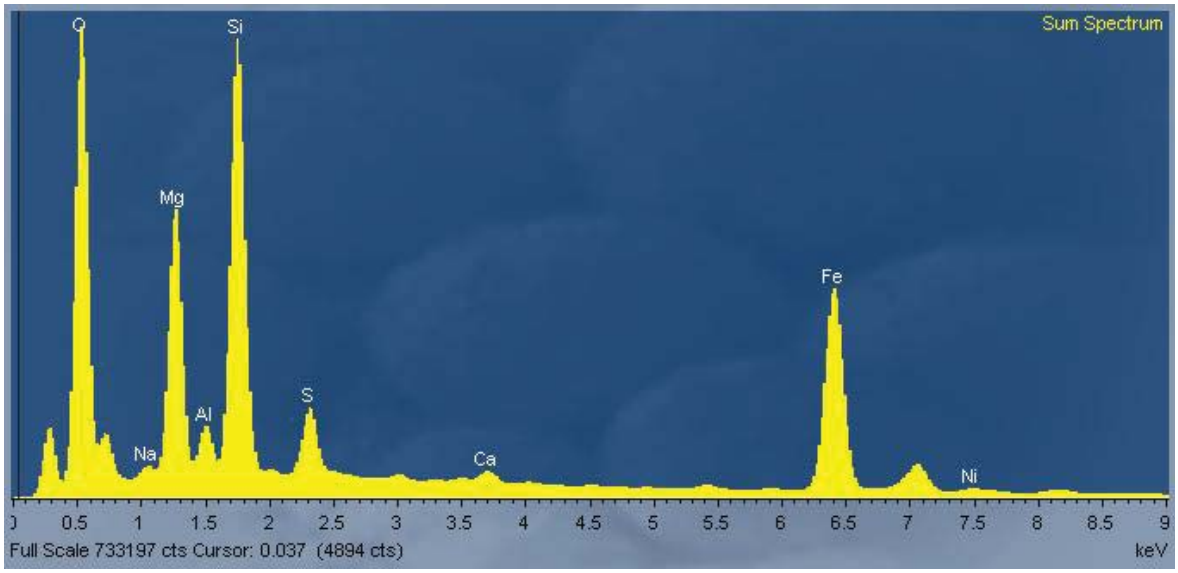

Figure 3.28- EDS spectrum of mapped area in Figure 3.27 confirms that Si, Mg, Fe and S are the main constituents of the meteorite matrix.
This spectrum has lower Mg/Si and lower Fe/Si than Mighei (Fig. 3.22a).

3.10 LON 94101 CM2.3

LON 94101 is a CM2 carbonaceous chondrite that was recovered by the Antarctic meteorites collection at the Lonewolf Nunataks, Antarctica, in 1994. It was broken to several pieces (e.g. Figure 3.29). The recovered weight of the meteorite is 2804.2g, and it has patches of fusion crust (2-3cm). It is described as black, highly fractured, and characterized by presence of rusted clasts and white spots. Its weathering classification is Be and fracturing category is C (AMN 18(2), 1995). One thin section of LON 94101 (50) was used for this study; this section was loaned from the NASA Antarctic meteorite collection at the NASA Johnson Space Center (JSC) in Houston. The thin section has an area of about 105 mm^2.

Figure 3.29- Photograph of piece of LON 94101.
The sample has reddish, greenish and white flecks on its surface. The source of the image is: http://curator.jsc.nasa.gov/antmet/amn/amnaug95/petdes.htm

3.10.1 Composition and mineralogy of LON 94101

About 2200 BSE images were obtained from the thin section of LON 94101 to investigate the detailed petrographic properties and relationships of carbonates and the other components. The constituents of LON 94101 can be also subdivided into two paragenetic phases - namely low and high temperature - that are present in different proportions of the whole bulk of the rock, with the highest abundance for low temperature phase. The high temperature constituents are olivine grains that are found in porphyritic chondrules, olivine fragments, pyroxene, spinel, Fe-Ni metal, apatite and pentlandite $(Fe, Ni)_9S_8$.

Chondrules in LON 94101 are elongated to spherical in shape, and up to 600 μm in diameter. The sizes of their olivine grains ranges from a few μm to 300 μm. Chondrules and chondrule fragments are composed of Mg-richolivine or/and Fe-rich olivine. Spinel grains are found within three loose clusters in the fine grained (<1μm) matrix. Each grain of spinel is polycrystalline and enclosed within an envelope of tochilinite (Figure 3.30). Very rare apatite (~5 μm across) was also observed within serpentine-tochilinite intergrowths. Pyroxene fragments are anhedral and in some cases form with tochilinite the entirety of a chondrule.

Fe-Ni metal, in the form of spherical blebs, occurs rarely in the fine grained (<1μm) matrix and olivine grains (mainly Mg-rich olivine). Sometimes these blebs reach a size of 30μm; however, the majority are 10 μm or less. Pentlandite is generally found in association with olivine fragments and olivine aggregates in chondrules (inter-chondrule materials) or/and rims around chondrules. Pentlandite is occasionally present within the fine grained (<1μm) matrix as isolated grains and inclusions within micro veins of Ca-carbonate. Negligible

amounts of Fe-sulphides occur as isolated grains in the fine grained matrix, and as inclusions within grains of calcite and serpentine pseudomorphs after calcite. Calcite grains are entirely or partly rimmed by Fe-sulphide. A small number of chondrules and chondrule fragments that are partly or near completely altered contain about 10-15% of Fe-sulphide and it occurs in chondrules and/or as rims around chondrule.

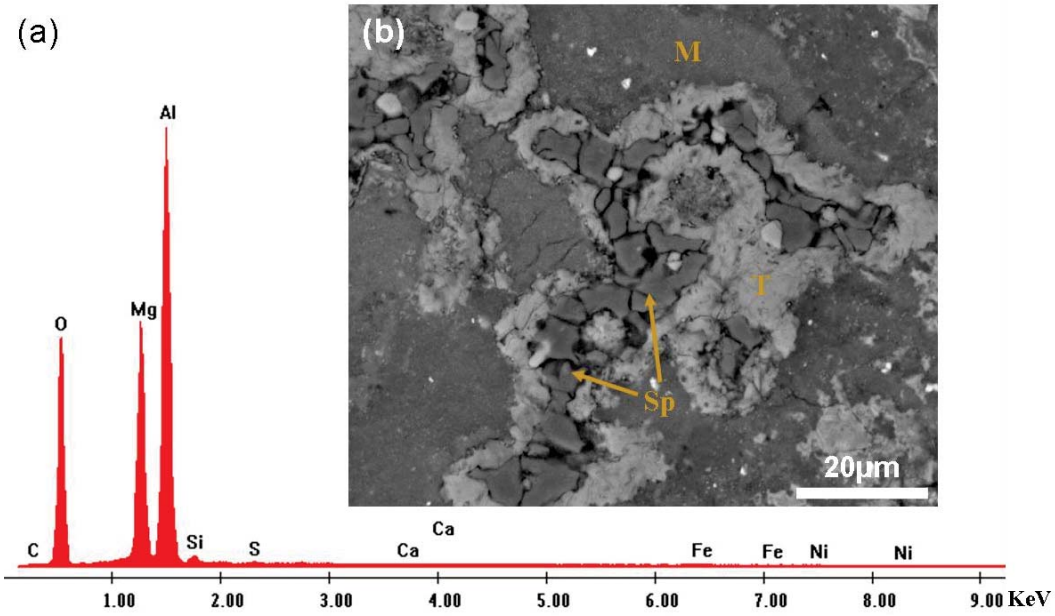

Figure 3.30- Occurrence of spinel in LON 94101.
(a) EDS spectrum of spinel grain in (b). (b) BSE image showing a spinel (Sp) aggregate enclosed by tochilinite (T). M is fine grained (<1µm) matrix that is texturally different to the adjacent matrix. The location of this map in the sample studied is shown in appendix D6.

The low temperature constituents LON 94101 comprise chondrule rims and fine grained matrix, in addition to Ca-carbonate and Fe-sulphide. The chondrule rims around chondrules and chondrule fragments comprise of very fine grained (<1µm) phyllosilicates that in some cases contain very small Fe-sulphide grains. The abundance of all LON 94101 constituents was determined by SEM point counting (Table 3.16). A characteristic feature of chondrule rims in LON 94101 is their low abundance (1.85 vol %) that is less than those in EET 96029 (5.52 vol%) and Mighei (5.28 vol%). The Fe-Ni metal was separately counted and its abundance is less than 0. 2 vol %.

The dominant minerals in the fine grained (<1µm) matrix are serpentine and tochilinite. Tochilinite is widely distributed in this meteorite, and has formed in many chondrules as a consequence of aqueous alteration. Tochilinite is also intergrown with serpentine in the fine grained matrix, it occurs around some calcite grains and as pseudomorphs after calcite, and as inclusions within other minerals. Carbonate minerals comprise calcite and aragonite, which occur as individual grains and micro-veins within the matrix. Other thin

sections (examined by Lindgren et al., 2011b) of LON 94101 contain sixteen xenoliths including twelve CI-like clasts, and another four different xenoliths that vary in size and composition (Lindgren et al., 2011b). Nine CI-like clasts are observed in the section of LON 94101 examined for current study. They have different shapes including rounded, elongate and irregular. They vary in size from about 50 to 500 µm. These nine xenoliths (CI-like clasts) are texturally different and finer grained than the chondrule rims and fine grained matrix, and in some cases are more fractured than the enclosing matrix. Small nodules of Fe-sulphide and tochilinite are also scattered within these CI-like clasts. Chemical analyses of the clasts are presented in Table 3.17.

Components		Vol%
Fine-grained (<1µm) matrix		63.0
	Pseudmorph structures (only tochilinite and/or Fe-sulphide)	13.0
	Olivine fragments	6.2
	Tochilinite	4.8
	Altered chondrules	3.1
	Ca-carbonate	1.3
	Pseudomorphs structures (calcite+ tochilinite and/or Fe-sulphide)	1.2
	Fe-sulphide, Fe-Ni metal and pentlandite	1.1
	Spinel	0.0
Chondrules		4.4
Chondrule rims		1.9
CI-like clast		0.1

Table 3.16- Abundance of the LON 94101 components.
Values determined by SEM point counting. The total number of points counted is 2324.

3.10.2 Alteration degree of LON 94101

LON 94101 is highly brecciated. As stated above, metallic Fe-Ni is very rare (<0.2vol %). Rubin et al. (2007) reported that the moderately altered CM2 chondrites contain 0.1-0.3 wt% metal. Some Fe-Ni metal inside olivine grains has been partly replaced with rinds of tochilinite. SEM point counting results indicate that the abundance of Fe-Ni metal in LON 94101, Mighei and EET 96029 is all less than 0.2 vol %. However, chondrule Mg, Fe silicate phenocrysts in LON 94101 appear more affected by aqueous alteration than Mg, Fe silicates in Mighei and EET 96029. Very rare chondrules in LON 94101 are entirely replaced, and other chondrules have been partially or near complete altered (Figure 3.31). Anhydrous silicates have been replaced by serpentine, tochilinite and Fe-sulphide. Calcite is found in chondrule and chondrule fragments as a replacement of Mg-rich olivine. It is remarkable that the calcite has not replaced Fe-rich olivine. Based on these observations

the alteration degree of LON 94101 is similar Mighei (CM2.3) or slightly more highly altered.

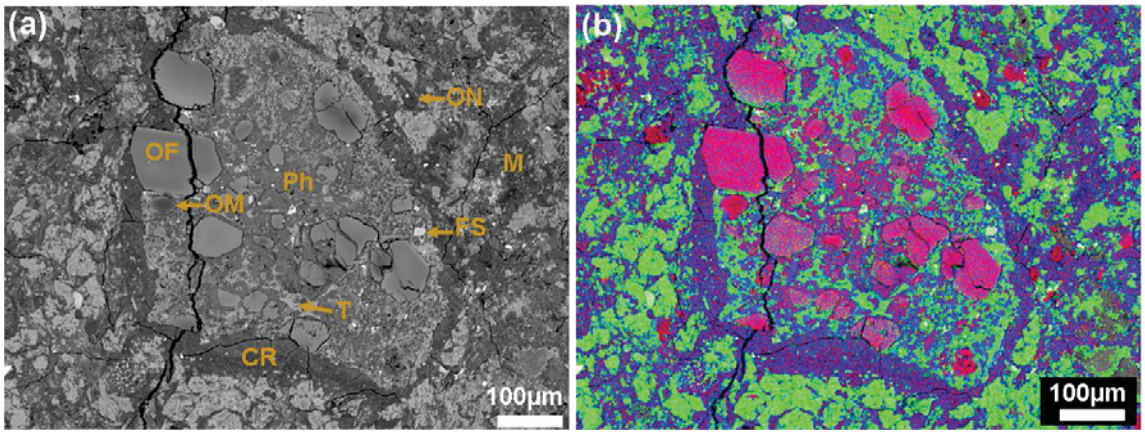

Figure 3.31- BSE image and elemental map of altered chondrule in LON 94101.
(a) BSE image showing near complete alteration of the chondrule. All Fe-rich olivine grains (OF) are likely to have been replaced by phyllosilicate (serpentine) (Ph) and tochilinite (T). Note that the chondrule rims (CR) and the fine grained (<1µm) matrix appear similar in texture, but there is much more tochilinite in the matrix. FS is Fe-sulphide; OM is Mg-rich olivine. (b) Combined elemental map of the same chondrule and adjacent materials in (a) showing the distribution of Fe, Mg and Si. This indicates that the chondrule rims and the fine grained matrix (free of tochilinite) contain the same materials. Note also that Fe is concentrated in locations of tochilinite. The location of this map in the sample studied is shown in appendix D6.

3.10.3 Chemical composition of LON 94101 matrix

X-ray element maps of small regions of the matrix of LON 94101 were obtained to determine the qualitative chemical composition (e.g Figure 3.32). Fe, Si and Mg are homogeneously distributed within in the chondrule rims and areas of fine grained (<1µm) matrix that are free of tochilinite and Fe-sulphide (see also Figure 3.31). Ca is locally concentrated in grains of Ca-carbonate and Ca-rich pyroxene. High concentrations of Mg and Si are found in locations of Mg-rich olivine, and Fe-sulphide and tochilinite respectively. An EDS X-ray spectrum (Figure 3.33) of the mapped area in Figure 3.32 confirms that Si, Mg, Fe and S are most abundant in the LON 94101. The spectrum of LON 94101 matrices was correlated with spectrum of EET 96029, and this indicates that the matrix of LON 94101 contains more Mg and less Fe than EET 96029 matrix, whereas the peaks of S and Si are nearly identical in relative intensity to each other (Figure 3.34).

CI-like clasts in LON 94101 have been also analyzed using EPMA (Table 3.17). The chemical composition of CI-like clasts is nearly identical (± 0.5-1.25 oxides wt%) to the composition of CI-like clasts in Pollen (Table 3.12).

Oxides wt%		Elements wt%	
Na_2O	0.48 ± 0.09	Na	0.36
MgO	22.85 ± 3.16	Mg	13.78
Al_2O_3	2.30 ± 0.70	Al	1.22
SiO_2	33.87 ± 3.55	Si	15.83
P_2O_5	0.15 ± 0.10	P	0.06
SO_2	3.68 ± 1.87	S	1.84
K_2O	0.14 ± 0.04	K	0.12
CaO	0.21 ± 0.14	Ca	0.15
TiO_2	0.09 ± 0.00	Ti	0.05
Cr_2O_3	0.31 ± 0.06	Cr	0.21
MnO	0.19 ± 0.04	Mn	0.15
FeO	15.29 ± 1.62	Fe	11.89
NiO	1.56 ± 1.10	Ni	1.23
		O	
Total	81.12	wt%	34.23
n	3		

Table 3.17- Mean chemical compositions of CI-like clasts in LON 94101 determined by EPMA. Data presented as mean ± SD, error values are calculated to 1σ. The full dataset with standard deviations is listed in appendix A.3.

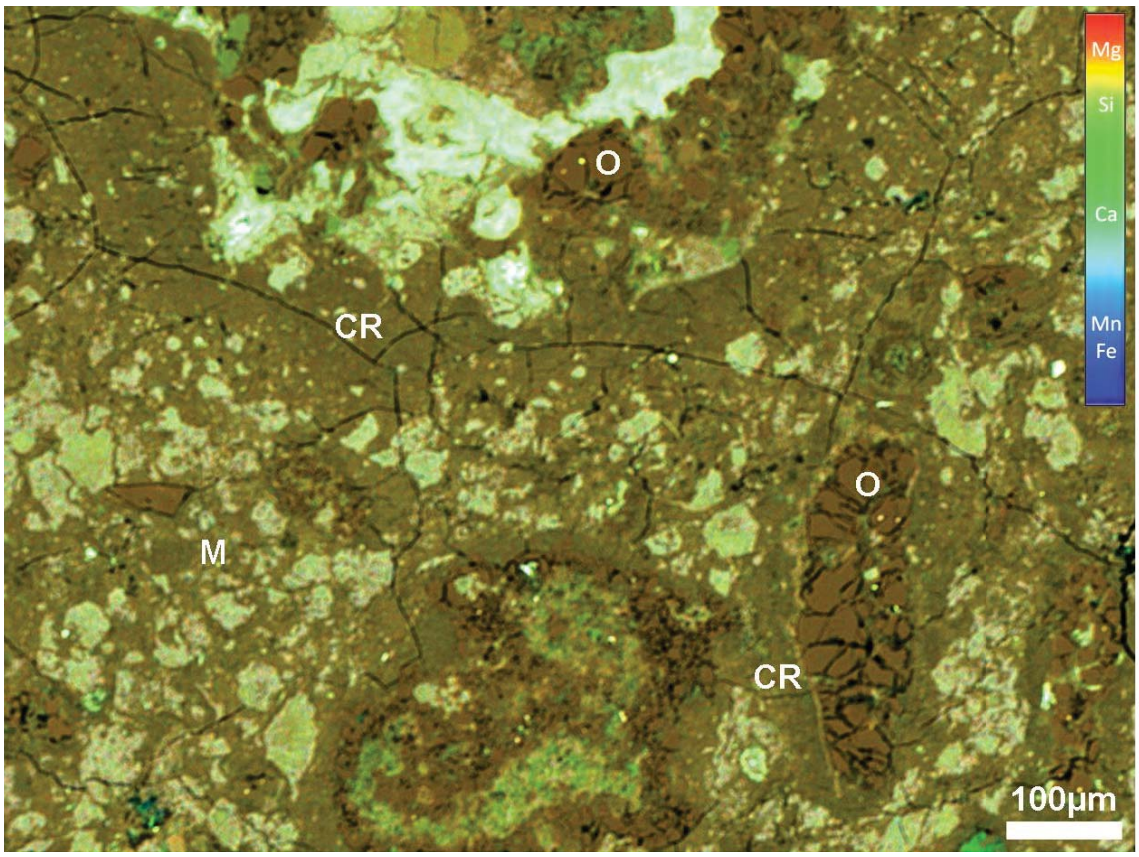

Figure 3.32- False colour multi-element X-ray map showing the distributions and concentrations of elements in LON 94101.
The concentrations of three elements Fe, Mg and Si are likely to be uniform throughout chondrule rims (CR) and the areas of fine grained (<1µm) matrix (M) where the tochilinite and Fe-sulphide are absent. O is Mg-rich olivine. The colour scale bar is provided in the upper right of the map. The location of this map in the sample studied is shown in appendix D6.

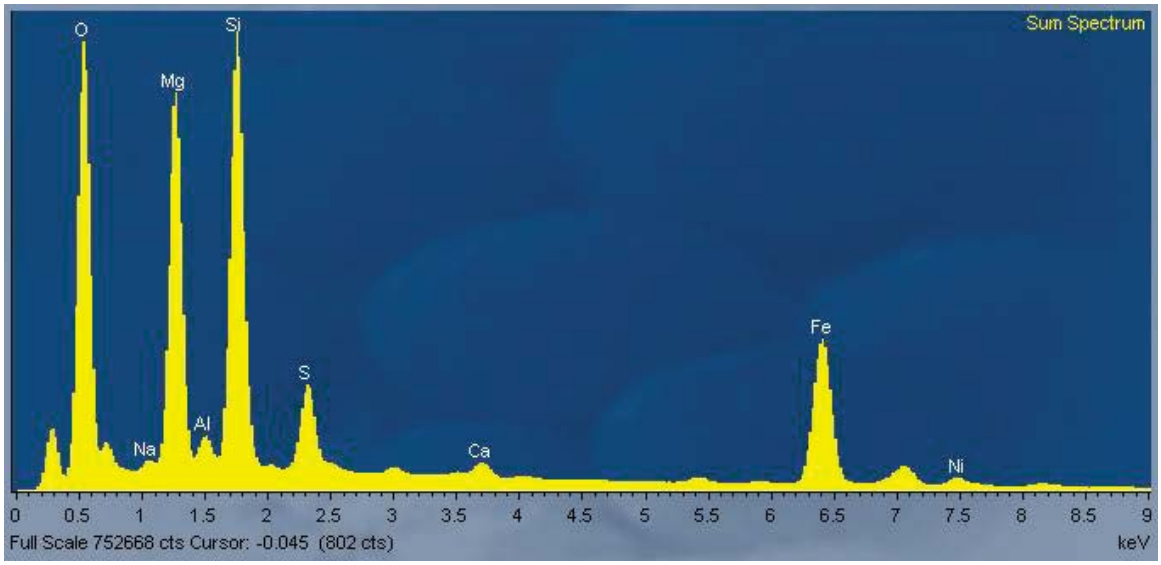

Figure 3.33- EDS spectrum from the mapped area in Figure 3.32.
It reveals that LON 94101 matrix has high contents of Mg and Si and a high Mg/Si ratio.

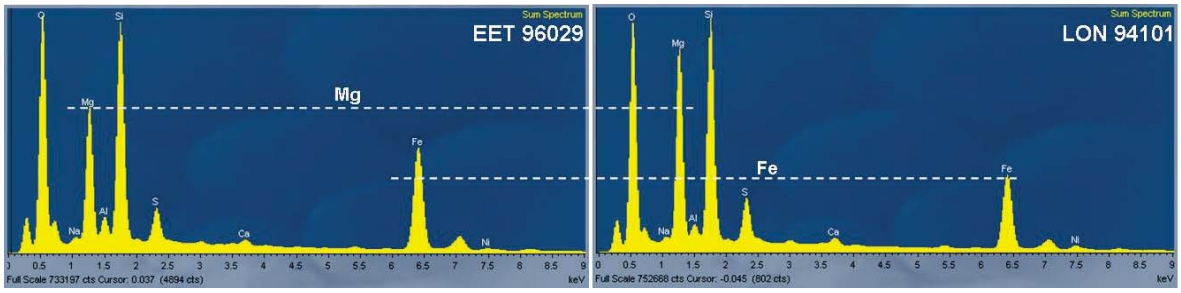

Figure 3.34- Correlation between peaks of Mg, Fe, Si and S in spectra of EET 96029 matrix (Fig. 3. 28) and LON 94101 matrix (Fig. 3.33).
Note that LON 94101 matrix contains more Mg and less Fe relative to Si than EET 96029.

3.11 Nogoya CM2.2/2.3

The Nogoya CM2 carbonaceous chondrite fell in Entre Rios, Argentina (32° 22′ S., 59° 50′ W.) in 1879, on June 30 in the evening. The total mass of the recovered meteorite is 4000g (Graham et al., 1985). It has a weathering level of W0 (Rubin et al 2007). One thin section of Nogoya (BM 84191) was obtained from the Natural History Museum, London for this study. It has an area of about 32 mm^2.

3.11.1 Composition and mineralogy of Nogoya

Using TEM and X-ray diffraction, Bunch and Chang (1980) reported that Nogoya contains Fe oxides (Fe_3O_4, Fe_2O_3), PCP, gypsum, pentlandite, zincian pentlandite, calcite, epsomite and relic pyrrhotite, forsterite and pyroxenes (both Ca rich and poor), and probably

antigorite and brucite. They also reported that Nogoya contains Fe-rich brucite, and Fe-serpentine around magnetite grains within some altered chondrules.

The current study indicates that Nogoya can be divided into two different parts, namely highly altered and less altered (Figure 3.35), that differ in mineralogy and alteration degree. The high altered part contains small amounts of preserved Mg-rich olivine grains in chondrules and chondrule fragments; however the margins of these grains have been affected by aqueous alteration. In this part of Nogoya, about 90-95% of the chondrules and chondrule fragments have been entirely or nearly completely replaced by tochilinite, phyllosilicates or calcite. Some pentlandite is present as individual grains and aggregates in the fine grained (<1μm) matrix, and around some calcite and olivine grains and/or as inclusions within them. Apatite is found rarely, and in conjunction with fibrous phyllosilicates (apatite intergrown with sheets of phyllosilicates). Isolated calcite grains are also scattered in this part. Very rare gypsum was observed and is mainly intergrown with calcite grains. This part of Nogoya has one CI-like clast that is irregular in shape, broken into several pieces, and contains small grains of Fe-sulphide.

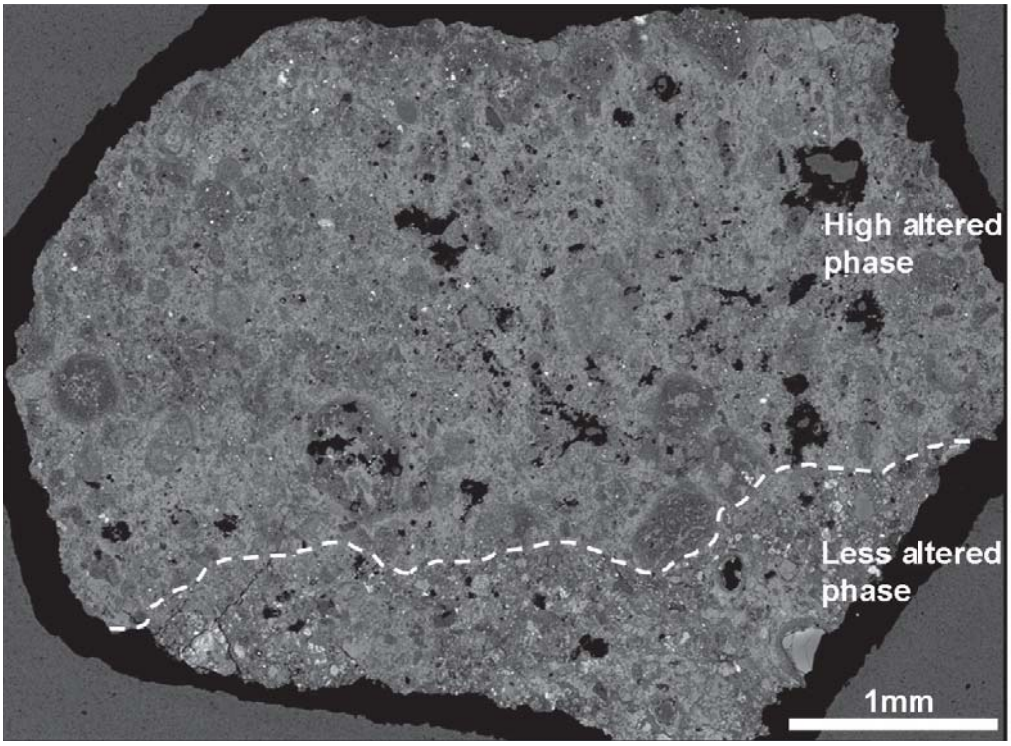

Figure 3.35- BSE image of the whole section of Nogoya that was used for this study.
This section has been subdivided into highly altered and less altered parts. The dashed line locates the boundary between the two. The orientation of this thin section relative to the main sample (hand specimen of the meteorite) is unknown, it most likely that the thin section was cut from the internal part of the meteorite as it free of fusion crust.

The less altered part represents about 20% of the whole sample. It contains olivine fragments that are rich in Mg and/or Fe. Their sizes range from a few microns to 250 microns. Some of these grains are rimmed. Pentlandite and Fe-sulphide are also found in the fine grained (<1μm) matrix of this part, but they are less abundant than pentlandite and Fe-sulphide in highly altered part. Carbonate minerals in this part comprise aragonite, calcite and dolomite. Pseudomorphs after Ca-carbonate minerals are composed of Mg-rich serpentine or tochilinite. Tochilinite also forms rims around pseudomorphs and some Ca-carbonate grains. The chondrule rims (<1μm) and fine grained (<1μm) matrix in Nogoya are texturally rough (coarser-grained than those in above described chondrites). The fine grained matrix is composed mainly of serpentine that contains abundant tochilinite clumps, whereas the chondrule rims contain serpentine that has small grains of tochilinite. The chondrule rims are equivalent in thicknesses to those in LON 94101, but more abundant. The abundance in volume percent of the Nogoya components is listed in Table 3.18.

Components		Vol%
Fine grained (<1μm) matrix		41.8
	Tochilinite grains	16.5
	Mg-phyllosilicate pseudomorphs	6.0
	Altered olivine with clay minerals	4.6
	Intergrowth tochilinite and pyrite	4.4
	Intergrowth tochilinite and phyllosilicates	3.7
	Pentlandite and Fe-sulphide	2.8
	Calcite	2.1
	Pyroxene	0.9
	Apatite	0.2
Mg-rich-Olivine fragments		10.1
Chondrule rims		6.3
Fe-rich-olivine		0.5

Table 3.18- Abundance of the Nogoya components.
Values determined by SEM point counting. The total number of points counted is 431.

3.11.2 The alteration degree of Nogoya

Nogoya was described by Bunch and Chang (1980) as a nearly completely altered meteorite as the most of anhydrous materials within it had been transformed to Mg and Fe serpentines. Texturally, Nogoya is unbrecciated (Rubin et al., 2007). The modal mineralogy of CM chondrites (Howard et al., 2011) showed that Nogoya contains 18.5 vol% Fe, Mg silicate and 75.8 vol% phyllosilicates. It was described as 'highly altered' by McSween (1979), and was classified as a CM 2.2 by Rubin et al. (2007). It is more altered than Mighei and less altered than Cold Bokkeveld (Browning et al., 1996; Howard et al.

2011). It contains very little metal (McSween and Richardson, 1977), 0.09 by vol%, occuring mainly in chondrules (Rubin et al., 2007). This is consistent with petrographic observations (discussed above) which indicate that the vast majority of Mg-rich olivine grains in the high altered part of the Nogoya thin section are altered or near complete altered, and indicate that the Fe-Ni metal is nearly absent in mafic silicates. Therefore the high altered phase of this section of Nogoya is classified as CM2.2 (Figure 3.36). The matrix of the less altered part is texturally analogous to the matrix of Mighei and EET 96029. Most of Mg-rich olivine grains are well preserved. In some cases they are etched in their margins, and have been replaced by calcite or phyllosilicates. The abundance of Fe-Ni metal in this region is less than 0.2vol%. Very rare grains of this metal were observed inside olivine grains and are intact. This part of Nogoya is breccia. Based on these observations, the alteration degree of less altered part of Nogoya is estimated to be CM2.3 (Figure 3.36).

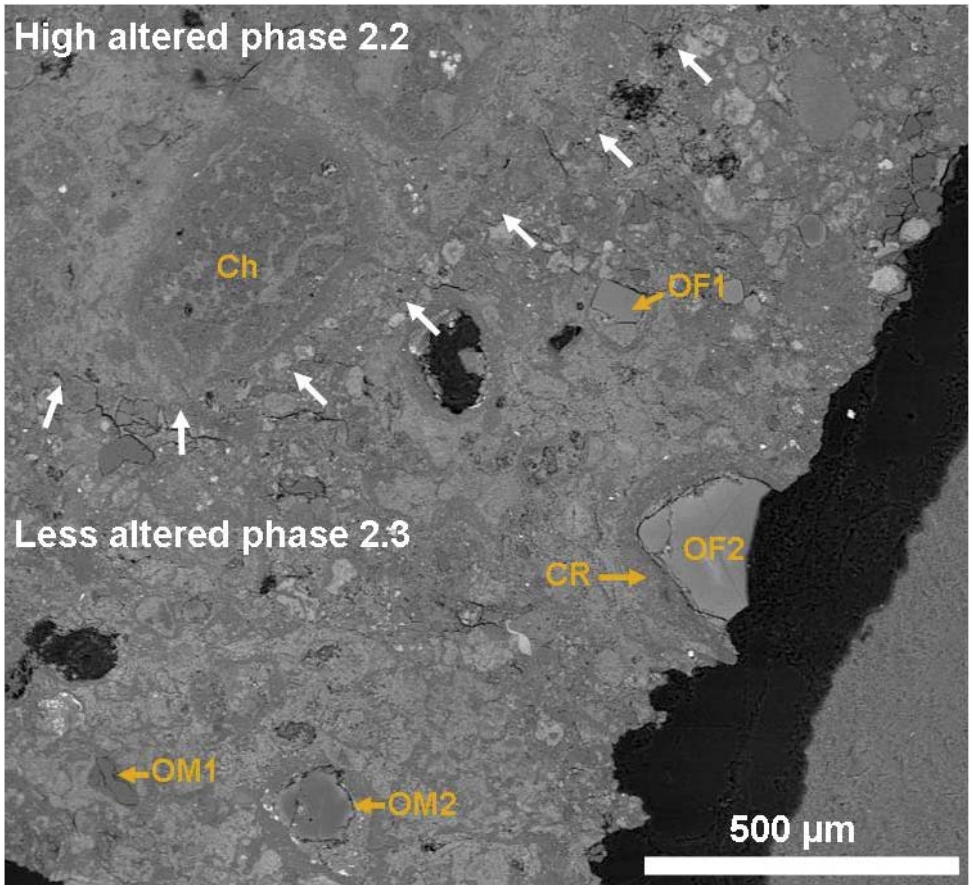

Figure 3.36- BSE image illustrating the alteration degrees of highly and less highly altered parts of Nogoya.
White arrows delineate the boundary between these two lithologies. Ch is partly altered chondrule in high altered region. The less altered region contains pristine olivine grains (OF1 and OM1), partly altered (OM2) and slightly altered in margins (OF2). OF1 and 2 are Fe-rich olivine, OM1 and 2 are Mg-rich olivine, CR is chondrule rims. The location of this map in the sample studied is shown in appendix D7.

3.11.3 The chemical composition of Nogoya matrices

Chemical analyses of Nogoya matrices have been presented by McSween and Richardson (1977) and Zolensky et al. (1993) and their analyses in wt% oxides and elements are presented in Table 3.19. As stated above, McSween and Richardson (1977) used a defocused beam to determine matrix chemical compositions, whereas a focused beam was employed by Zolensky et al. (1993). However, their analyses of the fine grained matrix show close agreement (± 0.5-1.5 wt%) (see Table 3.19).

	Zolensky et al. (1993)			McSween & Richardson (1977)
Oxides wt%	**Matrix**	**Chondrule rims**	**Average (matrix and chondrule rims)**	**Matrix**
Na2O	0.36	0.51	0.44	0.22
MgO	19.00	23.46	21.23	18.60
Al2O3	2.17	2.46	2.32	2.42
SiO2	28.97	33.85	31.41	26.70
P2O5	0.11	0.13	0.12	0.00
S	2.05	2.36	2.21	SO3= 4.84
K2O	0.06	0.11	0.09	0.70
CaO	0.28	0.58	0.43	0.57
TiO2	0.05	0.04	0.05	0.90
Cr2O3	0.33	0.36	0.35	0.36
MnO	0.20	0.18	0.19	0.19
FeO	27.63	25.98	26.81	26.4
NiO	2.18	2.59	2.39	1.56
Sum	83.39	92.61	88	83.46
Elements wt%	**Matrix**	**Rims**	**Average**	**Matrices**
Na	0.27	0.38	0.32	0.16
Mg	11.44	14.13	12.79	11.20
Al	1.14	1.29	1.22	1.27
Si	13.54	15.82	14.68	12.48
P	0.03	0.03	0.03	0.00
S	2.05	2.36	2.21	2.00
K	0.05	0.09	0.07	0.58
Ca	0.20	0.41	0.31	0.41
Ti	0.03	0.02	0.03	0.54
Cr	0.23	0.25	0.24	0.25
Mn	0.15	0.14	0.15	0.15
Fe	21.48	20.19	20.84	20.52
Ni	1.71	2.04	1.87	1.23
O	31.07	35.44	33.26	29.83
Sum	83.39	92.61	88.00	83.46
n	40	62	--	20

Table 3.19- Chemical analyses of Nogoya matrix in Zolensky et al. (1993) and McSween and Richardson (1977).
There is a slight difference between the analyses of the matrix in Zolensky et al. (1993) and McSween and Richardson (1977).

The data of Zolensky et al. (1993) show that the chondrule rims in Nogoya contains more of Mg (+2.69 element wt%) and Si (+2.28 element wt%) than the fine grained matrix.

Their data also indicate that the chondrule rims in Nogoya are enriched in Mg, Fe and Si (about + 4.25 element wt%) compared to those in Mighei, but the concentrations of these elements in fine grained (<1μm) matrix of both meteorites are similar to each other.

The data of Zolensky et al. (1993) are used for comparison with current work using synthesized spectrum (Figure 3.37a**)** of the average of the fine grained (<1μm) matrix and chondrule rims. An EDS spectrum (Figure 3.37b**)** was also obtained for this purpose from a small mapped region (Figure 3.38) in which the highly and less highly altered parts are included. The peaks for Mg, Fe, Si and S in both spectra (Figure 3.37) are very similar to each other (apart for O and Ca). The EDS spectrum of mapped area (Figure 3.38) has peaks of Mg and Fe are comparable relative to Si with those of the EDS spectrum obtained from LON 94101 (Figure 3.33).

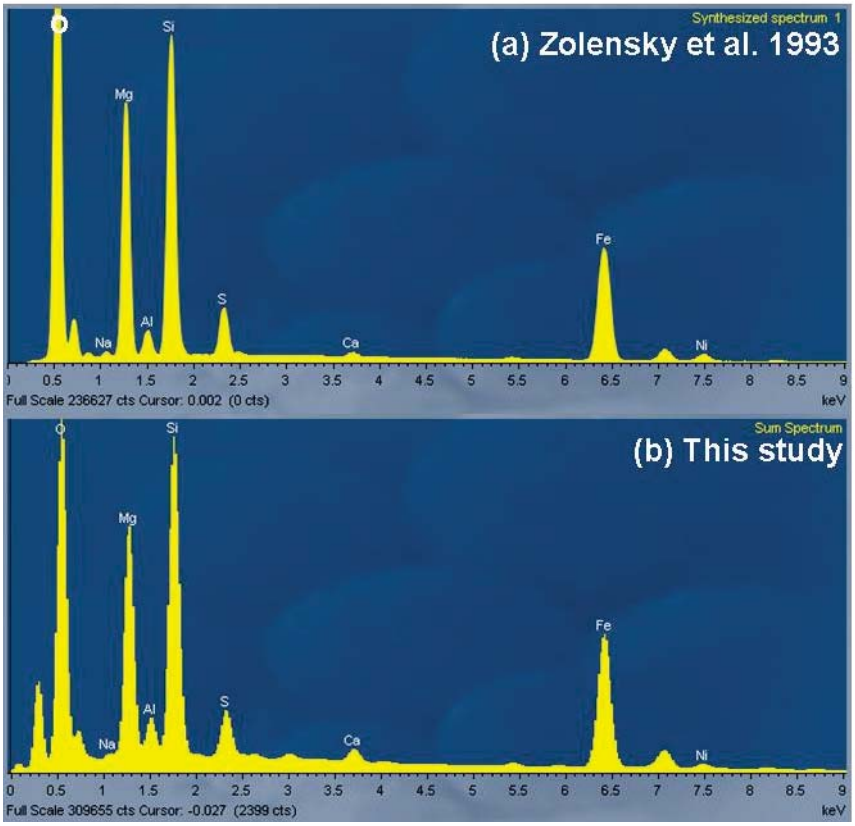

Figure 3.37- EDS spectra of Nogoya matrix.
(a) EDS spectrum of Nogoya matrices obtained from the composition of the matrix and chondrule rims (Zolensky et al., 1993). (b) EDS spectrum of small mapped area in Figure 3.38. The spectrum higher peak of Ca than (a) due to the presence of calcite in the area mapped. These spectra exhibit good agreement between the peaks of Fe, Mg, Si and S (apart for O). Note the Fe peaks in both spectra are lower than those of Mg.

Elemental mapping of several regions of Nogoya matrix (e.g. Figure 3.38) indicates that elements including Fe, Mg and Si are uniformly distributed within these materials, whereas S, Ni and Ca are concentrated in isolated pockets within the matrix.

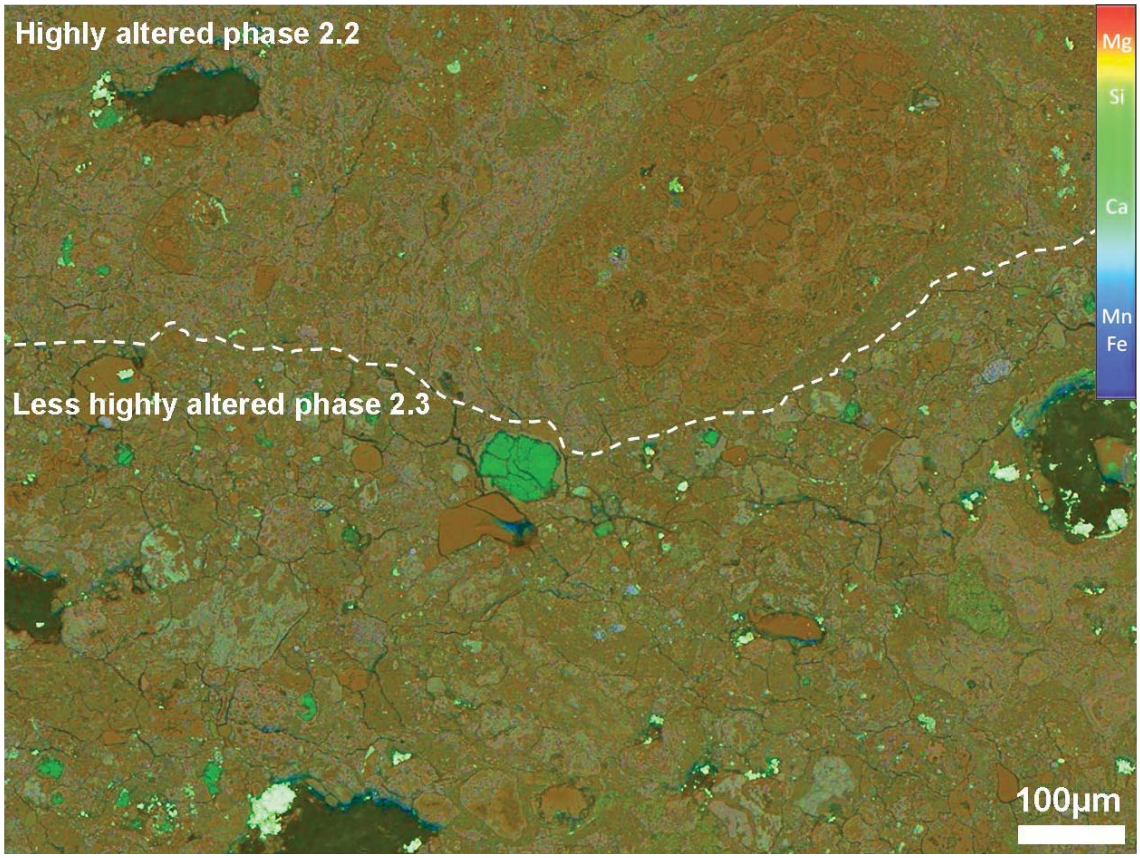

Figure 3.38- False colour multi-element X-ray map of Nogoya matrix.
This combined elemental map associated with colour scale bar (upright side) shows element distributions within a small region (~1mm^2) of Nogoya. Elements include Fe, Mg and Si are uniformly distributed. Note that the high intensity of green colour locates calcite grains and dark red locates Mg-olivine and pyroxene. The location of this map in the sample studied is shown in appendix D7.

EDS spectra of small mapped regions of highly and less highly altered parts indicate that the matrix of the less altered part contains slightly less Mg relative to Si (Figure 3.39). This is consistent with the fact that the matrix of CM chondrites becomes gradually enriched in Mg as consequence of progressive of aqueous alteration (e.g. Tomeoka and Buseck, 1985; Zolensky et al., 1993).

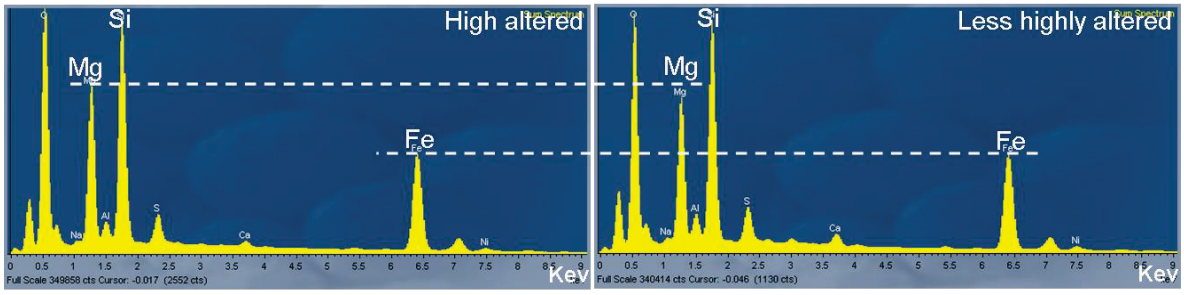

Figure 3.39- EDS spectra obtained from the matrix of highly altered and less highly altered parts in Nogoya.
These spectra reveal that slightly lower concentrations amounts of Mg are present in less altered part of Nogoya relative to the highly altered part.

3.12 Cold Bokkeveld CM2.2

The CM2 carbonaceous chondrite Cold Bokkeveld fell on 13th October, 1838, 0900 am, at Cape Province, South Africa (33º 8´ S., 19º 23´ E.). It was collected as several fragments (e.g. Figure 3.40); the weight of the largest stone is about 2.0 kg (Graham et al., 1985). The total mass of the meteorite is 5.2 kg (Meteoritical Bulletin database, web page, 2012). It has a weathering classification W0-1 (Rubin et al., 2007). One thin section of Cold Bokkeveld (P-4784) was obtained from the Natural History Museum, London. It has an area of about 110 mm^2 that contains a small part of the fusion crust.

Figure 3.40- Image of a fragment of Cold Bokkeveld showing a cracked fusion crust on its surface and unknown white inclusions within it.
The image taken from the Meteoritical Bulletin web page, database, http://www.lpi.usra.edu/meteor/metbull.php?code=5397

3.12.1 Composition and mineralogy of Cold Bokkeveld

Petrographic observations show that Cold Bokkeveld is composed of both high temperature and low temperature minerals. The high temperature minerals are Fe, Mg silicates that are present as isolated fragments and grains within chondrules or chondrule fragment. Olivine grains are scattered within the fine grained (<1μm) matrix and range in size from a few microns to 100 microns. The olivine grains in the areas of the fusion crust have been partially melted at their margins. Three types of porphyritic chondrules are found in the meteorite namely: (i) porphyritic chondrules that are composed of Mg-rich olivine grains, in some cases contain grains of Fe-Ni metal (~2-5 μm), and generally are rounded and sub-rounded in shape; (ii) chondrules containing large grains (~250 μm) of Fe-rich olivine and/or Mg-Fe olivine that are either partly altered or nearly completely altered to phyllosilicates or calcite; (iii) chondrules with porphyritic olivine-pyroxene (chondrules consist of a mixture of clinoenstatite and olivine) are also rarely found (see

Figure 3.42); most of the pyroxene grains in these chondrules have been replaced either by calcite or tochilinite. Most of the chondrules in Cold Bokkeveld are elongate and irregular in shape, and reach up 200 μm in length. The meteorite contains aggregates of spinel grains that are intergrown with calcite. Spinel inclusions were described by Greenwood et al. (1994) as one of four groups of CAIs that are present in Cold Bokkeveld. Hibonite inclusions, spinel-pyroxene inclusions, and spinel-pyroxene-olivine inclusions were the other three groups of CAIs (Greenwood et al., 1994). Pyroxene fragments are rarely observed within the fine grained (<1μm) matrix, but are present as inclusions within a few calcite grains. Fe-sulphides occur in the fine grained matrix and range in size from a few microns to ~50μm, and in some cases are partly or nearly completely replaced by tochilinite. Nearly completely altered Fe-sulphide is abundant between the olivine grains in chondrules.

The fine grained matrix (<1μm) in Cold Bokkeveld consists of phyllosilicates that are dominated by assemblages of tochilinite and tochilinite pseudomorphs after calcite (see section 5.3.4.2). Tochilinite is also found as rims around some Ca-carbonate grains (see Figure 5.19). Carbonate minerals in this meteorite are aragonite and calcite, and both minerals were recorded by Barber (1981). Chondrule rims in Cold Bokkeveld have been described in detail by Zega and Buseck (2003); they reported that the rims to different chondrules are similar in mineral constituents and bulk compositions. However, chondrule rims differ in thickness (ranging from 50μm to 200μm), and show a finer grain size in contact with the chondrules (the grain size of chondrule rims became finer towards the margin of chondrule). They are composed of a chrysotile-like phase, pentlandite, cronstedtite, polygonal serpentine, and tochilinite intergrown with serpentine. Chrysotile-like phase is described as the main mineral in these chondrule rims. It has a fibrous morphology and is rich in Mg (Zega and Buseck, 2003).

Lee (1993) has concluded that Cold Bokkeveld contains calcium sulphate filling fractures and secondary pores. The calcium sulphate was described as having been formed by melting of water ice in the parent body of the meteoritethat causedcalcite dissolution and re-crystallization as gypsum. This process was also described as the final diagenetic processes that took place before the fall of meteorite.

The matrix of Cold Bokkeveld was subdivided into four constituents by Greenwood et al. (1994) including; (i) dust mantles around chondrules, CAIs, etc.; (ii) clasts of fine-grained (<1μm) material; (iii) type I and II of PCP grains as stated in Tomeoka and Buseck (1985);

(iv) clastic matrix material as described by Metzler et al. (1992). The abundance (vol%) of the components in Cold Bokkeveld were determined and are listed in Table 3.20.

Components	Vol%
Fine grained (<1μm) matrix	64.5
Tochilinite-serpentine intergrowth	7.0
Partly altered chondrules	7.0
Tochilinite grains	6.9
Pseudomorphous structures after calcite	2.7
Completely altered chondrules	1.2
Ca-carbonate	0.9
Phyllosilicate fragments	0.5
Spinel	0.2
Mg-rich olivine fragments	4.1
Chondrule rims	3.6
Fe-rich olivine fragments	0.9
Preserved chondrules	0.5

Table 3.20- Abundance of the Cold Bokkeveld components. Values determined by SEM point counting. The total number of points counted was 971

3.12.2 Alteration degree of the Cold Bokkeveld

In common with other CM chondrites, Cold Bokkeveld is a breccia (Barber, 1981; Metzler et al., 1992). It contains about 86 vol% of hydrous materials including: serpentine, tochilinite, completely altered chondrules, chondrule rims and pseudomorphs after calcite (see Table 3.20). The high temperature components in chondrules and chondrule framents represent about 14 vol% of total bulk volume of the rock. Howard et al. (2011) have concluded that Cold Bokkeveld contains 16.4 vol% of Fe, Mg silicates and 77.4 vol% phyllosilicates. This indicates that rock has been extensively altered. It is as described the most altered CM chondrite (more than Nogoya), by Browning et al. (1996); more altered than Nogoya (Rubin et al., 2007); more altered than Nogoya or equivalent to it (Howard et al., 2011); less altered than Nogoya (McSween, 1979; Bunch and Chang, 1980). Rubin et al. (2007) have ranked Cold Bokkeveld as CM2.2 in their alteration sequence.

Petrographic observations and SEM point counting indicate the abundance of grains of Fe-Ni metal in fine grained matrix and inside olivine grains is very low (<0.2 vol%). Kimura et al. (2011) reported that highly altered chondrites such as Nogoya and Cold Bokkeveld contain scarce Fe-Ni metal, in which Ni ranges from 4.2 to 12.8 wt%. Cold Bokkeveld

contains isolated grains of pentlandite within fine grained (<1µm) matrix that have been partly or completely transformed to Mg-rich serpentine (Figure 3.41).

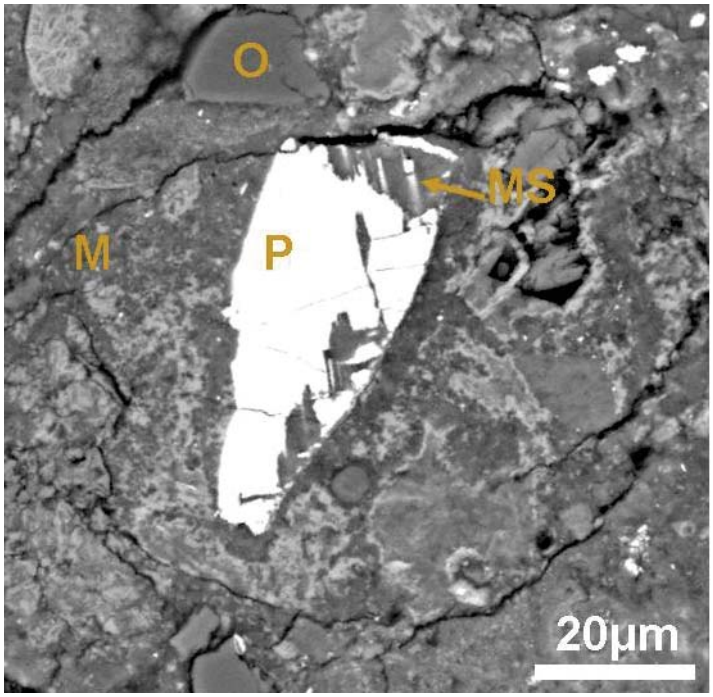

Figure 3.41- BSE image of altered pentlandite in Cold Bokkeveld.
The image shows pentlandite (P) that has been partly replaced by Mg-rich serpentine (MS). O is Mg-rich olivine, M is fine grained (<1µm) Matrix. The location of this map in the sample studied is shown in appendix D8.

The majority of Fe-rich olivine grains in this meteorite are likely to have been replaced by other minerals. Some of Mg-rich olivine grains in chondrules and chondrule fragments have also been highly affected by aqueous alteration. Based on these observations and previous results, Cold Bokkeveld is placed at the same stage of alteration as Nogoya (CM2.2).

3.12.3 The chemical composition of Cold Bokkeveld

Chemical analyses of the Cold Bokkeveld matrix have been summarized by McSween and Richardson (1977). Their analyses in oxide wt% have been converted to elements wt% and are listed in Table 3.21. As mentioned above, McSween and Richardson (1977) used a defocused beam to obtain the chemical analyses of CM matrices, but their chemical analyses of Cold Bokkeveld matrices in elements wt% are used for comparison with the current study (Figure 3.43). Their analyses indicate that the matrix of Cold Bokkeveld contains less Mg (-1.5 wt%) and more Fe (+3 wt%) than the Nogoya matrix.

Elemental mapping of small regions and the sample of the Cold Bokkeveld was undertaken (e.g Figure 3.42) to identify the distribution of elements, in particular Fe, Mg, Ca, Si and S. The presence of Ca and S together shows that some fractures in the meteorite are filled with calcium sulphate (see also Lee, 1993). Elemental mapping shows that Mg, Fe and Si are homogenously distributed within the fine grained (<1μm) matrix (areas free of tochilinite) and chondrule rims.

Oxides wt%		Elements wt%	
Na_2O	0.44	**Na**	0.33
MgO	16.2	**Mg**	9.76
Al_2O_3	3.12	**Al**	1.64
SiO_2	26.7	**Si**	12.48
SO_3	5.5	**S**	2.25
K_2O	0.07	**K**	0.07
CaO	0.34	**Ca**	0.24
TiO_2	0.1	**Ti**	0.06
Cr_2O_3	0.31	**Cr**	0.21
MnO	0.19	**Mn**	0.15
FeO	30.1	**Fe**	23.40
NiO	1.91	**Ni**	1.50
Total	84.98	**O wt%**	29.64
n	20		

Table 3.21- Chemical analyses in oxide and element wt% of the matrix of Cold Bokkeveld (McSween and Richard, 1977).

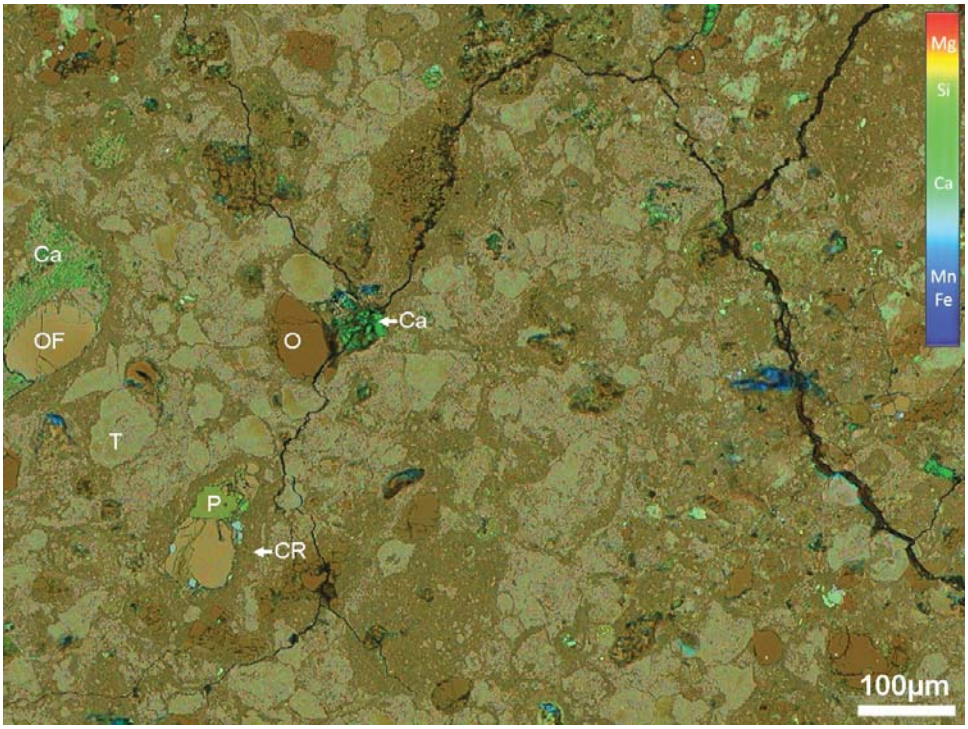

Figure 3.42- False colour multi-element X-ray map with colour scale (top) showing the distribution and concentration of elements in the matrix of Cold Bokkeveld.
The elements Fe, Mg and Si appear uniformly distributed throughout chondrule rims (CR) and the fine grained (<1µm) matrix in areas where tochilinite (T) is absent. O is Mg-rich olivine, Ca is calcite, OF is Fe-rich olivine and P is pyroxene within a porphyritic chondrule. The location of this map in the sample studied is shown in appendix D8.

An EDS spectrum of a small mapped area (in Figure 3.42) is used for comparison with synthesized spectrum of analyses by McSween and Richardson (1977) (Figure 3.43). Peaks of Mg, Fe and S in both spectra are nearly identical to each other. The two spectra show that matrix of the meteorite contains higher contents of Mg than Fe. The spectrum of Cold Bokkeveld matrices (this study) was compared with the EDS spectrum of Nogoya (this study Figure 3.37), and this indicates that the matrix of Nogoya contain more Mg and less Fe than Cold Bokkeveld.

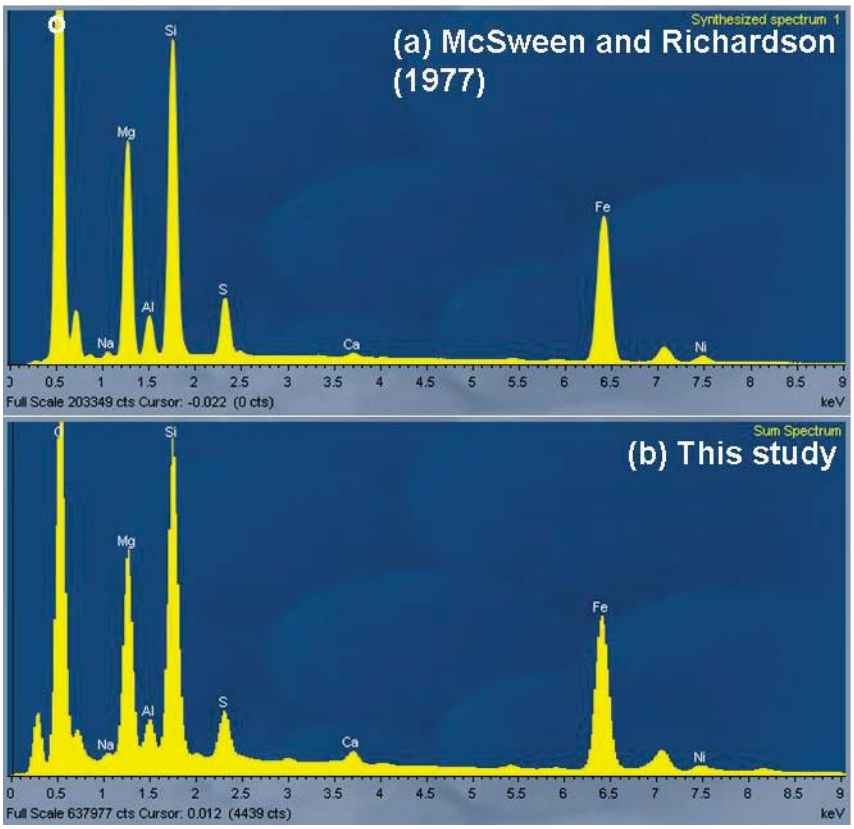

Figure 3.43- EDS spectra of Cold Bokkeveld matrix.
Comparison between two EDS spectra of Cold Bokkeveld matrices (a) synthesized spectrum of analyses of McSween and Richardson (1977) obtained using INCA software. (b) Spectrum of small mapped area (Figure 3.42) of Cold Bokkeveld. Relative peak heights are comparable between the two spectra (apart for O). Peaks of S, Mg are similar to each other, but peak of Fe is slightly greater in spectrum (b) (current study), which is possibly due to the occurrence of anhydrous materials in the mapped area (Figure 3.42).

3.13 QUE 93005 CM2.1

The CM2 chondrite QUE 93005 was collected by the Antarctic Search for Meteorites program (ANSMET) in 1993 at Queen Alexandra Range in Antarctica (84° 37' 23"S, 162° 1' 16"E). The total weight of the meteorite is 13.4 g and its dimensions in cm are 3.5 x 1.7 x 1.9. Fusion crust covers 90% of external surface of the meteorite and is also characterized by presence of flow marks (Meteoritical Bulletin database, web page, 2012). The meteorite has a weathering grade of A/Be (Grossman and Score, 1996). One polished thin section, QUE 93005 (10), was loaned from the NASA Antarctic meteorite collection for this study. It has an area of about 126mm^2.

3.13.1 Composition and mineralogy of QUE 93005

Quantatitive modal mineralogy by Howard et al. (2011) showed that QUE 93005 contains 11.1 vol% olivine, 1.4 vol% orthopyroxene, 1.7 vol% calcite, 1.5 vol% magnetite, 2.2 vol% sulphide, 20.8 vol% Fe-cronstedtite and 61.3 vol% Mg-rich serpentine. Fe-Ni metal was absent. Rubin et al. (2007) reported that QUE 93005 contains very little metallic Fe-Ni (less than 0.01 vol%). About 95-98% of mafic silicates within chondrules have been altered to hydrous minerals. Most of chondrules are therefore composed mainly of phyllosilicates and sulphides, however some have small cores of olivine. Rubin et al. (2007) reported that this chondrite contains about 8 vol% of carbonate and 1.2 vol% of sulphide (in most cases is pentlandite).

QUE 93005 is unbrecciated (Velbel et al., 2005; Rubin et al., 2007). Petrographic observations indicate that it contains abundant altered and near completed altered chondrules that range in size from a few hundred microns to more than 1mm. Most of them are rounded, sub rounded and elongated in shape, although some are irregular. The secondary minerals in these chondrules are tochilinite and Mg-serpentine. The remaining Mg–rich olivine grains in chondrules have etched margins and contain patches of alteration products. These chondrules also contain Fe-sulphide, and Fe-Ni grains within Mg-rich olivine. One radial pyroxene chondrule is found, well preserved and rounded in shape.

Some of the chondrules (altered/nearly completely altered) are characterized by the presence of pentlandite and or Fe-sulphide that occurs as a rim around altered grains. Reflected light imaging (Figure 3.44) additionally shows also that blocky pentlandite grains are present around carbonates and some olivine grains; they are also intergrown

with phyllosilicates around carbonate grains. The fine grained (<1μm) matrix is mottled with very small grains of pentlandite and Fe-sulphide. Very rare Mg-rich olivine fragments are scattered within the fine grained (<1μm) matrix. The chemical composition of olivine that was partly replaced by serpentine in QUE 93005 ranges between Fo_{77} and Fo_{99} (Velbel et al., 2005).

Rims around altered and near complete altered chondrules have two different textures: (i) rims are comparable in texture with the fine grained (<1μm) matrix (Figure 3.45); (ii) rims display grain size coarsening outward from the edge of the chondrule. The prominent feature in QUE 93005 is that some chondrule rims have radial fractures, comparable to the radial fractures around chondrules in EET 96029. As stated above, they were possibly formed as a consequence of expansion of chondrules during the alteration of primary materials. Most of these fractures in QUE 93005 have been later filled by calcite or calcite and pentlandite. Carbonate minerals occur in six types in QUE 93005, namely: calcite, dolomite, breunnerite, calcite-dolomite intergrowth, breunnerite-dolomite intergrowth and breunnerite-dolomite-calcite. The abundance in vol% of all constituents QUE 93005 is listed in Table 3.22.

Components	Vol%
Fine grained (<1μm) matrix	63.2
Altered and partly altered chondrule	22.7
Dolomite-calcite intergrowth	1.9
Dolomite	0.7
Calcite	0.7
Fe-sulphide and pentlandite	0.7
Breunnerite-dolomite-calcite intergrowth	0.3
Breunnerite	0.2
Olivine fragment	5.4
Chondrule rims	4.1
Apatite	0.1

Table 3.22- Abundance of the QUE 93005 components.
Values determined by SEM point counting. The total number of points counted is 882.

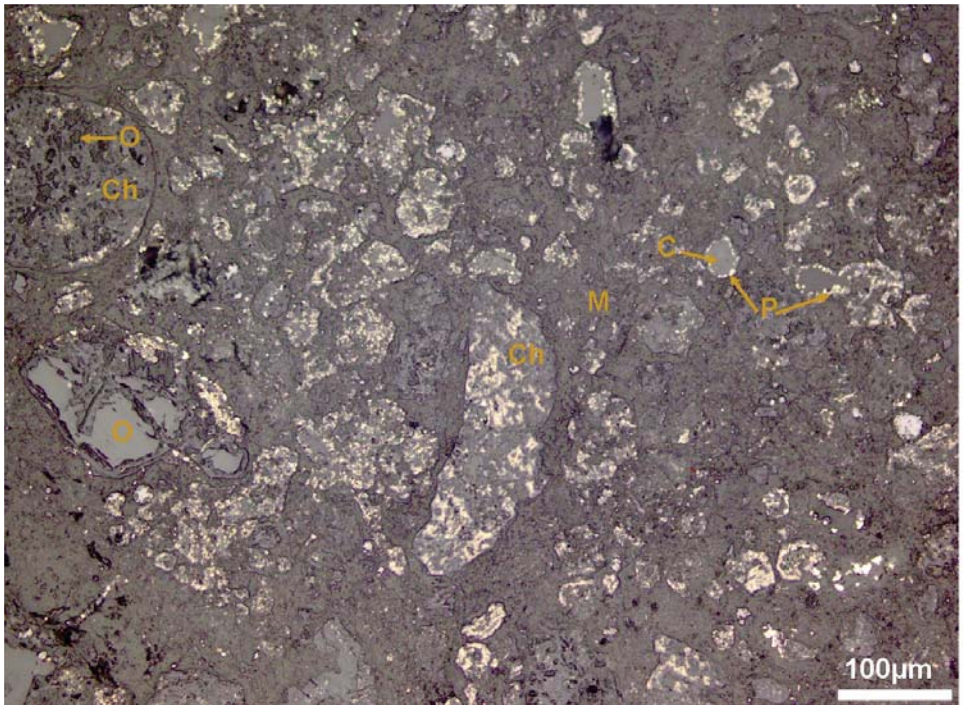

Figure 3.44- Reflected light image of QUE 93005.
The image shows the occurrence of Fe-sulphide and pentlandite (P) within the fine grained (<1µm) matrix (M) and chondrules (Ch). O is olivine, C is carbonate. The location of this map in the sample studied is shown in appendix D9.

3.13.2 Alteration degree of QUE 93005

QUE 93005 was described as a highly altered CM chondrite and was classified as CM2.1 by Rubin et al. (2007). The proportion of anhydrous materials (Fe, Mg silicates) is 12.4%, whereas the phyllosilicates represent 82.1% of the meteorite (Howard et al., 2011), and they described it as more altered than Cold Bokkeveld. Using MAI, Velbel et al. (2005) reported that QUE 93005 is more highly altered than Murchison. SEM point counting for this study showed that altered and partly altered chondrules, the fine grained (<1µm) matrix and chondrule rims (<1µm) together represent about 89 vol% of the total bulk of the meteorite. These petrographic observations indicate that the vast majority of the original anhydrous materials in QUE 93005 have been altered (e.g. Figure 3.45). Very little Fe-Ni metal is found surviving inside Mg-rich olivine grains, and most have been replaced by serpentine around their edges. Using these observations and published results (discussed above), the alteration degree of QUE 93005 is assigned as CM2.1.

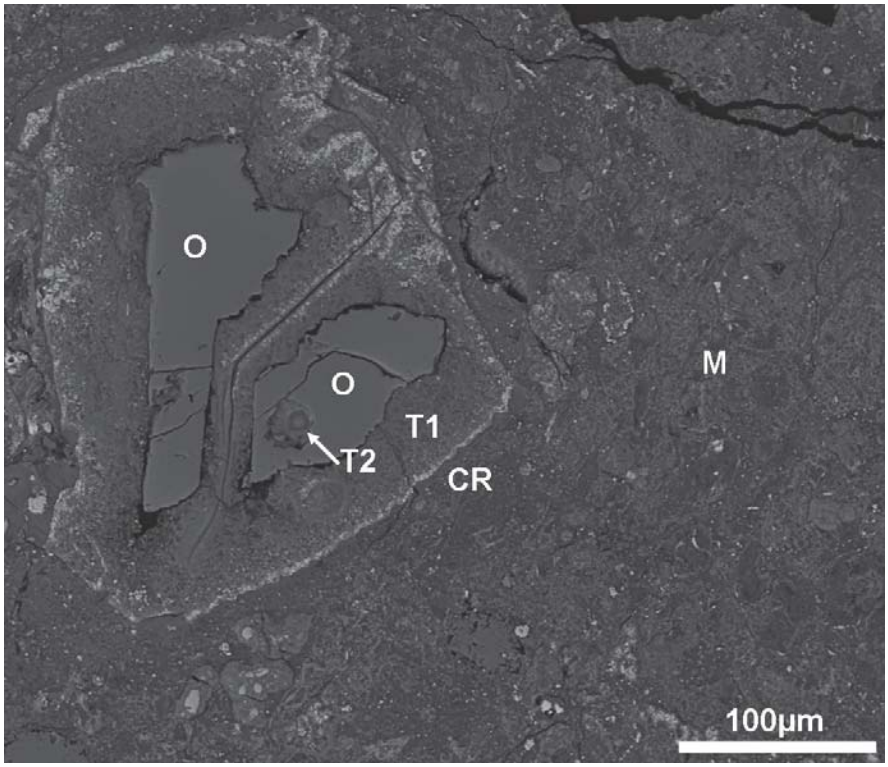

Figure 3.45- BSE image showing a near completely altered chondrule in QUE 93005.
O is olivine, T1 is serpentine that has replaced olivine, T2 is core of serpentine within olivine. Note the textures of the chondrule rims (CR) and the fine grained (<1µm) matrix (M) are similar to one other. The location of this map in the sample studied is shown in appendix D9.

3.13.3 The chemical composition of QUE 93005 matrices

Elemental mapping of small regions and the entire sample of QUE 93005 was undertaken (e.g. Figure 3.46) to investigate the distribution of elements, including Fe, Mg, Ca, Si, Ni and S. A Ca map of whole sample, combined with the BSE image, indicates that carbonate veins are common in this meteorite, and are present in the fine grained (<1µm) matrix and rims (<1µm) around the chondrules. The maps of Fe, Si and Mg show that these elements are somewhat homogeneously distributed within the fine grained matrix and chondrule rims. An EDS X-ray spectrum (Figure 3.47) of the mapped area in Figure 3.46 shows that Si, Mg, Fe and S are most abundant in QUE 93005. Comparison between the EDS spectrum of the matrix of Cold Bokkeveld (shown in Figure 3.43) and of QUE 93005 (Figure 3.47) reveals that QUE 93005 matrix contains less Fe and higher contents of Mg than Cold Bokkeveld.

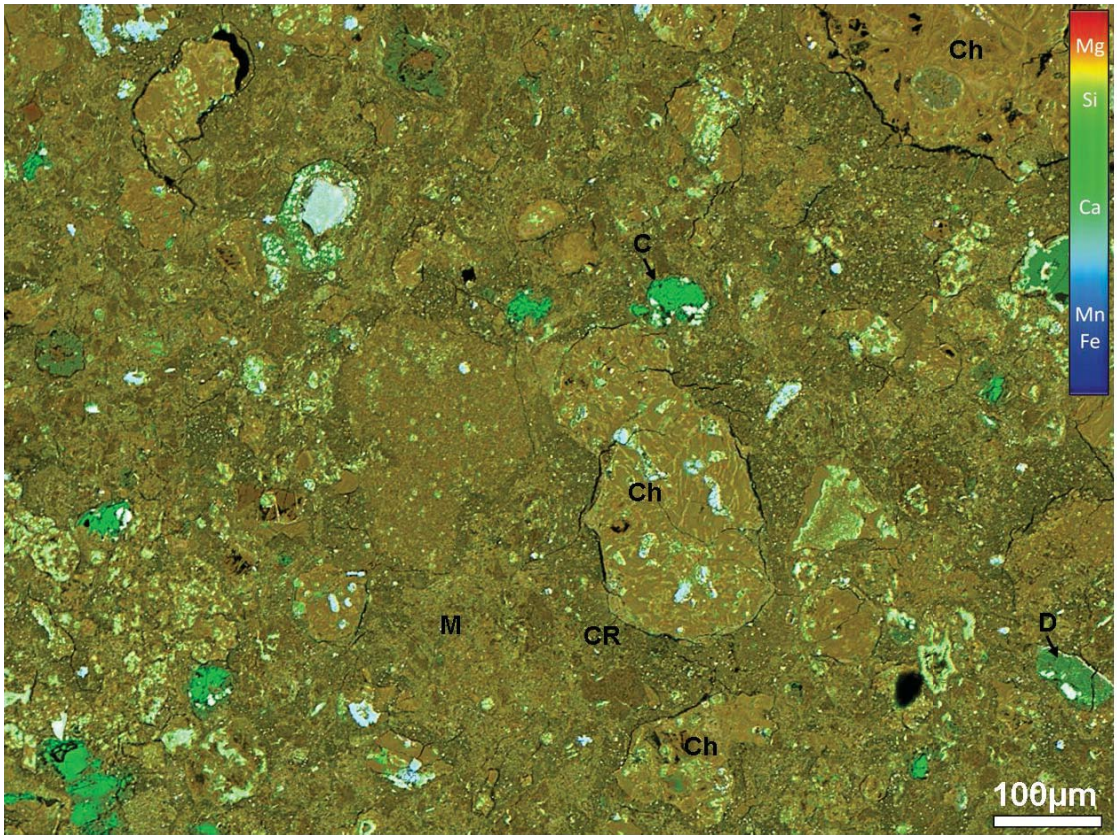

Figure 3.46- False colour multi-element X-ray map associated with colour scale (top) showing the distribution and relative concentration of elements in a small region in QUE 93005.
The elements Fe, Mg and Si appear uniformly distributed throughout chondrule rims (CR) and the fine grained (<1µm) matrix. C is calcite, Ch altered chondrules, CR chondrule rims, M is fine grained matrix, and D is dolomite in which the Ca is less concentrated than calcite (C). The location of this map in the sample studied is shown in appendix D9.

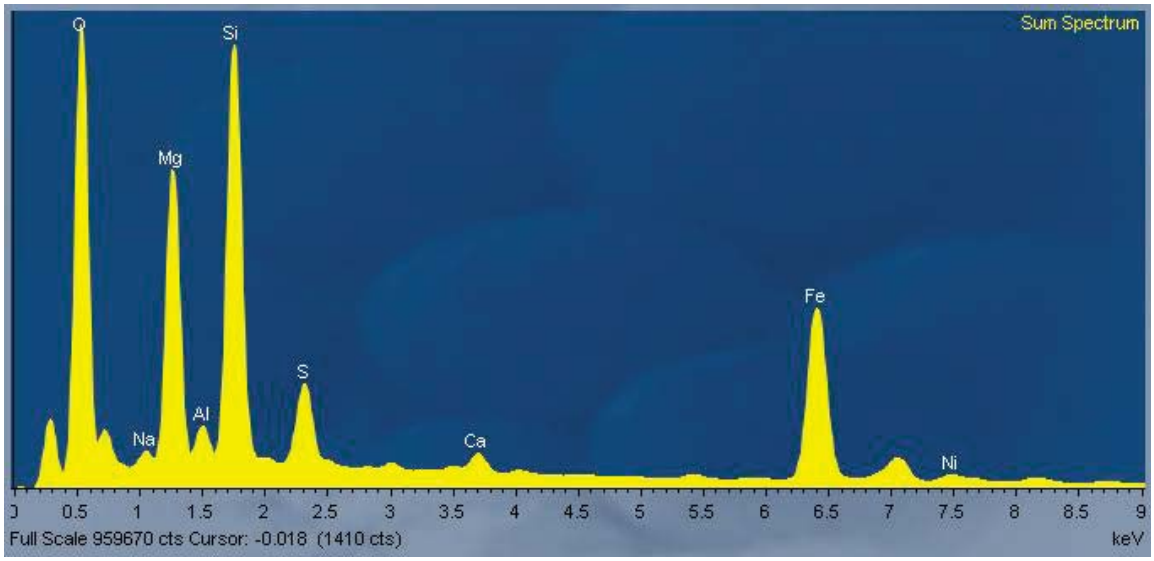

Figure 3.47- EDS spectrum from the mapped area in Figure 3.46.
It reveals that the QUE 93005 matrix contains high abundant Mg and Si relative to the matrix of Cold Bokkeveld.

3.14 LAP 031166 CM2.1/2.0

The CM1/2chondrite LAP 031166 was collected by US Antarctic Search for Meteorites program (ANSMET) in 2003 at LaPaz Ice field in Antarctica. The total mass of LAP 031166 is 15.083 g and it is divided in several pieces (Figure 3.48). Its weathering grade (described in section 1.4.2) is B. The fusion crust of this meteorite covers 80% of its external surface and is fractured with a purplish black colour, whereas the internal part is dull black. LAP 031166 is described as soft and somewhat friable (AMN 29(2), 2006). One thin section of LAP 031166 (sample number 15) was used for current study. It was loaned by the NASA Antarctic meteorite collection and has an area of about 100 mm^2.

Figure 3.48- Image showing the fragments of LAP 031166.
The image from the Meteoritical Bulletin web page, database,
http://www.lpi.usra.edu/meteor/metbull.php?code=35812

3.14.1 Composition and mineralogy of LAP 031166

Low magnification images of LAP 031166 show that it has a fabric that may have formed by burial compaction in its parent body. This phenomena has also been observed in some other CMs (e.g. Lee and Ellen, 2008; Lindgren, 2011). LAP 031166 is a highly altered meteorite in which the vast majority (~95%) of the original Fe, Mg silicates have been replaced by minerals including tochilinite, serpentine and calcite, and the meteorite contains ~90 vol% hydrous materials. The modal mineralogy (Howard et al., 2011) of highly altered CM1/2 and CM1 chondrites indicates that the abundance of phyllosilicates in these meteorites ranges from 86-88%. LAP 031166 contains very little Fe-rich olivine preserved within chondrules and chondrule fragments. A few grains of Mg-rich olivine occur in the fine grained (<1μm) matrix and within altered chondrules. Some of these grains appear as a preserved core within a tochilinite rim, others have been highly modified as a result of aqueous alteration (Figure 3.49). The meteorite contains completely, near

completely and partly altered chondrules (only two). They range in size from a few microns to about 300 µm. Fe-Ni metal grains are rarely (≤0.2 vol%) present inside Mg-rich olivine grains, and in most cases have been aqueously altered. Fe-Ni metal is absent from the fine grained matrix (<1µm).

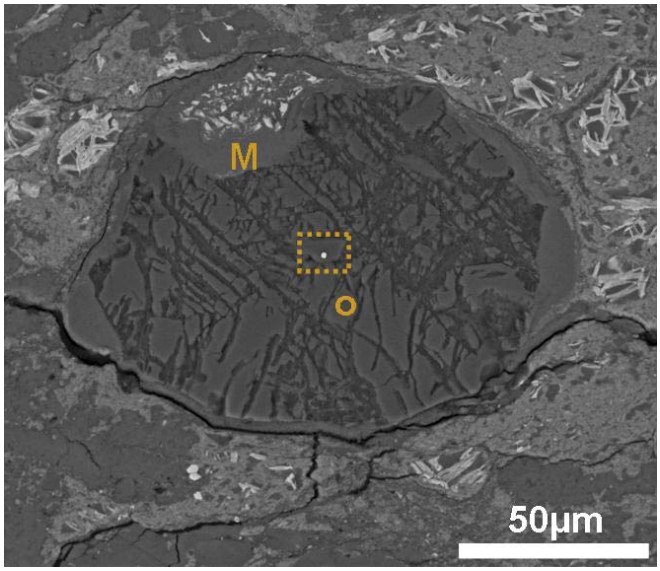

Figure 3.49- BSE image showing large Mg-rich olivine grain (O) that has been highly aqueously altered. M is Mg-serpentine, LAP 031166.
Note the preserved Fe-Ni grain within the square. The grain size of the olivine is 150 µm. The location of this map in the sample studied is shown in appendix D10.

Fe-sulphide is present mainly as rims around Mg-rich phyllosilicate pseudomorphs after calcite and some calcite grains; sometimes it occurs in conjunction with pentlandite (Fe-Ni-S) around these pseudomorphs. In some cases, Fe-sulphide is present as inclusions within pseudomorphs and calcite grains. Pentlandite is also found as blocky crystals around some olivine grains. The most remarkable feature in LAP 031166 is the extent of Mg-rich phyllosilicate pseudomorphism after calcite and their Fe-sulphide rims that are analogous to those in Pollen (CM2.4). Carbonate minerals in LAP 031166 are calcite and dolomite.

Rims to chondrules and chondrule fragments; are very rare; however a few chondrules have narrow rims (<50µm) that consist of tochilinite-serpentine intergrowths. The matrix of LAP 031166 is very finely crystalline and is divided into two phases: (i) one that is dark in BSE images and in which serpentine is dominant, (ii) a phase that is bright in BSE images composed mainly of tochilinite and cronstedtite (Figure 3.50). Some fractures that cross-cut the fine grained (<1µm) matrix are filled with either calcium sulphate or dolomite, but calcium sulphate is dominant (Figure 3.51). The abundance of the LAP 031166 constituents was determined by SEM point counting and is listed in Table 3.23.

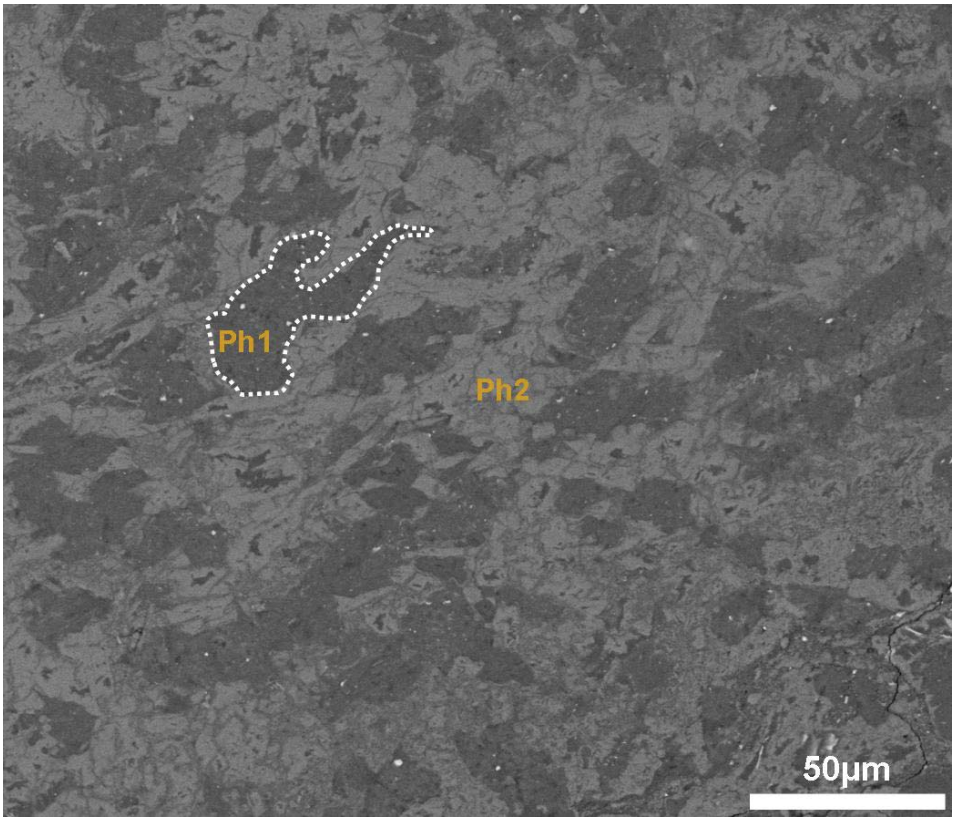

Figure 3.50- BSE image showing the fine grained matrix of LAP 031166.
This matrix is divided into two phases including serpentine-rich (Ph1) and tochilinite-rich (Ph2). The location of this map in the sample studied is shown in appendix D10.

Components		vol%
Fine grained (<1µm)	matrix dark-phase	41.9
Fine grained (<1µm)	matrix bright-phase	32.3
	Chondrules completely altered	7.5
	Chondrules near complete altered	5.6
	Mg-phyllosilicate Pseudomorphs after calcite	4.6
	Fe-sulfide fibres around Mg-phyllosilicates pseudomorphs	3.9
	Calcite	0.8
	Gypsum	0.8
	Partly altered olivine	0.1
	Pentlandite grains with Fe-Ni-S	0.5
Mg-rich olivine		1.2
Chondrules partly altered		0.5
Chondrule rims		0.5

Table 3.23- Abundance of the LAP 031166 components.
Values determined by SEM point counting. The total number of points counted is 1044.

3.14.2 The alteration degree of LAP 031166 CM2.1/2.0

LAP 031166 is a highly altered meteorite. It is apparently unbrecciated, and contains very rare blebs of Fe-Ni metal (≤0.2 vol%) in anhydrous silicate phenocrysts. As stated above, about 95% of Mg, Fe silicates in chondrules have been transformed to hydrous minerals. In

addition, the meteorite contains abundant cross-cutting micro-veins, more abundant than QUE 93005, Cold Bokkeveld and LON 94101. Bunch and Chang (1980) have reported that veining gradually increases from invisible in less altered Murchison and Murray, to rare in the highly altered Cold Bokkeveld and Nogoya, and to considerable occurrences in Orgueil (CI). Based on the petrographic observations and results of SEM point counting, LAP 031166 is assigned to be CM2.1/2.0, which is slightly more altered QUE 93005.

3.14.3 The chemical composition of LAP 031166 matrices

Chemical analysis of the fine grained (<1μm) matrix in LAP 031166 was carried out by EPMA. The bright and dark phases in this matrix were individually analyzed and the mean analyses of each phase are presented in Table 3.24. The analyses indicate abundant Mg, Si and Fe in the bright phase (Tochilinite-cronstedtite), whereas the dark phase (Serpentine) has higher concentrations of Si and Mg and substantially less Fe than the bright phase.

	Oxides wt%			**Elements wt%**	
	Tochilinite-cronstedtite	Serpentine		Tochilinite-cronstedtite	Serpentine
Na2O	0.24 ± 0.03	0.09 ± 0.01	**Na**	0.18	0.07
MgO	10.98 ± 0.66	26.11 ± 0.54	**Mg**	6.62	15.74
Al2O3	3.08 ± 0.19	1.75 ± 0.27	**Al**	1.63	0.92
SiO2	24.40 ± 1.20	37.77 ± 0.58	**Si**	11.41	17.66
CaO	0.17 ± 0.16	0.10 ± 0.05	**Ca**	0.12	0.07
FeO	43.37 ± 0.71	18.45 ± 0.48	**Fe**	33.71	14.35
K2O	0.03 ± 0.02	0.01 ± 0.00	**K**	0.03	0.01
P2O5	0.12 ± 0.12	0.01 ± 0.02	**P**	0.05	0.01
SO2	4.08 ± 0.66	0.36 ± 0.11	**S**	2.04	0.18
TiO2	0.19 ± 0.19	0.08 ± 0.02	**Ti**	0.12	0.05
Cr2O3	0.27 ± 0.03	0.07 ± 0.04	**Cr**	0.19	0.05
MnO	0.19 ± 0.08	0.24 ± 0.06	**Mn**	0.15	0.19
NiO	0.69 ± 0.16	0.20 ± 0.01	**Ni**	0.54	0.16
SUM	85.24	87.82	**O**	31.04	35.80
n	4	2			

Table 3.24- Chemical analyses of bright and dark phases in the fine grained matrix of the LAP 031166. Data presented as mean ± SD, error values are calculated to 1σ. The full dataset with standard deviation is listed in appendix A.4.

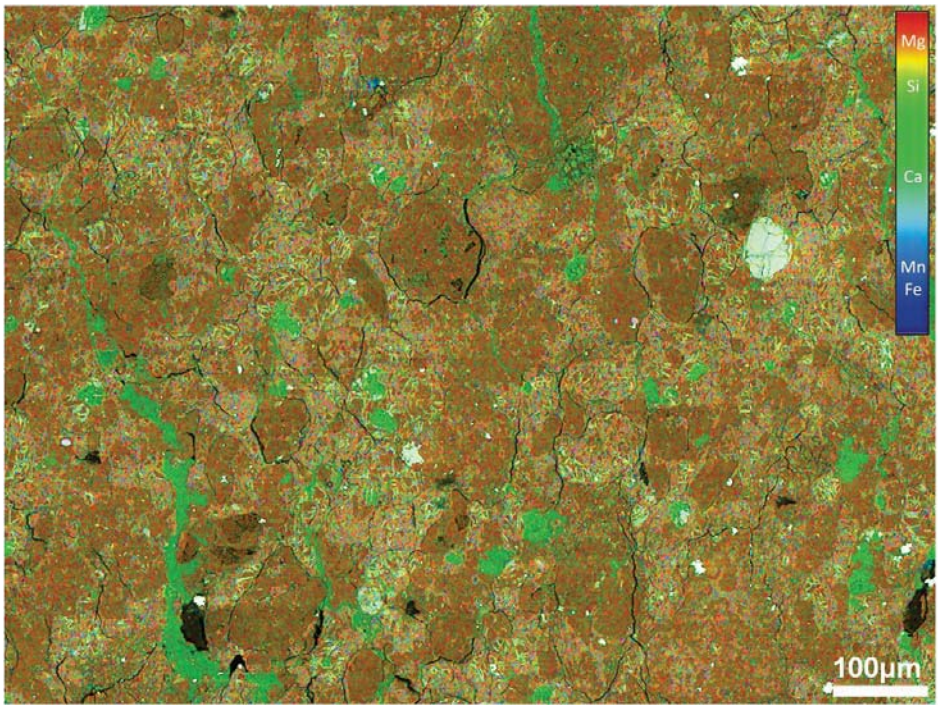

Figure 3.51- False colour multi-element X-ray map of a ~1mm^2 region of LAP 031166.
The map highlights the concentration and distribution of Si, Fe, Mg, S and Ca. Note the presence of gypsum micro-veins (green veins) cross-cutting the fine grained (<1µm) matrix. The colour scale bar is provided in the upper right part of the map. The location of this map in the sample studied is shown in appendix D10.

EDS spectra of small mapped areas (Figure 3.51) reveal the abundance of Si, Mg and Fe. Peaks of Fe, Mg, Si and S in the spectrum (Figure 3.52) of the small mapped area were compared with those in the spectrum of less altered QUE 93005 (Figure 3.47), and this indicates that QUE 93005 contains more Mg, and less Fe and S than the LAP 031166 matrix.

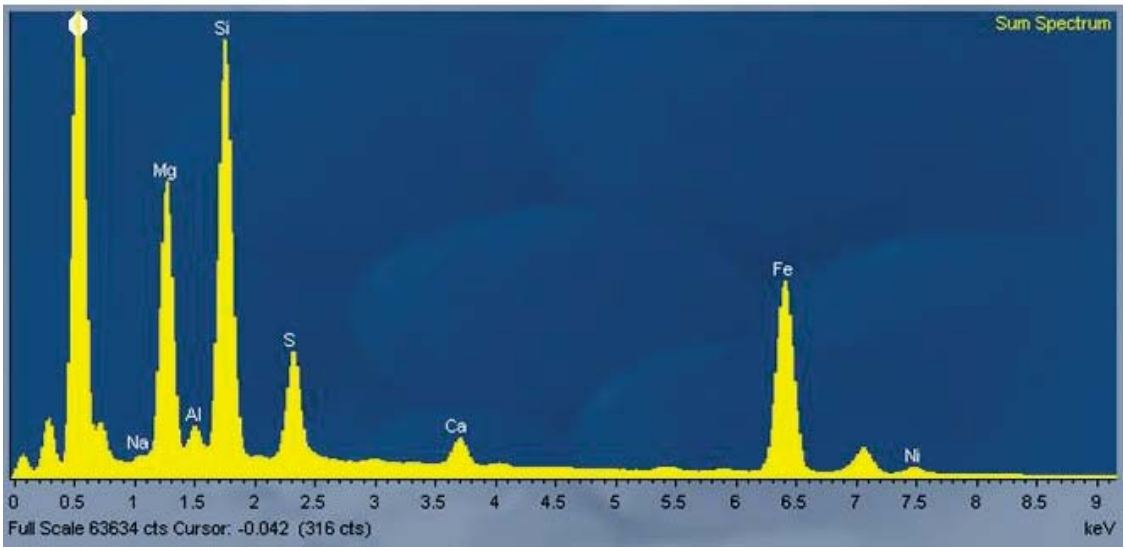

Figure 3.52- EDS spectrum of the small mapped area in Figure 3.51 showing the qualitative chemical composition of LAP 031166.

3.15 SCO 06043 CM2.0

The CM1 chondrite SCO 06043 was collected by US Antarctic Search for Meteorites program (ANSMET) in 2006 at Scott Glacier in Antarctica. The total mass of SCO 06043 is 27.6 g (Figure 3.53), and its weathering grade is B/CE. The fusion crust of this meteorite covers 10% of its external surface, has bubbles and is purple-black in colour. The interior part is black, and has fractures with evaporites and an oxidation rind (AMN 31(1), 2008). One thin section SCO 06043 (sample number 10) was used for current study that was loaned by the NASA Antarctic meteorite collection. The section has an area of about 85 mm^2.

Figure 3.53- Image showing the fragment of SCO 06043 meteorite. The image from the Meteoritical Bulletin, database, http://www.lpi.usra.edu/meteor/metbull.php?code=46404

3.15.1 Composition and mineralogy of SCO 06043

In common with LAP 031166, SCO 06043 shows a fabric by a preferred orientation of matrix that is probably a consequence of lithostatic compaction in the parent body. SCO 06043 is unbrecciated. Quantitative modal mineralogy (Howard et al. 2011) indicates that SCO 06043 contains 3.3 vol% olivine, 1.7 vol% calcite, 1.6 vol% magnetite, 2.7 vol% sulphide, 21.6 vol% Fe-cronstedtite and 66.0 vol % Mg-rich serpentine.

Petrographic observations show that SCO 06043 has very rare Mg, Fe silicate grains within chondrules or as fragments in the fine-grained (<1μm) matrix. This meteorite is highly altered, and about 98% of the chondrules are completely altered. The completely and near completely altered chondrules are mainly composed of tochilinite and Fe-cronstedtite, and in some cases have patches of Fe-sulphides and/or pentlandite. Fe-sulphide and pentlandite grains are also scattered within the fine grained (<1μm) matrix, and they are more

abundant in some areas. Pentlandite occurs also as blocky crystals in conjunction with dolomite and some remaining Mg-rich olivine grains. Chondrules lack rims, and all of them have sharp contacts with the fine grained (<1μm) matrix. The fine grained matrix in SCO 06043 is comparable to fine grained matrix in LAP 031166, as it can also be divided into bright BSE and dark phases. The bright BSE is more abundant than dark phase (Figure 3.54).

The thin section of SCO 06043 studied contains fractures that cross-cut the matrix and that are filled either with Ca-sulphate, calcite or dolomite. Some minerals (i.e. dolomite) within fractures in the fusion crust of SCO 06043 have been heated and texturally are different to the same minerals that are further from the crust (Figure 3.54). This suggests that at least some of the fracture fills formed prior to the fall of the meteorite. Some gypsum grains are intergrown with calcite, as was also observed for individual grains (gypsum and calcite) enclosed within Mg-rich serpentine. In some cases calcite has been replaced by gypsum. These petrographic observations also indicate that SCO 06043 has a more veins that cross-cut the fine grained (<1μm) matrix than LAP 031166. Mg-rich serpentine pseudomorphs after carbonate minerals (i.e. calcite and dolomite) are common in SCO 06043 and have thin rims of tochilinite (~0.25 μm). The abundance of all components of the SCO 06043 is listed in Table 3.25.

This sudy shows that areas in some of the samples studied (i.e. Pollen, Cold Bokkeveld, SOC 06043, LAP 031166 and QUE 93005) are made of fusion crust, which also contains calcite and/or dolomite grains, where the outer areas are texturally different to those in other areas of the sample. BSE images revealed that the internal part (labeled L2 in Figure 3.54a and b) of the fusion crust (i.e. the transition area located between the main area of the sample and the outer part of the fusion crust) differs from the outer part as the latter (labeled L1 in Figure 3.54a and b) contains large holes (20-70 μm in diameter), due to partial melting of silicate grains during the passage of the meteorite through the Earth's atmosphere (e.g. Lenart et al., 2010; Reimold et al., 2004). The contact between these two zones is not sharp, due to partial melting of the phyllosilicates matrix (see Figure 3.54). Investigations of meteorite fusion crust (Jesenice L6 chondrite) by Lenar et al. (2010) revealed that not all the minerals (olivines, pyroxenes and feldspar) at the surface had completely melted; in fact, these silicates reprecipitated as a glassy phase rich in Fe and Ni. They reported that structural changes to the thin fusion crust (~0.3mm) are a result of high temperatures (>1500 °C) associated with high pressure during passage through the atmosphere. Ivanov and Deutsch (2002) reported that calcite shocked to pressure >1 GPa

and temperatures >1227-1727 °C should be subjected to melting. Therefore, the absence of carbonate minerals at the surface and the outermost part of the fusion crust is most likely to be a result of these minerals melting during the passage of the meteorite through the Earth's atmosphere. Distribution of carbonate minerals (calcite and dolomite) within the second layer (labeled L2 in Figure 3.54a and b) is similar to those in the main areas of the sample (free of fusion crust), but have a darker appearance in BSE images and their outer areas are extensively degraded, which is consistent with alteration of the calcite or dolomite by high temperatures (e.g. Figure 3.54, Figure 5.14 d). The significance of the study of carbonate minerals in fusion crusts is to report that the heated carbonate was formed prior to the fall of the meteorite.

Components	Vol%
Fine grained (<1μm) matrix	72.6
Completely altered chondrule	15.0
Pseudomorphism after carbonate	7.2
Iron-sulphide	2.5
Chondrule partly altered	0.2
Mg-olivine	0.4
Tochilinite	0.8
Calcite	0.2
Dolomite	0.8
CI clast	0.3

Table 3.25- The abundance of the components of SCO 06043 in vol%. Determined by SEM point counting. The total point counted is 1265.

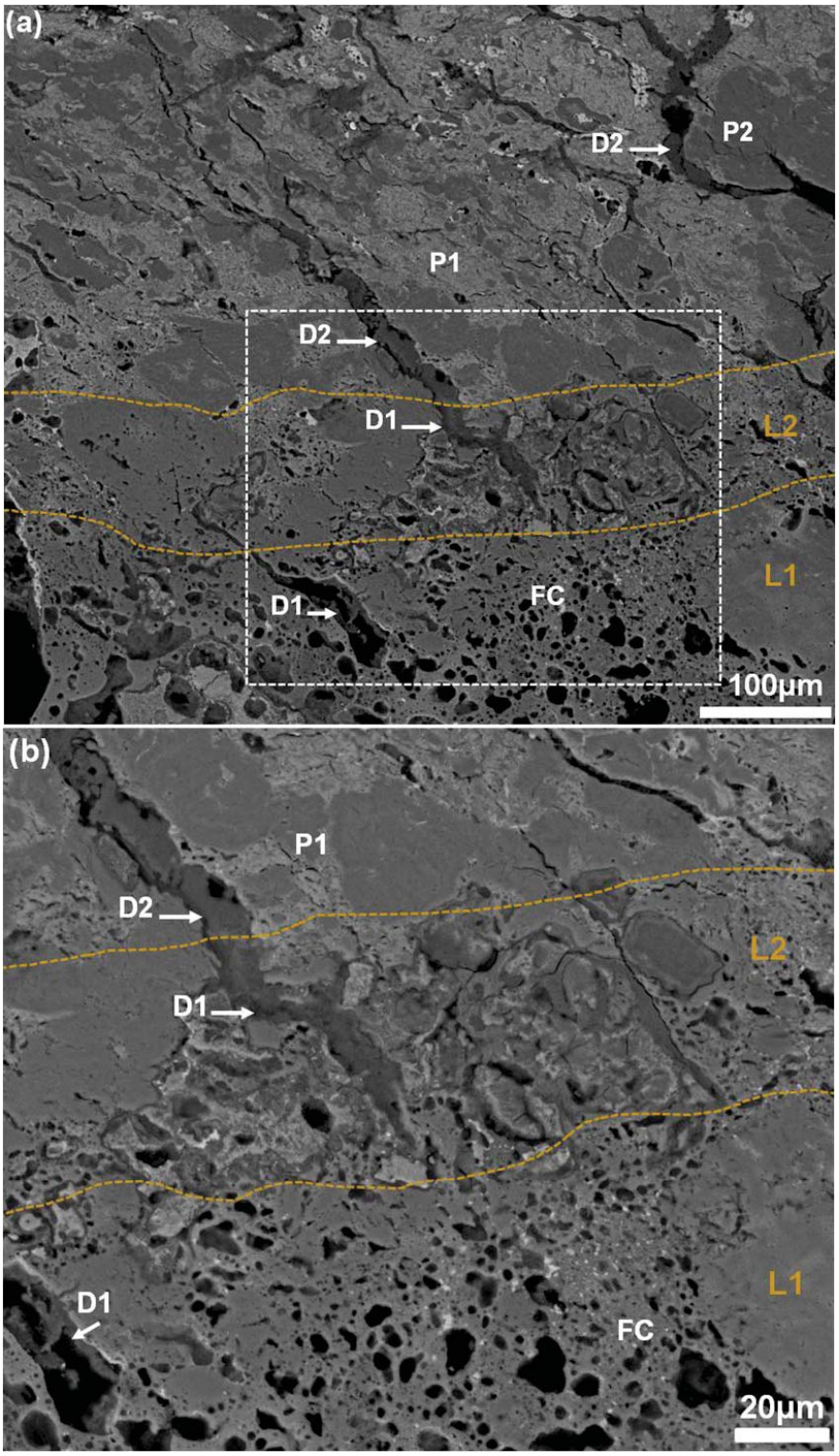

Figure 3.54- BSE image of SCO 06043 showing dolomite-filled fractures that cross-cut the fine grained matrix.
Dolomites (D1) within fractures cutting the fusion crust have been thermally altered in comparison with dolomite (D2) further from the fusion crust (FC). P1 is the bright BSE phase and P2 is dark BSE phase that comprises the fine grained (<1µm) matrix. (b) is boxed area in (a), L1 is the outer part of the fusion crust, L2 the internal part of the fusion crust, yellow lines are the boundaries (approximately) between L1 and L2.The location of this map in the sample studied is shown in appendix D11.

3.15.2 The alteration degree of SCO 06043 CM2.0

SCO 06043 is a nearly completely altered CM chondrite. SEM point counting showed that the hydrous materials within the fine grained (<1μm) matrix and completely altered chondrules represent about 94 vol% of the volume of the meteorite, whereas Mg, Fe silicates are very rare (<0.5 vol%) in this meteorite. Howard et al. (2011) reported that the SCO 06043 contains 87.6 vol% phyllosilicates and 6.3 vol% Fe, Mg silicates. They classified it as the high altered CM chondrite. The meteorite contains very rare metallic Fe-Ni (<0.2 vol%), found mainly within partly altered chondrules. These petrographic observations indicate that SCO 06043 is more altered than LAP 031166, so it is classified as CM2.0.

3.15.3 The chemical composition of SCO 06043 matrices

Chemical analyses of the fine grained matrix in SCO 06043 were carried out by EPMA. The bright and dark phases in this matrix were individually analyzed, and the mean compositions of each are presented in Table 3.26. As mentioned above, these phases are petrographically comparable to those in the fine grained matrix of LAP 031166, but the chemical analyses indicate that bright phase (Tochilinite-cronstedtite) of LAP 031166 has more Fe (+5 wt%) and less Mg (-3 wt%) than the bright phase (Tochilinite-cronstedtite) in SCO 06043. By contrast, the chemical analyses of the dark phases (Serpentine) of both meteorites are nearly identical to one another.

Oxides wt%			Elements wt%		
	Tochilinite-cronstedtite	Serpentine		Tochilinite-cronstedtite	Serpentine
Na_2O	0.35 ± 0.15	0.12 ± 0.02	**Na**	0.26	0.09
MgO	15.16 ± 0.67	26.49 ± 0.36	**Mg**	9.14	15.97
Al_2O_3	2.50 ± 0.26	2.09 ± 0.36	**Al**	1.32	1.10
SiO_2	26.12 ± 2.33	37.65 ± 0.33	**Si**	12.21	17.60
CaO	0.28 ± 0.31	0.02 ± 0.01	**Ca**	0.20	0.02
FeO	37.14 ± 0.67	17.14 ± 0.85	**Fe**	28.87	13.32
K_2O	0.07 ± 0.02	0.04 ± 0.02	**K**	0.06	0.03
P_2O_5	0.22 ± 0.30	0.04 ± 0.01	**P**	0.09	0.02
SO_2	3.84 ± 0.67	0.31 ± 0.13	**S**	1.92	0.16
TiO_2	0.11 ± 0.02	0.08 ± 0.00	**Ti**	0.07	0.05
Cr_2O_3	0.32 ± 0.05	0.40 ± 0.12	**Cr**	0.22	0.28
MnO	0.14 ± 0.10	0.20 ± 0.01	**Mn**	0.11	0.15
NiO	0.92 ± 0.30	0.61 ± 0.15	**Ni**	0.72	0.48
SUM	87.17	85.18	**O**	31.97	35.92
n	4	3			

Table 3.26- Chemical analyses of the dark and bright phases of the fine grained matrix in SCO 06043. Data presented as mean ± SD, error values are calculated to 1σ. The full dataset with standard deviations is listed in appendix A.5.

The concentration and distribution in elements including Si, Mg, Fe, S and Ca of small regions (~1mm^2) of SCO 06043 were described using multi-element X-ray mapping (e.g. Figure 3.55). Elemental mapping indicates that SCO 06043 is extensively veined in comparison to LAP 031166, QUE 93005 and Cold Bokkeveld, and the veins have high concentrations of Ca, or Ca and S, or Mg. Areas of the dark phase and some altered chondrules also have high concentrations of Mg and Si, whereas the high concentration of Fe is coincident with the bright phase.

EDS spectra of small mapped areas (e.g. Figure 3.56 obtained from Figure 3.55) show that SCO 06043 has high concentrations of Mg and Fe. Comparison between the EDS spectra of SCO 06043 and LAP 031166 indicates that matrices of both meteorites have similar concentrations of Mg and Fe, whereas the matrices of SCO 06043 have lower contents of S than LAP 031166.

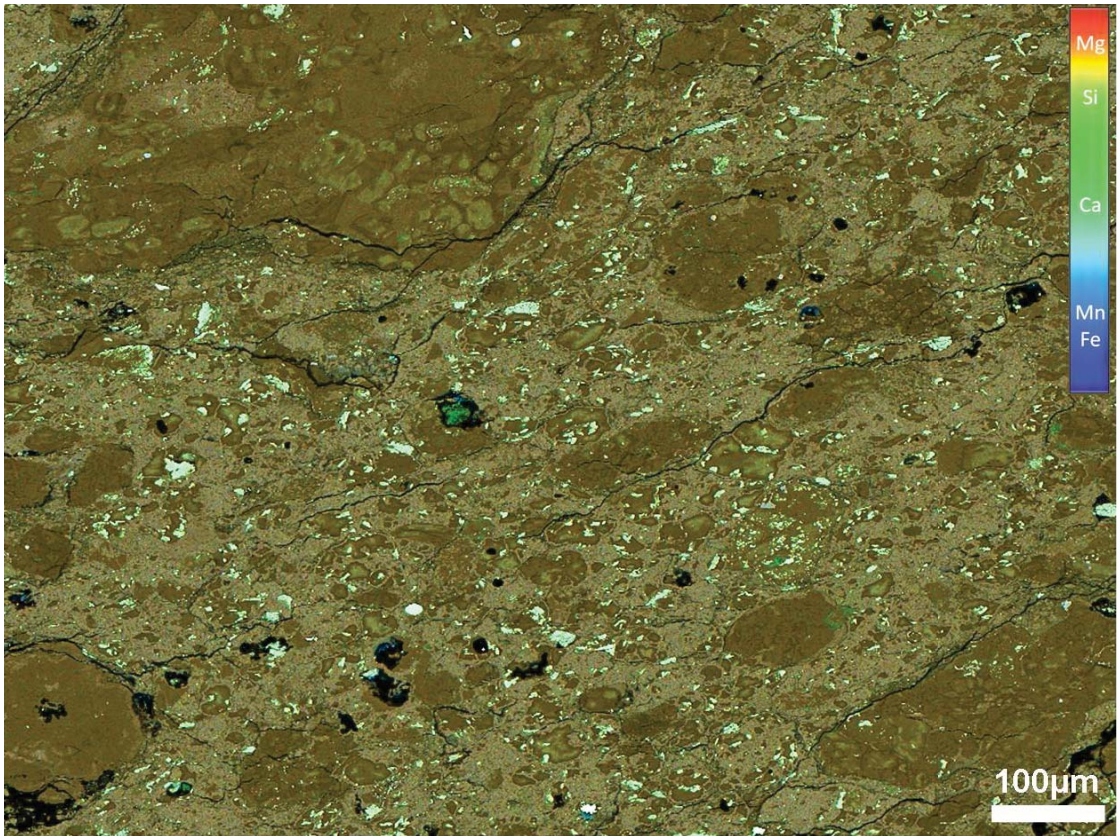

Figure 3.55- Combined elemental map of SCO 06043.
False colour multi-element X-ray map of small region ~1mm^2 of SCO 06043 highlighting the concentration and distribution of Si, Fe, Mg, S and Ca. Areas in dark red represent Mg-rich serpentine where the Mg and Si are concentrated. The bright phase occurs in light gray areas of the map where high contents of Fe are present. The colour scale bar is provided in the upper right part of the map. The location of this map in the sample studied is shown in appendix D11.

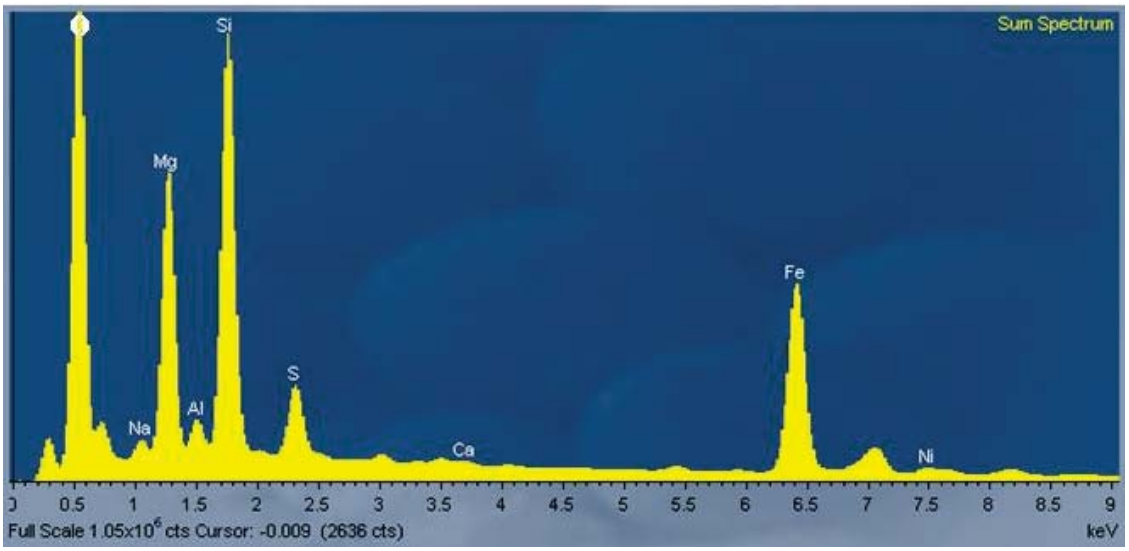

Figure 3.56- EDS spectrum of the mapped area in Figure 3.55 showing the qualitative chemical composition of SCO 06043.
The relative heights peaks of Mg and Fe are similar to those in the spectrum of LAP 031166 (Figure 3.52).

3.16 ALH 88045 CM2.0

ALH 88045 is a CM1 carbonaceous chondrite that was collected by the EuroMET consortium (European Meteorological Education and Training) at the Allan Hills of Antarctica, (76° 42' 18"S, 159° 5' 42"E), in 1988. The total mass of the meteorite is 18g (Wlotzka, 1990). A thin section of ALH 88045 (P11448) was provided by the Natural History Museum, London, and has an area of about 20 mm^2.

3.16.1 Composition and mineralogy of ALH 88045

ALH 88045 was described as an extensively altered chondrite by Bullock et al., (2010). It contains large sulphide grains (50-100 μm) within the fine grained (<1μm) matrix and around remaining chondrules. These sulphides are intergrown grains of pyrrhotite and pentlandite (Bullock et al., 2010). The matrix of ALH 88045 is composed mainly of serpentine that is free of anhydrous silicates (Zolensky et al. 1993) and it contains aggregates of carbonates that also occur as inclusions, sulphides, and assemblages of phyllosilicates (Wlotzka et al., 1989).

Petrographic observations made in the present study indicate that the fine grained (<1μm) matrix of ALH 88045 is composed of tochilinite (possibly with Fe-cronstedtite) and serpentine intergrowths, but tochilinite is more abundant. ALH 88045 has a very small number of Mg-rich olivine grains. It contains large grains of Fe-sulphide that are partially

or extensively replaced by Mg-serpentine. Blocky pentlandite is found around and within some Mg-rich serpentine pseudomorphs after calcite or Mg-rich olivine (e.g. Figure 3.57). Mg-rich serpentine pseudomorphs after calcite are moderately abundant in ALH 88045, and all these grains have thin rims of tochilinite (~0.25 μm). The carbonate in this meteorite is calcite that occurs as aggregates and as individual grains. The rims around some complete altered chondrules in ALH 88045 are similar to those around altered chondrules in LAP 031166. The rims around altered chondrules in ALH 88045 are very thin in thickness ((~1 to 2 μm or nearly absent around chondrules) and composed of a mixture of Mg-rich serpentine and tochilinite. Petrographic observations also indicate that the mineralogy of chondrule rims and the fine grained (<1μm) rims are comparable to each other. The abundance of ALH 88045 components is listed in Table 3.27.

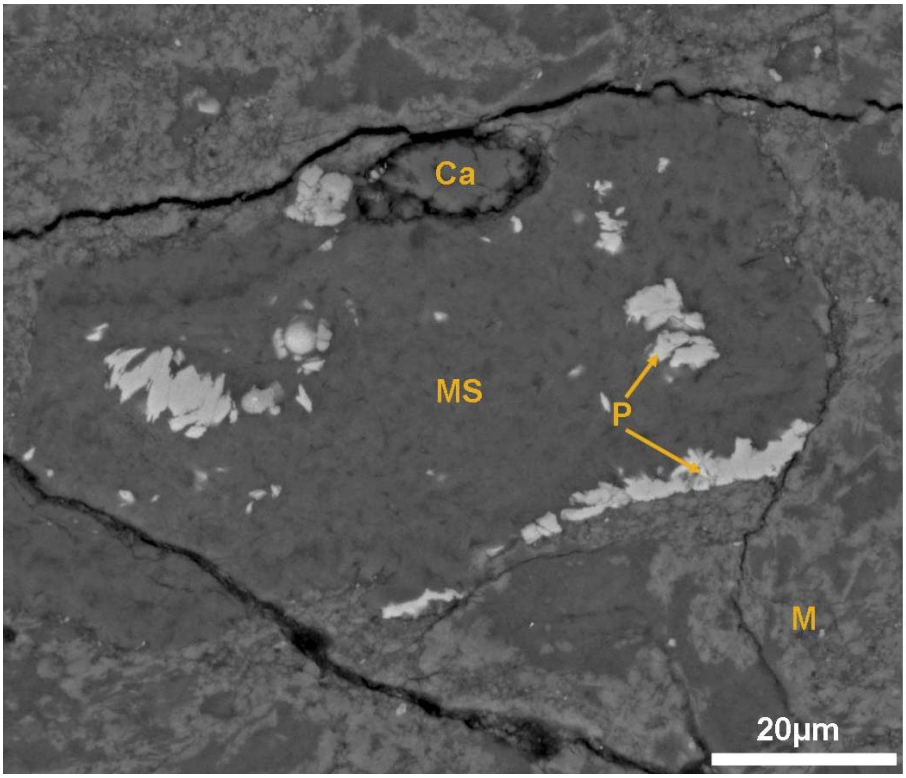

Figure 3.57- BSE image of ALH 88045 matrix.
BSE image showing the occurrence of pentlandite (P) within and around a Mg-rich serpentine (MS) grain. Ca is calcite and M is the fine grained (<1μm) matrix. The location of this map in the sample studied is shown in appendix D12.

Components	vol%
Fine grained (<1μm) matrix	53.5
Mg-rich serpentine spuedomorphs after calcite	19.1
Altered chondrules and chondrule fragments	21.0
Fe-sulphide	4.5
Calcite	1.9

Table 3.27- Abundance of ALH 88045 constituents as determined by SEM point counting. The total points counted is 160.

3.16.2 Alteration degree of ALH 88045

ALH 88045 was classified as a CM1 by Hutchison (2004) and Zolensky et al. (1997). Petrographic observation and SEM point counting show that about 99% of Mg, Fe silicates have been replaced by Mg-rich serpentine. The meteorite is also free of Fe-Ni metal. Therefore it is classified here as CM2.0.

3.16.3 The chemical composition of ALH 88045 matrices

Chemical analyses of chondrule rims have been performed by Zolensky et al. (1993) (Table 3.28). Their analyses show that these materials have high concentrations of Fe, Si and Mg. The content of Si in ALH 88045 rims is comparable to Si contents of bright phases in the fine grained (<1μm) matrix of SCO 06043 and LAP 031166 (±1.20 wt%), whereas the Mg contents increase from 6.62 ± 0.66 wt% in the bright phase of less altered LAP 031166, to 9.14 ± 0.36 wt% in bright phase of SCO 06043 and then 11.60 wt% in chondrule rims of completely altered ALH 88045. As mentioned above, the mineralogy of chondrule rims and the fine grained (<1μm) rims in ALH 88045 are similar, therefore the fine grained matrix in this study is assumed to have the same chemical composition as chondrule rims.

Chondrule rims			
Oxides wt%		**Elements wt%**	
Na2O	0.31	**Na**	0.23
MgO	19.25	**Mg**	11.60
Al2O3	2.32	**Al**	1.22
SiO2	28.67	**Si**	13.40
P2O5	0.12	**P**	0.03
S	2.75	**S**	2.75
K2O	0.09	**K**	0.07
CaO	0.39	**Ca**	0.28
TiO2	0.08	**Ti**	0.05
Cr2O3	0.5	**Cr**	0.34
MnO	0.2	**Mn**	0.15
FeO	27.02	**Fe**	21.00
NiO	1.94	**Ni**	1.52
Total	83.64	**O wt%**	30.99

Table 3.28- Chemical analyses of chondrule rims in ALH 88045 (Zolensky et al. 1993).
The fine grained (<1μm) matrix in ALH 88045 is assumed to have the same chemical composition as the chondrules rims.

Elemental mapping reveals that ALH 88045 contains high concentrations of Fe uniformly distributed throughout the fine grained matrix with the exception of areas that are

composed of Mg-rich serpentine. S and Ni however are found separately or together in isolated areas of the fine grained (<1μm) matrix (Figure 3.58).

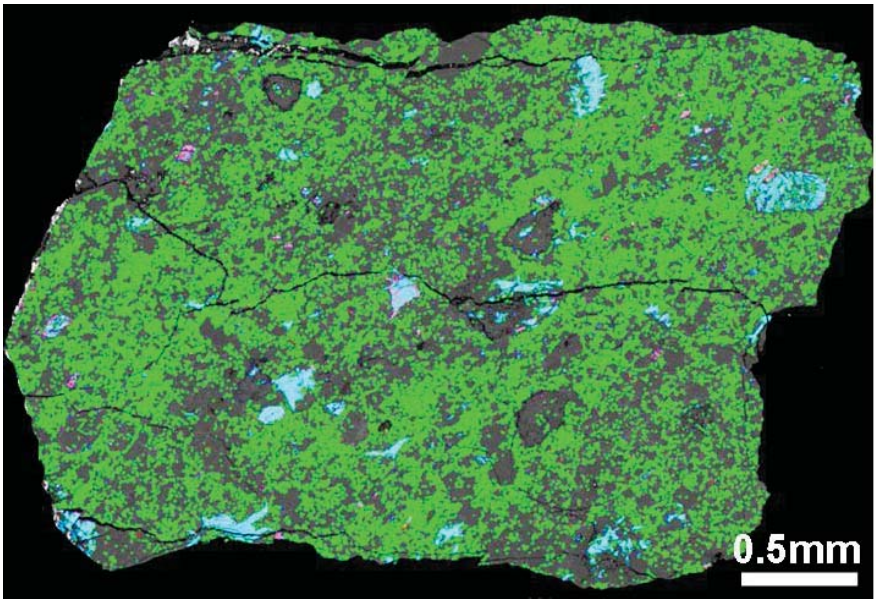

Figure 3.58- Combined element maps and electron image showing distribution and concentration of Fe, Ni and S throughout the sample of ALH 88045.
Fe is somewhat uniformly distributed within the fine grained (<1μm) matrix with exception for gray areas that identify calcite and Mg-rich serpentine.

Elemental mapping of several small areas of ALH 88045 (e.g. Figure 3.59) indicates that the meteorite is free of veins. It shows that Mg is homogeneously concentrated and distributed within areas of Mg-rich serpentine in the fine grained (<1μm) matrix and altered chondrules (Figure 3.59). The maps also show that high concentrations of Ca (i.e. carbonate minerals) are present only in a few isolated pockets in the fine grained matrix.

An EDS spectrum (Figure 3.60) obtained from small mapped area (Figure 3.59) of ALH 88045 shows slightly higher peak of Mg in comparison with EDS spectrum of SCO 06043 (Figure 3.56), but both spectra exhibit very good agreement between peaks of Fe.

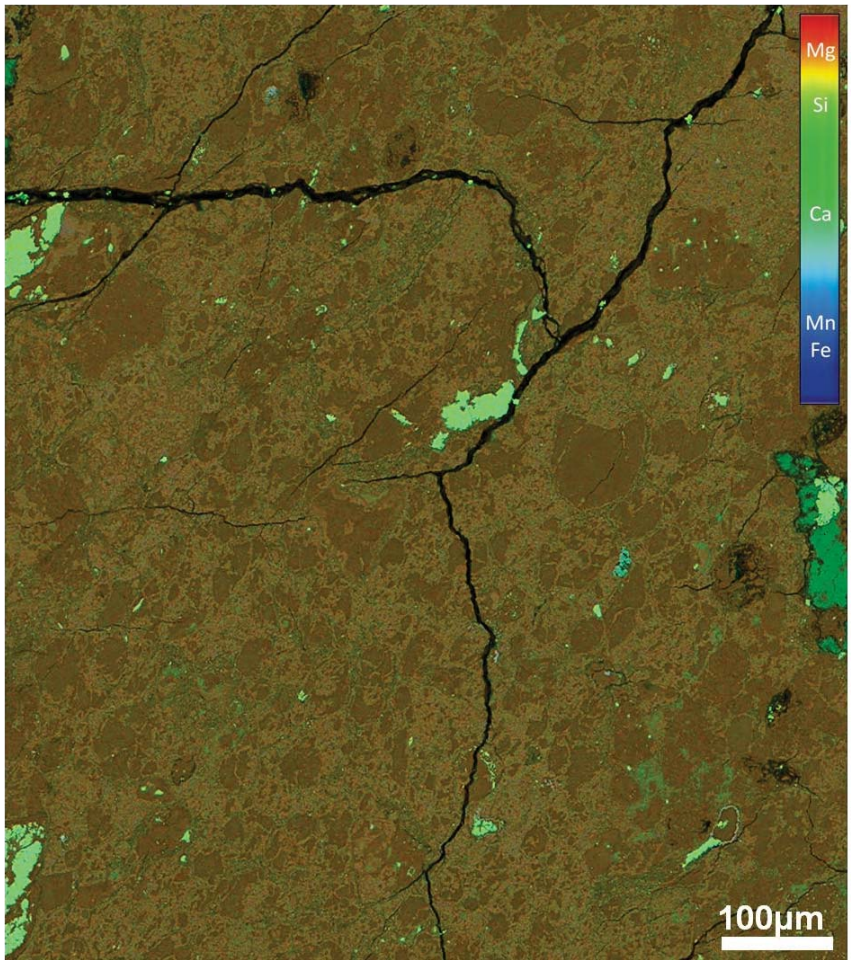

Figure 3.59- False colour multi-element X-ray map of a ~1mm^2 region of ALH 88045.
The map shows the concentration and distribution of Si, Fe, Mg, S and Ca. Areas in dark red colour are Mg-rich serpentine in completely altered chondrules and fine grained (<1µm) matrix. The bright gray areas locate Fe-cronstedtite. Green areas locate calcite grains. The colour scale bar is provided in the upper right part of the map. The location of this map in the sample studied is shown in appendix D12.

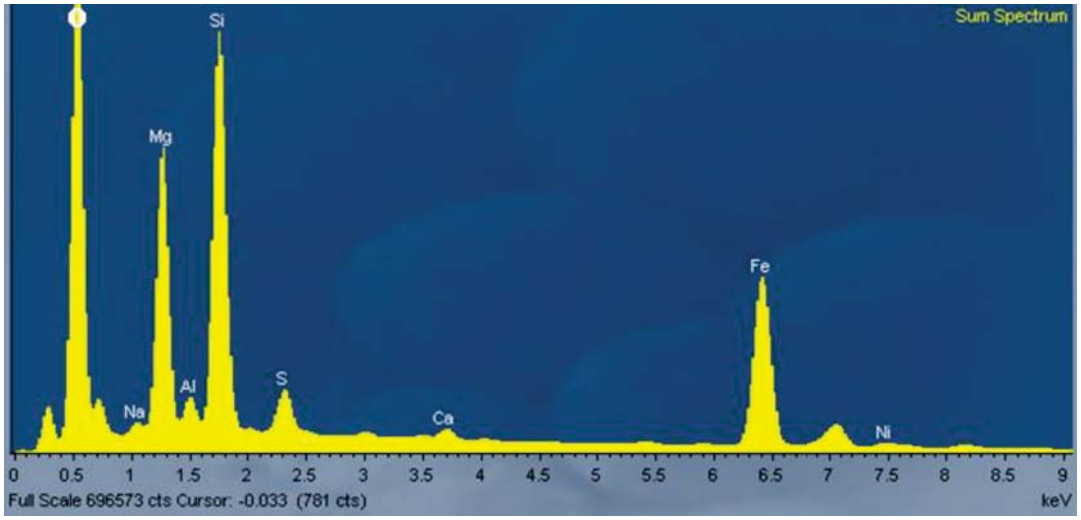

Figure 3.60- EDS spectrum of the small mapped area in Figure 3.59 showing the qualitative chemical composition of ALH 88045 matrix.
This spectrum indicates that ALH 88045 matrix contains slightly more Mg than the matrix of SCO 06043.

3.17 Summary

The samples studied have been ranked by degree of alteration, ranging from the least altered CM2.5 chondrite Murchison, to complete altered CM2.0 chondrite ALH 88045. Results of SEM point counting and petrographic observations were used, together with previous published data, to place these CM chondrites in this alteration sequence. Petrographic properties of the CM chondrites studied progressively vary, as a consequence of increasing of aqueous alteration. In addition to using the changing abundance of Fe-Ni metal and Fe-Mg silicates to determine the alteration sequences, this study also used the changing of properties of other minerals such as carbonates and Mg-rich serpentine pseudomorphs; and changing mineralogy and texture of fine grained (<1μm) matrix, chondrule rims and cross-cutting veins; as well as the occurrence of spinel and apatite (e.g. Figure 3.61). Some of these properties are related to the alteration degree of the CM chondrites and are summarized in Table 3.29.

Petrographic observations show that Murchison consists of a fine grained (<1μm) matrix within which phyllosilicate and tochilinite-cronstedtite intergrowths are dominant. The fine-grained (<1μm) matrix in Murray is mainly consisted of fine-grained (<1μm) phyllosilicates and Fe-sulphide and/or tochilinite-serpentine intergrowths. The fine-grained matrix in this meteorite is slightly coarser than the chondrule rims. The main component of Pollen is a fine-grained (<1μm) phyllosilicate-rich matrix that has been subdivided into two phases (see Figures 3.12-3.13) based on texture and mineral composition. Phase I fine grained (<1μm) matrix contains phyllosilicate that is almost free of Fe-sulphide and tochilinite. Phase II is composed of a fine grained (<1μm) phyllosilicate matrix that includes Fe-sulphide and tochilinite clumps, and is slightly coarser grained. The matrix of Mighei tends to be coarser and more fractured than the matrices of Murchison, Murray and Pollen. Mighei has a fine grained (<1μm) matrix that is characterized by abundant of Fe-sulphide and tochilinite (11.3 vol%). EET 96029 appears texturally and mineralogy analogous to Mighei. Some chondrule rims in EET 96029 are characterized by the presence of empty radial fractures, and these fractures may have formed as consequence of chondrule expansion during aqueous alteration (see Figure 3.26). The dominant minerals in the fine grained (<1μm) matrix of LON 94101 are serpentine and tochilinite. Tochilinite (13 vol%) is widely distributed in this meteorite, and has formed in many chondrules as a consequence of aqueous alteration.

The current study indicates that Nogoya can be divided into two different parts, namely highly altered (CM2.2) and less altered (CM2.3) (see Figure 3.35), that differ in mineralogy and alteration degree. The high altered part contains small amounts of preserved Mg-rich olivine grains in chondrules and chondrule fragments; however the margins of these grains have been affected by aqueous alteration. The less altered part represents about 20% of the whole sample and contains Mg-rich olivine fragments that more preserved than in highly altered part (see Figure 3.63). The fine grained (<1μm) matrix in Cold Bokkeveld consists of phyllosilicates that are dominated by assemblages of tochilinite (13.6 vol%) and tochilinite pseudomorphs after calcite (2.7 vol%). QUE 93005 contains abundant (22.7 vol%) altered and partly altered chondrules that range in size from a few hundred microns to more than 1mm. The prominent feature in QUE 93005 is that some chondrule rims have radial fractures, comparable to the radial fractures around chondrules in EET 96029. Most of these fractures in QUE 93005 have been later filled by calcite or calcite and pentlandite.

In respect of the fine grained (<1μm) matrix, the highly altered CM chondrites (CM2.1-CM2.0) show clear variation in the texture and mineralogy of these materials. The fine grained (<1μm) matrix in LAP 0660 CM2.1/2.0 is composed mainly of two phases, namely Mg-rich serpentine and tochilinite with Fe-cronstedtite that are separate from each other, but in SCO 06043 (CM2.0) Fe-serpentine (41 vol%) is more abundant than Mg-rich serpentine (31.5 vol%) and they are partly mixed. These phases are intergrown with each other in the completely altered ALH 088045 (CM2.0). The texture of fine grained (<1μm) matrix in less altered chondrites (CM2.5-CM2.3) is slightly coarser compared to the same materials in highly altered chondrites (CM2.2-CM2.0). Chemical analyses also indicate that Mg contents in fine grained (<1μm) matrix gradually increase with increasing of alteration degree.

Using the chemical analyses of the fine grained (<1μm) matrix (this study and Zolensky et al. 1993), this study supports the finding that Mg content increases in phyllosilicate matrix as alteration proceeds (e.g. Tomeoka and Buseck, 1985) and Fe/Si ratio of matrix decreases with increasing of alteration degree (McSween, 1979) (Figure 3.62)

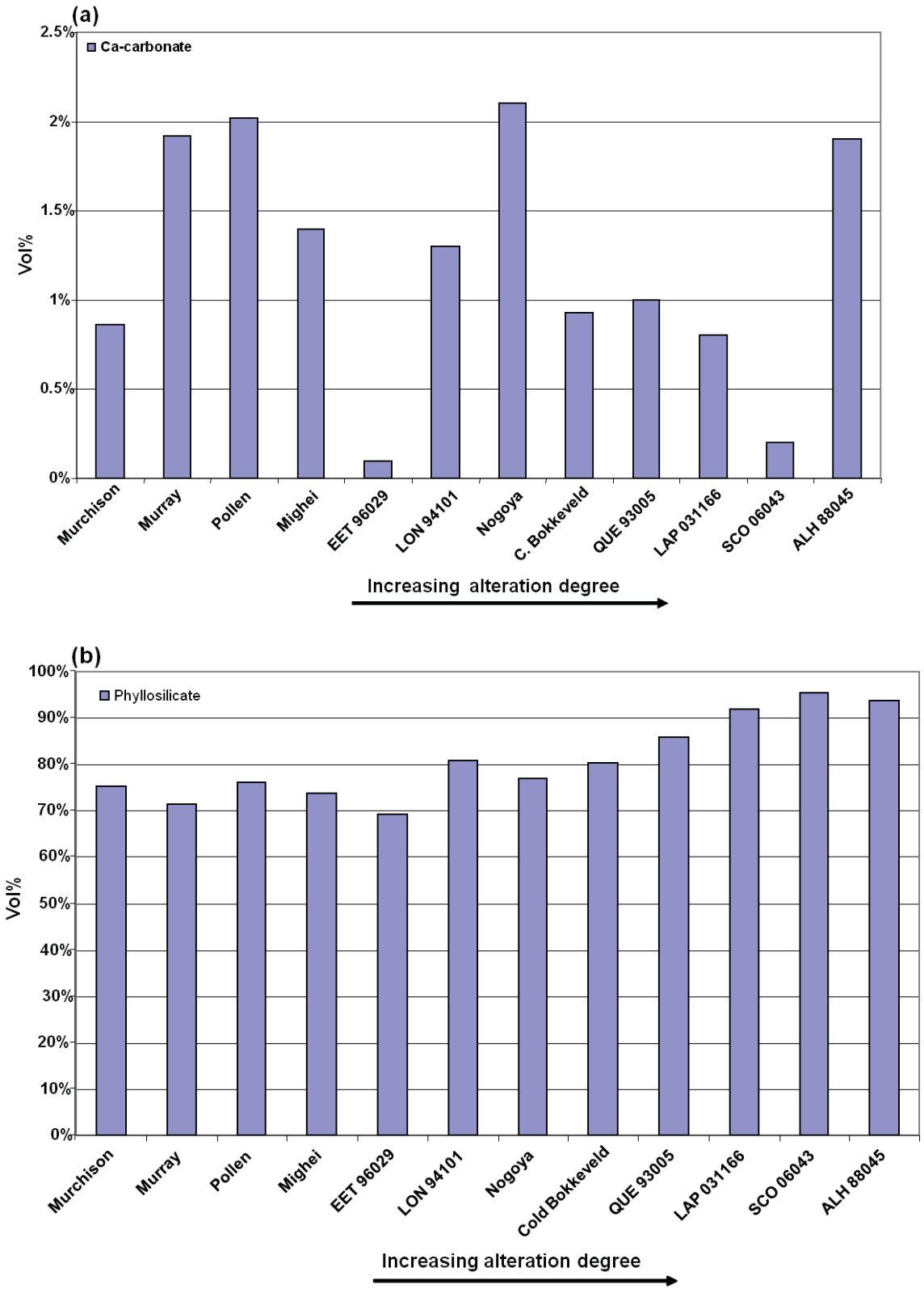

Figure 3.61- Variation in modal abundance of matrix phyllosilicates and Ca-carbonate in CM2 chondrites relative to their alteration degree.
(a) Bar chart bar showing the variation of the abundance of Ca-carbonate in CM2 chondrites used in this study relative to their alteration degree. (b) Bar chart showing the variation of the abundance of phyllosilicates (i.e. tochilinite, serpentine, Fe-cronstedtite, altered chondrules) that are found in fine grained (<1µm) matrix relative to alteration degree of the sample studied.

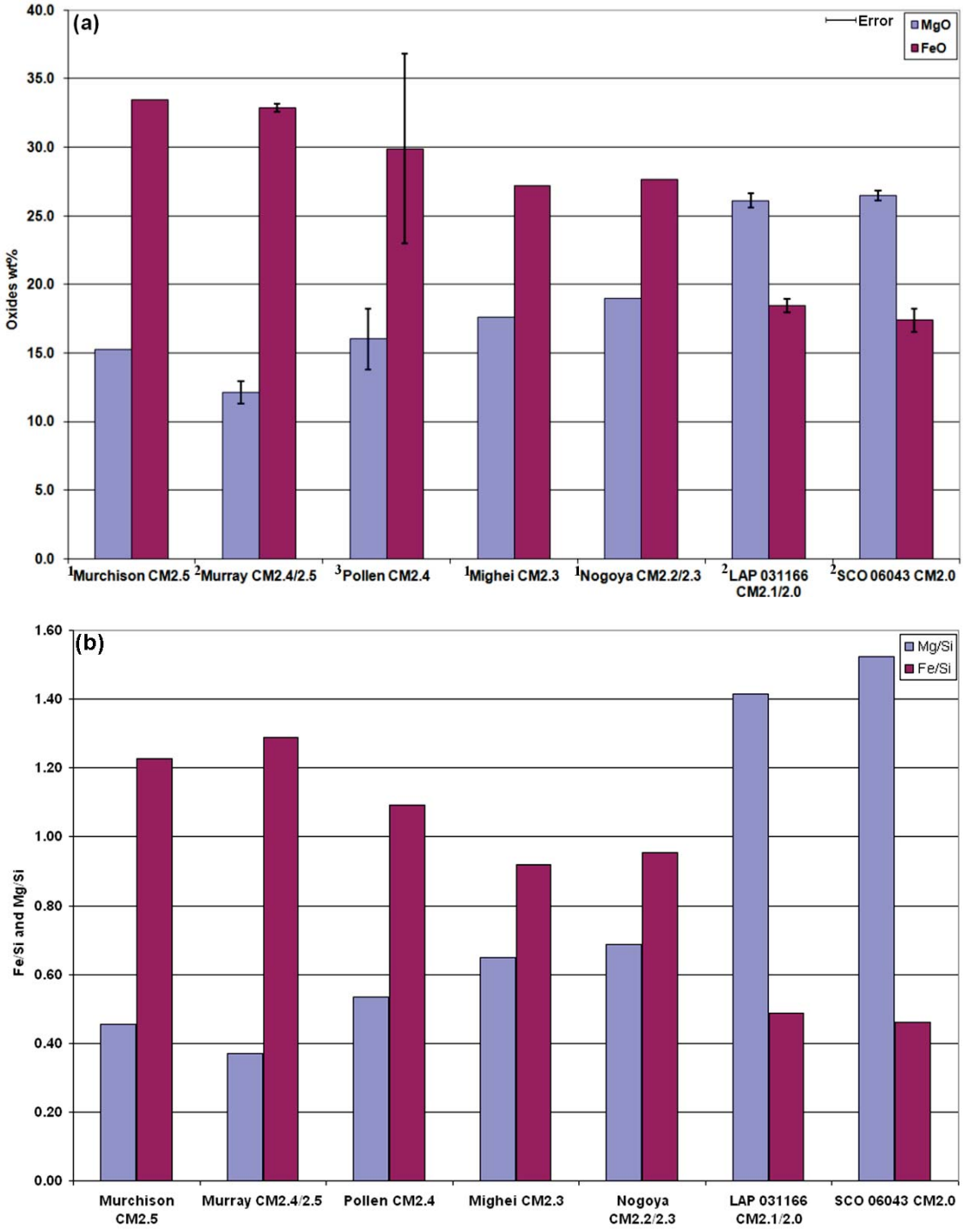

Figure 3.62- Histogram showing changing concentrations of Mg and Fe in fine grained matrix of CM chondrites as alteration proceeds.
(a) Histogram showing concentrations of MgO and FeO in the phyllosilicate matrix of some of the CM chondrites examined, 1 is analyses taken from Zolensky et al. (1993), 2 is analyses determined by EPMA, 3 is analyses carried out by Zeiss Sigma SEM. The variation of Fe content in Pollen matrix is a result of occurrence of tochilinite that is intergrown with phyllosilicates. (b) Histogram showing increasing and decreasing Mg/Si ratios and Fe/Si ratios respectively as alteration progresses. Note that all values of Mg, Fe and Si that are used in this comparison are the mean of chemical analyses listed above in this chapter.

Meteorite	Alteration degree	Fe,Mg silicates	Fe-Ni metal	Chondrule rims	Carbonates	Pseudomorphs after carbonate	Veining	Spinel	Apatite
Murchison	CM2.5	13 vol%	<0.2 vol%, preserved	0.7 vol%	aragonite, calcite	--	--	--	--
Murray	CM2.5/2.4	20.5 vol%	<0.2 vol%, slightly altered	6.5 vol%	aragonite, calcite	--	--	--	0.5 vol%
Pollen	CM2.4	12.1 vol%	<0.2 vol%, slightly altered	7 vol%	aragonite, calcite	3.2 vol%	--	--	--
Mighei	CM2.3	18.5 vol%	<0.2 vol%, moderately altered	5.3 vol%	aragonite, calcite	--	--	0.1 vol%	--
EET 96029	CM2.3	18 vol %	<0.2 vol%, moderately altered	5.5 vol%	calcite	--	--	0.1 vol%	--
LON 94101	CM2.3	10.6 vol %	<0.2 vol%, moderately altered	1.9 vol%	aragonite, calcite	14.2 vol%	calcite veins	0.4 vol%	0.1 vol%
Nogoya	CM2.3	11.5 vol %	<0.2 vol%	2.4 vol%	aragonite, calcite, dolomite	2 vol%	--	--	--
Nogoya	CM2.2	10.5 vol %	<0.2 vol%	3.9 vol%	calcite	4 vol%	--	--	0.2 vol%
Cold Bokkeveld	CM2.2	10 vol %	<0.2 vol%	3.6 vol%	aragonite, calcite	2.7 vol%	gypsum viens	0.2 vol%	--
QUE 93005	CM2.1	9.5 vol%	<0.2 vol%	4.1 vol%	calcite, breunnerite, dolomite	--	Calcite, dolomite viens	--	0.1 vol%
LAP 031166	CM2.1/2.0	1.5 vol%	<0.2 vol%	0.5 vol%	calcite	8.5 vol%	Calcite, gypsum veins	--	--
SCO 06043	CM2.0	0.5%	<0.2 vol%	absent	calcite, dolomite	7.2 vol%	dolomite veins	--	--
ALH 88045	CM2.0	--	--	absent	calcite	19.1 vol%	--	--	--

Table 3.29- Summary showing the alteration degree of samples studied and its relationship to the changing of occurrences and properties of primary and secondary minerals within the studied samples.

4

Carbonate minerals in CM2.5-CM2.3 chondrites

4.1 Introduction

This chapter describes in detail carbonate minerals that are found within the least altered, CM2.5-CM2.3 chondrites. These carbonates are present within the fine grained matrices of CM2.5 Murchison, CM2.4/2.5 Murray, CM2.4 Pollen, CM2.3 Mighei, CM2.3 EET96029 and CM2.3 LON 94101. The only carbonate minerals present within CM2.5-CM2.3 chondrites are the Ca-carbonates aragonite and calcite.

Full petrographic characterisation (e.g. texture, grain size, patterns of occurrence), chemical description (CL imaging, CL spectroscopy, X-ray mapping and EDS qualitative analyses and quantitative chemical analyses) of Ca-carbonate in each sample was carried out and is provided below. Crystallographic orientations of some aragonite and calcite grains in each sample have also been determined. Additionally, this chapter focuses on post-crystallization replacement and deformation (i.e. twinning and pseudomorphs after aragonite and calcite) of Ca-carbonates within these meteorites. Information from these aspects can be used to provide new insights to the sequence of events during the early stages of the evolution of the solar system. Description of pseudomorphs after carbonate minerals in some of samples examined were performed using BSE images, EDS qualitative analyses and quantitative chemical analyses, and interpretation of how they relate to the fine grained (<1μm) matrix are also provided. The description of twinning, mainly of calcite grains was carried out using BSE imaging, and EBSD mapping.

4.2 Carbonates in CM2.5 Murchison

4.2.1 Introduction

The first observation of calcite in Murchison was made by Fuchs et al. (1973) who found that it is ubiquitous within the matrix, but in some cases also present in white inclusions in the matrix of the meteorite. Aragonite and calcite in Murchison were identified by Barber (1981). Calcite in Murchison has two different occurrences, namely grains that are associated with 'PCP', and grains present in the fine grained (<1μm) matrix (Brearley, 1998). Brearley et al. (1999) found that the only carbonate mineral in Murchison is calcite. They also reported that subrounded and subhedral calcite grains occur in conjunction with 'PCP', and that individual and aggregate calcite occurs as isolated grains occurs in fine grained (<1μm) matrix. Benedix et al. (2003) reported that carbonate minerals in Murchison are calcite, in the form of subhedral to subrounded grains that range in size from 20-30 μm. Some of these calcite grains are surrounded by tochilinite and Fe-cronstedtite, and have sharp contacts with the matrix (here called fine grained (<1μm) matrix). Rubin et al. (2007) reported that Ca-carbonate is found in Murchison as isolated matrix grains. The modal mineralogy of CM chondrites by Howard et al. (2011) showed that Murchison contains 1.2 vol% of calcite. Lee et al. (2011) and Sofe et al. (2011) have reported that Ca-carbonate minerals (both calcite and aragonite) are present in Murchison.

4.2.2 Petrographic observations

Petrographic observations indicate that calcite and aragonite are both present in Murchison, and comprise 0.86 vol% of the total bulk volume of the meteorite (see Table 3.5). The distribution of aragonite and calcite grains within the fine grained (<1μm) matrix is different; aragonite crystals occur in two loose clusters (Figure 4.1), whereas calcite crystals are more uniformly distributed throughout the meteorite.

Aragonite and calcite were identified and distinguished from each other by EDS in combination with EBSD, and aragonite has been also confirmed by Raman spectroscopy (Figure 4.2). Small Raman shifts of calcite occur at 282 and 713 Δcm^{-1}, whereas aragonite produces small bands at 207 and 704 Δcm^{-1}.

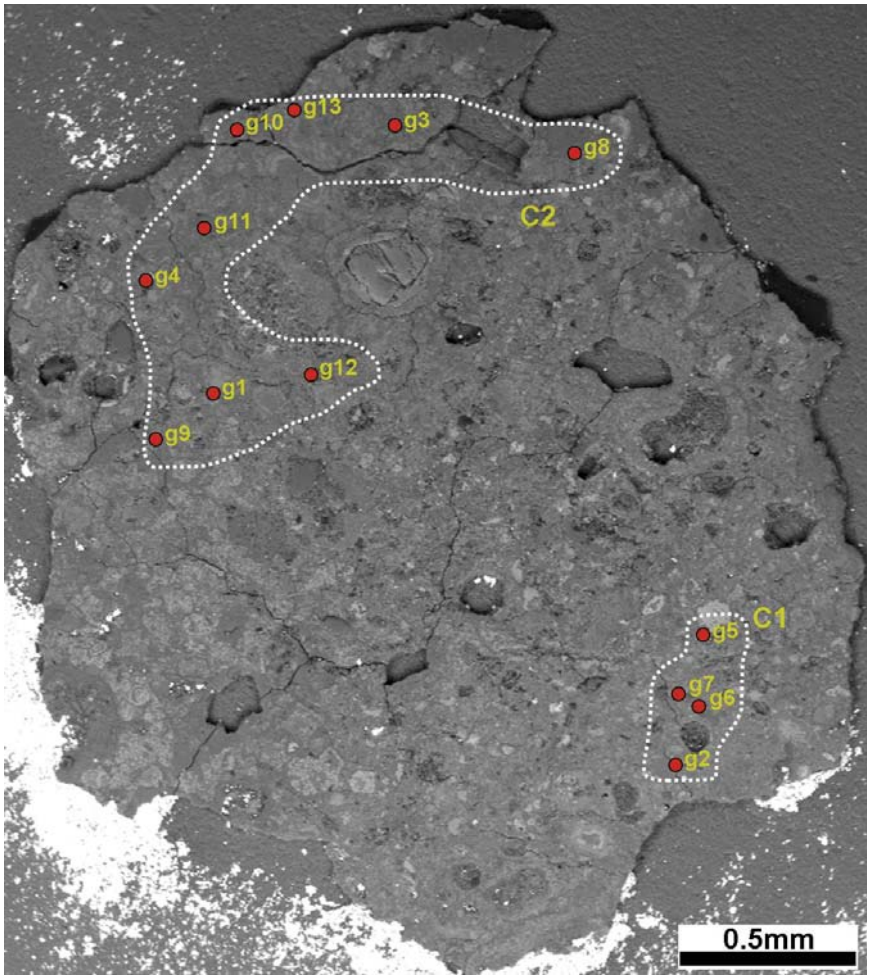

Figure 4.1- BSE image of the whole thin section of Murchison.
The image highlights the locations of two clusters of aragonite in the fine grained (<1µm) matrix (C1 and C2). C1 contains four grains, C2 contains nine grains.

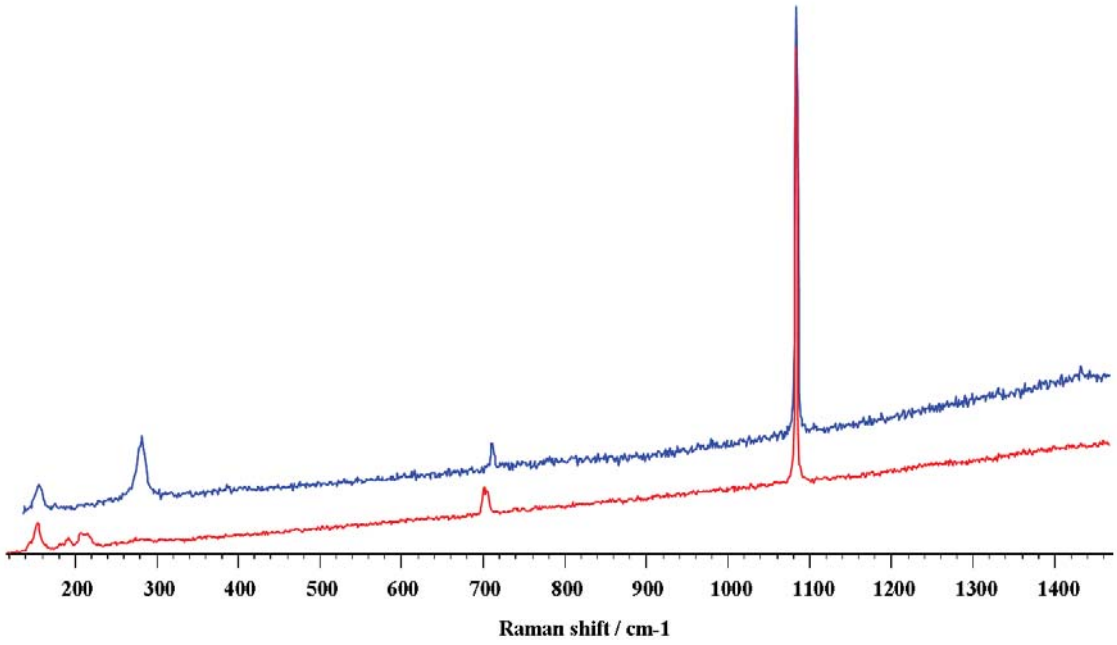

Figure 4.2- Raman spectra of Ca-carbonate grains in Murchison.
The blue spectrum was obtained from the calcite grain in Figure 4.4, the red spectrum was acquired from aragonite in Figure 4.3 b. The spectra illustrate typical Raman bands for calcite at wavenumber shifts of ~282 and ~713 cm^{-1} , and for aragonite at wavenumber shifts of ~207 and ~704 cm^{-1}.

Aragonite and calcite occur in the fine grained (<1μm) matrix both as individual and isolated grains and as aggregate grains. Calcite and aragonite are also intergrown with each other (see Figure 4.6). Some of the aragonite and calcite grains are highly fractured, but in most cases the enclosing materials are not cross-cut by these fractures, indicating that the crystals were probably broken prior to the formation of surrounding materials (e.g. tochilinite rims).

Calcite grains range in size from 10μm to 80 μm and have subhedral and euhedral crystal shapes; in many cases they are also irregular in shape. They occur as polycrystalline grains and as single crystals. They have two different petrographic relationships, namely grains that are totally or partly rimmed either by tochilinite or tochilinite with Fe-sulphides, and with/without inclusions of Fe-sulphides and/or tochilinite (e.g. Figure 4.3a). Fewer of the calcite grains are classified in the second type as free of inclusions and rims; some of these grains have euhedral shapes and sharp boundaries with a fine grained (<1μm) matrix, in some cases they have been slightly etched in their margins (see Figure 4.3 b), presumably due to aqueous processes. Very rarely, grains are likely to be pseudomorphs after Mg,Fe silicates (pyroxene or Mg-rich olivine) as they appear texturally similar to those calcite grains that are partly replaced forsteritic olivine in other chondrites (e.g. Figure 4.69 b). Only one grain is intergrown with pyroxene, indicates that pyroxene is partially replaced by calcite. A prominent feature in some calcite grains is a mottled appearance (vesicular texture) that is present as zones in the outer areas of a crystal or as a halo in a part of the grain (Figure 4.4), which possibly suggest that the formation of these parts of the grains was under different conditions in terms of temperature and the chemical composition of fluids. These features have previously been described as fluid inclusions (e.g. Saylor et al., 2001; Zolensky et al., 1999) that were found in carbonate minerals and other minerals in other CM chondrites.

The thin section studied contains thirteen crystals of aragonite, and as stated above they occur in two isolated clusters. C1 contains four grains and there are another eight grains in C2 (see Figure 4.1). Aragonite grains have euhedral and subhedral shapes that in most cases have sharp boundaries with fine grained (<1μm) matrix (e.g. Figure 4.3b). The size of the aragonite grains ranges from a few microns to 20 μm. They occur as single crystals and polycrystalline aggregates. Apparently, the aragonite grains in Murchison are un-mottled. Texturally therefore, aragonite grains are similar to the free of rims and inclusions. Most of aragonite grains are also free of inclusions and rims. Only two grains are partly surrounded by tochilinite and Fe-sulphides and three grains contain inclusions of

tochilinite or Fe-sulphide, which is presumably due to replacement. A few grains of aragonite exhibit very minor etching at the margins of the grains, which also indicates that Murchison is less affected by aqueous processes than other CM chondrites.

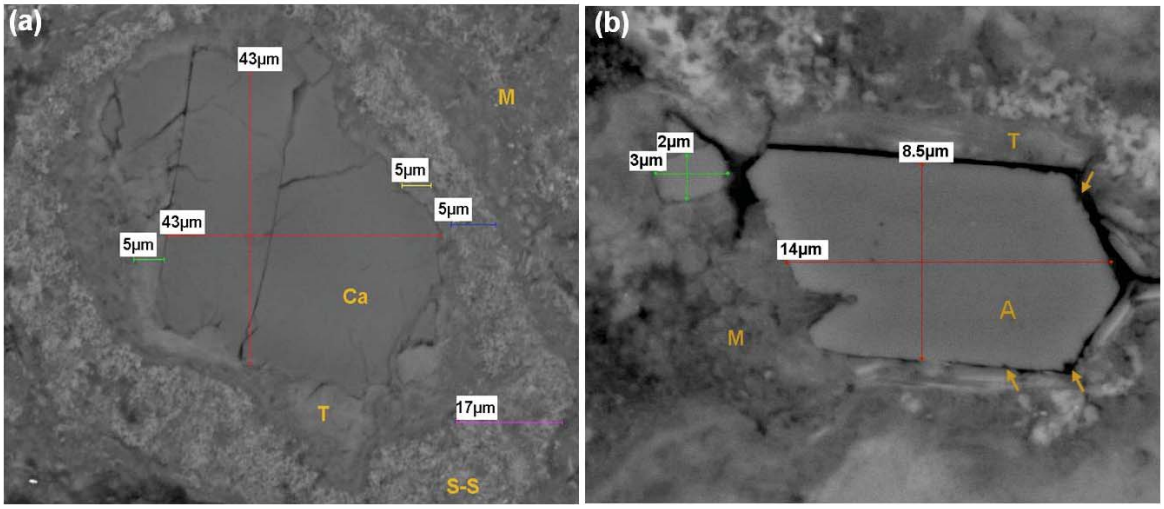

Figure 4.3- BSE images of aragonite and calcite in Murchison.
(a) Slightly fractured polycrystalline calcite grain (Ca) that is classified as calcite type I. This grain is rimmed with tochilinite (T) and the outer material is a layer of Fe-sulphide-serpentine intergrowth (S-S). M is fine grained (<1µm) matrix. (b) Euhedral aragonite grain (A) showing sharp boundaries with fine grained matrix (M). It is slightly etched at its margins (arrowed areas). A small grain in upper left side is also aragonite that has possibly broken from the large grain. The locations of these grains in the sample studied are shown in appendix D1.

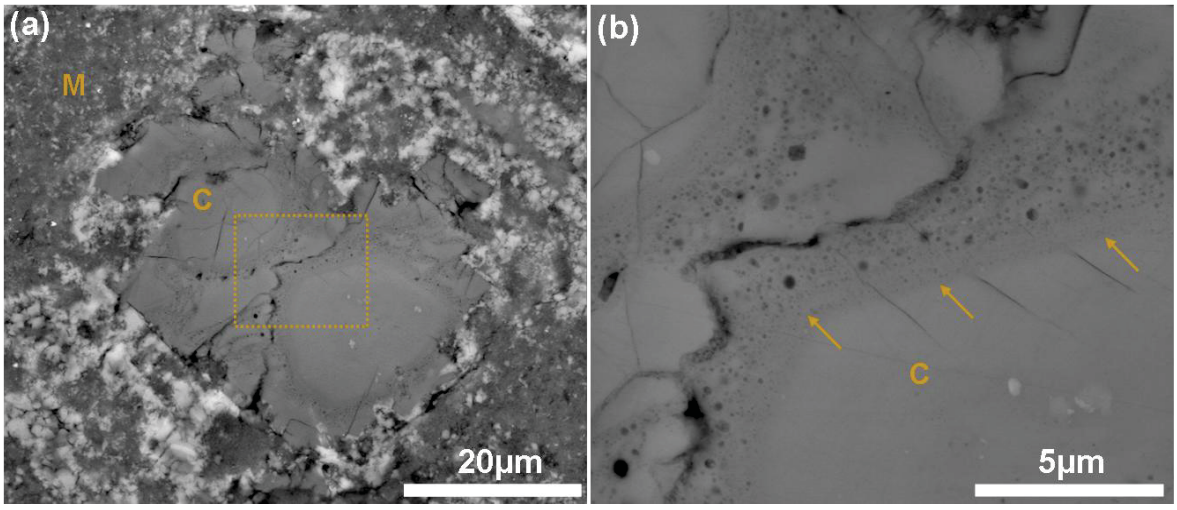

Figure 4.4- BSE images showing vesicular texture (fluid inclusions) in calcite grain.
(a) A calcite grain (C) is made of two crystals that contain vesicles (fluid inclusions) in their outer areas, M is fine grained (<1µm) matrix.(b) A part from calcite grain in (a) (delineated within a square) at high magnification showing the zones of the grain in which vesicles are present (arrowed areas). Note that these vesicles appear larger towards the edges of the grain. The location of this grain in the sample studied is shown in appendix D1.

It was also found that three of the aragonite crystals have been displaced by micro-faults and parts of these grains have been fragmented and mixed with the fine grained (<1µm) matrix (e.g. Figure 4.5).

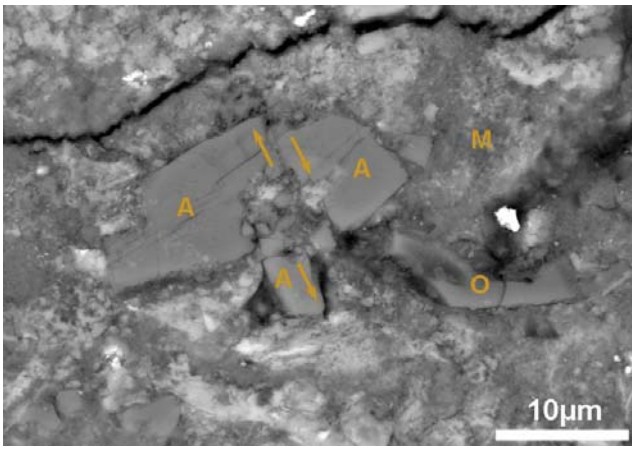

Figure 4.5- BSE image showing a typical micro-fault cutting aragonite in Murchison.
A is a split aragonite grain that has been displaced by a micro-fault; the up arrows exhibit the directions of this micro fault and the movement of the right part relative to the main part of the crystal, the lower arrow shows also the movement of another fragment from the main body. This grain contains inclusions of Fe-sulphides (bright areas in the middle of the grain) that are also separated into two parts (left is up and right is down). M is fine grained (<1µm) matrix. O is forsteritic olivine. The crystallographic orientation of this grain is pole figure in Figure 4.12, and is labelled g5. The location of this grain in the sample studied is shown in appendix D1.

Calcite-aragonite intergrowths also occur in Murchison, and two polymineralic grains were observed in this section. The first grain is a large crystal of calcite (~ 60 µm across) that contains a 'seed' crystal of aragonite located in one part of the grain (Figure 4.6).

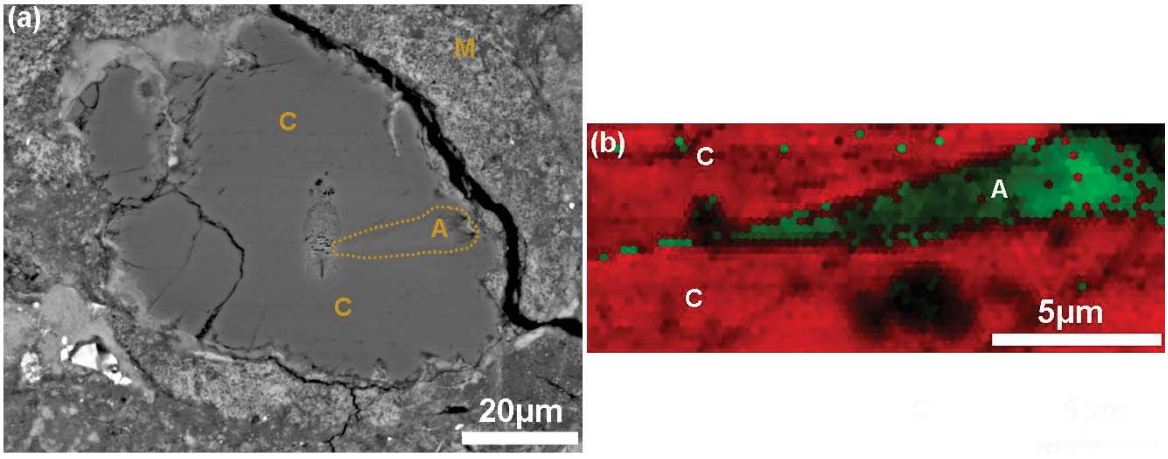

Figure 4.6- BSE and EBSD images of calcite-aragonite intergrowth.
(a) BSE image showing a small crystal of aragonite (A) within a large (90µm) crystal of calcite (C) M is fine grained (<1µm) matrix. (b) EBSD phase map of the aragonite and areas of calcite around it in (a) showing aragonite (A) in green and calcite (C) in red. The location of this grain in the sample studied is shown in appendix D1.

The second aragonite-calcite intergrowth contains two crystals of calcite and three crystals of aragonite, which are nearly completely enclosed by tochilinite (Figure 4.7). The two crystals of aragonite are on the outer edge, and have sharp and planar boundaries with calcite. The large crystal (10 µm) of aragonite has a euhedral habit and so must have crystallized within an open pore space; it is also remarkable that the crystallization of this aragonite was not hindered until the formation of the crystal was complete. The remaining void space then filled with two crystals of calcite.

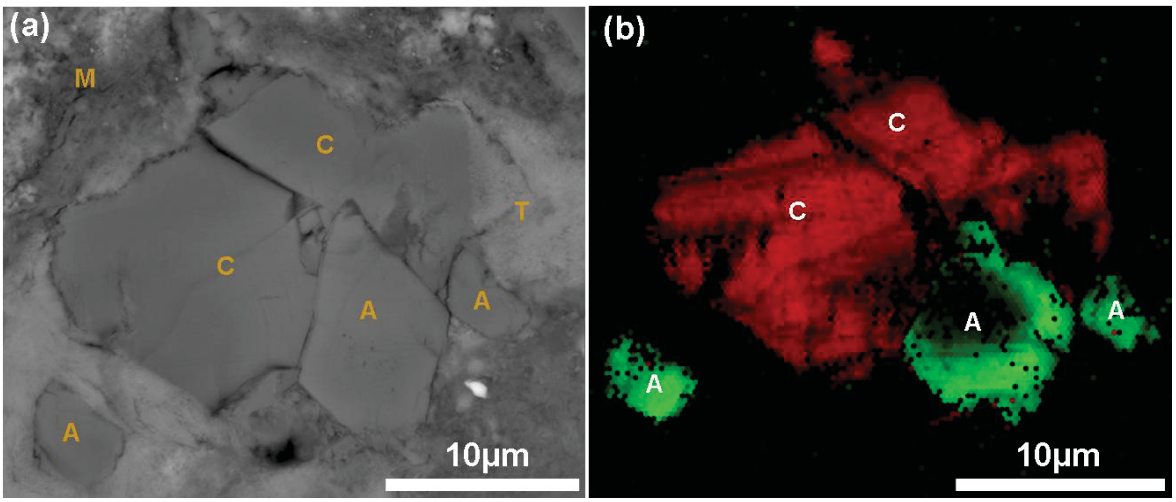

Figure 4.7- BSE and EBSD images of calcite-aragonite intergrowth.
(a) BSE image showing aragonite-calcite intergrowth. Three crystals of aragonite (A) and two larger crystals of calcite (C) are nearly completely surrounded by tochilinite (T). The large aragonite (10 µm) in the middle has sharp boundaries and an acute angle with calcite. (b) is EBSD phase map showing the aragonite in green and calcite in red. The location of this grain in the sample studied is shown in appendix D1.

4.2.2.1 Crystallographic orientations of carbonate crystals

The crystallographic orientations of aragonite (eight grains) and calcite (three areas of the sample) were determined using EBSD mapping and the results illustrated using pole figures. The c-axis of the hexagonal system of calcite and orthorhombic system of aragonite correspond to the normals to the planes {0001} and {001} respectively, and where perpendicular (makes 90º) with the surface of thin section, coincides with normal direction (ND) (see Figure 2.19).

The direction and angle of the c-axes of crystals are represented as points in the pole figure. Any point that is located in the centre of a pole figure is a crystal in which the c-axis is inclined 90º to the surface of the thin section, whereas points on the circumference of the pole figure are from those crystals whose c-axis is horizontally oriented in respect to

the thin section surface**.** Three large areas (~0.5 mm^2) of the sample, two of which contain both aragonite and calcite, were selected for high resolution EBSD mapping to determine whether these minerals have a preferred crystallographic orientation. EBSD mapping at higher magnification was also carried out for some of the aragonite and calcite grains for the same purpose.

The c-axes of two of the calcite grains in area 1 are vertically oriented relative to the surface of the thin section (Figure 4.8), so plot in the centre or very close, of the pole figure. These grains (C5 and C2) are completely enclosed by tochilinite and classified as calcite type one (described above). The c-axes of another four grains (grains C1, C3, C4 and C6 and sub-crystal in C5) plot both close to the centre and edge of the pole figure; these grains are texturally classified as calcite type two and are free of inclusions and rims. The c-axes of calcite grains in this area mostly lie in NE and SE quadrants of the pole figures. This map indicates that grains that are nearby have similar crystallographic orientations (i.e. C5 and C2).

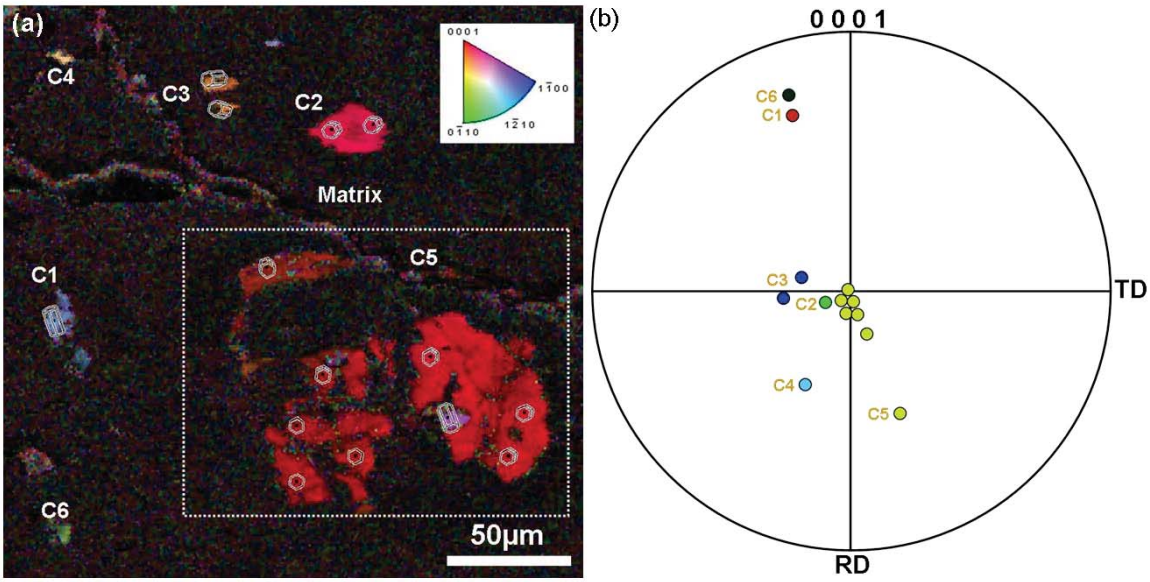

Figure 4.8- Crystallographic orientations of calcite grains of area 1 in Murchison.
(a) EBSD inverse pole figure map of area 1 showing the crystallographic orientation of calcite grains. The crystallographic orientation colour key of calcite with respect to normal direction is provided in the upper right. The c-axis orientations of each grain are indicated in the pole figure (b) (e.g. c-axes of C3 are blue). C5 is large (100 µm) polycrystalline calcite grain (within square) whose sub-crystals are vertically orientated and plot in the centre of the pole figure (b) or very close to it. Only a small sub-crystal is inclined at a low angle and is plotted further from the centre similar to other grains including C1, C3, C4 and C6 that are also inclined between high and low angles. In common with C1, the c-axis of C2 plots very close to the centre of the pole figure. The location of this map in the sample studied is shown in appendix D1.

The c-axes of the small cluster of calcite grains (14 grains) in area two are scattered in areas that are not close to the centre or the circumference of the pole figures and are distributed in all four quadrants (Figure 4.9). Only one grain (grain 13 in the map is labelled C13) has its c-axis inclined at a high angle to the surface of the thin section. Most of these grains are texturally classified as calcite type I (partly or totally rimmed with tochilinite and/or Fe-sulphides). It was also observed that some c-axes plot close to each other and so exhibit a similarity in crystallographic orientations (e.g. grains C3, C4, and C5). This may indicate that these grains crystallized at the same time, but in spite of this orientation similarity, they are located on the map far from each other. The pole figure of this map implies that the c-axes of calcite grains are generally inclined at angles that are close to each other.

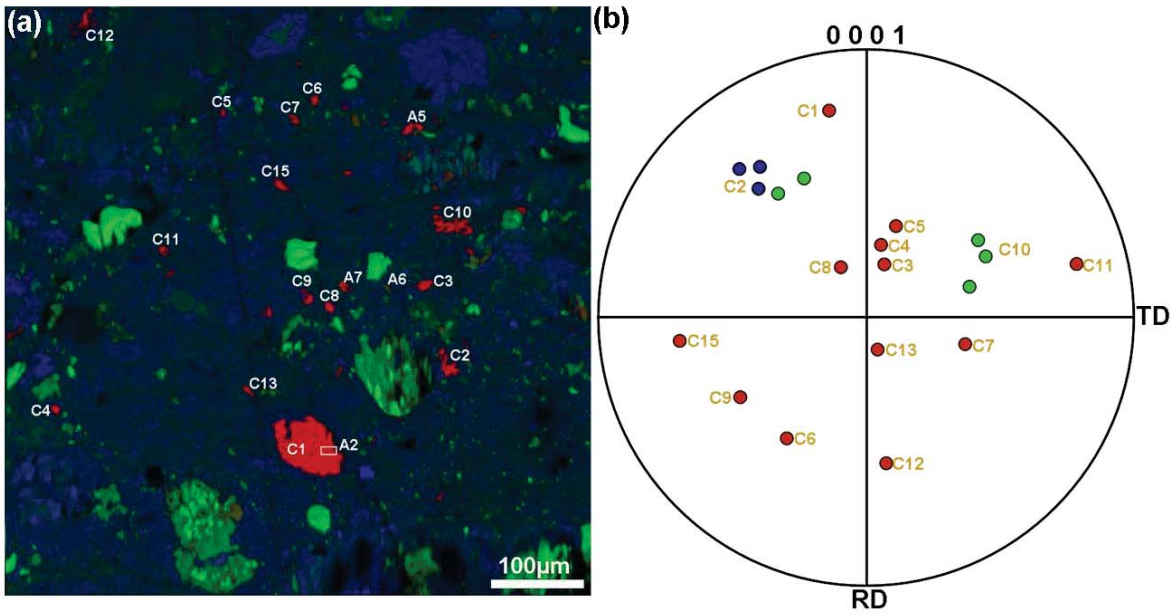

Figure 4.9- Crystallographic orientations of Ca-carbonate grains in area 2 in Murchison.
(a) X-ray element map showing the distribution of Ca which locates the Ca-carbonate (calcites are labelled C and aragonites are labelled A) grains in area two. It also shows the distribution of Mg and Fe. (b) Pole figure showing the orientations of c-axes of calcites grains in (a). Some grains such as C3, C4 and C5 show some similarity in their crystallographic orientations. The c-axis of C10 plots in two areas as it is a polycrystalline grain and contains microstructures (twins) in some areas, and both are nearly at the same angle. The c-axes of most other grains plot in intermediate areas of the pole figure (neither close to the centre nor to the edges); only the c-axis of C13 is close to vertical. The location of this map in the sample studied is shown in appendix D1.

All of the calcite grains in area three are partly or totally enclosed by tochilinite and/or Fe-sulphides, and some also contain inclusions of these minerals (Figure 4.10). These grains have crystallographic preferred orientations that are similar to those in area two. The c-axes of the grains are plotted around the circumference of the pole figure, but not very

close, thus they are inclined at angles that are similar to each other. Only one grain (grain C8) in this area has its c-axis inclined close to horizontal.

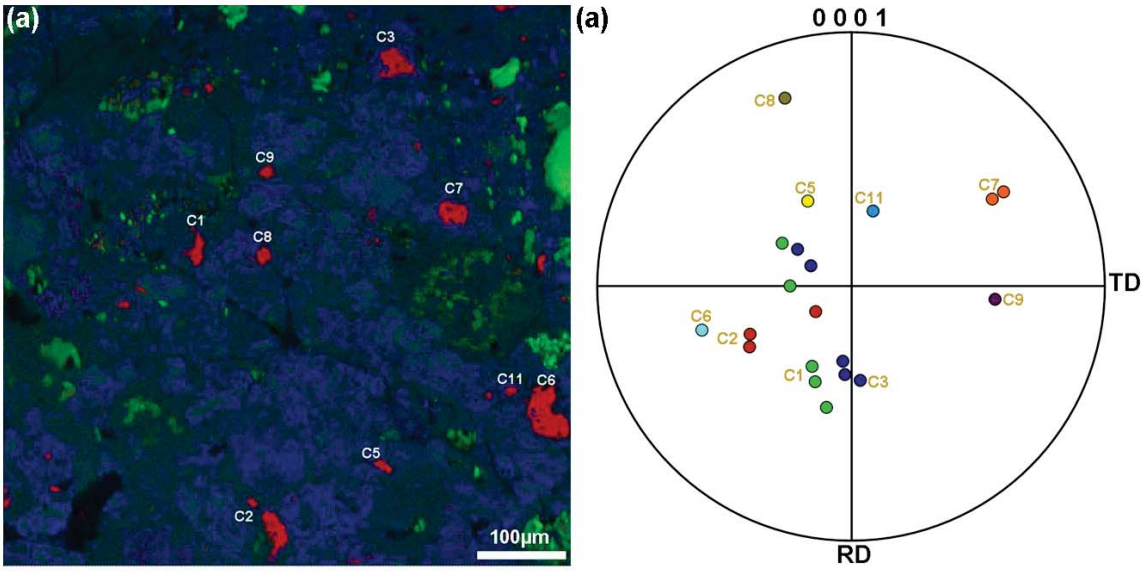

Figure 4.10- Crystallographic orientations of Ca-carbonate grains in area 3 in Murchison. (a) Element map showing the distribution of Ca which locates the calcite grains (labelled C). It also shows the distribution of Mg and Fe. (b) Pole figure showing the orientations of c-axes of calcite grains in (a). The points of the c-axes of each grain are colour coded. The c-axes of all of these grains plot in the middle areas of the pole figure, not close to its centre nor to its circumference, but they differ significantly in orientation. The location of this map in the sample studied is shown in appendix D1.

A combination of pole figures from the three mapped areas is shown in Figure 4.11a. The location of c-axes around the perimeter of the pole figure show that the majority of calcite grains in Murchison have a preferred inclination.A few grains have c-axes that are vertically inclined to the sample surface, and the other grains are inclined at angles between 76º to 20º. Most of the c-axes fall in the SE, NE and NW quadrants of the pole figure. It is known that the preferred orientation of Ca-carbonate grains in CM chondrites is a result of a directed stress during their crystallization (e.g. Lee and Ellen, 2008; Lindgren et al., 2011a). For example, if growth of crystals was controlled by static compaction in a parent body, then the crystals may show a preferred orientation perpendicular with stress directions (Figure 4.11 b). Nevertheless, it is difficult to determine the directions of stress without the three dimensional shape of a crystal (Lindgren et al., 2011a).

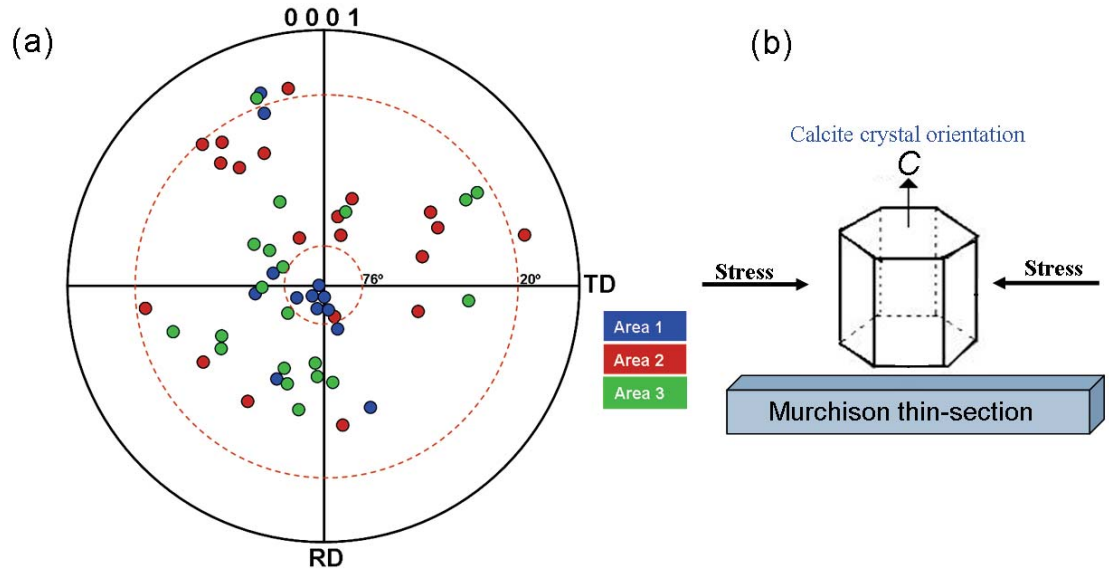

Figure 4.11- Crystallographic orientations of calcite grains in Murchison.
(a) Combination of pole figures from the three mapped areas in Murchison. The diagram shows the majority of calcite grains are inclined between 76º to 20º, and are also orientated NE, NW and SE. A few grains are inclined at a very high angle relative to the sample surface. (b) Schematic diagram showing the crystallographic orientation of calcite crystal that its c-axis is vertically inclined to the sample surface of Murchison and plots in the centre of the pole figure in (a). If the other crystals that plot in the centre and along NW-SE direction are euhedral in shape as shown in (b) then the directions stress probably are as shown in (b) (perpendicular with c axes of the crystals).

4.2.2.2 Crystallographic orientations of aragonite crystals and their relationship to the calcite

The crystallographic orientation of aragonite grains in Murchison generally shows a weak preferred orientation in the {001} pole figures (Figure 4.12). The c-axes of eight grains are orientated close to vertical and horizontal. However, comparison between aragonite grains in clusters one and two shows some variation in their orientations. The {001} poles of aragonite grains including 2, 5 and 7 that are located in cluster one (see Figure 4.1) plot close to the margins of the figures (Figure 4.12), which indicate that the aragonite grains in this cluster are inclined with their c-axes close to the horizontal, whereas the c-axes of grains 4, 9, 8, 3 and 13 in cluster are inclined at high angle (~40-65º) relative to the sample surface. Grains 5 and 13 are fragmented, so the c-axes of small fragments around these grains have crystallographic orientations that are inclined closer to horizontal than the main grains (e.g. Figure 4.13). Therefore the orientations of small fragments are excluded from the comparison between aragonite grains in both clusters. Grains 8 and 3 in cluster two are polycrystalline and yield multiple points in the {001} pole figures. Grain 3 contains three sub-crystals, two of which are inclined very close to vertical and another inclined near to horizontal relative to the surface of thin section (Figure 4.14). The EBSD map of grain 3 (Figure 4.14 a) suggests two different crystallization episodes within the pore space, the

first being a sub-grain formed within a part of a pore. The c-axis of this sub-grain plots close to horizontal in the pole figure (Figure 4.14 a). The overgrowth phase is two sub-grains in which the c-axes are inclined at a high angle. The sub-crystals in grain 3 and 8, and aragonite grains in cluster 1, in which the c axes lie near to the horizontal, possibly crystallized during the same period of time; this was probably at a different time to the second generation aragonite grains whose c-axes plot close to the centre of the pole figure.

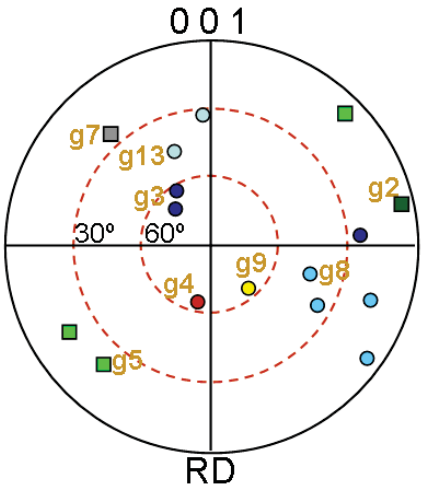

Figure 4.12- Pole figure showing the orientations of poles to the {001} planes of aragonite grains in Murchison.
The c-axes of aragonite grains in cluster 1 (square points) and some sub-crystals in grains (g3 and g8) in cluster 2 (circular points) are inclined at angles that are less than 30°, but the grains that are located in cluster 2 are orientated at a high angle.

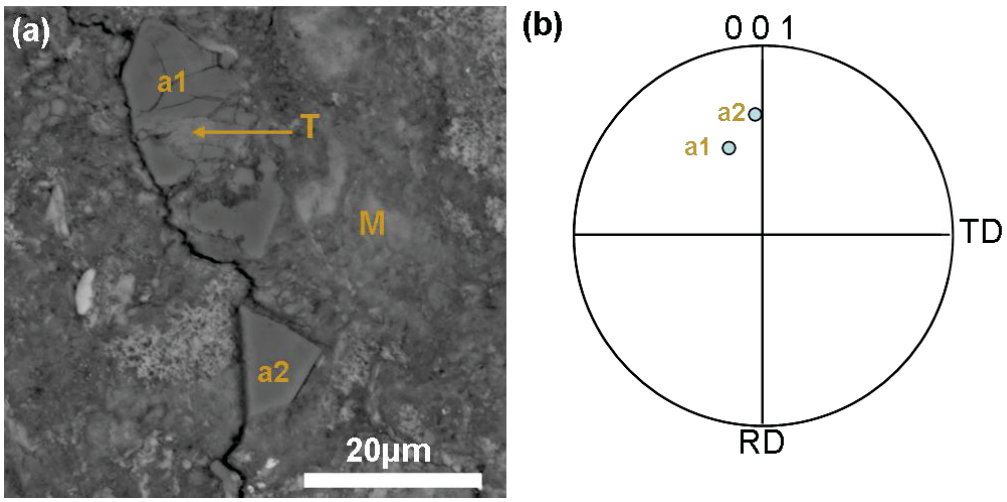

Figure 4.13- Pole figure of a broken aragonite grain.
(a) BSE image showing aragonite grain (g13 in cluster 2) that has fragmented into two parts (a1 and a2). The main grain (a1) contains tochilinite and serpentine in the middle part. (b) Pole figure for aragonite grains in (a) showing the difference of the crystallographic orientation between the main aragonite grain (a1) and fragment (a2). The location of this grain in the sample studied is shown in appendix D1.

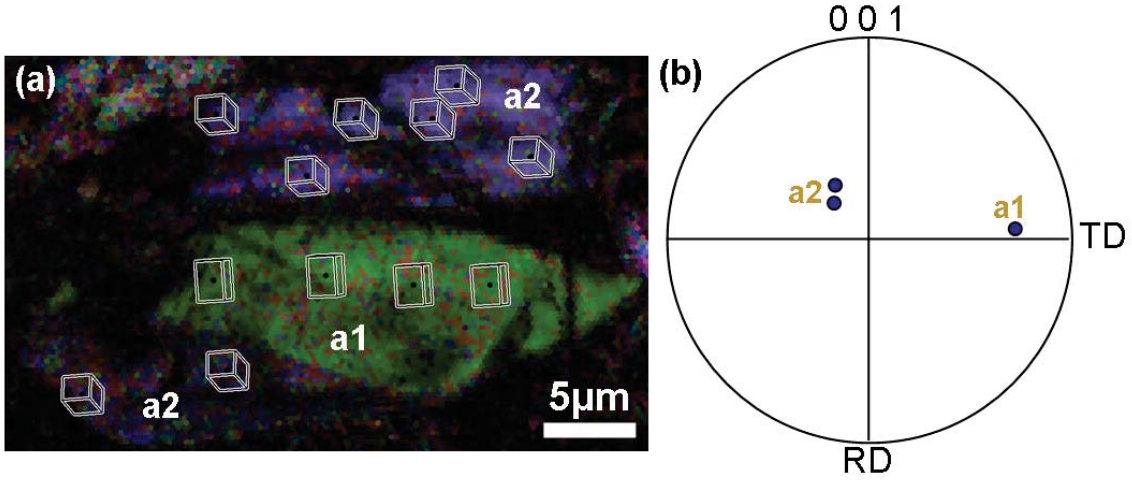

Figure 4.14- Crystallographic orientation map of a polycrystalline aragonite grain in Murchison. (a) EBSD map showing three sub-crystals intergrown within grain g3. The map suggests a1 is the first phase and a2 is overgrowth filling pore space. (b) Pole figure showing that the two sub crystals (labelled a2 in a) have c-axes are inclined close to the vertical, whereas the c-axis of sub-crystal (a1) is inclined close to the horizontal. The location of this grain in the sample studied is shown in appendix D1.

Understanding the relationships between aragonite and calcite is vital in determining the composition and temperature of fluids from which these minerals crystallized in the parent body of Murchison; it also can provide information on the formation time of aragonite relative to calcite. There are two possibilities with regard to the formation times of the two minerals: (i) calcite crystallized early and was later replaced by aragonite, but this is very unusual in terrestrial rocks, (ii) two distinct stages of mineral formation. Aragonite precipitated early from fluids whose properties reflected conditions including temperature and/or supply of elements, then changing conditions caused the crystallization of the later phase of calcite. The second scenario is favoured for two reasons: (i) in two aragonite-calcite intergrowths (see Figure 4.6a and Figure 4.7a), the aragonite is found only on one side of the grain and has well developed boundaries, the calcite resembling an overgrowth that is otherwise free of inclusions of aragonite, (ii) EBSD maps of both aragonite-calcite intergrowths (e.g. Figure 4.15b) also suggest two separate stages of mineral crystallization. The BSE image of aragonite-calcite intergrowth in Figure (4.7a) shows that each mineral is formed of multiple crystals, but the sub-crystals in each phase have a preferred orientation (Figure 4.15a) indicating that they formed at the same time. The c-axis of calcite (in Figure 4.7a) lies vertically relative to the sample surface, whereas the c-axis of aragonite has a low angle of ~25º relative to the c-axis of calcite (Figure 4.15), which is also consistent with two separate stages of mineralization. The traces of the calcite $\{11\bar{2}0\}$ and aragonite $\{110\}$ planes were overlain on the phase map of the aragonite-calcite intergrowth (Figure 4.7a), and clearly indicate that the two sets of planes lie parallel to each other (Figure

4.16). The similarity in orientations of {110} aragonite and $\{11\bar{2}1\}$ calcite suggests that one mineral has inherited the orientation of the other in part, although the c-axis differs in orientation, indicating that crystallographic interpretation of aragonite-calcite intergrowth is complicated.

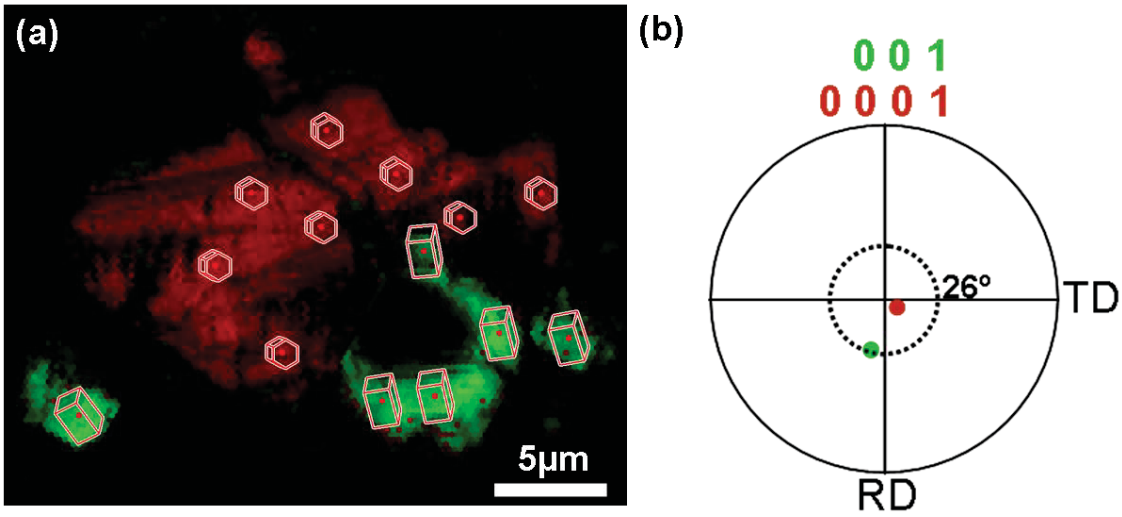

Figure 4.15- Crystallographic orientation of an aragonite-calcite intergrowth.
(a) EBSD map of aragonite-calcite intergrowth (in Figure 4.7a) showing aragonite (green) and calcite (red) with orientations overlain. (b) Pole figure showing the c-axes orientation of calcite (red) relative to aragonite (green).

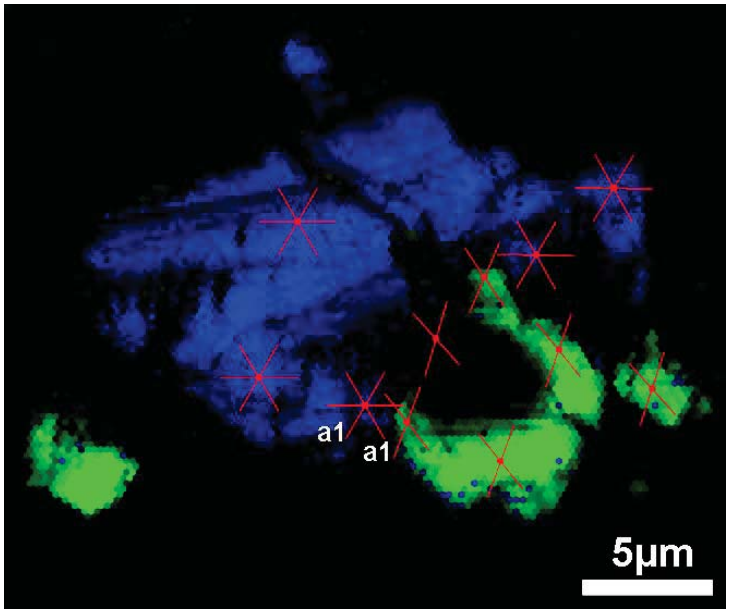

Figure 4.16- EBSD map of the aragonite (green) and calcite (blue) intergrowth (in Figure 4.7a).

Overlain on the map are the traces of the calcite $(11\bar{2}0)$ and aragonite (110) planes. Clearly the two sets of planes (a1) lie parallel to each other.

4.2.3 Chemical composition of Ca-carbonate in Murchison

The first chemical analyses (of three grains) of calcite in Murchison were reported by Armstrong et al. (1982); however two of these grains were found in refractory inclusions. Eight chemical analyses of carbonates in Murchison were carried out by Johnson and Prinz, (1993). CL characteristics of carbonate minerals in Murchison have been studied by Brearley et al. (1999) and Brearley (1998). Here CL of aragonite and calcite has been carried out, and coupled with elemental mapping by the Zeiss Sigma SEM and quantitative chemical analyses using EPMA.

4.2.3.1 SEM-CL imaging

CL characteristics of calcite in Murchison were described, and related to petrographic properties by Brearley (1998). He classified the CL characteristics in calcite grains that are associated with PCP into four types including: (i) grains exhibit no change in CL intensity, with the exception of shock-induced deformation twins, (ii) grains that demonstrate two different zones of irregular CL intensity, (iii) grains that contain corroded core of CL intensity and show increase of CL intensity towards the grain margins, (iv) grains that have very complex zoning that is asymmetric. He also reported that calcite grains in the fine grained (<1μm) matrix show the same four types of CL features with some variations in CL characteristics of grains that have asymmetric core regions of CL intensity. Instead, these cores have lower or higher CL intensity than outer areas. Grains in the fine grained (<1μm) matrix can have also one well developed face of high CL intensity that represents about half of the grain (Brearley, 1998).

Brearley et al. (1999) added that matrix calcite grains in Murchison show no change in CL intensity in the middle and brighter areas in the rims. They also reported that Murchison contains calcite grains with complex zoning in which patches of CL intensity are present, in some cases with an asymmetric low CL intensity core and outer areas that show significant variation in CL intensity, and grains illustrating asymmetrically oscillatory zoning.

Sofe et al. (2011a) classified CL characteristics of Ca-carbonate of CM2 chondrites including Murchison, Murray, Pollen, Mighei and Nogoya into several types, which have also been related three generations of calcite and one generation of aragonite.

In this study, CL imaging of six aragonite grains and eighteen of calcite grains was carried out. The CL properties of aragonite and calcite in the thin section examined are divided into several types, which are also related to the petrographic features of each mineral. For clarity and simplicity, four terms are used in this study to describe the luminescence of Ca-carbonate. These terms refer to four levels of SEM-CL intensity that describe increasing luminescence from very low to very high, and are used as following: very low CL intensity for quenched (dark areas), low CL intensity for dark gray areas, high CL intensity for light gray areas and very high CL intensity for bright areas (Figure 4.17).

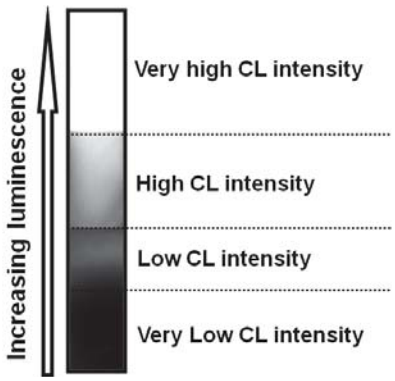

Figure 4.17- Scale of SEM-CL intensity ranging from very low to very high as seen in the PC window, these zones (low CL intensity etc.) obtained from calcite grains.

As described above, Ca-carbonates in Murchison are divided into several types, therefore the CL characteristics are related to these types and classified as following: (i) all six aragonite grains show invariant and low CL intensity throughout (Figure 4.18a); (ii) calcite replacing Mg,Fe silicates demonstrates no variation of high CL intensity throughout the grain, but is slightly patchy (not in specific areas) with small specks of very high CL intensity; (iii) grains that have a vesicular texture in the outer areas or as a halo in a part of the grain, can have high CL intensity in areas of the halo and zones, low CL intensity in areas inside these zones and halos, and other areas of the grain also show high CL intensity, in which some parts are also patchy with large spots of very high CL intensity (Figure 4.18b); (iv) only two grains of calcite type II (free of rims and inclusions) were imaged by CL, and both show high CL intensity at the edge of the grain, the subsequent zone being a symmetric overgrowth of very high CL intensity, (v) calcite type I (partly or totally rimmed) shows several varieties of SEM-CL intensity where: grains have the same patterns of CL intensity of calcite type II, grains can have a halo or layer of low CL intensity within very high CL intensity (Figure 4.18c), grains that demonstrate CL intensity

similar to that of calcite replacing Fe,Mg silicates, grains that demonstrate an irregular core of low CL intensity or very high CL intensity within the high CL intensity that covers other areas of the grain (Figure 4.18d).

It was also observed that very high CL intensity with very thin rims (~0.5-1 μm) of high CL intensity overlies some of grains of calcite type I. The abundance and characteristics of these CL types are provided in Table 4.1.

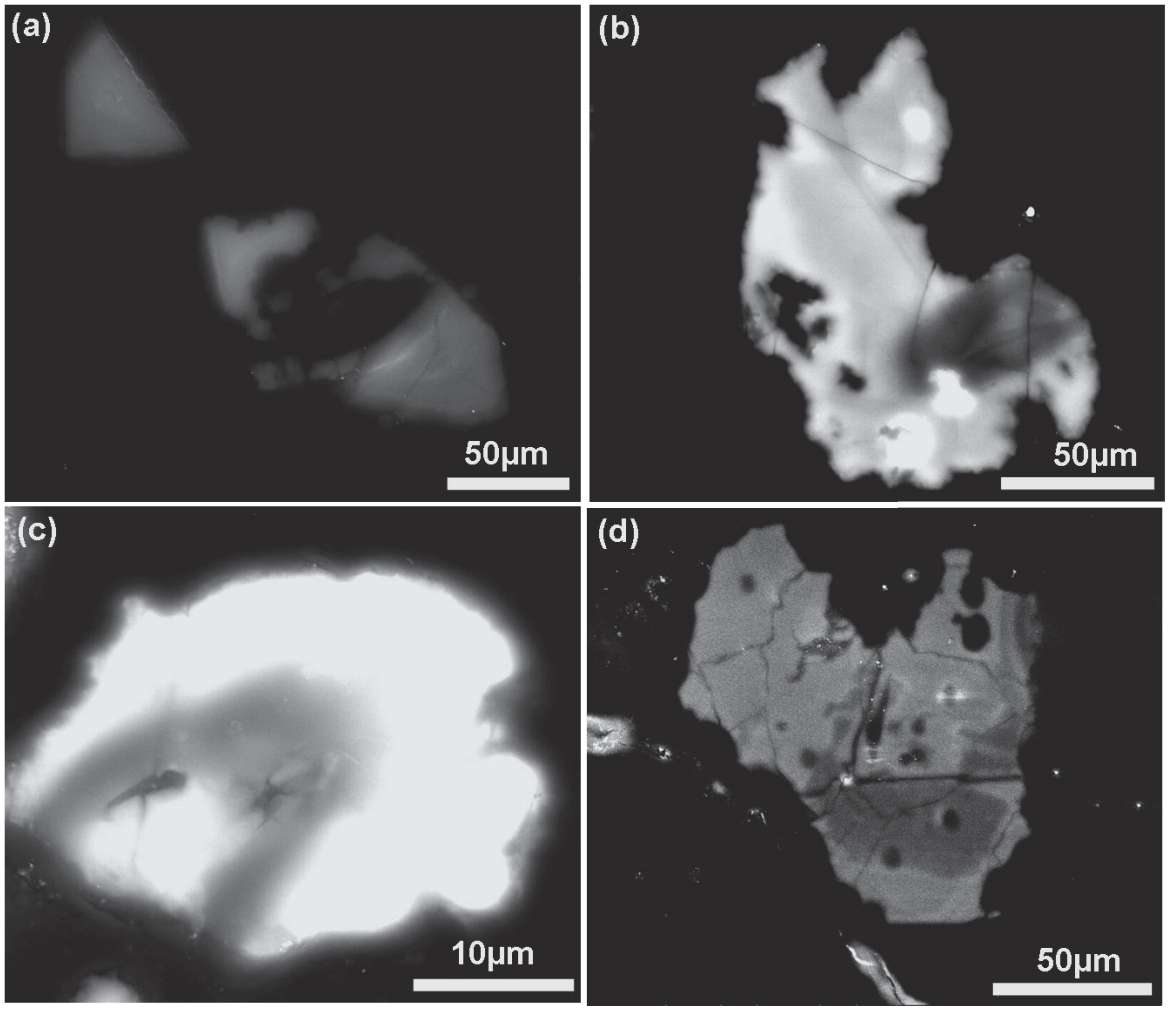

Figure 4.18- CL images showing patterns of SEM-CL intensity in Ca-carbonate from Murchison. (a) A typical CL type I aragonite grain, shown in Figure 4.13a, with low CL throughout the grain. (b) A typical CL type III that is present in grains with vesicular texture. (c) A typical CL type V that is observed in some grains of calcite type I (partly or totally rimmed). (d) A typical CL type VI showing an irregular core of low CL intensity with high CL intensity in other areas of the grain. The dark spots within the grain mark inclusions of phyllosilicates. The locations of these grains in the sample studied are shown in appendix D1.

Grain type	SEM-CL type	SEM-CL characteristics	Abundance
A, , C, C-R, P.	I	Low or high CL throughout a grain, in some cases contains patches of very high CL intensity (e.g. calcite replacing olivine, aragonite shows only low CL).	6 A, 2 C, 1 C-R, 1 P.
--	II	Complex zoning mainly found in polycrystalline grains and in most cases shows all four levels of CL intensity within one grain (from very low CL to very high CL).	--
P	III	High CL over halo areas, low CL in areas inside the halo, high CL in other areas of the grains with presence of large patches (~20 μm) of very high CL.	2 P.
C, F.	IV	Core of high CL on the edge, overgrowth zone of very high CL.	1 C, 2 F.
C	V	Very high CL in all areas, but contains halo or layer of low CL cross cutting the grain.	2 C
P, C	VI	Irregular core of low or very high CL within high CL	3 C, 3 P,
C	VII	Very high CL intensity with thin rims (~0.5-1 μm) of high CL	1 C

Table 4.1- Characteristics and abundance of SEM-CL types and their relationships to Ca-carbonates phases in Murchison.
Note CL type II was not observed in Murchison, but it characterises calcite grains in some other meteorites. A is aragonite, C is completely rimmed, F is calcite grains free of rims, P is calcite grains partly rimmed with tochilinite and/or Fe-sulphides, C-R is calcite raplicing olivine. Total number of grains imaged is 24. Note the abundance of each CL type is assigned by numbers, e.g. 6 A means 6 grains of 24 grains imaged show CL type I, and A means these 6 grains are aragonite.

4.2.3.2 X-Ray mapping

Qualitative elemental mapping of the whole Murchison sample, selected regions and some Ca-carbonate grains was conducted, using the Sigma SEM with INCA software. The Ca X-ray maps reveal that Ca-carbonates are present as somewhat isolated clusters and as large (80-100 μm) isolated polycrystalline grains in the fine grained (<1μm) matrix. Ca maps of small regions of Murchison also show that Ca-carbonate grains have crystallized close to each other in discrete small pockets (e.g. Figure 4.19).

Element mapping of the grain that contains an aragonite-calcite intergrowth (Figure 4.20) shows the presence of S and Fe, particularly at the margins of the calcite. This suggests that the fluids from which the aragonite and calcite were precipitated was also involved in formation of the surrounding materials (i.e. tochilinite), as the composition of fluids gradually became less saturated with calcium carbonate (Figure 4.20).

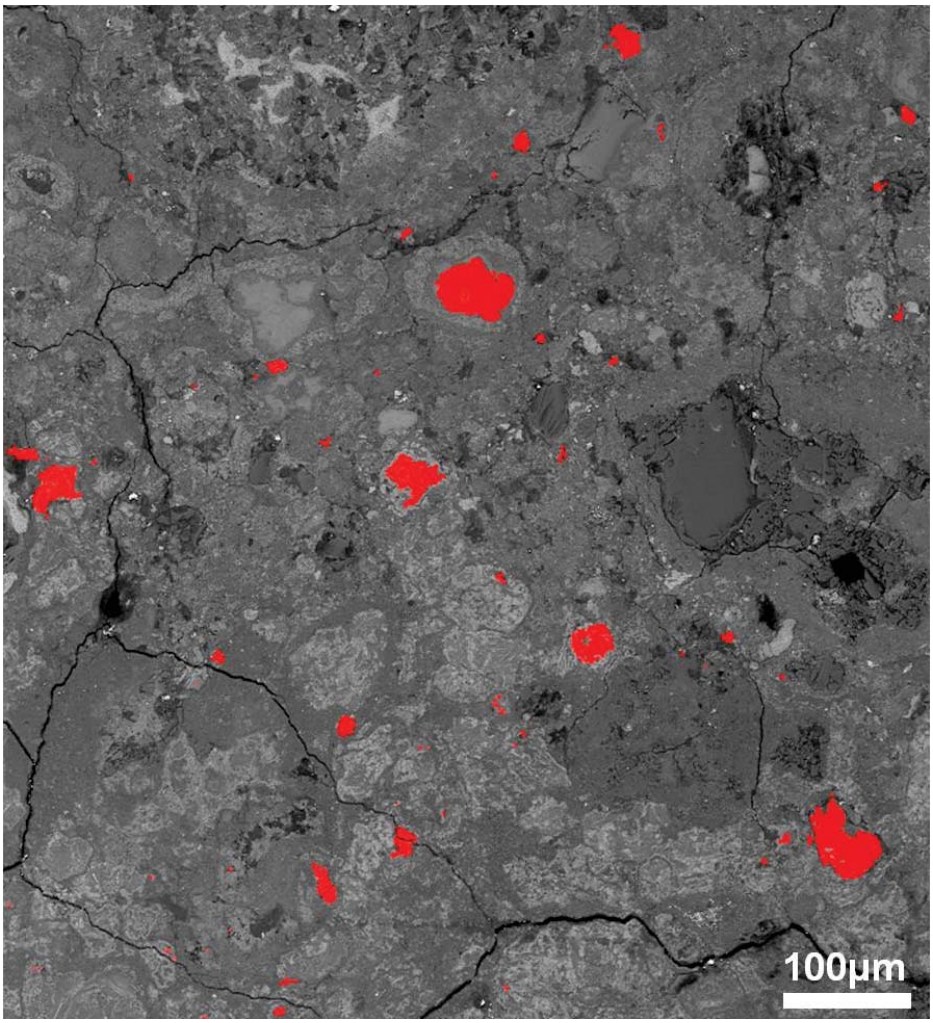

Figure 4.19- Calcium ED X-ray map combined with BSE image of small region in Murchison showing the occurrence of a calcite (red areas) cluster in the fine grained (<1µm) matrix. The location of this map in the sample studied is shown in appendix D1.

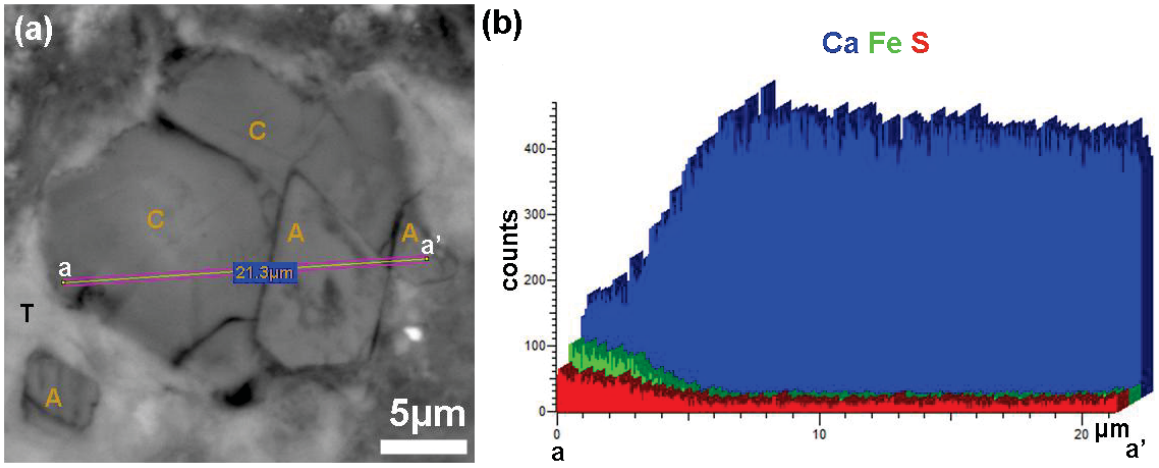

Figure 4.20- X-ray map of calcite-aragonite intergrowth.
(a) BSE image of aragonite-calcite intergrowth, A is aragonite, C is calcite T is tochilinite. (b) EDS analyses of Ca, Fe and S along the line (a-a') in (a) showing the presence of Fe and S in aragonite and calcite, and the increase of these elements towards the calcite margins. The location of this grain in the sample studied is shown in appendix D1.

4.2.3.3 Quantitative chemical analyses

Fourteen grains of calcite that show variations in CL intensity (i.e. types III, IV, VII) and four grains of aragonite that are large enough for the 5μm beam size of the EPMA were chemically analysed, and the mean of these analyses are shown in Table 4.2. Care was taken to collect data from areas of aragonite and calcite grains that were completely free of inclusions and sufficiently far from the fine grained (<1μm) matrix. Despite these reactions, one was excluded from the four analyses of aragonite, as it has very high concentrations of Fe and Mg, probably from adjacent materials. Generally, the analyses show that the aragonite and calcite grains are rich in Fe, with concentrations up to 1.28 and 0.98 mol% $FeCO_3$ respectively. Areas of high and low CL intensity in large (30-100 μm) calcite grains (e.g. Figure 4.18d) show low $FeCO_3$ contents (an average of 0.62 mole%). It was also observed that some calcite grains that are near to aragonite (i.e. in the same area as an aragonite cluster) have $FeCO_3$ with concentrations up to 1.67 mol%. The most remarkable feature is that the calcite grain which is intergrown with aragonite (shown in Figure 4.7a) has high $FeCO_3$ and $MgCO_3$ contents of 3.25 mol% and 0.90 mol% respectively, and the intergrown aragonite has 1.16 mol% $FeCO_3$ and 0.33 mol% $MgCO_3$. This chemical relationship is consistent with qualitative chemical analyses (shown in Figure 4.20) and suggests the possibility that the formation of these minerals was by fluids that gradually gained higher concentrations of elements including Fe, Mg and S. Since some calcite grains in the meteorite are rimmed by tochilinite, logically the formation of calcite was prior to that of their rims. It is clear that aragonite crystallization began at the edge of the fine grained (<1μm) matrix, and the overgrowth was calcite that was later enclosed within its tochilinite envelope.

Mole %	**aragonite**	**calcite**	**wt%**	**aragonite**	**calcite**
$CaCO_3$	98.48 ± 0.06	98.81 ± 0.97	**Ca**	38.56	38.74
$MgCO_3$	0.28 ± 0.05	0.18 ± 0.26	**Mg**	0.07	0.04
$SrCO_3$	0.04 ± 0.04	0.00 ± 0.00	**Sr**	0.03	0.00
$FeCO_3$	1.20 ± 0.07	0.98 ± 0.73	**Fe**	0.65	0.54
$MnCO_3$	0.00 ± 0.00	0.02 ± 0.08	**Mn**	0.00	0.01
n	3	14			

Table 4.2- Mean of the quantitative chemical analyses of Ca-carbonates in Murchison.
The analyses were carried out by EPMA. Concentrations below detection limit are assumed to be zero. Data presented as mean ± SD, error values are calculated to 1σ. Full dataset is listed in appendix B.1 in Mole% with average and standard deviation.

4.2.4 Post crystallization deformation of Ca-carbonate in Murchison

Petrographic observations indicate that some calcite and aragonite grains in Murchison display evidence of two shock events that have induced twinning, and some of the calcite grains have been completely transformed to Mg-rich serpentine.

4.2.4.1 Calcite twin morphology

Twins in terrestrial calcite crystals have been used as tool to understand deformation history and palaeostress orientations (e.g. Rowe and Rutter, 1990; González-Casadoa and García-Cuevasb 1999). Many researchers have mentioned that the thickness of twinning lamellae relates to thermal deformation (Rowe and Rutter, 1990; Ferrill 1991). It is also thought that twinning morphology, such as width and spacing, plays an important role, reflecting that rocks which have these calcite crystals formed in an environment near the surface of the parent body of the meteorite (e.g. Lindgren et al. 2011a).

Burkhard (1993) has classified the appearance of deformation of calcite twins into four types including: thin twins (~0.5 μm); tabular thick; curved, tapered, and lensoid thick twins; and thick patchy twins modified by dynamic recrystallisation (Figure 4.21). He related each type to a particular temperature using about 150 thin sections of calcite from the Helvetic zone at the western end of the Aar massif, Switzerland. The twin lamellae of calcite are altered by deformation temperature. Micro twins and straight lamellae (<1μm) form at very low temperatures, twin lamellae with a thickness between 1-5 μm formed under thermal conditions of about 150ºC, curved twins and thick patchy twins are related to high temperatures of approximately above 200ºC and 250 ºC respectively (Burkhard, 1993). His chart (Figure 4.21) was used here to describe the twins of calcite and aragonite. The twin morphology of Ca-carbonate was mainly described using BSE images and some EBSD maps.

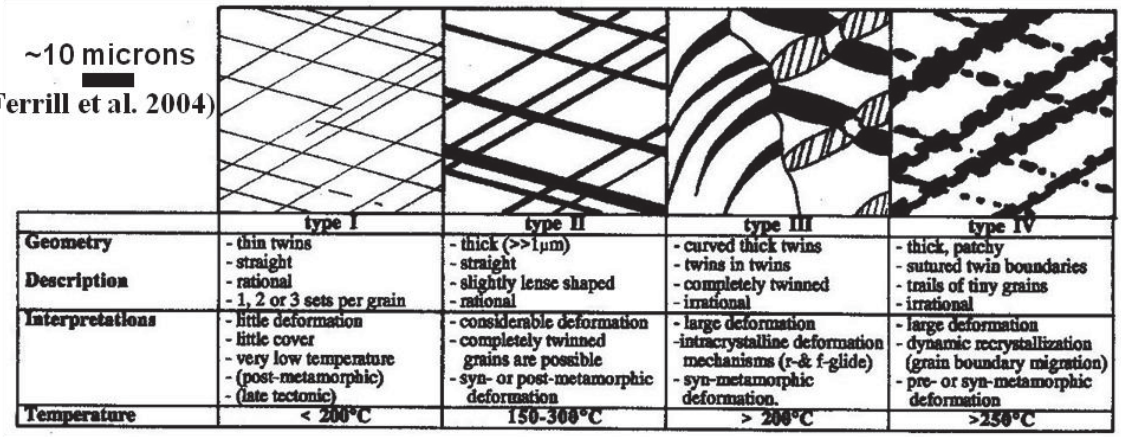

	type I	type II	type III	type IV
Geometry Description	- thin twins - straight - rational - 1, 2 or 3 sets per grain	- thick (>>1μm) - straight - slightly lense shaped - rational	- curved thick twins - twins in twins - completely twinned - irrational	- thick, patchy - sutured twin boundaries - trails of tiny grains - irrational
Interpretations	- little deformation - little cover - very low temperature - (post-metamorphic) - (late tectonic)	- considerable deformation - completely twinned grains are possible - syn- or post-metamorphic deformation	- large deformation -intracrystalline deformation mechanisms (r-& f-glide) - syn-metamorphic deformation.	- large deformation - dynamic recrystallization (grain boundary migration) - pre- or syn-metamorphic deformation
Temperature	< 200°C	150-300°C	> 200°C	>250°C

Figure 4.21- Schematic diagram showing the relationship between temperature and the width of calcite twinning, from Burkhard (1993).
The scale has been added to this twinning classification chart by Ferrill et al. (2004).

Calcite grains in Murchison have {$\bar{1}$018} e-twins, and also have multiple phases of twinning, as evidenced by the offset of twins that are cross-cut by other twins (Lindgren and Lee, 2011). Petrographic observations and EBSD mapping show that a few calcite grains in Murchison are decorated by thin straight twin lamellae (~0.5 μm), that in most cases are one set (Figure 4.22). Only one small fragment of aragonite had straight thin twins (see Figure 4.20). The thickness of lamella in most cases was less than ~0.5 μm, indicating that the Ca-carbonate in Murchison was deformed at temperatures of less than 200º.

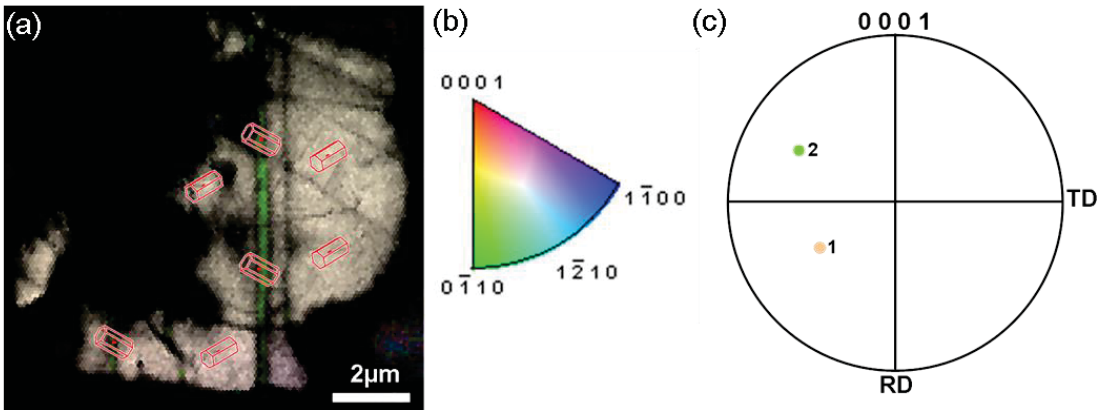

Figure 4.22- EBSD data from a calcite grain in Murchison.
(a) EBSD inverse pole figure map showing the difference between the orientations of the main crystal (brownish) and twins (green). (b) Crystallographic orientation colour key for calcite relative to ND. (c) pole figure showing the c-axes orientation of calcite (brownish) relative to its twins (green)

4.2.4.2 Pseudomorphs after Ca-carbonate in Murchison

Pollen (CM2 chondrite) has multiple generations of carbonates, one of which has been partly or completely transformed to Mg-rich phyllosilicates (Sofe et al., 2010b). Petrographic observations made for this study indicate that pseudomorphs after carbonate minerals are common in CM2 chondrites. The pseudomorphs have inherited structural details of the original crystals such as iron sulphide inclusions, grain outlines and tochilinite rims. Ca-carbonate grains in Murchison are well preserved, so free of any alteration. However, very rarely grains of Mg-rich serpentine that are rimmed with tochilinite or/and Fe-sulphides, and in some cases contain inclusions of tochilinite or/and Fe-sulphides, are found in Murchison. The texture and occurrences of the rims and inclusions are similar to those around and within some grains of calcite type II, which suggests that Mg-rich serpentine may have replaced some calcite grains in Murchison.

4.3 Carbonates in CM2.5 Murray

4.3.1 Introduction

Murray contains calcite in chondrules and as aggregates in the matrix that have formed by alteration and replacement processes (Bunch and Chang, 1980). Features of calcite grains in Murray and Murchison are similar to each other. Calcite grains in Murray are in most cases surrounded by alteration products to a thickness of about 1μm and, rarely, 10μm (Benedix et al., 2003). Murray has 2.3 vol% of Ca-carbonate (both aragonite and calcite) (Lee and Ellen, 2008). Calcite grains have anhedral to subhedral shapes, are 10-60 μm in size, and fairly homogeneously distributed throughout the fine grained matrix (Lee and Ellen, 2008). The relationship between calcite and tochilinite-serpentine intergrowth or one of these minerals has been described in order of abundance by Lee and Ellen (2008) as follows: (i) one or more grain of calcite is found within an envelope of serpentine-tochilinite, (ii) fractures that cross-cut calcite grains are filled with tochilinite, (iii) calcite grains are partly surrounded with thin layer of tochilinite (1-3 μm), (iv) calcite grains are interpenetrated with one or more aggregates of radial-fibrous tochilinite, (v) needle shaped tochilinite crystals occur within calcite.

4.3.2 Petrographic observations

Petrographic observations for this study indicate that Murray contains both calcite and aragonite. More than 800 grains of calcite were studied in thin section (P13114). SEM

point counting results show that Murray contains 1.9 vol% Ca-carbonate. These minerals are observed only in the fine grained (<1µm) matrix, which is also consistent with Lee and Ellen (2008). A Ca X-ray map of the whole sample indicates that the Ca-carbonate grains are mainly found in areas of the fine grained matrix that are associated with tochilinite and Fe-sulphides (Figure 4.23, see also Figure 3.8).

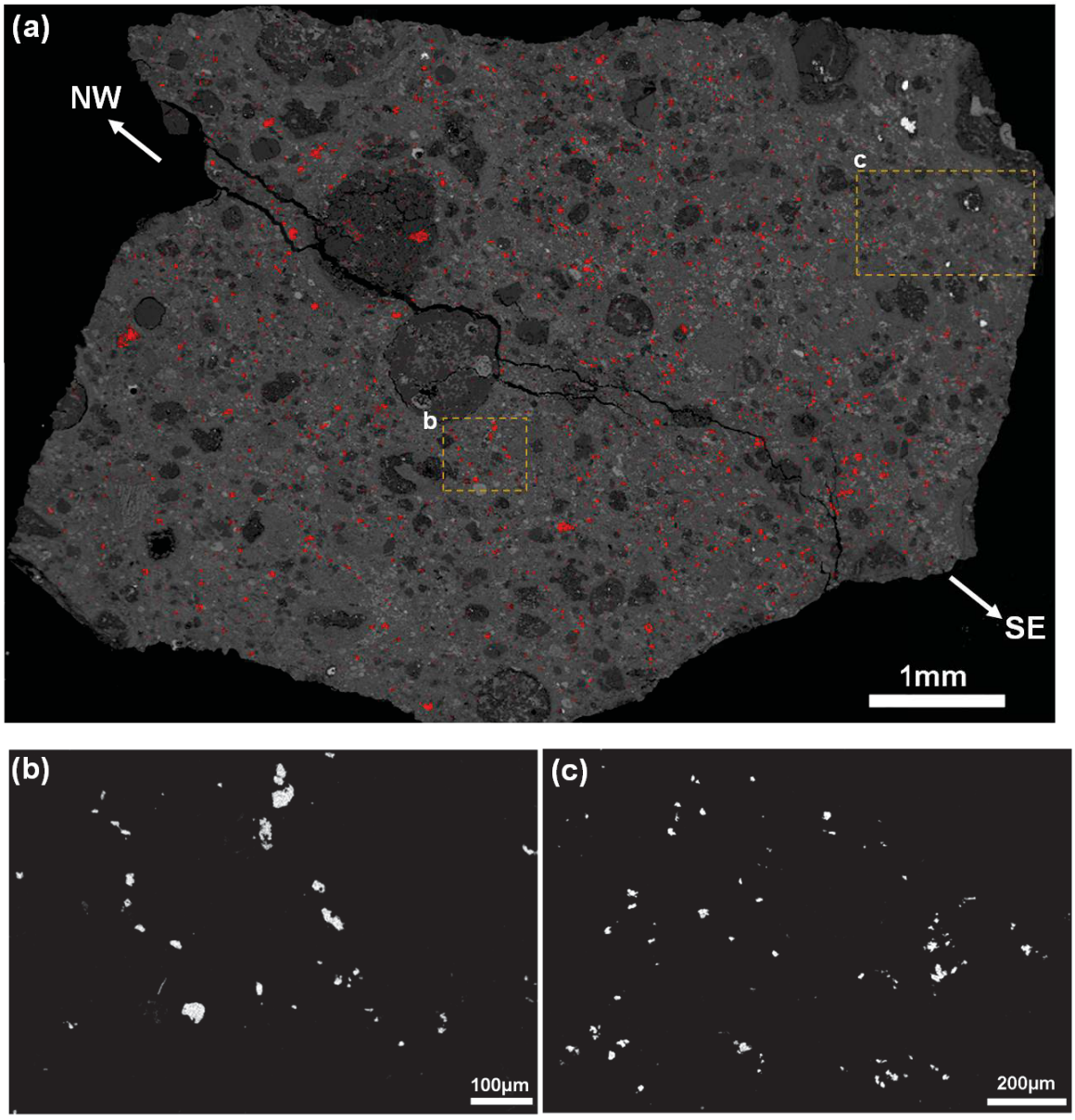

Figure 4.23- Calcium ED X-ray maps of Murray.
(a) Combined Ca map with BSE image of the whole sample showing the distribution and concentrations of Ca (red areas), which locates all Ca-carbonate grains, and a few grains of pyroxene and apatite. Ca-carbonate grains occur in two different contexts, including discontinuous veins that are shown in (b), white areas and isolated small clusters (c, white areas). Calcite grains in the boxed area were mapped for crystallographic orientation. Note the fabric of the meteorite is NW-SE is parallel to the elongation of tochilinite and Fe-sulphide clumps (white areas) in (a).

Generally, Ca-carbonate grains in Murray are likely to have crystallized in permeable zones, as these minerals are precipitated within micro-pores that are close to each other and appear in the fine grained (<1μm) matrix as discontinuous veins (Figure 4.23a-b). It was also observed that some Ca-carbonate grains have crystallized very close to each other in small clusters in the matrix (Figure 4.23a-c). The calcite grains range in size from a few microns (2 or 3μm) to 120 μm. Most of the aggregate grains and polycrystalline grains have a size between ~50μm and 120 μm.

4.3.2.1 Calcite

Unlike calcite grains in Murchison, most calcite grains in Murray either have narrow rims of Fe-sulphides and/or tochilinite, or lack rims. They have a variety of shapes that are classified in order of abundance as following: subrounded, irregular, elongate, euhedral (hexagonal and orthorhombic), and anhedral. It is also possible to divide the calcite grains into three types: (i) calcite type I is partly or completely rimmed by Fe-sulphide and/or tochilinite, and in some cases contains inclusions of one or both of the rim materials, or apatite. The thickness of rims around this calcite type ranges from >1μm to ~10μm. The characteristics of some grains of calcite type I are consistent with petrographic observations by Lee and Ellen (2008) (described above) where some Murray calcite grains are interpenetrated with radial-fibrous tochilinite, (ii) calcite type II grains are free of rims and have sharp contacts with the fine grained (<1μm) matrix; in this type inclusions of Fe-sulphides and/or tochilinite, or apatite are rare, (iii) a few grains of calcite are classified as pseudomorphs after olivine or pyroxene. It was also observed that the texture of calcite replacing pyroxene is homogeneous (appears as one crystal), whereas the calcite replacing olivine has a granular appearance (contains numerous small crystals) and in some cases has Fe-sulphide inclusions. Many of the calcite grains are likely to have been influenced by later aqueous processes, as they are slightly etched at their margins (Figure 4.24a), and more etched than Ca-carbonate grains in Murchison (see Figure 4.3b). The presence of phyllosilicates as inclusions within calcite grains is common. These inclusions are texturally and chemically comparable to phyllosilicates in the fine grained (<1μm) matrix; moreover some calcite grains have been significantly replaced by phyllosilicates (e.g. Figure 4.24b).

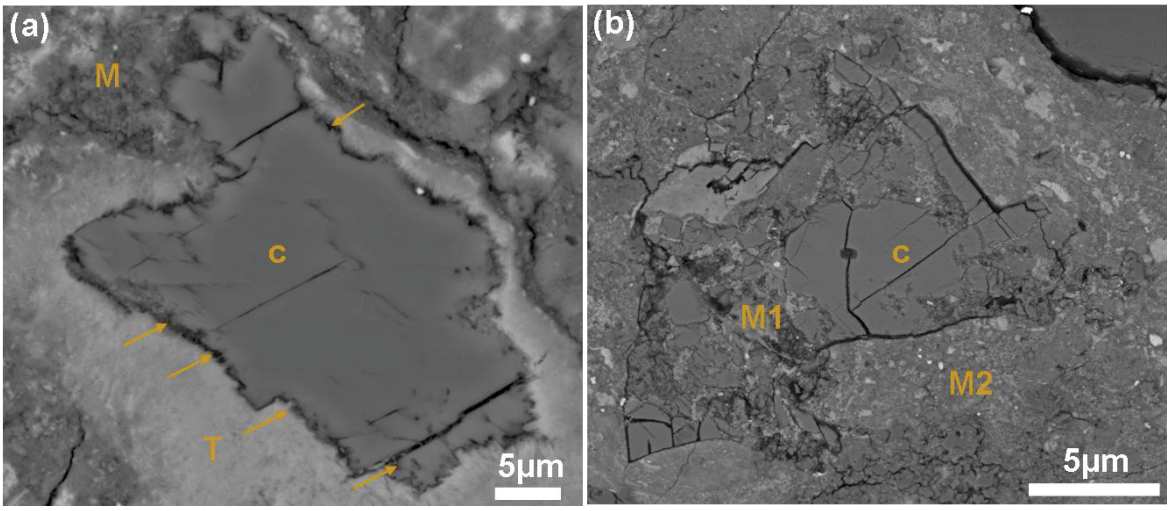

Figure 4.24- BSE images of calcite grains in Murray showing dissolution and replacement.
(a) Calcite grain (c) (type I) that is enclosed by tochilinite (T) and shows etching at its edges (arrowed areas) as a result of late aqueous process; M is fine grained (<1µm) matrix. (b) large (~40 µm) crystal of calcite (c) (type II) shows evidence of replacement by phyllosilicates (M1) that occur inside the grain and are texturally comparable to constituents of fine grained matrix (M2). The locations of these grains in the sample studied are shown in appendix D2.

The growth patterns of some grains of calcite type I suggest at least two phases of crystallization within a single grain. The first phase represents crystallization of calcite within a pore space, whereas the second is a calcite overgrowth; they show a difference in texture that probably signifies a hiatus in crystallization (Figure 4.25 a). Some calcite grains can also have one to three growth zones throughout all areas of a grain (Figure 4.25 b).

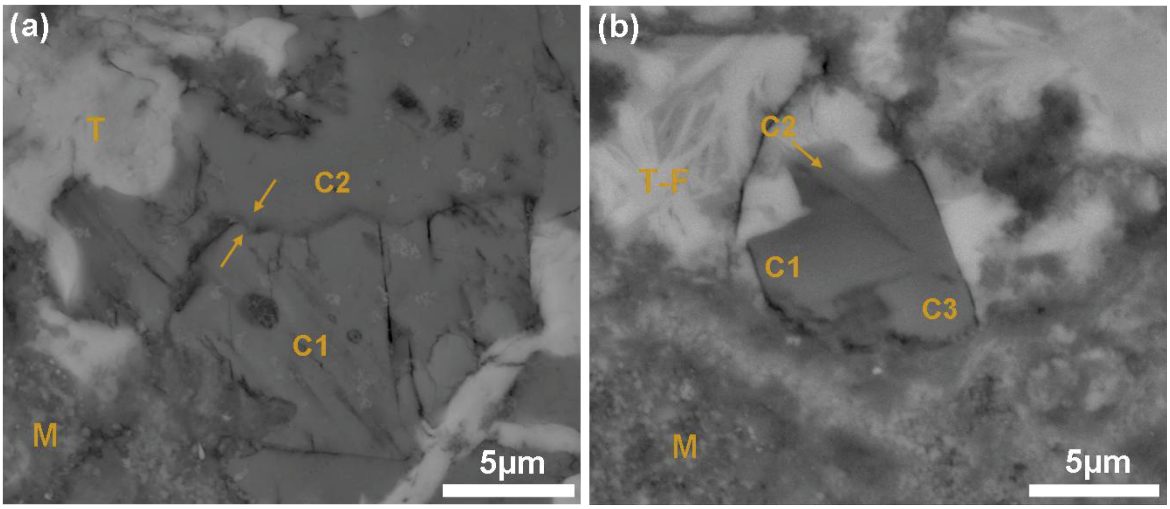

Figure 4.25- BSE images showing two or three phases of calcite within one grain.
(a) calcite grain type I demonstrates two generations of calcite, the first (C1) is a polycrystalline grain that has an irregular boundary (arrowed) with a calcite overgrowth (C2). (b) Calcite grain type I showing three zones growth (C1-C3). M is fine grained (<1µm) matrix, T is tochilinite, T-F is tochilinite Fe-sulphide intergrowth. The locations of these grains in the sample studied are shown in appendix D2

Apatite has a close relationship to some grains of calcite type I that occur close to each other in two areas of the sample. These calcite grains can have apatite as inclusions (inside the grain) or as a discontinuous thin layer (~1 μm) around the calcite (Figure 4.26).

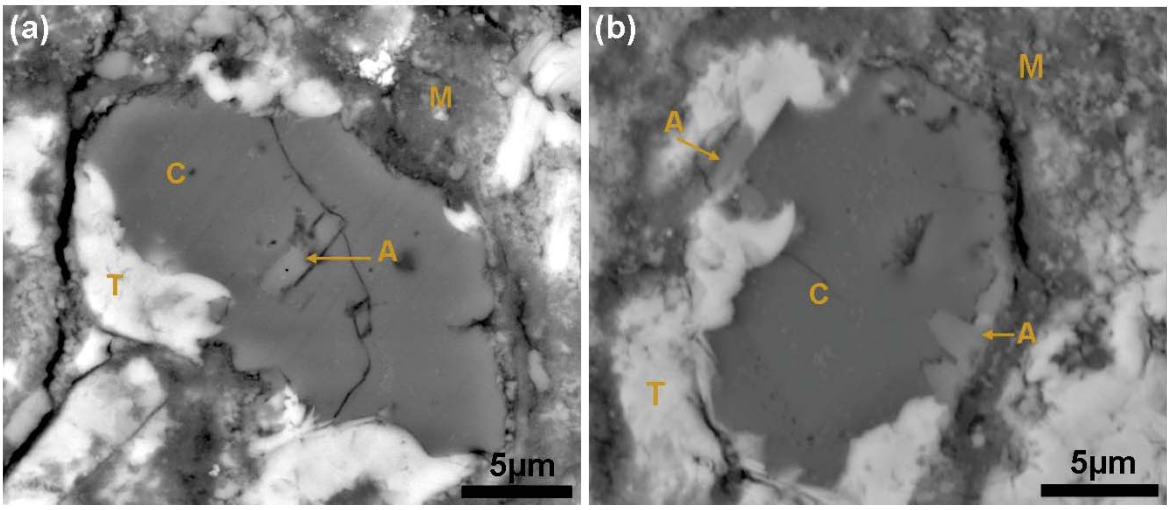

Figure 4.26- BSE images showing the relationship between calcite type I and apatite.
(a) Calcite grain type I (C) is partly surrounded by tochilinite (T) and contains an inclusion of apatite (A). (b) Calcite grain type I is partly replaced with apatite (A) and tochilinite (T). M is fine grained (<1μm) matrix. The locations of these grains in the sample studied are shown in appendix D2

4.3.2.2 Aragonite

Petrographic observations of aragonite in Murray have been reported by Lee and Ellen (2008). They found sixteen aragonite grains in two thin sections. The grains occur as single grains in a loose cluster in the fine grained (<1μm) matrix. Two clusters that contain eleven grains were found in one section (thin section P13115), whereas the second section (thin section P13114) has one cluster of five crystals of aragonite. Their results showed that some aragonite crystals are broken into two or more pieces, and all aragonite grains are surrounded by a tochilinite-serpentine intergrowth or fine grained (<1μm) phyllosilicates.

4.3.2.3 Crystallographic orientations of the calcite crystals

The crystallographic orientations of calcite grains in three areas of the sample examined were determined by EBSD. Calcite in these areas occurs as isolated grains and in two different manners, including isolated clusters and discontinuous veins. These areas are located far from each other in the sample. EBSD maps at high magnification were also obtained from some polycrystalline grains, and single grains that are very similar in their petrographic features. The first area mapped (Figure 4.27a) has one cluster of seventeen

calcite grains. The c-axes of most of these grains are inclined at high angles that range between 45º to 80º; only two grains (C7 and C11) have c-axes that are inclined close to horizontal (~15º) relative to the sample surface; nevertheless they contain sub-crystals that have c-axes that plot between about 60º-80º in the pole figure (Figure 4.27b). It is also clear that the majority of c-axes of calcite grains in the area (1) plot in three quadrants of the pole figure, namely NE, NW and SE. Generally, the c-axes of these grains are oriented around the centre of the pole figure (Figure 4.27d), which is probably related to the fabric of the rock. An EBSD map at high magnification was also acquired from five crystals including C17, C16, C15, C14 and C13 located close to each other, and that are similar in texture with rims of Fe-sulphide. The c-axes of these grains show preferred orientations at high angles in four quadrants that cluster around the centre of the pole figure (Figure 4.27c). This result suggests that calcite grains with similar textural features may also have similar crystallographic orientations.

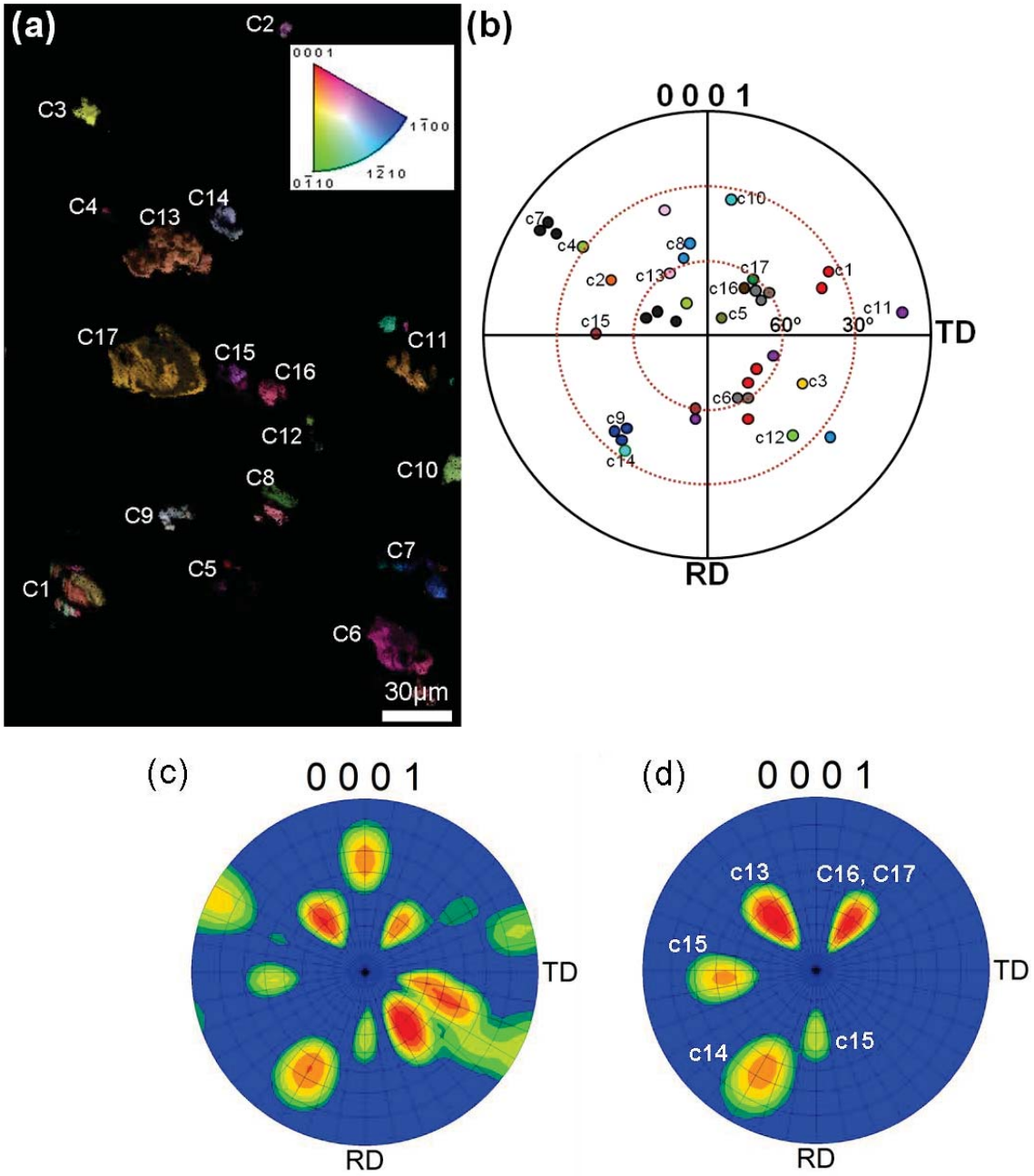

Figure 4.27- Crystallographic orientations of a small cluster of calcite grains (area 1) in Murray. (a) EBSD map showing the seventeen grains of calcite. The crystallographic orientation colour key for calcite relative to the normal direction is provided in the upper right of the map. (b) Pole figure showing the c-axes of calcite grains in (a). The c-axis of each grain is plotted in a different colour. Some grains have several points and in some cases different areas in the pole figure, as they are polycrystalline grains (all plots of e-twinning were omitted from this map). (c) Pole figure of orientations of all calcite grains in the area 1, the grid line divisions represent 10º. (d) Pole figure showing the orientations of grains C17, C16, C15, C14 and C13. The location of this map in the sample studied is shown in appendix D2.

An EBSD map was obtained from a small area in which calcite has crystallized in discontinuous zones, and parallel to the elongation of tochilinite and Fe-sulphides in same area (NW-SE) (the boxed area in Figure 4.23). This may help to correlate the orientations of these crystals with those formed within isolated clusters. The area contains two zones in

each of which at least five grains of calcite have crystallized (Figure 4.28a-b). The crystallographic orientations of the eight grains reveal a weak preferred orientation, but the c-axes of five grains (C1, C3, C5, C6 and C7) are inclined at angles between ~45º to 75º, and all grains in this map with the exception of C5 and sub-crystal of C2 lie in the NW and SW quadrants. Generally the c-axes of all grains lie in a plane parallel to the elongation of tochilinite and Fe-sulphides in the same area (NW-SE). The c-axes of grains C1, C3 and C4 that are located in the same discontinuous vein are inclined at angles between about 60º to 33º, whereas crystals C5, C6 and C7 found in the second discontinuous vein are inclined at angles between about 75º to 45º.

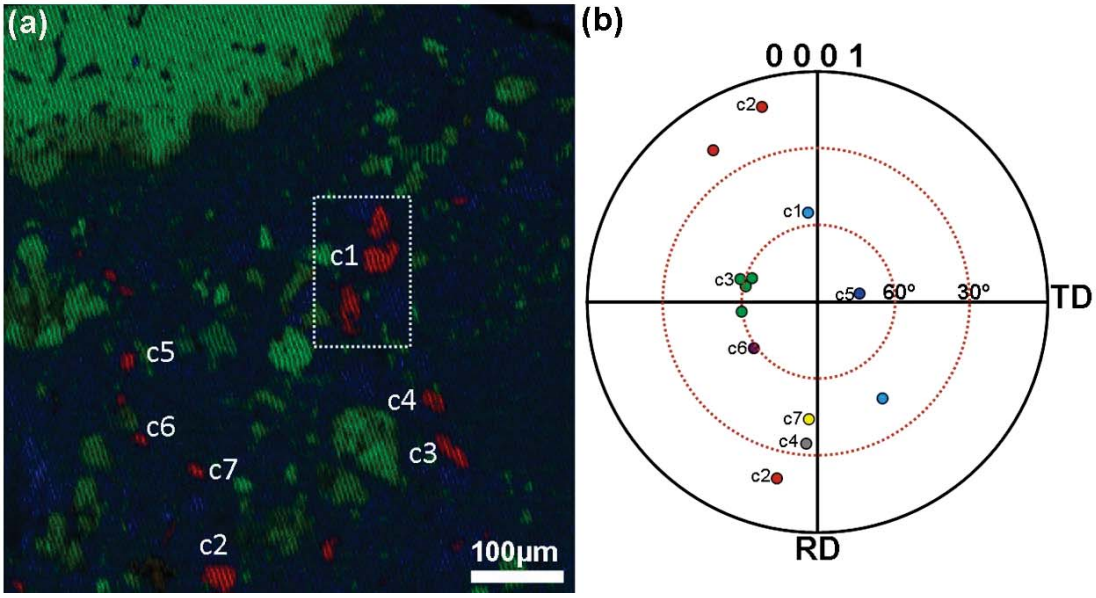

4.28- Discontinuous micro veins of calcite (area 2) in Murray.
(a) X-ray element map showing the distribution of Ca which locates the calcite grains (labelled c) that occur as single grains and in discontinuous veins. The map shows also Mg and Fe distribution in the area. (b) Pole figure showing the orientations of the c-axes of calcite grains in (a). The c-axis of each grain is plotted in the pole figure in a different colour. The c-axes of the calcite grains in these discontinuous veins are mainly orientated in NW and SW quadrants. Grains in boxed are labelled as grain 1. The location of this map in the sample studied is shown in appendix D2.

The third mapped area contains five crystals of calcite. C1 and C4 are completely rimmed by tochilinite (calcite type I), and the other three crystals are free of rims (type II). The c-axes of grains C1 and C4 are orientated close to 30º from the horizontal, with the exception of the c-axis of a sub-crystal in grain C4, which is inclined very close to the vertical and also to the direction of the c-axis of C5. Grains C2 and C3 lie between ~ 45º and less than 30º, however the c-axes of C2 twins are orientated at a low angle of ~15º. The c-axes of calcite grains in this area plot mainly in the SW and SE quadrants of the pole figure. The

EBSD map of this area also indicates that some calcite grains that are similar in petrographic features can also have similar crystallographic orientations.

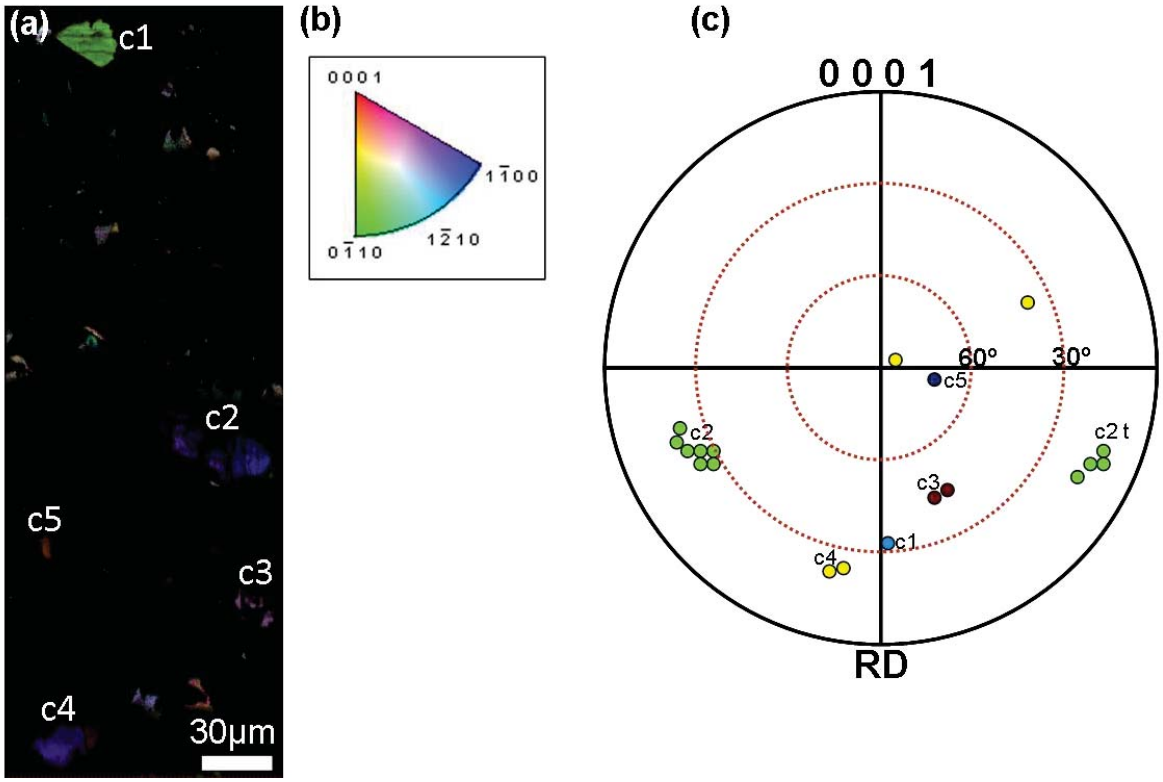

Figure 4.29- Calcite orientation in the small area (3) of Murray.
(a) EBSD map of area (3) containing five crystals of calcite. (b) Crystallographic orientation colour key for calcite relative to the normal direction. (c) Pole figure of calcite grains (a) showing the orientations and directions of these grains relative to the sample surface, c2t is the plot of c-axes of twins in C2, so is excluded from the description. The location of this map in the sample studied is shown in appendix D2.

A combination of pole figures from the three mapped areas is shown in Figure 4.30. The pole figure illustrates the difference between plots of the c-axes of calcite grains in three mapped areas. It shows that the c-axes of grains in area 1 are mainly inclined at a high angle, between 60º- 80º, whereas the c-axes of most calcite grains in area 2 and area 3 are inclined at between 30º- 60º. The pole figure shows that a few grains have c-axes that are inclined at low angles ranging between 15º-30º. Generally, the c-axes of calcite grains plot in four quadrants around the centre of the pole figure and are mainly inclined between 30º-80º. The majority of c-axes of calcite grains in Murray lie in a plane that is NW-SE and parallel to the fabric of the rock (see Figure 4.23a). Some calcite grains that are close to each other and have similar petrographic features are also similar in crystallographic orientations, example C17, C16, C15, C14, C13 and C6 in area1, and C4 and C1 in area 2

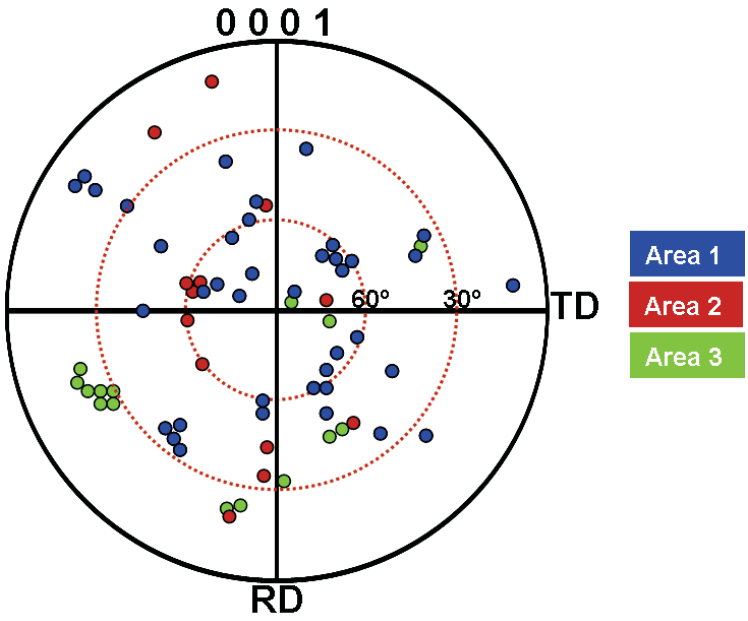

Figure 4.30- Combination of pole figures of the three mapped areas in Murray.
The aggregate pole figure shows that the c-axes of most calcite grains are inclined between 30º-80º and lie in all four quadrants and around the centre of the pole figure. The majority of the c-axes of grains in areas 1 and 2 lie in the NW-SE plane. The plots of the c-axes of twins in the calcite grains were omitted. The locations of these mapped areas in the sample studied are shown in appendix D2.

4.3.2.4 Crystallographic orientations of the aragonite crystals

The crystallographic orientation of aragonite grains in Murray was reported by Lee and Ellen (2008). Most of the aragonite grains are euhedral. The aragonite grains with an equant crystal habit and grain size of ~10-15 µm have c-axes that are near vertical. The aragonite crystals with elongate and prismatic shapes are up to 75 µm, and whose c-axes are roughly parallel to the sample surface. The orientation of the c-axes of small pieces of aragonite within faulted grains shows a very slight difference to the c-axes orientation of the main grain. The c-axes of an aragonite cluster (five grains) in thin section P13114 plot near to the margins in the pole figure and are roughly oriented E-W relative to the thin section. The c-axes of aragonite grains in thin section P13115 are oriented roughly NE-SW, relative to the orientation of that thin section as plotted by Lee and Ellen (2008). The orientation of the c-axes (NE-SW) is related to the direction of elongation of tochilinite-serpentine intergrowth in the area where one of the aragonite clusters is found. An aragonite crystal in P13115 is broken into pieces that exhibit a significant difference in orientations of their c-axes (Lee and Ellen, 2008). In this study, the majority of c-axes of calcite grains in the sample studied (P13114) lie in the NW-SE plane, parallel to the fabric of the rock (see Figure 4.23a). This indicates that the c-axes of both aragonite and calcite in Murray are inclined parallel to the same fabric of the meteorite.

4.3.3 Chemical composition of Ca-carbonate in Murray

Calcite grains in Murray were chemically analysed and mapped using the EPMA and the Sigma SEM, respectively. The FEI Quanta SEM was used to acquire SEM-CL images of calcite grains, and subsequent CL spectroscopy of some of these grains was also undertaken.

4.3.3.1 SEM-CL imaging

CL imaging of the Ca-carbonates in Murray indicates that aragonite is un-zoned. Previous CL images calcite grains have indicated that the majority either have homogenous contrast or irregular variations in SEM-CL intensity. Only a few grains show no variation in SEM-CL intensity with well defined zone growths (Lee and Ellen, 2008).

In this study, 114 CL images were acquired of Murray calcite grains. Most of these grains are partly or completely rimmed by tochilinite or/and Fe-sulphide (calcite type I), and the other grains are free of rims (calcite type II). The chart in Figure 4.17 was used as guidance to classify CL properties of Murray calcite into eleven CL types that are summarised in Table 4.3. These CL types were also related to petrographic properties of the calcite grains. The majority of CL types were observed in calcite that is partly rimmed with Fe-sulphides and calcite that is free of rims. Most calcite grains that are located close to each other and/or show similarity in petrographic features have the same CL characteristics or show very slight differences. For instance, C13 and C17 in Figure 4.27a occur in the same cluster (e.g. Figure 4.23b) and are classified as calcite type I partly rimmed with Fe-sulphides, and are identical in CL characteristics (see Table 4.3 CL type viii and Figure 4.31 a-b). Furthermore, the complex zoning is only observed in polycrystalline grains that are free of rims. It is clear that grains with similar CL characteristics probably crystallized from fluids that were similar in chemical composition.

Grain type	SEM-CL type	SEM-CL characteristics	Abundance
P, F	I, observed in Murchison	Low or high CL throughout the grain and in some cases contains patches of very high CL intensity.	8 P, 5 F
P,F	II	Complex zoning mainly found in polycrystalline grains and in most cases shows all four levels of CL intensity within one grain (from very low CL to very high CL).	1 P, 2 F
P, F, C	III, is similar to that in Murchison	Well defined halo of high or very high CL, low CL in areas inside the halo, high CL in other areas of the grain and in some cases contains large (~20 μm) patches of very high CL.	15 P, 1 F, 1 C
P, F, C	IV	Core of very high CL on the edge of the grain, overgrowth zone of high CL. (In Murchison the opposite: the very high is high CL and the high is very high CL).	3 P, 5 F, 1 C
P, C	V	High CL throughout the grain with a well defined thin layer of low CL that cross-cuts the grain. (In Murchison the high CL is very high CL).	1 P, 1 C
P, F, C	VI	Irregular core of high or very high CL, subsequent with thin layer of low CL (~1 μm), high CL overgrowth filling the pore space. (Similar to that in Murchison, but the irregular core in Murchison is low or very high CL).	2 P, 1 F, 2 C
P, F, C	VII	High CL throughout the grain, in some cases rimmed with very high CL. (In Murchison is very high CL with thin rims (~0.5 μm) of high CL).	5 P, 2 F, 5 C
P, F	VIII	Low CL with a triangle or hexagonal shaped crystal in one part, subsequent high CL of hexagonal habit, high CL growth filling the pore space.	13 P, 1 F
P, F, C	IX	Large (5-10 μm) core of low or very low CL in apart of the grain, in some cases is well developed, and the subsequent band is high CL.	17 P, 8 F, 2 C
P, F	X	Well defined band of high CL in some cases contains core of low CL, overgrowth zone of low or very low CL filling the space.	3 P, 2 F
P, F, C	XI	High CL through out the grain and contain very small core of low CL in apart of the grain.	3 P, 1 F, 3 C

Table 4.3- Characteristics and abundance of CL types of calcite in Murray and their relationships to the calcite types.
F= calcite grains free of rims and inclusions, P= calcite grains partly rimmed with tochilinite and/or Fe-sulphides, C= calcite grains completely rimmed with tochilinite and/or Fe-sulphides. Note the abundance of each CL type is assigned by numbers, e.g. 8 P means 8 grains of 114 grains imaged show CL type I, and P means these 8 grains are partly rimmed.

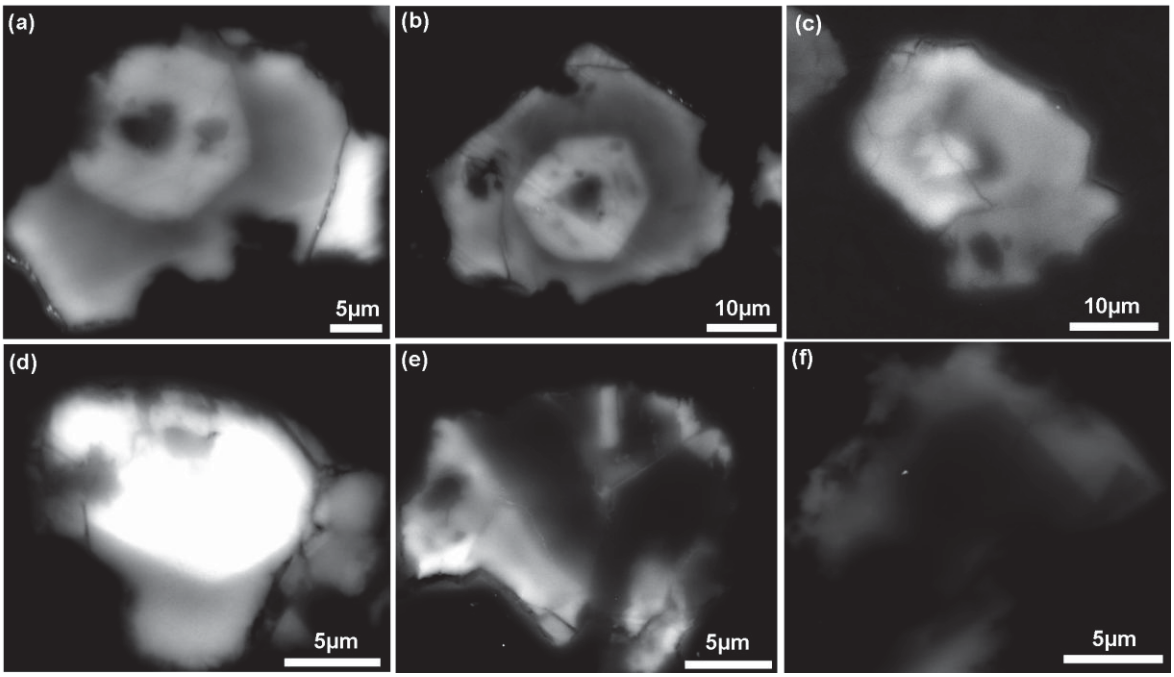

Figure 4.31- Typical images of SEM-CL types of calcite grains in Murray, that are summarised in Table 4.3.
(a-b) A CL type viii from two calcite grains that are partly rimmed with Fe-sulphides and are located close to each other. (c) A CL type vi calcite grain that is completely rimmed with Fe-sulphides. (d) CL type iv grain that is free of a rim. (e) A CL type II grain showing complex zoning in polycrystalline a calcite grain that is free of a rim. (f) CL type ix from calcite grain that is partly rimmed by tochilinite. locations of these grains in the sample studied are shown in appendix D2

4.3.3.1.1 CL spectroscopy of zoned calcite grains in Murray

CL emission spectra comprising 57 analyses of 15 zoned Ca-carbonate grains were obtained by EPMA. Results show a significant difference in CL spectra corresponding to the SEM-CL intensity variations within a grain or between grains. Lee and Ellen (2008) found that CL emission of aragonite crystals in Murray has a single peak (green) at ~490 nm, whereas zoned areas of calcite have peaks at ~430 nm (blue) and ~600 nm (orange= Mn^{2+} peak). The CL spectroscopy results presented here show that some calcite grains only have an emission peak at ~430 nm, whereas other grains exhibit two emissions peaks at ~430 nm and ~600 nm (Figures 4.32 and 4.33). Only 7 out of 15 grains analyzed have CL emission peaks at ~430 nm and ~600 nm. Eight grains have a high intensity of emission at ~430 nm with/without a very weak CL at ~600 nm. The results of CL spectroscopy are summarised in Table 4.4 and Table 4.5. The intensity value of each peak is noted in these tables. The results (Table 4.4) show that the highest intensity peaks of CL emission at ~430 nm were produced from areas of grains in CL images with very high SEM-CL and high SEM-CL intensities, with the highest intensity values in CL spectra for areas of grains very high CL in their images. The highest peaks of CL emission at ~600 nm are from areas of high SEM-CL intensity (see Table 4.5). Some grains that are located close to each other

and/or show similar petrographic features and/or have the same SEM-CL type can also have similar CL spectra, but the values of CL emission, especially at ~430 nm depend upon the SEM-CL intensity within the specific analyzed area. For instance, grains 1 and 2 (Table 4.4) are free of rims and show complex zoning (CL type ii), hence both grains only have emissions at ~430 nm (e.g. Figure 4.32), despite these grains showing all four SEM-CL intensity grades (from very low CL to very high CL), and the CL spectra obtained of all four SEM-CL zones. Furthermore, grains 6 and 7 (Table 4.4), located close to each other in the sample, are partly rimmed with tochilinite, and their SEM-CL type is (x); these grains also have two CL emissions at ~430 nm and ~600 nm. In addition, it was observed that all analysed grains that have CL type (x) can also have CL emissions at ~430 nm and ~600 nm.

			Intensity of CL emission at ~430 nm (in arbitary units) and related to SEM-CL characteristics			
No.	**Grain type**	**SEM-CL type**	**Very low SEM-CL**	**Low SEM-CL**	**High SEM-CL**	**Very high SEM-CL**
1	Free of rims	ii	--	100, 225	375, 700	1300
2	Free of rims	ii	50, 150	225	500	700
3	Partly rimmed	iii	--	200	400	1000
4	Partly rimmed	v	--	300	700, 750	--
5	Partly rimmed	vi	--	275	600	2200
6	Partly rimmed	x	100	150, 250,150, 300	450, 900	--
7	Partly rimmed	x	50	175	450	--
8	Partly rimmed	ix	--	325	500, 900	--
9	Complete rimmed	ix	--	150, 140	570, 625	--
10	Partly rimmed	ix	90	--	580	--
11	Free of rims	x	--	--	100, 125, 150	150, 275
12	Free of rims	x	--	40	40, 60	100
13	Partly rimmed	x	--	700	500, 1000	850
14	Free of rims	xi	--	950	750	1225
15	Complete rimmed	xi	30	70	70	--

Table 4.4- Summary of CL spectroscopy results of calcite grains in Murray.
The table shows the occurrences and values of CL emissions at ~430 nm of zoned grains. Every analysis of specific location is provided here, for example grain 1 has two values (100 arb. and 225 arb.) from a low SEM-CL intensity zone as two analyses were obtained from different areas in the low intensity zone of the grain. Note each analysis has CL emission at ~430 nm. All CL spectra and SEM-CL images of analysed grains are displayed in appendix C.1. The CL emission intensity is in arbitary units.

			Intensity of CL emission at ~600 nm (in arbitary units) and related to SEM-CL characteristics			
No	Grain type	SEM-CL type	Very low SEM-CL	Low SEM-CL	High SEM-CL	Very high SEM-CL
4	Partly rimmed	v	--	150	150, 150	--
5	Partly rimmed	vi	--	--	325	--
6	Partly rimmed	x	100	100, 100, 300	200, 200	--
7	Partly rimmed	x	125	70	125	--
13	Free of rims	x	--	--	300	--
12	Free of rims	x	--	40	70, 40,	40
11	Free of rims	x	--	--	--	100

Table 4.5- Summary of CL spectroscopy results from calcite grains in Murray.
The table shows the occurrences and values of CL emissions at ~600 nm of zoned calcite grains. Only seven of the analysed grains have CL emissions (peaks) at ~600 nm. Note the no. of grain in this table means the same as in Table 4.4. All CL spectra and SEM-CL images of analysed grains are displayed in appendix C.1. CL emission intensity is in arbitrary units.

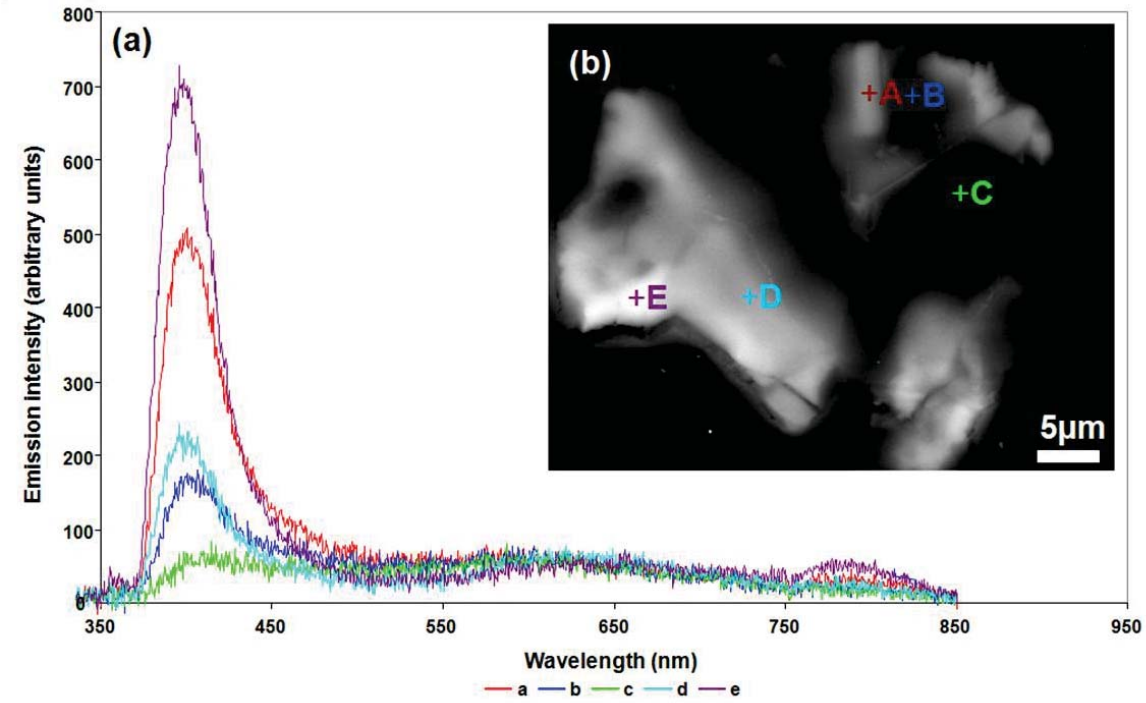

Figure 4.32- Results of CL imaging and spectroscopy of calcite grain in Murray.
(a) Spectra showing CL emissions from analyzed zones in (b) (grain no. 2 in Table 4.4). The spectra have peaks at ~430 nm, whereas the CL emissions from the zones at ~600 nm are very weak. (b) SEM-CL image showing complex zoning (CL type ii) from which the six spectra in (a) were obtained. The analyses of each point are represented in the spectra by different colour. The grain shows the four CL grades (from very low to very high CL), and the areas with very high SEM-CL intensity have the highest CL emission at ~430 nm. The location of this grain in the sample studied is shown in appendix D2.

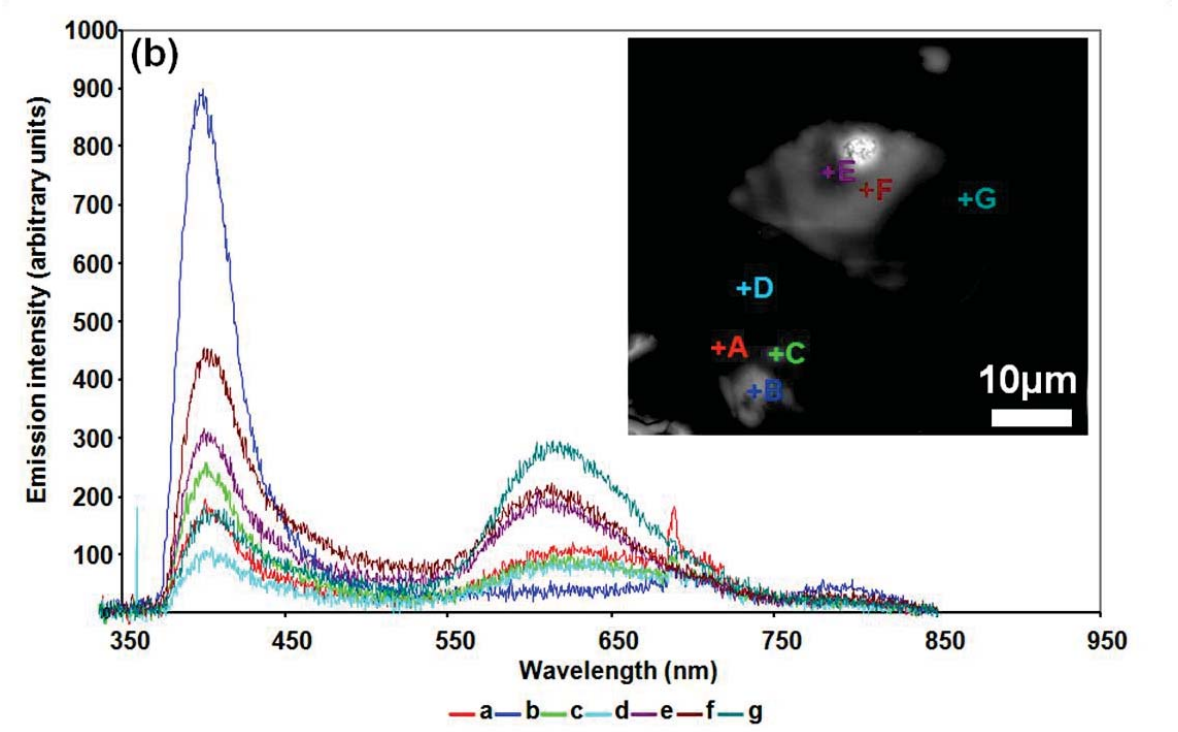

Figure 4.33- Results of SEM-CL imaging and spectroscopy of zoned calcite grain in Murray. (a) Spectra showing the occurrence of CL emissions from analysed zones in (b). The spectra have peaks at ~430 nm, and also show CL emissions from some of these zones at ~600 nm. (b) CL image of zoned calcite grain from which the seven spectra in (a) were obtained. The analyses of each point are represented by a different colour. The areas with strong SEM-CL intensity (here is high CL) have the highest CL emission at ~430 nm. The location of this grain in the sample studied is shown in appendix D2.

4.3.3.2 X-Ray mapping

Qualitative element mapping of the whole Murray sample, selected regions and some Ca-carbonate grains was carried out using the Sigma SEM with INCA software. As stated above, the Ca X-ray maps reveal that the Ca-carbonate grains are either gathered together in isolated areas or in discontinuous veins (see Figure 4.23 a, b and c).

Petrographic observations and element mapping show that some calcite grains are replaced with thin rims (~1 µm) of apatite or zoned calcite enriched with Fe (e.g. Figure 4.34). In some cases these grains are found close to each other. Some calcite grains that are partly or completely rimmed with Fe-sulphides have a strong relationship with S as the boundaries between these grains and Fe sulphides appear in element maps as transitional zones enriched with S, Fe and Ca (Figure 4.35).

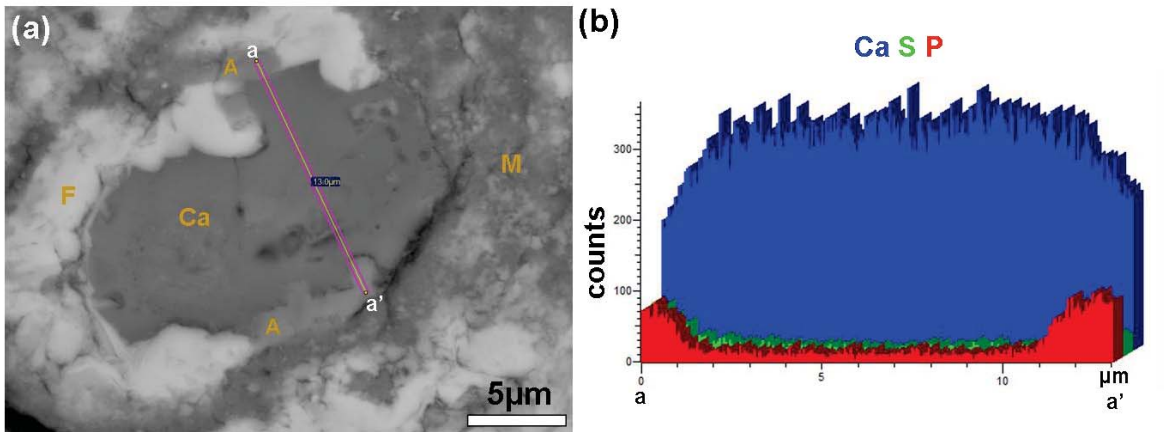

Figure 4.34- Image and EDS analyses of a replaced calcite grain by apatite at its rim.
(a) BSE image of an apatite-calcite intergrowth, A is apatite, C is calcite, F is Fe-sulphide and M is fine grained (<1µm) matrix. (b) EDS analyses of Ca, S and P along the line (a-a') in (a) showing increase of P and S in point a, and increase of P and decrease of S in a'. The location of this grain in the sample studied is shown in appendix D2.

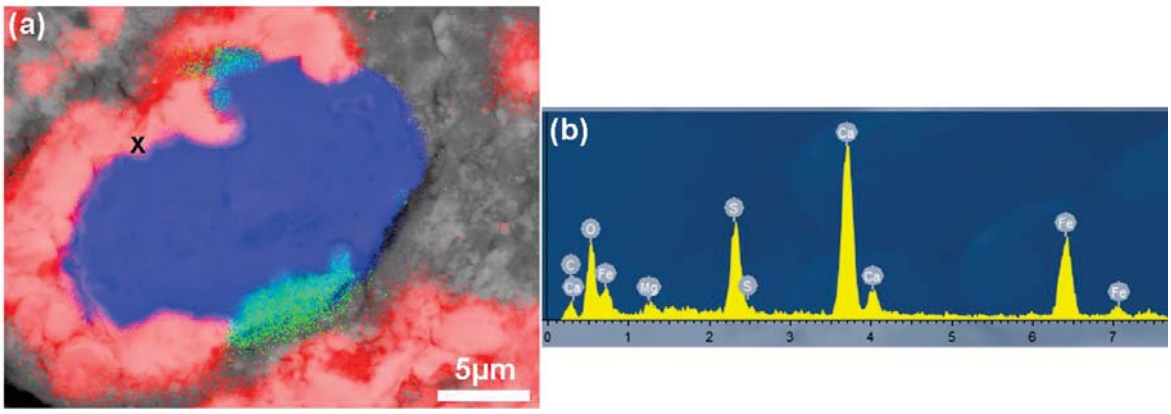

Figure 4.35- Compositional data from a replaced calcite grain by apatite at its rims.
(a) X-ray element map combined with BSE image shows the distribution of P Ca, S within the calcite grain and surrounding materials in Figure 4.34. Note the presence of S and Ca in the boundary between Fe-sulphides and the calcite. (b) EDS spectrum obtained from point x in (a) showing a qualitative chemical analysis of the boundary between the calcite and the Fe-sulphide. The spectrum confirms the presence of the constituent minerals of calcite and Fe-sulphide.

4.3.3.3 Quantitative chemical analyses

Chemical analyses of aragonite (4 analyses from one grain) and calcite (21 analyses from 7 grains) were reported by Lee and Ellen (2008). Their analyses showed that aragonite contains 0.37 mole% $MgCO_3$ and 1.61 mole% $FeCO_3$, whereas calcite contains 0.18 mole% $MgCO_3$, 0.24 mole% $MnCO_3$ and 1.44mole% $FeCO_3$.

17 grains of calcite with variations in SEM-CL (very low to very high intensity) were chemically analysed by EPMA. The average of the analyses is listed as mol% and wt% in Table 4.6. All analyses were obtained from areas that were far enough from the fine

grained (<1μm) matrix or inclusions within the grain. 3 analyses of the 35 were omitted from the average of the analyses, as they show very high concentrations of Fe relative to other analyses. The mean of chemical analyses of calcite in mol% is consistent with data in Lee and Ellen (2008), although this study indicates that two grains can have higher concentrations of Mn^{2+} in comparison with other analyses (Table 4.7). These two grains are partially rimmed with tochilinite, located close to each other, and also show the same CL intensity type (type x). Five analyses of these two grains show that the concentration of Mn^{2+} ranges from 0.52 mol% to 1.19 mol%, but in all other grains Mn is below detection limit.

Mole %	**calcite**	**Wt%**	**calcite**
$CaCO_3$	98.23 ± 0.51	**Ca**	37.61
$MgCO_3$	0.14 ± 0.17	**Mg**	0.03
$SrCO_3$	0.00 ± 0.00	**Sr**	0.00
$FeCO_3$	1.54 ± 0.27	**Fe**	0.82
$MnCO_3$	0.09 ± 0.25	**Mn**	0.04
total	100.00	**total**	38.5
n= 32 of 17 grains			

Table 4.6- Mean of the quantitative chemical analyses of calcite grains in Murray.
Concentrations below detection limit are assumed to be zero. Data presented as mean ± SD, error values are calculated to 1σ.Full dataset is listed in appendix B.2 in Mole% with average and standard deviation.

A				**B**			
Mole %	**calcite**	**Wt%**	**calcite**	**Mole %**	**calcite**	**Wt%**	**calcite**
$CaCO_3$	97.66 ± 0.72	**Ca**	34.76	**$CaCO_3$**	98.31 ± 0.38	**Ca**	38.11
$MgCO_3$	0.32 ± 0.23	**Mg**	0.07	**$MgCO_3$**	0.11 ± 0.14	**Mg**	0.03
$SrCO_3$	0.00 ± 0.00	**Sr**	0.00	**$SrCO_3$**	0.00 ± 0.00	**Sr**	0.00
$FeCO_3$	1.48 ± 0.12	**Fe**	0.73	**$FeCO_3$**	1.57 ± 0.27	**Fe**	0.85
$MnCO_3$	0.55 ± 0.39	**Mn**	0.27	**$MnCO_3$**	0.00 ± 0.00	**Mn**	0.00
Total	100.01	**Total**	35.83	**Total**	99.99	**Total**	38.99
n= 5 of 2 grains				**n=** 27 of 15 grains			

Table 4.7- Comparison between the chemical composition of two adjacent calcite grains (A) and another fifteen grains in Murray (B).
The mean of the analyses of two grains shows more Mn than the other 15 grains that lack Mn (Table B). Data presented as mean ± SD, error values are calculated to 1σ.

4.3.4 Post crystallization deformation of Ca-carbonate in Murray

Petrographic observations show that some calcite grains have been replaced by phyllosilicate minerals that are comparable with materials of the fine grained (<1μm) matrix (Figure 4.24 b), and other grains have twin lamellae.

4.3.4.1 Calcite twin morphology

Twins in calcite grains were described using BSE images and the reference chart is displayed in Figure 4.21. Two types of twins are described from about thirty calcite grains in this meteorite. Twin lamellae of these grains differ in width and shape from grain to grain, and the deformation twinning also ranges from partly deformed over part of the calcite grain to high deformation over all areas of a grain. Some grains can have one or two sets of straight and thin twins, which are classified as twinning types (I) according to the chart (Figure 4.21); additionally, a few grains show thick and patchy twins with sutured boundaries, and this twinning is classified as type (IV) (Figure 4.36 a-b).

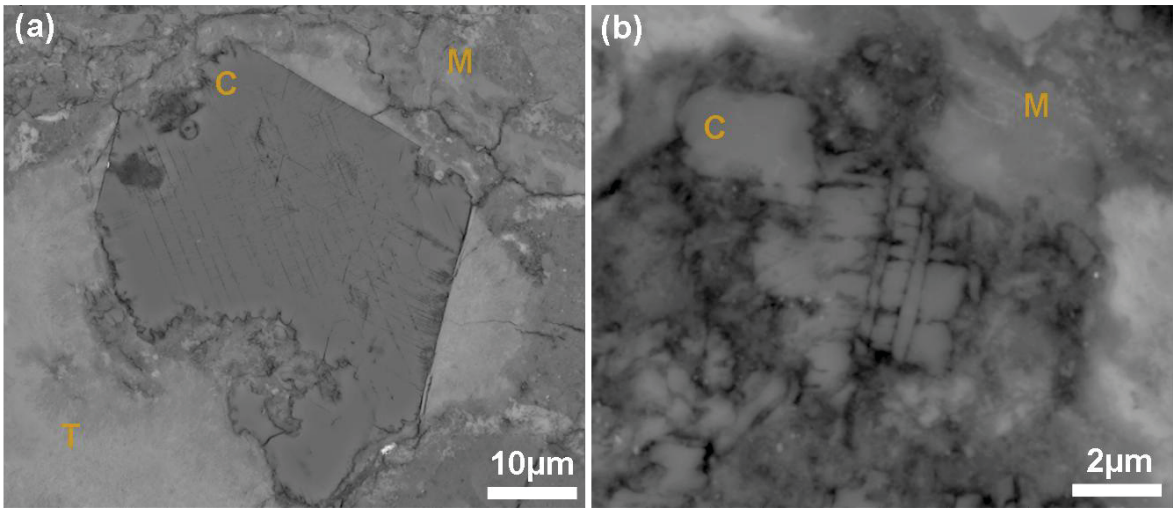

Figure 4.36- BSE images showing calcite twins in Murray.
(a) Subhedral calcite grain shows two sets of straight and thin twins (~0.3 µm) that occur throughout the grain. (b) Calcite grain displays patchy twins in the right part of the grain with sutured twin boundaries. M is fine grained (<1µm) matrix, C is calcite and T is tochilinite. The location of thes grains in the sample studied is shown in appendix D2.

4.4 Carbonates in CM2.4 Pollen

4.4.1 Introduction

In contrast to other CM2 chondrites, carbonate minerals in Pollen have received much less attention. Sofe et al. (2010b) reported that Pollen contains 2.02 vol% aragonite and calcite, present as individual and aggregate grains.

4.4.2 Petrographic observations

About 700 calcite grains and only 10 grains of aragonite are present in an area of about 45 mm^2 of the Pollen sample. Three generations of calcite were recognised from their

petrographic relationships with each other, and with matrix phyllosilicates. They are classified as following: (I) calcite grains that are completely rimmed by tochilinite-serpentine and, in some cases, contain inclusions of tochilinite, (II) calcite that has replaced forsteritic olivine and pyroxene, (III) calcite free of rims and inclusions. As stated in section 3.8.1, the Pollen matrix is composed of phase I fine grained (<1μm) matrix, consisting of phyllosilicate that is almost free of Fe-sulphide and tochilinite grains, and phase II that is composed of fine grained (<1μm) phyllosilicate, which has abundant Fe-sulphide and tochilinite clumps, and is slightly coarser grained. Aragonite grains, calcite completely rimmed by tochilinite-serpentine and calcite free of inclusions are found in the phase II matrix (Figure 4.37). Calcite replacing Mg,Fe silicates is present in both phase I and II grained (<1μm) matrix. Generally, the distribution of aragonite and calcite are different, such that aragonite grains occur in two loose clusters, whereas calcite grains are more homogeneously distributed (Figure 4.37). In common with Murray, Ca-carbonate grains are likely to have crystallized in small clusters, and in some cases occur as discontinuous veins of calcite.

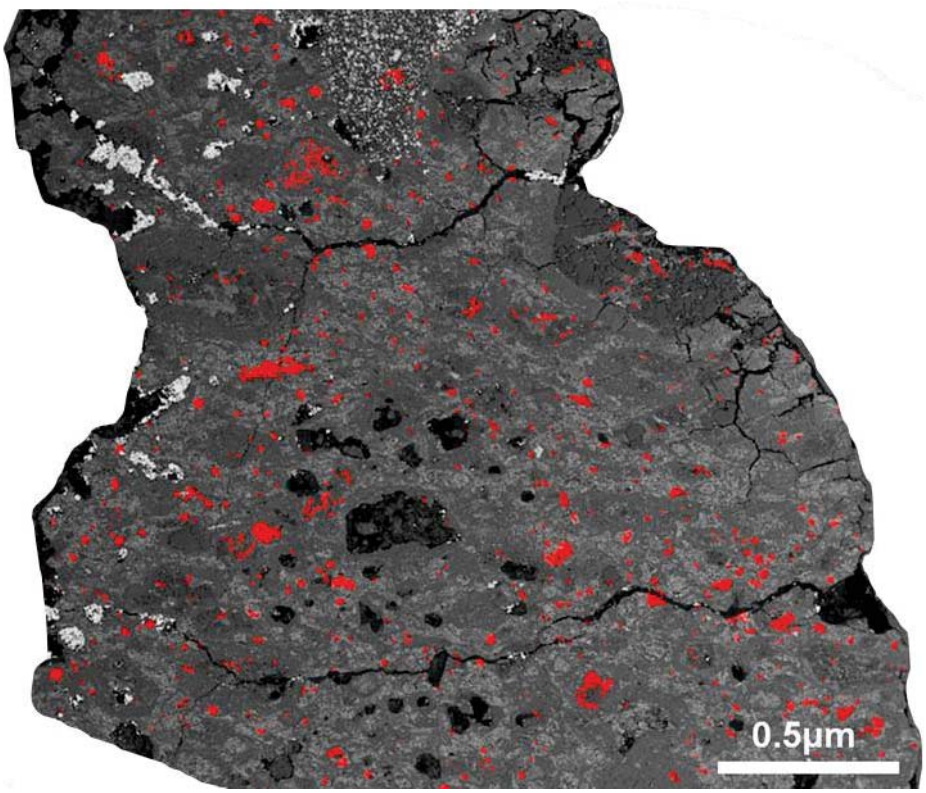

Figure 4.37- Calcium X-ray map combined with BSE image of a small region of Pollen.
The map shows the concentration and distribution of Ca, which locates all Ca-carbonate grains. Note the majority of these grains occur in areas that are dominated by Fe-sulphides and tochilinite (bright areas), EDS spectra obtained from tochilinite crystals are shown in Figure 4.52 (x3, x4 and x5). The calcite grains (red areas) occur in isolated small areas and in small discontinuous veins. The location of this map in the sample studied is shown in appendix D3.

Calcite grains in Pollen range in size from 1 μm to 50 μm and in some cases are ~150 μm in length. Most of these grains are subhedral, subrounded or irregular in shape.

A prominent feature of the calcite generation I (Figure 4.38a) is that every crystal is rimmed by tochilinite-serpentine, which ranges in thickness from ~0.5 μm to 2 μm. In some cases, fibres of Fe-sulphides are also present around or within this calcite, and the Fe-sulphide fibres range in length from 1 μm to 3 μm. The majority of these calcite grains have been totally or partially replaced by Mg-rich phyllosilicates to leave tochilinite-serpentine rimmed pseudomorphs (Figure 4.38b), which comprise 3.15 vol% of the meteorite. Generation II calcite then replaced chondrule and forsteritic-olivine/pyroxene, which contains patches of blocky pentlandite (Figure 4.38b). This generation of calcite has a mottled appearance and exhibits sharp contacts with surrounding materials; however it is observed that the calcite replacing pyroxene has a cryptocrystalline texture (see Figure 4.49). The third generation is calcite that is free of rims and inclusions, and is comparable in texture and appearance to most aragonite grains (Figure 4.38 c-d). This generation of calcite is less abundant (0.4 vol%) than the other two. It was also found that calcite replacing Fe,Mg silicates is more abundant in Pollen (2% out of 700 grains in the sample) than calcite of the same origin in Murray (1% out of 800 grains in the sample).

Textures of some grains of calcite generation I (rimmed by tochilinite-serpentine) show clear evidence of calcite precipitation within pore space (Figure 4.39). These grains show at least two phases of calcite crystallization that clearly differ in texture and the second appears as a calcite overgrowth.

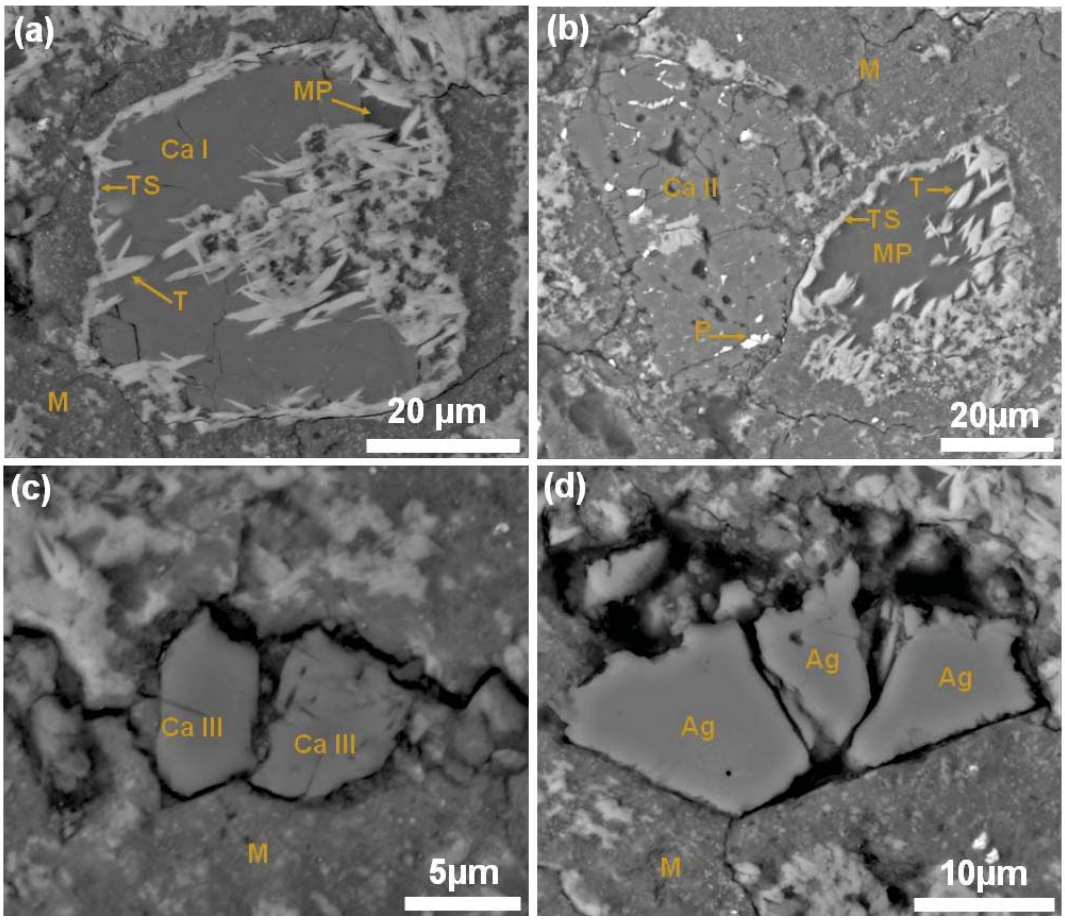

Figure 4.38- BSE images illustrate four generations of Ca-carbonates in Pollen.
(a) Calcite generation I (Ca I) that is rimmed with serpentine-tochilinite intergrowths (TS) and contains fibres of tochilinite (T). This grain has been partly replaced by Mg-rich serpentine (MP). (b) Two different types of pseudomorphs including replacement of forsteritic olivine with calcite (Ca II) that is assigned to be the second generation of calcite, and Mg-rich serpentine (MP) that has totally replaced a calcite grain. Note that the rims around the grain are similar to those around the calcite in (a). (p) is blocky pentlandite within the calcite. (c) Calcite generation three (Ca III) that is free of rims and inclusions. (d) Aragonite crystal (Ag) shows the same the texture and appearance of calcite generation III (in c). M is fine grained (<1µm) matrix. The locations of these grains in the sample studied are shown in appendix D3.

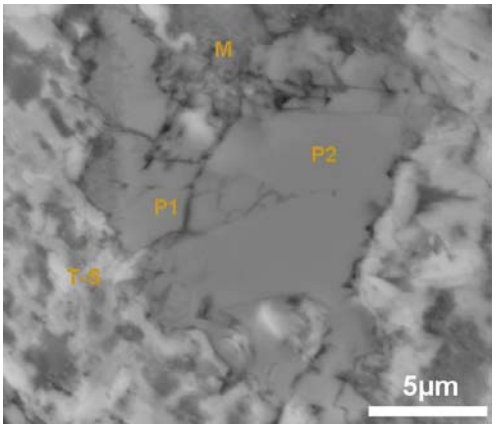

Figure 4.39- BSE image showing a grain rimmed by tochilinite-serpentine that contains of two phases of calcite.
The first phase (P1) is fractured calcite that is formed within open pore space, and the subsequent phase (P2) is a calcite overgrowth. M is fine grained (<1µm) matrix. T-S is tochilinite-serpentine. The location of this grain in the sample studied is shown in appendix D3.

One crystal of aragonite was found within a polycrystalline grain of calcite and was identified unequivocally from is its CL spectrum (see Figure 4.43). Another nine aragonite crystals were distinguished from calcite by their Raman spectra. These nine occur as single grains within the fine grained (<1μm) matrix. Aragonite grains occur in two isolated clusters. One cluster (C1) contains three grains and the other (C2) contains six grains. Only one grain (grain 9) was found isolated and is far from C2 (Figure 4.40). The size of aragonite grains ranges from ~3 μm to 20 μm. Most of these grains are fractured and have sharp boundaries with the fine grained (<1μm) matrix (e.g. Figure 4.38d); only one grain has inclusions of Fe-sulphides.

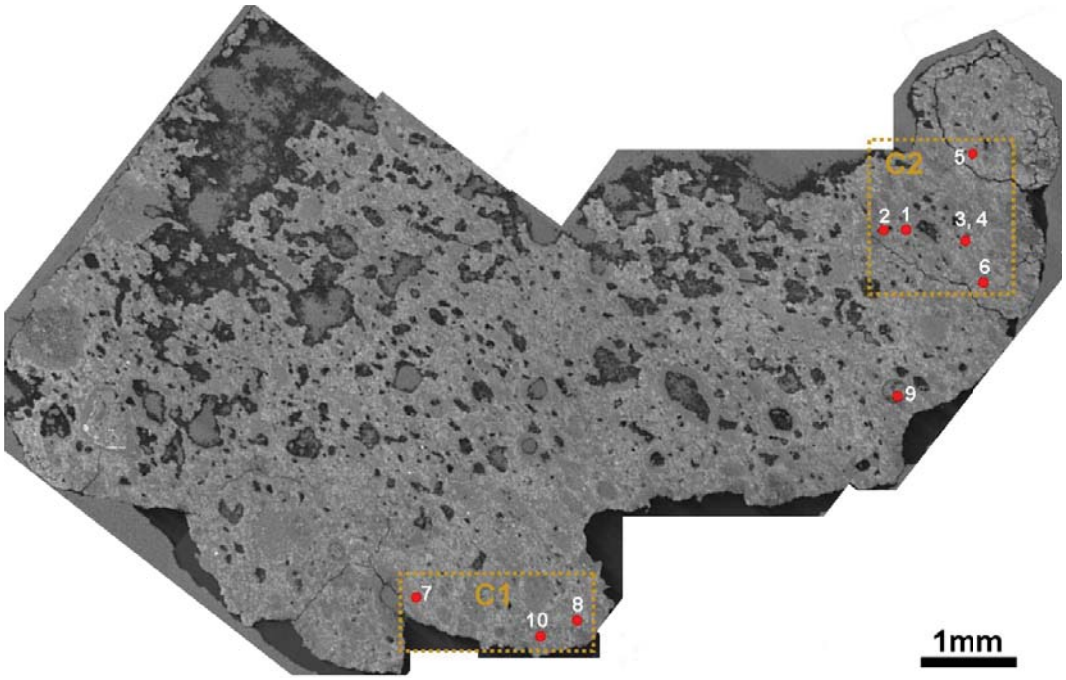

Figure 4.40- BSE image of whole thin section of Pollen showing the location of two clusters of aragonite in the fine grained (<1μm) matrix (C1 and C2).
C1 contains three grains of aragonite, C2 contains six grains of aragonite. Note that only grain 9 is isolated. Dark areas are pores within the sample.

4.4.2.1 Crystallographic orientation of calcite

Crystallographic orientation mapping was carried out for some calcite grains in Pollen, in particular the calcite replacing Fe,Mg silicates that have two different textures (calcite replacing olivine and calcite replacing pyroxene). Calcite replacing forsteritic olivine has a mottled appearance and is likely to be composed of sub-crystals (see Figure 4.38 b). In most cases, the c-axes of these sub-crystals within the large (~20 μm) grain are inclined at the same orientations and directions (Figure 4.41).

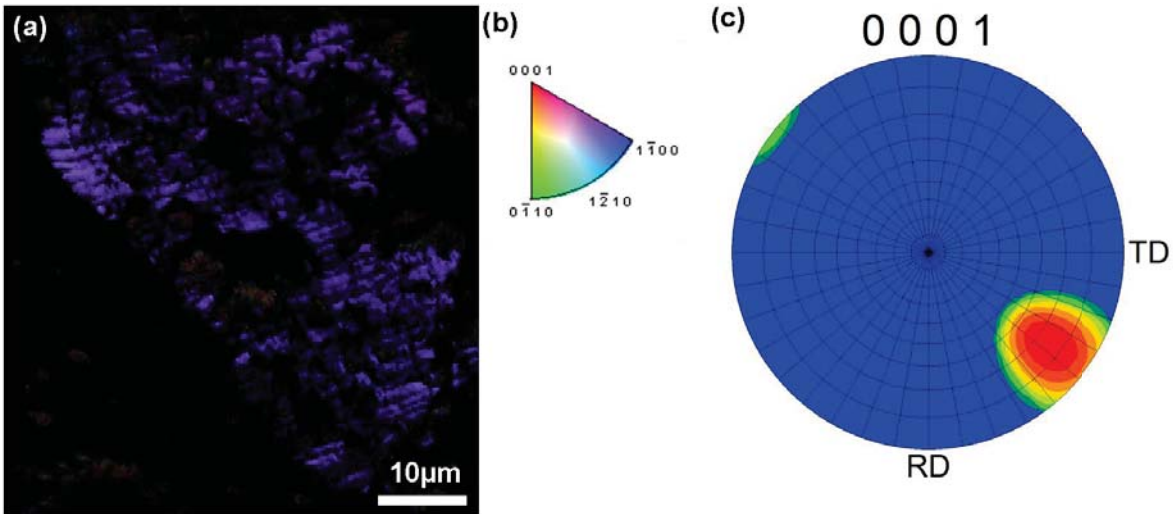

Figure 4.41- EBSD results from a large calcite grain replacing forsteritic olivine.
The BSE image of the grain is in Figure 4.38b (labelled C II). (a) Inverse pole figure map showing orientations of sub-crystals within the grain, which are represented by the same colour. (b) Crystallographic orientation colour key for calcite relative to the normal direction. (c) Pole figure texture showing orientations of the calcite sub-grains in (a). The grid line divisions represent 10º. Note that all sub-crystals are orientated at the same angle and in the same direction. The location of this grain in the sample studied is shown in appendix D3.

4.4.2.2 Crystallographic orientation of aragonite

Crystallographic orientations of 5 aragonite grains were determined. The {001} pole figure (Figure 4.42) shows that these grains have a crystallographic preferred orientation with their c-axes approximately in the plane (~60º) close to the centre of the pole figure, with the exception of the c-axis of grain 9, that is nearly inclined to the horizontal relative to the sample surface. This suggests that the aragonite grains in C1 and C2 could have been formed at the same time, whereas grain 9 probably formed at a different time.

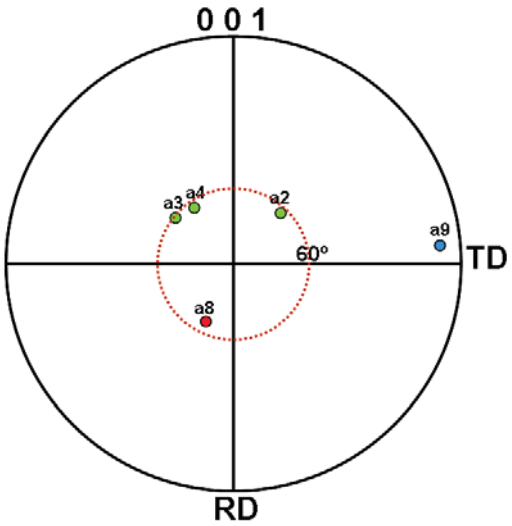

Figure 4.42- Pole figure showing the orientations of poles to the {001} planes of the 5 aragonite grains that were sufficiently large to be mapped by EBSD.
Grains in green are located in C2, a8 is grain 8 in C1 (BSE image of this grain is shown in Figure 4.38d), a9 is grain 9 that is located far from C1 and C2. Note four grains in C1 and C2 plot at about 60º and around the centre of the pole figure, but a9 plots close to the circumference of the figure. The grain size of the grains ranges from 10 µm to 20 µm.

4.4.3 Chemical composition of Ca-carbonate in Pollen

Aragonite and calcite grains in Pollen have been chemically analysed and mapped using the EPMA and the Sigma SEM respectively. The FEI Quanta SEM was used to acquire SEM-CL images of some aragonite and calcite grains and subsequent CL spectroscopy of some of these grains was also undertaken.

4.4.3.1 SEM-CL imaging

SEM-CL images were obtained from 48 grains of calcite, 1 grain from aragonite and of the aragonite-calcite intergrowth. The patterns of SEM-CL in images of the grains were also related to their petrographic features.

SEM-CL characteristics of Ca-carbonate in Pollen are classified into 7 types. Five of these types were observed in some calcite grains from Murray that include: I, II, V, IX and VIII. Type VII is rarely present in Murchison (calcite grains) and also characterises some calcite grains in Murray. Type XII is only observed in calcite grains from Pollen (described in Table 4.8). CL type I shows a high SEM-CL intensity throughout a grain but in some cases contains patches of very high CL. This type characterizes some calcite grains in Murchison and Murray, but is more abundant in Pollen, which is probably related to a greater stability of compositions. It was also observed that all grains that have replaced forsteritic olivine

exhibit CL type I. CL type I also characterizes most calcite grains that are completely rimmed by tochilinite-serpentine. CL type VIII (described in Table 4.3 and Table 4.8) is more common in Murray than Pollen; it is seen in only one grain in Pollen, which also indicates that fluid compositions fluctuated during the precipitation of calcite grains.

Grain type	SEM-CL type	SEM-CL characteristics	Abundance
C, R, F	I (observed in Murray and Murchison)	Low or high CL throughout the grain, in some cases contains patches of very high CL.	19 C, 3 F, 2 R, 1 C-A
C	II (observed in Murray)	Complex zoning mainly found in polycrystalline grains and typically shows all four levels of CL intensity (from very low CL to very high CL) within a grain.	4 C
C, A	V (observed in Murchison, Murray)	High CL throughout the grain with well defined thin layer (0.2-1 μm) of low CL cross-cutting the grain.	3 C, 1 A
C	IX (observed in Murray)	Large (5-10 μm) core of low or very low CL in a part of the grain, in some cases is well developed, and the subsequent band is high CL, but in some cases in Pollen a grain can has third band of high CL or very high.	7 C, 2 F
C, F	VII (observed in Murchison)	Very high CL throughout the grain with rims of high CL.	4 C
C	VIII (observed in Murray)	Low CL with a triangle or hexagonal shaped crystal in one part, subsequent high CL of hexagonal habit, high CL growth filling the pore space.	1 C
C	XII (observed only Pollen)	High CL throughout the grain with rims of very high CL.	1 C

Table 4.8- Characteristics and abundance of CL types of Ca-carbonate grains in Pollen and their relationship to petrographic features.
F is calcite grains free of rims, C is completely rimmed with tochilinite-serpentine (type I), R is calcite replacing olivine (type II), A is aragonite, C-A is calcite-aragonite intergrowth. Total number of grains imaged is 48. Note the abundance of each CL type is assigned by numbers, e.g. 19 C means 19 of the 48 grains imaged show CL type I, and C means these 19 grains are completely rimmed.

4.4.3.1.1 CL spectroscopy of zoned calcite grains in Pollen

CL emission spectra were obtained from 106 analyses of 26 zoned Ca-carbonate grains in Pollen. One grain contains both aragonite and calcite. CL intensities of zoned gains in Pollen show differences between the grains and also between zones within a grain. Generally, all the grains analysed emit CL at ~430 nm, but the peak intensity of CL emission varies with the SEM-CL characteristic of the analysed point (low CL etc.). All CL emission values at ~430 nm are listed in Table 4.9. It is clear the highest intensities (up to 1600 counts) of CL emission were produced from areas that are characterised by high and very high SEM-CL intensity, whereas areas with low and very low CL intensity can have peaks with values that range between '100 to 700' counts. 19 grains of the 26 also have emission peaks at ~600 nm; the values of these peaks were determined approximately

and are listed in Table 4.9. The results show that the areas with low and very low intensity can have the highest intensity peaks at ~600 nm, reaching up to 420 counts, but areas with very high SEM-CL intensity produce smaller peaks at ~600 nm, in comparison with areas of low and high SEM-CL intensity. The results also show the aragonite grain analysed to have a peak at ~530 nm (Figure 4.43).

Intensity of CL emission at 430 nm according to SEM-CL characteristics						
No.	**Grain type**	**SEM-CL type**	**Very low SEM-CL**	**Low SEM-CL**	**High SEM-CL**	**Very High SEM-CL**
1	C	vii	--	--	825	1000,1000
2	C	v	250	550	800	--
3	F	vii	--	--	625	1500
4	R	i	--	--	825, 825, 625	--
5	C	ii	--	--	400,250, 240,200	1100,1100,800, 750
6	C	i	--	--	425,575,1025	--
7	C	i	125	--	430	575, 575
8	C	viii		290	550,400	700,700
9	C	i	--	--	400,350	550
10	C	i	--	100	560	1025
11	R	i	--	--	550,700,525,450	--
12	C	xii	--	--	325,360	570
13	C	ix	--	200,300	350	800
14	C	v		425	825	850
15	C	ix	450	700	720	925
16	C	ix	--	220	1200, 1000, 900	--
17	C	ix	--	650	1200,800, 580	1300
18	C	vii	--	--	950, 600, 500	1600, 1380
19	F	ix	--	200	550, 425	--
20	F	i	--	--	400,420,380,350,200, 200,	--
21	C	i	--	--	825,500,500	--
22	C	v	--	--	325	925,750
23	A-C	i	--	--	650,620,580,430,900, 1110,1100	1300,1050, 980
24	C	ix	--	200	600,1020,1080, 1200	--
25	C	ix	--	--	850,600,350,250	--
26	C	ix	--	250,250,200	725	--

Table 4.9- Summary of CL spectroscopy results from Pollen.
The table shows the occurrences and values of CL emissions at ~430 nm in all Ca-carbonate grains analysed. Each spot analysis of a specific location has an emission intensity that is represented as a peak at ~430 nm in the spectrum. The value of each peak is represented by a number (intensity counts) in this table; for example grain 3 has emission intensities of 625 and 1500 (counts) from high and very high CL areas respectively. C= calcite completely rimmed (type I), R= calcite replacing olivine (type II), F= calcite free of rims and inclusions (type III), A-C= aragonite-calcite intergrowth. The CL emission intensities are quantified in arbitrary units.

(a)			Intensity of CL emission at 600 nm according to SEM-CL characteristics			
No.	**Grain type**	**SEM-CL type**	**Very low SEM-CL**	**Low SEM-CL**	**High SEM-CL**	**Very High SEM-CL**
2	C	v	--	150	200	--
4	R	i	--	--	300,240,250	--
5	C	ii	300,250	--	280,170,150	180,180
7	C	i	325	--	280,150	200
8	C	viii	--	225	150	--
9	C	i	--	--	220	--
10	C	i	--	300	--	200
12	C	xii	--		--	170
13	C	ix	--	150,150, 120	--	--
15	C	ix	--	350	210,250	--
16	C	ix	--	--	210	--
18	C	vii	--	400,420	--	--
19	F	ix	300	--	150,180	--
20	F	i	--	--	220,250,220	--
26	C	ix	--	300	250	--
24	C	ix	150		100	--
22	C	v	--	200	150,200	--
14	C	v	--	150	--	--
23	A-C	i	--	--	220	--
(b)			**Occurrence of CL emission at ~550 nm according to SEM-CL characteristics**			
No.	**Grain type**	**SEM-CL type**	**Very low SEM-CL**	**Low SEM-CL**	**High SEM-CL**	**Very high SEM-CL**
23	A-C	--	--	--	--	1200,850,450

Table 4.10- Summary of CL spectroscopy results of calcite and aragonite in Pollen.
(a) Summary of CL spectroscopy results showing the occurrences and values of CL emissions at ~600 nm of some of grains analyzed; 19 grains of the grains analysed have CL emission peaks at ~600 nm. Note the no. of grain in this table means the same grain in Table 4.9. (b) Table showing the values of CL intensities at ~550 nm that were produced from very high CL intensity area in sub-crystal of aragonite in calcite grain (see also Figure 4.43). C= calcite completely rimmed (type I), R= calcite replacing olivine (type II), F= calcite free of rims and inclusions (type III), A-C= aragonite-calcite intergrowth. All CL spectra and CL images of analysed grains are displayed in appendix C.2.The CL emission is quantified in arbitrary units.

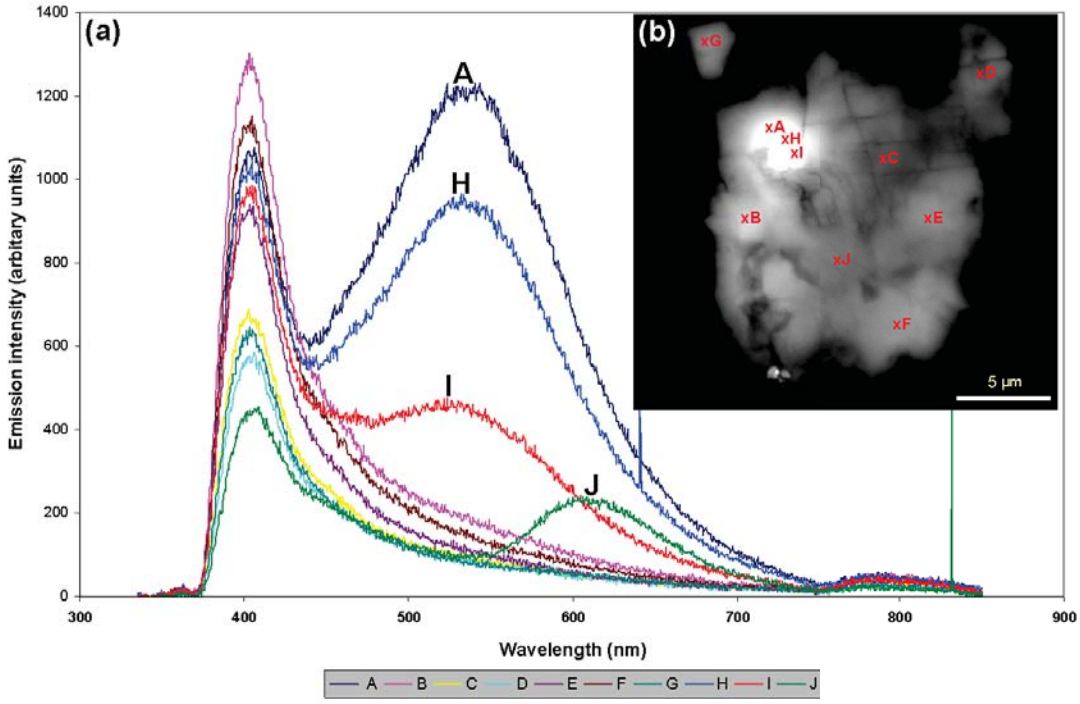

Figure 4.43- CL spectroscopy of the aragonite and calcite intergrowth in Pollen.
(a) Emission spectra from the zoned calcite-aragonite intergrowth in (b). A, H and I are from very high SEM-CL intensity areas of the crystal of aragonite that have peaks at ~530 nm, whereas the calcite spectrum of area J has a Mn^{2+} peak at ~620 nm. Intrinsic spectra of calcite B, C, E, F and G show significant emission maxima that are at ~430 nm. (b) SEM-CL image of the grain. The location of this grain in the sample studied is shown in appendix D3.

4.4.3.2 X-Ray mapping:

Qualitative element mapping of the whole Pollen sample, selected regions and some carbonate grains was carried out using the Sigma SEM with INCA software. Element mapping shows that calcite grains rimmed by serpentine-tochilinite and with/without Fe-sulphides are likely to have precipitated from fluids from which these rims were formed. These grains show a strong relationship with S and Fe and appear slightly zoned with Fe and S (Figure 4.44).

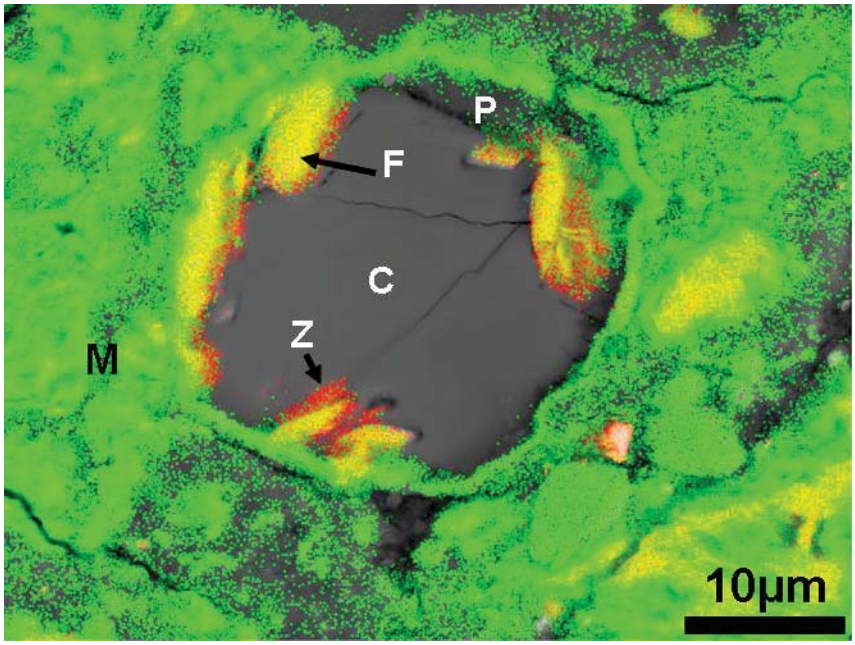

Figure 4.44- Element map (S and Fe) combined with BSE image of the calcite grain (C) and the surrounding materials in Pollen.
Note the presence of S and Fe in some margins (labelled Z) of the grain. M is fine grained (<1µm) matrix, F is fibres of Fe-sulphides; P is Mg-phyllosilicate replacing calcite. The location of this map in the sample studied is shown in appendix D3.

4.4.3.3 Quantitative chemical analyses of Ca-carbonate in Pollen

Thirty five grains of calcite that show differences in petrographic features as well as variations in CL characteristics were chemically analysed by EPMA. All analyses were from areas far enough from the margins of the grain, and also from Fe-sulphide inclusions, to avoid contamination. The averages of the analyses are listed in mol% and wt% in Table 4.11.

Mole %	calcite	Wt%	calcite
CaCO3	98.26 ± 1.48	Ca	38.20
MgCO3	0.34 ± 0.57	Mg	0.08
SrCO3	0.00 ± 0.01	Sr	0.00
FeCO3	1.37 ± 1.07	Fe	0.74
MnCO3	0.02 ± 0.06	Mn	0.10
Total	99.99	Total	39.12
***n*= 66 analyses from 35 grains**			

Table 4.11- Mean of the quantitative chemical analyses of calcite grains in Pollen.
Concentrations below detection limit are assumed to be zero. Data presented as mean ± SD, error values are calculated to 1σ.Full dataset is listed in appendix B.3 in Mole% with average and standard deviation.

Three analyses of one grain of aragonite were obtained, but they show very high concentrations of $FeCO_3$ (up to 5 mol%) that are probably related to small inclusions of Fe-sulphides within the grain, so analyses of this grain are excluded from the study.

Comparison between chemical analyses of three calcite types in Pollen show slightly variation in the range of $FeCO_3$ concentrations between calcite replacing forsteritic olivine (phase II), completely rimmed calcite (phase I) and calcite free of rims (phase III) (Table 4.12). The analyses from zoned polycrystalline grains that show large variations in CL intensity also show variations in chemical composition from sub-crystal to sub-crystal within a grain (Figure 4.45). This suggests that the sub-crystals were probably formed from fluids of different chemical compositions.

Mole %	**calcite I**	**calcite II**	**calcite III**	**Wt%**	**calcite I**	**calcite II**	**calcite III**
CaCO3	98.36 ± 1.65	98.15 ± 0.92	98.05 ± 1.46	**Ca**	38.44	37.55	38.15
MgCO3	0.31 ± 0.53	0.18 ± 0.16	0.63 ± 0.88	**Mg**	0.07	0.04	0.14
SrCO3	0.00 ± 0.00	0.00 ± 0.00	0.01 ± 0.03	**Sr**	0.00	0.00	0.01
FeCO3	1.31 ± 1.2	1.65 ± 0.93	1.27 ± 0.70	**Fe**	0.71	0.88	0.68
MnCO3	0.02 ± 0.05	0.01 ± 0.05	0.04 ± 0.07	**Mn**	0.01	0.01	0.02
Total	100	100	100	**Total**	54.92	53.83	54.61
***n* (analyses)**	40	14	12		40	14	12
***n* (grains)**	23	6	6		23	6	6

Table 4.12- Comparison between the chemical analyses (averages) of three types of calcite in Pollen. Calcite I is completely rimmed, calcite II is replacing olivine, calcite III is free of rims and inclusions. Data presented as mean ± SD, error values are calculated to 1σ.

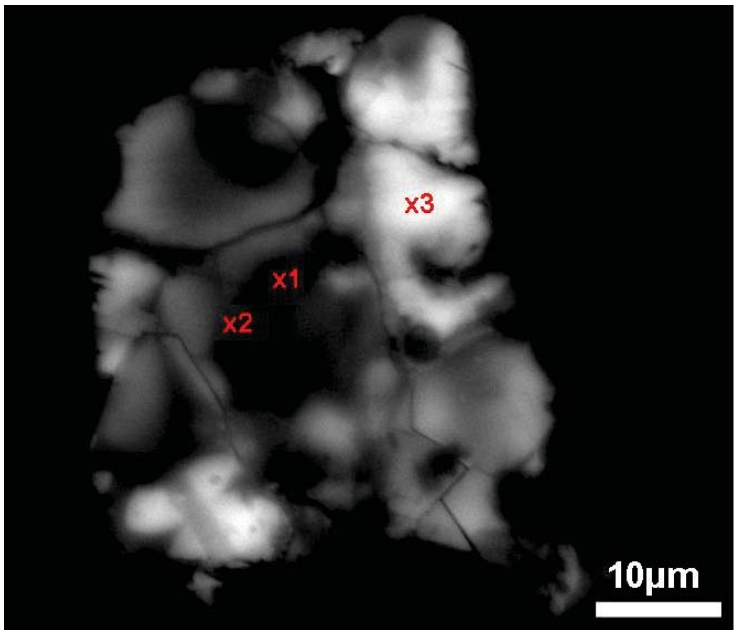

Mole%	CaCO3	MgCO3	SrCO3	FeCO3	MnCO3	Total
point 1	98.96	0.12	0.00	0.78	0.14	100
point 2	98.72	0.16	0.00	0.91	0.21	100
point 3	98.03	0.58	0.00	1.38	0.00	100
Wt%	**Ca**	**Mg**	**Sr**	**Fe**	**Mn**	**Total**
point 1	38.00	0.03	0.00	0.42	0.07	53.95
point 2	38.23	0.04	0.00	0.49	0.11	54.47
point 3	38.39	0.14	0.00	0.76	0.00	55.02

Figure 4.45- SEM-CL image of a polycrystalline calcite grain showing high magnitude variations of CL intensity from sub crystal to sub crystal within the grain.
Chemical analyses of three points (x1, x2, x3) are provided in mole and wt% in table below the image. The analyses show a difference in chemical composition between the sub-crystals from which the three analyses were obtained. The first two analyses (x1 and x2) were from a very low CL intensity band and x3 was obtained from a very high CL intensity band. Note that x3 has more Fe and Mg than x1 and x2. The location of this grain in the sample studied is shown in appendix D3.

4.4.4 Post crystallization deformation of Ca-carbonate in Pollen

Petrographic observations indicate that most calcite grains were affected by late deformations related to thermal and aqueous processes. The majority of calcite grains that are completely rimmed with serpentine-tochilinite (phase I) show shock induced twins within a grain and/or replacement by Mg-rich serpentine, whereas some grains of calcite free of rims (phase III) and calcite replacing olivine (phase II) show only shock induced twins.

4.4.4.1 Calcite twin morphology

BSE images and EBSD maps show that ~50 of the grains of calcite in Pollen 50 examined have shock induced twins. 40 grains display one set or two sets of twins (type I) (using twinning classification chart in Figure 4.21). The lamellae in these grains are straight and

thin, and cross-cut the grain (Figure 4.46). Another 10 grains exhibit twin type II (two perpendicular sets of twins) in all areas of a grain, or a small part of it; lamellae in these grains are straight and thick (>>1µm).

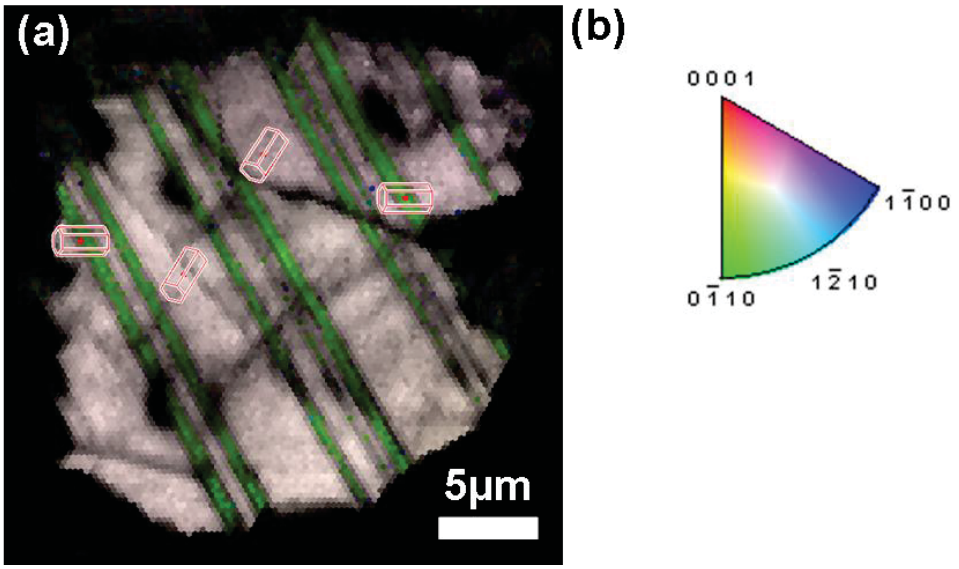

Figure 4.46- EBSD inverse pole figure map showing one set of type I twins within a (phase I) completely rimmed calcite grain.
The lamellar twinning is straight and thin (<1µm). (b) Crystallographic orientation colour key for calcite relative to the normal direction. The location of this grain in the sample studied is shown in appendix D3.

4.4.4.2 Pseudomorphs after Ca-carbonate in Pollen

Petrographic observations reveal that pseudomorphs of Mg-rich serpentine, after most of the phase I completely rimmed calcite grains, formed by the direct transformation of calcite grains into Mg-rich serpentine. The pseudomorphs inherited structural details of the calcite crystals such as Fe-sulphide and/or tochilinite inclusions, and tochilinite-serpentine rims (Figure 4.47 d). The texture of Mg-rich serpentine after calcite is aphanitic that differs from the fine grained (<1µm) matrix. Four distinctive types of Mg-serpentine pseudomorphs are recognised and designated as stages I to IV (Figure 4.47 a-d). Stage I is characterised by the partial or very slight transformation of calcite into Mg-rich serpentine (Figure 4.47 a). Stage II displays moderate (~ 40-50% of the calcite) transformation of calcite to Mg-rich serpentine (Figure 4.47 b), stage III represents near complete replacement of calcite (Figure 4.47 a), and in stage IV the calcite crystals have been completely replaced by Mg-rich serpentine. Boundaries between calcite and Mg-rich serpentine are in most cases transitional, containing a mixture of Mg-rich serpentine with calcite, and chemically showing high contents of Mg and Ca. Texturally this zone is pitted, and in most cases the margins of calcite in these areas are etched (Figure 4.47 a-c).

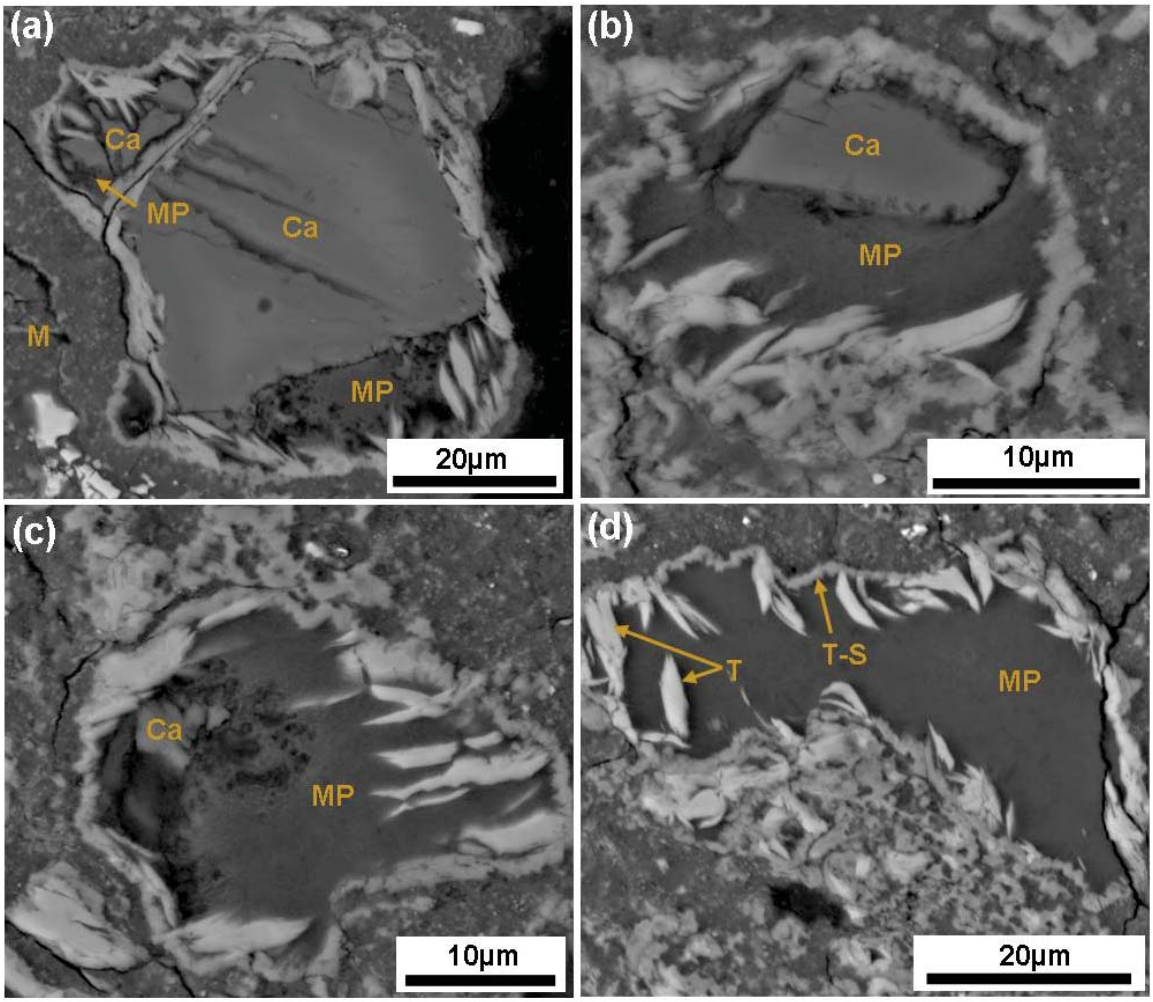

Figure 4.47- BSE images showing the stages of pseudomorph formation of phase I calcite, rimmed with tochilinite-serpentine intergrowths.
(a) Stage I, partial replacement of calcite (Ca) by Mg-rich serpentine (MP). M is fine grained (<1µm) matrix. (b) Stage II, moderate replacement of calcite (Ca) by Mg-rich serpentine (MP). (c) Stage III, near complete replacement of calcite (Ca) by Mg-rich serpentine. (d) Stage IV, complete replacement of calcite by Mg-rich serpentine (MP). T is tochilinite, T-S is tochilinite-serpentine rims. Note the areas around calcite in (c) are dissolved and also shows the presence of small grains of calcite in Mg-serpentine. The location of this grains in the sample studied is shown in appendix D3.

4.4.4.2.1 Chemical composition of Mg-rich serpentine pseudomorphs after calcite

Sixteen grains of Mg-rich serpentine were chemically analysed by EPMA. The average of the analyses is listed as element wt% and oxide wt% in Table 4.13. Mg-rich serpentine pseudomorphs in Pollen are enriched with Mg (27.50 wt% MgO) and show less FeO (11.32 wt%) compared with phyllosilicates from the fine grained (<1µm) matrix, chondrule rims and CI-like clasts in the meteorite (see Table 3.12). X-ray mapping also shows that the Mg is homogenously distributed within the Mg-rich serpentine pseudomorphs, whereas the Fe is only concentrated in the margins and in some areas of the grain (Figure 4.48). This is consistent with quantitative chemical analyses which show that

the concentration of Mg is less variable than Fe, which ranges between 10.11 to 15.17 (wt% FeO) (see appendix no. A-6).

Oxide wt%		Element wt%	
Na_2O	0.28 ± 0.14	**Na**	0.21
MgO	27.50 ± 0.61	**Mg**	16.58
Al_2O_3	1.27 ± 0.09	**Al**	0.67
SiO_2	36.91 ± 1.65	**Si**	17.25
SO_2	0.37 ± 0.33	**S**	0.19
K_2O	0.09 ± 0.02	**K**	0.07
CaO	0.18 ± 0.04	**Ca**	0.13
P2O5	0.01 ± 0.01	**P**	0.00
TiO_2	0.07 ± 0.01	**Ti**	0.04
Cr_2O_3	0.23 ± 0.05	**Cr**	0.16
MnO	0.26 ± 0.03	**Mn**	0.20
FeO	11.32 ± 1.59	**Fe**	8.80
NiO	0.52 ± 0.18	**Ni**	0.41
		O	34.29
Total%	79.01	**Total%**	79.01
n= 22 of 16 grains			

Table 4.13- Average EPMA analyses of Mg-rich serpentine pseudomorphs in Pollen.
Data presented as mean ± SD, error values are calculated to 1σ. The full data set is listed in appendix A.6 with average and standard deviation.

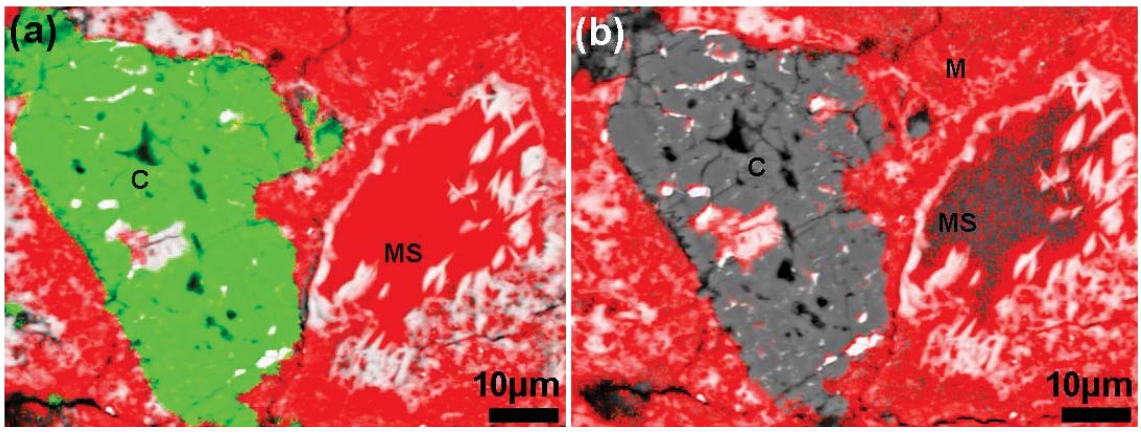

Figure 4.48- X-ray element map combined with BSE image of a Mg-rich serpentine pseudomorph after calcite and calcite replacing olivine.
(a) Element map showing the distribution of Ca (green) and Mg (red) within calcite replacing forsteritic olivine (c), Mg-rich serpentine pseudomorphs (MS) and the surrounded materials. (b) Map showing the concentration and distribution of Fe (red) within Mg-serpentine (MS) and surrounded materials in (a). Note the Mg in Mg-rich serpentine is homogeneous distributed (in a), but Fe is heterogeneously distributed and only concentrated in the margins and in some other areas of the grain. The BSE image of this map is shown in Figure 4.38b. M is the fine grained (<1µm) matrix. The location of these grains in the sample studied are shown in appendix D3.

4.4.5 TEM work of calcite, phyllosilicates and tochilinite intergrowths in Pollen

FIB cross-sections for TEM work were extracted from three grains that contain the following minerals: (i) pyroxene-calcite intergrowth (~4.5 μm sized cross-section) (Figure 4.49a), (ii) stage I pseudomorph, which is intergrowth of calcite, Mg-rich serpentine and tochilinite fibres (~5 μm sized cross-section) (Figure 4.50a), (iii) fine grained (<1μm) matrix, fibres of tochilinite and serpentine intergrown with Mg-rich serpentine (~10 μm sized cross-section) (Figure 4.52a). The FIB method used for this purpose is explained in Chapter 2. Two types of data were acquired by TEM, namely: (i) electron diffraction patterns that provided information on crystal structure, (ii) high resolution images that were used to characterise the microstructure of the materials within the intergrowths, and at their mutual boundaries.

TEM results from the pyroxene-calcite intergrowth show that the calcite is featureless apart from some strain contrast probably related to dislocations. Pyroxene exsolution lamellae are parallel to the interface with calcite on both sides (left and right), which reveals that pyroxene was replaced by calcite (Figure 4.49b). The interfaces between calcite and pyroxene are sharp (Figure 4.49c). EDS X-ray spectra of calcite and pyroxene in this sample were obtained using the Sigma SEM (Figure 4.49 d-e). The spectrum of pyroxene shows that it is enstatite, composed mainly of Mg and Si, with very low concentrations of calcium or iron.

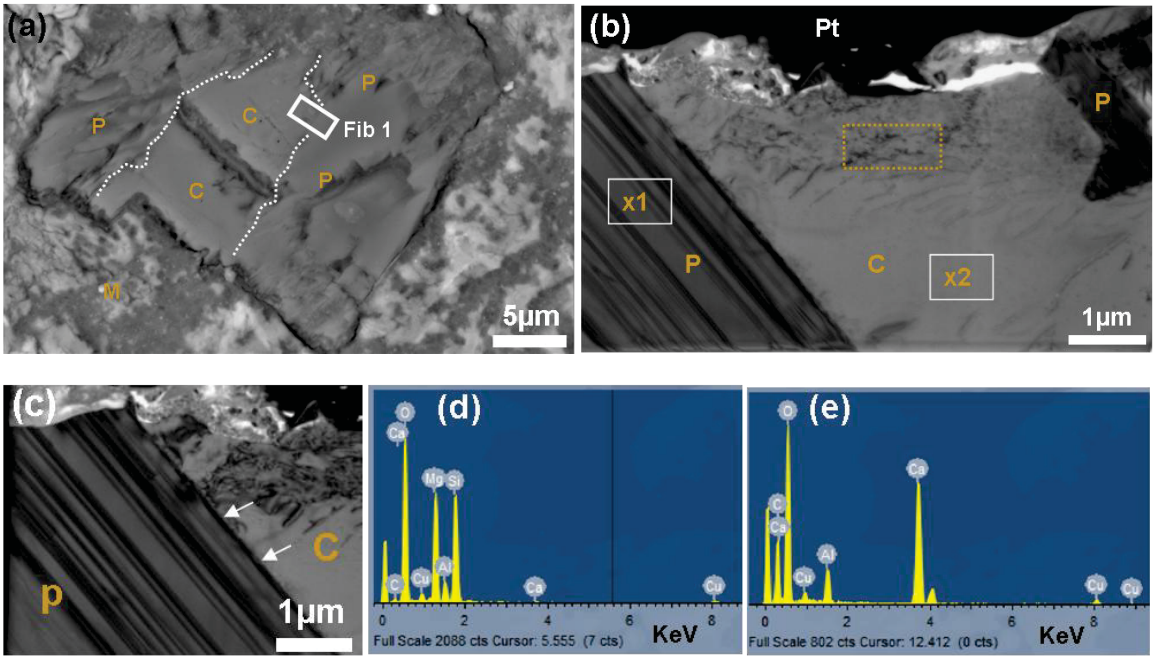

Figure 4.49- SEM and TEM data from a calcite-pyroxene intergrowth in Pollen.
(a) BSE image showing the location of FIB 1 (boxed region), C is calcite, P is pyroxene, M is fine grained (<1µm) matrix, and dashed lines represent the boundaries between calcite and pyroxene. (b) Bright-field TEM image showing the microstructure of calcite (c) and pyroxene (p). The calcite contains dislocations in the upper part (e.g. yellow square). Pt is platinum protection around the sample. (c) TEM image of a region in the upper left part in (b) showing the presence of dislocations in upper part of the calcite and sharp boundary between the calcite (c) and pyroxene (p) (indicated by white arrows). The edges of the pyroxene have been replaced by calcite. (d) EDS spectrum of pyroxene obtained from x1 in b showing this pyroxene is enstatite. (e) EDS spectrum of calcite obtained from x2 in b. Al and Cu are contaminants. The location of this grain in the sample studied is shown in appendix D3.

TEM images of calcite, Mg-rich serpentine and tochilinite fibres within a stage I pseudomorph (Figure 4.50) show clear variations in microstructure between the three. Calcite contains sub crystals that are intergrown with Mg-rich serpentine (Figure 4.50a), indicating that calcite formed prior to Mg-rich serpentine. Mg-rich serpentine is poorly crystalline, and exhibits a spongy texture (porous) that has fibres and wavy flakes intermixed with voids (Figure 4.50 c-d). The sub-crystals of tochilinite within the Mg-rich serpentine show a denser texture than the Mg-rich serpentine (Figure 4.50 c-d). It was also observed that the tochilinite crystals are intergrown with fine fibres of Mg-rich serpentine (Figure 4.50 d), indicating that Mg-rich serpentine formed later. EDs X-ray spectra of the minerals in this FIB sample were also obtained, using the Sigma SEM (x1, x2, x3 and x4 in Figure 4.50). The spectra confirm the presence of calcite, Mg-rich serpentine and tochilinite. A diffraction pattern of tochilinite indicates a d-spacing of 10.9 Å, which is characteristic of tochilinite (Figure 4.51).

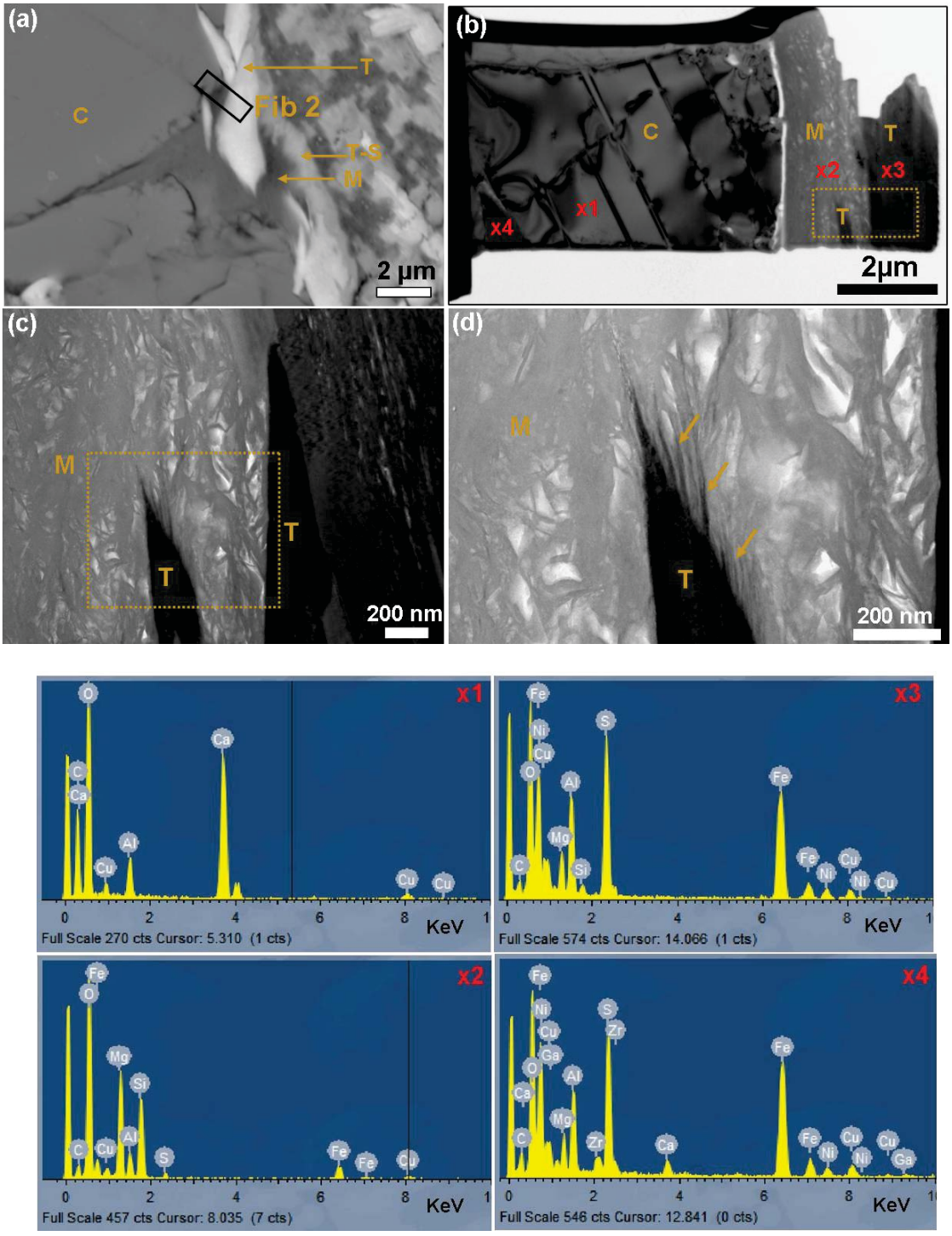

Figure 4.50- SEM and TEM information on calcite, Mg-rich serpentine and tochilinite fibres within a stage I pseudomorph from Pollen.
(a) BSE image showing the location from which the FIB 2 was extracted (boxed region). T is tochilinite, M is Mg-rich serpentine, C is calcite and T-S is tochilinite-serpentine rims. (b) Bright-field TEM image showing morphologic variations between calcite (C) Mg-rich serpentine pseudomorphs after calcite (M) and tochilinite (T). Note the calcite sub-crystals are terminated by Mg-rich serpentine. (c) Bright field TEM image of boxed area in (b) showing the spongy and porous texture of the Mg-rich serpentine (M). Within it is a crystal of tochilinite (T) that is likely to have formed earlier. (d) Bright field TEM image of the boxed area in (d) showing the boundary between the tochilinite (T) and Mg-rich serpentine (M) (e.g. arrowed area). The fibres of poorly crystalline Mg-serpentine are intergrown with the tochilinite. x1 is EDs spectrum of calcite obtained from x1 in (b), x2 is EDs spectrum of Mg-rich serpentine obtained from x2 in (b), x3 is EDs spectrum of tochilinite obtained from x3 in (b), x4 is EDS spectrum of tochilinite inclusion in the calcite obtained from x4 in (b). Al and Cu are contaminants. The location of this grain in the sample studied is shown in appendix D3.

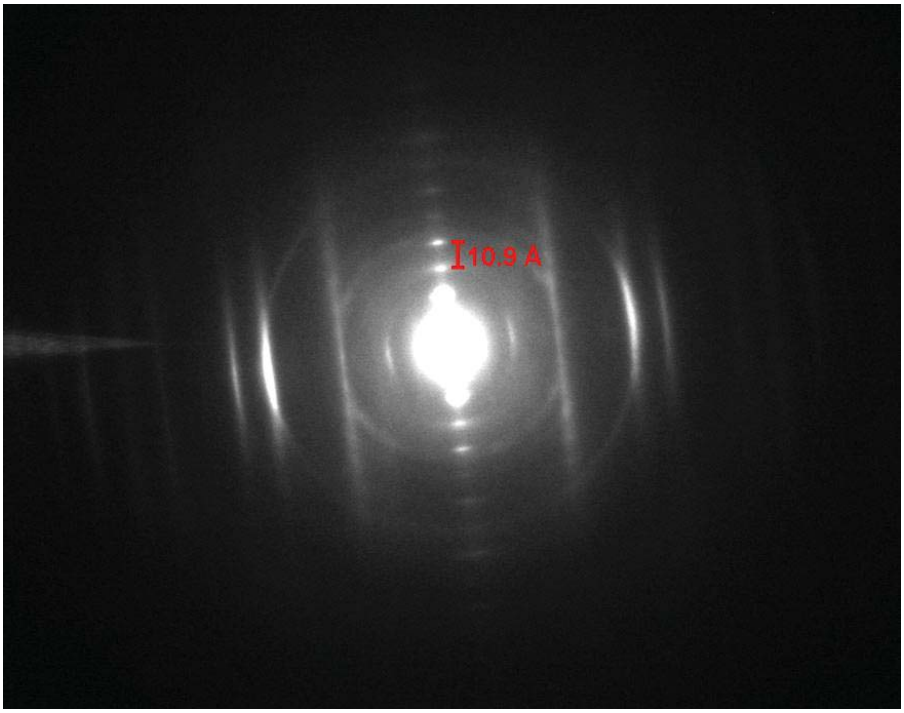

Figure 4.51- Diffraction pattern of tochilinite in Pollen.
The main row of spots has a characteristic spacing of 10.9 Å.

TEM results from FIB 3 (Figure 4.52 a) that is the contact between a type II calcite grain and a stage IV pseudomorph, which contains, from left to right, fine grained (<1μm) matrix, tochilinite-serpentine intergrowth, Mg-rich serpentine and tochilinite fibres, shows that these materials have complicated microstructural relationships (Figure 4.52 b). The fine grained matrix and rims contain small tabular and plate-like crystals (Figure 4.52 b); similar crystals were also observed in phyllosilicates in the Nawapali CM2 chondrite by Barber (1981). These crystals are additionally intergrown with fibres of Mg-rich serpentine and small crystals of tochilinite, mainly in areas towards the rims. The TEM results also show that the Mg-rich serpentine is poorly crystalline, and dominated by fibres with pores between (Figure 4.52 c-d). The interface between tochilinite and Mg-rich serpentine shows that fibres of Mg-rich serpentine are intergrown with tochilinite (Figure 4.52 d). X-ray spectra of the materials in this FIB sample were obtained by the Sigma SEM (x1, x2, x3, x4, x5 and x6 in Figure 4.52). These spectra confirm the presence of Mg-rich serpentine, tochilinite-serpentine rims around the pseudomorphs and tochilinite fibres. Diffraction patterns of tochilinite-serpentine intergrowth in this sample show a combination of rings and spots (Figure 4.53). The rings have a d-spacing of ~10.9 Å that represents tochilinite, whereas the spot patterns represent the serpentine, and the d-spacing is ~7.3 Å.

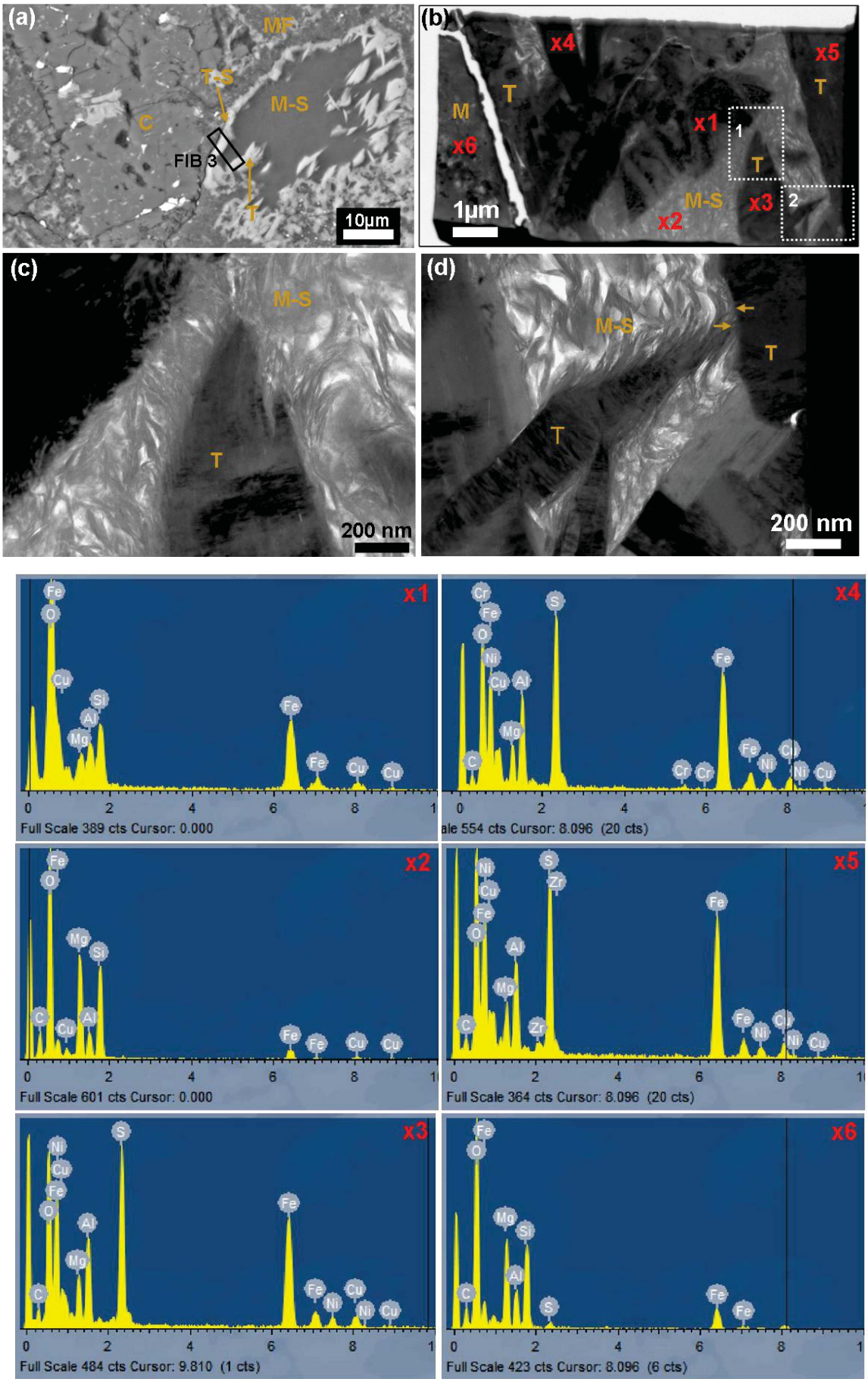
(a)
MF
T-S
M-S
C
FIB 3
T
10µm
(b)
x4
x5
T
M
T
x6
x1
1
T
M-S
x3
2
x2
1µm
(c)
M-S
T
200 nm
(d)
M-S
T
T
200 nm
x1
Full Scale 389 cts Cursor: 0.000
x4
ale 554 cts Cursor: 8.096 (20 cts)
x2
Full Scale 601 cts Cursor: 0.000
x5
Full Scale 364 cts Cursor: 8.096 (20 cts)
x3
Full Scale 484 cts Cursor: 9.810 (1 cts)
x6
Full Scale 423 cts Cursor: 8.096 (6 cts)

Figure 4.52- TEM and SEM results from fine grained (<1µm) matrix, Mg-rich serpentine pseudomorphs and tochilinite-serpentine intergrowths in Pollen.
It is the contact between type II calcite and a stage IV pseudomorph. (a) BSE image showing the location from which the FIB 3 was extracted (boxed region). T-S is tochilinite-serpentine intergrowth, M-S is Mg-rich serpentine, C is calcite, T is fibres of tochilinite and MF is fine grained matrix. (b) Bright-field TEM image showing in the left part the fine grained matrix (M) and tochilinite rims (T) that contain small tabular and platelike crystals. In middle areas of the image these crystals are intergrown with the fibres of Mg-rich serpentine (M-S) and crystals of tochilinite (T). (c) Bright field image of small region in b (boxed area 1) showing fibres of Mg-rich serpentine (M-S) in contact with pores that are formed within tochilinite (T). Note the plate-like crystal (probably serpentine) in the upper left corner. (d) Bright-field image of small region in b (boxed area 2) also showing clear evidence of termination (arrowed area) of Mg-rich serpentine (M-S) fibres with tochilinite (T). x1 is EDs spectrum of sub grain of serpentine x1 in (b). x2 is EDs spectrum of Mg-rich serpentine obtained from x2 in (b). Note the high concentrations of Mg and Si in x2 compared to x1. x3, x4 and x5 are EDs spectra obtained from tochilinite crystals (in b) at x3, x4 and x5 respectively. These crystals contain high contents of S and are free of Si. x6 EDs spectrum of fine grained (<1µm) phyllosilicate obtained from x6 in (b). The location of this grain in the sample studied is shown in appendix D3.

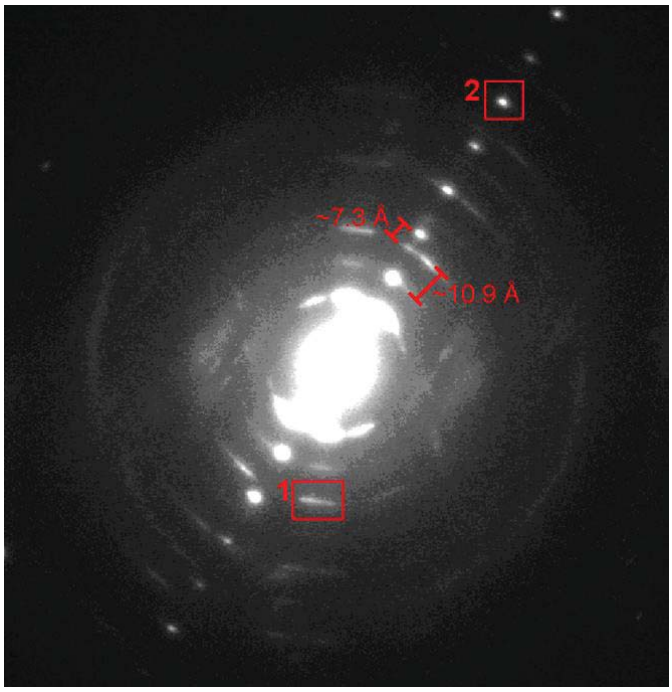

Figure 4.53- Diffraction patterns of the tochilinite-serpentine intergrowth.
Selected area diffraction pattern of serpentine-tochilinite intergrowth in Figure 4.53 b. Tochilinite has ring patterns (e.g. boxed area 1) with spacing of about 10.9 Å, and the serpentine has spot patterns (e.g. boxed area 2) and spacing of about 7.3 Å with rings patterns of tochilinite.

4.5 Carbonates in CM2.3 Mighei

4.5.1 Introduction

The presence of carbonate minerals in Mighei was reported by Smith and Kaplan (1970), and Vdovykin (1973). Smith and Kaplan (1970) found that the carbonate minerals contain 21% carbon. Carbonates in Mighei were chemically analysed by Johnson and Prinz (1993). Oxygen isotopic compositions of the carbonates were determined by Benedix et al. (2003).

The quantitative modal mineralogy of CM chondrites (Howard et al., 2011) showed that Mighei contains 1.2 vol% of calcite.

4.5.2 Petrographic observations

Petrographic observations show that only Ca-carbonate minerals (both aragonite and calcite) are present in Mighei, and these minerals comprise 1.35 vol% of the rock. The distributions of aragonite and calcite grains within the fine grained (<1μm) matrix are likely to be comparable to one another. Aragonite grains were distinguished from calcite using EBSD mapping and Raman spectroscopy. Element maps and BSE images show that Ca-carbonate minerals are mainly found in areas that are associated with tochilinite-serpentine intergrowths (Figure 4.54).

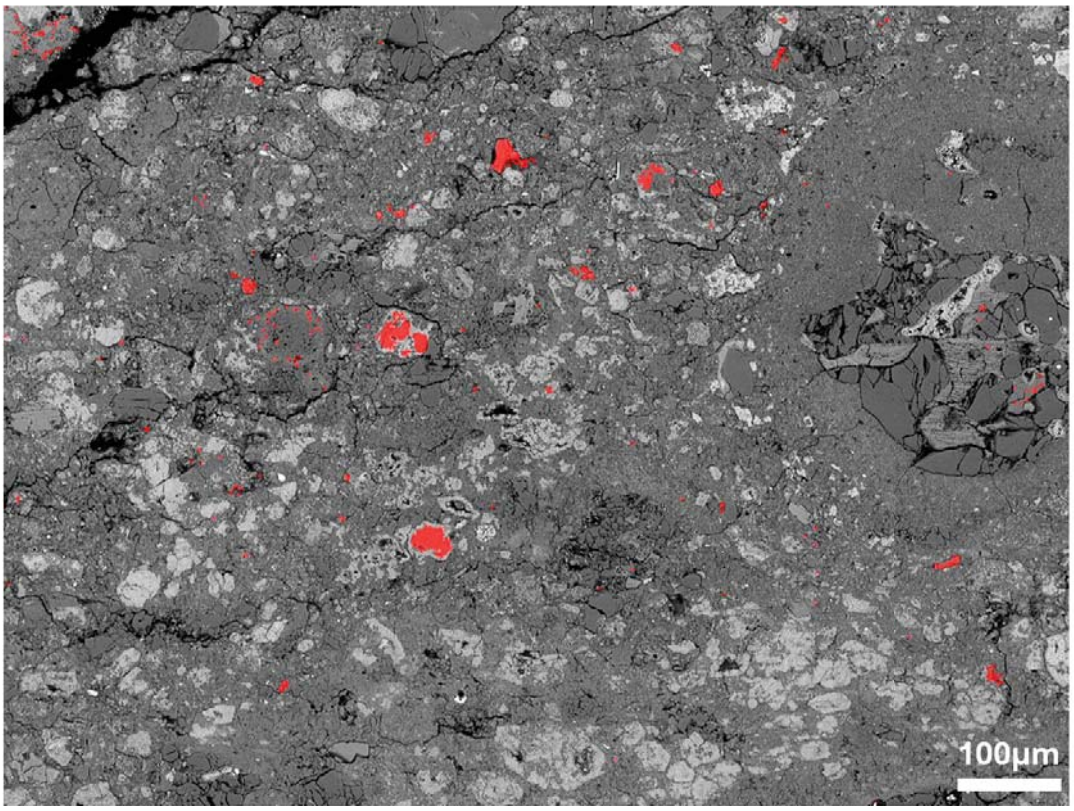

Figure 4.54-Ca X-ray map combined with a BSE image of small region in Mighei.
Ca (red) locates all Ca-carbonate grains and grains of Ca-rich pyroxene within chondrules. Note the Ca-carbonates are mainly present in areas of the fine grained (<1μm) that are associated with tochilinite-serpentine intergrowths. The location of this map in the sample studied is shown in appendix D4.

Most of the calcite grains are found in isolated clusters in the fine grained (<1μm) matrix. They range in size from 2 or 3μm to 60 μm. Their shapes include euhedral, subhedral, irregular and elongated. Grains of euhedral and subhedral shape occur very close to each

other in some areas of the sample, and exhibit sharp boundaries (or at least two boundaries) with enclosing materials (Figure 4.55), which suggests that these grains were formed within pore space and then enclosed within the tochilinite-serpentine intergrowth.

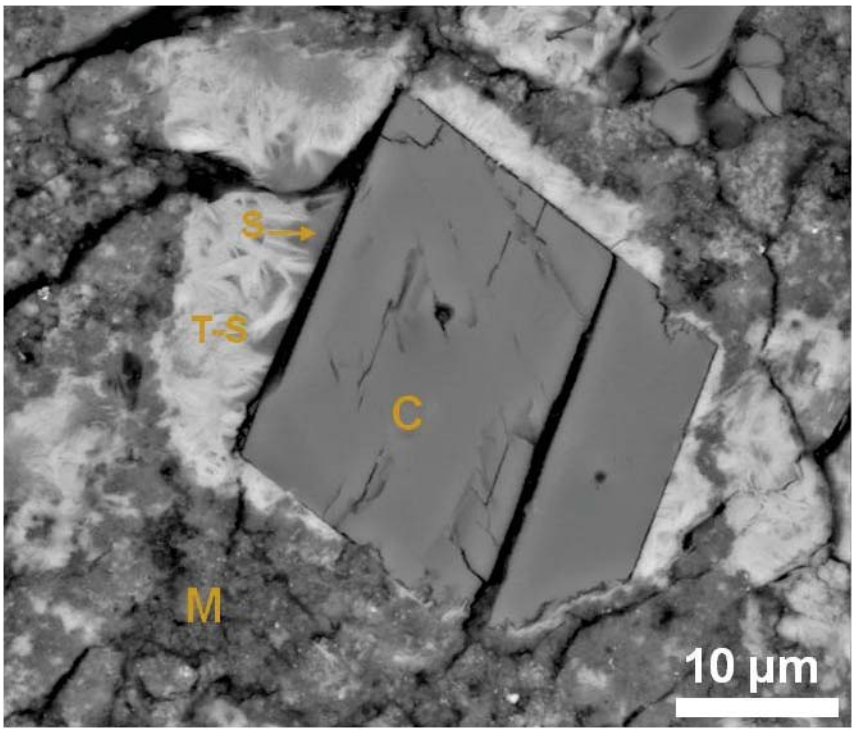

Figure 4.55- BSE image of a eubhedral calcite grain enclosed within tochilinite-serpentine. The calcite grain (c) has sharp boundaries with surrounded materials including serpentine (S) and tochilinite and serpentine intergrowth (T-S). M is fine grained (<1µm) matrix. The location of this grain in the sample studied is shown in appendix D4.

The majority of calcite grains are single crystals, though few are aggregates. Calcite grains in Mighei are also present in three contents including: (i) the majority of calcite grains are enclosed by radial fibrous tochilinite aggregates that in some cases are interpenetrating with the calcite grains (ii) some grains are free of inclusions, (iii) two aggregate calcite grains are found within chondrules replacing Mg, Fe silicates. An unusual feature of Mighei calcite is the presence of vesicular texture (fluid inclusions) that overprints all areas of a few grains (4 grains) of calcite that are enclosed by tochilinite-serpentine intergrowths (Figure 4.56a). These features also characterise parts of some calcite grains in Murchison (described above in section 4.2.2). It was additionally found that some calcite grains which are enclosed by tochilinite-serpentine intergrowths are etched in their outer areas but show pristine textures in other areas of the grain (Figure 4.56b). However, most calcite grains that are surrounded by tochilinite and are well preserved (e.g. Figure 4.55), and in some cases show at least two calcite generations (calcite and calcite overgrowth) that clearly crystallised within a pore space (Figure 4.57).

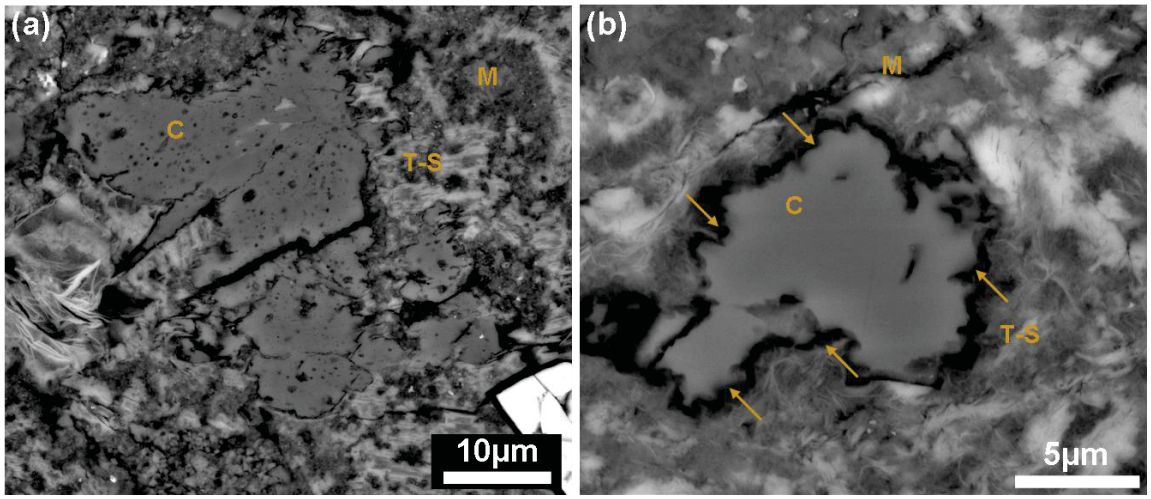

Figure 4.56- BSE images of calcite grains in Mighei showing two different textures.
(a) Calcite grain with a vesicular texture that covers all areas of the grain. (b) Calcite grain that is etched at its edges (arrowed), but internally it has a better preserved than the grain in (a). The locations of these grains in the sample studied are shown in appendix D4.

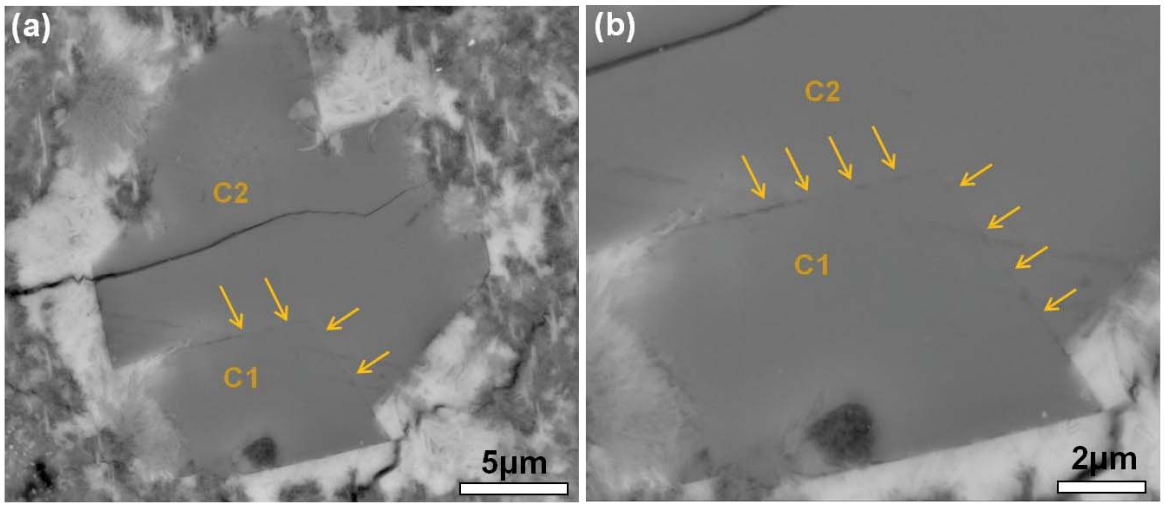

Figure 4.57- BSE images showing two generations of calcite within one grain.
(a) Grain that contains two phases of calcite. Phase one (C1) is a well defined crystal formed on the edge of pore space and the C2 is calcite overgrowth (arrowed) filling the remaining space. (b) BSE image at high magnification showing the boundary between the two phases in (a). The location of this grain in the sample studied is shown in appendix D4.

The thin section studied contains sixteen crystals of aragonite. Aragonite grains in Mighei are more widely distributed throughout the sample in comparison to the occurrence of aragonite in less altered chondrites (i.e. Murchison, Murray and Pollen) (Figure 4.58).

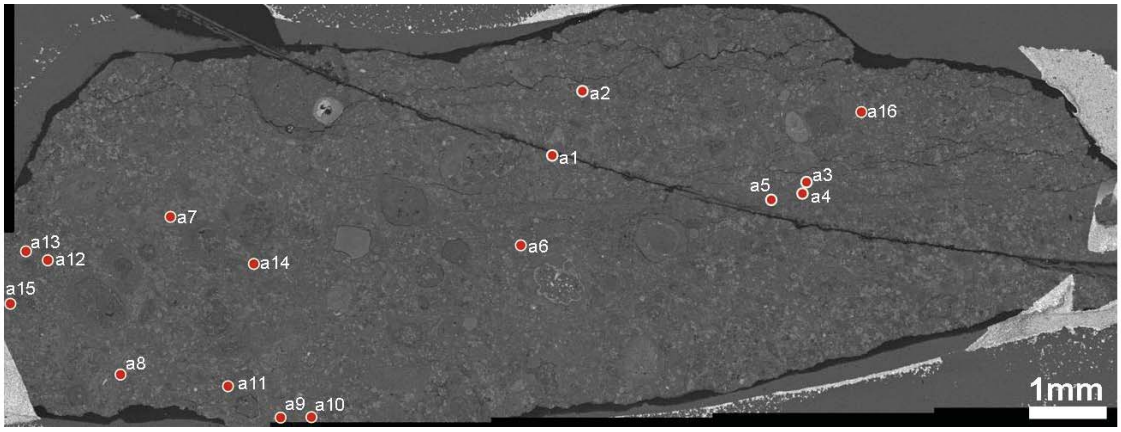

Figure 4.58- BSE image of the whole sample of Mighei showing the locations of aragonite grains.

Aragonite grains in Mighei have a size of 10 µm to ~90 µm. They have euhedral, subhedral, sub-rounded and elongated shapes. Only one grain is enclosed within Fe-sulphide-tochilinite intergrowth, but all other grains are free of inclusions and rims. It is clear that the grain size of aragonite in Mighei is greater than those in less altered chondrites (aragonite size in Murchison is ≥ 20 µm, in Murray is ~10-15 µm (lee and Ellen, 2008), and in Pollen is ~3-20 µm). Most of the grains are etched at their margins (Figure 4.59); small pores are also present inside two grains.

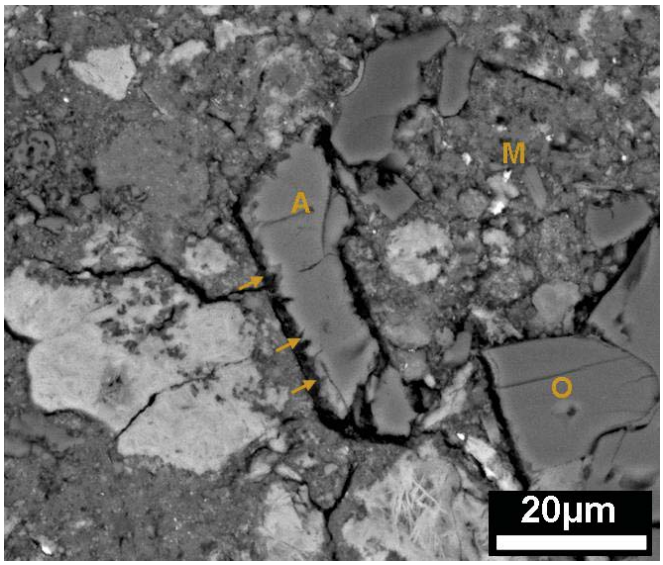

Figure 4.59- BSE image showing the occurrence of a grain of aragonite in Mighei.
A is an elongate aragonite grain that is etched in the margins (arrowed). M is fine grained (<1µm) matrix, O is olivine. The location of this grain in the sample studied is shown in appendix D4.

4.5.3 Crystallographic orientation of aragonite grains

EBSD mapping and BSE imaging shows that 6 of the aragonite grains (a1, a3, a4, a5, a13 and a14 in Figure 4.58) in Mighei are polycrystalline. Crystallographic orientation mapping of five of these grains reveals some variation, or slight variation in directions of the c-axes of the constituent sub-crystals, but in most cases the c-axes of the sub-crystals of each grain are inclined at nearly the same angle (e.g. Figure 4.60). Only one (a1) of these six grains contains three sub-crystals that have c-axes are inclined at the same direction and orientation relative to the sample surface (Figure 4.61). Generally, the c-axes of aragonite grains in Mighei show a weak preferred orientation (Figure 4.61). The majority of the c-axes of these grains are inclined at between ~30º to ~60º to the horizontal. The pole figure (Figure 4.61) shows that the c-axes of some single aragonite grains and some sub-crystals within polycrystalline grains are nearly inclined at the same angle, indicating that they were probably formed at same time.

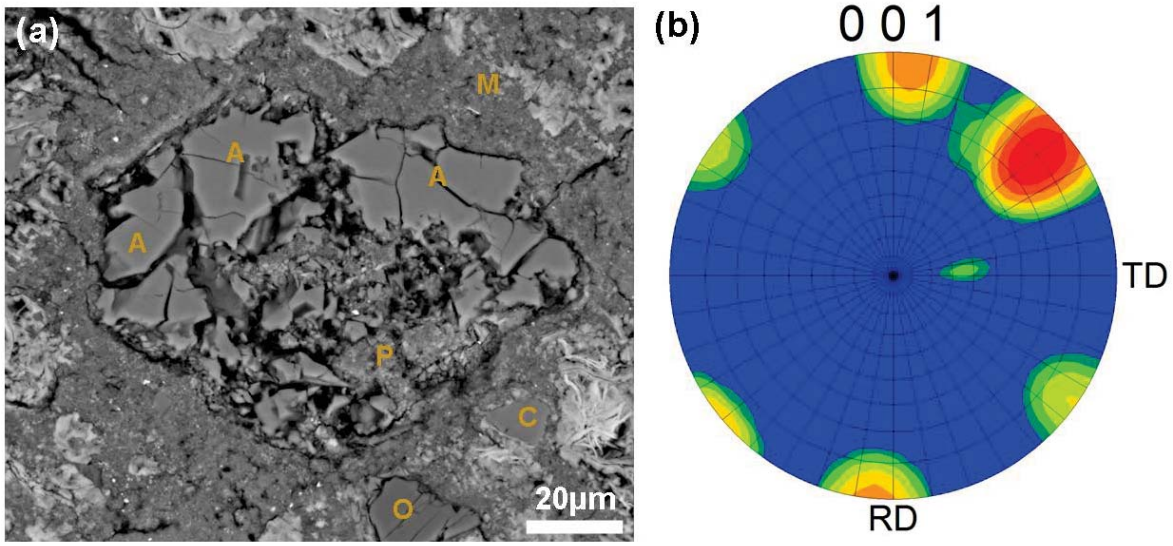

Figure 4.60- Crystallographic orientation data from a polycrystalline aragonite grain in Mighei (grain a7).
(a) BSE image of polycrystalline aragonite grain (a7). The grain contains several sub-crystals (A) that have probably been (sub-crystals inside the grain) partly replaced by phyllosilicate (P). O is olivine, C is calcite and M is fine grained (<1µm) matrix. (b) Pole figure texture showing orientations of the aragonite sub-crystals in (a). The grid line divisions represent 10º. Note all the c-axes of sub-crystals are orientated at the edge of the pole figure (nearly parallel to the sample surface), but the direction of the c-axes are different. The location of this grain in the sample studied is shown in appendix D4.

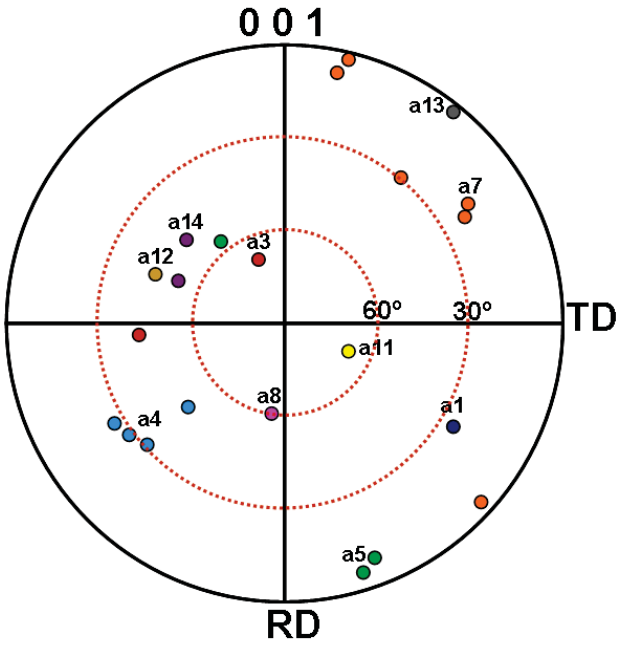

Figure 4.61- Crystallographic orientations of aragonite grains in Mighei.
Pole figure showing the orientations of poles to the {001} planes of aragonite grains (located in Figure 4.58). Each grain is labelled in a different colour, c-axes of sub crystals within one grain are labelled in the same colour. Note the majority of c-axes of aragonite grains are inclined at angles between ~30º and ~60º.

4.5.4 Chemical composition of Ca-carbonate grains in Mighei

Five chemical analyses of Mighei carbonates were carried out by Johnson and Prinz (1993). In this study CL images of aragonite and calcite were acquired using the Quanta 200F SEM and coupled with elemental mapping using the Zeiss Sigma SEM and quantitative chemical analyses by EPMA.

4.5.4.1 CL imaging of Ca-carbonates in Mighei

6 grains of aragonite and 47 grains of calcite were imaged by SEM-CL. The CL characteristics of the grains imaged were also related to their petrographic features. The Ca-carbonate grains in Mighei show 8 different SEM-CL types that are described in Table 4.14. Seven of these SEM-CL types also characterise some Ca-carbonate grains in Murchison, Murray and Pollen. The new SEM-CL type characterises one grain of aragonite and two grains of calcite in Mighei, and is assigned in this study as CL type XIII. It is described as oscillatory zoning that shows a sequence of thin layers (0.2-1 µm) of low, high and very high CL intensity within a grain (Figure 4.62 a-b). Generally, CL images of Ca-carbonate grains in Mighei indicate that most grains imaged have well-defined growth patterns that distinctly contain a sharp boundary between CL bands (e.g. Figure 4.62 c-d).

Most imaged grains have CL type IX (described in Table 4.14) and most zoned grains are completely rimmed. Four grains of aragonite show only low CL intensity throughout a grain that also characterises all aragonite grains imaged in Murchison. The other two aragonite grains show CL type II and CL type XIII. Some grains that are located close to each other and some sub-crystals within polycrystalline grains can also have similar SEM-CL intensity types.

Grain type	SEM-CL type	SEM-CL characteristics	Abundance
C, A	I (observed in Murchison, Murray, Pollen)	Low or high CL throughout the grain, in some cases contains patches of very high CL.	7 C, 4 A
C, A, F	II (observed in Murray, Pollen)	Complex zoning mainly found in polycrystalline grains and in most cases showing all four levels of CL intensity (from very low CL to very high CL) within a grain.	6 C, 1 A, 2 F, 1 P
P, C	V (observed in Murchison, Murray, Pollen)	High CL throughout grain with well defined thin layer (0.2-1 μm) of low CL cross-cutting the grain. (In Murchison the high CL is very high CL)	3 C
P, F, C	VII (observed in Murchison, Pollen)	Very high CL throughout the grain with rims of high CL.	1 F, 3 C
P	VIII (observed in Murray)	Low CL with a triangle or hexagonal shaped crystal in one part, subsequent high CL of hexagonal habit, high CL growth filling the pore space.	1 P
C, P, F	IX (observed in Murray, Pollen)	Large core (5-10 μm) of low or very low CL in apart of a grain, in some cases well developed; the subsequent band is high CL, but in most cases in Mighei the subsequent is band very high CL.	12 C, 4 P, 2 F
P, C	X (observed in Murray)	Well defined band of high CL in some cases contains core of low CL, overgrowth zone of low or very low CL filling the space.	2 C
C, A	XIII	Oscillatory zoning that shows sequence of thin layers (0.2-1 μm) of low, high and very high CL.	3 C, 1 A

Table 4.14- Characteristics and abundances of the CL types of Ca-carbonate grains in Mighei and their relationship to petrographic features.
F is calcite grains free of rims, C is completely rimmed, A is aragonite. P= calcite grains partly rimmed with tochilinite and/or Fe-sulphides. Total number of grains imaged is 53. Note the abundance of each CL type is assigned by numbers, e.g. 6 C means 6 grains of 53 grains imaged show CL type I, and C means these 6 grains are completely rimmed.

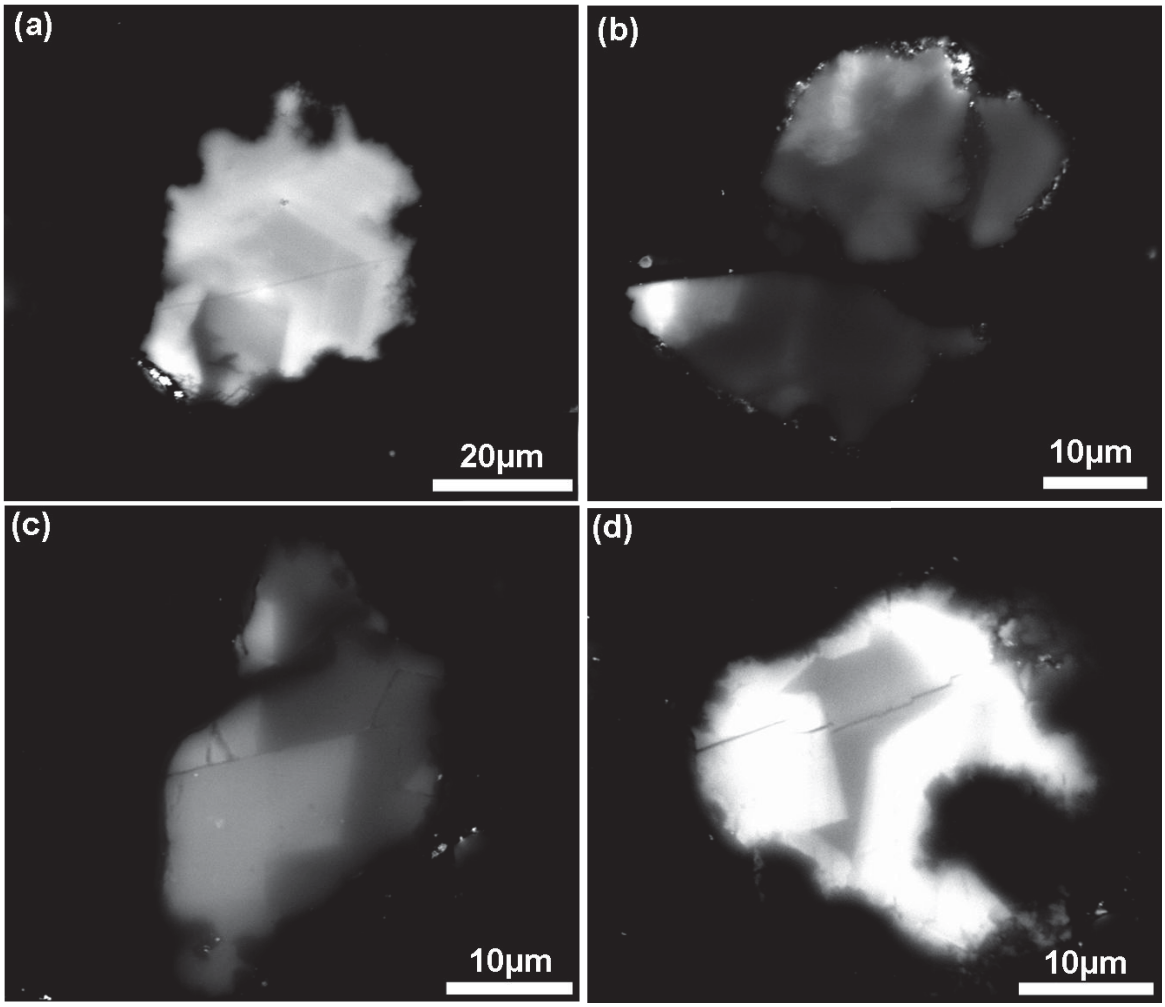

Figure 4.62- CL images of Ca-carbonate grains in Mighei.
(a) CL image of a completely rimmed calcite grain showing CL type XIII. (b) CL image of a polycrystalline grain of aragonite that displays also CL type XIII. (c) Completely rimmed calcite grain that displays CL type X. (d) Partly rimmed calcite grain showing CL type IX. Note CL images in c and d showing well defined sharp boundary that define two different zones. The locations of these grains in the sample studied are shown in appendix D4.

4.5.4.2 Quantitative chemical analyses of Ca-carbonate grains in Mighei

Ten grains of aragonite and twenty three grains of calcite that show differences in petrographic features as well as variations in CL characteristics were chemically analysed. Only two of the grains analysed are calcite replacing olivine, the other calcite grains being completely and partly rimmed by Fe-sulphides with/without tochilinite. All analyses have been taken from areas that are far enough from the margins of the grain and also from inclusions within the grain. The average of the analyses of aragonite and calcite is listed in mol% and wt% in Table 4.15. The two analyses of calcite replacing olivine are excluded from comparison between the analyses of calcite and aragonite as these two analyses show unusually high concentrations of $FeCO_3$ (2.85 mol%) and $MgCO_3$ (1.43 mol%).

On average, aragonite grains in Mighei have lower concentrations of $FeCO_3$ and $MgCO_3$ than aragonite grains in Murchison. Calcite grains (completely rimmed) in Mighei contain 1.45 ± 0.70 mol% $FeCO_3$, whereas calcite grains in Murchison show contents of $FeCO_3$ up to 0.98 ± 0.73 mol%.

Mol%	**$CaCO_3$**	**$MgCO_3$**	**$SrCO_3$**	**$FeCO_3$**	**$MnCO_3$**	**SUM**	***n***
Calcite A	98.23 ± 0.99	0.24 ± 0.31	0.00 ± 0.01	1.45 ± 0.70	0.08 ± 0.13	100.00	33
Calcite B	95.72 ± 1.70	1.43 ± 1.31	0.00 ± 0.00	2.85 ± 0.39	0.00 ± 0.00	100.00	2
Aragonite	98.97 ± 0.17	0.03 ± 0.04	0.05 ± 0.04	0.95 ± 0.14	0.00 ± 0.00	100.00	15
Wt%	**Ca**	**Mg**	**Sr**	**Fe**	**Mn**	**SUM**	***n***
Calcite A	38.62	0.06	0.00	0.87	0.05	39.59	33
Calcite B	37.34	0.34	0.00	1.70	0.00	39.38	2
Aragonite	39.00	0.01	0.05	0.57	0.00	39.48	15

Table 4.15- Mean of the quantitative chemical analyses of Ca-carbonate grains in Mighei.
The analyses obtained from 10 and 23 grains of aragonite and calcite respectively. Concentrations below detection limit are assumed to be zero. The full data set is listed in appendix B.4 with average and standard deviation. Calcite A is calcite completely or partly rimmed. Calcite B is calcite replacing olivine. Data presented as mean ± SD, error values are calculated to 1σ.

It was observed that the Mn^{2+} is present at relatively high concentrations in some calcite grains that are located close to each other, and they have also similar petrographic features and CL characteristics. Mn^{2+} is present only in some zoned sub-crystals in polycrystalline grain in areas that are equivalent in CL characteristics. For instance, chemical analyses of three zoned calcite grains (Table 4.16) reveal that the Mn^{2+} is only present in areas of low CL intensity (see Figure 4.63). These grains are found close to each other, completely rimmed with Fe-sulphides and display very similar SEM-CL characteristics (Figure 4.63b). The bands of low CL intensity in these grains are likely to have precipitated from the same solution and probably at the same time. Two aragonite grains, a4 and a5, are located very close to each other in the sample (see Figure 4.58). These grains are also nearly identical in chemical composition; grain a4 contains 1.05 mol% $FeCO_3$, 0.03 mol% $MgCO_3$ and 0.06 mol% $SrCO_3$, whereas grain a5 contains 1.18 mol% $FeCO_3$, 0.02 mol% $MgCO_3$ and 0.05 mol% $SrCO_3$. Mn^{2+} is absent from both.

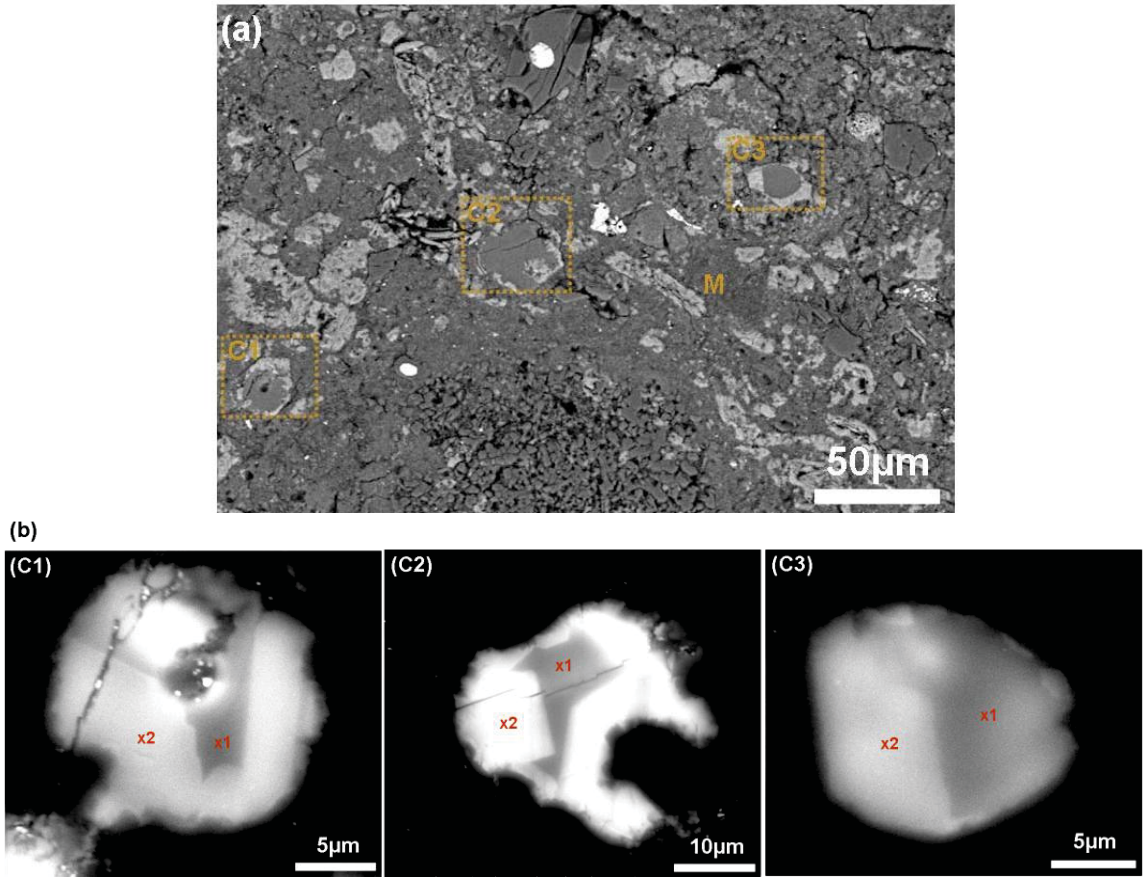

Figure 4.63- Image and chemical analyses of three zoned calcite grains located close to one another in Mighei.
(a) BSE image showing the location of three grains (named C1, C2 and C3) that are completely rimmed with Fe-sulphide. M is fine grained (<1µm) matrix. (b) SEM-CL images of the three calcite grains (C1, C2 and C3) in (a). Note the grains are similar in CL characteristics, x1 and x2 are the locations from which the chemical analyses were obtained. The chemical analyses are listed in Table 4.16. Mn^{2+} is present in low CL intensity areas (x1 in each grain), but is absent in areas of high and very high CL intensity (x2 in each grain). The location of this map in the sample studied is shown in appendix D4.

Mole%	$CaCO_3$	$MgCO_3$	$SrCO_3$	$FeCO_3$	$MnCO_3$	Sum
C1 point1	97.76	0.30	0.00	1.81	0.13	100.00
C1 point 2	97.54	0.34	0.00	2.11	0.00	100.00
C2 point 1	98.49	0.07	0.01	1.35	0.09	100.00
C2 point 2	97.64	0.37	0.00	1.99	0.00	100.00
C3 point 1	98.67	0.07	0.00	1.18	0.09	100.00
C3 point 2	98.93	0.01	0.00	1.06	0.00	100.00

Table 4.16- Chemical analyses in mol% of three zoned calcite grains in Mighei.
BSE images, CL images and locations of analyses are shown in Figure 4.63.

4.5.5 Post crystallization deformation of Ca-carbonate in Mighei

Petrographic observations indicate that only a few calcite grains (~8 grains) have one set of twins (type I) that cross-cut the grain. The twin lamellae in these grains are straight and very thin (0.2-0.5 µm).

4.6 Carbonate minerals in CM2.3 EET 96029

4.6.1 Introduction

Petrographic observations and Raman analyses show that EET 96029 contains only calcite, and SEM point counting found 0.12 vol%. The abundance of calcite in EET 96029 is therefore described as very rare, given the area of the sample studied (~125 mm^2), the total points counted (1739), and in comparison with previously discussed meteorites that have a greater abundance of Ca-carbonates. For example, Murchison contains 0.86 vol % Ca-carbonate that occurs within an area of about 6 mm^2.

4.6.2 Petrographic observations

X-ray mapping and petrographic observations indicate that EET 96029 calcite grains are within small isolated clusters and discontinuous veins (Figure 4.64). The Ca X-ray map of whole sample reveals that calcite grains are likely to have formed parallel to the compactional fabric of the rock X-ray mapping of small regions of EET 96029 (Figure 4.65) shows that calcite grains are homogenously distributed within the fine grained (<1μm) matrix.

Calcite grains in EET 96029 occur as single and also as aggregate grains that are enclosed within the tochilinite-serpentine intergrowth, and as polycrystalline grains embedded in the fine grained (<1μm) matrix with/without rims of tochilinite-serpentine. Very rare grains of calcite replacing forsteritic olivine were also found in EET 96029. In one of these, calcite has replaced a chondrule of about 300 μm diameter. Generally, the size of calcite grains ranges from ~3 μm to ~60 μm. The calcite grains in EET 96029 take several different forms that, in order of abundance, are as follows: subrounded (48% out of the calcite grains), subhedral (28% out of the calcite grains), irregular (15% out of the calcite grains) and elongated (9% out of the calcite grains). All calcite grains in the meteorite, with the exception of calcite replacing olivine, are highly etched at their margins, and in most cases have large pores (2-10 μm) inside the area of the grain (Figure 4.66 a-b). Some grains contain patches of phyllosilicates that are comparable to phyllosilicates of the fine grained (<1μm) matrix.

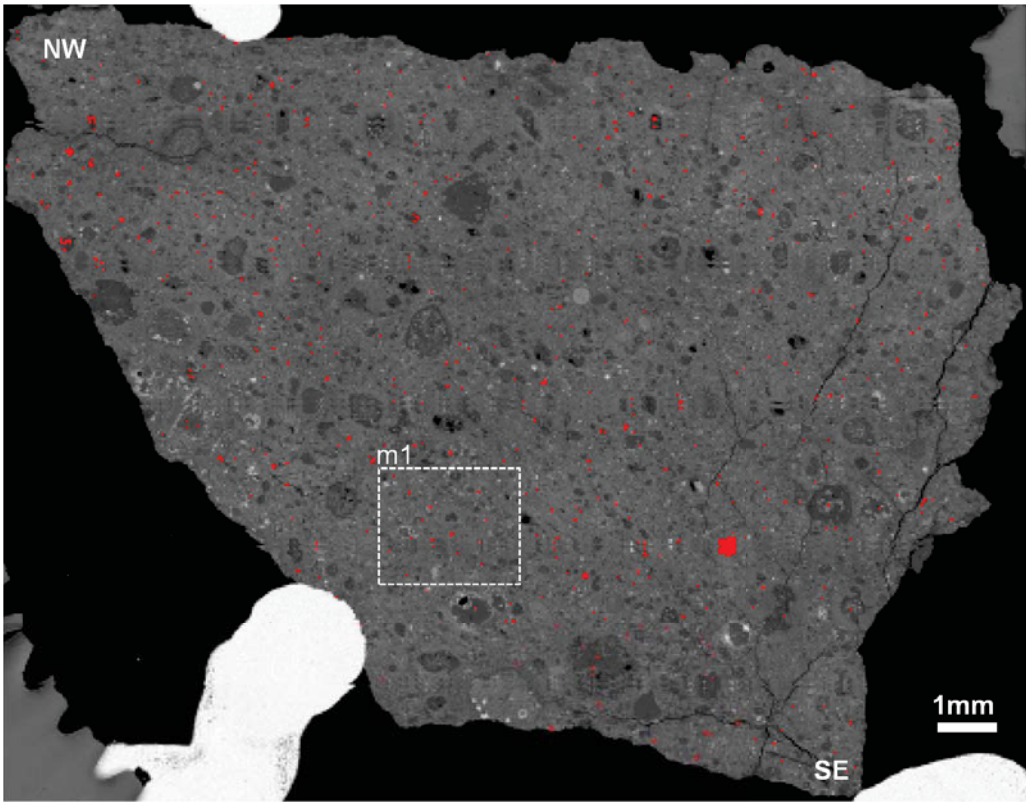

Figure 4.64- Combined Ca X-ray map with BSE image of whole sample of the EET 96029.
The map shows the distribution and concentrations of Ca (red areas) within the meteorite, which locates all of Ca-carbonate grains, and a few grains of pyroxene. Note Ca is concentrated in small discontinuous veins and within very small isolated clusters. Note also the presence of Ca along the compactional fabric of the rock that is oriented SE-NW, the image is denoted with compass bearing directions (N, S, E, W).

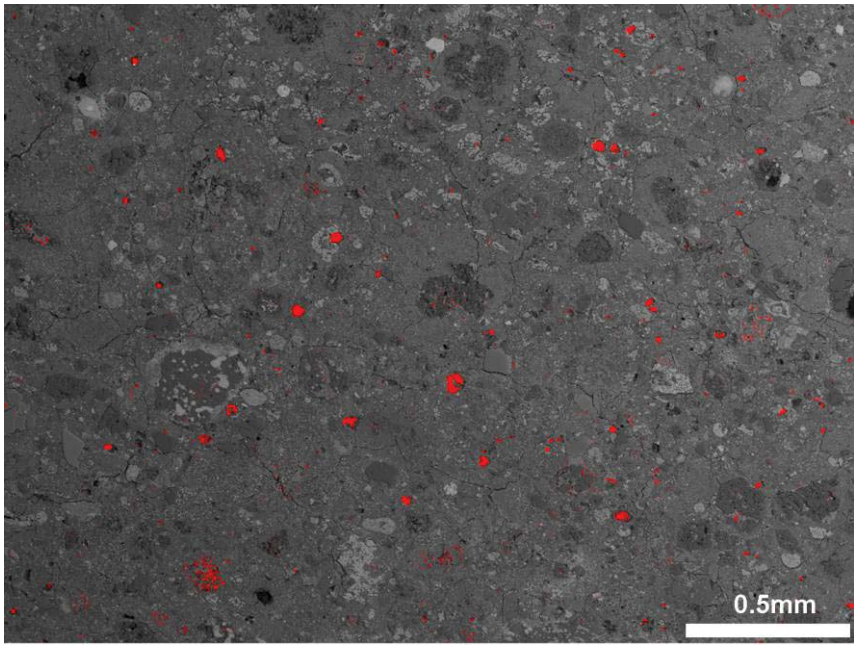

Figure 4.65- Combined Ca X-ray map with BSE image of small region of EET 96029.
The Ca (red areas) locates all calcite grains and a few grains of pyroxene within some chondrules. Note these calcite grains (large red areas) are fairly uniformly distributed within fine grained (<1μm) matrix. The location of this map in the sample studied is labelled m1 in figure 4.64.

All calcite grains in EET 96029, with the exception of calcite replacing olivine, have a habit similar to that of aragonite grains in Mighei, in particular grains that are free of rims (Figure 4.66 a) suggestingthat aragonite has probably been replaced by calcite. None of the rimmed and un-rimmed calcite grains are in contact with the matrix; instead pores are present between the grain and surrounding materials (Figure 4.66 a-b). These pores have a width of about 1-3 μm. Some of the calcite grains have been highly etched to leave small grains with large pores (2-10 μm). Other grains are observed to have completely dissolved away to leave only empty holes (e.g. Figure 4.67). Petrogrphic observations show that large numbers of small holes are present in the fine grained (<1μm) matrix of this meteorite, and are likely to have formed as a consequence of calcite dissolution.

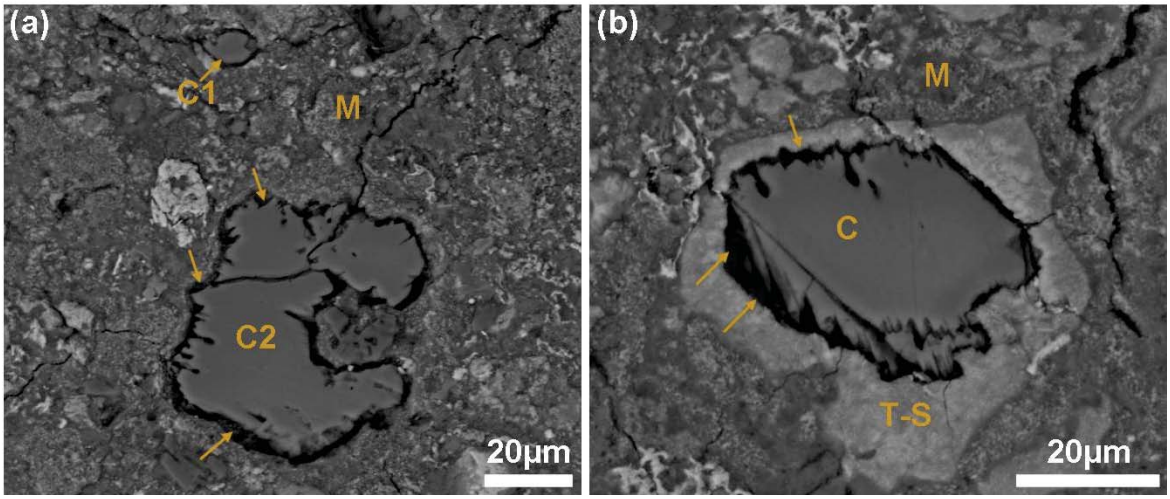

Figure 4.66- BSE images of calcite grains in EET 96029.
(a) Two calcite grains. C1 is single grain and C2 is polycrystalline grain. Both grains are highly etched around their margins and also surrounded by pores (arrowed areas) from calcite dissolution. (b) Large calcite grain (~40 μm) (C) enclosed within a tochilinite-serpentine intergrowth (T-S). The margins of the grain have been highly dissolved to leave large holes (2-5 μm) (arrowed areas) between the calcite and tochilinite-serpentine intergrowth. M is fine grained matrix. The locations of these grains in the sample studied are shown in appendix D5.

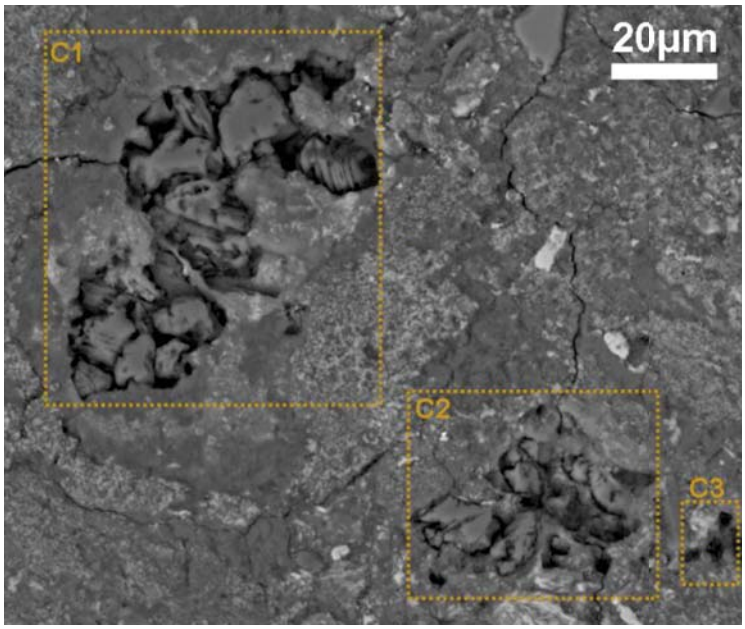

Figure 4.67- BSE image showing the high intensity of dissolution of calcite in EET 96029. C1 and C2 calcite grains have been highly etched and large proportions (~55%) have been lost. C3 is a hole left after the dissolution of a calcite grain. The location of this map in the sample studied is shown in appendix D5.

4.6.3 Chemical composition of calcite grains in EET 96029

Chemical analyses of calcite grains were obtained by EPMA. X-ray maps of whole sample and small regions were acquired by the Zeiss Sigma SEM, and CL images of calcite grains were also obtained by the Quanta 200F SEM.

4.6.3.1 CL imaging of calcite grains

CL images of thirty calcite grains, including rimmed and un-rimmed grains, were obtained. CL studies indicate that only one SEM-CL type is present among the rimmed and un-rimmed calcite grains (Figure 4.68). This type of CL intensity also characterises some Ca-carbonate grains in previously described meteorites. It is CL type I that exhibits high CL intensity throughout a grain, and in some cases contains patches of very high CL intensity. CL intensity type I characterises the majority of aragonite grains in previously described meteorites. This provides additional insights into the link between calcite in EET 96029 and aragonite in other CM chondrites.

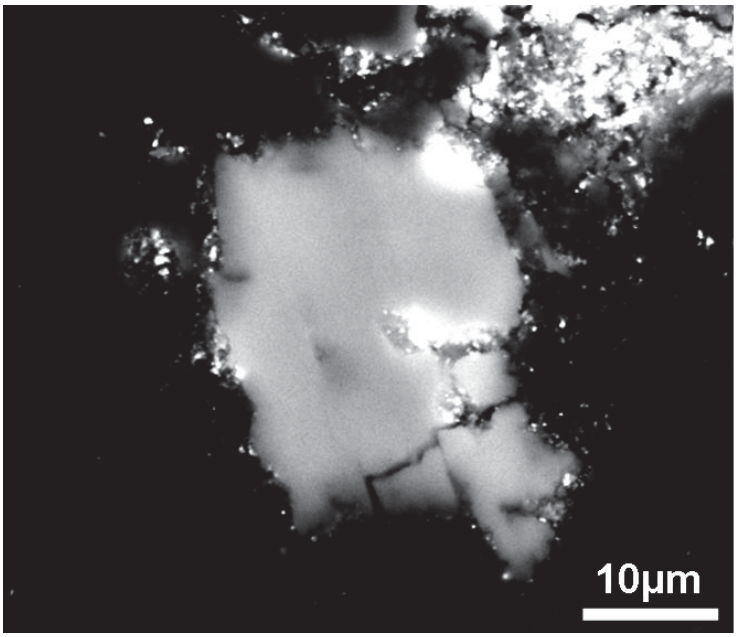

4.68- SEM-CL image of an un-rimmed calcite grain in EET 96029.
The grain shows high CL intensity over all areas. The presence of very high CL intensity in some areas of the grain is charging that has devolved around the holes. The location of this grain in the sample studied is shown in appendix D5.

4.6.3.2 Quantitative chemical analyses of calcite grains

Twenty nine chemical analyses of twenty four calcite grains were acquired by EPMA (Table 4.17). Only five of the grains analysed were completely rimmed or partly rimmed with tochilinite-serpentine intergrowth; the other nineteen were free of rims. All analyses were obtained from areas that were far enough from rims and inclusions. Only one analysis has been omitted, as it shows very high concentration of Fe and Mg that is probably related to the surrounding materials. Some calcite grains that are close to each other have very similar chemical compositions. Generally, high concentrations of Mn^{2+} above detection limits were only observed in seven grains that in most cases were close to each other. The concentration of $MnCO_3$ in calcite grains in EET 96029 ranges between 0.1 to 2.5 mol%. BSE image of the grains that show very high contents of $MnCO_3$ (e.g. 2.5 mol%) has confirmed that the analyses were correctly located within the grain.

Mol%		Wt%	
CaCO3	98.44 ± 1.42	**Ca**	38.98
MgCO3	0.17 ± 0.34	**Mg**	0.04
SrCO3	0.00 ± 0.01	**Sr**	0.00
FeCO3	1.17 ± 0.51	**Fe**	0.65
MnCO3	0.22 ± 0.61	**Mn**	0.12
Total	100.00	**Total**	39.79
***n*= 29 analyses from 24 grains.**			

Table 4.17- Mean of the quantitative chemical analyses of calcite grains in EET 96029. Concentrations below the detection limit are assumed to be zero. Data presented as mean ± SD, error values are calculated to 1σ. The full data set is listed in appendix B.5 with average and standard deviation.

4.6.4 Post crystallization deformation of Ca-carbonate in EET 96029

Petrographic observations indicate that only a few calcite grains are decorated with one set of twinning type I that cross-cuts a grain. Twin lamellae in these grains are straight and very thin.

4.7 Carbonate minerals in CM2.3 LON 94101

4.7.1 Introduction

The first observation a millimetre sized vein of twinned calcite in LON 94101 was by Sofe et al. (2010a). A microstructure study of this vein was undertaken by Lindgren et al. (2010, 2011a). Sofe et al. (2011b) have reported that both aragonite and calcite occur in LON 94101.

4.7.2 Petrographic observations

Carbonate minerals in LON 94101 are aragonite and calcite. About 2000 BSE images have been obtained from the sample to investigate the detailed petrographic context of these minerals. Calcite and aragonite were distinguished from each other by EBSD mapping and laser Raman spectroscopy. Calcite in LON 94101 is present in four generations (Figure 4.69) including: (i) grains completely rimmed with tochilinite, and in many cases partly or wholly replaced by tochilinite-serpentine intergrowths or tochilinite; in some cases this calcite also contains inclusions of tochilinite, (ii) calcite replacing forsteritic olivine, which in many cases contains patchy inclusions of pentlandite, (iii) calcite grains free of inclusions and rims, (iv) micro to millimetre-sized veins of calcite; micro veins are associated with blocky grains of pentlandite. SEM point counting results showed that the

Ca-carbonate (aragonite and calcite) comprise 1.29 vol% of the rock by volume, with the exception of calcite grains that are partly replaced by tochilinite-serpentine intergrowths, that were separately counted and represent 1.20 vol% of the meteorite. X-ray maps and SEM point counting revealed that LON 94101 has more abundant calcite than other CM2 chondrites. The Ca X-ray map of LON 94101 (Figure 4.70) indicates that calcite grains occur in small isolated clusters, in discontinuous veins, and in millimetre and micrometer sized veins. The map also shows that the majority of small calcite grains occur in one large area (left half of the map in Figure 4.70), whereas the right hand part of the map has less numerous but coarser calcite grains (i.e. most areas in the left half of the map Figure 4.70).

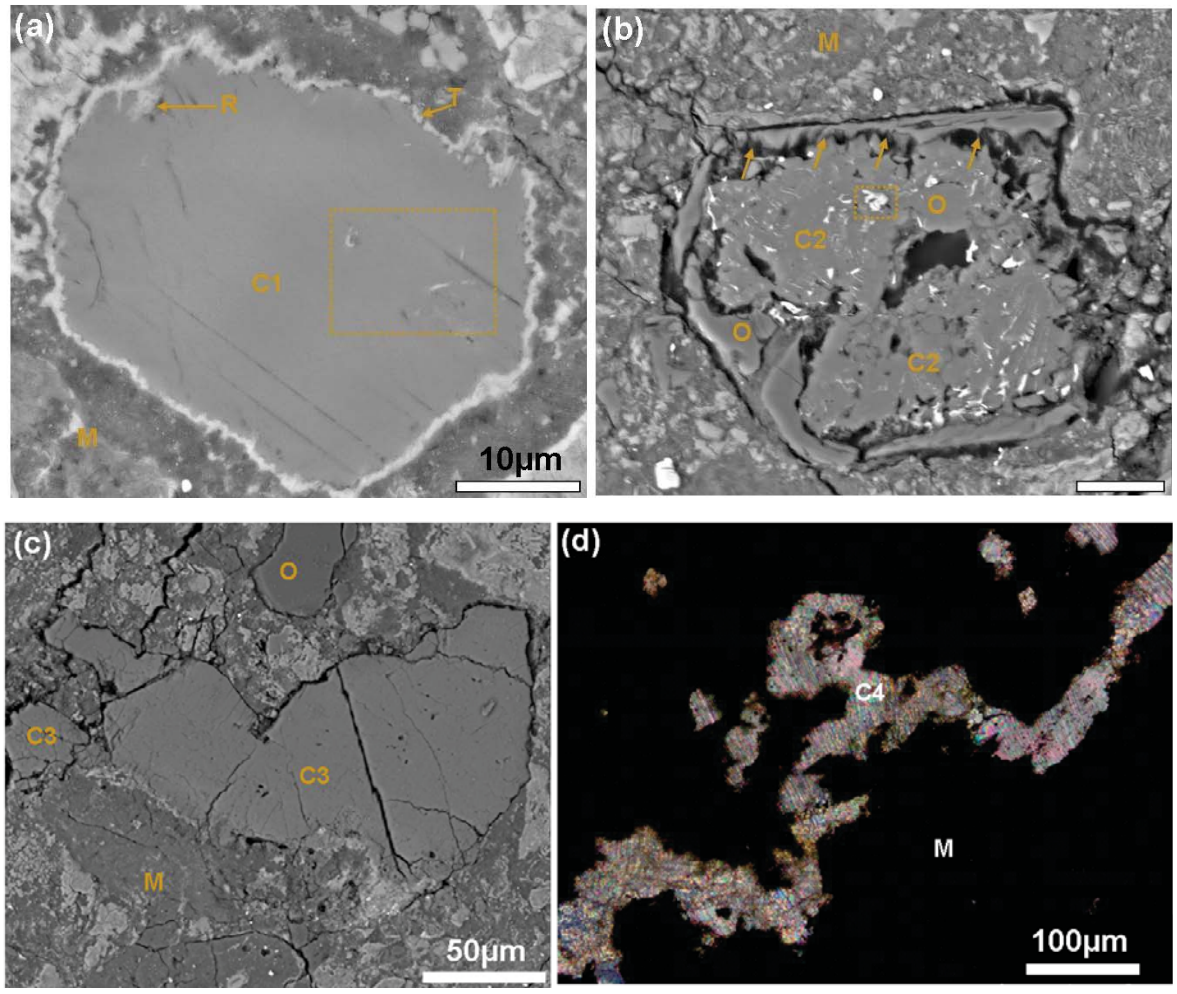

Figure 4.69- BSE images of four generations of calcite in LON 94101.
(a) Calcite generation I (C1) that is rimmed by a serpentine-tochilinite intergrowth (T) and contains small patches of tochilinite (white crystals in the boxed area). The grain has been slightly replaced by tochilinite (R). (b) Image showing calcite generation II (C2) that has replaced forsteritic olivine (O). The image shows unaltered areas of olivine (O) inside and around the calcite; these areas are also highly etched (arrowed areas). The calcite contains blocky grains of pentlandite (e.g. boxed area). (c) BSE image showing a large (80 µm) grain of calcite generation II (C3) that is free of rims and differs in texture to calcite grains in (a) and (b), O is olivine, M is fine grained (<1µm) matrix. (d) Transmitted light image between crossed polarisers showing part of a twinned calcite vein (C4) within fine grained matrix (M) (from Sofe et al. (2010)). The locations of these grains in the sample studied are shown in appendix D6.

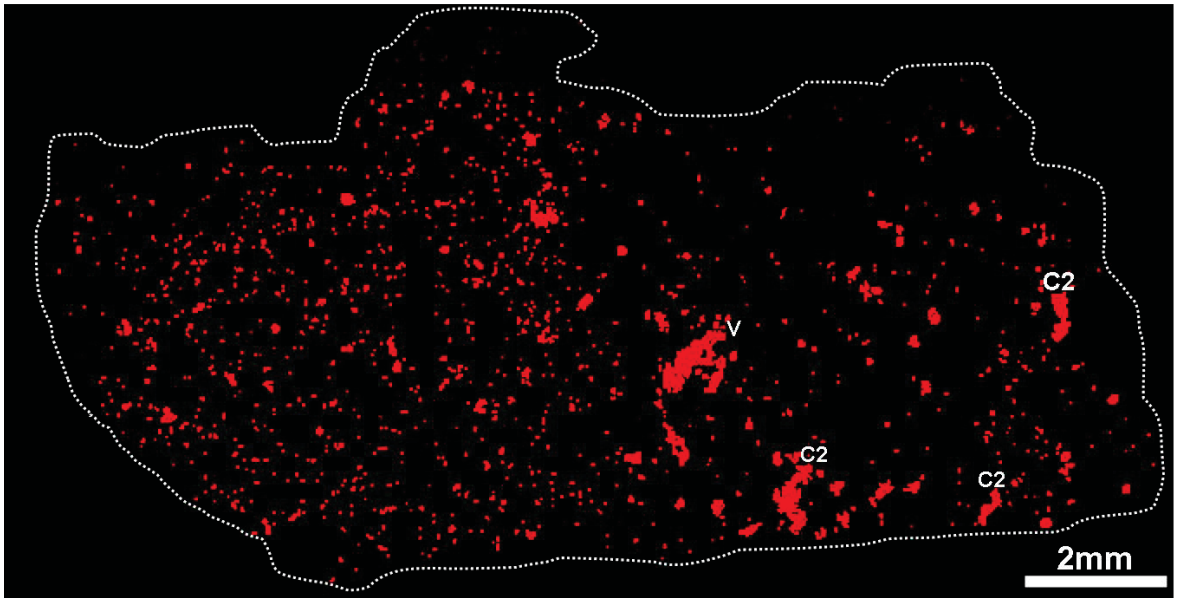

Figure 4.70- Ca X-ray map of whole sample of LON 94101.
The map shows the distribution of Ca (red areas), which locates all Ca-carbonate grains, and a few grains of pyroxene. Note the Ca is concentrated in small discontinuous veins and within very small isolated clusters, and also within large (~2mm in length) vein (v). Ca is more abundant within left half of the sample than the right half. Fine grained (<1µm) matrix and high temperature phases are black in the map. The dashed line is the edge of the thin section. C2s are large (1-1.5 mm in length) grains of calcite after olivine.

Calcite grains in LON 94101 can have different shapes that in order of abundance are: subrounded (38% of the calcite grains), irregular (27% of the calcite grains), elongated (18% of the calcite grains), subhedral (14% of the calcite grains), euhedral (3% of the calcite grains). Rimmed and un-rimmed grains range in size from ~1µm up to ~100 µm across, and in some cases can be ~150 µm in length. Calcite replacing olivine shows different sizes, in some cases reaching ~300 µm across and ~200 µm in length. LON 94101 contains a large twinned calcite vein that is ~3.8 mm in length and ~250 µm in width, and also contains a few small veins that are ~100 µm in length by a few microns in width.

In LON 94101 calcite occurs as monocrystalline and polycrystalline grains. Rimmed and un-rimmed calcite grains, and calcite replacing olivine are slightly fractured, whereas the calcite in the millimetre-sized vein is highly fractured and intensity twinned. A few grains in this meteorite show slight etching of their margins. Calcite in the millimetre sized vein is totally free of inclusions, has direct contact with the fine grained (<1µm) matrix, and is composed of numerous sub-grains (Figure 4.71a). Areas along the large vein are mainly composed of calcite and phyllosilicate intergrowth, and areas towards the vein gradually became enriched with calcite. A few small areas in the fine grained matrix in LON 94101

also consist of calcite-phyllosilicate intergrowth. A few single calcite grains that are free of rims and inclusions are texturally comparable to the calcite in the large vein; these single grains were probably formed at the same time as the calcite vein from the same fluids, and were broken from it during deformation (Figure 4.71).

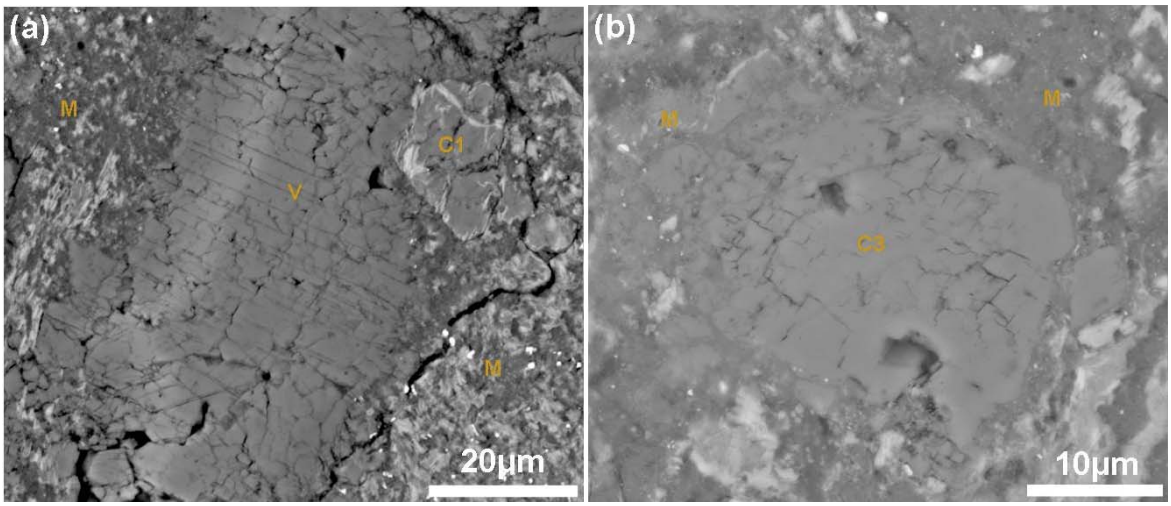

Figure 4.71- BSE images of calcite grain and part of calcite vein in LON 94101.
(a) The texture of part of twined calcite in the large vein (v). C1 is a calcite grain rimmed with tochilinite. Note the presence of twins that cross-cut the calcite vein and the sub-grains in the vein. Note also the boundary between C1 and calcite vein that suggests the calcite vein is calcite overgrowth. (b) The texture of single grain (C3) that is comparable to the texture of calcite vein, and this grain also is composed of several sub-grains. The locations of these grains in the sample studied are shown in appendix D6.

Twenty six aragonite grains were found in LON 94101. These grains occur mainly in the left half of the sample where the majority of small calcite grains are also found (Figure 4.72, see also Figure 4.70). They are concentrated in the interior of the sample, whereas the outer parts zone of the thin section are almost free of aragonite. However, aragonite grains in LON 94101 are more widely distributed in the meteorite compared with those in less altered chondrites (i.e. Murchison, Murray, and Pollen).

Aragonite grains in LON 94101 are similar in texture to calcite grains that are free of rims. They have irregular boundaries with the fine grained (<1µm) matrix, and in most cases are etched at their margins. Pores are also present between the edges of some grains and the fine grained (<1µm) matrix that were probably formed by the dissolution. All aragonite grains in LON 94101 are free of inclusions and rims, but in most cases are highly fractured. They range in size from ~3 µm to ~ 40 µm, and occur in shapes that, in order of abundance include: subhedral, subrounded and irregular.

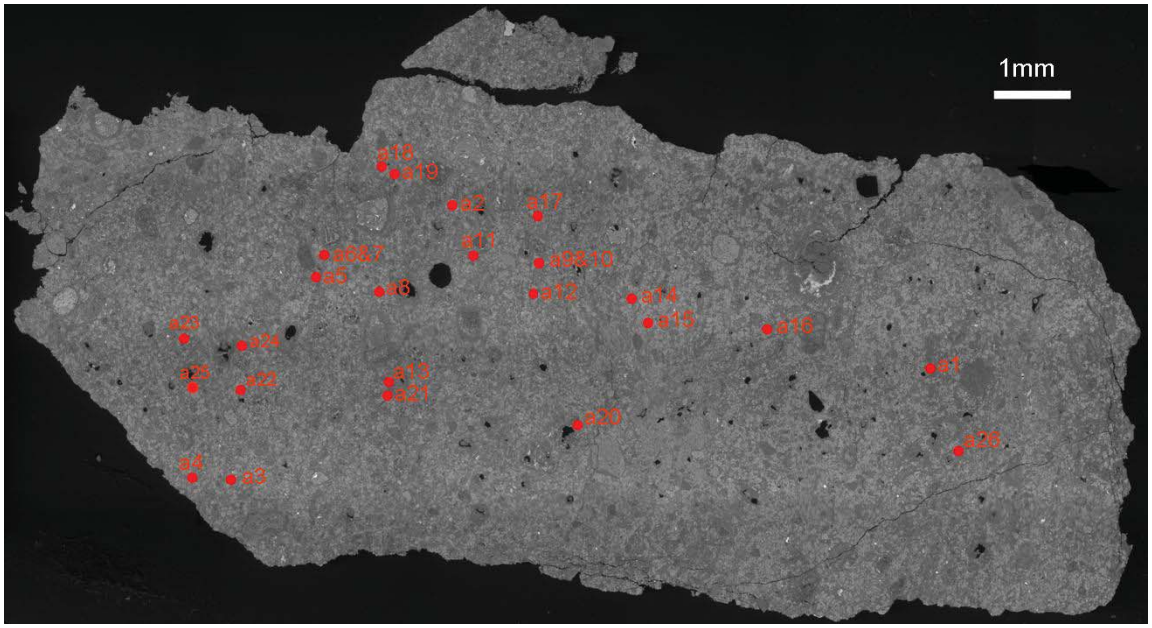

Figure 4.72- BSE image of the whole of LON 94101 with the locations of the 26 aragonite grains marked.
Note that more than 20 grains occur in the left half of the sample, but the right half contains only 6 grains. It is clear also that the outer parts of the sample are nearly free of aragonite. Each grain is labelled in this map with an identifying number.

4.7.3 Crystallographic orientation of Ca-carbonate grains

EBSD results from calcite in LON 94101 have been discussed by Lindgren et al. (2011a). Crystallographic orientation maps of some calcite grains in LON 94101 that were obtained for this study were also used by Lindgren et al. (2011a). Lindgren et al. (2011a) reported that the c-axes of 65 single calcite grains are inclined close to the vertical and horizontal, and the majority of these grains (47 grains) show a preferred crystallographic orientations that occur at a low angle (<45º from the horizontal) relative to the sample surface. They also reported that the c-axes of the majority of calcite grains in the vein are inclined <45º from the surface of the sample, and mainly plot in the NE and S-SW quadrants of the pole figure, with the exception of the c-axes of a few grains that are inclined more and less than 45º. EBSD mapping of five grains of calcite replacing olivine show that the c-axes of four grains are inclined close to the vertical, whereas the c-axis of the fifth grain is inclined close to the horizontal (Lindgren et al., 2011a).

EBSD maps also show that calcite grains that are located close to each other and have similar petrographic features can have also c-axes that are inclined at nearly the same angle (e.g. Figure 4.73 a-b). It was observed that the c-axes of some Ca-carbonate grains (aragonite and calcite) that are located close to each other are inclined at nearly the same angle (e.g. Figure 4.73 c-d).

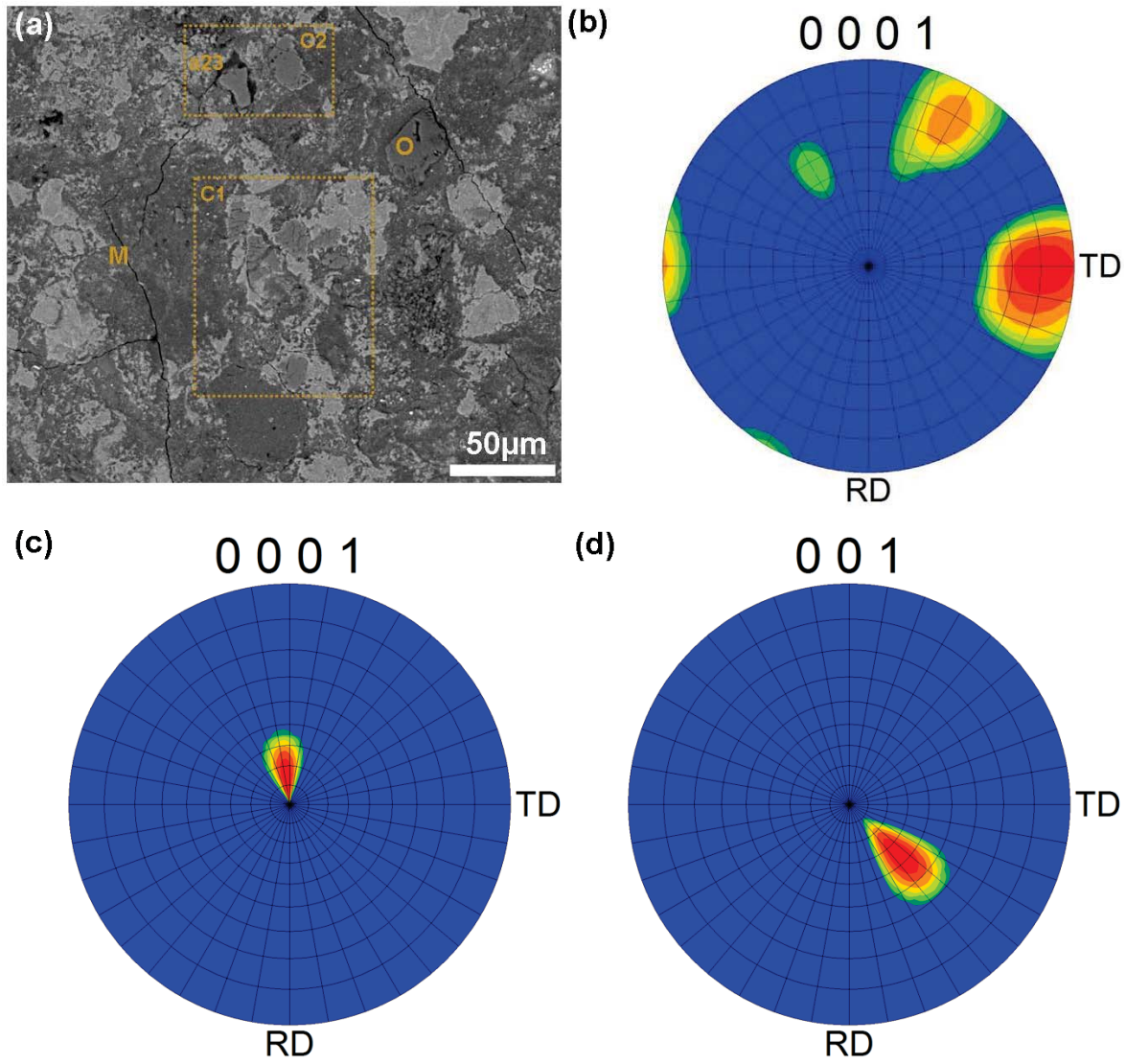

Figure 4.73- Crystallographic orientations of Ca-carbonate grains in LON 94101.
(a) BSE image showing the location of a small cluster (boxed area C1) that contains five completely rimmed calcite grains and one partly rimmed calcite grain. It also shows the location of an aragonite grain (a23) and partly rimmed calcite grain (C2), M is fine grained (<1µm) matrix and O is olivine grain. (b) Pole figure showing the orientations of calcite crystals in boxed area (C1) in (a). Note the c-axes of these crystals are inclined at low angle to the thin section surface. (c) Plot showing c-axis orientation of the calcite C2 in (a) that is inclined at a very high angle. (d) Pole figure texture showing the orientation of the c-axis of the aragonite (a23) in (a) that is inclined very close to the vertical. Note the c-axes of aragonite (a23) and calcite (C2) in (a) are inclined at similar angles. Grid line divisions represent 10º. The location of this map in the sample studied is shown in appendix D6.

EBSD mapping of aragonite grains in LON 94101 was a challenge, as the majority of these grains are either surrounded by holes or highly fractured, which causes charging over and around a grain; this hinders setup of the EBSD scans, or produces EBSD maps of very poor quality. However EBSD maps of eight well preserved aragonite grains were successfully obtained. The pole figure containing orientations of these eight grains (Figure 4.74) shows that the c-axes of three (a7, a18, a22) are inclined at low angles (< ~25º) relative to the sample surface, whereas the c-axes of another five (a5, a6, a13, a21, a23) are

inclined at high angles (~ 60º to ~ 80º). The results also show that the c-axes of some grains that are found close to one another are inclined at nearly the same angle (e.g. a21 and a13; a5 and a6, see Figure 4.74 and Figure 4.72). The c-axes of aragonite grains plot in the NW, SE and SW quadrants; however most aragonite c-axes lie NW-SE, which is at 90º to the long axis of the vein. This suggests that the growth of aragonite was controlled by compression, which is probably perpendicular to the c-axes of aragonite grains (see Figure 4.74). Crystallographic orientation maps of aragonite in LON 94101 suggest that two different generations of aragonite may have formed including aragonite grains with c-axes that are inclined at high angles (>60º) and aragonite grains that have c-axes are inclined at low angles (<30º) relative to the sample surface.

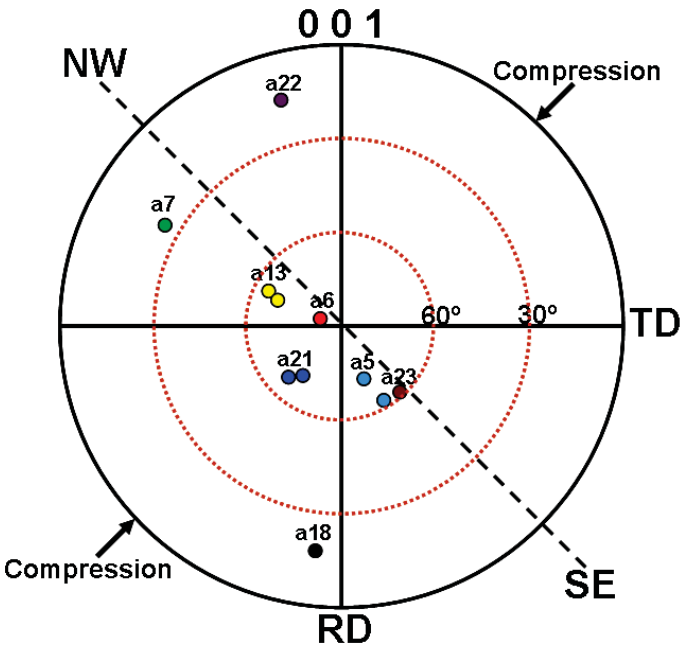

Figure 4.74- Pole figure showing the orientations of poles to the {001} planes of aragonite grains in LON 94101.
Note the c-axes of the aragonite grains are inclined either at low angle (<30º) or at high angle (>60º). Note that most aragonite c-axes lie in a NW-SE, which is possibly perpendicular to compression under which the aragonite was crystallized.

4.7.4 Chemical composition of Ca-carbonate grains in LON 94101

Twenty seven chemical analyses of single calcite grains and the calcite vein in LON 94101 were carried out using the Zeiss Sigma SEM by Lindgren et al. (2011a). In this study CL imaging of aragonite and calcite has been acquired using Quanta 200F SEM, and the EPMA was used to determine the chemical composition of aragonite and calcite in LON 94101.

4.7.4.1 SEM-CL imaging of Ca-carbonates in LON 94101

SEM-CL images were acquired from calcite in the large vein, 30 grains of completely rimmed calcite and 8 grains of aragonite. SEM-CL characteristics of all grains imaged are summarized in Table 4.18. The most common SEM-CL intensity type of Ca-carbonate grains in LON 94101 is CL type I. SEM-CL intensity type I characterises some Ca-carbonate grains in Murchison, Murray, Pollen, Mighei and all calcite grains in EET 96029. Calcite in the large vein exhibits high SEM-CL intensity (Figure 4.75 a); it also shows low SEM-CL intensity along the boundaries of shock induced twins (Figure 4.75 b). Calcite in the large vein also has patches with a very high SEM-CL intensity. All 8 aragonite grains only have CL type I (Figure 4.76 a). SEM-CL characteristics of aragonite in LON 94101 are identical to those of aragonite grains in Murchison (see Figure 4.18 a, and Figure 4.76 a) and most aragonite grains imaged in Mighei. The stability of SEM-CL intensity throughout the vein and aragonite grains indicates that the fluids from which the aragonite and calcite in the vein were invariant in composition. Twelve grains of completely rimmed calcite have CL type VII, only two grains of completely rimmed calcite exhibit CL type V and another two grains show CL type X (e.g. Figure 4.76 b). CL characteristics of Ca-carbonate in LON 94101 and EET 96029 are less complex than those in less altered chondrites.

Grain type	SEM-CL type	SEM-CL characteristics	Abundance
A, C, V	I (observed in, Murchison, Murray, Pollen, Mighei, EET 96029)	Low or high CL throughout the grain, in some cases contains patches of very high CL.	8 A, 14C, V
C	V (observed in Murchison, Murray, Pollen, Mighei)	High CL throughout a grain with a well defined thin layer (~0.5-1 μm) of low CL cross-cut the grain. (Murchison the high CL is very high CL).	2 C
C	VII (observed in Murchison, Pollen, Mighei)	Very high CL throughout the grain with rims of high CL	12 C
C	X (observed in Murray, Mighei)	Well defined band of high CL in some cases contains core of low CL, overgrowth zone of low or very low CL filling the space.	2 C

Table 4.18- Characteristics and abundance of SEM-CL types of Ca-carbonate in LON 94101 and their relationship to petrographic features.
C is completely rimmed, A is aragonite. V is calcite in the large vein. Total number of grains imaged is 38. Note the abundance of each CL type is assigned by numbers, e.g. 14 C means 14 grains of 38 grains imaged show CL type I, and C means these 14 grains are completely rimmed.

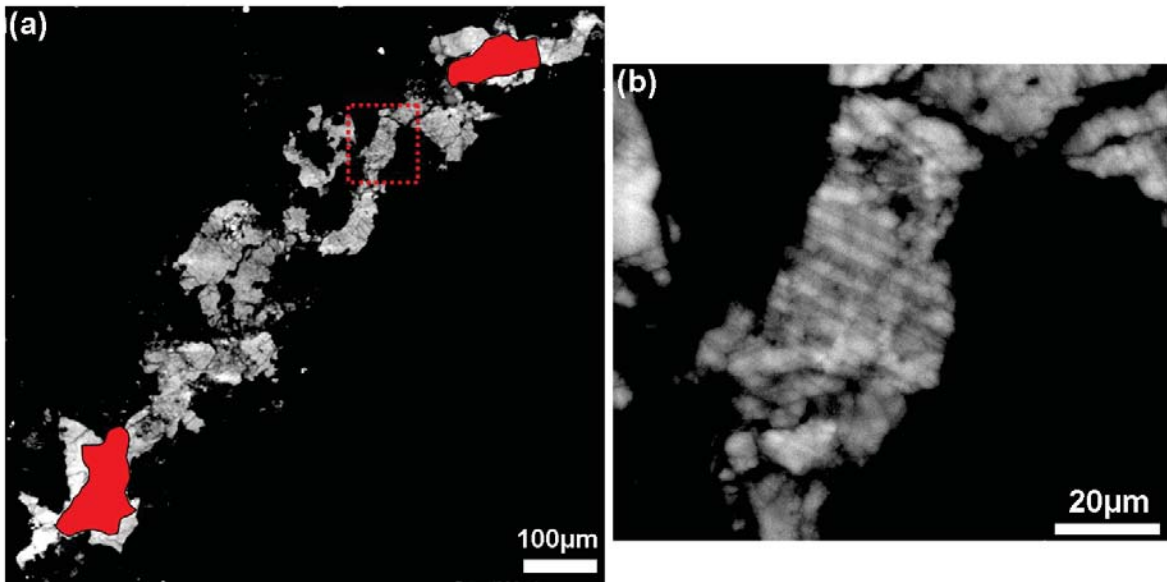

Figure 4.75- SEM-CL image of calcite in the large vein.
(a) CL image showing SEM-CL type I that characterizes the calcite. Holes within the vein are coloured with red. (b) CL image at high magnification from a small part (boxed area) in (a) showing high CL intensity throughout this part of the vein. Note the presence of low CL intensity along shock induced twins. The location of this map in the sample studied is shown in appendix D6.

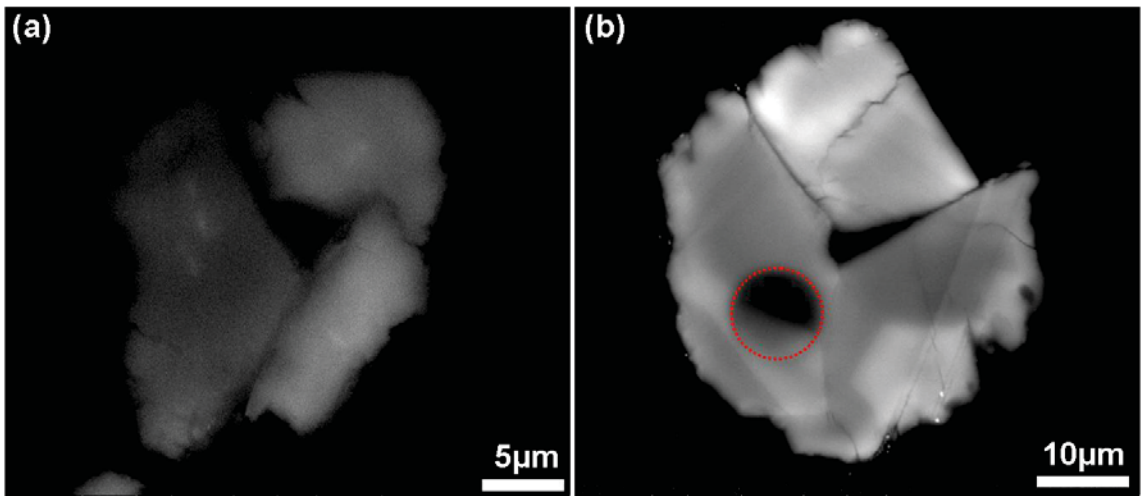

Figure 4.76- SEM-CL images of Ca-carbonate grains in LON 94101.
(a) CL image of aragonite (a13) that contains three sub-crystals that show CL type I, in this case low CL intensity extends throughout the grain. (b) CL image of completely rimmed calcite grain showing CL type X. Area within the red circle is excluded of this comparison as it was burnt by the beam during the chemical analyses by EPMA. The locations of these grains in the sample studied are shown in appendix D6.

4.7.4.2 Quantitative chemical analyses of Ca-carbonate minerals in LON 94101

Thirty grains of Ca-carbonate in LON 94101 were chemically analysed and data obtained from aragonite, completely rimmed calcite, calcite free of rims, the calcite vein and calcite replacing forsteritic olivine. The mean analyses of theses grains are listed in Table 4.19.

This data shows that calcite replacing forsteritic olivine contains more $FeCO_3$ than the calcite vein, rimmed and un-rimmed calcite grains, and aragonite.

The calcite vein has lower concentrations of $FeCO_3$ than the other Ca-carbonates in LON 94101. The three analyses of calcite vein were obtained from the upper, middle and lower parts. These three areas of the vein are nearly identical in their chemical composition. The chemical analyses of three grains of un-rimmed calcite that are similar in texture to the calcite vein (e.g. Figure 4.71 b) show high contents of $FeCO_3$ (+0.53 mol%) in comparison to the calcite vein. However, two of these grains show only a very slight difference in chemical composition from the calcite vein. It was also observed that some aragonite grains and completely rimmed calcite grains that crystallized close to one another can also show a strong similarity in their chemical composition (e.g. Table 4.20). The analyses also show that the completely rimmed calcite contains less of $MgCO_3$ than other Ca-carbonates (calcite vein, calcite replacing olivine) in LON 94101.

Generally, completely rimmed and un-rimmed calcite in LON 94101 contains less $FeCO_3$ than calcite grains in Murray CM2.5. Aragonite in LON 94101 also contains less $FeCO_3$ (-0.17 mol%) than aragonite in Murchison.

Mole%	**$CaCO_3$**	**$MgCO_3$**	**$SrCO_3$**	**$FeCO_3$**	**$MnCO_3$**	**Sum**	***n***
Aragonite	99.01 ± 0.31	0.14 ± 0.18	0.07 ± 0.02	0.79 ± 0.17	0.00 ± 0.00	100	13
Calcite vein	99.65 ± 0.04	0.12 ± 0.02	0.00 ± 0.00	0.23 ± 0.03	0.00 ± 0.00	100	3
Calcite completely rimmed	99.32 ± 0.08	0.00 ± 0.00	0.00 ± 0.00	0.68 ± 0.08	0.00 ± 0.00	100	8
Calcite free of rims	98.94 ± 0.66	0.29 ± 0.36	0.00 ± 0.00	0.76 ± 0.31	0.00 ± 0.00	100	3
Calcite replacing olivine	97.90 ± 1.41	0.17 ± 0.14	0.00 ± 0.00	1.93 ± 1.2	0.00 ± 0.00	100	3
Wt%	**Ca**	**Mg**	**Sr**	**Fe**	**Mn**	**Sum**	***n***
Aragonite	39.00	0.03	0.06	0.43	0.00	39.53	13
Calcite vein	39.27	0.03	0.00	0.13	0.00	39.43	3
Calcite completely rimmed	39.72	0.00	0.00	0.38	0.00	40.10	8
Calcite free of rims	39.04	0.07	0.00	0.42	0.00	39.53	3
Calcite replacing olivine	37.71	0.04	0.00	1.02	0.00	38.77	3

Table 4.19- Mean of the quantitative chemical analyses of Ca-carbonate grains in LON 94101. The analyses were obtained from 13 and 17 grains of aragonite and calcite respectively. Analyses below detection limit are assumed to be zero. Data presented as mean ± SD, error values are calculated to 1σ. The full data set is listed in appendix B.5 with average and standard deviation.

Mole%	CaCO3	MgCO3	SrCO3	FeCO3	MnCO3	SUM
a14	99.10	0.03	0.09	0.78	0.00	100.00
a15	99.15	0.04	0.08	0.73	0.00	100.00
c8	99.23	0.00	0.00	0.77	0.00	100.00
c6	99.24	0.00	0.00	0.76	0.00	100.00
Wt%	**Ca**	**Mg**	**Sr**	**Fe**	**Mn**	**SUM**
a14	39.02	0.01	0.08	0.43	0.00	39.53
a15	39.22	0.01	0.07	0.40	0.00	39.70
c8	39.35	0.00	0.00	0.42	0.00	39.77
c6	39.72	0.00	0.00	0.43	0.00	40.15

Table 4.20- Typical chemical analyses of Ca-carbonate grains that crystallized close to each other. Note aragonite grains a14 and a15 are close to each other (see Figure 4.72), and these grains show a very slight difference in their chemical composition. Two grains of completely rimmed calcite (c8 and c9) are found in same clusters in fine grained (<1µm) matrix, and their chemical compositions are almost identical.

The chemical analyses confirm that several generations of Ca-carbonate were involved in the parent body of LON 94101 and crystallised from fluids of different chemical compositions. In most cases, grains that are close to each other show a similarity in chemical composition, indicating that they are likely to have precipitated from fluids of the same chemistry.

4.7.5 Post crystallization deformation of calcite in LON 94101

All calcite types in the examined section of LON 94101 show the evidence of impact induced twinning, whereas most of the calcite grains that are completely rimmed with tochilinite-serpentine have been partly or totally transformed into tochilinite-serpentine intergrowth.

4.7.5.1 Calcite twin morphology

Using EBSD mapping, Lindgren et al. (2011a) reported that the twins of calcite examined in LON 94101 are e-twins on {-1018} planes. They reported that some of the calcite grains and calcite vein are twinned. They also reported that the twins of calcite in LON 94101 are straight, have a thickness of about 2-4 µm, the space between the twins range between 2 to 4 µm, and only one set of twins is found in a single calcite grain. However, further petrographic observations show that some of the single calcite grains contain two sets of twins; the first set is thick a patchy twin classified as type IV twinning (using the chart stated in Figure 4.21) and cross-cut a grain; the lamella thickness of this twins ranges from ~1µm to ~2µm. The second set are thin straight twins (~0.5 µm) (twinning type I) that are perpendicular to the first set (Figure (4.77 a). Some of the single calcite grains can also

have one set of thick straight twins (twins type II) (~0.5µm to ~2µm) that cross-cut a grain, and in some cases these grains are also partially deformed with thin straight twins (Figure 4.77 b). Petrographic observations also showed that all calcite in the large vein is deformed with one set of thick straight twins parallel to those in the single grains (see Figure 4.71 a and Figure 4.77 b). Note that the sample was placed in a specific position (shown in Figure 4.72) during the acquisition of BSE images and EBSD maps of the meteorite. Calcite grains in LON 94101 contain abundant deformation twins, but the aragonite grains do not show evidence for this deformation. Calcite grains are likely to have been exposed to at least two or three thermal deformations (<200ºC, 150-300ºC, >250ºC) that took place prior to the formation of aragonite grains.

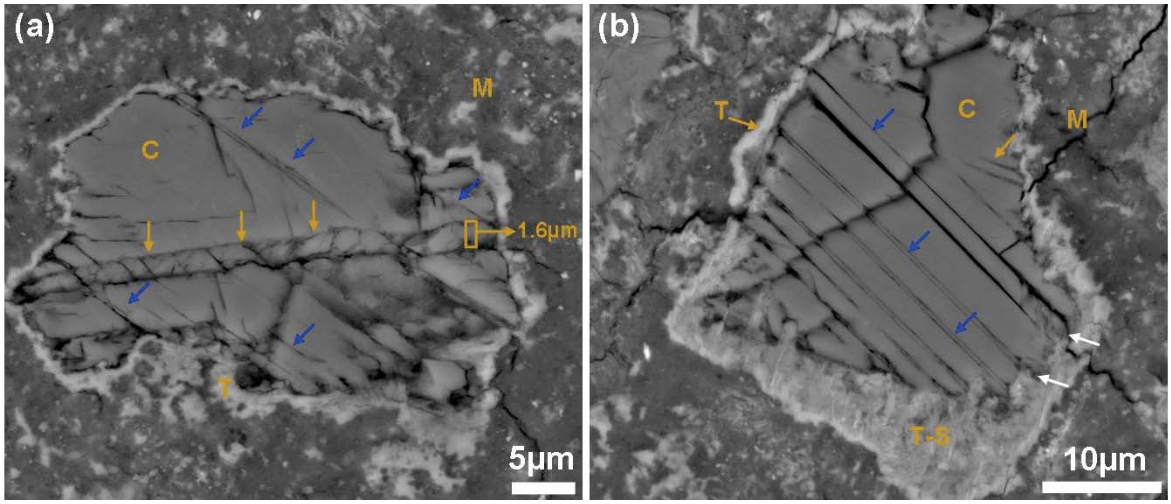

Figure 4.77- BSE images of calcite grains containing twins in LON 94101.
(a) Completely rimmed calcite grain (C) shows thick patchy twin lamella (1.6 µm) (arrowed with yellow) perpendicular with the second set of thin twins (arrowed with blue). (b) Completely rimmed calcite grain (C) that is decorated with thick straight twins (arrowed with blue) that cross-cut the grain. The grain is also partially twinned with thin straight lamellae (1.5 µm) (arrowed with yellow). This calcite grain has been partly replaced by tochilinite-serpentine intergrowths (T-S). Note the lamellar twins are also replaced by these materials (white arrows). M is fine grained (<1µm) matrix, T tochilinite rims. The locations of these grains in the sample studied are shown in appendix D6.

4.7.5.2 Pseudomorphs after calcite in LON 94101

Petrographic observations of LON 94101 show that most of the completely and nearly completely rimmed calcite grains have transformed into tochilinite-serpentine intergrowths. The replaced rimmed calcite grains inherited structural details of the calcite such as tochilinite rims and inclusions. The tochilinite-serpentine pseudomorphs form 12.91% of total bulk volume of the meteorite. The relationship between tochilinite-serpentine pseudomorphs and calcite rimmed by tochilinite can be classified as follows: (i) calcite is partly replaced by tochilinite-serpentine; (ii) calcite is moderately transformed

into tochilinite-serpentine; (iii) calcite is nearly completely replaced by tochilinite-serpentine; (iv) calcite is completely replaced by tochilinite-serpentine (Figure 4.78).

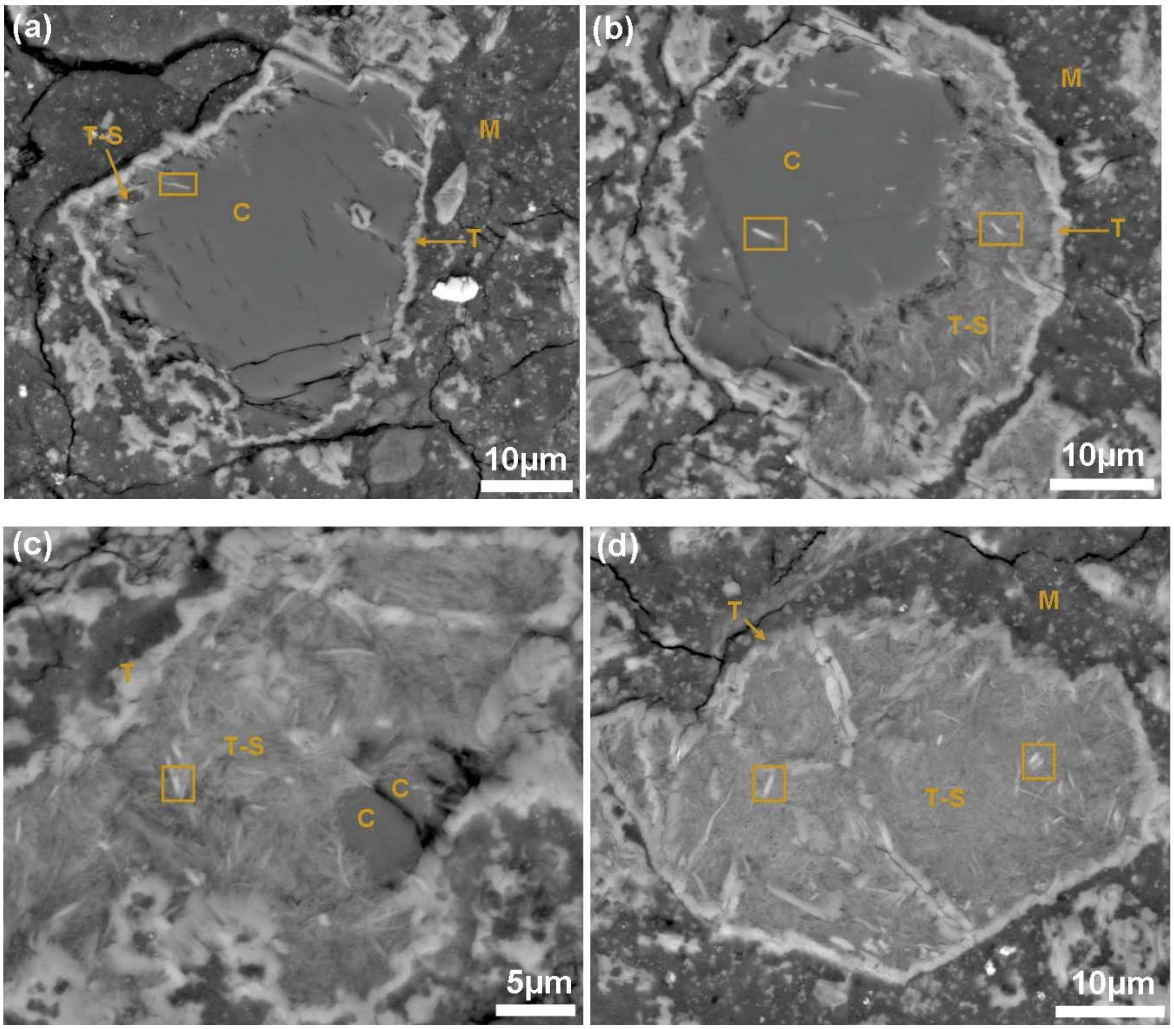

Figure 4.78- BSE images showing the stages of formation of pseudomorphs after calcite rimmed with tochilinite in LON 94101.
(a) Partial replacement of calcite (C) by tochilinite-serpentine (T-S). Boxed area shows the occurrence of Fe-sulphide within the calcite. (b) Moderate replacement of calcite (C) by tochilinite-serpentine (T-S). Note the inclusions of Fe-sulphide (e.g. boxed area) that have increased in the calcite with increasing alteration. (c) Near complete replacement of calcite (C) with tochilinite-serpentine. (d) Complete transformation of calcite into tochilinite-serpentine (T-S). Note in b, c and d the final phase of pseudomorphs has inherited the tochilinite rims (T) and Fe-sulphide inclusions (e.g. boxed areas) that initially present in the calcite. T is tochilinite rims. M is fine grained (<1µm) matrix. The locations of these grains in the sample studied are shown in appendix D6.

The first three types of calcite (from partly to nearly completely altered) represent 1.2 vol% of the total bulk volume of the meteorite. Petrographic observations also showed that some of the calcite grains that are rimmed by tochilinite are well preserved. The presence of Fe-sulphide as inclusions within the calcite rimmed with tochilinite gradually increases with increasing calcite replacement into tochilinite-serpentine intergrowth. For instance, calcite grains that are partly or slightly altered to tochilinite-serpentine contain fewer

inclusions than moderately and nearly completely altered grains. In most cases the well preserved calcite grains rimmed with tochilinite are free of Fe-sulphide inclusions, or contain very rarely patches of these materials, whereas the partly altered calcite and moderately altered calcite contains slight and high amounts of Fe-sulphides respectively (e.g. Figure 4.78 a-b).

It is clear that starting point of the transformation of calcite into tochilinite-serpentine was the formation of Fe-sulphide (probably tochilinite) as inclusions within the calcite. It was observed that the twin microstructure of calcite rimmed grains has been transformed into tochilinite-serpentine (see 4.77 b); this indicates that formation of twins was probably prior to replacement by tochilinite-serpentine intergrowths.

4.7.5.2.1 Chemical composition of pseudomorphism of tochilinite-serpentine intergrowth after calcite in LON 94 101

The chemical composition of seven pseudomorphs after calcite was undertaken by EPMA. Chemical analyses and EDS spectra indicate that the tochilinite-serpentine pseudomorphs differ in chemical composition from area to area in the meteorite, in some cases from grain to grain in the same area of the meteorite, so the amounts of Fe, Mg and S in these pseudomorphs fluctuate. It was also found that a few grains of the pseudomorphs are enriched in Ca, but high contents of Fe and S are also present. These grains are located within small clusters in the meteorite, and are composed mainly of tochilinite-calcite intergrowths. Based on these chemical analyses (Table 4.21), the pseudomorphs after calcite can be classified into three phases including: (i) phase 1, in which the tochilinite-serpentine intergrowth is enriched in Fe and S, (ii) phase 2 represents tochilinite-serpentine intergrowth that is enriched in Si and Mg, (iii) phase 3 is tochilinite-calcite intergrowth (Figure 4.79) that is enriched in Ca and also contains high concentrations of Fe and S.

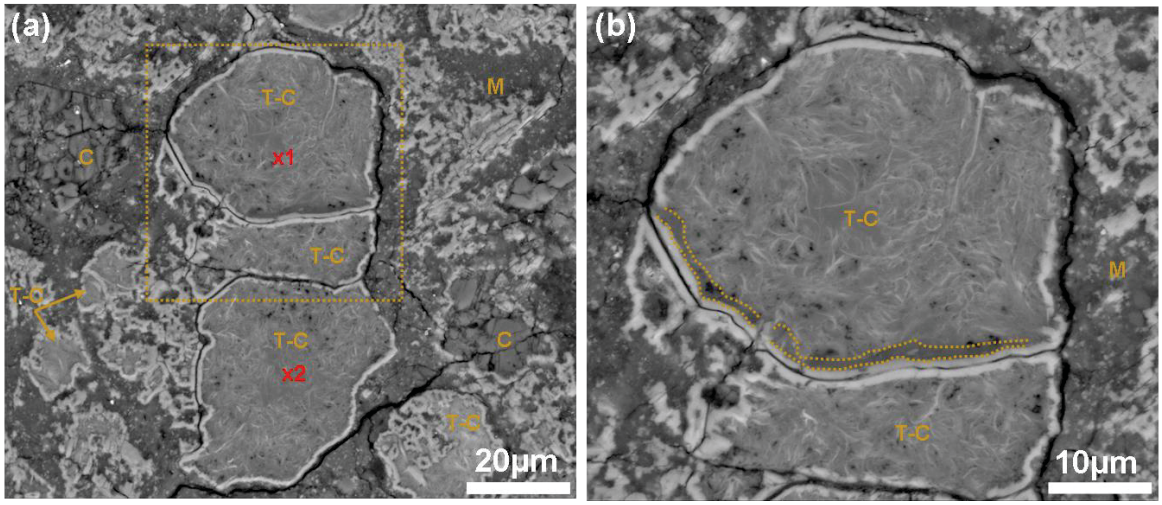

Figure 4.79- BSE images of pseudomorphs after calcite in LON 94101.
(a) Small area of fine grained (<1µm) matrix (M) contains several tochilinite-calcite pseudomorphs (T-C) after calcite, x1 and x2 were chemically analysed (the analyses are presented in Table 4.21), c is calcite grain. (b) BSE image at high magnification of the boxed area in (a) showing remnants of calcite (areas between detached lines) within tochilinite-serpentine intergrowths (T-S). The locations of these grains in the sample studied are shown in appendix D6.

Oxide wt%	Phase1	phase 2	Phase 3	Element wt%	Phase1	Phase 2	Phase 3
Na_2O	0.32 ± 0.07	0.29 ± 0.08	0.04 ± 0.02	Na	0.24	0.21	0.03
MgO	13.79 ± 1.55	24.13 ± 0.07	2.94 ±0.87	Mg	8.31	14.55	1.77
Al_2O_3	2.36 ± 0.20	1.81 ± 0.23	0.48 ± 0.23	Al	1.25	0.96	0.25
SiO_2	17.18 ± 0.49	29.43 ± 1.14	1.58 ± 0.34	Si	8.03	13.76	0.74
SO_2	16.42 ± 0.37	8.71 ± 3.19	8.14 ± 1.81	S	8.22	4.36	4.07
K_2O	0.05 ± 0.01	0.10 ± 0.03	0.01 ± 0.00	K	0.04	0.08	0.01
CaO	0.15 ± 0.04	0.11 ± 0.02	41.75 ± 4.16	Ca	0.11	0.08	29.84
P2O5	0.02 ± 0.01	0.02 ± 0.01	0.02 ± 0.00	P	0.01	0.00	0.00
TiO_2	0.04 ± 0.00	0.04 ± 0.00	0.01 ± 0.01	Ti	0.02	0.03	0.00
Cr_2O_3	0.17 ± 0.05	0.24 ± 0.05	0.08 ± 0.00	Cr	0.12	0.17	0.05
MnO	0.19 ± 0.05	0.21 ± 0.04	0.03 ± 0.03	Mn	0.15	0.16	0.00
FeO	37.57 ± 2.48	21.74 ± 0.32	11.97 ± 4.33	Fe	29.2	16.90	9.31
NiO	2.89 ± 0.48	1.70 ± 0.50	1.00 ± 0.12	Ni	2.27	1.34	0.79
Total%	91.16	88.53	68.06	O	33.18	35.93	21.15
n	3	2	2	n	3	2	2

Table 4.21- The mean of the chemical analyses of the pseudomorphs after calcite in LON 94101.
Phase 1 is a tochilinite-serpentine intergrowth with high concentrations of Fe. Phase 2 is tochilinite-serpentine intergrowths with high concentrations of Si and Mg. Phase 3 shows high concentrations of Ca. Data presented as mean ± SD, error values are calculated to 1σ. The full data set is listed in appendix A.7 with average and standard deviation.

4.8 Isotope results

Results of petrographic and compositional analysis of carbonates in CM chondrites in this study have shown that each meteorite contains multiple generations. Results have also show that CM carbonate minerals are a rich source of information on the conditions and timing of aqueous alteration of their parent body. Oxygen isotopic compositions are an additional and powerful tool to understand conditions under which the carbonate minerals crystallized (Benedix, 2003). The isotopic results may therefore be interpreted in the context of the evolution of the meteorite as a whole, and a much broader understanding of parent body evolution can be achieved by integration of the isotope results with those obtained by other techniques.

4.8.1 Previous work

Results of previous oxygen isotope work (Clayton and Mayeda, 1984; Grady et al., 1988; Benedix et al., 2003) on calcite of CM chondrites are presented in Table 4.22. The previous results show that calcite oxygen isotope compositions in CM2 chondrites (Murchison, Murray, Pollen, Mighei, Cold Bokkeveld and Nogoya) range from 20.0 to 35.5 ‰ for $\delta^{18}O$ and from 8.0 to 17.6 ‰ for $\delta^{17}O$. Tyra et al. (2007) reported that oxygen isotope compositions of carbonate in the paired Antarctic CMs EET 96006, EET96016, EET 96017 and EET 96019 do not plot to the terrestrial fractionation line (TFL), which they interpreted as a consequence of the presence of extraterrestrial carbonate with terrestrial carbonate in their samples. However, work recently published by Tyra et al. (2012) (using a Cameca IMS 6F SIMS) identified 3 isotopically distinct types of calcite in the name Antarctic CM (Table 4.23). These calcite types are petrographically different and comprise small blocky calcite grains in which inclusions are rarely present (type 1) and large calcite grains contain inclusions of tochilinite, phyllosilicate and sulphide (type 2). One analysis of a calcite vein (classified as type 3) was also included in their study (Table 4.23). They found that oxygen isotopic analyses of type 1 and type 2 calcite fall in an array of carbonates analyzed by Benedix et al. (2003), whereas the oxygen isotopic composition of calcite type 3 (calcite vein) has a distinct value (see Table 4.23), which indicates its origin by terrestrial weathering.

Author	Sample	$\delta^{18}O$ (‰)	$\delta^{17}O$ (‰)	$\Delta^{17}O$ (‰)	Mineral	*n*
Clayton and Mayeda (1984)	Murchison	35.1	16.7	-1.6	Calcite	1
Grady et al. (1988)	Murchison	+27.2 to + 34.5	--	--	Calcite*	12
	Murray	+35.1	--	--	Calcite*	1
	Pollen	+ 33.8	--	--	Calcite*	1
	Mighei	+28.8	--	--	Calcite*	1
	Cold Bokkeveld	+26.6 to +29.8	--	--	Calcite*	2
	Nogoya	+30.0 to +30.4	--	--	Calcite*	2
Benedix et al. (2003)	Murchison	26.6 to 35.5	13.2 to 15.9	-0.67 to -1.02	Calcite	4
	Murray	35.2 to 35.3	17.5 to 17.6	0.72 to -0.87	Calcite	2
	Mighei	29.7	14.1	-1.38	Calcite	1
	Nogoya	20.0 to 28.1	8.0 to 12.8	-1.85 to -2.44	Calcite	3
	Cold Bokkeveld	28.3	13.1	-1.65	Calcite	1

Table 4.22- Oxygen isotopic compositions of calcite in some CM2 chondrites (falls).
More than two analyses are shown in range from lowest to highest value. These data obtained from Clayton and Mayeda (1984); Grady et al. (1988); Benedix et al. (2003). * is all carbonate assumed to be calcite that analysed only for $\delta^{18}O$ by Gardy et al. (1988).

	$\delta^{18}O$ (‰)	$\delta^{17}O$ (‰)	$\Delta^{17}O$ (‰)	*n*
Type 1 calcite	28.8 to 37.8	13.9 to 20.9	1.9 to -2.0	23
Type 2 calcite	16.8 to 21.1	6.1 to 10.1	-0.7 to -3.6	8
Calcite vein*	-5.3	-3.3	-0.5	1

Table 4.23- Oxygen isotopic analyses of calcite in the EET CM2 chondrites.
More than two analyses are shown in range from lowest to highest value (see also Figure 4.81). From Tyra et al. (2012).

4.8.2 Oxygen isotopic compositions of Ca-carbonate in LON 94101

The NanoSIMS 50L at the Open University was used to determine whether oxygen isotope compositions vary between Ca-carbonate generations, in order to help refine models of parent body evolution and grains in LON 94101 were analysed. This meteorite is suitable because it contains four generations of calcite (calcite rimmed with tochilinite, calcite free of rims, calcite replacing olivine, calcite vein) and aragonite, which are distinct in their petrographic characteristics and chemical composition (see Table 4.19). Four of the calcite grains rimmed with tochilinite (three of them zoned), three areas of the calcite vein, six grains of aragonite, one grain of calcite replacing olivine and one grain of calcite free of rims were analysed for oxygen isotopic compositions using a spot size of 5 μm. (Tyra et al. (2012) used an ion beam spot with size of 10 μm). Analysis of calcite replacing olivine is not discussed further, as an area of Fe-rich material was exposed during measurement. It covered <10% of the 5μm raster but it is unclear if it was silicate or sulphide. There was

also a 10 ‰ drift in $\delta^{18}O$ coincident with detection of Fe. Calcite replacing olivine contains Fe-sulphide, and LON 94101 has 1.93 mol% of $FeCO_3$ as this calcite is intergrown with Fe-sulphide (see Figure 4.69 b). Therefore, Fe-sulphide is present in nano-scale inclusions within the calcite, so this type of calcite is inappropriate for oxygen isotopic analysis. One analysis of calcite free of rims was also excluded, as it shows low oxygen and Ca counts, and also very high Fe and Mg counts, and high ^{17}OH, which suggests that the area possibly contains matrix.

The variation in O isotopic values obtained from Ca-carbonate in LON 94101 is significant for either $\delta^{18}O$ or $\delta^{17}O$ (ANOVA, p=0.00 $\delta^{18}O$, p=0.00 $\delta^{17}O$). Calcite rimmed with tochilinite has an average $\delta^{18}O$ of 37.5 ± 0.65‰ and $\delta^{17}O$ of 20.9 ± 1.3‰. The calcite vein has average $\delta^{18}O$ of 18.4 ± 0.3‰ and $\delta^{17}O$ of 9.0 ± 0.5‰. Aragonite has an average $\delta^{18}O$ of 39.9 ± 0.57 ‰ and $\delta^{17}O$ of 20.4 ± 1.1 ‰. The analyses therefore show three distinct populations of $\delta^{18}O$ (calcite, calcite vein and aragonite), but only two distinct populations of $\delta^{17}O$ (one for rimmed calcite and aragonite, and another for calcite vein). The average of $\delta^{17}O$ of aragonite shows a very slight difference to calcite rimmed with tochilinite. The average $\Delta^{17}O$ of aragonite is -0.34 ± 1.1‰, the average $\Delta^{17}O$ of calcite grains is 1.43 ± 1.1‰ and the average $\Delta^{17}O$ of calcite vein is -0.53 ± 0.5 ‰.

The $\delta^{18}O$, $\delta^{17}O$, and $\Delta^{17}O$ for 6 grains of aragonite, 3 areas of calcite vein, and 7 grains of calcite rimmed with tochilinite in LON 94 101 are listed in Table 4.24.

The isotopic compositions of aragonite, calcite rimmed with tochilinite and the calcite vein are plotted on a graph of $\delta^{17}O$ versus $\delta^{18}O$ (Figure 4.80). These points plot along and very slightly above or below the terrestrial fractionation line (TFL) (see Miller et al., 2002). The calcite vein has significantly lower $\delta^{17}O$ and $\delta^{18}O$ than calcite grains and aragonite, and plots very close to the calcite type 2 described by Tyra et al. (2012) (Figure 4.81). Tyra et al. (2012) classified the calcite vein in the Antarctic CM2s as a weathering product and its oxygen isotopic composition (found by Tyra et al., 2012) (see Table 4.23) lies far from the calcite vein in LON 94101 (Figure 4.81). This helps prove that the calcite vein in LON 94101 is extraterrestrial. The composition of terrestrial carbonate was estimated by Tyra et al. (2007) as ~ -9 ‰ for $\delta^{18}O$ and ~ 0 ‰ for $\Delta^{17}O$.

Calcite	**$\delta^{17}O$ (‰)**	**2σ (‰)**	**$\delta^{18}O$ (‰)**	**2σ (‰)**	**$\Delta^{17}O$ (‰)**	**2σ (‰)**
Calcite grain 1, point 1	20.7	2.2	37.1	0.7	1.4	2.3
Calcite grain 1, point 2	19.3	2.2	37.7	0.7	-0.3	2.3
Calcite grain 3, point 2	22.8	2.2	38.1	0.7	2.9	2.3
Calcite grain 3, point 3	22.6	2.2	38.4	0.7	2.6	2.3
Calcite grain 4, point 1	20.5	2.2	37.5	0.7	1.0	2.3
Calcite grain 4, point 1	20.5	2.2	37.5	0.7	1.0	2.3
Calcite grain 4, point 2	19.9	2.2	36.4	0.7	0.9	2.3
Calcite vein, point 1	8.8	2.2	18.7	0.7	-0.9	2.3
Calcite vein, point 2	8.7	2.2	18.0	0.7	-0.7	2.3
Calcite vein, point 3	9.6	2.2	18.5	0.7	0.0	2.3
Aragonite	**$\delta^{17}O$ (‰)**	**2σ (‰)**	**$\delta^{18}O$ (‰)**	**2σ (‰)**	**$\Delta^{17}O$ (‰)**	**2σ (‰)**
Aragonite 1, point 1	19.5	1.4	39.09	1.2	-0.79	1.9
Aragonite 2, point 1	21.0	1.4	39.62	0.9	0.39	1.7
Aragonite 3, point 1	19.1	1.4	40.34	0.9	-1.91	1.7
Aragonite 6, point 1	19.7	1.4	39.52	1.2	-0.89	1.9
Aragonite 9, point 1	21.1	1.4	39.96	1.2	0.30	1.9
Aragonite 11, point 1	22.0	1.4	40.63	0.9	0.88	1.7

Table 4.24- Oxygen isotopic compositions of calcite rimmed with tochilinite, the calcite vein and aragonite in LON 94101 measured by NanoSIMS 50L.
Note that two analyses obtained from calcite grain 1, two analyses obtained from calcite grain 3, three analyses obtained from calcite grain 4, three analyses obtained from 3 different areas of calcite vein, and one analysis of each grain of six aragonite grains.

The oxygen isotope composition of aragonite in LON 94101 is slightly higher than calcite rimmed with tochilinite and the type 1 calcite of Antarctic chondrites in $\delta^{18}O$ (Tyra et al., 2012), suggesting that the aragonite formed at a different time from calcite. Benedix et al. (2003) reported that the oxygen isotope compositions of calcite falls (Murchison, Murray, Mighei, Nogoya and Cold Bokkeveld) ranges from +20.0 to + 35.7% for $\delta^{18}O$, which indicates that calcite grains in CM2 chondrites have lower $\delta^{18}O$ than aragonite. Clayton and Mayda (1984) and Grady et al. (1988) also show calcite in some falls (Murchison, Murray, Mighei, Pollen, Nogoya and Cold Bokkeveld) with a range from + 26.6 to + 35.1 for $\delta^{18}O$ (see Table 4.22).

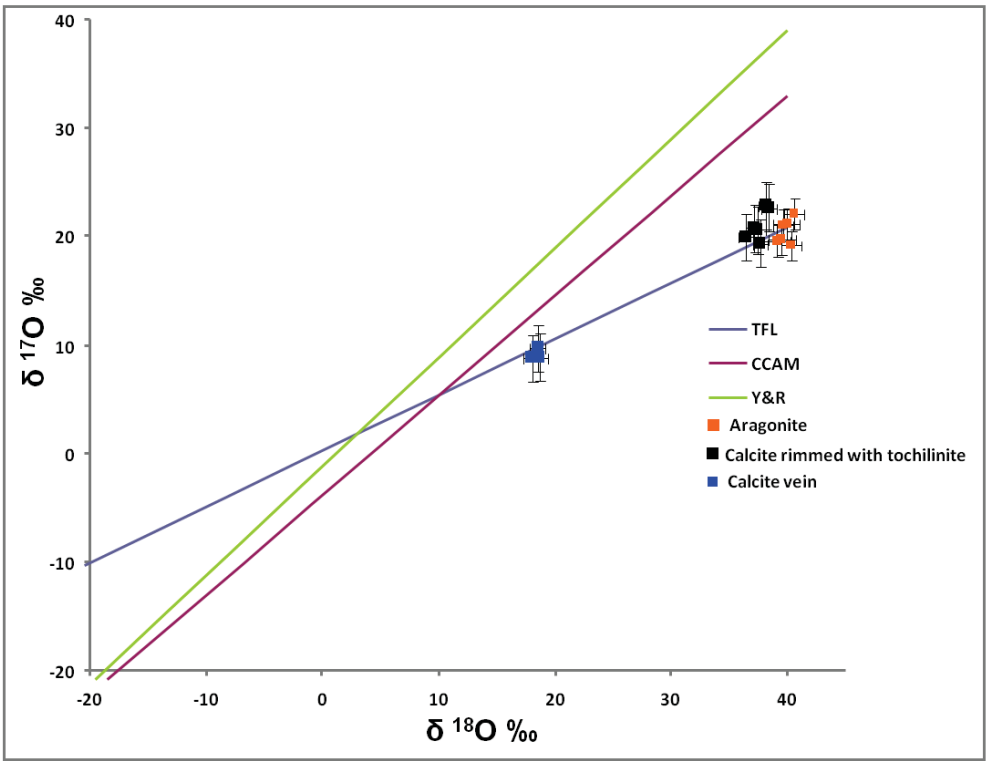

Figure 4.80- Three-isotope plot (δ ^{18}O versus δ ^{17}O) relative to SMOW of analysed Ca-carbonate grains in LON 94101.
TFL is the terrestrial fractionation line (Miller et al., 2002), CCAM is the carbonaceous chondrite anhydrous mineral mixing line (Clayton et al., 1977), Y&R is the Young & Russell line (Young and Russell, 1998) are all shown for reference.

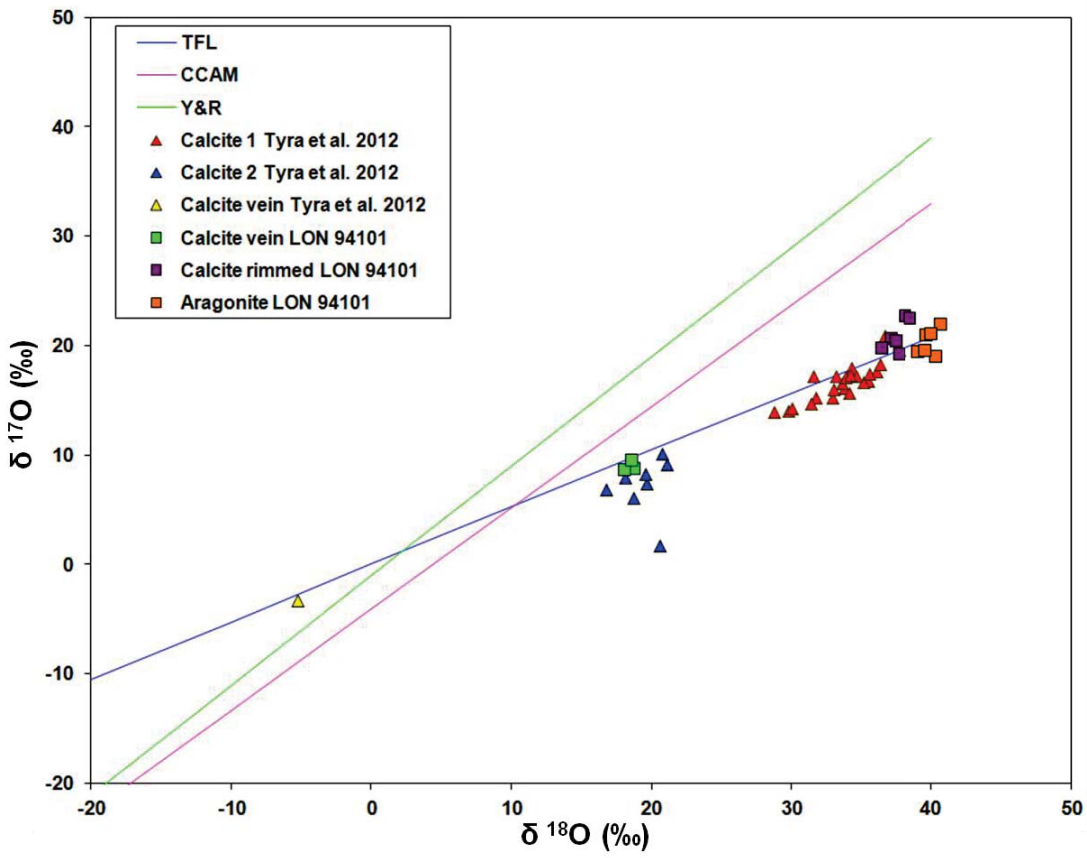

Figure 4.81- SIMS-derived oxygen isotopic compositions (relative to SMOW) of calcite and aragonite in LON 94101, and the three calcite types reported by Tyra et al. (2012).
The plot shows three populations for calcite and one for aragonite. Note that oxygen isotope compositions of calcite vein in LON 94101 lie very close to calcite type 2 (Tyra et al. (2012) that is extraterrestrial and far from oxygen isotope compositions of terrestrial calcite vein of Tyra et al. (2012). Note also that the oxygen isotope compositions of calcite rimmed with tochilinite in LON 94101 lie close to calcite type 1 of Tyra et al. (2012).

The terrestrial fractionation line (TFL) is usually plotted on a $\delta^{17}O$ vs $\delta^{18}O$ graph for reference only. It is along this line that all minerals formed on the Earth and moon by mass-dependent fractionation of oxygen isotopes (e.g. melting) will plot. The gradient of the line is 0.52, which defines the slope of mass-dependent fractionation on any planetary body. Primitive asteroids plot in a separate part of the $\delta^{17}O$- $\delta^{18}O$ graph to the Earth-moon system, as they formed in a different part of the solar nebula, which had a different initial O isotope composition. Any mass-dependent fractionation process on an asteroid will cause its O isotopes to move along the 0.52 line. However, in the case of carbonaceous chondrite parent bodies, they have two components with different initial O isotope compositions; namely high temperature silicates, and water and carbon dioxide ices, which must have formed in different parts of the solar nebula. As the carbonates in CM2 meteorites formed by mixing of oxygen from these two reservoirs, their O isotope compositions will lie along a mixing line between ice and primary silicates, which has a gradient of ~0.62 (Benedix et al., 2003).

4.9 Summary

The petrographic observations of less altered CM2 chondrites (CM2.5-CM2.3) show that they contain only Ca-carbonate minerals (both aragonite and calcite). These minerals vary in abundance, chemical composition and also in their relationships with the fine grained (<1μm) matrix between subtypes of samples studied. The petrographic characteristics of these minerals are briefly summarised and related to the alteration degree of each sample studied, as shown in Table 4.25

Sub type	2.5	2.5	2.4	2.3	2.3	2.3
Meteorite	**Murchison**	**Murray**	**Pollen**	**Mighei**	**EET 96029**	**LON 94101**
Abundance of aragonite	very rare (13 grains in 6mm^2)	very rare (5 grains in 102mm^2)	very rare (10 grains in 45mm^2)	rare (16 grains in 96mm^2)	--	common (26 grains in 105mm^2)
Aragonite-calcite intergrowth	present (2 grain)	--	present (1 grain)	--	--	--
Aragonite occurrence	2 clusters	2 clusters	2 clusters	scattered	--	scattered
Aragonite size	<20µm	10-15µm, 75µm length	<20µm	<90µm	--	<40µm
Dissolution of aragonite	preserved	preserved	preserved	etched	--	etched
Aragonite twinning	one grain twined	twined	--	--	--	--
CL types aragonite	I	I	I	I& XIII	--	I
Calcite veins	--	--	--	--	--	present
Pseudomorphs after calcite	0.2vol%	--	3.2vol%	--	--	14.2vol%
Presence of calcite replacing olivine	0.3% of the calcite grains	1.1% of the calcite grains	2.3% of the calcite grains	0.4% of the calcite grains	0.5% of the calcite grains	2.9% of the calcite grains
Dissolution of calcite	preserved	preserved	preserved	slightly etched	95% of the grains are etched	slightly etched
Calcite twinning	2% of the grains are tiwinned	3% of the grains are tiwinned	3% of the grains are tiwinned	0.7% of the grains are tiwinned	0.5% of the grains are tiwinned	3.4% of the grains are tiwinned
No. of CL types	6 types	11 types	7 types	8 types	1 type	5 types
Timing of calcite relative to aragonite	aragonite prior to calcite	calcite prior to aragonite	--	--	--	--
Presence of fluid inclusions	4 grains in 6mm^2	--	--	5 grains in 45mm^2	--	--

Table 4.25- Summary of the main petrographic variations of aragonite and calcite in samples studied (CM2.5-CM2.3).
Note the aragonite data of Murray published by Lee and Ellen (2008) are used in this study.

The occurrence of carbonate minerals (aragonite and calcite) and pseudomorphs after calcite relative to the alteration degree of CM chondrites (CM2.5 to CM2.3) can be summarized as follows: Aragonite present in less altered CM chondrites (Murchison, Murray and Pollen) and moderately altered CM chondrites (Mighei and LON 94101) with the exception of EET 96029, which contains only calcite. Aragonite occurs mainly as isolated clusters in less altered CM chondrites (e.g. Figure 4.1), whereas moderately altered CM chondrites contain larger and more widely distributed aragonite grains. Murchison contains two grains of aragonite-calcite intergrowth, which are nearly completely enclosed

by tochilinite (e.g.Figure 4.7). The crystals of aragonite in the aragonite-calcite intergrowth are on the outer edge, and have sharp and planar boundaries with calcite. The crystallographic orientation maps of aragonite grains in Murchison, Pollen and LON 94101 reveal two generations that differ in orientation. Some grains have their c-axes inclined at high angles to the surface of the thin section (around the centre of the pole figure), while other grains have c-axes that are inclined at low angles (close to the circumference of the pole figure) relative to the thin section surface (e.g. Figure 4.42 and Figure 4.74). These two generations may have formed consecutively, as the orientation map of an aragonite grain in Murchison suggests two different crystallization episodes within a pore space (see Figure 4.14).

About 95% of aragonite grains in the samples studied (Murchison, Mighei and LON 94101) show homogeneous SEM-CL characteristics (i.e. low or high CL throughout a grain (e.g. Figure 4.18)), which indicates that the aragonite precipitated from chemically stable fluids. However, two aragonite grains in Mighei show SEM-CL type II (complex zoning) and SEM-CL type XIII (oscillatory zoning), and one aragonite grain in Pollen shows SEM-CL type V (High CL throughout the grain with well defined thin layer (0.2-1 μm) of low CL cross-cutting the grain).

CM chondrites (CM2.5 to CM2.3) contain several calcite generations (see Figure 4.38 and Figure 4.69) that are classified as follows: calcite free of rims and inclusions, that is comparable in texture and appearance to most of the aragonite grains (e.g. Figure 4.38 c-d).The majority of calcite grains in EET 96029 are free of rims and inclusions, and, in common with aragonite grains in other CMs (Murchison, Pollen, Mighei and LON 94101), the grains are euhedral and have sharp contacts with the matrix. It is thus possible that the aragonite was replaced by calcite in the parent body of EET 96029, or within a small region (on the scale of millimetres) in the parent body of CM chondrites. Calcite free of rims and inclusions exhibits more complex CL patterns than aragonite grains. This indicates that this calcite precipitated from fluids that were compositionally less stable than those from which aragonite crystallized.

CM chondrites (Murchison, Pollen, Mighei, EET 96029 and LON 94101) contain calcite rimmed with tochilinite and/or Fe-sulphide, which in many cases have been replaced by Mg-rich serpentine and/or tochilinite. SEM-CL characteristics of rimmed calcite are more complex than those of other carbonate minerals (aragonite, calcite free of rims) in these CM chondrites. However, the most complicated SEM-CL characteristics have been found

in grains from Murray (CM2.5/2.4), Pollen (CM2.4) and Mighei (CM2.3) (e.g. Table 4.3 and Figure 4.31), while SEM-CL characteristics gradually become simpler towards the moderately altered CM2.3 chondrites (LON 94101 and EET 96029). SEM-CL characteristics of calcite rimmed with tochilinite provide good evidence that this calcite was precipitated from small pockets of water by nucleation of a seed crystal within one part of a void, growing to fill the pore until the space or solution was used up (i.e. SEM-CL type viii, see Figure 4.31a-b).

Petrographic observations of calcite replacing original anhydrous minerals (i.e. pyroxene and Mg-rich olivine) show that calcite after pyroxene is free of inclusions (e.g. Figure 4.49a) whereas calcite replacing olivine often contains inclusions of sulphide, and is composed of numerous sub-crystals (Figure 4.38b). Calcite replacing Mg-rich olivine is found in all the studied CM chondrites (Murchison, Murray, Pollen, Mighei, EET 96029 and LON 94101), but varies in abundance from meteorite to meteorite. It represents ~3% of the calcite grains, and regions replaced exceed ~300 μm in LON 94101 (CM2.3).

Micro to millimetre-sized veins of calcite are present in LON 94101 (CM2.3); micro veins are associated with blocky grains of pentlandite. BSE images of the calcite vein (millimetre-sized) in LON 94101 show that this calcite overgrows calcite rimmed with tochilinite (Figure 4.71 a), suggesting that the calcite vein formed later. Pseudomorphs of calcite grains (calcite rimmed with tochilinite and/or Fe-sulphide) made of Mg-rich serpentine, or Mg-rich serpentine intergrown with tochilinite, are present mainly in LON 94101 (CM2.3). Mg-rich serpentine after calcite is also present in Pollen (CM2.4). TEM results show that the Mg-rich serpentine is not crystalline, but rather dominated by fibres with pores between them (see Figure 4.52 c-d). Chemical analyses of these pseudomorphs indicate that Mg-rich serpentine pseudomorphs formed from fluids that were richer in Mg than Fe, whereas tochilinite-serpentine pseudomorphs are likely to have crystallized from solutions that contained high concentrations of Fe, S and Ni.

Oxygen isotope analyses reveal that the calcite vein has significantly lower $\delta^{17}O$ and $\delta^{18}O$ than calcite grains and aragonite, and plots very close to the calcite type 2 described by Tyra et al. (2012) (see Figure 4.81). The oxygen isotope composition of aragonite in LON 94101 is slightly higher than calcite rimmed with tochilinite and the type 1 calcite of Antarctic chondrites in $\delta^{18}O$ (Tyra et al., 2012), suggesting that the aragonite formed at a different time from calcite.

5

Carbonate minerals in CM2.2/2.3 to CM2.1 chondrites

5.1 Introduction

This chapter describes carbonate minerals that are present in moderately and highly altered CM chondrites (CM2.2/2.3 to CM 2.1). The carbonate minerals are found mainly in the fine grained (<1μm) matrix of CM2.2/2.3 Nogoya, CM2.2 Cold Bokkeveld and CM2.1 QUE 93005. The carbonate minerals within the CM2.2/2.3 to CM2.1 meteorites are aragonite, calcite, dolomite, Ca-poor dolomite and breunnerite.

Petrographic description (distribution, texture, grain size etc.) and chemical characterisation (CL imaging, X-ray mapping, EDS qualitative analyses and quantitative chemical analyses) of carbonates in each sample is provided in this chapter. This chapter also highlights post-crystallization/replacement and deformation (i.e. twinning and pseudomorphs after calcite, aragonite and dolomite) of carbonate minerals.

5.2 Carbonates in CM2.2/2.3 Nogoya

5.2.1 Introduction

Bunch and Chang (1980) reported that chondrules and aggregates in Nogoya contain calcite that formed as the result of replacement. Carbonate minerals in Nogoya and other chondrites were analysed for their carbon and oxygen isotopic compositions by Grady et al. (1988). Benedix et al. (2003) found that calcite grains are present mainly as products of replacement in chondrules in Nogoya. They occur as aggregates that contain patches of

small grains of sulphides. A vein of calcite is found in the meteorite, and the vein is in contact with the aggregate grain of calcite. Single grains of calcite are occasionally present. Dolomite was reported to be observed in Nogoya by Johnson and Prinz (1993) who chemically analysed its calcite and dolomite. De Leuw et al. (2010) found that Nogoya contains 1.4 vol% carbonate minerals, and dolomite was present as a single grain 20 μm in size. Calcite occurs as single grains (20-30 μm) and aggregates (<70 μm) (De Leuw et al. 2010). The PSD-XRD quantitative modal mineralogy of CM chondrites by Howard et al. (2011) showed that Nogoya contains 1.1 vol% of calcite. Aragonite and dolomite were described in Nogoya by Sofe et al. (2011b).

5.2.2 Petrographic observations

Petrographic observations show that three carbonate minerals are present in Nogoya, namely aragonite, calcite and dolomite. As described in section 3.12.1, Nogoya contains two different lithologies, which are highly altered (CM2.2) and less altered (CM2.3), and these two differ in mineralogy and alteration degree (see Figure 3.35). The less altered lithology (CM2.2) contains aragonite, calcite and dolomite, whereas the highly altered one (CM2.3) contains only calcite (Figure 5.1). Nogoya has 2.1 vol % Ca-carbonate overall.

Calcite in the CM2.2 lithology is found in a variety of contexts that include: (i) grains free of inclusions and rims that occur in contact with the fine grained (<1μm) matrix, (ii) calcite grains that are enclosed within serpentine or serpentine and Fe-sulphide intergrowths, (iii) calcite grains that are entirely or partially surrounded by blocky grains of pentlandite, which are also present as inclusions within some grains, (iv) calcite intergrown with fibres of serpentine with and without blocky grains of pentlandite, (v) calcite grains that are surrounded by thin rims (0.5-1 μm) of tochilinite, (vi) calcite replacing Mg, Fe silicates; this calcite contains very small inclusions of pentlandite. Some of these grains are found within large altered chondrules (1mm); in some cases, also, parts of Mg, Fe silicates are found around or within this calcite.

Calcite in the CM2.2 lithology occurs as single grains and aggregates and with a grain size ranging from a few microns to ~80 μm. One grain calcite replacing Mg, Fe silicates has a grain size of about 200 μm. The majority of calcite grains in this lithology are irregular or sub-rounded. Some grains have only one or two sharp boundaries with surrounding materials, but the outer areas of these boundaries are clearly embayed or replaced by phyllosilicates. It was also observed that most calcite grains are likely to have dissolved in

their outer and internal areas. The vesicular texture (fluid inclusions) is also present in some grains or whole parts of some calcite grains in this part of studied sample (Figure 5.2). Some grains that are free of rims and inclusions and others are surrounded by thick rims of serpentine. The fluid inclusions are very abundant in the highly altered part.

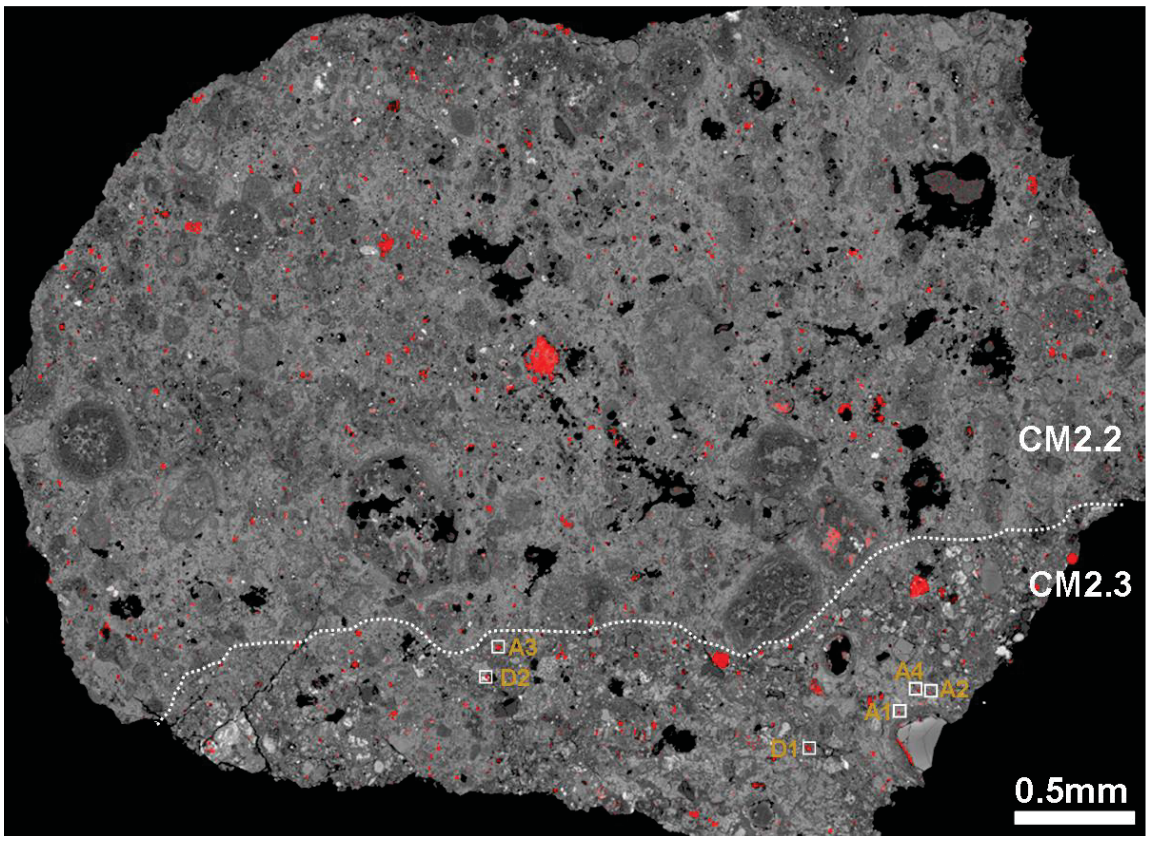

Figure 5.1- Ca X-ray map combined with BSE image of whole sample of Nogoya.
Note the variation in lithology between the less altered (CM2.3) and highly altered lithology (CM2.2) (separated with line). Ca (red areas) in this map locates all calcite grains in the sample; along with aragonite grains (A1-A4) and dolomite grains (D1 and D2) in the less altered lithology.

The CM2.3 lithology contains four grains of aragonite and two grains of dolomite. Calcite grains are petrographically different to grains in the CM2.2 lithology. Calcite grains in this lithology occur in three contexts, including: (i) a few grains of calcite which are free of inclusions and rims, and have a grain size of 2 or 3 μm to ~ 40 μm; (ii) a few grains replacing olivine, where some of the olivine grains are partly or totally replaced by calcite (Figure 5.3 a), (iii) calcite is partly or totally rimmed by tochilinite. In most cases, this calcite contains inclusions of Fe-sulphide. This variety of calcite has also been partly or nearly completely replaced by either tochilinite or Mg-rich serpentine (Figure 5.3 b). It has a grain size ranging from ~5μm to ~20μm. It exhibits in most cases one or more sharp boundaries with enclosed materials.

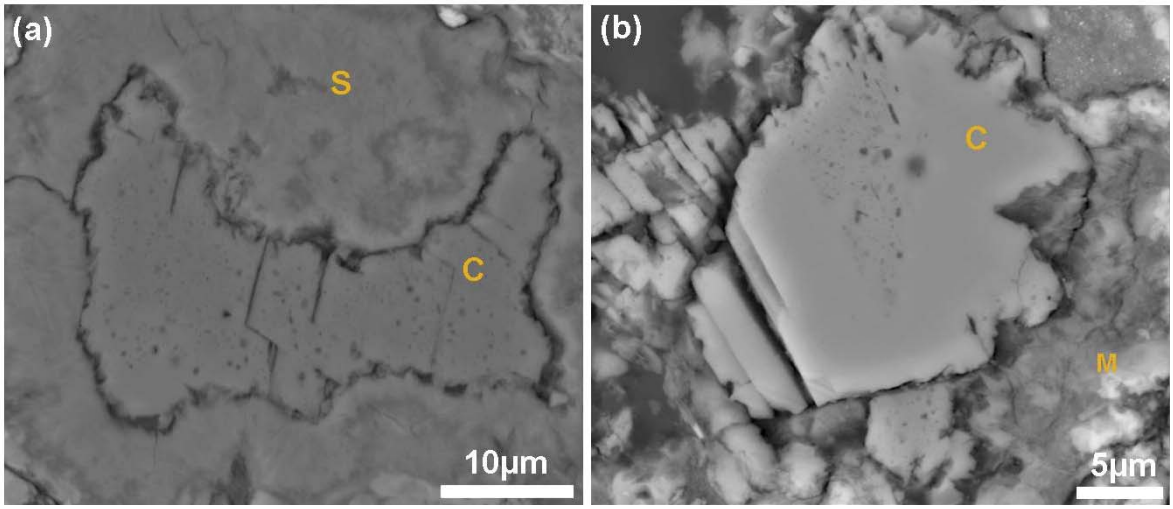

Figure 5.2- BSE images showing the occurrence of fluid inclusions in calcite grains of Nogoya.
(a) Calcite grain (C) enclosed with thick layer of serpentine (S), and the grain is etched in the margins; note the vesicular texture in all areas of the grain. (b) Calcite grain (C) in direct contact with fine grained (<1µm) matrix (M). Part of the grain has vesicular texture, note the other areas of the grain that occur as growth band. The locations of these grains in the sample studied are shown in appendix D7.

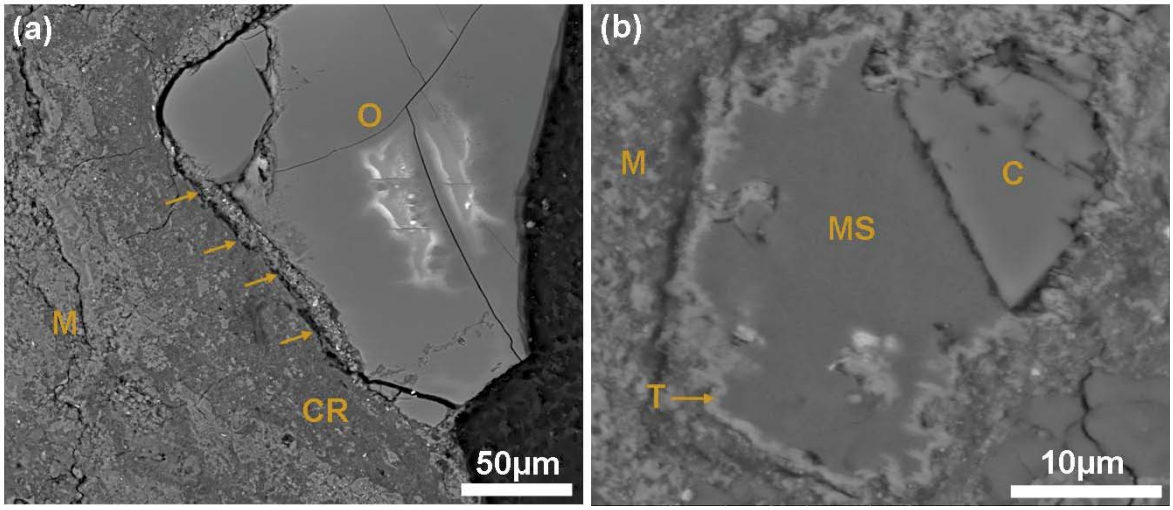

Figure 5.3- BSE images of calcite grains in the CM2.3 lithology of Nogoya.
(a) BSE image showing a large (200 µm) fragment of olivine (O) that has been partly replaced by calcite (arrowed areas). M is fine grained (<1µm) matrix, CR is chondrule rims. (b) Calcite grain (C) is near completely replaced by Mg-rich serpentine (MS). T is tochilinite rim. The locations of these grains in the sample studied are shown in appendix D7.

Three aragonite grains occur in a small cluster in the CM2.3 lithology (see Figure 5.1); they are free of rims and inclusions and have a grain size of about 5 µm. These grains were identified by Raman spectroscopy, but EBSD mapping and chemical analyses were hindered, due to their small size and the presence of holes around the grains. Another grain (A3) was found to be isolated, but shows a size of about 20µm and occurs in conjunction with Mg-rich serpentine pseudomorphs, which have replaced some of calcite grains in this

part of Nogoya. Both aragonite (A3) and Mg-rich serpentine are surrounded by thin rims of tochilinite (0.5-1 μm). Holes around the outer areas of the aragonite (A3) contain very small amounts of aragonite that are likely to be the remains of dissolution of the margins of the main grain (Figure 5.4 a).

As stated above, the CM2.3 lithology contains two grains of dolomite (see Figure 5.1). One grain (Figure 5.4 b) is subhedral in shape, surrounded by a thin rim of serpentine and is intergrown with blocky grains of pentlandite; it has size of ~ 15μm. The other grain is elongated in shape (see Figure 5.7 a). It is about 30μm long and its average width is about 15 μm. A small grain of pentlandite occurs as an inclusion within it. This dolomite grain and a small grain of Mg-rich serpentine (~2μm) are both enclosed with thin rims of cronstedtite (0.3 μm).

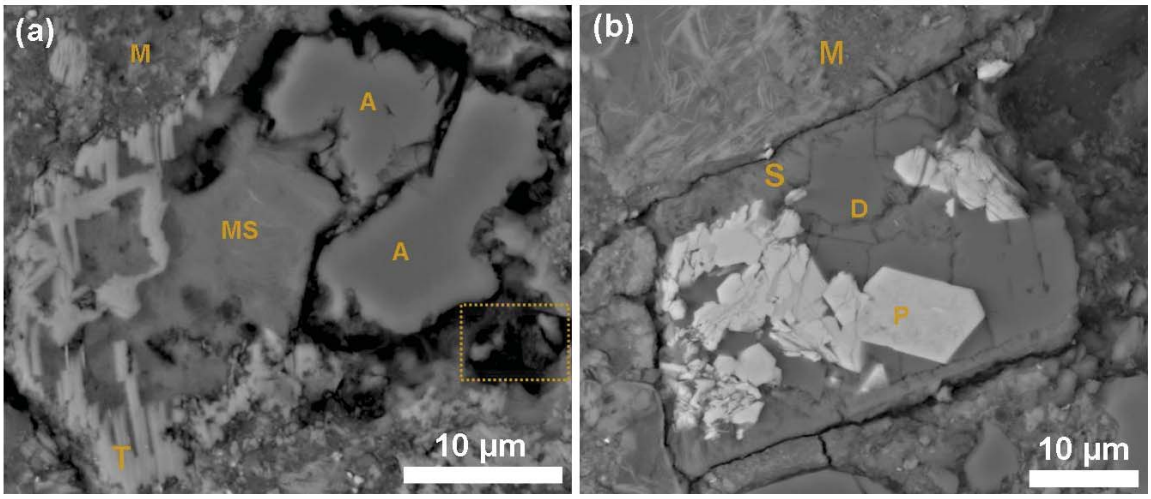

Figure 5.4- BSE images of aragonite and dolomite in the CM2.3 lithology of Nogoya.
(a) BSE image of aragonite (A) (A3 in Figure 5.1). Areas of this grain have probably been dissolved as the holes around the grain contain small fragments of aragonite (e.g. boxed area). Mg-rich serpentine (MS) is likely to be a pseudomorph after aragonite. T is tochilinite. (b) Dolomite grain (D) (D2 in Figure 5.1) is intergrown with pentlandite (P) and both are rimmed by serpentine (S). M is fine grained (<1μm) matrix. The locations of these grains in the sample studied are shown in Figure 5.1.

5.2.3 Chemical composition of carbonate minerals in Nogoya

Thirteen chemical analyses of carbonate minerals in Nogoya were carried out by Johnson and Prinz (1993). Their analyses showed that dolomite has $FeCO_3$ concentrations ranging from 3.6 to 5.2 mol% and $MnCO_3$ from 3.0 to 5.6 mol%. Twenty one chemical analyses of calcite grains and two chemical analyses of dolomite in Nogoya were acquired by De Leuw et al. (2010). Their analyses showed that dolomite has an average of 4.1 ± 0.5 mol% $FeCO_3$ and 3.1 ± 0.6 mol% $MnCO_3$, whereas calcite contains 0.69 ± 0.66 of $FeCO_3$ and

0.31 ± 0.27 of $MnCO_3$. In this study, CL images of calcite grains were obtained, and coupled with elemental mapping using the Zeiss Sigma SEM and quantitative chemical analyses by EPMA.

5.2.3.1 CL imaging

CL images were obtained from 42 grains of calcite that differ in petrographic features (e.g. grains of calcite free of rims, calcite replacing olivine etc.). Some of these grains are located in the CM2.3 lithology and others in the CM2.2 lithology, but the majority are from the CM2.2. CL characteristics of these calcite grains are summarized as following: (1) the majority (38) of the grains have CL type I (low or high CL through out a grain, but in very cases the grain has patches of very high CL) (Figure 5.5); (2) CL type VII characterizes four calcite grains. This type is described as very high CL intensity and covers all areas of a grain with thin rims (0.2-1 μm) of high CL intensity; (3) only one grain showed CL type IX, that is a very low CL intensity core and the subsequent band is high CL.

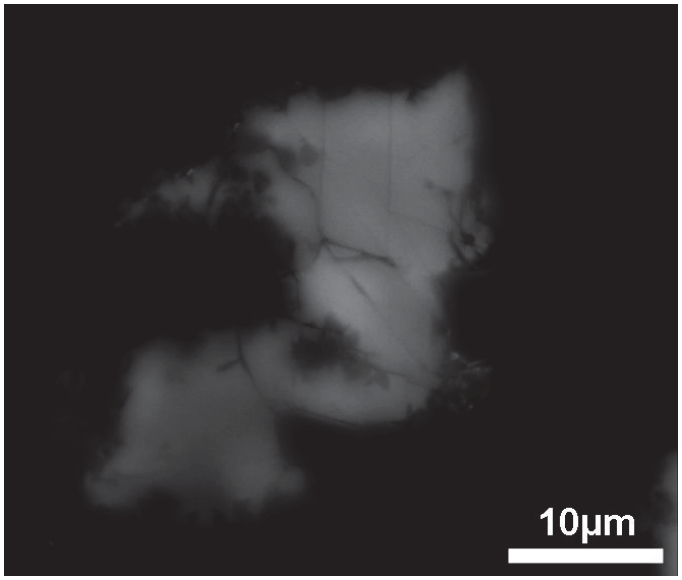

Figure 5.5- CL image of a calcite grain in Nogoya.
The image shows CL type I, in this case low CL intensity through out the grain. This CL type characterizes the majority of calcite grains in Nogoya. The location of this grain in the sample studied is shown in appendix D7.

5.2.3.2 Quantitative chemical analyses of carbonate minerals in Nogoya

Fourteen grains of calcite that vary in petrographic features were chemically analysed. The two dolomite grains and one grain of aragonite were also analysed by EPMA. All analyses were obtained from areas that are free of inclusions and sufficiently far from surrounding

materials. The means of these analyses are listed in Table 5.1 and Table 5.2. The aragonite analysed in Nogoya shows lower $FeCO_3$ (~0.25 to 1.0 mol%) in comparison with aragonite analyses of less altered meteorites (discussed above). Chemical analyses show that the calcite grains (completely rimmed and free of rims) in LON 94101 are nearly identical in $FeCO_3$ (mean 0.68 ± 0.08 mol%) to calcite grains in the CM2.3 lithology of Nogoya. Chemical analyses show also that the two dolomite grains are rich in $FeCO_3$ (8.29 mol%) and $MnCO_3$ (2.45). These grains show higher $FeCO_3$ values than found by Johnson and Prinz (1993) and De Leuw et al. (2010) (Table 5.1). However, one of the two grains analysed is richer in $FeCO_3$ (+ ~5.5 mol%) in comparison with the other dolomite grain, that also contain less $MnCO_3$ (Table 5.3).

Wt %	Ca	Mg	Sr	Fe	Mn	SUM	*n*
Aragonite (A3)	41.90	0.03	0.13	0.28	0.00	59.55	1
Calcite	41.80	0.10	0.00	0.49	0.00	59.34	17
Dolomite	20.09	10.75	0.00	4.89	1.43	54.17	4
Mole%	**$CaCO_3$**	**$MgCO_3$**	**$SrCO_3$**	**$FeCO_3$**	**$MnCO_3$**	**Sum**	***n***
Aragonite (A3)	99.26	0.12	0.14	0.47	0.00	100.00	1
Calcite	98.79± 1.05	0.38 ± 0.58	0.00 ± 0.00	0.83 ± 0.55	0.00± 0.00	100.00	17
Dolomite	47.42± 3.71	41.84 ± 0.95	0.00 ± 0.00	8.29 ± 2.78	2.45 ± 1.05	100.00	4
Dolomite[1] 1993	56.07	36.23	--	3.80	3.87	100.00	3
Dolomite[2] 2010	53.05 ± 1.1	39.80 ± 0.02	0.00	4.05± 0.5	3.10±0.6	100.00	2

Table 5.1- Chemical analyses of carbonate grains in Nogoya.
The analyses were obtained from 1 grain of aragonite (A3), 14 grains of calcite and 2 grains of dolomite. Data presented as mean ± SD, error values are calculated to 1σ. Dolomite[1] is the average of dolomite analyses by Johnson and Prinz (1993), dolomite[2] is the average of dolomite analyses by De Leuw et al. (2010). The full dataset with standard deviation is listed in appendix B-7.

Wt%	Ca	Mg	Sr	Fe	Mn	Sum	No. analyses
CM2.2	41.76	0.13	0.00	0.52	0.00	42.41	11
CM2.3	41.88	0.04	0.00	0.43	0.00	42.34	6
Mol%	**$CaCO_3$**	**$MgCO_3$**	**$SrCO_3$**	**$FeCO_3$**	**$MnCO_3$**	**Sum**	**No. analyses**
CM2.2	98.61	0.50	0.00	0.88	0.00	100.00	11
CM2.3	99.10	0.16	0.00	0.74	0.00	100.00	6

Table 5.2- Chemical analyses of calcite grains in the CM2.2 and CM2.3 lithologies of Nogoya.

Mol%	$CaCO_3$	$MgCO_3$	$SrCO_3$	$FeCO_3$	$MnCO_3$	Sum
Dolomite 1- point 1	46.18	40.75	0.00	10.56	2.51	100.00
Dolomite 1- point 3	42.87	42.39	0.00	10.82	3.92	100.00
Dolomite 2- point 1	51.41	41.37	0.00	5.64	1.58	100.00
Dolomite 2- point 2	49.21	42.83	0.00	6.16	1.80	100.00

Table 5.3- Chemical analyses of two dolomite grains in the CM2.3 lithology of Nogoya.
Note the differences in $FeCO_3$ and $MnCO_3$ between the two grains.

5.2.4 Post crystallization deformation of carbonates in Nogoya

BSE images of carbonate grains in Nogoya indicate that a few of the calcite grains exhibit shocked induced twining. The lamellar twins in these grains are straight and thin (~0.5 µm), which are classified as twinning type I. Petrographic observations also show that some calcite grains in Nogoya have been replaced by Mg-rich serpentine.

5.2.4.1 Pseudomorphs after carbonates in Nogoya

The meteorite contains 6.03 vol% pseudomorphs after calcite. These materials are mainly present in the CM2.3 lithology and formed only from the calcite grains that are rimmed with tochilinite. The calcite grains have been partially, moderately or totally replaced by Mg-rich serpentine (e.g. Figure 5.6). The texture of Mg-rich serpentine after calcite in Nogoya is comparable to Mg-rich serpentine pseudomorphs after calcite in Pollen. Mg-rich serpentine in the CM2.3 lithology of Nogoya shows a very fine texture compared with the matrix. One grain of aragonite (A3) is also found in conjunction with Mg-rich serpentine that probably has partly replaced the aragonite (Figure 5.4 a).

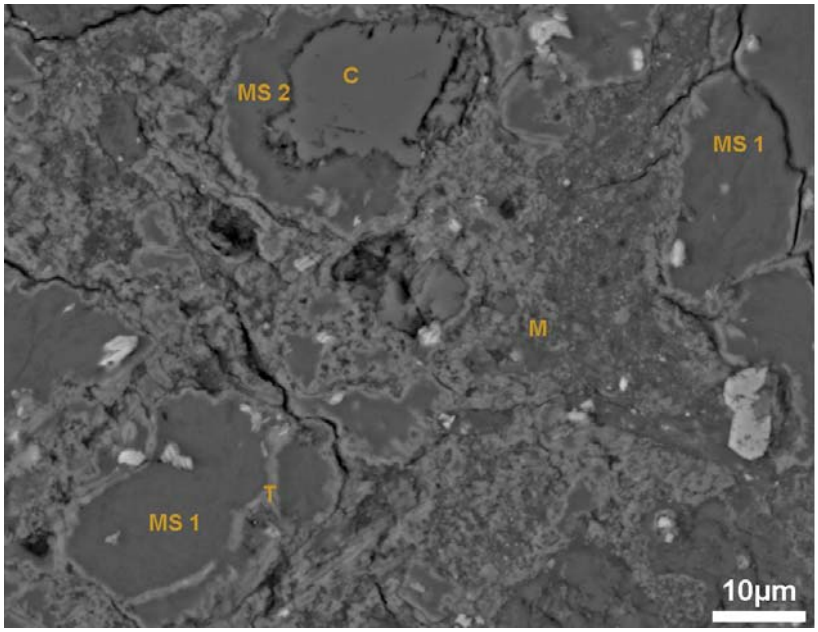

Figure 5.6- BSE image showing the replacement of calcite by Mg-rich serpentine in the CM 2.3 lithology of Nogoya.
MS 1 is Mg-rich serpentine that has completely replaced calcite, MS 2 is Mg-rich serpentine that has partly replaced calcite (C). M is fine grained (<1µm) matrix. The location of this map in the sample studied is shown in appendix D7.

5.2.5 TEM of dolomite and associated minerals & Mg-rich serpentine after calcite

Samples for TEM work were cut using the FIB technique from the two dolomite grains and enclosing materials including the rims to the grain and the fine grained (<1μm) matrix. The third sample was extracted from Mg-rich serpentine that has replaced calcite; this sample contains both Mg-rich serpentine and calcite. The data obtained from this work are: (i) electron diffraction patterns which are used to identify minerals from their crystal structure, (ii) high resolution images that are used to describe the internal structure of the sample and relationships between minerals.

The first sample (~8 μm in length) contains a part of dolomite grain 1, rims around the grain and Mg-rich serpentine (see Figure 5.7 a). TEM images show that the dolomite contains a sub-grain (D2) (Figure 5.7 a-d) between the main dolomite grain (D1) and the cronstedtite rim (R). This sub grain has a mottled texture and part of it contains fibres that are terminated by the main grain of the dolomite (D1) that has fewer defects. These grains are likely to have formed in different orientations (see Figure 5.7 c). Results also show that the rim around this dolomite grain is composed mainly of plate and ribbon shaped crystals that are characteristic of cronstedtite (Barber, 1981) as well as containing fractures that correspond to the boundary between the rims and dolomite sub-grain (Figure 5.7 c). The plate-like crystals in these rims appear darker than the ribbon-like crystals. The darker areas in TEM images of cronstedtite crystals in Cold Bokkeveld were described as crystal that was more strongly diffracting electrons by Greenwood et al. (1994). These rims contain fibres (Figure 5.7 c) that terminate with the dolomite sub-grain (D2). The TEM data shows that the Mg-serpentine is poorly crystalline and composed mainly of fibres in contact with pores (Figure 5.7 d). The sequence of events can be summarised as follows: (i) the main grain of dolomite (D1) was initially formed; (ii) subsequent event is the formation of the sub-grain (D2); (iii) the cronstedtite rim then crystallized. The differences in texture between the dolomite sub-grain and the main dolomite grain and the features of the boundary between these grains suggest that different conditions were probably involved during the formation of these dolomite crystals. EDS spectra of grains in this foil were obtained using the Sigma SEM with INCA software. Spectra confirm the presence of dolomite, cronstedtite and Mg-rich serpentine (Figure 5.7 x1-x6). Diffraction patterns of cronstedtite (Figure 5.8) correlate well with its chemical composition (Figure 5.7 x2).

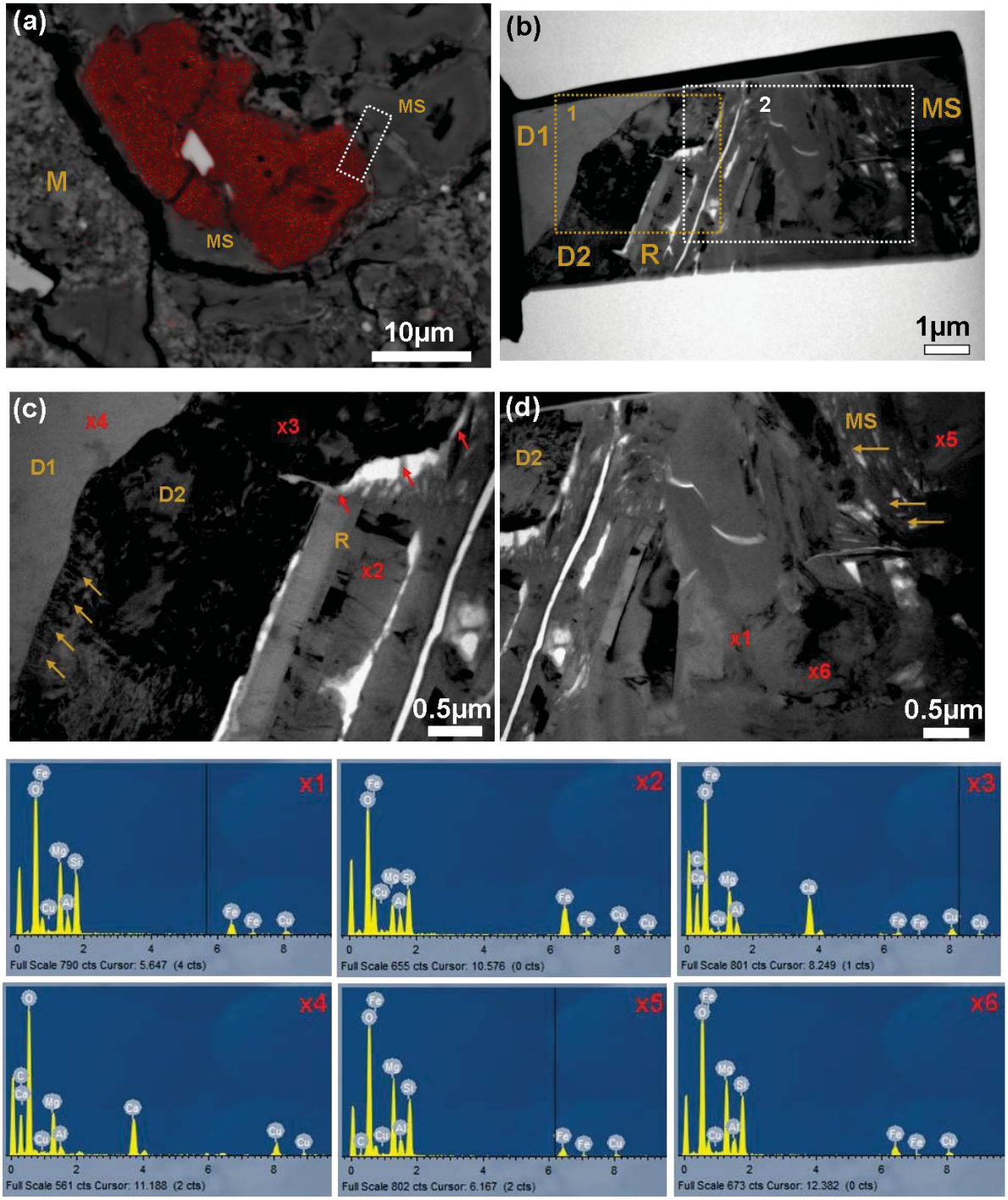

Figure 5.7- BSE image and bright-field TEM images of a dolomite grain and enclosing materials in Nogoya.
(a) Ca X-ray map combined with BSE image showing the location from which FIB 1 was extracted (boxed area). The red area is the dolomite grain, MS is Mg-rich serpentine, M is fine grained (<1µm) matrix. (b) TEM image showing the overall textural variations between the materials examined in this foil. D1 is the main grain of dolomite, D2 is the dolomite sub-grain, R is cronstedtite rim, MS is Mg-rich serpentine. (c) Bright field TEM image of the boxed area 1 in (b). Note the difference in texture between the D1, D2 and R. Note also the small fibres in D2 (yellow arrows) that are perpendicular with D1 and the fibres in R (arrowed in red) that terminate D2. (d) Bright field TEM image of the boxed region 2 in (b) showing the 'spongy' texture of Mg-rich serpentine (MS) (upper left part of the image). x1 is EDs spectrum of serpentine obtained from x1 in (d). x2 is EDS spectrum of cronstedtite obtained from x2 in (c). x3 and x4 are EDs spectra obtained of dolomite D2 and D1 respectively in (c). x5 and x6 are EDS spectra of serpentine obtained from x5 and x6 in (d). Note that the Al and Cu in these spectra are contaminants. The locations of this grain in the sample studied are shown in Figure 5.1 (D1).

Greenwood et al. (1994) showed that the diffraction patterns of cronstedtite rimming spinel-pyroxene in Cold Bokkeveld has spots in the basal row with spacing of about 0.71 nm, and their observations are in close correlation with this study, which shows the diffraction patterns of cronstedtite rims around the dolomite contain spots with spacing of ~0.72 nm (Figure 5.8).

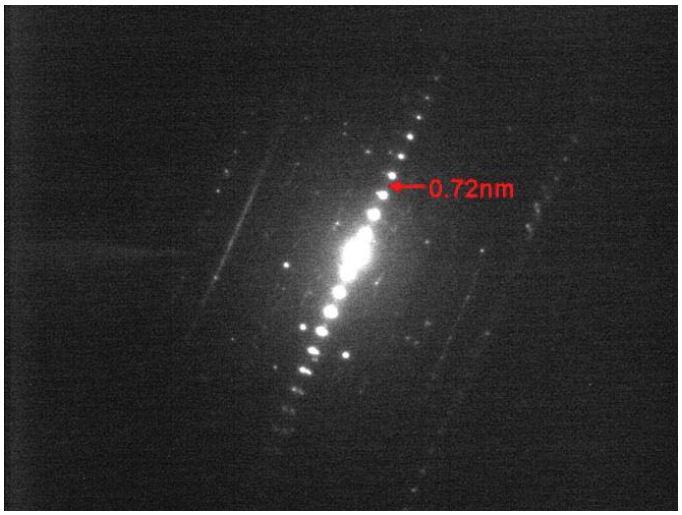

Figure 5.8- Selected area electron diffraction pattern of cronstedtite rims around dolomite. The d-spacing of the spots is about 0.72 nm.

TEM results from part of dolomite grain 2, rims around the grain and a part from the fine grained (<1μm) matrix (Figure 5.9 a) display clear variations in microstructure between these materials (Figure 5.9 b). The dolomite is composed of several sub-grains that are separated from each other by micro-fractures. Some of these dolomite crystals show a mottled texture, whereas other sub-grains have no mottling or are slightly mottled (Figure 5.9 b). These dolomite grains are likely to have crystallized in different orientations. The closest dolomite sub-grain to the rims (D2 in Figure 5.9 c) is similar in texture to the sub-grain D2 in Figure 5.7 c in the previously examined dolomite grain (probably formed at the same time). Results also show that the rims around the dolomite are composed of plate and ribbon like crystals and wavy crystals (phyllosilicates). The interface between the dolomite and the rims is sutured, but it is clear that the crystals in these rims are formed on the surface of the dolomite, and the phyllosilicate has replaced dolomite (Figure 5.9 c-d). TEM results further show that the fine grained (<1μm) matrix has wavy crystals with many pores (Figure 5.9 c-d); TEM images of Cold Bokkeveld by Greenwood et al. (1994) also showed that the phyllosilicates can have several short wavy crystals. EDS spectra of grains in this foil (obtained by Sigma SEM with INCA software) indicate that inclusions of Fe-Ni sulphide occur within the dolomite (Figure 5.9 x1, x2).

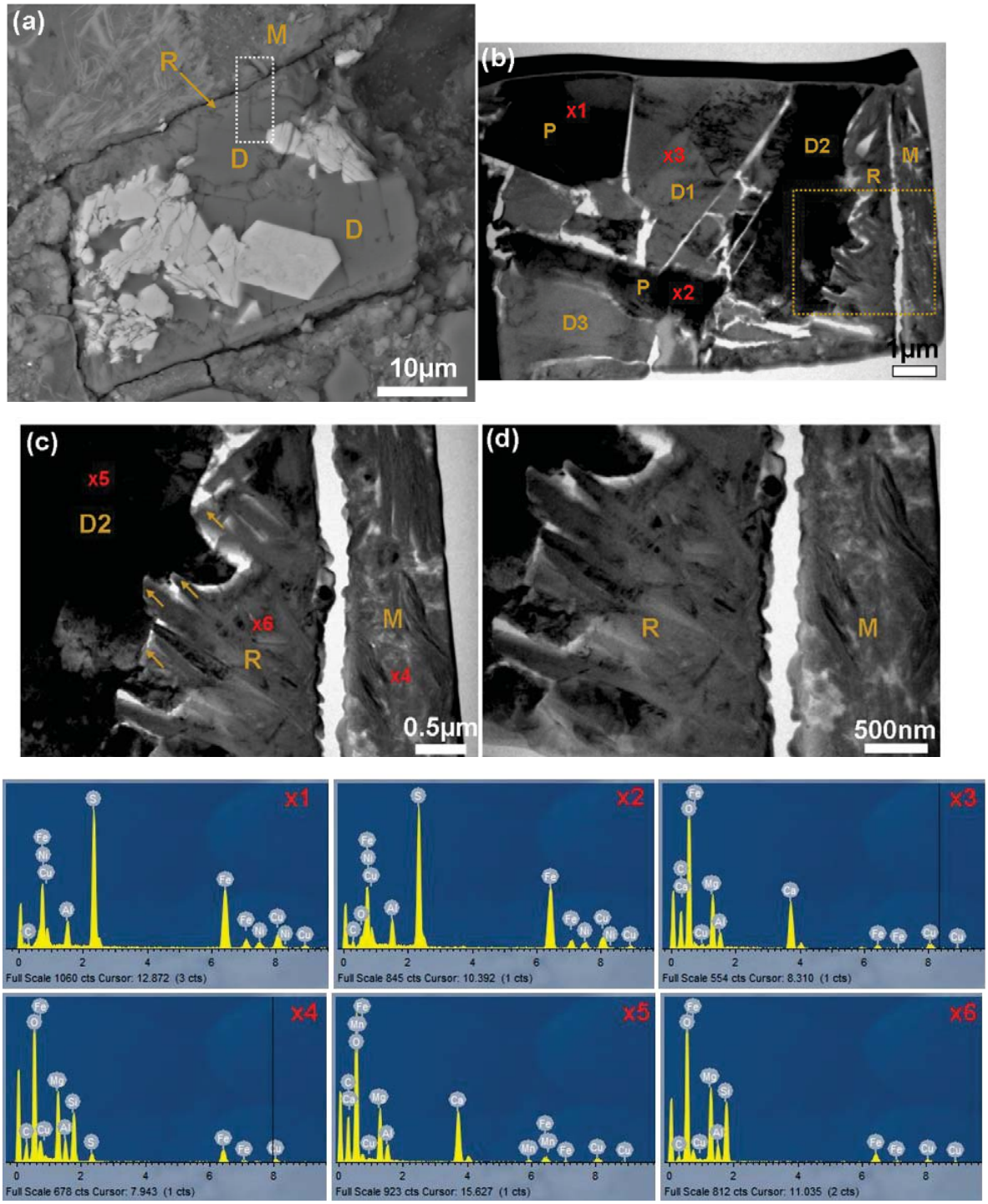

Figure 5.9- BSE image and bright-field TEM images of dolomite grain and surrounding materials in Nogoya. The grain is shown as D2 in Figure 5.1.
(a) BSE image showing the location of FIB 2 (boxed region) that contains rims (R), part of the dolomite (D) and fine grained (<1µm) matrix (M). (b) Bright-field image showing morphologic variations between dolomite sub-grains (D1, D2 and D3), rims (R), Fe-Ni sulphide (P) and the fine grained (<1µm) matrix (M). Note the difference in texture between D1 (slightly mottled), and D2 (mottled subgrains). (c) Bright-field image at high magnification of the boxed area in (b) showing the interface (arrowed area) between the dolomite sub-grain (D2) and the rims (R). The phyllosilicate is likely to have replaced the dolomite. Note the micro crystals (arrowed) of these rims have grown into the dolomite. (d) Bright-field image shows the difference in texture of the rims (R) that are denser than the materials of the fine grained matrix (M), which composed mainly of wavy crystals with pores. x1 and x2 are EDs spectra of Fe-Ni sulphide grains obtained from x1 and x2 respectively in (b). x3 is an EDS spectrum of dolomite from x3 in (b). x4 is an EDs spectrum of phyllosilicate obtained from the fine grained matrix x4 in (c). x5 is EDS spectrum of dolomite from x5 in (c). x6 is Eds spectrum of phyllosilicate obtained from the rims x4 in (c). Al and Cu are contaminants. White areas in b, c and d are pores.

The spectra obtained from the rims around the dolomite and the matrix also reveals that these materials are phyllosilicates (see Figure 5.9 x4 and x6). Diffraction patterns of these phyllosilicates (Figure 5.10) have rings and indicate that phyllosilicate of the rims is coarser. The rings of diffraction patterns from the rims have spacing of about 0.71 nm (Figure 5.10).

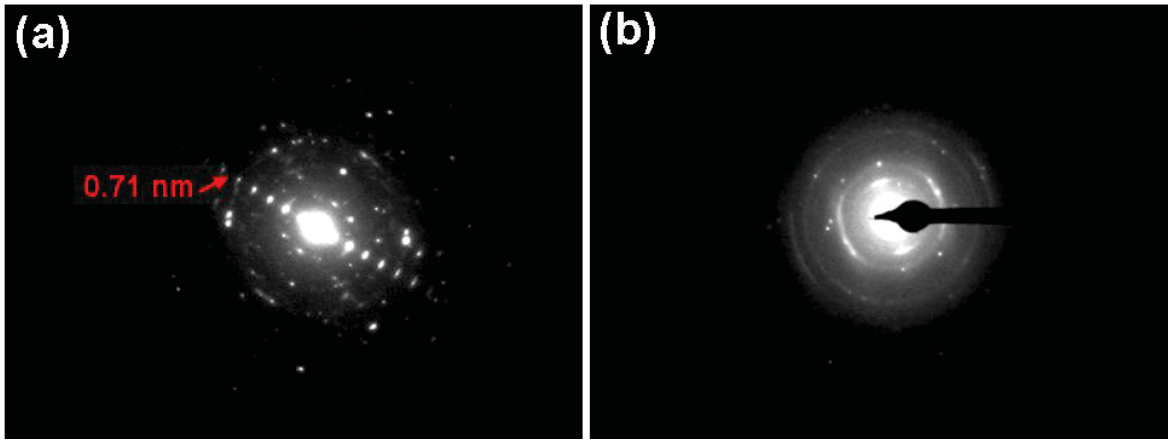

Figure 5.10- Selected area electron diffraction patterns of phyllosilicates.
(a) Diffraction patterns of the rims around dolomite that have spacing between the spots with about 0.71 nm. (b) Diffraction pattern of phyllosilicate of the fine grained matrix that form rings. Note the difference between these diffraction patterns that indicates the phyllosilicates in fine grained (<1µm) matrix are finer and randomly oriented.

FIB 3 contains a calcite grain and Mg-rich serpentine after calcite (Figure 5.11 a). This foil was removed from a grain that is located in less altered lithology (CM2.3) of Nogoya. TEM results from of this sample show that the Mg-rich serpentine is poorly crystalline and has a spongy, porous texture. It is composed of fibres and wavy flakes with pores and also contains grains of tochilinite and serpentine that show a denser texture (Figure 5.11 c-d). The internal structure of the Mg-rich serpentine and tochilinite sub-grains in this sample are comparable to those in Pollen (see Figure 4.50 c-d). These results help confirm that the calcite is likely to have been replaced by Mg-rich serpentine (Figure 5.11 b). It was also observed that the fibres of Mg-rich serpentine have initially formed on the surface of the tochilinite sub grains, indicating the Mg-rich serpentine post dates the sub-grains of tochilinite (Figure 5.11 d). EDs spectra (Figure 5.11 x1 and x2) confirm the presence of Mg-rich serpentine and tochilinite-serpentine intergrowth (contains Mg, Fe and Si) in this sample, and shows that the chemical composition of Mg-rich serpentine is equivalent to Mg-rich serpentine in Pollen (see also Figure 4.52 x2).

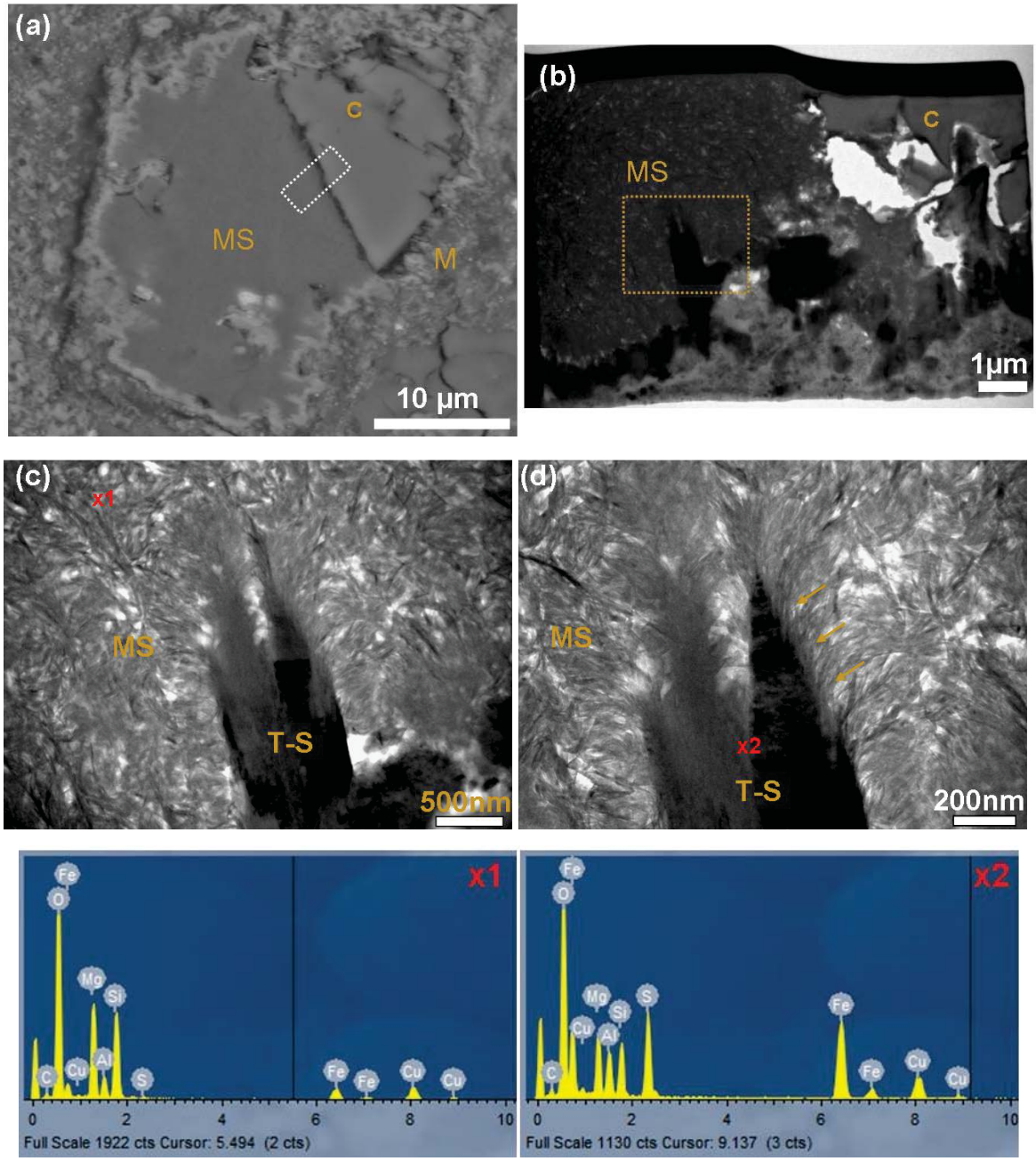

Figure 5.11- BSE image and bright-field TEM images of Mg-rich serpentine and calcite in Nogoya. (a) BSE image showing the location from which the FIB 3 was extracted. C is calcite, MS is Mg-rich serpentine, M is fine grained (<1µm) matrix. (b) Bright field image showing the internal structure of Mg-rich serpentine (MS) and calcite (c). Note the calcite is likely to be etched and replaced by serpentine and the presence of the seed crystals in the boxed area. (c) Bright-field image at high magnification of the boxed area in (b). The image shows clearly variation in texture between Mg-serpentine (MS) and the tochilinite and serpentine (T-S). These sub-grains are darker as the electrons were strongly diffracted. (d) Bright field image at high magnification showing the interface between the tochilinite-serpentine sub grains (T-S) and the main grain (MS). Note the fibres of serpentine (arrowed area) are terminated by the sub-grains. X1 is EDs spectrum of Mg-rich serpentine obtained from x1 in (c). x2 is EDs spectrum of tochilinite-serpentine obtained from x2 in (d). Cu and Al are contaminants. The locations of these grains in the sample studied are shown in appendix D7.

Diffraction patterns of Mg-rich serpentine phyllosilicate show rings indicating that these materials are composed of many randomly orientated crystals (Figure 5.12a). Diffraction patterns of the tochilinite-serpentine intergrowth in this sample show a combination of

rings and spot patterns (Figure 5.12b). The rings have spacing of ~1.08nm that represent tochilinite, whereas the spot patterns represent serpentine. The spacing between the spots of serpentine is ~0.72nm**,** yielding a combined spacing of 1.8nm for both minerals.

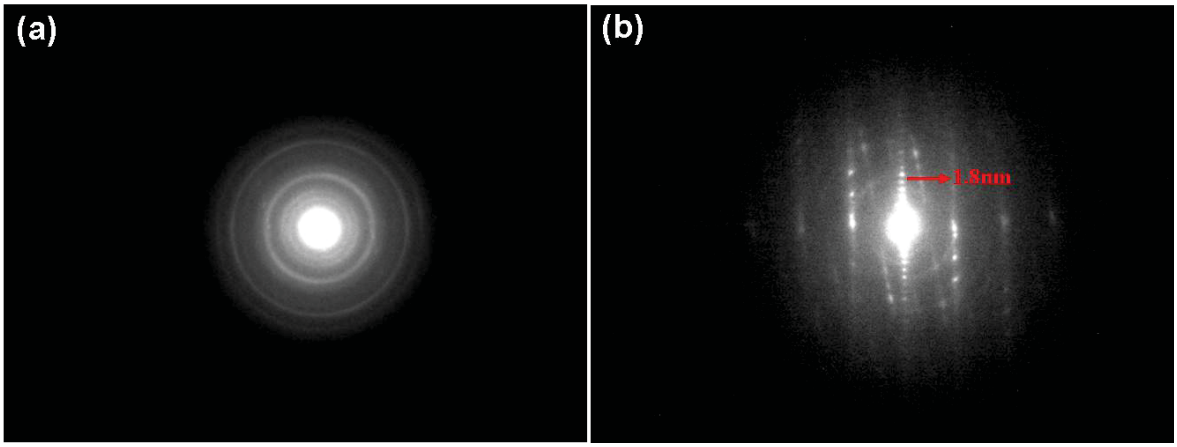

Figure 5.12 Diffraction patterns of Mg-rich serpentine and the tochilinite-serpentine intergrowth in Nogoya.
(a) Diffraction pattern of Mg-rich serpentine that has rings, indicating very fine crystallize. (b) Diffraction pattern of tochilinite-serpentine. Tochilinite spots have a spacing of about 1.08 nm, and the spots of serpentine have a spacing of about 0.72 nm giving an aggregate spacing of ~ 1.8 nm. Note the difference between these diffraction patterns indicates the tochilinite-serpentine is coarser than Mg-rich serpentine.

5.3 Carbonates in CM2.2 Cold Bokkeveld

5.3.1 Introduction

Ca-carbonate (both aragonite and calcite) are found in Cold Bokkeveld, and TEM previous work indicates that aragonite postdates calcite (Barber, 1981). Carbonate minerals in Cold Bokkeveld and other chondrites have been analysed for carbon and oxygen isotopic composition by Grady et al. (1988). One grain of dolomite, and calcite grains in Cold Bokkeveld were chemically analysed by Johnson and Prinz (1993). Calcite in Cold Bokkeveld is present as single grains surrounded by PCP (i.e. intergrown tochilinite and serpentine), and margins of calcite grains in Cold Bokkeveld show evidence of alteration as these grains contain alteration products in the form of sheetsof altered minerals (Benedix et al. , 2003). Ca-carbonate grains in Cold Bokkeveld range in size from 20 µm to 40 µm (Rubin et al., 2007). Cold Bokkeveld contains 1.9 vol% of calcite ranging in size from 20 µm to 40 µm, but a few aggregate grains are 40-90 µm. Rims of Fe-sulphide or PCP surround most of calcite grains (De Leuw et al., 2010). The PSD-XRD quantitative modal mineralogies of CM chondrites by Howard et al. (2011) found that Cold Bokkeveld contains 1 vol% of calcite.

5.3.2 Petrographic observations

Petrographic observations of Cold Bokkeveld made here show that only Ca-carbonates (both aragonite and calcite) are found. SEM point counting demonstrated that Cold Bokkeveld contains 0.93 vol% Ca-carbonate, and that these grains are present only in the fine grained (<1μm) matrix. The calcite grains range in size from a few microns (2 or 3 μm) to 100 μm. They are found in a variety of shapes, which are, in order of abundance irregular, subrounded, subhedral and euhedral. They occur as isolated grains in small clusters, as single or polycrystalline grains, but only rarely as aggregate grains. The X-ray map (Figure 5.13) also indicates that the calcite grains are mainly found in isolated clusters and discontinuous microveins. The map also shows the presence of Ca-sulphate (gypsum) within fractures that cross-cut the fine grained matrix, as reported by Lee (1993).

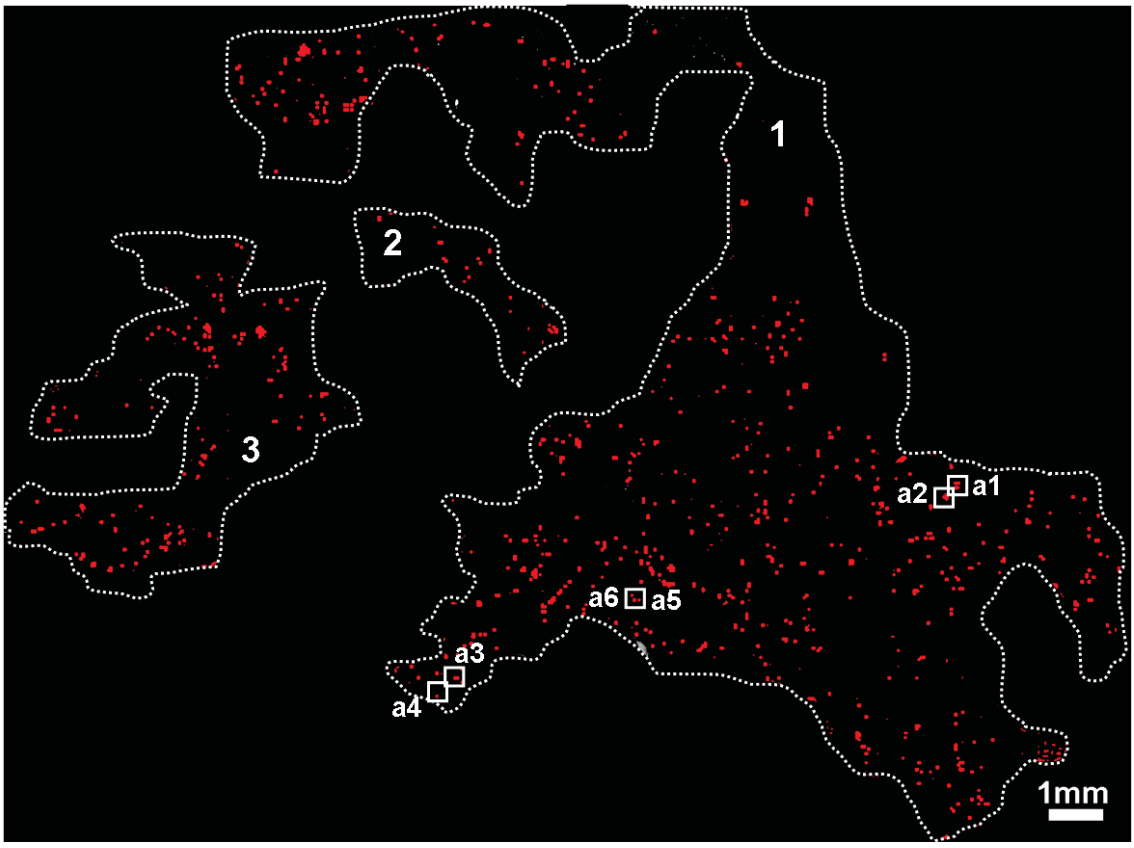

Figure 5.13- Ca X-ray map of the whole sample of the Cold Bokkeveld.
The sample studied consisted of three isolated pieces of rock (1, 2 and 3). The map reveals the distribution of Ca (red areas) within these three pieces. Ca locates all Ca-carbonate grains, a few grains of Ca-rich pyroxene and discontinues micro veins of Ca-sulphate. The white boxed areas reveal the locations of the six aragonite grains.

The margins of calcite grains are either etched or have been replaced by tochilinite-serpentine intergrowths. The calcite grains can be petrographically classified into four types, which in order of abundance are: (i) calcite grains completely rimmed by tochilinite;

the majority of these grains have been partly, moderately or totally replaced by tochilinite-serpentine intergrowths or Mg-rich serpentine, (ii) a few grains of calcite replacing olivine were also observed, these grains containing patches of Fe-sulphide (Figure 5.14 a), (iii) a few grains are in direct contact with the fine grained (<1µm) matrix and are also free of inclusions. The examined sample also contains five grains of calcite enclosed by tochilinite-cronstedtite intergrowth and contains large cores (10 µm) of spinel inclusions (Figure 5.14 b). Greenwood et al. (1994) also reported spinel in conjunction with calcite in Cold Bokkeveld. A part of the studied sample is made of fusion crust, which also contains calcite grains that are texturally different to those in other areas of the sample. They have a darker appearance in BSE images and their outer areas are extensively degraded, which is consistent with alteration of the calcite by high temperatures (Figure 5.14 d).

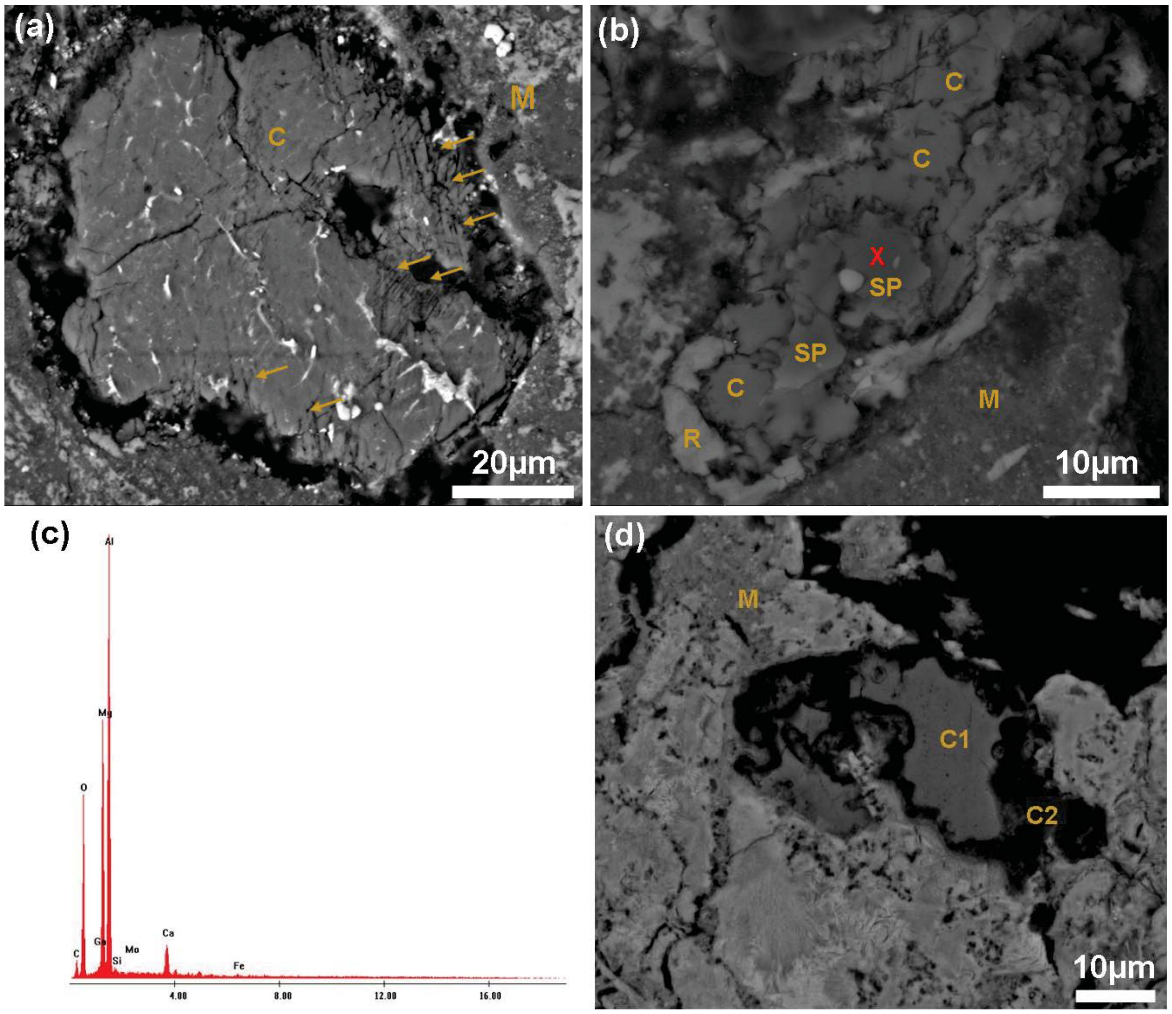

Figure 5.14- BSE images and X-ray spectra of calcite grains in Cold Bokkeveld.
(a) BSE image of calcite (C) replacing olivine. The grain is partly twined (arrowed areas), and note the presence of Fe-sulphide (bright areas) within the grain. (b) Calcite (C) grain enclosed by tochilinite-cronstedtite intergrowth (R). The grain contains large core (10 µm) of spinel (SP), M is fine grained (<1µm) matrix. (c) EDS spectrum that was used to confirm the identity of the spinel in (b). The spectrum obtained from area labelled X in b. (d) BSE image of a calcite grain in the fusion crust of the sample examined. The outer areas of the grain (C2) are degraded, whereas the internal area of the grain is unaltered. The locations of these grains in the sample studied are shown in appendix D8.

Six grains of aragonite were identified in Cold Bokkeveld using Raman spectroscopy and EBSD mapping. All six grains were found in area 1 of the studied sample, and in three different locations, each with two grains (see Figure 5.13). Aragonite grains have subhedral, subrounded and elongated shapes. They are embedded in the fine grained (<1μm) matrix without inclusions and rims, and show textures that are comparable to those of the calcite grains in which inclusions and rims are absent. Four of these grains range in size from 20 μm to 80 μm and one grain (a1) is 60 μm in length. The margins of all six aragonite grains are either slightly or highly dissolved; holes around some of these grains contain remains of aragonite left after dissolution (e.g. Figure 15.5).

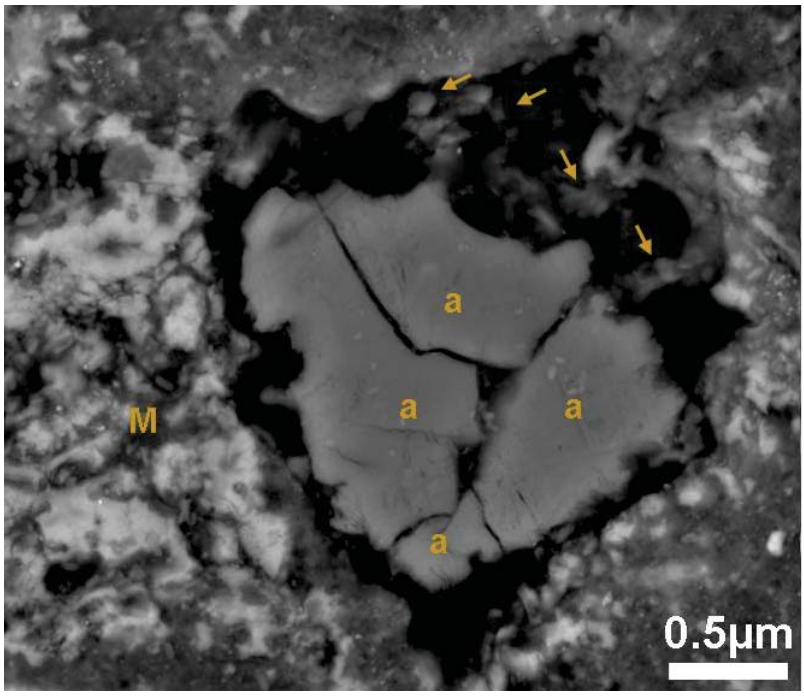

Figure 5.15- BSE image of an aragonite grain in Cold Bokkeveld.
Note the margins of this aragonite, a, has been dissolved, and the holes around the grain contain very small grains of aragonite left after dissolution. The location of this grain in the sample studied is shown in appendix D8.

5.3.2.1 Crystallographic orientation of aragonite grains in Cold Bokkeveld

The crystallographic orientation of five aragonite grains (a2, a3, a4, a5 and a6) was determined by EBSD mapping. In common with some other meteorites (e.g. Pollen, LON 94101), the c-axes of aragonite grains in this meteorite are mainly inclined in two different orientations. Three grains (a2, a3 and a4) each consist of a few sub grains. The c-axes of the sub-grains in each grain are inclined and orientated very close to each other (e.g. Figure 5.16). The crystallographic orientation of five aragonite grains shows two different preferred inclinations in the {001} pole figures (Figure 5.17). The c-axes of the sub-grains

in a2 and a4 are inclined close to vertical (~80º), whereas the c-axes of the grains a5 and sub-grain of a3 are orientated at about 15º relative to the sample surface. However, the c-axis of the a6 is inclined approximately 45º to the pole figure horizontal. The pole figure also indicates that the c-axes of these grains are orientated close to an E-W direction (Figure 5.17).

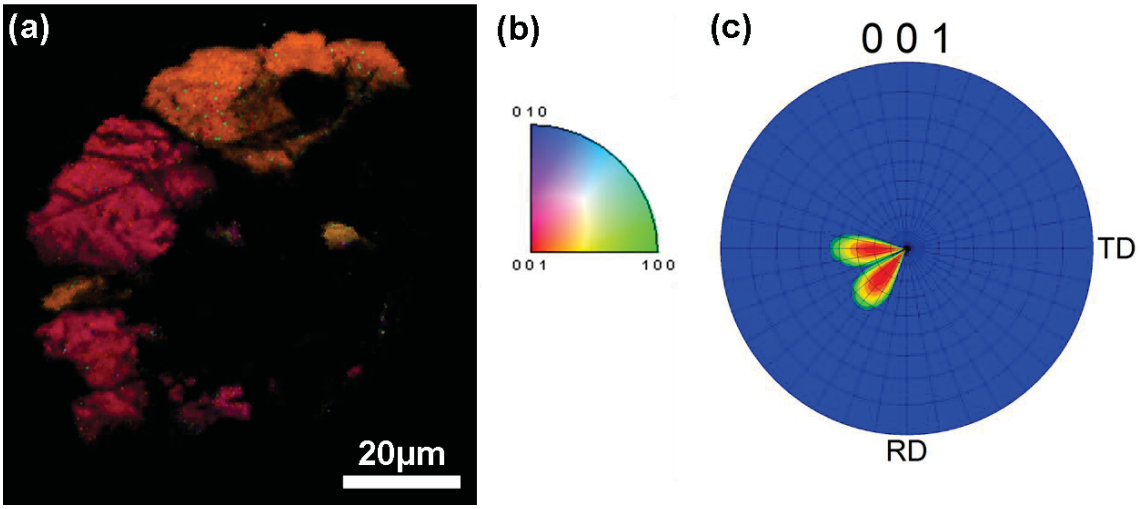

Figure 5.16- Crystallographic orientation map of the polycrystalline aragonite grain in Cold Bokkeveld.
(a) EBSD map of the a2. The grain is composed of large (15 µm) sub-grains and smaller aragonite grains that are present in holes around the main grain. (b) Crystallographic orientation colour key for aragonite relative to ND. (c) Pole figure showing orientations of the subgrains in a2; the grid line divisions represent 10º. Note that all sub-grains are close to the centre of the pole figure. The location of this grain in the sample studied is shown in appendix D8.

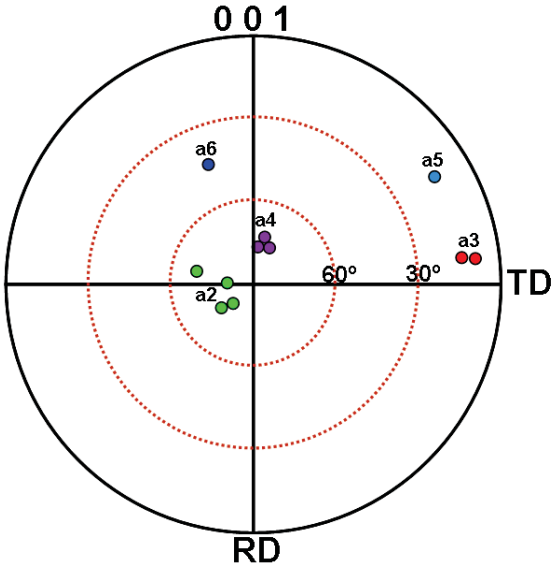

Figure 5.17- Crystallographic orientation of aragonite grains in Cold Bokkeveld.
Pole figure showing the orientations of poles to the {001} planes of five aragonite grains. Sub-grains of each grain (a2, a3, a4) are plotted in the same colour. Note the aragonite grains in the meteorite have two different inclinations that are near to the centre (i.e. a2 and a4) and near to the margins of the pole figure (i.e. a3 and a5). Only the c-axis of a6 is inclined between 60º and 30º, and at about 45º.

5.3.3 Chemical composition of Ca-carbonate in Cold Bokkeveld

Calcite and dolomite in Cold Bokkeveld were chemically analysed by Johnson and Prinz (1993). The chemical composition of its calcite grains were also reported by De Leuw et al. (2010). In this study, SEM-CL imaging and chemical analyses of Ca-carbonate in Cold Bokkeveld were carried out using the Quanta 200F SEM and EPMA respectively. BSE images were obtained after the chemical analyses to verify the locations of the analyses and as a consequence a few analyses have been excluded.

5.3.3.1 CL imaging

CL images were obtained from 26 calcite grains and two aragonite grains. The majority of imaged calcite grains are completely rimmed by tochilinite. CL characteristics of the grains are summarised in Table 5.4. CL of Ca-carbonate in Cold Bokkeveld is classified into four types of CL intensity, namely: I, II, IV and VII. Calcite free of rims and most of the completely rimmed calcite grains have CL type I. The two aragonite grainsshow low CL intensity (CL type I) throughout a grain, which also characterises the majority of aragonite imaged in some of the meteorites above described.

Grain type	SEM-CL type	SEM-CL characteristics	Abundance
A, C, F	I (observed in, Murchison, Murray, Pollen, Mighei, EET 96029, Nogoya)	Low or high CL throughout a grain, in some cases contains patches of very high CL.	A1, C15, 4F
C	II (observed in Murray, Pollen, Mighei)	Complex zoning mainly found in polycrystalline grains and in most cases showing all four levels of CL intensity (from very low CL to very high CL) within a grain.	1C
C	X (observed in Murray, Mighei, LON 94101)	Well defined band of high CL in some cases containing core of low CL, overgrowth zone of low or very low CL filling the space. In Cold Bokkeveld the high CL is very high intensity.	1C
C	VII (observed in Murchison, Pollen, Mighei, Nogoya)	Very high CL throughout the grain with thin rims (0.2-1 μm) of high CL	7C

Table 5.4- Characteristics and abundance of CL types of Ca-carbonate in Cold Bokkeveld and their relationship to petrographic features.
A is aragonite, C is completely rimmed calcite, F calcite free of rims. Total number of grains imaged is 29. The abundance of each CL type is indicated by numbers, e.g. 4F means 4 grains imaged show CL type I, and F means these 6 grains are free of rims.

5.3.3.2 Quantitative chemical analyses

Twenty six grains of Ca-carbonate were chemically analysed. The analyses were obtained from aragonite, calcite completely rimmed, calcite free of rims and calcite replacing olivine. The mean of the analyses are presented in Table 5.5. This data shows that the aragonite and completely rimmed calcite contain similar contents of Fe, but these Fe concentrations are less than those in calcite replacing olivine. The amount of $FeCO_3$ in calcite replacing olivine is 1.53 mol%. However, the high concentrations of $FeCO_3$ (>1 mol%) also occur in a few grains that in some cases are located close to each other (e.g. Table 5.6). The analyses also show that aragonite in Cold Bokkeveld has more $FeCO_3$ than aragonite in Nogoya. The Fe content of aragonite grains in Cold Bokkeveld is nearly identical to those in Mighei.

Mol%	$CaCO_3$	$MgCO_3$	$SrCO_3$	$FeCO_3$	$MnCO_3$	Sum	*n*
Aragonite	98.90 ± 0.28	0.11 ± 0.10	0.08 ± 0.02	0.92 ± 0.25	0.00 ± 0.00	100.00	5
Calcite rimmed	99.05 ± 0.21	0.02 ± 0.02	0.00 ± 0.00	0.93 ± 0.22	0.00 ± 0.01	100.00	16
Calcite free of rims	98.87 ± 0.16	0.04 ± 0.01	0.00 ± 0.00	1.09 ± 0.15	0.00 ± 0.00	100.00	4
Calcite replacing olivine	98.42	0.05	0.00	1.53	0.00	100.00	1
Wt%	**Ca**	**Mg**	**Sr**	**Fe**	**Mn**	**O**	**Sum**
Aragonite	42.11	0.03	0.07	0.55	0.00	17.07	60.05
Calcite rimmed	41.96	0.01	0.00	0.55	0.00	16.93	59.48
Calcite free of rims	42.28	0.01	0.00	0.65	0.00	17.09	60.10
Calcite replacing olivine	41.09	0.01	0.00	0.89	0.00	16.73	58.92

Table 5.5- Mean of the quantitative chemical analyses of Ca-carbonates in Cold Bokkeveld. Concentrations below detection limit are assumed to be zero. Data presented as mean ± SD, error values are calculated to 1σ. The full dataset with standard deviation is listed in appendix B-8.

Mol%	$CaCO_3$	$MgCO_3$	$SrCO_3$	$FeCO_3$	$MnCO_3$	Sum
Calcite 1	98.89	0.03	0.00	1.08	0.00	100.00
Calcite 2	98.82	0.04	0.00	1.14	0.00	100.00

Table 5.6- Typical analyses of two calcite grains in Cold Bokkeveld. The grains are free of inclusions and are located close to each other. Note these grains are nearly identical in chemical composition.

5.3.4 Post crystallization deformation of calcite in Cold Bokkeveld

BSE images and EBSD maps indicate that most of the calcite grains in Cold Bokkeveld exhibit evidence of shock induced deformation. BSE images also indicate that the majority

of completely rimmed calcite grains are likely to be on the way to becoming fully transformed into tochilinite-serpentine intergrowths.

5.3.4.1 Calcite twin morphology

Petrographic observations and EBSD mapping show that most calcite grains in Cold Bokkeveld are either partly or totally decorated with lamellar twining. However, the twinning of calcite grains in Cold Bokkeveld is less common than in LON 94101. The deformation twinning in the meteorite ranges from weak deformation over a small area of a grain, to intense deformation in all areas of the grain. Twinned calcite grains can have one or two sets of twins. Three types of twinning are observed in these grains, which in order of abundance are: one set or two sets of thin straight twins (1 μm) that cover all areas of a grain (e,g. Figure 5.18 a); one set of thick straight twins that occurs across a grain making an acute angle with another set of thin twins (~0.5 μm), that in most cases are present in a part of the grain (Figure 5.18 c); a few grains have thick straight twins cross-cut by thick patchy twin lamellae.

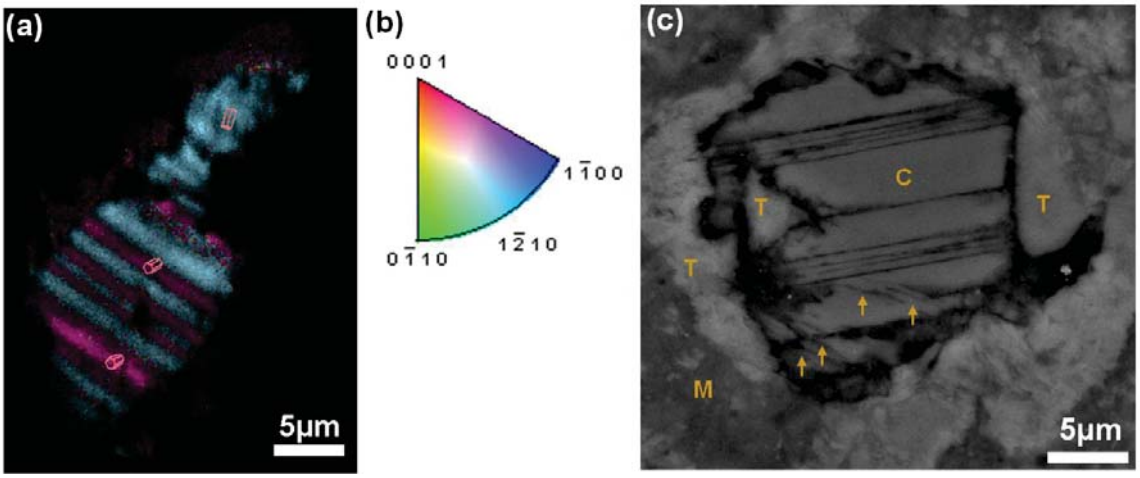

Figure 5.18- Images showing partially and totally twinned in calcite grains in Cold Bokkeveld. (a) EBSD map of a twined calcite grain. Note the twins (purple colour) are parallel, thin (1 μm), straight and penetrate the grain. (b) Crystallographic orientation colour key for calcite relative to the normal direction. (c) BSE image of a calcite grain (C). The grain are totally decorated with one set of thick and straight twins, and partly twinned with lens-shaped twins (arrowed area). T is tochilinite, M is fine grained (<1μm) matrix. The locations of these grains in the sample studied are shown in appendix D8.

5.3.4.2 Pseudomorphs after calcite in Cold Bokkeveld

BSE images of Cold Bokkeveld show that some of the completely rimmed calcite grains have been replaced by tochilinite-serpentine intergrowths or Mg-rich serpentine. The meteorite contains 2.37 vol% of these pseudomorphs after calcite. In this case, the margins

of the calcite grains were gradually transformed into tochilinite-serpentine or Mg-rich serpentine. In common with completely rimmed calcite grains in Pollen and LON 10194, the completely rimmed calcite grains in Cold Bokkeveld show four phases of transformation of the calcite into pseudomorphs. These are partly, moderately, near complete and complete replacement of calcite by the tochilinite-serpentine intergrowth or Mg-rich serpentine (e.g. Figure 5.19 a-d). Petrographic observations show that the pseudomorphs after calcite in Cold Bokkeveld differ between areas of the meteorite. These pseudomorphs are present in three forms, which in order of abundance are: (i) tochilinite-serpentine pseudomorphs that are highly enriched with tochilinite in comparison to serpentine, (ii) pseudomorphs that are likely to be intermediate between tochilinite and serpentine (e.g. Figure 5.19 d); these are identical to those in LON 94101 (see Figure 4.78), (iii) pseudomorphs that are mainly composed of Mg-rich serpentine, which are very rare in this meteorite in comparison to Pollen and Nogoya.

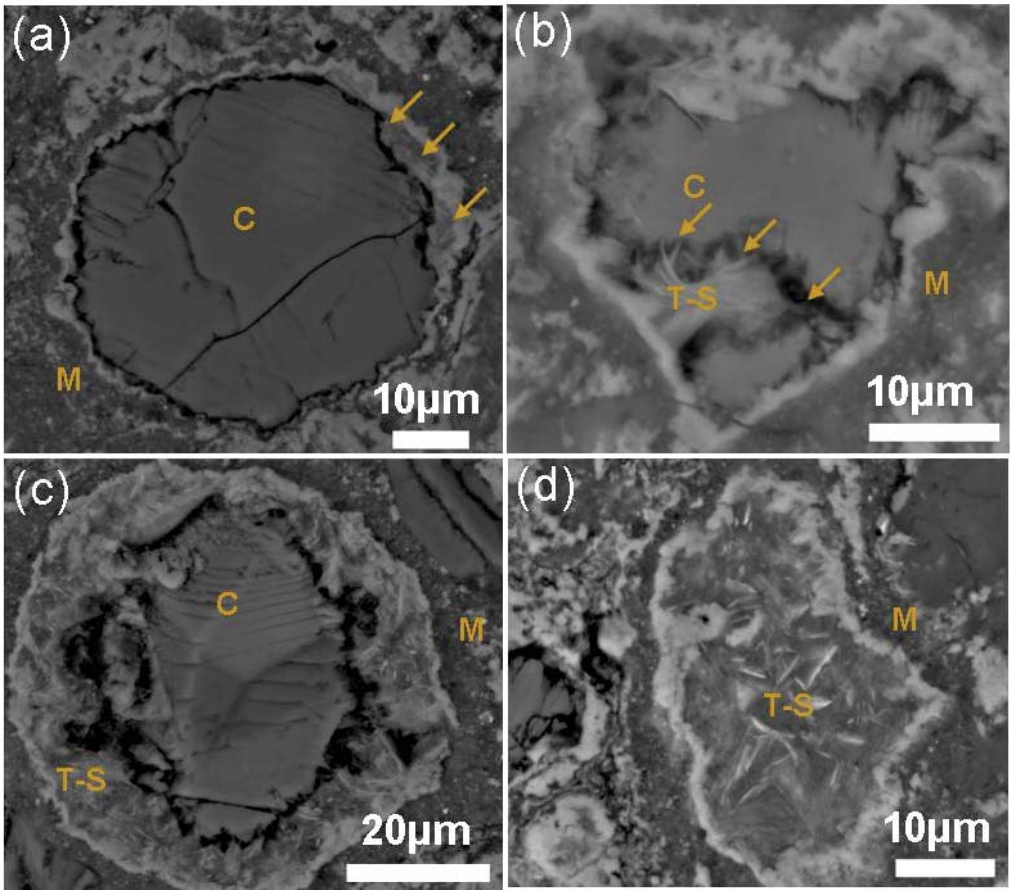

Figure 5.19- BSE images of pseudomorphs after calcite in Cold Bokkeveld.
(a-b) BSE images of calcite grains (C) that have been partly replaced by tochilinite-serpentine (T-S) (arrowed areas). (C) Calcite grain (C) is moderately replaced by tochilinite-serpentine (T-S). (d) Calcite grain that has been completely replaced by tochilinite-serpentine (T-S). M is fine grained (<1µm) matrix. Note the calcite grains in a, b and c are mainly consumed from their edges inwards. The locations of these grains in the sample studied are shown in appendix D8.

5.3.4.2.1 Chemical composition of pseudomorphs calcite in Cold Bokkeveld

Chemical compositions of 12 pseudomorphs after calcite were acquired by EPMA. Based on these analyses (Table 5.7) and also on the petrographic observations (discussed above), the pseudomorphs can be classified into three types: (i) type 1 in which the tochilinite-serpentine intergrowth is enriched in Fe and S, and contains less Mg than Fe, (ii) type 2 represents tochilinite-serpentine intergrowths that are enriched in Mg and Fe and concentrations of these elements (Mg and Fe) are similar, (iii) type 3 is mainly composed of Mg-rich serpentine that is enriched in Mg and Si in comparison to Fe.

Oxides wt%	Type 1	Type2	Type 3	Element wt%	Type 1	Type 2	Type 3
Na_2O	0.11 ± 0.03	0.08 ± 0.03	0.06 ± 0.01	Na	0.08	0.06	0.01
MgO	15.27 ± 0.55	22.53 ± 1.49	28.94 ± 0.83	Mg	9.21	13.58	17.45
Al_2O_3	1.88 ± 0.23	1.78 ± 0.18	1.51 ± 0.23	Al	0.99	0.94	0.80
SiO_2	17.49 ± 0.19	28.58 ± 3.37	36.15 ± 2.37	Si	8.17	13.36	16.90
SO_2	17.20 ± 2.80	8.09 ± 2.43	3.37 ± 1.68	S	8.61	4.05	1.69
K_2O	0.07 ± 0.04	0.08 ± 0.01	0.05 ± 0.01	K	0.06	0.06	0.04
CaO	0.16 ± 0.07	0.32 ± 0.13	0.18 ± 0.02	Ca	0.12	0.23	0.13
P_2O_5	0.05 ± 0.04	0.06 ± 0.04	0.04 ± 0.01	P	0.02	0.03	0.02
TiO_2	0.04 ± 0.03	0.06 ± 0.01	0.08 ± 0.02	Ti	0.02	0.03	0.05
Cr_2O_3	0.28 ± 0.19	0.09 ± 0.04	0.09 ± 0.05	Cr	0.19	0.06	0.05
MnO	0.15 ± 0.04	0.19 ± 0.09	0.23 ± 0.06	Mn	0.12	0.15	0.18
FeO	36.86 ± 0.27	23.70± 3.27	14.44 ± 2.57	Fe	28.65	18.42	11.22
NiO	2.75 ± 0.24	1.87± 0.27	1.05 ± 0.34	Ni	2.16	1.47	0.82
Total %	92.29	87.43	86.18	O	33.89	34.98	36.87
n	2	5	4	No. analyses	2	5	4

Table 5.7- The mean of chemical compositions (wt%) of the pseudomorphs after calcite in Cold Bokkeveld.
Type 1 tochilinite-serpentine intergrowths contain abundant of Fe and S. Type 2 tochilinite-serpentine intergrowths have contents of Fe and Mg in comparable concentrations. Type 3 is mainly composed of Mg-rich serpentine and has higher concentrations of Mg and Si than Fe. Note the contents of Mg, Si increase from type 1 to 3, whereas Fe and S gradually from type 3 to 1. Data presented as mean ± SD, error values are calculated to 1σ. The full dataset with standard deviation is listed in appendix A-8.

5.4 Carbonate minerals in CM2.1 QUE 93005

5.4.1 Introduction

Rubin et al. (2007) found that QUE 93005 contains carbonate minerals that range in size from 20 to 70 μm. Ca-carbonates represent about 20% of the carbonates in QUE 93005;

the majority of carbonate minerals in QUE 93005 contain considerable concentrations of Ca, Mg, Fe and Mn. QUE 93005 contains 2.3 vol % of carbonate, which is calcite and dolomite; calcite present as aggregate grains that are irregular in shape, and range in size from 50 to 100 μm, whereas dolomite appears as single grains that range in size from 10 to 30 μm. Pentlandite is mainly present as rims around the dolomite grains, and as inclusions within the most of calcite grains (De leuw et al., 2009). The PSD-XRD quantitative modal mineralogies of CM chondrites by Howard et al. (2011) showed that QUE 93005 contains 1.7 vol% of calcite. Lee et al. (2011) showed that QUE 93005 contains four distinct carbonate minerals that are breunnerite, calcite, dolomite and Ca-poor dolomite.

5.4.2 Petrographic observations

Petrographic observations, EDS spectral analyses and Raman spectroscopy have shown that QUE 93005 contains four carbonate minerals, namely breunnerite, calcite, dolomite and Ca-poor dolomite. The abundance of these minerals is listed in Table 5.8. They were distinguished from each other by EDS and Raman spectroscopy. Raman spectroscopy shows that calcite has peaks at 282 and 713 Δcm^{-1} (Figure 5.20, see also Figure 4.2), whereas small Raman shifts of dolomite occur at 300 and 721 Δcm^{-1} and breunnerite produces bands at 318 and 729 Δcm^{-1}. The Ca-poor dolomite was mainly identified by X-ray analyses, and show lower concentration of Ca than dolomite. These minerals are found in QUE 93005 in a variety of grain types including: (i) calcite as single grains, (ii) dolomite as single grains, (iii) calcite and dolomite intergrowths, (iv) breunnerite as single grains, (v) breunnerite-dolomite intergrowths, (vi) breunnerite, Ca-poor dolomite and calcite intergrowths. The Ca X-ray map of the whole sample (Figure 5.21a) shows that carbonate minerals, including calcite and dolomite, are homogenously distributed throughout the meteorite. Unlike the previously discussed meteorites, the dolomite and calcite in QUE 93005 are also found in fine-grained (<1μm) chondrule rims (e.g. Figure 5.21 b). However, grains of breunnerite; breunnerite-dolomite intergrowths; breunnerite, Ca-poor dolomite and calcite intergrowths mainly occur in the matrix between chondrules. These minerals are absent from the fusion crust of the sample, and occur very rarely in areas close to the fusion crust (Figure 5.22).

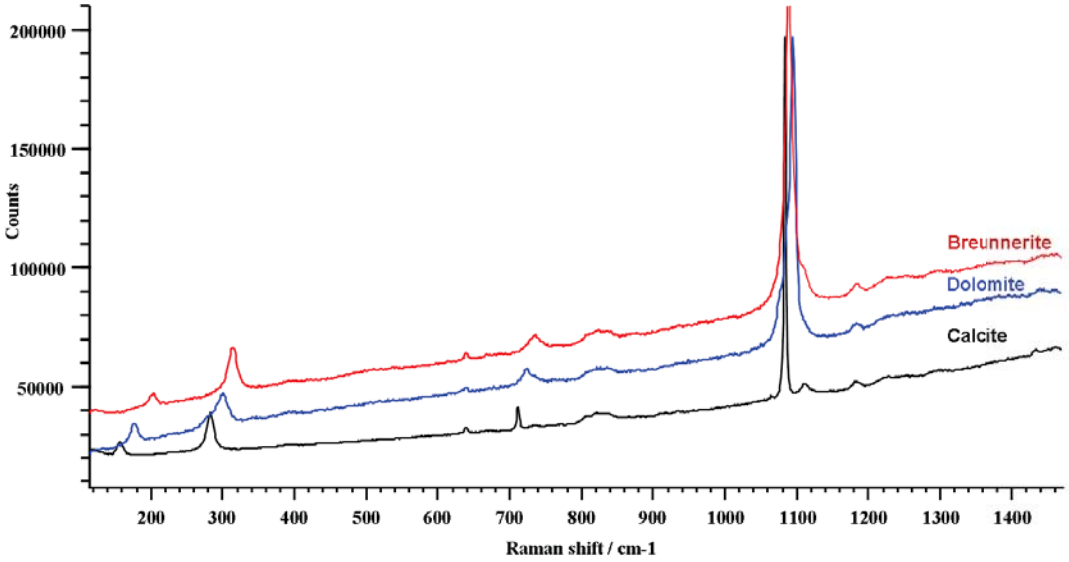

Figure 5.20- Raman spectra of carbonate minerals in QUE 93005.
The black spectrum was obtained from a calcite grain, the blue spectrum from a dolomite grain and the red spectrum from a breunnerite grain. The spectra illustrate typical Raman bands for calcite at wavenumber shifts of ~282 and ~713 cm^{-1}, dolomite at shifts of ~300 and ~721 cm^{-1}, and breunnerite at ~318 and ~729 cm^{-1}.

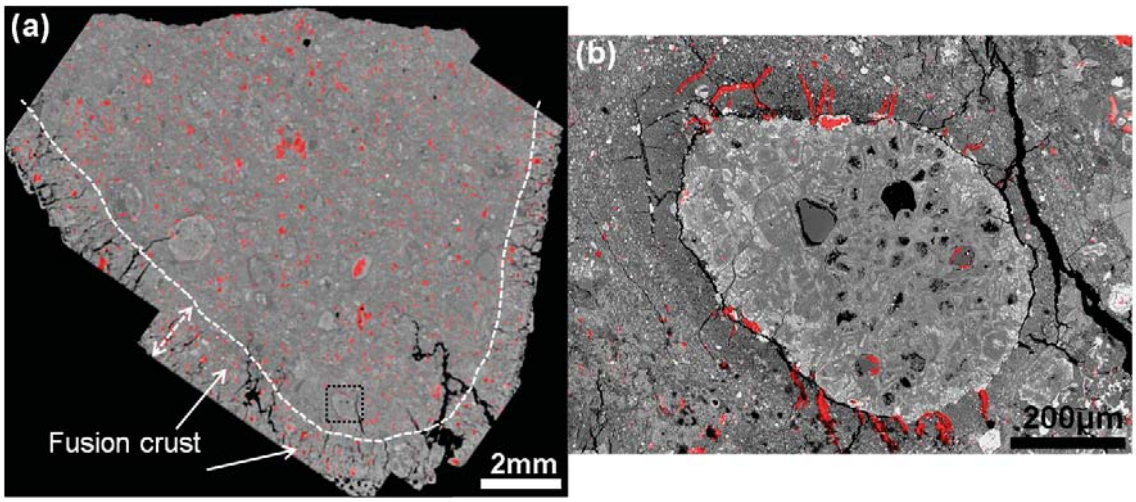

Figure 5.21- Calcium ED X-ray maps of QUE 93005.
(a) Combined Ca map with BSE image of whole sample of QUE 93005 showing the distribution and concentration of the Ca (red areas) within the meteorite. Ca in this map locates all grains and veins of calcite and dolomite. Note the Ca is uniformly distributed within all areas of the meteorite. (b) Combined Ca map (red areas) with BSE image of a small area (boxed area in a) showing the presence of calcite veins (red areas) within the chondrule rims, which are not present in any other meteorites analysed here.

Carbonate abundance in QUE 93005	Vol%
Dolomite-calcite intergrowth	1.9
Breunnerite-dolomite-calcite intergrowth	0.3
Dolomite	0.7
Calcite	0.7
Breunnerite	0.2
Total	**3.9**

Table 5.8- Abundance of carbonate minerals in QUE 9005 as determined by SEM point counting. The total number of points that counted was 882.

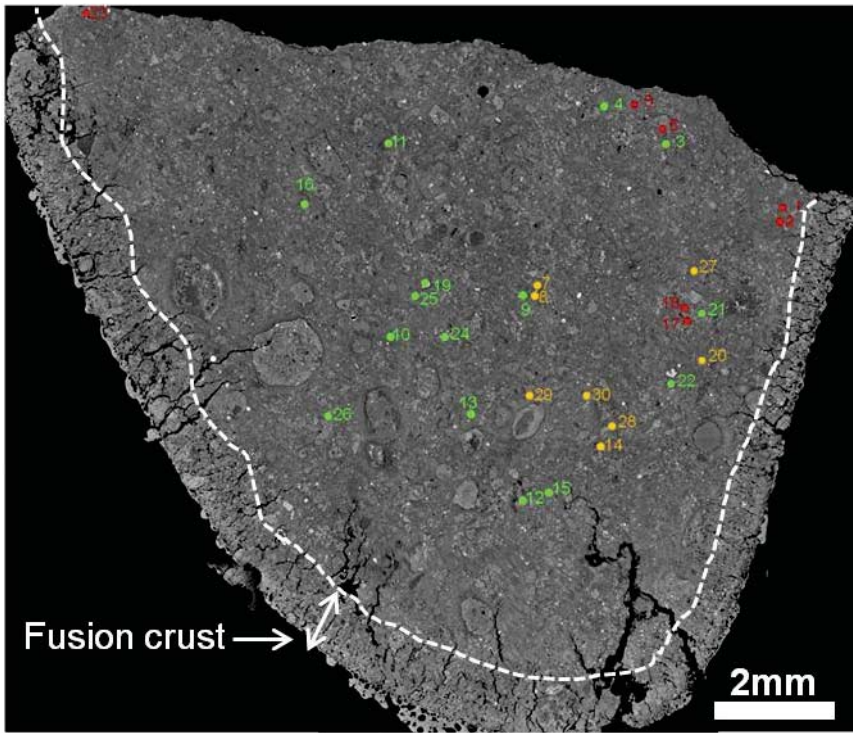

Figure 5.22- BSE image of the whole sample of QUE 93005.
The image shows the locations of breunnerite grains (yellow spots), breunnerite-dolomite intergrowths (red spots), and breunnerite, Ca-poor dolomite and calcite intergrowths (green spots). Note that these three phases of carbonate minerals are mainly present in the interior of the sample. The fusion crust and most areas along the fusion crust are free of these minerals.

5.4.2.1 Calcite grains and veins

QUE 93005 contains 0.7 vol% of calcite, occurring as single grains and as calcite veins. Calcite veins are present mainly within the chondrule rims around altered or nearly completely altered chondrules. As discussed in section 3.10.1, fractures cross-cutting chondrule rims are likely to have been formed as a consequence of chondrule expansion by aqueous alteration of mesostasis clases and olivine/pyroxene. They remain empty in EET 96029 (e.g. Figure 3.26), and most of these fractures are partially or completely filled with calcite in QUE 93005 (e.g. Figure 5.21 b). Veins of calcite are also present in the fine-grained (<1μm) matrix (Figure 5.23 b). In some cases, they have a length of several

hundred micrometres, but their width ranges from 4 to 8 µm. A few of these calcite veins are associated with very small grains of pentlandite.

Calcite grains in QUE 93005 are mainly present in the fine grained (<1µm) matrix; they occur as isolated grains (range from ~ 2µm to 120 µm) and also as large polycrystalline grains (~ 200 µm in length). They are sub-rounded to irregular in shape, and in very rare cases are subhedral. Calcite grains can be classified into two types, which are: (i) calcite replacing olivine that contains of Fe-sulphides or blocky grains of pentlandite, (ii) calcite grains that probably crystallized within pore space. These are in direct contact with fine grained (<1µm) matrix, and some of these grains contain fibres of phyllosilicates in their outer parts and/or inclusions of Fe-sulphides (Figure 5.23 a). Some of these grains have also been partly replaced by phyllosilicates that are comparable to those in the fine grained matrix, (iii) very rare calcite grains that are enclosed by rims of intergrown pentlanite-phyllosilicate, which are similar to the rims around the dolomite grains. De Leuw et al. (2010) reported that pentlandite rims are only present around dolomite grains.

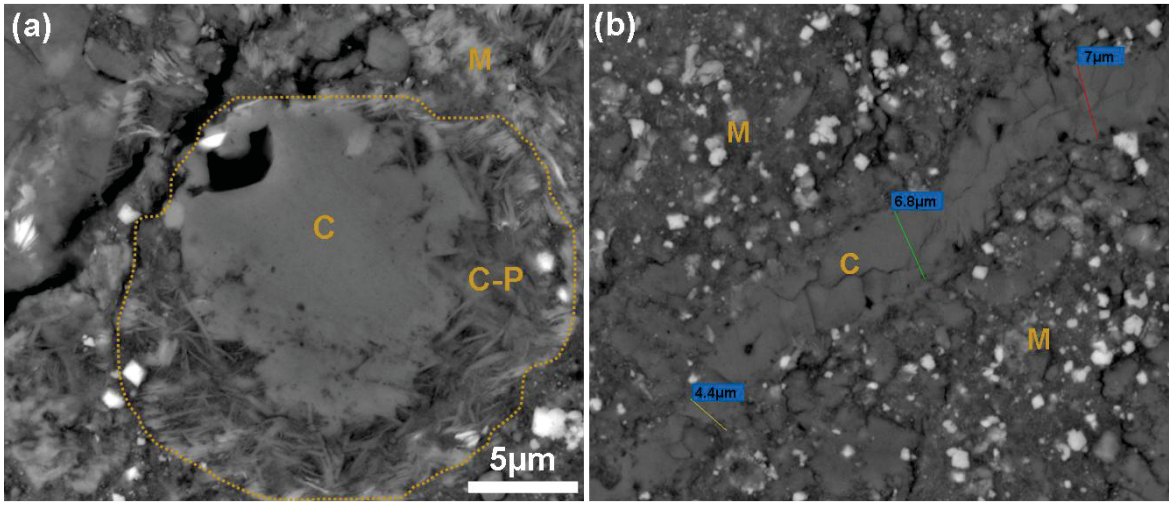

Figure 5.23- BSE images showing the occurrence of a calcite in QUE 93005.
(a) BSE image of a calcite grain (C) that is intergrown with fibres of phyllosilicates (C-P). (b) Calcite (c) filled fracture cross-cutting the fine grained (<1µm) matrix (M). The locations of these grains in the sample studied are shown in appendix D9.

5.4.2.2 Dolomite grains

QUE 93005 contains 0.7 vol% of dolomite, that is present as single grains and in very rare cases as dolomite veins. Dolomite grains in QUE 93005 range in size from 3µm to 70µm, and occur in shapes that are sub-rounded, elongate and irregular. De Leuw et al. (2010) reported that each grain of dolomite in this meteorite is rimmed with pentlandite, but the

petrographic observations of this study show that single dolomite grains are present in three different relationships, which in order of abundance are (i) dolomite grains partly or entirely enclosed within an envelope of pentlandite-phyllosilicate that ranges in thickness from 4 to 6 µm (Figure 5.24 a); the pentlandite occurs as blocky crystals and/or needles, (ii) dolomite grains that are free of rims, in some cases fibres of phyllosilicates are intergrown with these dolomite grains (e.g. Figure 5.24 b), (iii) in very rare cases fractures in fine grained (<1µm) matrix are filled with dolomite.

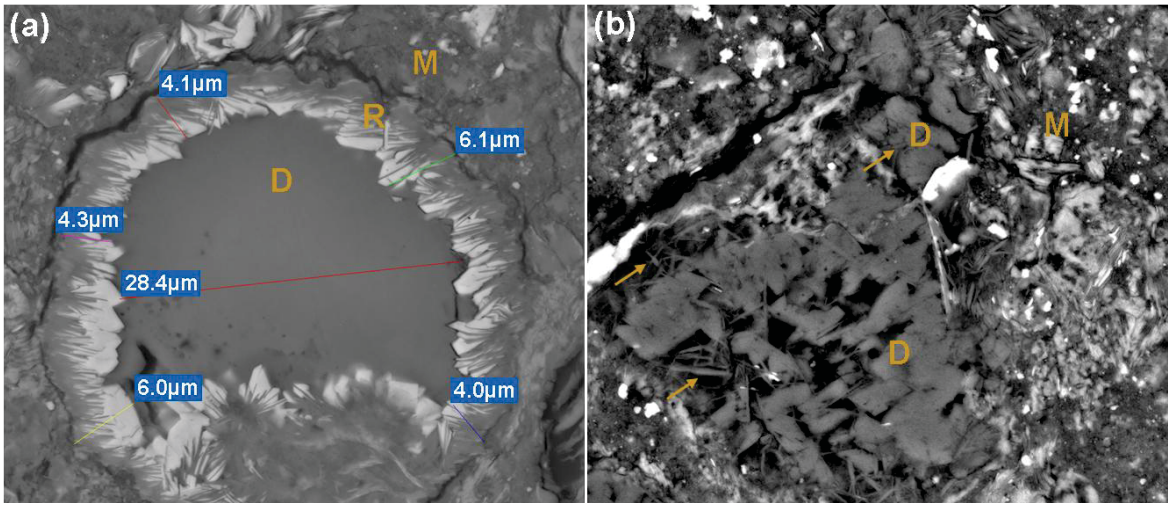

Figure 5.24- BSE images of dolomite in QUE 93005.
(a) A dolomite grain (D) that is rimmed by a pentlandite-phyllosilicate intergrowth (R). Note the crystals of pentlandite (white) are blocky or needle-shaped. (b) Dolomite (D) is intergrown with fibres of phyllosilicate (arrowed). M is fine grained (<1µm) matrix. The locations of these grains in the sample studied are shown in appendix D9.

5.4.2.3 Calcite-dolomite intergrowth

Calcite-dolomite intergrowths occupy 1.9% of the total volume of the rock. They occur as single grains (~5µm to ~60µm), polymineralic aggregates (~120µm across) and large veins (0.8-1 mm). Single grains of intergrown calcite-dolomite are completely or partly rimmed by the same materials that are found around some of the single dolomite grains (see Figure 5.25 a). Calcite-dolomite intergrowths are also present as grains that are free of rims. In most cases, calcite-dolomite intergrowths occur in contact with fine grained (<1µm) matrix, but some sub-grains within these assemblages are partly rimmed by of pentlandite-phyllosilicate intergrowths (Figure 5.25 b).

Grains of calcite, dolomite and blocky pentlandite together fill micro fractures cross-cutting the fine grained (<1µm) matrix of QUE 93005. A large vein (~ 800 µm in length and ~ 100 µm across) was also observed in this meteorite. This vein is mainly composed of

calcite and dolomite. Petrographic observations also show that some dolomite crystals are found as small inclusions within the calcite grains (e.g. Figure 5.26). However, the boundaries between calcite and dolomite within some single grains are sharp and planar, and show growth patterns (e.g. Figure 5.25a).

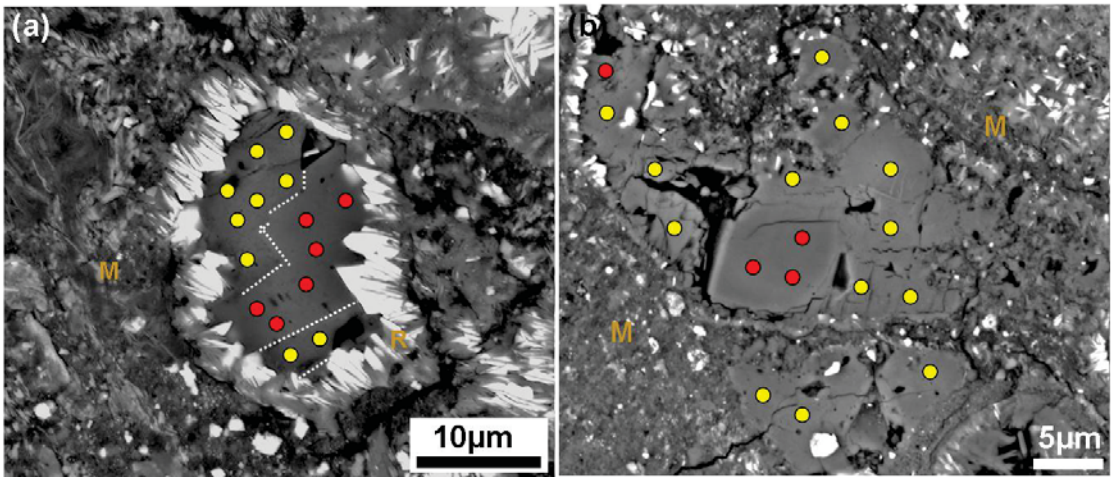

Figure 5.25- BSE images of calcite-dolomite intergrowths in QUE 93005.
(a) BSE image showing a calcite-dolomite intergrowth (yellow spots calcite, red spots dolomite) that is enclosed by rims of a pentlandite-phyllosilicate intergrowth (R). Note the boundaries between calcite and dolomite is sharp and planar. (b) BSE image showing a calcite-dolomite intergrowth in contact with the fine grained (<1µm) matrix (M). The grain in the upper left side of the image is partly rimmed. Note the euhedral dolomite (red) in this image and also the boundaries between calcite and dolomite that show two phases of crystallization. The locations of these grains in the sample studied are shown in appendix D9.

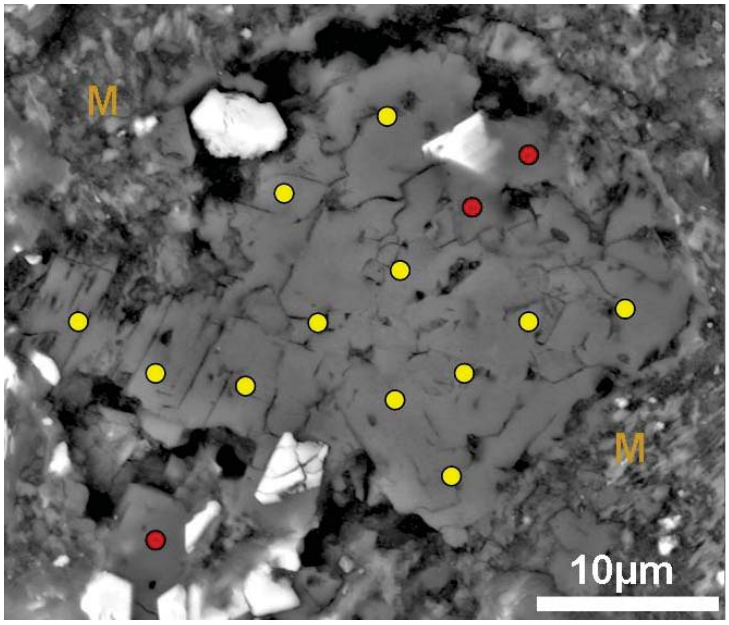

Figure 5.26- BSE image showing the occurrence of small inclusions of dolomite within a calcite grain. Dolomite is indicated by red spots and calcite the yellow spots. The location of this grain in the sample studied is shown in appendix D9.

5.4.2.4 Breunnerite grains

The sample of QUE 93005 contains eight single grains of breunnerite that have been recognised by their Raman spectrum (see Figure 5.20) and EDS spectrum (Figure 5.27 b). These grains are located fairly close to each other in the sample (see Figure 5.22). They range in size from ~10 µm to 60 µm. These breunnerite grains are fractured and are abundant in flakes of phyllosilicates (Figure 5.27 a). In some cases, sub grains of breunnerite within the main grain are partly rimmed by Fe-sulphide (Figure 5.27 a).

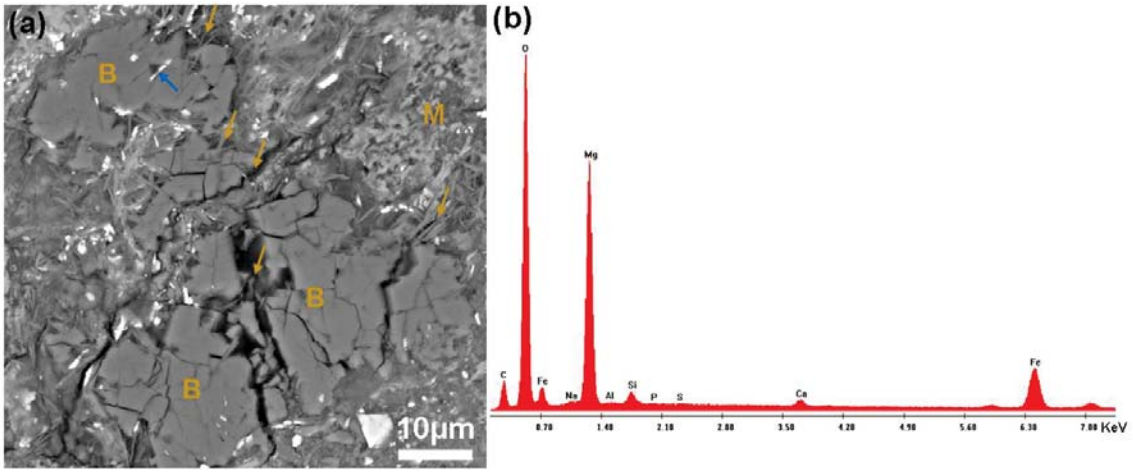

Figure 5.27- BSE image and EDS spectrum of a breunnerite grain in QUE 93005.
(a) BSE image of breunnerite (B) that contains with sheetsof phyllosilicates (yellow arrows). Some sub grains in this breunnerite are partly rimmed with Fe-sulphide (blue arrow). M is fine grained (<1µm) matrix. (b) EDS spectrum from breunnerite in (a). Note the small peak of Si that is probably related to the phyllosilicate inclusions within the breunnerite. The location of this grain in the sample studied is shown in appendix D9.

5.4.2.5 Breunnerite-dolomite intergrowth

QUE 93005 contains at least seven large grains of a breunnerite-dolomite intergrowth that range in size from ~20 µm to 70 µm. Six of these grains occur in three clusters, each with two grains, and the seventh grain is isolated (see Figure 5.22). These seven grains are in direct contact with fine grained (<1µm) matrix, and occur in two different patterns, namely grains free of inclusions (Figure 5.28 a) and grains that are intergrown with fibres of phyllosilicate and Fe-sulphides (Figure 5.28 b). In this respect, the boundaries between breunnerite and dolomite are sharp and also exhibit overgrowth patterns (e.g. Figure 5.28 a).

It was also observed that some dolomite grains in the sample contain small grains of breunnerite that occur mainly at the margins of the dolomite (Figure 5.29 a-b).

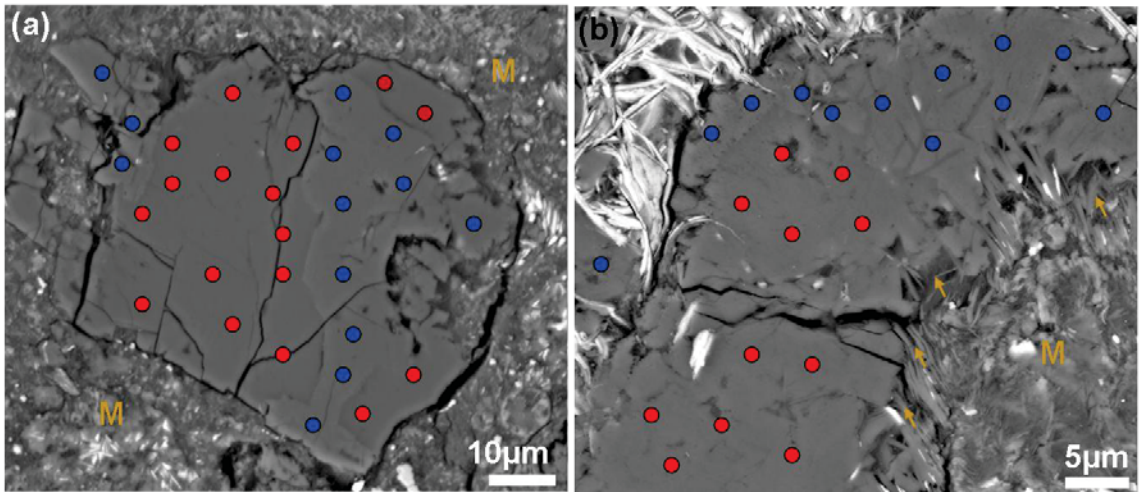

Figure 5.28- BSE images of breunnerite-dolomite grains in QUE 93005.
(a) BSE image of a large grain (80 µm) contains that breunnerite (blue) and dolomite (red). Note the breunnerite is more porous and brighter (i.e. higher atomic number) than dolomite, and the boundary between these minerals is gently curved. (b) BSE image showing breunnerite (blue) that occurs together with dolomite (red). Both are associated sheets of phyllosilicates (yellow arrows) and Fe-sulphides fibres (white areas in upper right side of the image). The locations of these grain in the sample studied are shown in appendix D9.

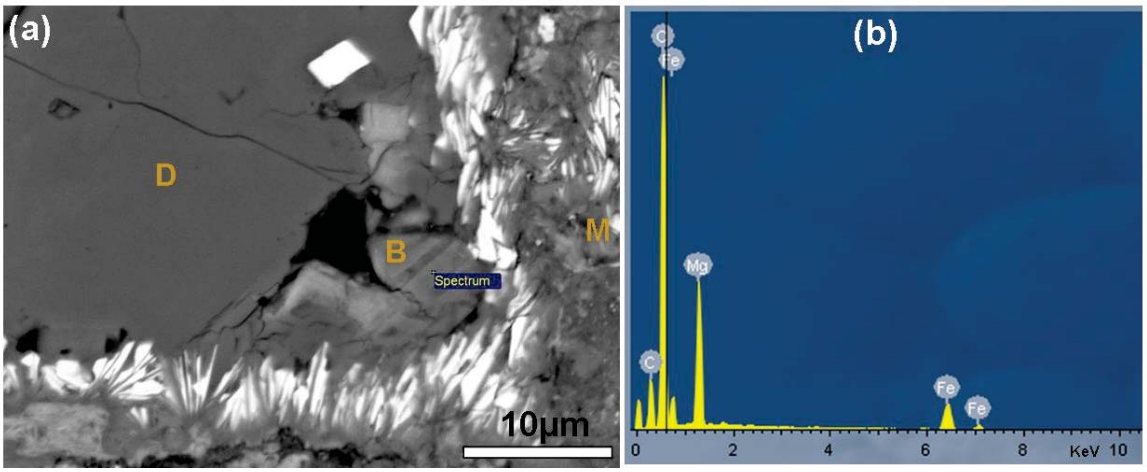

Figure 5.29- The occurrence of small grains of breunnerite in the margins of dolomite in QUE 93005.
(a) BSE image showing dolomite (D) grain that is partially lined by breunnerite (B). M is fine grained (<1µm) matrix. (b) EDS spectrum that was obtained from breunnerite in (a). The location of this grain in the sample studied is shown in appendix D9.

5.4.2.6 Breunnerite, Ca-poor dolomite and calcite intergrowth

Fifteen grains of breunnerite-(Ca-poor dolomite)-calcite were found in the sample of QUE 93005. These grains are scattered in the middle area of the sample. They range from 50 to 300 µm in size and have rounded, subrounded and subhedral shapes. Three types of carbonates are present within each of these fifteen grains. The first phase is breunnerite, which often occurs at the margins of grain. The subsequent phase is Ca-poor dolomite that occurs as a narrow strip (in most cases is ~3 to 6 µm) between the breunnerite and calcite;

it is also found as very small veins within the breurrenite. The third phase in these polymineralic grains is calcite, which is mainly present in the centre of these grains (see Figure 5.30a). It was also observed that phyllosilicates and Fe-sulphides occur as small inclusions within the breunnerite and Ca-poor dolomite, whereas these minerals are absent from the calcite. Most of the polymineralic grains (the main grains) are partially or entirely rimmed by phyllosilicate-sulphide intergrowths (Figure 5.30a). The calcite in these polymineralic grains shows two different textures that are either free of cleavages or have cleavages with planes occurring that meet nearly at right angles (Figure 5.30 a). The difference in morphology between the three minerals is readily detectable in BSE images. These petrographic observations indicate that the hardness of these three minerals gradually increases towards the breunnerite (Figure 5.30 b).

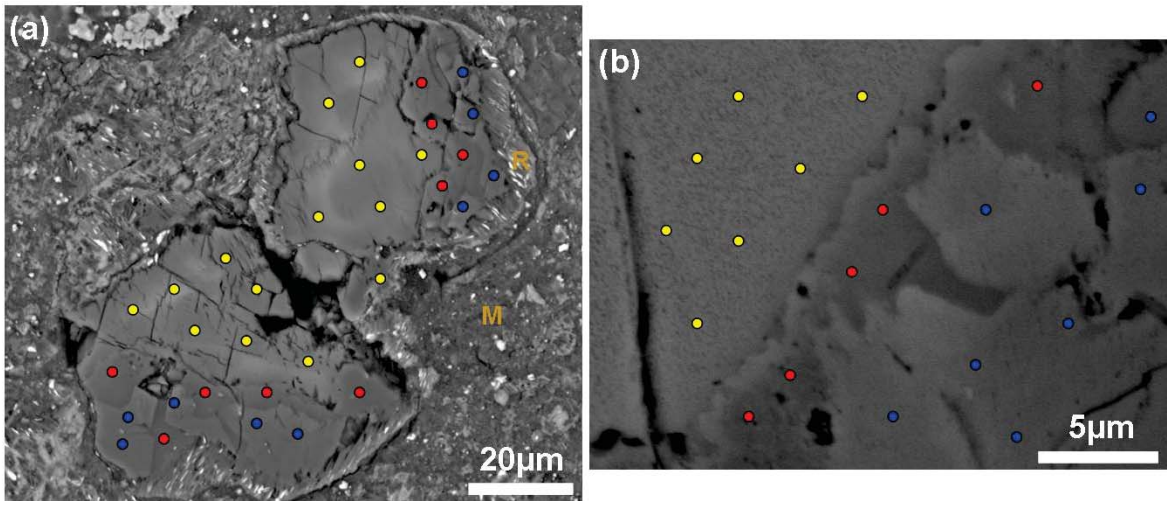

Figure 5.30- BSE images of intergrown breunnerite, Ca-poor dolomite and calcite in QUE 93005. (a) BSE image showing a polymineralic grain that contains at the margins breunnerite (blue). Ca-poor dolomite (red) occurs as a narrow rim between the breunnerite and calcite (yellow). Note in the lower left part of the grain the boundaries between the breunnerite and Ca-poor dolomite are sharp and gently curved. The calcite (yellow) is composed of two sub-grains, which are: sub-grain (in the middle area of the upper part of the grain) which shows a smooth surface and a sub-grain that contains cleavages which cover most areas of the calcite. R is a rim around the grain that consists of phyllosilicates-sulphide intergrowths. M is fine-grained (<1µm) matrix. (b) BSE image of small part of polymineralic grain showing the external variations between breunnerite (blue), Ca-poor dolomite (red) and calcite (yellow). The locations of these grains in the sample studied are shown in appendix D9.

5.4.3 Chemical composition of carbonate minerals in QUE 93005

Calcite and dolomite in QUE 93005 were chemically analysed by De Leuw et al. (2010). The mean of their analyses showed that the calcite has 0.43 ± 0.26 mol% $FeCO_3$, 0.22 ± 0.39 mol% $MnCO_3$ and 0.25 ± 0.22 mol% $MgCO_3$. The dolomite contains 7.2 ± 1.9 mol% of $FeCO_3$, 4.7± 1.2 mol% of $MnCO_3$ and 35.9 ± 2.8 mol% $MgCO_3$. In this study, CL

images of calcite and dolomite were obtained using the Quanta 200F SEM. X-ray maps of the four carbonate minerals were obtained using the Zeiss Sigma SEM, and the chemical analyses of these carbonates were acquired using the Zeiss Sigma SEM and EPMA.

5.4.3.1 CL imaging

CL imaging was carried out on 33 carbonate grains (single calcite, single dolomite, calcite-dolomite, breunnerite-dolomite, breunnerite-(Ca-poor dolomite)-calcite).

CL characteristics of carbonate minerals in QUE 93005 are classified into six CL types. These CL types are summarised and related to mineral generation in Table 5.9.

Mineral	CL SEM type	CL SEM characteristics	Abundance
Calcite	I	Low or high CL throughout the grain, in some cases contains patches of very high CL.	15 grains
Calcite	VII	Very high CL throughout a grain with rims of high CL.	4 grains
Calcite	X	Well defined band of high CL. In some cases contains core of low CL, overgrowth of low or very low CL filling the pore space.	2 grains
Breunnerite-dolomite	IX	Large band (5-10 μm) of low or very low CL in a part of a grain, in some cases is well developed, and the subsequent band is high CL.	1 grain
Breunnerite-dolomite	XIII	Oscillatory zoning shows sequence of thin layers (0.2-1 μm) of low, high and very high CL.	1 grain
Breunnerite, dolomite	XIV	Very low CL intensity through out a grain.	10 grains

Table 5.9- Characteristics and abundance of CL types of carbonate minerals in QUE 93005. The total number of grains imaged is 33.

The calcite in this meteorite shows CL type I and CL type VII (Figure 5.31 and Figure 5.32). CL imaging also shows that the majority of breunnerite-dolomite grains are un-zoned and classified as XIV (very low CL intensity through out a grain) (e.g. Figure 5.32). A few grains of breunnerite-dolomite can have CL type IX and CL type X (Figure 5.33 b-d).

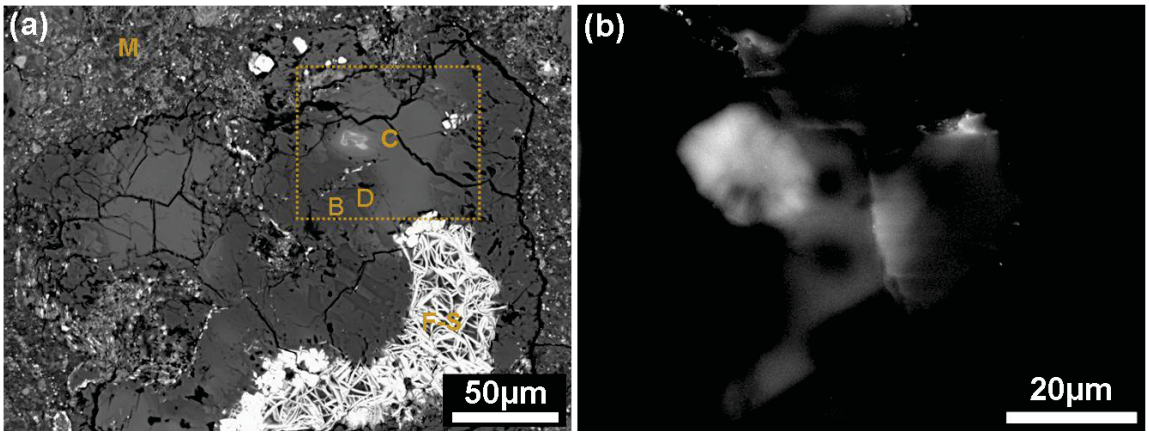

Figure 5.31- CL intensity type X of calcite, Ca-poor dolomite and breunnerite in QUE 93005.
(a) BSE image showing large grain (~150 µm) of calcite (C), Ca-poor dolomite (D) and breunnerite (B). M is fine grained (<1µm) matrix; F-S is fibres of Fe-sulphide that crystallized within this carbonate grain. (b) CL image of small area (boxed area) in (a). In this image both breunnerite and dolomite show very low CL intensity, whereas the calcite has features of CL type (X). The location of this grain in the sample studied is shown in appendix D9.

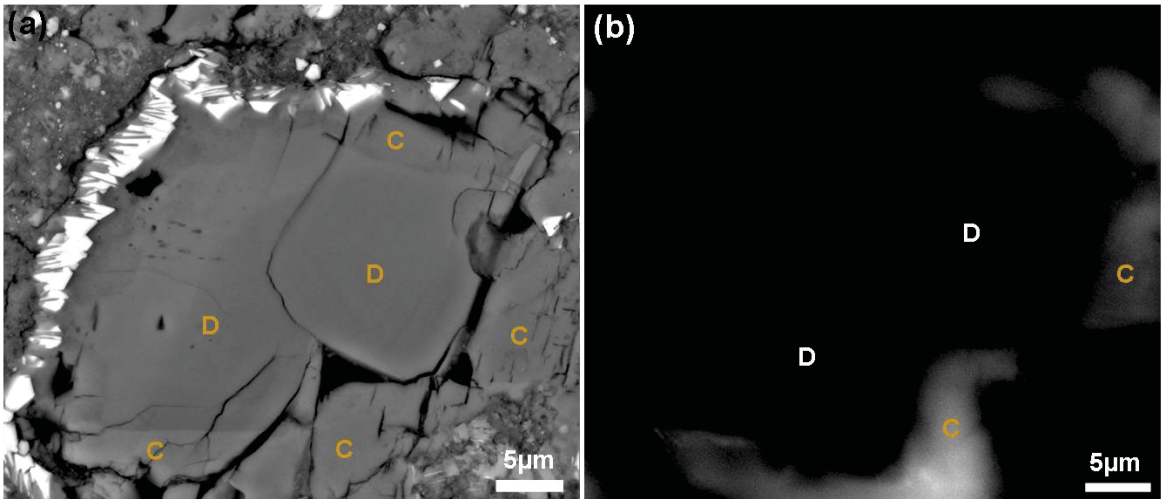

Figure 5.32- CL image of a calcite-dolomite intergrowth in QUE 93005.
(a) BSE image of calcite (C) and dolomite (D) intergrown. (b) CL image of calcite-dolomite in (a). Note the dolomite shows very low CL intensity (CL type XIV) (D) throughout the grain, whereas the calcite (C) shows characteristics of CL type I. The location of this grain in the sample studied is shown in appendix D9.

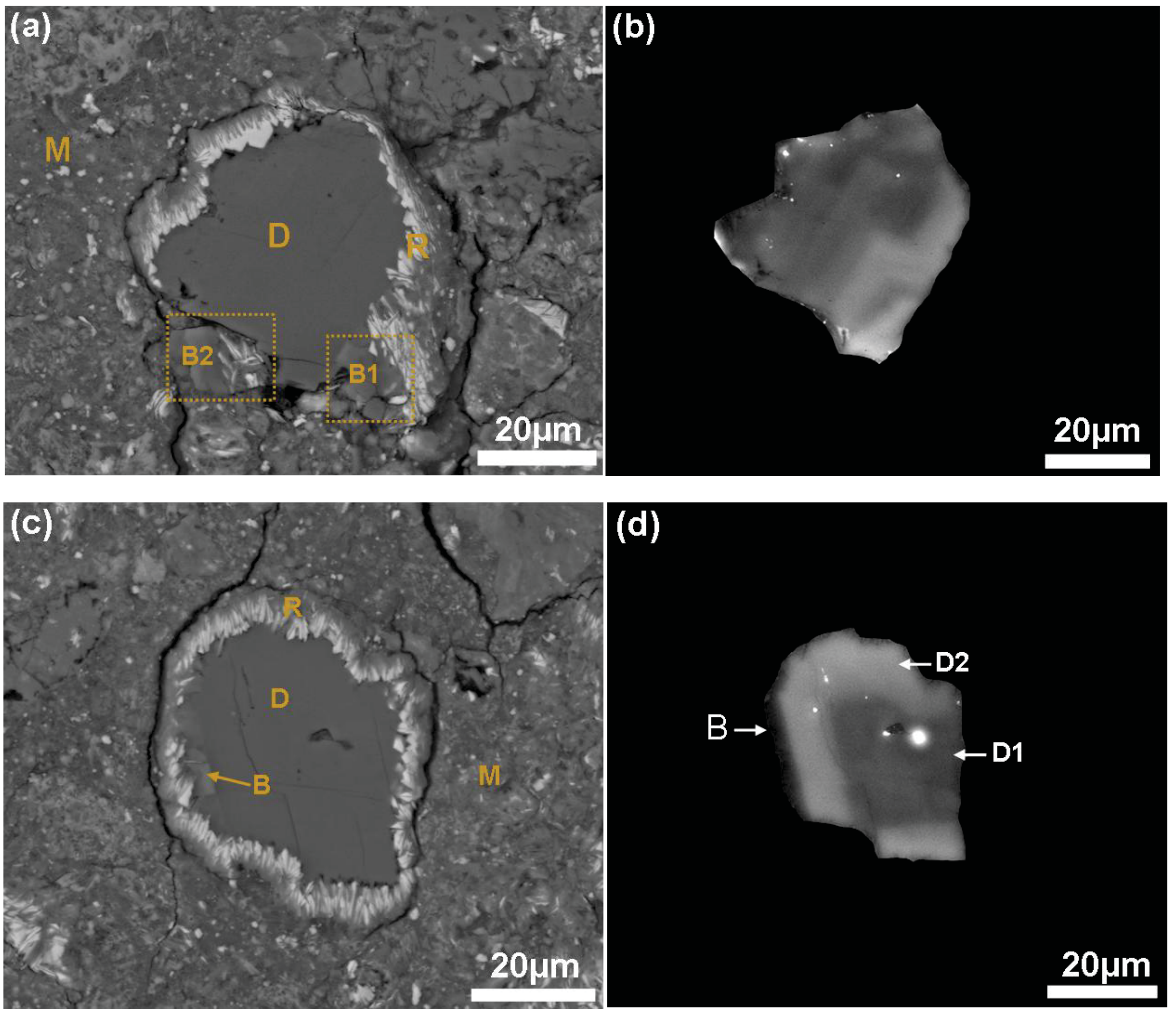

Figure 5.33- BSE and SEM-CL images breunnerite-dolomite intergrowths in QUE 93005.
(a) BSE image showing dolomite grain (D) that is partly rimmed with breunnerite (B1). Note a small fragment of breunnerite (B2) that is likely to be broken from the main breunnerite (B1). (b) CL image of the dolomite grain in a. This dolomite shows a sequence of thin layers (0.2-1 µm) of low CL, high CL (XIII). (C) BSE image of dolomite grain (D) that is partly rimmed with breunnerite (B). R is rims of pentlandite-phyllosilicate, M is fine grained (<1µm) matrix. (d) CL image of the dolomite grain in (c) showing CL type IX. This dolomite contains a broad zone of low CL intensity (D1) and overgrowth of high CL intensity (D2) and a thin layer of low CL intensity of breunnerite (B) that formed last. Note that the boundaries between the three zones are sharp and planar. The locations of these grains in the sample studied are shown in appendix D9.

5.4.3.2 X-Ray mapping

Qualitative element mapping of the whole sample, selected areas and some carbonate grains was conducted using the Sigma SEM with INCA software. Elemental mapping of polymineralic grains of breunnerite, Ca-poor dolomite and dolomite (e.g. Figure 5.34) shows that the Ca is mainly concentrated in the centre of these grains where the calcite has crystallized, and gradually decreases towards the areas of Ca-poor dolomite. The Ca is nearly absent in areas of breunnerite where Fe and Mg are dominant (Figure 5.34 and Figure 5.35).

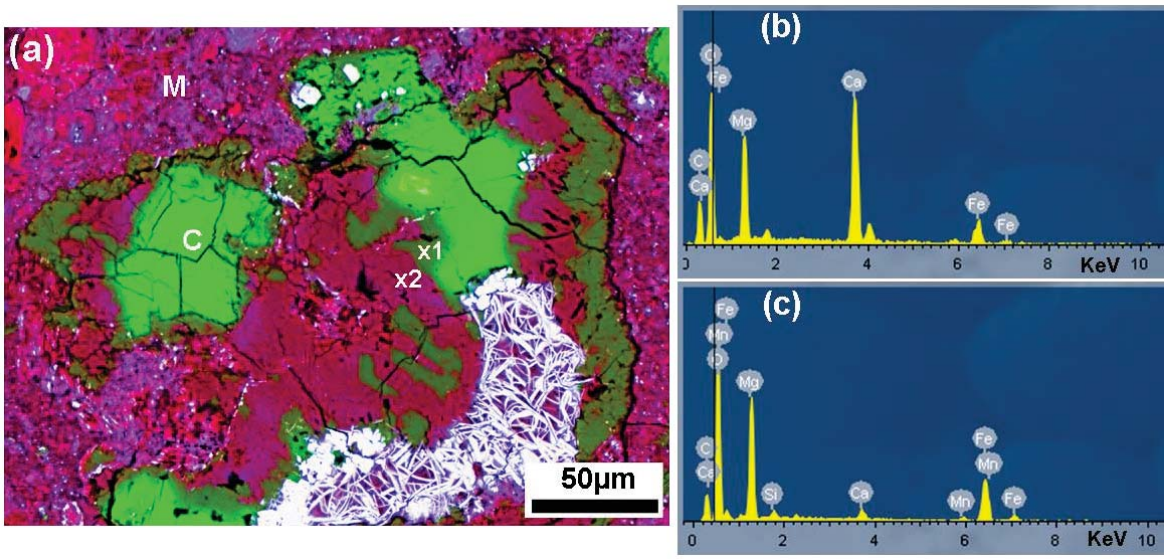

Figure 5.34- X-ray element map and EDS spectra of a polymineralic grain in QUE 93005.
(a) Element map combined with electron image of polymineralic grain of breunnerite (X2), Ca-poor dolomite (X1) and calcite (C). BSE image of this grain is shown in Figure 5.31 (a). The map shows the distribution of Ca, Fe and Mg within this grain. Note that all areas of calcite (green) are surrounded by a thin layer (1-5 µm) of Ca-poor dolomite (dark green) that contains less Ca. Note also that Ca-poor dolomite occurs as narrow veins within breunnerite (dark red). M is fine grained (<1µm) matrix. (b) EDS spectrum obtained from Ca-poor dolomite (X1) in (a). (c) EDS spectrum obtained from breunnerite (X2). Note the difference of Ca peaks between the two areas X1 and X2. The location of this map in the sample studied is shown in appendix D9.

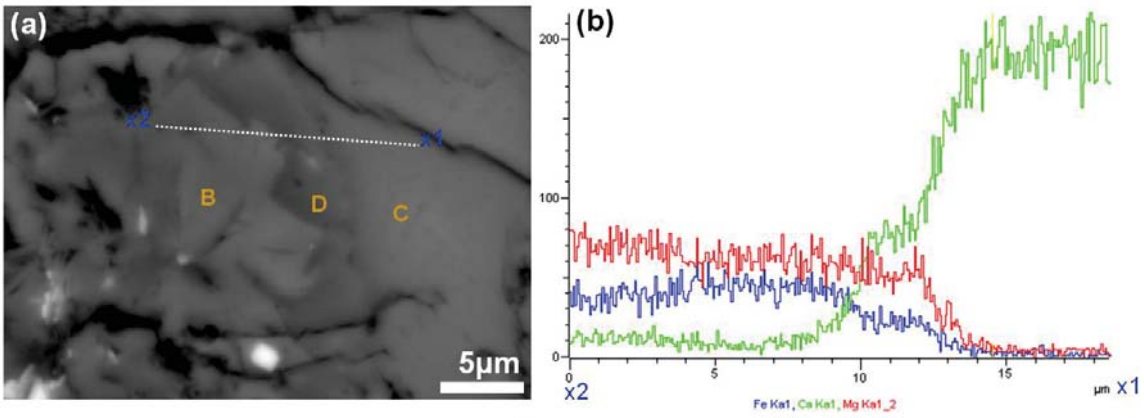

Figure 5.35- X-ray map of small area of a polymineralic grain in QUE 93005.
(a) BSE image showing the presence of the three minerals breunnerite (B), Ca-poor dolomite (D) and calcite (C) within a small area of the polymineralic grain. (b) EDS analyses of Ca, Fe and Mg along the line (x1-x2) in (a) showing the concentration of these elements within the three phases. The location of this grain in the sample studied is shown in appendix D9.

5.4.3.3 Quantitative chemical analyses

Carbonate minerals in QUE 93005 were chemically analysed using the Zeiss Sigma SEM (EDX) and EPMA. The analyses of these minerals using EDX show very close alignment with analyses by EPMA (Table 5.10). The quantitative chemical analyses of carbonates in

QUE 93005 are consistent with EDS analyses, which reveal that the breunnerite is enriched in Fe and Mg in comparison to Ca-poor dolomite and single grains of dolomite. However, chemical analyses by EDX show that breunnerite and Ca-poor dolomite have high concentrations of SiO_2 2.46 ± 1.01 and 3.53 ± 1.69 respectively, as these minerals are intergrown with sheets of phyllosilicates that are more abundant in Ca-poor dolomite than breunnerite. The quantitative chemical analyses show that Ca-poor dolomite has less $CaCO_3$. (~8 mol%) than dolomite grains, and $MnCO_3$ is more abundant in dolomite than Ca-poor dolomite.

				EDX				
	$CaCO_3$	**$MgCO_3$**	**$SrCO_3$**	**$FeCO_3$**	**$MnCO_3$**	**$NiCO_3$**	**SiO_2**	***n***
Breunnerite	3.54 ± 1.35	59.92 ± 5.30	0.04 ± 0.10	33.64 ± 3.63	2.86 ± 1.64	0.00 ± 0.00	2.46 ± 1.01	25
Ca-poor dolomite	40.72 ± 2.32	45.17 ± 2.06	0.02 ± 0.07	12.43 ± 1.52	1.65 ± 0.99	0.00 ± 0.00	3.53 ± 1.69	20
Dolomite	52.61 ± 1.84	35.40 ± 2.29	0.00 ± 0.00	7.40 ± 1.89	4.56 ± 0.93	0.00 ± 0.00	--	18
Calcite in polymineralic	97.89 ± 1.09	0.52 ± 0.33	0.00 ± 0.00	0.78 ± 0.31	0.81 ± 0.56	0.00 ± 0.00	--	17
Calcite grain	99.47 ± 0.45	0.17 ± 0.20	0.00 ± 0.00	0.33 ± 0.35	0.02 ± 0.09	0.00 ± 0.00	--	18
				EPMA				
	$CaCO_3$	**$MgCO_3$**	**$SrCO_3$**	**$FeCO_3$**	**$MnCO_3$**	**$NiCO_3$**	**SiO_2**	***n***
Breunnerite	1.90 ±1.16	61.90 ± 5.63	0.00 ± 0.00	34.10 ± 2.70	2.00 ± 1.81	0.03 ± 0.05	--	2
Ca-poor dolomite	43.12	44.50	0.04	10.52	1.77	0.05	0.76	1
Dolomite	51.40 ± 0.99	35.6 ± 2.45	0.00± 0.01	8.40 ± 1.81	4.50 ± 1.05	0.00 ± 0.04	--	12
Calcite in polymineralic	96.99 ± 1.55	0.74 ± 0.55	0.00 ± 0.00	1.27 ± 0.45	0.98 ± 0.66	0.02 ± 0.03	--	5
Calcite grain	99.38 ± 0.44	0.06 ± 0.12	0.04 ± 0.04	0.39 ± 0.16	0.11 ± 0.21	0.02 ± 0.03	--	9
				De Leuw et al. 2010				
	$CaCO_3$	**$MgCO_3$**	**$SrCO_3$**	**$FeCO_3$**	**$MnCO_3$**	**$NiCO_3$**	**SiO_2**	***n***
Calcite	99.0 ± 0.8	0.25 ± 0.22	--	0.43 ± 0.26	0.22 ± 0.39	--	--	40
Dolomite	52.1 ± 1.7	35.9 ± 2.8	--	7.2 ± 1.9	4.7 ± 1.2	--	--	16

Table 5.10- Mean of the quantitative chemical analyses (mole%) of carbonate minerals in QUE 93005. The analyses were obtained using the Zeiss Sigma SEM (EDX) and EPMA. Data presented as mean ± SD, error values are calculated to 1σ. For comparison, the average of dolomite and calcite analyses by De Leuw et al. (2010) is also included in this table. Full dataset with standard deviation is listed in appendix B-9.

The analyses of calcite and dolomite grains are also consistent with findings by De Leuw et al. (2010). EPMA analyses show that the single calcite grains in QUE 93005 contain less $FeCO_3$ than calcite grains in Cold Bokkeveld (-0.16 mol%). EPMA analyses show that dolomite grains in Nogoya and QUE 93005 have nearly similar contents of $FeCO_3$.

5.5 Summary

Petrographic observations of moderately to highly altered CM2 chondrites (CM2.2/2.3 to CM2.1) have shown that they contain Ca-carbonate minerals (both aragonite and calcite), breunnerite, Ca-poor calcite and dolomite. These minerals vary in abundance, chemical composition and also in their relationships with fine grained (<1μm) matrix from subtype to subtype of samples studied. The petrographic variations of these minerals are briefly summarized, and related to the alteration degree of each sample studied, in Table 5.11.

Alteration degree	**2.3/2.2**	**2.2**	**2.1**
Chondrite	**Nogoya**	**Cold Bokkeveld**	**QUE 93005**
Abundance of aragonite	4 grains in 32mm^2	6 grains in 110mm^2	--
Aragonite-calcite intergrowth	--	--	--
Aragonite occurrence	2 clusters	3 clusters	--
Aragonite size	5-20μm	20-80μm, 60μm length	--
Dissolution of aragonite	etched	etched	--
Aragonite twining	--	--	--
CL types of aragonite	--	I	--
Veins	--	present as gypsum	calcite
Pseudomorphs after calcite	6vol%	2.7vol%	--
Calcite replacing olivine	2.5 % of the calcite grains	1.8% of the calcite grains	1.6% of the calcite grains
Calcite twining	1.2% of the calcite grains	5.6% of the calcite grains	0.5% of the calcite grains
No. of CL types of calcite	3 types	4 types	3 types
Dolomite	2 grains in 32mm^2	--	0.7vol%
CL SEM types of dolomite	--	--	2 types
Breunnerite	--	--	0.3vol%
Ca-poor dolomite	--	--	0.2vol%

Table 5.11- Summary showing the main petrographic properties of carbonates in samples studied of subtypes CM2.3/2.2-CM2.1.

The occurrence of carbonate minerals and pseudomorphs after carbonate, relative to the alteration degree of CM chondrites (CM2.2/2.3 to CM2.1) can be summarized as following: Aragonite occurs as single grains in the less altered lithology (CM2.3) of Nogoya and Cold Bokkeveld (CM2.2). Aragonite in these meteorites occurs mainly as isolated clusters in the fine-grained (<1μm) matrix (e.g. Figure 5.13). It shows homogeneous SEM-CL characteristics (i.e. low or high CL throughout a grain), suggesting that the aragonite precipitated from chemically stable fluids. In common with some other meteorites (e.g. Pollen, LON 94101), the c-axes of aragonite grains in Cold Bokkeveld are mainly inclined in two different orientations. Some grains have their c-axes inclined at

high angles to the surface of the thin section (around the centre of the pole figure), while grains have c-axes that are inclined at low angles (close to the circumference of the pole figure) relative to the thin section surface (e.g. Figure 5.17).

CM2.2/2.3 to CM2.1 chondrites contain several calcite generations that are classified as follows: Calcite free of rims and inclusions that occurs in contact with the fine grained (<1μm) matrix. It is present in Nogoya and Cold Bokkeveld and QUE 93005. Calcite rimmed with tochilinite and/or Fe-sulphide occurs in Nogoya, Cold Bokkeveld and QUE 93005. Calcite rimmed with tochilinite and/or Fe-sulphide in Nogoya and Cold Bokkeveld has been partially, moderately or totally replaced by Mg-rich serpentine and/or tochilinite. Calcite replacing Mg,Fe silicates are found in CM2.2/2.3 to CM2.1 chondrites but differ in abundance from meteorite to meteorite, with a grain size ranging from a few micros to ~ 200μm. These grains contain patches of Fe-sulphide (e.g. Figure 5.14a). Calcite grains in CM chondrites (Nogoya, Cold Bokkeveld, QUE 93005) show 5 types of SEM-CL characteristic (I, II, VII, X, IX), whereas SEM-CL characteristics of calcite grains in CM2.5 to CM2.3 chondrites (e.g. Murray, Pollen, Mighei) show 13 types.

Dolomite is found mainly in the highly altered CM chondrite QUE 93005 (0.7 vol%), but it is rarely present (only two grains) in the less altered lithology of Nogoya (CM2.3). Dolomite intergrown with calcite is also present in QUE 93005 and represents ~1.9 vol% of total bulk volume of the rock. Petrographic observations show that dolomite inclusions occur in calcite grains in QUE 93005 (CM2.1) (e.g. Figure 5.26), indicating that this dolomite is likely to have been replaced by calcite. CL images of some dolomite grains in QUE 93005 show zonation (CL types: IX and XIII) (e.g. Figure 5.33), which reveals changes in the chemical composition of fluids during growth.

This study shows that chemically complex carbonate minerals occur mainly in QUE 93005 (dolomite-breunnerite grains and aggregates of breunnerite-(Ca-poor dolomite)-calcite cement). BSE images and EDS X-ray maps of polymineralic grains breunnerite-(Ca-poor dolomite)-calcite cement show that the breunnerite initially formed at the margins of pore spaces; subsequently, Ca-poor dolomite and then calcite cement filled the pore space. BSE and CL images of dolomite-breunnerite grains reveal that dolomite is most likely to have crystallized first within the pore space, to be followed by breunnerite. The occurrence of these minerals in QUE 93005 suggests that conditions of aqueous alteration differ from area to area of the parent body/ies.

Pseudomorphs of calcite grains (calcite rimmed with tochilinite and/or Fe-sulphide) made of Mg-rich serpentine, or Mg-rich serpentine intergrown with tochilinite, are present mainly in Nogoya and Cold Bokkeveld. Mg-rich serpentine in Nogoya is comparable to Mg-rich serpentine pseudomorphs after calcite in Pollen. Pseudomorphs in Cold Bokkeveld are classified into three types: (i) type 1 in which the tochilinite-serpentine intergrowth is enriched in Fe and S, and contains less Mg than Fe, (ii) type 2 represents tochilinite-serpentine intergrowths that are enriched in Mg and Fe and similar concentrations of these elements (Mg and Fe), (iii) type 3 is mainly composed of Mg-rich serpentine that is enriched in Mg and Si in comparison to Fe.

6

Carbonate minerals in CM2.1/2.0 to CM2.0 chondrites

6.1 Introduction

This chapter describes in detail carbonate minerals that occur in near completely and completely altered CM2.1/2.0-CM2.0 chondrites. These carbonates are mainly present in the fine grained (<1μm) matrix (as grains, aggregates, and veins) and in chondrule rims (as veins) of LAP 031166 (CM2.1/2.0), SCO 06043 (CM2.0) and ALH 88045 (CM2.0). Carbonate minerals in these CM2.1/2.0 chondrites are calcite and dolomite. This chapter provides full petrographic description (e.g. patterns of occurrence, grain size, texture) and chemical characterisation (CL imaging, X-ray mapping, EDS qualitative analyses, quantitative chemical analyses) of these carbonates. Information about the pseudomorphs after carbonate and replacement of carbonate are also provided, and this chapter further outlines how the carbonate pseudomorphs are related to those are found in less and moderately altered chondrites (e.g. Pollen and LON 94101).

6.2 Carbonates in CM2.1/2.0 LAP 031166

6.2.1 Petrographic observations

The weathering classification of LAP 031166 is B (AMN 29(2), 2006). Elemental mapping of the whole sample and small areas of it shows that LAP 031166 contains Ca-sulphate that fills fractures that cross-cut the fine grained (<1μm) matrix (e.g. Figure 6.1). The meteorite contains 0.8 vol% of Ca-sulphate. Ca-sulphate veins are more common in this meteorite than in any of the other CM chondrites examined in this study. Petrographic observations, Raman spectroscopy and EDS spectra indicate that LAP 031166 contains

both calcite (0.77%) and dolomite (rare). This volume of calcite occurs in area of about 100mm^2, which indicates that the carbonates are rare in comparison with other meteorites studied. For instance, LON 94101 has 1.29 vol% of Ca-carbonate that occur within an area of about 105mm^2. Furthermore, calcite grains are concentrated in a few areas of the sample, whereas most other areas are free of calcite. Petrographic observations and EDS spectra reveal that the majority of calcite grains that were originally present have recrystallized to Mg-rich serpentine. Some of calcite grains have also been partly or totally replaced by Ca-sulphate (Figure 6.1 and Figure 6.2 c), which is probably a weathering product because sulphates in Antarctic meteorites were described as weathering products by Jull et al. (1988).

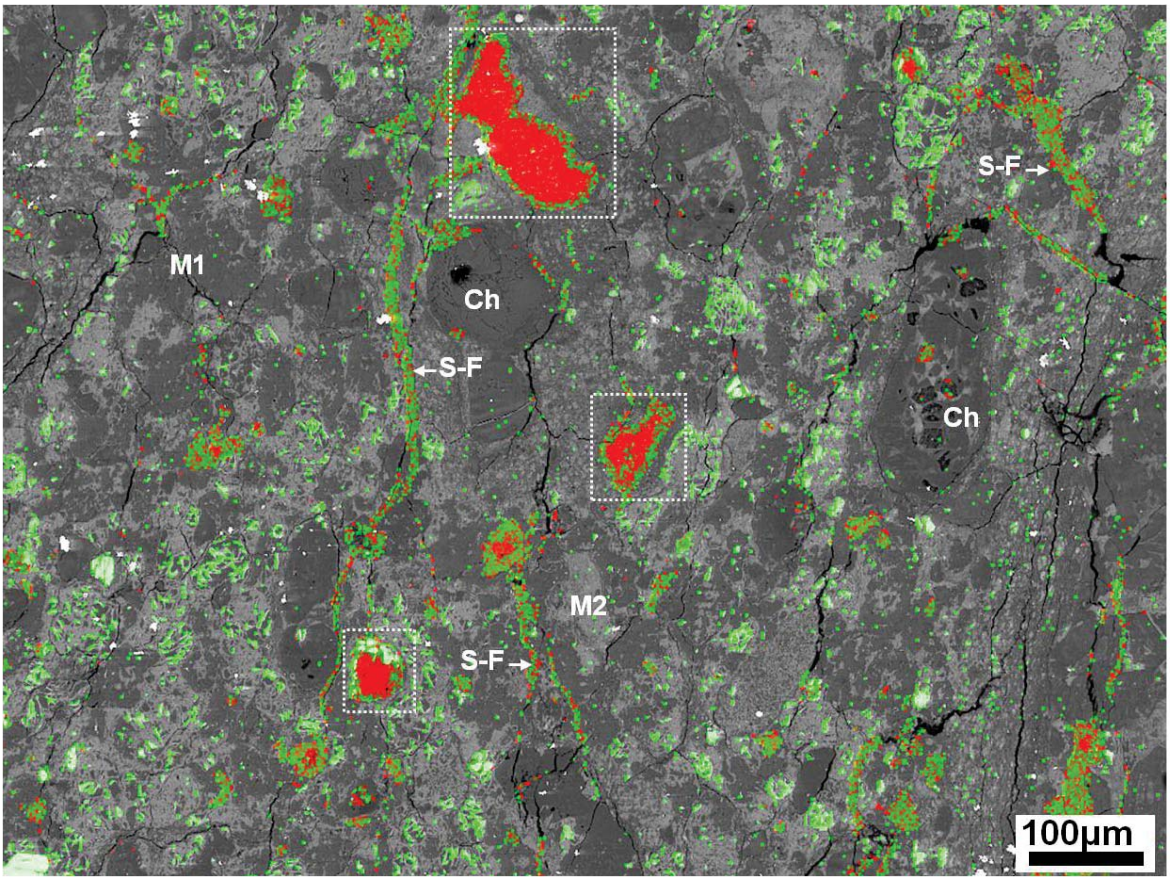

Figure 6.1- Combined elemental map (Ca and S) with BSE image of a part of LAP 031166. The image shows the presence of Ca-sulphate veins (S-F) that cut the fine grained (<1µm) matrix. Ca-sulphate is also present around and within some calcite grains (boxed areas). M1 is fine grained matrix (dark phase). M2 is fine grained matrix (bright phase). Ch denotes chondrule fragments. The location of this map in the sample studied is shown in appendix D10.

Calcite in LAP 031166 is present mainly as single grains within the fine grained (<1µm) matrix. They are subrounded, subhedral or irregular in shape. The majority of the calcite grains are rimmed by Fe-sulphide and/or Fe-serpentine and contain inclusions of Fe-sulphides and/or tochilinite that occur as small angular grains or fibres (Figure 6.2 a).

These inclusions have been partly or near completely replaced by Mg-rich serpentine. The crystals of Fe-sulphide (pentlandite) within these calcite grains range in size from ~1 µm to ~5 µm and in some cases are euhedral in shape and show overgrowths patterns with calcite (Figure 6.2 a and c). The tochilinite fibres range in length from ~1 µm to ~10 µm. The edges of a few grains of calcite occur in direct contact with fine grained (<1µm) matrix, and sometimes these calcite grains contain small inclusions of Fe-sulphide (Figure 6.2 b).

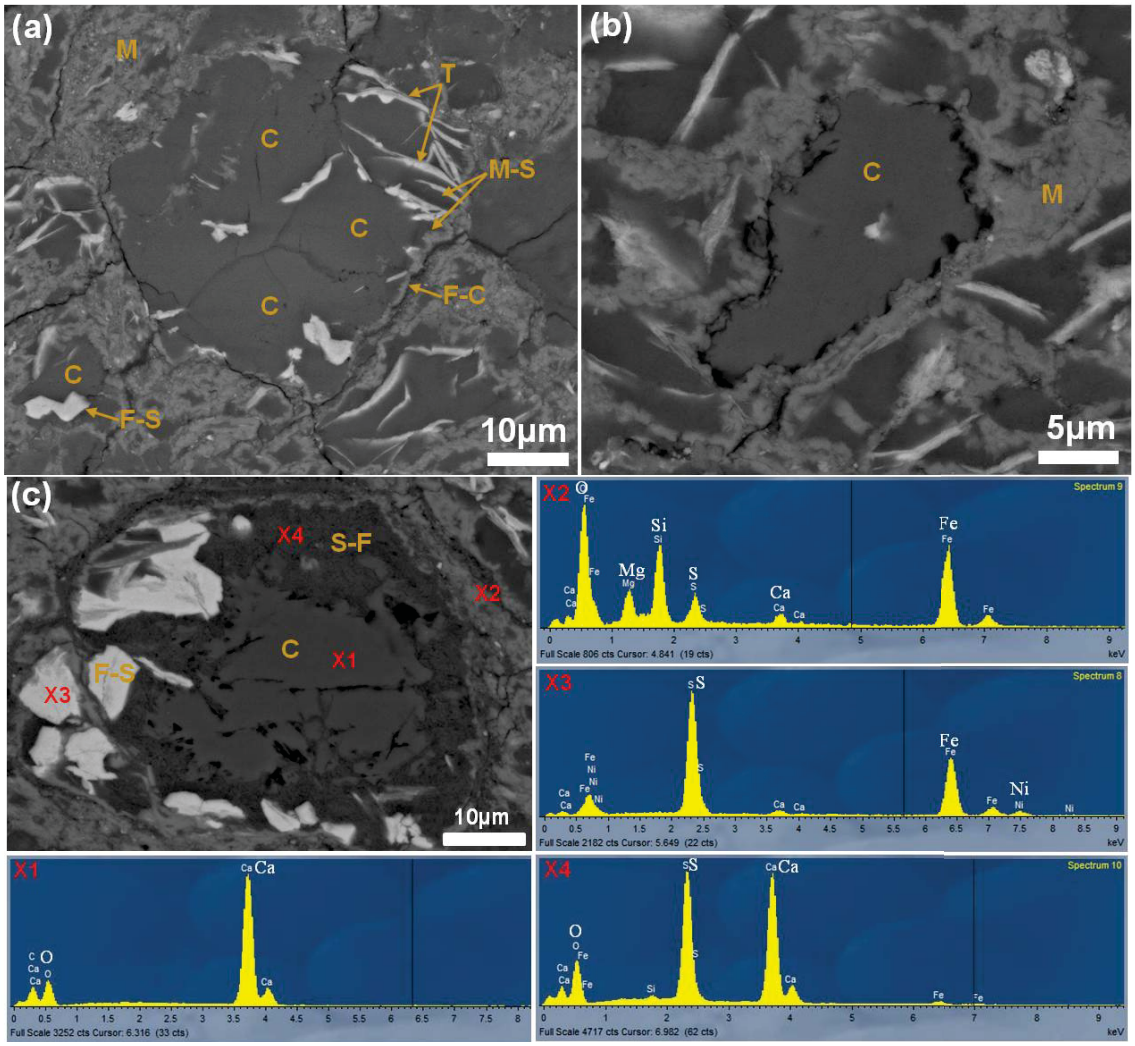

Figure 6.2- BSE images of calcite grains in LAP 031166.
(a) BSE image showing calcite grain (c) that has been partly replaced by Mg-rich serpentine (M-S). This grain is surrounded by thin rims (0.5 µm) of Fe-cronstedtite (F-C) and contains inclusions of tochilinite (T). M is fine grained (<1µm) matrix. (b) BSE image showing calcite grain (C) in contact with the fine grained matrix (M). (c) BSE image showing a calcite grain (C) that has been partly replaced by Ca-sulphate (S-F) and is also partially rimmed by blocky grains of Fe-sulphide (F-S). EDS was used to confirm the identity of each mineral. X1 is an EDS spectrum of calcite obtained from X1 in (c). X2 is an EDS spectrum of the fine grained matrix obtained from X2 in (c). X3 is an EDS spectrum of Fe-sulphide obtained from X3 in (c). X4 is an EDS spectrum of Ca-sulphate obtained from X4 in (c). The locations of these grains in the sample studied are shown in appendix D10.

Calcite also forms pseudomorphs after Mg-rich olivine. Matrix calcite grains range in size from about 3 µm to 80 µm, but calcite replacing olivine has a grain size of up to 600µm. It

was also observed that a large mass (300 μm in length) of calcite-phyllosilicate intergrowth is present in this meteorite.

Dolomite is very rare and it occurs as small grains within a fracture that cross-cuts the fine grained (<1μm) matrix and also around and within a few calcite grains (e.g. Figure 6.3).

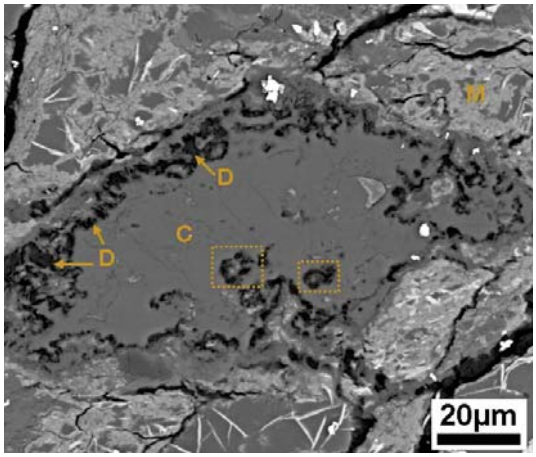

Figure 6.3- BSE image of a calcite grain in LAP 031166 that contains dolomite.
Note the dolomite occurs around grain margins (D) and in boxed areas within the calcite (C). This relationship suggests that calcite has been partly replaced by dolomite. M is fine grained (<1μm) matrix. The location of this grain in the sample studied is shown in appendix D10.

6.2.2 Chemical composition of calcite in LAP 031166

CL images of calcite grains in LAP 031166 were acquired using the Quanta SEM, and coupled with elemental mapping using the Zeiss Sigma SEM and quantitative chemical analyses by EPMA.

6.2.2.1 SEM-CL imaging

CL images of 20 grains of calcite were obtained. These grains exhibit only SEM-CL type I, i.e. a high SEM-CL intensity throughout a grain and in some cases contains patches of very high SEM-CL intensity.

6.2.2.2 Quantitative chemical analyses of calcite grains

Twenty one chemical analyses of twenty calcite grains were obtained by EPMA (Table 6.1). Only one of the grains measured is free of rims and all other grains are rimmed by Fe-sulphide and/or Fe-serpentine. The analyses were obtained from areas that are free from inclusions and sufficiently far from rims. $FeCO_3$ contents in grains examined range between 0.78 to 2.06 mol%.

Mole%		Wt%	
$CaCO_3$	98.52 ± 0.65	**Ca**	40.81
$MgCO_3$	0.26 ± 0.32	**Mg**	0.06
$SrCO_3$	0.00 ± 0.00	**Sr**	0.00
$FeCO_3$	1.22 ± 0.40	**Fe**	0.70
$MnCO_3$	0.00 ± 0.00	**Mn**	0.00
Sum	100.00	**Sum**	41.57
***n*= 21 analyses from 20 grains**			

Table 6.1- Mean of the quantitative chemical analyses of calcite grains in LAP 031166. Concentrations below detection limit are assumed to be zero. Data presented as mean ± SD, error values are calculated to 1σ. The full dataset with standard deviation is listed in appendix B-10.

6.2.3 Post crystallization deformation of calcite grains in LAP 031166

Petrographic observations reveal that calcite grains in LAP 031166 are free of twins. The majority of calcite grains that are rimmed by Fe-sulphide and/or Fe-serpentine have been partly, near completely or completely replaced by Mg-rich serpentine.

6.2.3.1 Pseudomorphs after Ca-carbonate in LAP 031166

Results of SEM point counting indicate that LAP 031166 contains 4.6 vol% of Mg-rich serpentine after calcite. Petrographic observations indicate that calcite grains are rimmed by Fe-sulphide and/or Fe-serpentine have been partly, near completely or totally replaced by Mg-rich serpentine. The pseudomorphs have inherited the orginal rims and inclusions around and within the calcite grains (Figure 6.4 a-b). Petrographic observations indicate also that the textures of pseudomorphs after calcite in LAP 031166 are identical to those in Pollen (see Figure 4.47 and Figure 6.4). It was also found that most of the Fe-sulphide and tochilinite inclusions and rims within and around the Mg-rich serpentine in LAP 031166 have been partly or totally replaced by Fe-serpentine (Figure 6.4 a-b).

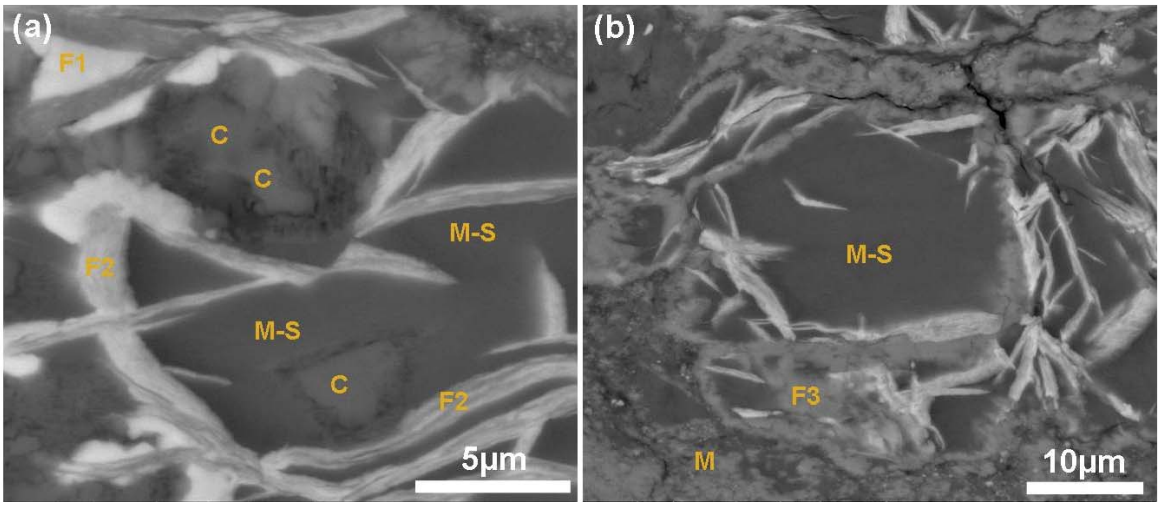

Figure 6.4- BSE images of Mg-rich serpentine pseudomorphs after calcite in LAP 031166.
(a) BSE image showing calcite grain (C) that has been near completely replaced by Mg-rich serpentine. Note the rims around the grain that are Fe-sulphide (F1), and an intergrowth of Fe-sulphide with Fe-serpentine (F2). Fe-sulphide is likely to have been partly replaced by Fe-serpentine. (b) Calcite grain that has totally transformed to Mg-rich serpentine (M-S). Note here areas of Fe-sulphide have been totally replaced by Fe-serpentine (F3), which is similar in texture to the bright phase of the fine grained (<1µm) matrix (M). The locations of these grains in the sample studied are shown in appendix D10.

6.2.3.1.1 Chemical composition of Mg-rich serpentine pseudomorphs after calcite

Chemical analyses of ten grains of the Mg-rich serpentine after calcite were carried out by the EPMA. The average of these analyses is shown in element wt% and oxide wt% in Table 6.2. Mg-rich serpentine pseudomorphs in LAP 031166 are rich in MgO (27.26 wt%) and SiO_2 (39.27 wt%), but have lower FeO (14.42 wt%). The chemical composition of the Mg-rich serpentine in LAP 031166 is nearly identical to the Mg-rich serpentine pseudomorphs in Pollen. Specifically the Mg-rich serpentine pseudomorphs in Pollen have 27.50 MgO wt%, 36.91 SiO_2 wt% and 11.32 FeO wt%.

Oxides wt%		Elements wt%	
Na_2O	0.15 ± 0.06	**Na**	0.11
MgO	27.26 ± 1.11	**Mg**	16.44
Al_2O_3	2.35 ± 0.11	**Al**	1.24
SiO_2	39.27 ± 1.53	**Si**	18.35
CaO	0.07 ± 0.04	**Ca**	0.05
FeO	14.42 ± 1.48	**Fe**	11.21
K_2O	0.11 ± 0.04	**K**	0.09
P_2O_5	0.02 ± 0.03	**P**	0.01
SO_2	2.48 ± 2.44	**S**	1.24
TiO_2	0.08 ± 0.01	**Ti**	0.05
Cr_2O_3	0.31 ± 0.04	**Cr**	0.21
MnO	0.21 ± 0.06	**Mn**	0.16
NiO	0.58 ± 0.44	**Ni**	0.46
Sum	87.30	**O**	37.68
n= 11 analyses of 10 grains.			

Table 6.2- Average microprobe analyses of Mg-rich serpentine pseudomorphs in LAP 031166 determined by EPMA.
Data presented as mean ± SD, error values are calculated to 1σ. The full dataset with standard deviation is listed in appendix A-9.

6.3 Carbonates in CM2.0 SCO 06043

6.3.1 Introduction

Quantitative modal mineralogy shows that SCO 06043 contains 1.7 vol% calcite (Howard et al. 2011). Lindgren et al. (2012) reported that carbonate minerals in SCO 06043 are calcite and dolomite that occur as single grains and calcite-dolomite intergrowths, and dolomite is also present as veins near to the fusion crust. They reported that carbonate minerals in SCO 06043 have a size range of ~10 to 60 μm. In this study, SEM point counting showed that SCO 06043 contains 0.24 vol% calcite and 0.79 vol% dolomite.

6.3.2 Petrographic observations

Petrographic observations and Raman and X-ray spectrscopy indicate that only calcite and dolomite are present in SCO 06043. X-ray maps of the whole sample and of small areas within it show that calcite and dolomite are present as single grains, aggregates and veins (Figure 6.5). In common with some other Antarctic meteorites (e.g. LAP 03166), SCO 06043 contains Ca-sulphate that occurs as isolated grains and as veins filling fractures that cross-cut the fine grained (<1μm) matrix. Ca-sulphate is also present around a few calcite grains, and in this respect the calcite is likely to have been replaced by sulphate. As stated above, Ca-sulphates in the Antarctic meteorites used in this study are likely to be terrestrial weathering products.

In addition to the presence of carbonate veins, the Ca X-ray map of the whole sample studied, and petrographic observations, indicate that carbonate minerals crystallized in small isolated areas, which are scattered through the fine grained (<1μm) matrix (Figure 6.5).

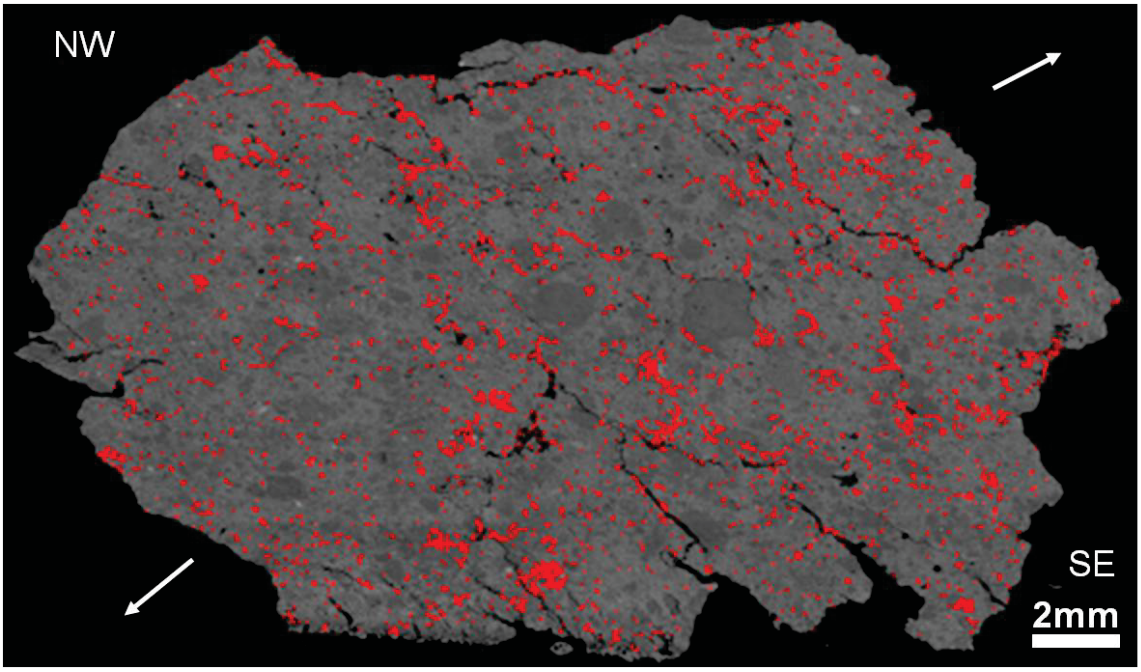

Figure 6.5- Combined Ca X-ray map with BSE image of the whole sample examined of SCO 06043. The map shows the distribution and concentration of the Ca (red areas) that locates calcite, dolomite and gypsum within the meteorite. Note the Ca is concentrated in the right hand part of the sample. Note also that Ca-rich areas are elongated along the NW and SE direction, and this elongation is likely to represent NE-SW oriented extension (white arrows). The figure is denoted with compass directions (N, S, E, W).

6.3.2.1 Calcite grains

Single grains of calcite are rare (0.24 vol%). The majority of these grains are surrounded by thin rims of tochilinite (0.2-0.5 μm), and have been partly replaced by Mg-rich serpentine. Rare calcite free of rims is also present in this meteorite. The majority of calcite grains are ~3μm to 30μm, however a few grains have a size of ~60 μm. Calcite grains in SCO 06043 are subhedral, irregular and subrounded in shape. In most cases, they have been etched around their margins.

6.3.2.2 Dolomite grains and veins

SCO 06043 contains 0.79 vol% of dolomite that is present as single matrix grains and also within fractures that cross-cut the fine-grained (<1μm) matrix. The abundance of dolomite grains in SCO 06043 is similar to QUE 93005 (0.7 vol% of single dolomite grains).

Lindgren et al. (2012) reported that SCO 06043 contains dolomite veins that are ~10 µm in width and 500 µm in length, which is also consistent with the petrographic observation of this study. In this study, these veins are described as extraterrestrial products. As stated in section 3.16.1, the dolomite within fractures in the fusion crust of SCO 06043 has been heated and texturally is different to dolomite located further from the crust (see Figure 3.54). Dolomite grains in SCO 06043 occur as grains free of rims and grains surrounded by rims of tochilinite (possibly tochilinite-serpentine intergrowth). Petrographic observations show also that some of the completely rimmed dolomite grains occur together with Mg-rich serpentine. In most cases, they are also associated with a few grains of pentlandite that range in size from ~1µm to 10µm. This pentlandite occurs as euhedral grains that followed by dolomite crystallisation (see Figure 6.6). Single dolomite grains in this meteorite range in size from 3µm to 50µm, and are sub-rounded, elongated, euhedral and irregular in shape. BSE images show also that margins and outer areas in some dolomite grains are brighter than other areas of the same grains (Figure 6.6), and qualitative chemical analyses by EDS indicates that the bright areas are enriched in Fe relative to grain interiors.

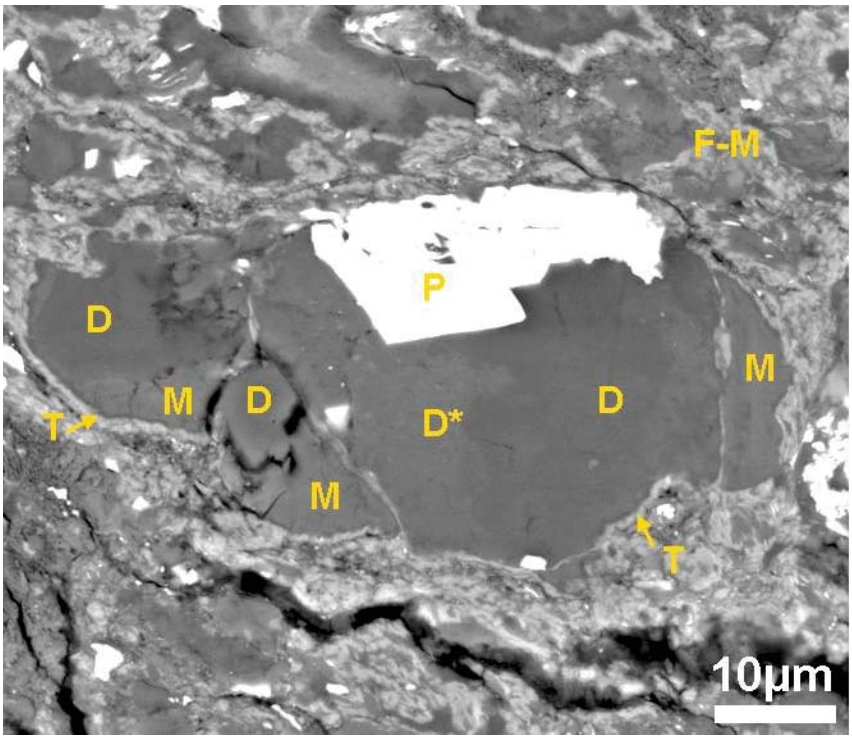

Figure 6.6- BSE image of a dolomite grain in SCO 06043.
The image shows that dolomite (D), Mg-rich serpentine (M) and pentlandite are enclosed within thin rims (0.2-0.5 µm) of a tochilinite-serpentine intergrowth (T). Note the Mg-rich serpentine is likely to have replaced dolomite. The pentlandite and dolomite show overgrowth patterns, which suggest that dolomite formed after pentlandite. F-M is fine grained (<1µm) matrix. D* is dolomite that is brighter than other areas of dolomite in the grain and so has a higher mean number. The location of this grain in the sample studied is shown in appendix D11.

6.3.2.3 Calcite-dolomite intergrowth

The meteorite contains several bimineralic grains where calcite and dolomite are intergrown. Calcite-dolomite intergrowths occur as single grains (grains composed of two areas: dolomite and calcite) or as aggregates that are ~50 µm to ~120 µm in size and contains several sub-grains of dolomite and calcite (e.g. Figure 6.7). In some cases, calcite-dolomite intergrowths are also associated with a few grains of pentlandite that have sharp boundaries with dolomite or calcite. It was also observed that some calcite grains contain small inclusions of dolomite, indicating the dolomite has been almost entirely replaced by calcite (Figure 6.7). However, calcite is often surrounded by dolomite, and in some cases the interfaces between calcite and dolomite are sharp.

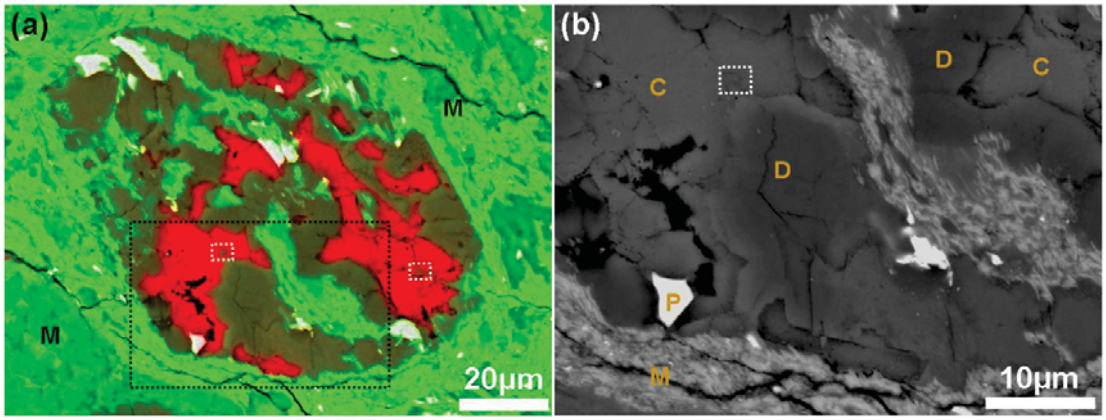

Figure 6.7- X-ray map and BSE image of calcite-dolomite intergrowth in SCO 06043.
(a) Element map (Ca and Mg) combined with BSE image of calcite-dolomite intergrowth. Dark green areas are dolomite, red areas are calcite and white areas are pentlandite. Note the presence of the dolomite inclusions within the calcite (white squares) that suggest the dolomite has been replaced by calcite M is matrix (light green). (b) BSE image at high magnification of the boxed areas in (a). Note the presence of dolomite (boxed area) in calcite (C). The dolomite (D) is darker than calcite (C). P is pentlandite and M is fine grained (<1µm) matrix. The location of this map in the sample studied is shown in appendix D11.

6.3.3 Chemical composition of calcite dolomite in SCO 06043

SEM-CL images of calcite grains in SCO 06043 were acquired using the Quanta SEM, and coupled with elemental mapping using the Zeiss Sigma SEM and quantitative chemical analyses by EPMA.

6.3.3.1 SEM-CL imaging

SEM-CL imaging of 15 grains of calcite in SCO 06043 were acquired. These calcite grains exhibit only SEM-CL type I that displays high SEM-CL intensity throughout a grain and in some cases contains patches of very high intensity.

6.3.3.2 Quantitative chemical analyses of calcite and dolomite grains

Twenty four chemical analyses from twenty two calcite grains were acquired by EPMA (Table 6.3). The $FeCO_3$ contents of the grains examined range from 0.15 to 2.00 mol%. Calcite grains in SCO 06043 have contents of $FeCO_3$ up to 0.90 ± 0.45mol%, whereas calcite grains in LAP 031166 contain 1.22 ± 0.40 mol% $FeCO_3$. Calcite of polymineralic grains in QUE 93005 contains 0.74 ± 0.55 mol% $MgCO_3$, 1.27 ± 0.45 mol% $FeCO_3$ and 0.11 ± 0.21 $MnCO_3$. The chemical composition of calcite in dolomite grains in SCO 06043 is shown in Table 6.3.

Mole%	**$CaCO_3$**	**$MgCO_3$**	**$SrCO_3$**	**$FeCO_3$**	**$MnCO_3$**	***n***
calcite grain	98.58 ± 0.75	0.37 ± 0.25	0.01 ± 0.02	0.90 ± 0.45	0.14 ± 0.16	18
calcite in dolomite	97.34 ± 2.67	1.55 ± 1.95	0.00 ± 0.00	0.76 ± 0.29	0.35 ± 0.56	6
Wt%	**Ca**	**Mg**	**Sr**	**Fe**	**Mn**	***n***
calcite grain	39.34	0.09	0.01	0.51	0.08	18
calcite in dolomite	41.30	0.40	0.00	0.49	0.22	6

Table 6.3- Mean chemical compositions of calcite in SCO 06043.
The total number of single grains of calcite and calcite intergrown with dolomite that were analyzed is 18 and 6 respectively. Data presented as mean ± SD, error values are calculated to 1σ. The full dataset with standard deviation is listed in appendix B-11.

Twenty two dolomite grains and two areas of a dolomite vein in SCO 06043 were chemically analysed by EPMA. The averages of these analyses are listed in Table 6.4. In common with analyses of the calcite vein in LON 94101, the analyses of the dolomite veins in SCO 06043 show very low contents of $FeCO_3$ (0.69 mol%) (see Figure 7.8) compared with other dolomite grains in this meteorite, it was also observed that $MnCO_3$ is absent in the dolomite vein.

As stated above, BSE images show that some dolomite grains contain margins or areas that are brighter than other areas of the same grains (e.g. Figure 6.6). EDS spectra and quantitative chemical analyses show that the bright areas in some dolomite grains have more $FeCO_3$ (about + 3 mol%) and $MnCO_3$ (about + 2 mol%) than other areas of the same grain.

Dolomite grains in SCO 06043 contain less $FeCO_3$ (- 0.18 mol%) than in QUE 93005 (EPMA analyses). The concentrations of $MnCO_3$ in dolomite grains in both meteorites (Nogoya and SCO 06043) differ slightly.

Mole%	$CaCO_3$	$MgCO_3$	$SrCO_3$	$FeCO_3$	$MnCO_3$	*n*
Dolomite grain	53.13 ± 3.99	39.14 ± 4.01	0.00 ± 0.00	4.73 ± 1.68	3.00 ± 1.44	40
Dolomite vein	55.47 ± 2.28	43.83 ± 2.15	0.00 ± 0.00	0.69 ± 0.13	0.00 ± 0.00	2
Wt%	**Ca**	**Mg**	**Sr**	**Fe**	**Mn**	***n***
Dolomite grain	22.33	9.99	0.00	2.97	1.86	40
Dolomite vein	21.47	10.30	0.00	0.37	0.00	2

Table 6.4- Mean of the quantitative chemical analyses of dolomite in SCO 06043.
The total number of dolomite grains and areas of vein that were analyzed is 40 and 2 respectively. Note that the dolomite vein contains very low concentrations of Fe, and Mn is also absent. Data presented as mean ± SD, error values are calculated to 1σ. The full dataset with standard deviation is listed in appendix B-11.

6.3.4 Post crystallization deformation of calcite grains in SCO 06043

Petrographic observations show that carbonate minerals in SCO 06043 are free from twins, but the majority of these carbonate grains (calcite and dolomite) have been partly, near completely or completely replaced by Mg-rich serpentine.

6.3.4.1 Pseudomorphs after Ca-carbonate in SCO 06043

Results of SEM point counting indicate that SCO 06043 contains 7.2 vol% of Mg-rich serpentine pseudomorphs after carbonate minerals. Mg-rich serpentine in SCO 06043 has mainly replaced calcite, but some of dolomite grains have been also transformed into Mg-rich serpentine. These carbonate grains are often surrounded by thin rims (0.2-0.5 μm) of tochilinite (possibly tochilinite-serpentine intergrowth) (e.g. Figure 6.8 see also Figure 6.6). Petrographic observations show that the Mg-rich serpentine pseudomorphs have inherited structural details such as rims (tochilinite) and inclusions (Fe-sulphide or/and pentlandite) that were present originally within the calcite and dolomite grains (e.g. Figure 6.8).

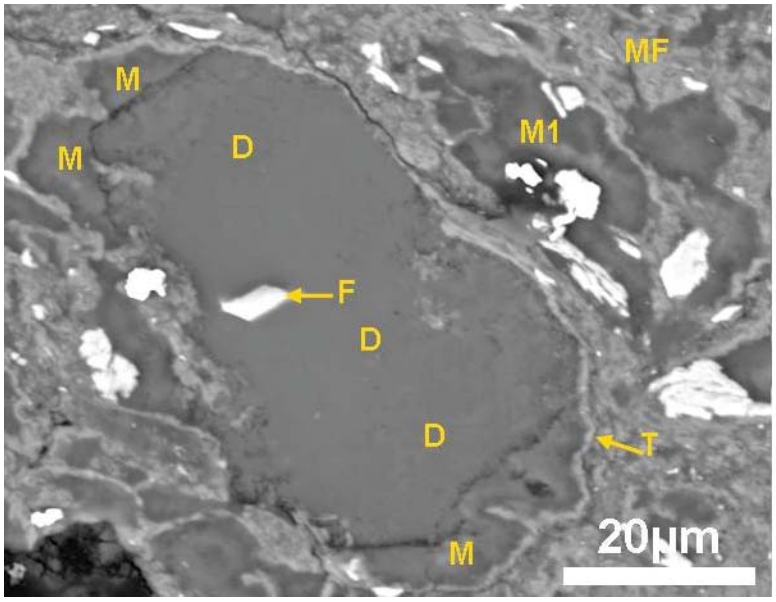

Figure 6.8- BSE image of Mg-rich serpentine replacing dolomite in SCO 06043.
The image shows a dolomite grain (D) that has been partly replaced by Mg-rich serpentine (M). Dolomite and Mg-rich serpentine are both enclosed by thin rims (~0.5 µm) of tochilinite (T). M1 is small grain of Mg-rich serpentine that is likely to have replaced calcite or dolomite. This grain is also rimmed by tochilinite. MF is fine grained (<1µm) matrix. F is Fe-sulphide inclusion in the dolomite grain. The location of this grain in the sample studied is shown in appendix D11.

6.3.4.1.1 Chemical composition of Mg-rich serpentine pseudomorphs after calcite and dolomite

Ten grains of Mg-rich serpentine after calcite and dolomite were chemically analysed by EPMA. The average of these analyses is presented as element wt% and oxide wt% in Table 6.5. In common with Pollen and LAP 031166, Mg-rich serpentine pseudomorphs in SCO 06043 are enriched in MgO (26.04 wt%) and SiO_2 (33.77 wt%). However, Mg-rich serpentine pseudomorphs in SCO 06043 contain higher concentrations of FeO (21.06 ± 2.59 wt%) in comparison with Pollen and LAP 031166 in which the Mg-rich serpentine pseudomorphs have 11.32 ± 1.59 wt% and 14.42 ± 1.48 wt% Fe respectively.

Oxides wt%		Element wt%	
Na_2O	0.20 ± 0.04	**Na**	0.15
MgO	26.04 ± 1.10	**Mg**	15.70
Al_2O_3	2.48 ± 0.46	**Al**	1.31
SiO_2	33.77 ± 3.07	**Si**	15.79
CaO	0.04 ± 0.02	**Ca**	0.03
FeO	21.06 ± 2.59	**Fe**	16.37
K_2O	0.05 ± 0.04	**K**	0.05
P_2O_5	0.01 ± 0.02	**P**	0.01
SO_2	3.11 ± 3.33	**S**	1.55
TiO_2	0.07 ± 0.02	**Ti**	0.04
Cr_2O_3	0.33 ± 0.19	**Cr**	0.23
MnO	0.13 ± 0.03	**Mn**	0.10
NiO	0.31 ± 0.20	**Ni**	0.24
Total	87.61	**O**	36.04
***n*= 14 analyses of 10 grains**			

Table 6.5- Average microprobe analyses of Mg-rich serpentine pseudomorphs in SCO 06043. The analyses were obtained by EPMA. Data presented as mean ± SD, error values are calculated to 1σ. The full dataset with standard deviation is listed in appendix A-10.

6.4 Carbonates in CM2.0 ALH 88045

ALH 88045 contains Ca-carbonates (calcite or aragonite) that occur mainly as aggregates (Zolensky et al. 1997). The results of SEM point counting show that ALH 88045 contains 1.91 vol% of calcite.

6.4.1 Petrographic observations

Raman spectroscopy indicates that calcite only is present in ALH 88045. Calcite occurs as single grains and aggregates that are scattered throughout the fine grained (<1μm) matrix (Figure 6.09). Single grains range in size from ~2 μm to ~30 μm, and are irregular or sub rounded in shape. The majority of these grains are free of inclusions and rims, but their outer margins have been etched**.** Calcite aggregates are 50-250 μm in size, irregular and sub rounded in shape. Some of these aggregates have silicates (pyroxene and olivine) or pentlandite between the calcite grains (e.g. Figure 6.10). In some cases, pentlandite is present as inclusions within calcite. Petrographic observations show that Mg-rich serpentine pseudomorphs are moderately abundant in ALH 88045, but all of them are free of calcite. All Mg-rich serpentine grains in this meteorite have thin rims of tochilinite.

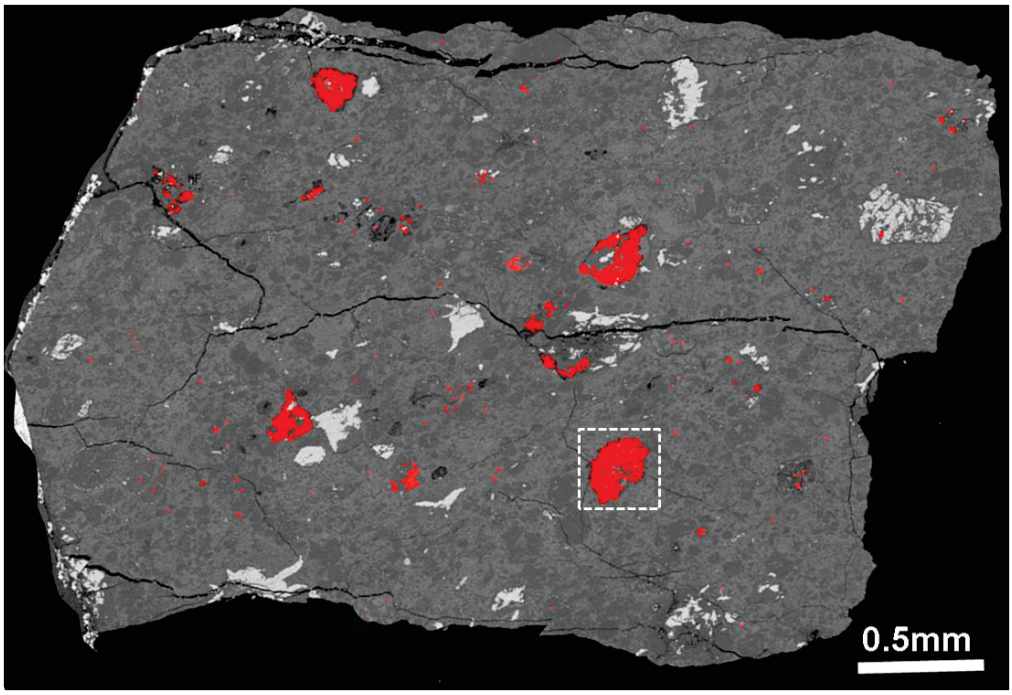

Figure 6.9- Combined Ca X-ray map and BSE image of the whole sample of ALH 88045.
This image shows the presence of calcite (red areas) within the ALH 88045. Note the meteorite contains large aggregates of calcite (50-250µm).

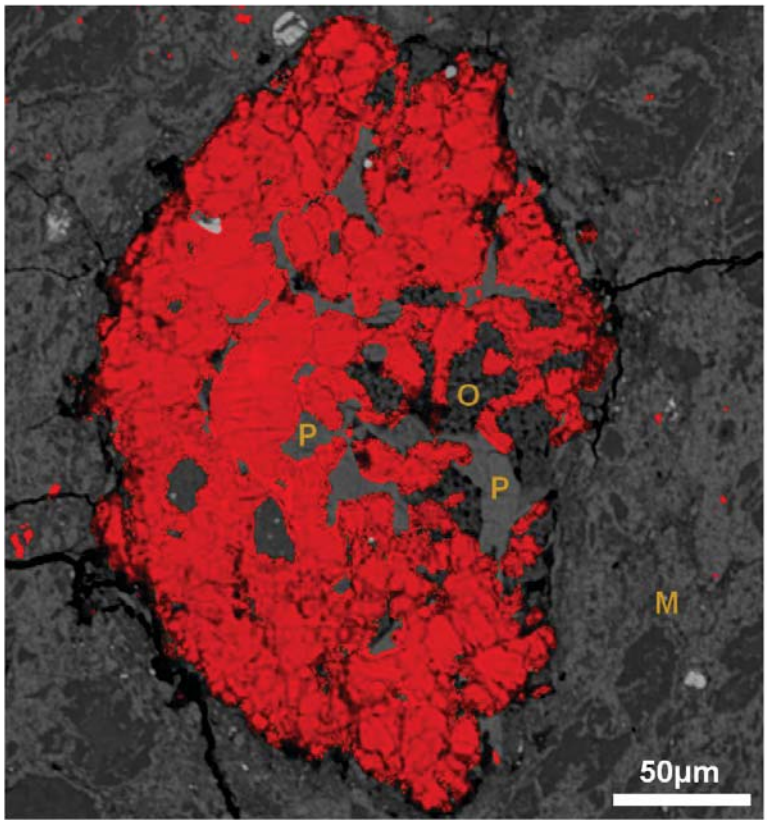

Figure 6.10- Combined Ca X-ray map with BSE image of calcite aggregate in ALH 88045.
The image shows a large calcite (red) aggregate (250µm) that contains pyroxene (P) and olivine (O) that is mainly present between the calcite grains. Pyroxene and olivine are likely to have been replaced by calcite. M is fine grained (<1µm) matrix. The location of this map in the sample studied is shown Figure 6.9 (boxed areas).

6.4.2 Chemical composition of calcite in ALH 88045

6.4.2.1 Quantitative chemical analyses of calcite grains

Ten chemical analyses from nine calcite grains were obtained by EPMA (Table 6.6). The analyses show that the calcite grains are enriched in $MnCO_3$ (0.50 ± 0.42 mol%) and nearly identical in $FeCO_3$ (0.90 ± 0.45) to calcite grains in SCO 06043.

Mole%		Wt%	
$CaCO_3$	98.16 ± 0.82	Ca	40.92
$MgCO_3$	0.52 ± 0.42	Mg	0.13
$SrCO_3$	0.00 ± 0.00	Sr	0.00
$FeCO_3$	0.82 ± 0.18	Fe	0.47
$MnCO_3$	0.50 ± 0.42	Mn	0.29
Total	100	Total	41.81
***n* = 9 analyses of 9 grains.**			

Table 6.6- Mean of the quantitative chemical analyses of calcite in ALH 88045.
The analyses were obtained by EPMA. Data presented as mean ± SD, error values are calculated to 1σ.
The full dataset with standard deviation is listed in appendix B-12.

6.5 Summary

Petrographic observations of high altered (CM2.1/2.2.0) and completely altered CM chondrites (CM 2.0) show that they contain calcite, dolomite and calcite-dolomite intergrowths. These minerals vary in abundance, chemical composition and also in their relationships with fine grained (<1μm) matrix from subtype to subtype of the samples studied. The petrographic variations of these minerals are briefly summarized and related to alteration degree of each sample studied in Table 6.7.

The occurrence of carbonate minerals (calcite and dolomite) and pseudomorphs after carbonate relative to the alteration degree of CM chondrites (LAP 031166, SCO 06043, ALH 88045) can be summarized as follows: Calcite in the CM2.2/2.3 to CM2.1 chondrites are found in a variety of contexts that include; Calcite free of rims and inclusions that occurs in contact with the fine grained (<1μm) matrix; Calcite grains that are enclosed within serpentine or serpentine and Fe-sulphide intergrowths. These grains have been partly, nearly completely or completely replaced by Mg-rich serpentine. Calcite also forms pseudomorphs after Mg-rich olivine. Calcite replacing olivine in LAP 031166 has a grain size of up to 600μm.

Calcite grains in LAP 031166, SCO 06043 and ALH 88045 exhibit only SEM-CL type I, i.e. a high SEM-CL intensity throughout a grain, and in some cases contain patches of very high SEM-CL intensity. Calcite grains in LAP 031166 are similar in Fe contents to calcite grain in Pollen. .

SCO 06043 CM2.0 dolomite is present as single matrix grains and also within fractures that cross-cut the fine-grained (<1μm) matrix. The abundance of dolomite grains in SCO 06043 is similar to QUE 93005 (0.7 vol% of single dolomite grains). The meteorite contains several bimineralic grains where calcite and dolomite are intergrown. Calcite-dolomite intergrowths occur as single grains (grains composed of two areas: dolomite and calcite) or as aggregates that are ~50 μm to ~120 μm in size, and contain several sub-grains of dolomite and calcite (e.g. Figure 6.7). It was also observed that some calcite grains contain small inclusions of dolomite, indicating that dolomite has been almost entirely replaced by calcite (Figure 6.7).

Pseudomorphs of calcite grains (calcite rimmed with tochilinite and/or Fe-sulphide) made of Mg-rich serpentine are present mainly in LAP 031166. Petrographic observations also indicate that the textures of pseudomorphs after calcite in LAP 031166 are identical to those in Pollen (see Figure 4.47 and Figure 6.4). In common with Pollen and LAP 031166, Mg-rich serpentine pseudomorphs in SCO 06043 are also enriched in MgO and SiO_2.

Alteration degree	**CM2.1/2.0**	**CM2.0**	**CM2.0**
Chondrite	**LAP 031166**	**SCO 06043**	**ALH 88045**
Calcite	0.8 vol%	0.2 vol%	1.9 vol%
Veins	gypsum	gypsum, dolomite	--
Calcite replacing olivine	2.5 % of the calcite grains	--	rare
Pseudomorphs after calcite	8.5 vol%	7.2 vol%	abundant 19.1 vol%
Calcite twinning	--	--	--
No. of SEM-CL types of calcite	1	1	--
Dolomite grains	2 grain in 100mm^2	0.8 vol%	--
CL types of dolomite	--	--	--
Calcite-dolomite intergrowths	--	3% of the carbonate grains in the sample	--

Table 6.7- Summary of the main petrographic properties of carbonates in the samples of CM2.1/2.0-CM2.0 meteorites studied.

7

Discussion

7.1 Introduction

Aqueous alteration of chondritic meteorites is indicated by the presence of secondary minerals such as phyllosilicates, carbonates, sulphates, oxides (i.e. magnetite), and secondary sulphides (Brearley, 2003). As stated in section 1.2.4, there are several possibilities regarding the location and conditions that formed the secondary minerals: (i) minerals that formed at high temperature (e.g. olivine and pyroxene) reacted with water vapor within the solar nebula as the temperature fell to about 375 K. (e.g. Grossman and Larimer, 1974); (ii) anhydrous dust in the solar nebula experienced hydration as a consequence of shock wave passage (Ciesla et al., 2003); (iii) during the pre-accretionary phase, aqueous alteration took place within short-lived small parent bodies (~ten metres), which were later disrupted, the altered contents and unaltered materials ultimately accumulating with each other in the final asteroidal parent body (Metzler et al., 1992; Bischoff, 1998); (iv) aqueous alteration took place within the asteroidal parent bodies of meteorites (Kerridge and Bunch, 1979; Zolensky and McSween, 1988; Browning et al., 1996).

Endress and Bischoff (1996) showed that carbonates in CI chondrites are likely to have formed as a consequence of aqueous solutions circulating in the parent body of CI chondrites. They found that carbonate grains formed as fragments of an earlier generation of carbonate veins. By contrast, veins in CM chondrites are very rare (Brearley, 2003). However, Ca-sulphate veins cross-cutting the matrix were observed in Cold Bokkeveld, and used as evidence for the last stage of asteroidal alteration by Lee (1993). Hanowski

and Brearley (2001) used vein fillings within chondrule constituents and multiple phases of chondrule alteration in ALH 81002 to argue that alteration took place after accretion. The presence of Fe-rich aureoles within CM chondrites was the consequence of alteration of metal and movement of Fe in the matrix. This observation also supports the idea of alteration taking place on the parent body (Hanowski and Brearley, 2000). The new observations of a large calcite vein in LON 94101 (see Figure 4.69 d), carbonate veins in QUE 93005 (e.g. Figure 5.21 b and Figure 5.23 b) and dolomite veins in SCO 06043 (see Figure 3.54) also provide support for asteroidal alteration. These veins are strong evidence that water movement took place within the parent bodies of CM chondrites, but most likely during later stages of aqueous alteration. In addition to carbonate veins in CM chondrites, observations of compositional zoning carbonates of the Y91198 CM2 chondrite together with their Mn-Cr dates were used by Brearley et al. (2001) to argue that the aqueous activity occurred on the parent body of CM2 chondrites. CL images of carbonate minerals (e.g. Figure 4.34 a-b), and X-ray maps of polymineralic carbonate grains in QUE 93005 (e.g. Figure 5.34 a) and SCO 06043 (e.g. Figure 6.7) obtained in the present study further strengthen the model of asteroidal alteration. Properties of carbonates and their relationship with water movement in the parent body/ies of the CM chondrites are discussed in more detail below.

7.2 The timing of carbonate crystallization relative to the sequence of events in the early solar system

The timescale of aqueous alteration on parent bodies of carbonaceous chondrites has been discussed by several authors. Using Rb-Sr techniques, Macdougall et al. (1984) estimated that aqueous alteration of CI chondrites took place about 50 Ma after accretion. Endress et al. (1996) and Hutcheon and Phinney (1996) used the ^{53}Mn-^{53}Cr isotope system to show that aqueous alteration of CI chondrites started less than 20 Ma after CAI formation. Brearley and Hutcheon (2000) documented that carbonates in ALH84034 formed after about 10 Ma after CAI. Brearley and Hutcheon (2000) reported that the most altered chondrites contain the lowest values of ^{53}Mn/^{55}Mn. They also concluded that aqueous alteration commenced within a few million years of the formation of CAIs and probably continued for about 15 million years. Based on ^{53}Mn/^{55}Mn value of dolomite in QUE 93005 and ALH 83100, De Leuw et al. (2009) concluded that aqueous alteration on the CM chondrites parent body/ies began synchronously with the formation of CAIs, or after a short period of time, and lasted at least 4 million years. They reported that carbonate minerals in less altered chondrites are older than those in highly altered CI chondrites. The

crystallization of dolomite in QUE 93005 was at 3.93±0.23 Ma after the formation of the oldest solids in the solar system at 4568 Ma (i.e. ~ 4564 Ma) (Lee et al., 2012). Fujiya et al. (2012) reported that the age of carbonate in four CM chondrites (Murchison, Y791198, ALH 83100 and Sayama) is 4,563.4+0.4/-0.5 Ma, which is about 4.8 Ma after the formation of CAI.

From the discussion, and results of this study, carbonate minerals in the studied CMs chondrites are likely to have crystallized very shortly after formation of CAIs. Petrographic observations, chemical analyses and isotope analyses of CM carbonates reveal that several episodes of carbonate formation occurred on the CM parent body/ies, but only one of these multiple generations of calcite probably formed at a similar time to CAIs (Figure 7.1). This study also shows that the carbonate minerals were subjected to several processes after crystallization, including replacement, dissolution and shock-induced twining. Each of these processes is discussed in more detail in the following sections.

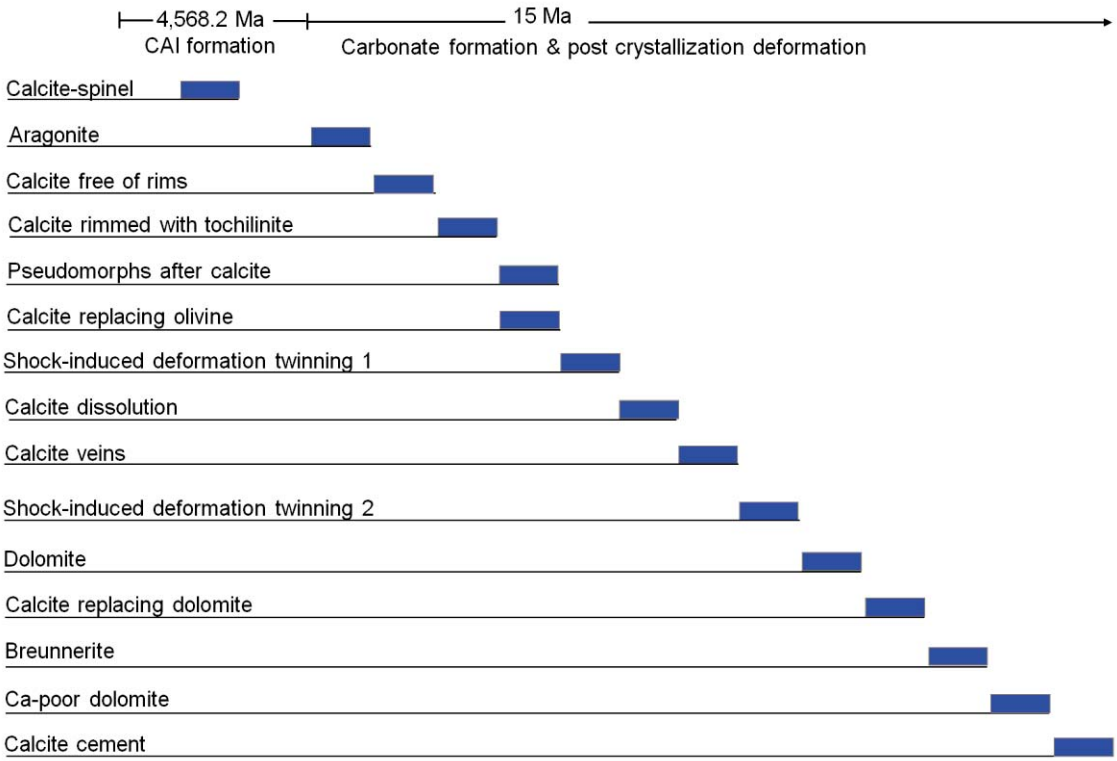

Figure 7.1- Summary of relative chronology of the formation of carbonate minerals and post-crystallization processes.
Based on the suggestion by Brearley and Hutcheon (2002), aqueous alteration is assumed here to have extended about 15 Ma after CAIs. The age of CAI formation is 4568.2 Ma as reported by Bouvier and Wadhwa (2010).

7.2.1 Formation of calcite-spinel intergrowth

Petrographic observations in this study show that Cold Bokkeveld only contains calcite-spinel assemblages (merely five aggregates). In these grains, spinel occurs as a core in calcite, which is also rimmed by PCP (tochilinite-cronstedtite intergrowths) (see Figure 5.14 b). This type of calcite is termed as calcite in CAI, and may not have formed in situ in the Cold Bokkeveld parent body. This calcite could have been formed by replacement of Mg, Fe silicates, but calcite intergrown with spinel is free of Mg, Fe silicate and/or Fe-sulphide inclusions, which characterise calcite after olivine (e.g. Figure 5.14 a). Overall, it is difficult to identify the origin of this calcite, as it is very rarely present in the studied CMs chondrites, and occurs only in conjunction with spinel. Therefore it is excluded from the comparison with other carbonate minerals that clearly formed within the parent body/ies of CMs chondrites.

Calcite within Murchison CAIs was observed by Armstrong et al. (1982). It was also observed in CAIs in Cold Bokkeveld by Greenwood et al. (1994) and within CAIs in LEW 90500 by Hua et al. (1999). Armstrong et al. (1982) suggested that calcite in the Murchison 'Blue Angel' CAI was formed on a small planetary body by one of two different processes; (i) as a consequence of the dissolution of matrix minerals at low temperature and pressure conditions that produced fluids with high concentrations of Ca^{2+} and HCO_3^-, with subsequent precipitation of calcite within pores in the CAIs; (ii) as the result of a metamorphic reaction between a Ca-rich mineral (e.g. melilite) and CO_2 rich fluids. Greenwood et al. (1994) favoured the possibility that calcite within CAIs had formed by aqueous alteration at low temperature and pressure. However, Hua et al. (1999) reached the conclusion that calcite spinel-fassaite CAIs in LEW 90500 were present prior to the incorporation of inclusions into their location in LEW 90500, and further suggested that the calcite could have formed by the replacement of melilite.

7.2.2 Aragonite formation

The occurrence of aragonite and other carbonate minerals relative to the alteration degree of CM chondrites is shown in Figure 7.2. It is remarkable that CM chondrites contain several Ca-carbonate generations that formed at different times. As found in this study, the Ca-carbonate generations are: (i) aragonite; (ii) calcite free of rims and inclusions that is similar in texture to aragonite; (iii) calcite rimmed with tochilinite, that in many cases has been replaced by Mg-rich serpentine and/or tochilinite; (iv) calcite replacing olivine; (v) calcite veins, (vi) calcite replacing dolomite and (vii) calcite cement (calcite that is

intergrown with breunnerite and Ca-poor dolomite, see Figure 5.30). Understanding the relationships between aragonite and calcite is vital in determining the composition and temperature of fluids from which these minerals crystallized in the CM2 parent body, and can also provide information on their relative timing of formation.

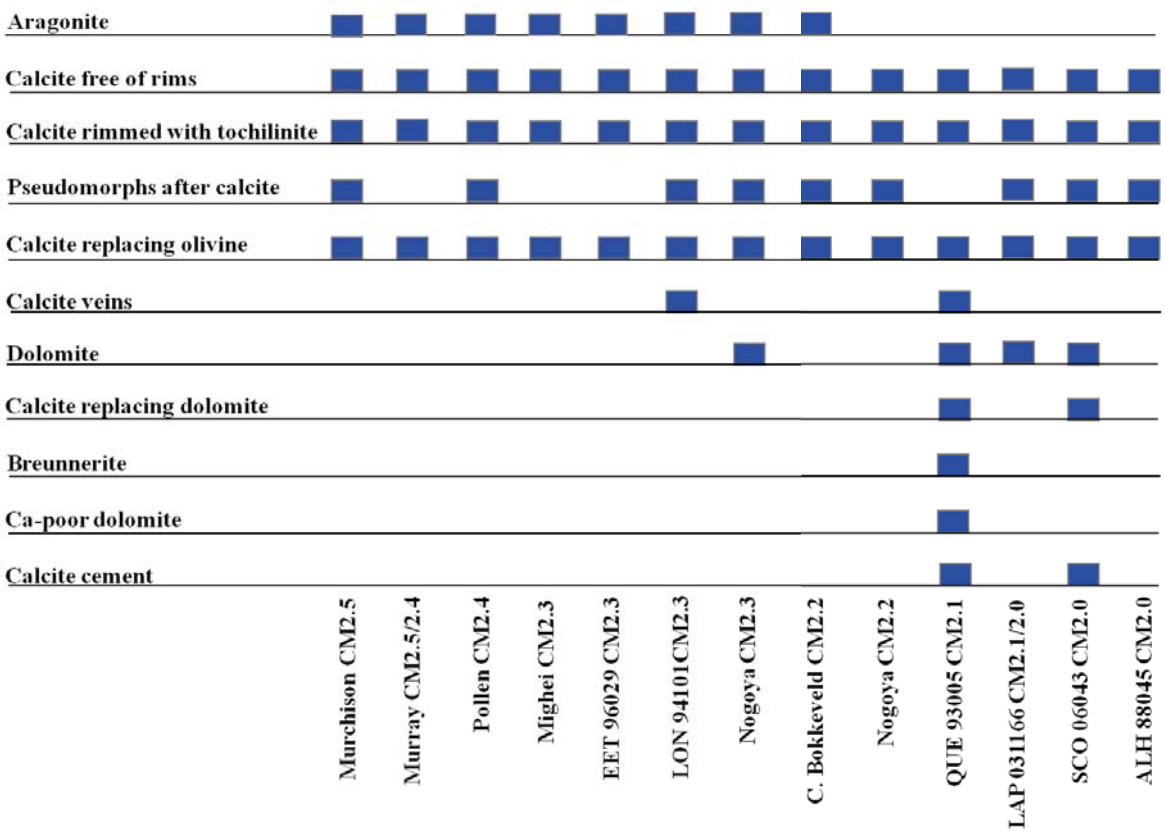

Figure 7.2- The occurrence of carbonates relative to alteration degree of CM chondrites. The presence of carbonates in each sample studied is indicated in blue.

7.2.2.1 Relative timing of aragonite formation

In this study, aragonite is inferred to mark the first generation of Ca-carbonate to crystallize in the parent body/ies of CMs chondrites. Lee and Ellen (2008) however reported that the matrix of Murray contains rare grains of aragonite that crystallized after calcite; they also suggested that aragonite formed after the matrix (phyllosilicates) and tochilinite-serpentine rims, as the aragonite grains have sharp boundaries with these materials. Barber (1981) found calcite intergrown with aragonite in Cold Bokkeveld, and concluded that the aragonite formed after calcite. Based on the experimental results by Morse et al. (1997), Lee and Ellen (2008) introduced a model for the evolution of fluid chemistry within CM2 chondrites. They argued that the crystallization of calcite from solutions supersaturated with respect to $CaCO_3$ changed to aragonite by an increase of

solution Mg/Ca (at about 0.04 (discussed below in section 7.2.2.2)) at a constant temperature, or by an increase in temperature at constant Mg/Ca.

However, results in this study of aragonite grains in Murchison reveal that there are two possibilities with regards to the formation time of calcite relative to aragonite: (i) calcite crystallized early and was later replaced by aragonite, so this is very unusual in terrestrial rocks, (ii) two separate stages of mineral formation, where aragonite precipitated early from fluids of a specific temperature and elemental composition, and then changing fluid properties caused the later crystallization of calcite. The second scenario is favoured for two reasons: (i) in two Murchison aragonite-calcite intergrowths (see Figures 4.6a and 4.7a), the aragonite is found only in one part of the grain, and has sharp boundaries with the calcite that is clearly an overgrowth otherwise free of inclusions of aragonite, (ii) EBSD maps of both aragonite-calcite intergrowths (e.g. Figure 4.15) also suggest two separate stages of mineral crystallization. The BSE image of an aragonite-calcite intergrowth in Figure 4.7a shows that each mineral is formed from multiple sub-crystals, but the sub-crystals have a preferred orientation (Figure 4.15a) indicating that while the sub-grains of each mineral formed at the same time, the aragonite and calcite formed at different times.

The model for CM2 aqueous alteration in Benedix et al. (2003) indicated that the process of aqueous alteration was continuous, and more highly altered meteorites contain carbonate with lower values of $\delta^{17}O$ and $\delta^{18}O$. Tyra et al.′s (2012) model also suggests that calcite grains with higher values of $\delta^{17}O$ and $\delta^{18}O$ crystallized before calcite grains with lower values. By applying these models to LON 94101, the aragonite must have formed before calcite. This is because aragonite in LON 94101 has a $\delta^{18}O$ of 39.9 ± 0.57 ‰ and $\delta^{17}O$ of 20.4 ± 1.1‰, whereas calcite grains in same meteorite has a lower $\delta^{18}O$ of 37.5 ± 0.65‰, although similar $\delta^{17}O$ of 20.9 ± 1.3‰ (see Figure 4.80). Therefore, the initial water on the parent bodies of CM2 chondrites produced carbonate with high oxygen isotope values, and these values fell as water obtained oxygen from reaction with anhydrous silicates (olivine/pyroxene). This model is consistent with the findings of Benedix et al. (2003) and Tyra et al. (2012).

The crystallographic orientation maps of aragonite grains in some of the studied samples reveal two generations that differ in orientation. Some grains have their c-axes inclined at high angles to the surface of the thin section (around the centre of the pole figure) and other grains have c-axes that are inclined at low angles (close to the circumference of the

pole figure) relative to the thin section surface (e.g. Figure 4.42 and Figure 4.74). These two generations may have formed consecutively, as the orientation map of an aragonite grain in Murchison suggests two different crystallization episodes within a pore space. The first is a sub-grain formed within a part of pore with c-axis inclined at high angle, and the second is a sub-grain that has its c-axis inclined to the horizontal (see Figure 4.14). Changing crystallographic orientation of these crystals was probably due to changes in the direction of pressure during the crystallization of aragonite in the parent body, so that aragonite crystals aligned themselves according to ambient pressure.

Aragonite forms needles which are orientated in the same direction in the sample (Murchison, Murray, Pollen, LON 94101, and Cold Bokkeveld). The most likely setting for generating the stress that caused the crystallographic preferred orientation of the aragonite needles is burial and compaction in shallow crustal levels of the parent body (Lee and Ellen, 2008). Stress can also be caused on the parent body by impact gardening (e.g. Lindgren et al. 2011a; Rubin, 2012), and explosive degassing (e.g. Brearley, 2006). Trigo-Rodriguez et al. (2006) also suggested that the fabric and foliation of chondrite are probably a result of impact. However, impact stress is very short-lived so that aragonite needles would not have had time to grow in a crystallographic preferred orientation during those events. Lee and Ellen (2008) related the preferred orientation of aragonite needles in Murray to the static stress field, rather than being impact related (e.g. Trigo-Rodriguez et al., 2006).

7.2.2.2 Factors promoting the formation of aragonite in parent body/ies of CM2 chondrites

Two Ca-carbonate minerals, i.e. aragonite and calcite, are common in a terrestrial sediments and rocks. Magnesium plays an important role in the morphology and growth of Ca-carbonate in terrestrial solutions (e.g. Folk, 1974). Fernández-Díaz et al. (1996) noted that the presence of Mg^{2+} ions in fluids hinders crystallization of calcite, as adsorption of Mg^{2+} on crystal faces poisons crystal growth. Davis et al. (2000) also found that Mg^{2+} inhibits calcite growth owing to incorporation of magnesium in the lattice of calcite. Studies on terrestrial carbonates have found that the crystallization of aragonite or calcite in seawater is controlled by temperature, and by magnesium absorption on calcite (Burton and Walter, 1991; Morse et al., 1997).

Choudens-Sánchez and González (2009) experimented with crystallization in cave systems to clarify the roles of fluid Mg/Ca ratio, and instantaneous supersaturation on the

mineralogy and composition of Ca-carbonate. They concluded that a combination of a saturated liquid in terms of $CaCO_3$ and Mg/Ca ratios controls the transition between the aragonite crystallization and the aragonite plus calcite crystallization zones in fluids with diverse ratios of Mg/Ca. As discussed above, the main factors that control the crystallization of calcite and aragonite are magnesium concentrations and temperature, but the relationship of these two factors in terrestrial minerals is unlikely to be simple (Wasylenki et al., 2005). Morse et al. (1997) used results of experiments from seawater-based solutions to explore the role of temperature in the crystallization of aragonite versus calcite and also the incorporation of Mg into calcite. Using Mg/Ca values of solutions from 0 to ~5.5 and temperatures of water from 0 to 35ºC, Morse et al. (1997) concluded that in sea water, and at under ~6ºC, calcite can be crystallized, and at a critical Mg/Ca ratio crystallization changes from calcite to aragonite by an increase of temperature (Figure 7.3). Their results also show that the precipitation of aragonite occurs where the Mg/Ca ratio is ~>0.5, and increases at a temperature of >~7ºC as Mg/Ca increases. The precipitation of calcite occurs mainly where Mg/Ca values are below ~0.5 at all temperatures.

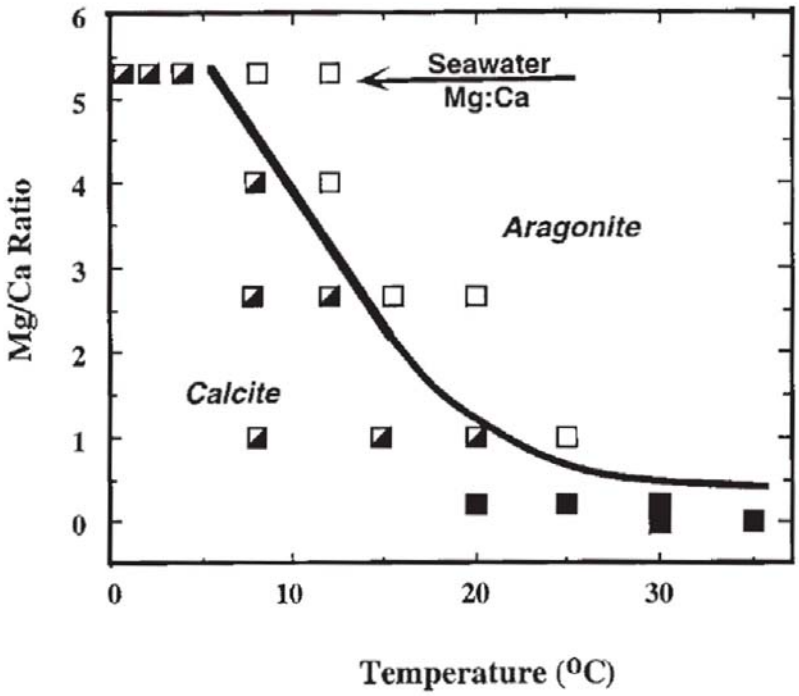

Figure 7.3- Mg/Ca ratio and temperature related to the polymorphs of $CaCO_3$ precipitated from sea water, from Morse et al. (1997).
Aragonite plots in white squares, calcite plots in black squares; divided squares (white and black) are aragonite formed on calcite that crystallized initially.

Lee and Ellen (2008) used the results from Morse et al. (1997) to conclude that the change from calcite to aragonite precipitation in the parent body of Murray was probably as a

result of temperature rise or increase of solution Mg/Ca ratio. Clayton and Maydea (1984) determined the temperature of solutions from which calcite in CM chondrites precipitated to be less than 20ºC.

In this study, the following equations were used to determine the Mg/Ca ratios of solutions from which aragonite or calcite precipitated, and so to test the Morse et al. (1997) model:

$$Mg/Ca\ Calcite/aragonite = \frac{Mole\%MgCO_3}{Mole\%CaCO_3}$$

$$Mg/Ca_{Fluid} = \frac{Mg/Ca_{Calcite/aragonite}}{D_{Mg,Calcite/aragonite}}$$

The average composition (in mole%) of calcite and aragonite was used to determine the Mg/Ca ratio of each mineral. Riciputi et al. (1994) used 0.044 as the partition coefficient for Mg into calcite, which was also used by Lee and Ellen (2008) to determine the Mg/Ca ratio of the solution from which the calcite grains in Murray precipitated. Lee and Ellen (2008) used 0.0013 (Gaetani and Cohen, 2006) as the partition coefficient for Mg into aragonite. The value of the partition coefficient for Mg into aragonite used in this study is also 0.00133, as determined by Gaetani and Cohen (2006), who experimentally determined the partition coefficients for aragonite/solution at 5°C to 75°C. Calculated Mg molar ratios relative to Ca for fluids in equilibrium with meteoritic aragonite were plotted on the graph (shown in Figure 7.3) of Morse et al. (1997) to explore the roles of temperature and Mg/Ca of fluids during the precipitation of aragonite (Figure 7.4). Fluids in equilibrium with aragonite in Murchison CM2.5 and Murray CM2.5/2.4 [2.209 and 2.92 respectively, note that the Mg/Ca of aragonite in Murray obtained from Lee and Ellen (2008)] have a higher Mg/Ca than those calculated for moderately altered chondrites such as LON 94101 CM2.3, Nogoya CM2.3/2.2 and Cold Bokkeveld CM2.2 (1.05, 0.94 and 0.83 respectively). However, a solution in equilibrium with aragonite in Mighei CM2.3 has a very low Mg/Ca ratio (0.24) in comparison with other moderately altered CM2.3-CM2.2 chondrites. Thus the formation of aragonite in Mighei is more likely to have been controlled by an increase in temperature at a constant Mg/Ca rather than by the Mg/Ca ratio alone (Figure 7.4). Oxygen isotope results from carbonate in Murchison were used by Clayton and Mayeda (1984 and 1999) to determine that phyllosilicates and carbonate precipitated in equilibrium with the same fluid and temperature (about 0 to 25ºC). Given the low Mg/Ca of ambient

solutions (0.24), aragonite in Mighei is most likely to have crystallized from a fluid at > ~ 35ºC.

Chemical analyses of aragonite show that the $FeCO_3$ concentrations are higher in less altered CM2.4/2.5 chondrites than in the CM2.3 chondrites (Figure 7.5). This observation is consistent with findings by De Leuw et al. (2010), that the Fe contents of calcite in CM chondrites decreases with increasing degree of alteration. However, aragonite in Cold Bokkeveld CM2.2 has a higher content of $FeCO_3$ than in the less altered lithology CM2.3 of Nogoya. Generally, aragonite in CM2.5-CM2.4 crystallized from fluids that have higher concentrations of Fe than those from which the aragonite grains in the CM2.3 crystallized.

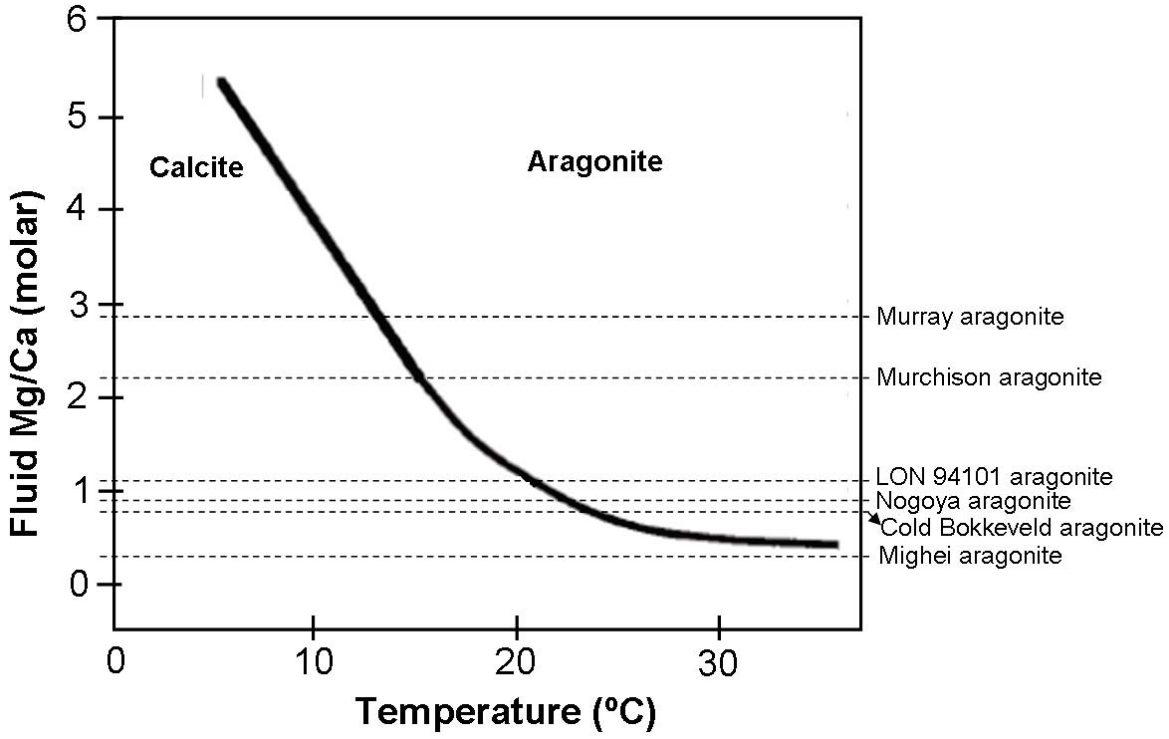

Figure 7.4- Graph showing the influence of Mg/Ca ratio and temperature on the precipitation of aragonite in CM chondrites.
Values of Mg/Ca ratio of fluids from which aragonite grains were precipitated are plotted in this graph, which is modified after Morse et al. (1997). Note the value of Mg/Ca ratio fluid of aragonite in Murray is obtained from Lee and Ellen (2008). A solution in equilibrium with aragonite in Mighei CM2.3 is comparable to a solution in equilibrium with calcite. It seems that aragonite in Mighei formed at a much higher temperature than in other meteorites.

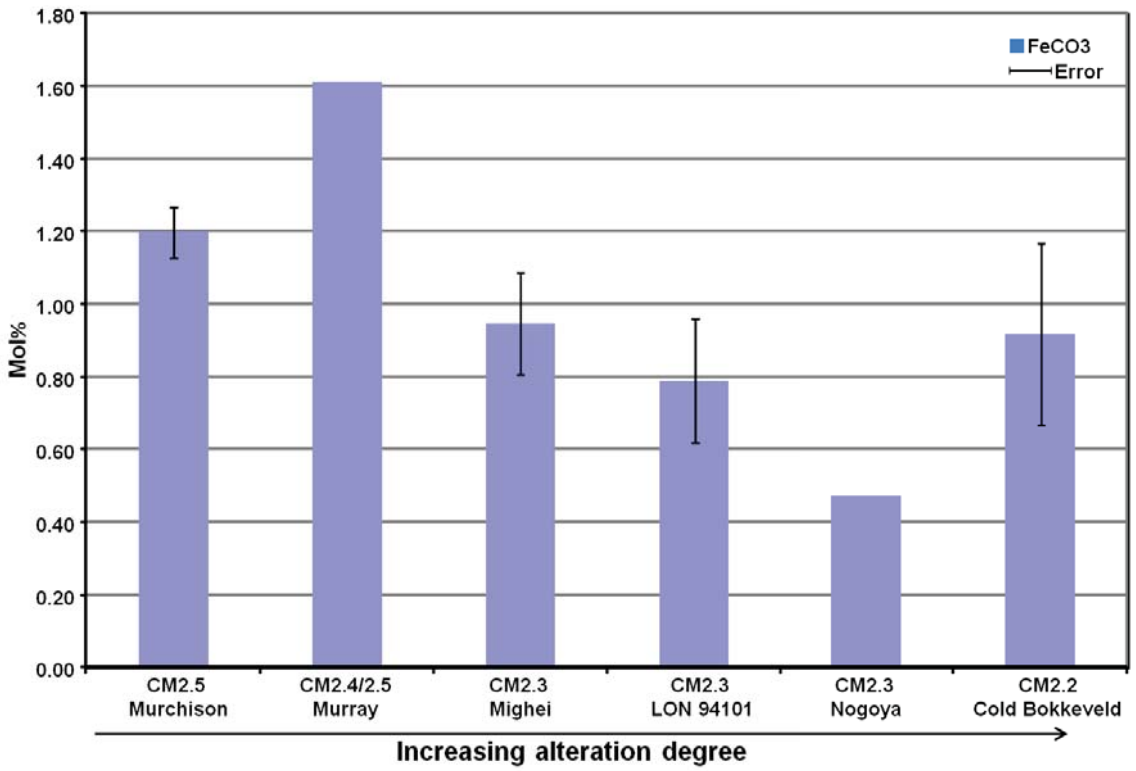

Figure 7.5- Histogram of Fe concentrations of aragonite in the studied CM chondrites.
Note that the two CM2.5 and CM2.4/2.5 chondrites have high Fe contents, but the Fe falls in the moderately altered chondrites (CM2.3 to CM2.2/2.3) (using EPMA). Chemical analyses of aragonite in Murray were obtained from Lee and Ellen (2008) (using EPMA).

7.2.2.3 Behaviour and source of fluids from which aragonite grains were precipitated in parent bodies of CM2 chondrites

Grimm and McSween (1989) concluded that the water for aqueous alteration was a direct consequence of the melting of accreted ice by the decay of ^{26}Al with a half-life 717,000 years, and this now the generally accepted heat source.

Chondrule glasses are believed to have been extremely susceptible to aqueous alteration (Hanowski and Brearley, 2001). Howard et al. (2011) reported that glassy mesostasis altered early to saponite, and dissolution of these materials also supplied elements such as Al, Na, Ca and Si to solution. Thus, Ca ions that were used for carbonate formation are likely to have been sourced from the hydration of chondrule mesostases or from the matrix of CM chondrites, which also provided all other elements (i.e. Mg, Fe, Mn and S) (De Leuw et al., 2010).

Petrographic observations of this study show that Fe-rich olivine is likely to have been altered earlier than Mg-rich olivine (e.g. Figure 3.15). This observation is consistent with Tomeoka et al. (1989), who reported that the hydration of Fe-rich minerals (fayalite and

metal) was first, and was followed by alteration of Mg-rich minerals (forsterite and pyroxene). The model by Tomeoka et al. (1989) suggests that calcite precipitated from solutions rich in Ca^{+} and CO_3^{2-}, and after hydration of olivine and pyroxene. The hydration of Ca-rich pyroxene (e.g. diopside ($CaMgSi_2O_6$); ferrohedenbergite ($CaFeSi_2O_6$) was probably another source of Ca used in the formation of Ca-carbonate during early stages of aqueous alteration. The formation of Ca-carbonate after the dissolution of diopside is described in the following equation:

$$CaMgSi_2O_6 + CO_2 + H_2O = CaCO_3 + MgSi_2O_4(OH)_2$$

It was reported by Wasson and Rubin (2009) that the source of carbonate ions is ambiguous. They suggested that CO_2 formed by energetic nebular processes lead to the production of reactive organics, which oxidized later on the parent body/ies of carbonaceous chondrites. They also suggested that $CaCO_3$ is most abundant in areas of the parent bodies that contained reactive organic matter. Tyra et al. (2012) suggested that shock depressurization may have caused solutions to degas CO_2 that was needed to commence the carbonate precipitation.

Aragonite is present only in the less altered and moderately altered CM2.5-CM2.2 chondrites (see Figure 7.2). It occurs mainly as isolated clusters within these meteorites (e.g. Figure 4.1), with the exception of Mighei and LON 94101, that contain larger and more widely distributed aragonite grains. This reveals that the aragonite precipitated from isolated regions of fluids that varied slightly in chemical composition, in terms of distance in the parent body (more details are provided in section 8.1). Howard et al. (2009) reported that severe limitation of water flow by the low permeability of CM chondrites parent bodies was probably the reason why fluids initially varied in composition. Fluid chemistry was controlled by the composition of anhydrous phases exposed to water, and the precipitation of Fe and Mg phyllosilicates in different areas of the same meteorite. Lee and Ellen (2008) found that aragonite grains in Murray formed in isolated clusters from films of solutions (high Mg/Ca ratio) that were present on scales of less than tens or hundreds of micrometers. These fluids were mainly concentrated within areas of high porosity and permeability in the matrix of Murray (Lee and Ellen, 2008). The presence of aragonite grains in small isolated clusters in the CM2 chondrites studied here supports the model that they were precipitated from isolated fluid reservoirs that slightly differed in chemical composition. It was also found in this study that aragonite grains that are in close proximity

to each other are similar in chemical composition, also indicating that they precipitated from the same fluid volume (see Table 4.20).

The formation of aragonite grains within small isolated areas of CM chondrites (Murchison, Murray, Pollen, Nogoya (less altered lithology) and Cold Bokkeveld) implies that fluid were locally depositing aragonite, but aragonite grains are more widely distributed in Mighei and LON 94101. Aragonite grains in these two CMs are also more abundant and larger in size in comparison to those in other CM chondrites. This suggests that the fluids from which aragonite precipitated were less localized in the parent body/ies of Mighei and LON 94101, and water may have flowed in the parent regions of some moderately altered CM chondrites. The majority of aragonite grains in the samples studied show homogeneous SEM-CL characteristics (e.g. Figure 4.18a and Figure 4.76a). This indicates that the precipitation of aragonite was from chemically stable fluids. However, some grains with oscillatory SEM-CL zoning are present in Mighei (CM2.3) (see Figure 4.62 a), which suggests that aragonite in Mighei precipitated from fluids that fluctuated in chemical composition. The low intensity of luminescence in the majority of aragonite grains (e.g. Figure 4.18a) is probably a consequence of absence of Mn^{2+}, and chemical analyses confirm that $MnCO_3$ is below detection limits. By contrast, the luminescence of calcite is known to be controlled by Mn^{2+} in the crystals, whereas the quenching of the crystal is due to ferrous activation (Marshall, 1988; Habermann et al., 1998). More discussion about the factors that control the luminescence of calcite is provided in Section 7.2.3.2.

7.2.3 Calcite crystallization

Calcite in CMs chondrites has a variety of petrographic relationships, namely free of rims and inclusions, rimmed with tochilinite and/or Fe sulphide, replacing olivine, and veins. Calcite free of rims and inclusions is less abundant than calcite rimmed with tochilinite, and calcite replacing olivine, and occurs as grains in direct contact with the fine grained (<1μm) matrix.

7.2.3.1 Formation of calcite free of rims and inclusions

Calcite free of rims and inclusions is comparable in texture and appearance to most of the aragonite grains (e.g. Figure 4.38 c-d), but in very rare cases this calcite contains minor inclusions of tochilinite (e.g. Figure 6.2 b). Unlike aragonite, calcite free of rims and inclusions occurs in all CM chondrites (see Figure 7.2). It is rare in the most highly altered

CM chondrites, though it is more common and grains are coarser in EET 96029, LON 94101 and QUE 93005. It exhibits more complex CL patterns than aragonite grains. This indicates that this calcite precipitated from fluids that were less compositionally stable than those from which aragonite crystallized.

In the models for aqueous alteration by Tomeoka et al. (1989) and Howard et al. (2009,2011) the formation of phyllosilicates commenced early, and these phyllosilicates are a result of aqueous alteration of anhydrous Mg,Fe silicates. As the majority of the calcite and aragonite that is free of rims and inclusion occur in direct contact with phyllosilicates, these minerals may have formed during or immediately after the phyllosilicates, and immediately after each other (aragonite and calcite free of rims and inclusions). As discussed in section 7.2.21, aragonite is most likely to have crystallized before calcite. There are two possibilities for the formation of aragonite and calcite free of rims relative to the tochlinite that is intergrown with another type of calcite (e.g. Figure 4.38 a). Calcite free of rims and inclusions and aragonite has either crystallized at a different time relative to tochilinite (probably before), or crystallized from isolated fluids that were supersaturated with only Ca^{2+} and CO_3^{2-}, and lacked sulphur. In support of the second possibility, it is known that alteration conditions differed from location to location in parent body (e.g. Johnson and Prinz, 1993; Riciputi et al., 1994; more discussion is also provided in section 8.1). This study has found that the chemical compositions and petrographic features of carbonate minerals do vary on the scale of micrometers.

Petrographic observations show that the majority of calcite grains in EET 96029 are free of rims and inclusions, and in common with aragonite grains in other CMs, the grains are euhedral and have sharp contacts with matrix. It is thus possible that the aragonite was replaced by calcite. In common with aragonite in Mighei and LON 94101, calcite free of rims in EET 96029 is also widely distributed in the meteorite. It seems therefore that EET 96029 is a piece of parent body where aragonite grains crystallized in isolated areas (on the scale of millimetres) and later transformed to calcite. Calcite free of rims and inclusions in EET 96029 exhibits only SEM-CL type I, that also characterises the majority of aragonite grains, and so possibly supports the relationship between aragonite and calcite in EET 96029. The chemical composition of calcite free of rims and inclusions in Pollen (CM2.4), EET 96029 (CM2.3) and LON 94101 (CM2.3) is plotted in a histogram in Figure 7.6. In Pollen (CM2.4) this calcite shows the highest amounts of $MgCO_3$ and $FeCO_3$ in comparison to the moderately altered (CM2.3) chondrites (EET 96029 and LON 94101). The high $FeCO_3$ concentration of the rim-free calcite is consistent with early crystallization

because the Fe content of calcite decreases with an increase in degree of alteration (De Leuw et al., 2010) (Figure 7.6).

Chemical analyses of carbonate minerals show that aragonite has higher concentrations of Sr^{2+} than calcite. Assuming that aragonite was replaced by calcite in EET 96029, then Mg and Sr were lost during replacement. Studies of terrestrial rocks by Yoshioka et al. (1986) confirm Mg and Sr are lost during the transformation of aragonite to calcite.

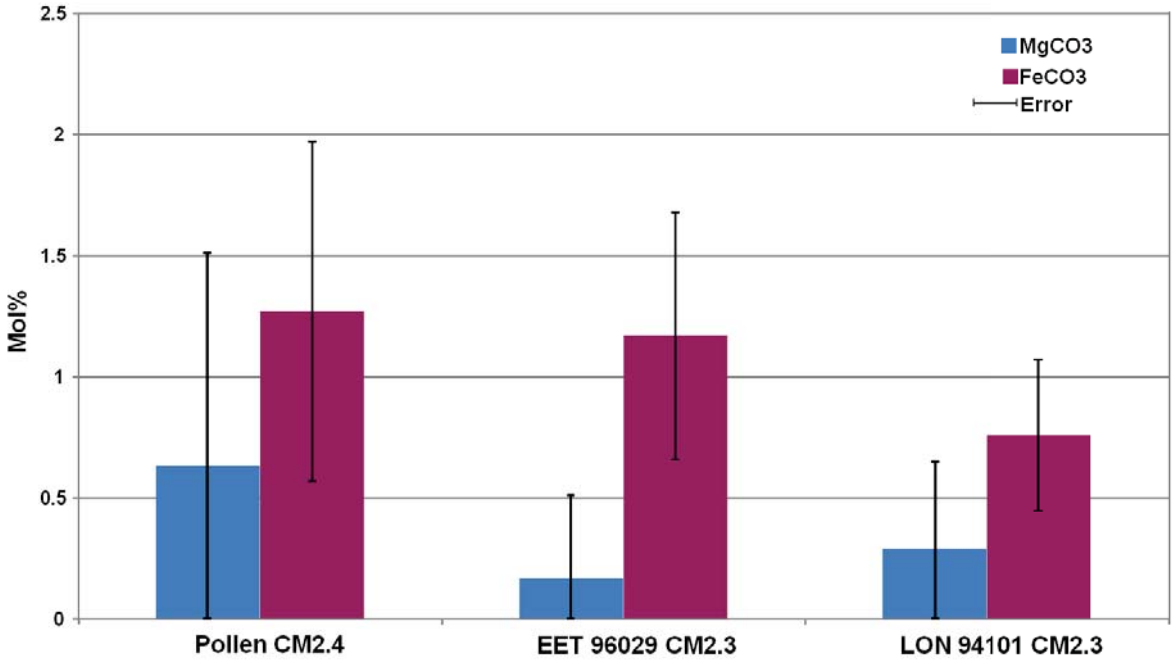

Figure 7.6- Histogram of Fe and Mg concentrations in calcite free of rims and inclusion in CM2.4 and CM2.3 chondrites.
Note that calcite in CM2.4 Pollen has higher concentrations of Fe and Mg than CM2.3 chondrites.

Riciputi et al. (1994) and Lee and Ellen (2008) used 0.044 as the partition coefficient for Mg to determine the Mg/Ca ratio of solutions from which calcite grains in Murray and other CM chondrites precipitated. Calculated molar ratios (relative to Ca) of Mg for solutions in equilibrium with calcite free of rims and inclusions are shown in Figure 7.7. It is clear that solutions in equilibrium with this calcite in the CM2.4 and CM 2.3 chondrites had a lower Mg/Ca ratio than calculated for aragonite in CM chondrites (see Figure 7.7), which is also consistent with findings by Lee and Ellen (2008). As discussed above, Lee and Ellen (2008) found that the change in crystallization from calcite to aragonite in the parent body was probably due to an increase in fluid Mg/Ca or temperature. The Mg/Ca values of fluids in equilibrium with calcite free of rims and inclusions (in different meteorites) are also similar between different meteorites, whereas the Mg/Ca values of

solutions in equilibrium with aragonite vary much more from meteorite to meteorite, probably the precipitation of calcite free of rims was from more open regions than those from which aragonite was precipitated (Figure 7.7).

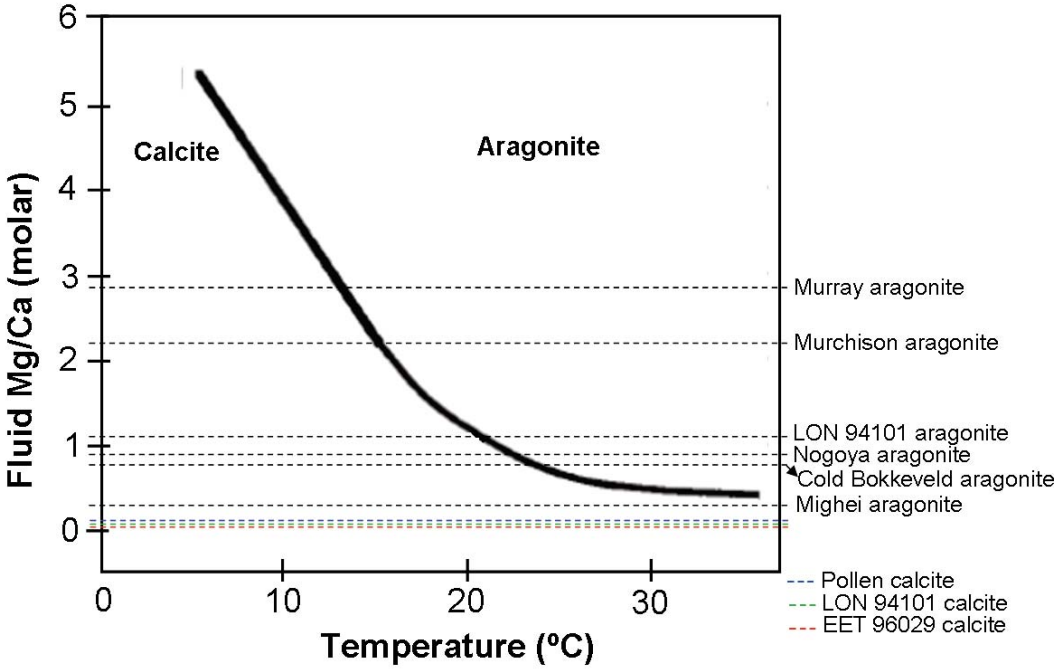

Figure 7.7- Graph showing the influence of Mg/Ca ratio and temperature on the precipitation of aragonite and calcite free of rims and inclusions in moderately and less altered CM chondrites. Values of Mg/Ca ratio of fluids from which aragonite and calcite grains precipitated are plotted in this graph, which is modified after Morse et al. (1997). The value of Mg/Ca ratio of aragonite in Murray was determined by Lee and Ellen (2008). Unlike aragonite, Mg/Ca values of fluids in equilibrium with calcite free of rims and inclusions are all very similar.

7.2.3.2 Formation of calcite rimmed with tochilinite and/or Fe-sulphide

Calcite grains rimmed with tochilinite and/or Fe-sulphide were present in all samples studied (Figure 7.2), but differ in abundance from meteorite to meteorite. This calcite is more abundant than aragonite and calcite free of rims and inclusions. It is infrequent in QUE 93005 and EET 96029, but more common in Pollen, LON 94101, Cold Bokkeveld and LAP 031166.

As described in previous chapters, this calcite has been partly or totally replaced by Mg-rich serpentine. It was also found that the fine grained (<1μm) matrix of some CMs (e.g. Pollen) can be subdivided into two phases, namely a phyllosilicate matrix that is almost free of Fe-sulphide and tochilinite, and a phyllosilicate matrix that includes Fe-sulphide and tochilinite clumps (see Figure 3.13). The calcite occurs in conjunction with Fe-sulphide and tochilinite. A prominent feature of this calcite is that every grain is partly or

totally rimmed by tochilinite and/or Fe-sulphide (e.g. Figure 4.38 a). The rims are most likely to have been formed immediately after the calcite. Tochilinite is inferred to have formed from the reaction between kamacite (Fe, Ni metal) and a solution that contained S during its movement within chondrules (Tomeoka et al., 1989), whereas chondrule mesostasis dissolution supplied elements such as Al, Na, Ca and Si to fluids (Howard et al., 2011). These Ca ions were then consumed during calcite crystallization (De Leuw et al., 2010).

As discussed previously, the calcite grains rimmed with tochilinite in LON 94101 have lower $\delta^{18}O$ values than aragonite grains, so this calcite probably formed after aragonite. Variation in oxygen isotopic compositions between two different types of calcite (rimmed calcite and calcite replacing olivine) in an Antarctic CM2 was used by Tyra et al. (2012) to argue that these two types formed at different times and under different conditions. Using this isotopic variability and the presence of these two types in all CM chondrites, Tyra et al. (2012) also suggested that the precipitation of rimmed calcite (classified by them as type 1) was prior to calcite replacing olivine (classified by them as type 2).

CL zoning of calcite grains of CM2.5 and CM2.4 chondrites has been reported by Brearley et al. (1999), Brearley (2001) and Lee and Ellen (2008). Work reported here shows that the SEM-CL characteristics of calcite rimmed with tochilinite and/or Fe-sulphide are more complex than those of other carbonate minerals in the samples studied. However, the most complicated SEM-CL characteristics have been found in grains from less altered CM chondrites (CM2.5-CM2.4), and SEM-CL characteristics become simpler in the more highly altered CM chondrites (CM2.2-CM2.0). For instance, calcite grains rimmed with tochilinite and/or Fe-sulphide in Murray and Pollen exhibit SEM-CL types from 7 to 11 (see Table 4.3 and Table 4.8), but only 1-3 CL types have been observed in calcite grains in highly altered meteorites (CM2.2-CM2.0).

SEM-CL characteristics of the rimmed calcite provide evidence that it was precipitated from small pockets of water by nucleation (from a seed crystal) within one part of a pore, and grew to fill the pore until the space or solution was consumed (e.g. Figure 4.31). The occurrence of CL zoning on the scale of micrometers shows that solution compositions changed during precipitation of these calcite grains. The presence of a variety of CL patterns in calcite grains in less altered CM chondrites reveals fluctuating fluid chemistry, which was more stable (relative to the time it took calcite crystals to grow) during the formation of calcite grains in highly altered CMs chondrite.

The difference in SEM-CL characteristics between the rimmed calcite and aragonite, also suggests that the two minerals formed under different conditions and from different fluids. As stated above, the luminescence of calcite is known to be controlled by the concentration of Mn^{2+} in the crystal, whereas the quenching is due to Fe^{2+} (Marshall, 1988; Habermann et al., 1998). In some cases Mn^{2+} is present in relatively high concentrations in rimmed calcite grains (mainly in CM2.5/2.4 and CM 2.3) that are located close to each other, and they have also similar petrographic features and CL characteristics (e.g. Table 4.7, Table 4.16 and Table 4.20).

In an effort to understand better the luminescence and quenching of CL in calcite, CL spectroscopy of some of Ca-carbonate grains in Murray and Pollen was undertaken (see sections 4.3.3.1.1 and 4.4.3.1.1 for more details). CL spectra of calcite and aragonite have peaks at ~530 nm and at ~620 nm respectively, which are the Mn^{2+} activated emission bands. Generally, all points analysed also luminesce at ~430nm, which is the intrinsic CL, but the intensity of CL emission varies with SEM-CL characteristics of the analysed points (i.e. low SEM-CL intensity etc.). One possible reason for the intrinsic CL in calcite at ~420 nm is due to electron recombination of Ca^{2+} and CO_3^- (Calderon et al., 1984). This study shows that the highest intensities of CL emission at ~430 nm were produced from areas characterised by high and very high SEM-CL intensity, whereas areas with low and very low SEM-CL intensity produce peaks the lowest intensities of CL emission (e.g. Table 4.9 and Table 4.10). Thus SEM-CL images are mainly of emission at ~430nm, and reveal variations during crystallization of trace or major element incorporation, but the identity of the CL activator remains unknown.

Calculated molar ratios (relative to Ca) of Mg for solutions in equilibrium with calcite rimmed with tochilinite, and/or Fe-sulphide in all samples examined is lower than those calculated for solutions in equilibrium with aragonite. However, the molar Mg/Ca values calculated for solutions in equilibrium with rimmed calcite (Table 7.1) correspond well with the molar Mg/Ca values for fluids in equilibrium with calcite free of rims (see Figure 7.7). Generally, this study provides good evidence that the change from precipitation of aragonite to calcite in the parent body/ies of CM chondrites was mainly controlled by a fall in the Mg/Ca of the solution, which is also consistent with findings by Lee and Ellen (2008). For example, chemical analyses of calcite grains (8 analyses) in LON 94101 show that $MgCO_3$ is below detection limits, whereas the concentration of $MgCO_3$ in aragonite is 0.14 mole% (average of 13 analyses). Fluids in equilibrium with aragonite in LON 94101 have 1.05 Mg/Ca, but fluids in equilibrium with calcite in the meteorite appear to have 0

Mg/Ca (i.e. <0.0003 Mg/Ca which is calculated from the approximate minimum concentration of Mg detectable by EPMA). Thus, calcite and aragonite were formed from different fluids, and most probably during different times.

Chondrites	Mean solution Mg/Ca	n
Murchison CM2.5	0.04	14
Murray CM2.5/2.4	0.03	32
Pollen CM2.4	0.07	40
Mighei CM2.3	0.06	32
EET 96029 CM2.3	0.04	29
LON 94101 CM2.3	0.00	08
Nogoya CM2.3/2.2	0.09	17
Cold Bokkeveld CM2.2	0.00	16
QUE 93005 CM2.1	0.01	09
LAP 031166 CM2.1/2.0	0.06	21
SCO 06043 CM2.0	0.09	18
ALH 88045 CM2.0	0.12	09

Table 7.1- Calculated mean Mg/Ca values of fluids in equilibrium with calcite rimmed with tochilinite and/or Fe-sulphide.
Note Mg/Ca values increase with increasing degree of alteration in highly altered CM chondrites (CM2.1 to CM2.0).

Chemical analyses show that the highest $FeCO_3$ concentrations are found in calcite grains rimmed with tochilinite and/or Fe sulphide (Figure 7.8) of the less altered chondrites (CM2.5/2.4). The exception is calcite in LAP 031166 (CM2.1/2.0) which is similar in $FeCO_3$ concentration to calcite in Pollen. The analyses also show the Fe content of calcite in highly altered CM2.1/2.0 to CM2.0 chondrites falls as aqueous alteration progresses.

Fluids from which Ca-carbonates precipitated (or recrystallizated) are believed to have become richer in Mg as alteration progressed (Riciputi et al., 1994; Lee and Ellen, 2008). However, De Leuw et al. (2010) suggested that Mn and Mg concentrations of calcite do not correspond with the alteration degree of CM chondrites. This study shows that the highest concentrations of $MgCO_3$ and $MnCO_3$ are recorded in ALH 88045 (CM2.0), and Mn is below detection limits in moderately altered CM2.3-CM2.2 chondrites (LON 94101, Nogoya and Cold Bokkeveld). Negligible concentrations of Mn were also found in less altered CM2.5-CM2.4 chondrites and some of the moderately altered CM2.3 chondrites. It was also observed that calcite grains in the highly altered CM2.1/2.0 and CM2.2 chondrites contain Mn and Mg that increase with increasing of alteration degree (see Figure 7.8). Based on the concept of increasing Mg content of the meteorite matrix with increase of alteration of CM chondrites (e.g. Tomeoka and Buseck, 1985; Browning et al., 1996; Howrad et al., 2011), this study shows that the Mg content in calcite does not follow the

pattern of overall fluid evolution of CM chondrites, and Mg only corresponds with increasing alteration degree in highly altered CM2.2 to CM2.0 chondrites (see Figure 7.8 and Table 7.1).

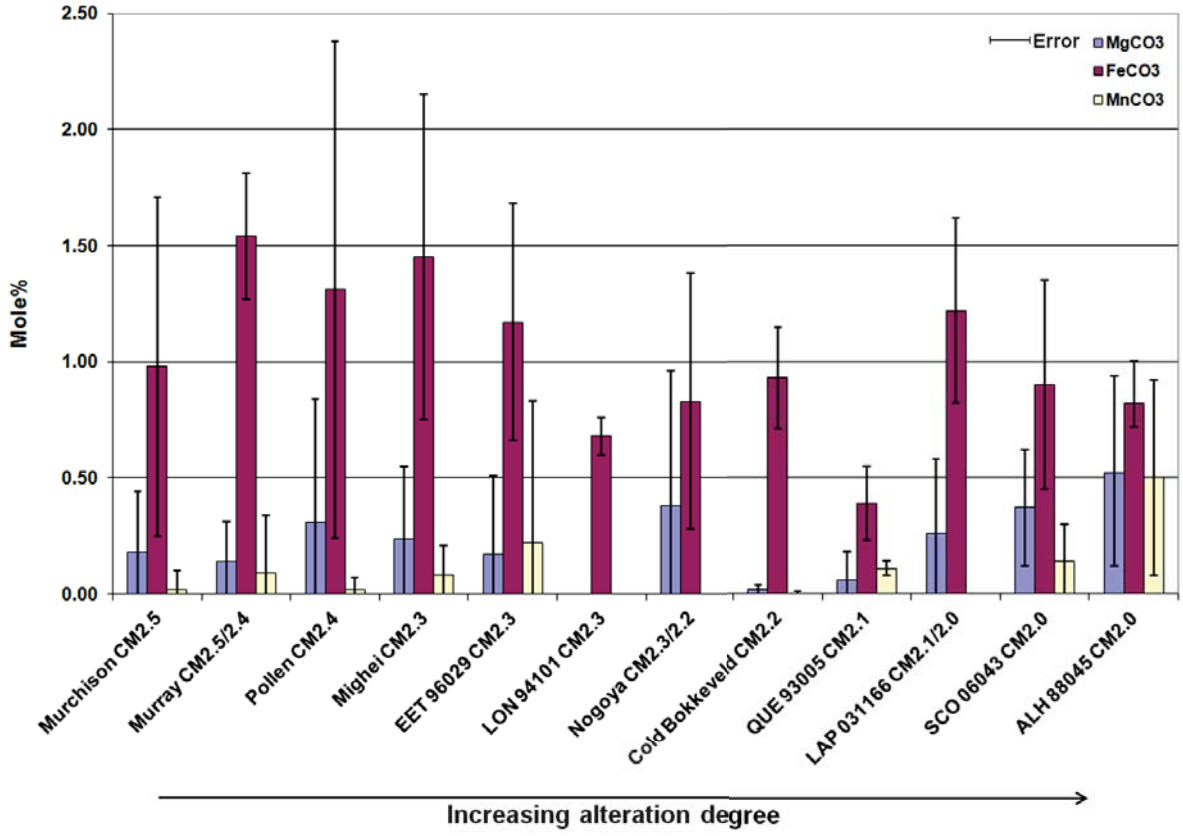

Figure 7.8- Histogram of mean $MgCO_3$, $MnCO_3$ and $FeCO_3$ concentrations of rimmed calcite in the CM chondrites studied.
Note Mg and Mn in highly altered CM2.2 to CM2.0 chondrites increase with degree of aqueous alteration and Fe correspondingly falls.

Fluid inclusions (~0.2µm) were observed in calcite grains (rimmed and free of rims) in Murchison (CM2.5), Mighei (CM2.3) and Nogoya (CM2.3/2.2) (see Figure 4.4, Figure 4.56 and Figure 5.2). Fluid inclusions are tiny fluid filled parts of a crystal, which formed from ambient solutions during or after crystallization (Zolensky and Bondar, 1982). Fluid inclusions were also found in Ca-carbonate in LON 94101, and in Ca and Ca/Mg carbonate in ALH 84029 (CM2) by Saylor et al. (2001), who described their origin as extraterrestrial. Zolensky et al. (1999) studied aqueous fluid inclusions in halite and sylvite in Monahans (1998) H5 chondrites by heating and freezing experiments, and concluding that the fluids are brines. The occurrence of fluid inclusions within overgrowth zones in calcite grains in Murchison and Nogoya suggests that these zones in calcite were formed under different conditions than other areas of the grain. These inclusions can be used to understand the conditions that existed during the formation of the enclosing crystals, but this requires

heating and freezing measurements to clarify if they are brines as reported by Zolensky et al. (1999).

7.2.3.3 Calcite after Mg, Fe silicates

Calcite in chondrules and aggregates of Murray and Nogoya was described as replacive by Bunch and Chang (1980). Incomplete replacement of pyroxene and olivine by calcite was also noted in Nogoya by Benedix et al. (2003). Calcite replacing silicates has also been described in other Antarctic CM chondrites (Tyra et al., 2007). The conclusion of this previous work is that this replacive calcite is pre-terrestrial (Benedix et al., 2003; Tyra et al., 2007).

Petrographic observations of calcite replacing original anhydrous minerals (i.e. pyroxene and Mg-rich olivine) show that calcite after pyroxene is free of inclusions and is coarsely crystalline (see Figure 4.49 a), whereas calcite replacing olivine often contains inclusions of sulphide, and is composed of numerous sub-crystals (e.g. Figure 4.38 b). Calcite after pyroxene is rarely present in CM chondrites. TEM results from a pyroxene-calcite intergrowth (Section 4.4.5) confirms that pyroxene has been replaced by calcite, and the EDS spectrum of pyroxene (Figure 4.49 d) indicates that it is enstatite with little Ca. The presence of minor Ca in the enstatite may nonetheless have facilitated replacement. Calcite replacing Mg-rich olivine is found in all studied CM chondrites, but varies in abundance from meteorite to meteorite. It becomes more abundant and coarser grained with increasing degrees of alteration of the CM chondrites. For example, calcite replacing olivine is rare in Murchison (CM2.5), but is more common, and regions replaced exceed ~300 μm in LON 94101 (CM2.3), and ~600 μm in LAP 031166 (CM2.0). Mg-rich olivine containing calcite was observed in many of the CM chondrites studied (e.g. Figure 4.69 b), confirming that this calcite has mainly replaced forsterite (Mg_2SiO_4), not fayalite (Fe_2SiO_4).

Calcite replacing anhydrous silicates in Antarctic CM chondrites was classified as calcite type 2 by Tyra et al. (2012). Oxygen isotope analyses show that this calcite has an average $\delta^{18}O$ of 19.4% ± 1.5% suggesting that it had formed after another generation of calcite in the same meteorite (type 1) (Tyra et al., 2012).

Olivines in terrestrial rocks are unstable in contact with water in the shallow crust and transform rapidly into minerals including serpentines, iddingsite (a mixture of goethite and phyllosilicates), bowlingite-saponite and iron hydroxides (Delvigne et al., 1979).

Replacement of quartz (typically more stable than olivine) by calcite has been observed in studies of authigenic minerals in terrestrial rocks (e.g. Walker, 1957). This implies that olivine could also be readily replaced by calcite.

The mechanisms by which calcite may replace olivine can be understood from laboratory experiments. Experiments were carried out by Andreani et al. (2009) by percolation of CO_2-rich brine through peridotites, in an effort to understand the relationships between the heterogeneity of rock, water flow and chemical reactions. They found that elements including Si, Mg and Ca, were progressively liberated during these experiments; this was due to the continuous dissolution of olivine and diopside, the formation of Ca-carbonate after the dissolution of diopside is discussed in section 7.2.2.3. The first layer of alteration material that was observed on olivine was magnetite ± siderite ($FeCO_3$), the second alteration product being Ca-rich magnesite. They also observed a nanometer-scale porous zone between magnesite and olivine, which was partly filled by siderite and amorphous phyllosilicates (probably sepiolite). Andreani et al. (2009) also found that the rate of siderite and magnesite crystallization is controlled by the concentration of Fe that is supplied by the dissolution of olivine and diopside. They reported that areas of reduced water flow are characterised by carbonate crystallization, as local solutions became supersaturated, pH was high, and conditions were also slightly more reducing in these areas. They concluded that the heterogeneity of pore systems and local regeneration of the reactant controls carbonation efficiency. They described the carbonation of forsterite by the following reaction:

$$Mg_2SiO_4 + 2CO_2 = 2MgCO_3 + SiO_2$$

Hövelmann et al. (2011) undertook experiments using samples of primary olivine and products of olivine weathering (deweylite = magnesium silicate $Mg_3Si_2O_5(OH)_4$), and solutions with an average salt content similar to that of sea water. These experiments were performed under hydrothermal conditions, in an attempt to understand the carbonation of partially serpentinized and weathered peridotites. They found that the original samples (olivine, deweylite) were partially replaced by calcite in Na-Ca-Cl solutions. Their experiments also showed that in NaCl solutions, the fluids became supersaturated in respect of Mg and Si with reaction time, large pores formed in the reaction area of deweylite as a result of the dissolution, whereas the olivine was altered into magnesite. Hövelmann et al. (2011) also reported that minerals including magnesite, silica, dolomite, calcite and siderite can be formed by the reaction of CO_2 in solution with peridotite. Observations showed that calcite crystallizes in close proximity to the surfaces of olivine

and deweylite aggregates. The reactions which produced calcite after olivine (pure forsterite) can be described as following:

1. The solution became slightly acidic due to dissolution of CO_2, this acidic solution caused the olivine to dissolve:

$$Mg_2SiO_4 + 4H^+ = 2Mg^{2+} + SiO_{2(aq)} + 2H_2O$$

2. There was an increase in the activity of bicarbonate as a consequence of pH increase

$$H_2CO_3 = H + HCO_3^-$$

3. Calcite formed on the dissolved area as the solution contained high concentrations of Ca^{2+} and bicarbonate:

$$Ca^{2+} + 2HCO_3^- = CaCO_3 + H_2CO_3$$

The liberation of Mg and Si from Mg-rich olivine during its replacement by calcite in the parent body/ies of CM chondrites increased the concentrations of these elements in the surrounding fluids. But the source of Ca that was required to replace olivine is still unknown, in particular during the replacement of large chondrules (300 to 600μm) by calcite (e.g. LON 94101, LAP 031166). It is also unclear how Mg and Si were consumed. This is discussed in detail below.

Chemical analyses of calcite replacing olivine in Pollen and LON 94101 (Table 4.12 and Table 4.19) showed that it has high concentrations of $FeCO_3$, which is probably related to the Fe-sulphide inclusions. Thus the Fe content of calcite replacing olivine cannot be used as a tool to explore the alteration of the studied CM chondrites.

7.2.4 Pseudomorphs after calcite rimmed with tochilinite and/or Fe-sulphide

Pseudomorphs of calcite grains made of Mg-rich serpentine, or Mg-rich serpentine intergrown with tochilinite, are present mainly in the moderately and highly altered CM chondrites. However, a few Mg-rich serpentine pseudomorphs after calcite occur in Murchison (CM2.5), and they are also common in Pollen (CM2.4). Mg-rich serpentine after calcite is more abundant than tochilinite-serpentine pseudomorphs in the studied CM chondrites. Pseudomorphs after calcite in the highly altered CM chondrites (LAP 031166, SCO 06043, ALH 88045) are only Mg-rich serpentine, and increase in abundance with increasing degrees of alteration (Figure 7.9). This is consistent with findings by Tomeoka and Buseck (1985) that serpentine minerals become richer in Mg with increasing aqueous

alteration. Howard et al. (2011) also concluded that Mg-rich serpentine becomes more abundant as aqueous alteration of CM2 chondrites increases.

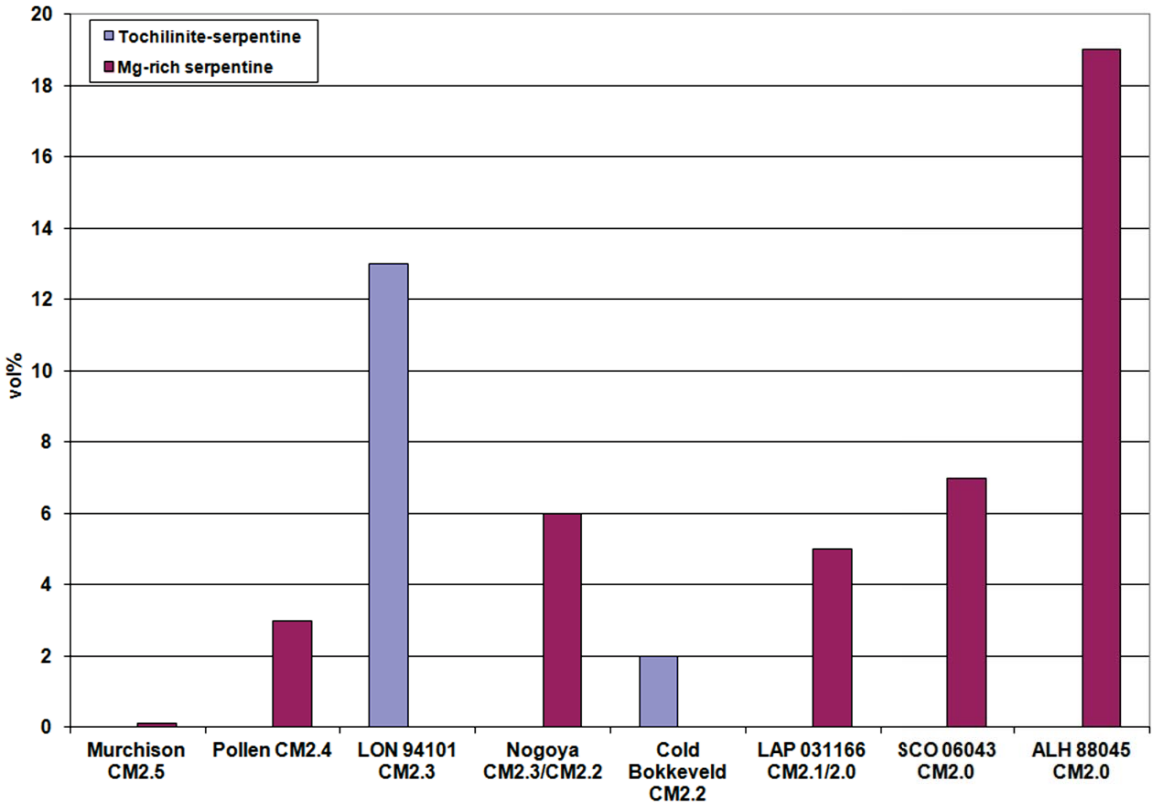

Figure 7.9- Histogram showing the abundance in vol% of pseudomorphs after calcite in the CM chondrites studied.
Note that the highly altered CM chondrites contain only Mg-rich serpentine, whereas tochilinite-serpentine pseudomorphs occur only in the moderately altered CM chondrites.

The sequence of formation of pesudomorphs after calcite can be summarised as follows:

1. The initial process was crystallization of calcite in pore spaces in the meteorite matrix. These voids probably were left after the melting of ice crystals or dissolution of anhydrous silicates in situ. Grimm and McSween (1989) mentioned that the presence of water during aqueous alteration was a direct consequence of melting of ice, accreted to the carbonaceous chondrites parent body/ies.
2. Partial replacement of calcite by tochilinite and/or sulphides.
3. Replacement of calcite by Mg-rich-phyllosilicate (Figure 4.47) or tochilinite-serpentine (Figure 4.78) by solutions with high concentrations of ions including Fe^{2+}, Mg^{2+} and Si^{4+}. Based on the chemical composition of the product (Figure 7.10), Mg-rich serpentine pseudomorphs (mainly present in the highly altered CM chondrites) formed from fluids that were richer in Mg than Fe, whereas tochilinite-serpentine pseudomorphs (present only in moderately CM chondrites) are likely to have

crystallized from solutions that contained high concentrations of Fe, S and Ni. This is consistent with hypotheses (e.g. McSween, 1979) that solutions at later stages in the alteration sequence were dominated by Mg, a result of the later dissolution of the more stable Mg-rich silicates.

4. This study suggests that calcite after Mg-rich olivine, and Mg-rich serpentine or serpentine-tochilinite intergrowth after calcite, formed at the same time or probably immediately after each other. Elements including Fe, Mg and Si were released from Mg-rich olivine and so may have been used for the replacement of calcite by Mg-rich serpentine. The Ca and CO_3 released from calcite may then have contributed to the replacement of Mg-rich olivine by calcite. A good example of these two mineral pairs is in Pollen. Two grains of calcite after Mg-rich olivine and Mg-rich serpentine after calcite are found close to each other (Figure 4.38 b). In this case it is most likely that calcite replaced olivine after the Mg-serpentine had replaced tochilinite-rimmed calcite.

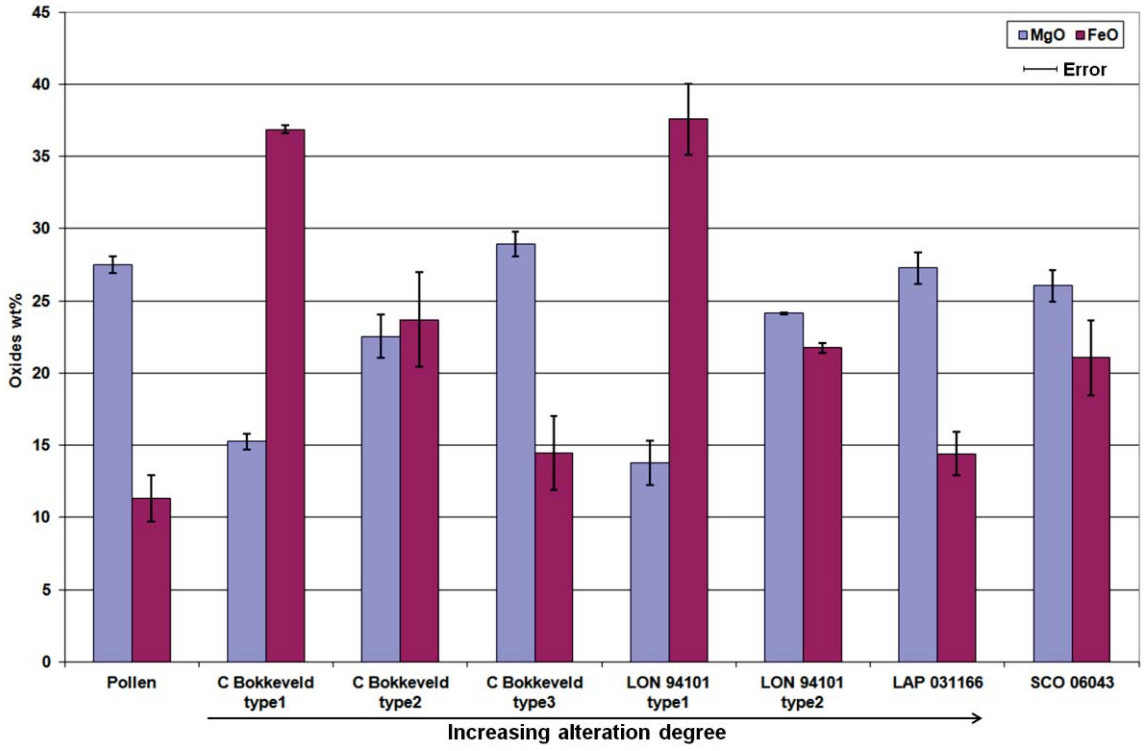

Figure 7.10- Histogram showing the variation of mean MgO and FeO concentrations in pseudomorphs after calcite in the studied CM chondrites.
Note that Cold Bokkeveld and LON 94101 contain three (type1= tochilinite-serpentine with high contents of Fe, type2= tochilinite-serpentine that are riched in Mg and Fe, type3= Mg-rich serpentine) and two types (type1= tochilinite-serpentine with high contents of Fe, type2= tochilinite-serpentine that are riched in Mg and Fe) of pseudomorphs respectively, which vary in concentrations of the Fe and Mg. Note the Mg contents of the Mg-rich serpentine pseudomorphs in LAP 031166 is slightly different to the Mg-rich serpentine pseudomorphs in Pollen, note also that the petrographic features of the pseudomorphs in Pollen are identical to those in LAP 031166 (see Figure 4.47 and Figure 6.4).

7.2.4.1 The mechanism of pseudomorph formation

An important question to answer is whether the replacement reactions were driven by solid state diffusion processes or dissolution and reprecipitation. Many studies of terrestrial rocks have been carried out in laboratory experiments to understand the mechanism of the pseudomorphism of minerals (e.g. Delvigne et al., 1979; Maliva and Siever, 1988; Putnis, 2002; Putnis et al., 2005; Xia et al., 2009).

Results obtained here suggest that the reaction between Mg-rich olivine grains and solutions dissolved the Mg-rich olivine. Fluids in contact with calcite then became supersaturated with respect to Mg-phyllosilicates. Thus, the constituents of calcite have been removed and replaced by constituents of the Mg-phyllosilicates. As discussed above, the Ca that was released by replacement may have been used to produce calcite pseudomorphs after olivine. In both cases the new crystals have retained the overall morphology of the parent crystals (i.e. isovolumeteric replacement), but their chemical compositions have changed totally. Replacement proceeded from the outer surface of the calcite grain and moved inwards, which caused the Mg-phyllosilicate to preserve the external shape of the calcite. In some cases, crystallographic information of calcite has been inherited by Mg-phyllosilicates, e.g. some Mg-phyllosilicate pseudomorphs exhibit a hexagonal shape. Serpentine pseudomorphs after olivine are also distinguished by their outlines, which characterise the parent crystals (Velbel et al., 2012). The rates of dissolution of calcite and precipitation of Mg-phyllosilicates must have been equal. Textural preservation of the parent crystal indicates that the dissolution rate of the parent crystal was equal to the crystallization rate of the new phase (Maliva and Siever, 1988).

Solid-fluid interactions were most probably involved in forming the Mg-phyllosilicate pseudomorphs because a replacement reaction that constructs the replacive phase with morphology and structural details of parent mineral typically entails solid-solution interactions (e.g. Putnis et al., 2005). Laboratory experiments on replacement reactions at the solid-fluid interface in the model system KBr-KCl-H_2O (KBr crystals and saturated fluids of KCl), showed that the main control of the replacement mechanism is porosity generation, by which fluids gain contact with the reaction interface (Putnis et al., 2005). Experimental results by Putnis et al. (2005) also showed that fluid-solid equilibrium can only be preserved in a fluid boundary layer (formed as a result of original crystal dissolution), whose thickness is controlled by the dissolution rate of the original phase, epitaxial nucleation of the new phase and rate of the mass transfer across the solution.

Petrographic observations of Pollen indicate that the porosity was formed within calcite grains prior to Mg-phyllosilicate (see Figure 4.47 a, c), and also before calcite formation after Mg-rich olivine (see Figure 4.69 b). Thus, the etching of calcite grains allowed fluids to access grain interiors and was followed by epitaxial crystallization of Mg-phyllosilicates.

The parent body conditions that controlled calcite transformation into Mg-phyllosilicate are related to the chemical equilibrium of fluids and solids at the reaction interface, and temperature and pH of the fluids. Putnis (2002) explained that the rates of dissolution and crystallization of minerals are highly variable, based on conditions such as pH and solution composition etc. For example, experiments under hydrothermal conditions were conducted by Xia et al. (2009) to understand the mechanism and kinetics of pseudomorphic mineral replacement reactions, specifically of pentlandite by violarite ($FeNi_2S_4$). Their results showed that the replacement rate increases with temperature, from 80 to 125 ºC, and decreases when the temperature exceeded 210 ºC. They also showed that pH has a role in replacement. They concluded that only between over pH 1 and less than pH 6 (acid regime), and in the nanometer scale of pseudomorphic transformation of pentlandite into violarite, could the product phase (violarite) inherit the crystallographic orientation of pentlandite. It was also observed by Sjoberg and Rickard (1984) that the relationship of the calcite dissolution rate to the concentration of H^+, at a temperature of 25ºC and pH less than 4 is directly proportional, the dissolution rate is independent in respect of H^+ concentrations at greater than pH 5.5, and there is a transitional zone between pH <4 and pH > 5.5. On the other hand, the dissolution rate of forsterite (Fo_{91}) is six times lower than that of fayalite in a deoxygenated atmosphere at a pH of 2-7 at 25ºC (Wogelius and Walther, 1991). It has also been reported by Zolensky et al. (1989) that the aqueous alteration of CM chondrites was characterized by a pH of 7 to greater than 12 and at temperatures of 1 to about 25ºC.

Based on the literature data and the results of this study, the pH values of fluids during the formation of these pseudomorphs are likely to have fluctuated within a range of acid + basic. Probably, the etching of calcite and olivine would require slightly acidic fluid pH (~6-7) and the recrystallization of calcite after olivine and Mg-phyllosilicates after calcite was by alkaline fluid pH (~7-8), at a temperature of 1 to about 25ºC. It also seems that these pseudomorphs formed in a low-energetic environment, as has been reported also by Browing and Keil (1997).

7.2.5 Ca-carbonate dissolution and its reprecipitation as calcite veins

Petrographic observations show that Ca-carbonate grains (calcite and aragonite) in the less altered CM chondrites (Murray and Murchison) are better preserved than those in moderately and highly altered CM chondrites (e.g. Figure 4.3). Partly and totally dissolved calcite grains (un-rimmed and rimmed) are mainly present in EET 96029 (CM2.3) (e.g. Figure 4.67). Partly dissolved aragonite and calcite grains are also observed in Mighei (CM2.3), LON 94101 (CM 2.3), Nogoya (CM2.3/2.2), Cold Bokkeveld (CM 2.2) and QUE 93005 (CM 2.1) (e.g. Figure 4.59, Figure 5.4 a, and Figure 5.15). As discussed in Section 7.2.4.1, Sjoberg and Rickard (1984) outlined how changing pH affects the rate of calcite dissolution at 25ºC. Therefore the dissolution of calcite grains in the parent body/ies of CM chondrites was probably the result of changing of pH of fluids surrounding some of the grains. It is also known that the amounts of dissolved CO_2 in sea water control the dissolution and preservation of $CaCO_3$, by which the pH of sea water also changes (e.g. Naik and Naidu, 2008). Results of this study suggest that after the dissolution of Ca-carbonate grains, Ca and CO_3 ions were transported by fluids through asteroidal regoliths and reprecipitated as calcite within fractures that cross-cut the fine grained matrix (e.g. Figure 4.71 a). It is also likely that some of the Ca that remained in fluids after the replacement of calcite by Mg-rich serpentine was also consumed during the formation of calcite veins. This is consistent with findings by Lee (1993) that the source of Ca-sulphate veins in Cold Bokkeveld was dissolution of calcite and metal sulphides that reprecipitated as gypsum. It was also reported by Lindgren et al. (2011a) that the calcite vein in LON 94101 appears to have been formed by water flow within the parent body of the meteorite.

BSE images of the calcite vein in LON 94101 shows that this calcite overgrows calcite rimmed with tochilinite (Figure 4.71 a), suggesting that the calcite vein formed later. The calcite vein in LON 94101 has low concentrations of Fe in comparison with other calcite and aragonite grains in the same meteorite (see Table 4.19). De Leuw et al. (2010) reported that calcite formed in the later stages of aqueous alteration contains less Fe than that formed earlier. This finding also suggests that the calcite vein originated from different solutions compared to the calcite and aragonite grains in the enclosing matrix.

The calcite vein in LON 94101 was analysed for its oxygen isotopic composition, and has distinct values ($\delta^{18}O$ of 18.4 ± 0.3% and $\delta^{17}O$ of 9.0 ± 0.5%) compared to aragonite and rimmed calcite grains in the same meteorite (see Table 4.24). These values (average of $\delta^{18}O$ is 19.4% ± 1.5%) are comparable to calcite replacing olivine in Antarctic CM2

chondrites, as reported by Tyra et al. (2012) (see Figure 4.81). This common composition suggests that calcite replacing olivine, and the calcite vein, precipitated after matrix calcite and aragonite grains, and suggests that they may have been sourced from dissolution of earlier Ca-carbonate grains.

Petrographic observations show that at least two episodes of shock deformation have generated the two sets of twins in some of the calcite grains (e.g. Murray, Pollen, LON 94101), and one set of twins in the LON 94101 calcite vein. Lindgren et al. (2011a) suggested that the e-twinning and microstructure of the calcite vein in LON 94101 were a consequence of impact processing in the parent body of the meteorite, rather than deformation in the Antarctic ice. As discussed in section 4.8.2, Tyra et al. (2012) reported calcite veining as a terrestrial weathering product in an Antarctic CM2 chondrite. It has a distinct oxygen isotopic composition which lies on TFL, far from the calcite vein in LON 94101 (see Figure 4.81). This comparison supports the hypotheses (of this study and Lindgren et al. 2011a) that the calcite vein in LON 94101 is pre-terrestrial.

Twinned calcite grains are mainly present in the less altered and moderately altered chondrites (Murchison, Murray, Pollen, LON 94101 and Cold Bokkeveld). These grains and the calcite vein in LON 94101 have been subjected to stress after their formation, probably due to impact gardening (e.g. Lindgren et al., 2011a). This conclusion is in agreement with the calcite twins in Murchison being attributed to impact processes (Brearley et al., 1999). It is known that calcite twins can form at low temperatures, while dolomite twins develop at higher temperatures (Barber and Wenck, 1979). Calcite deformation at a temperature of <170ºC produces thin twins, whereas thick twins occur at >200ºC (Ferrill et al., 2004). It was also observed by Rowe and Rutter (1990) that the thicknesses of twins correspond to the deformation temperature. Calcite twin width and morphology in the samples studied were described using a schematic diagram in Figure 4.21, in an effort to estimate the paleo-temperature of deformation that took place in the parent body/ies. The results show that the majority of calcite deformation was at a temperature ranging from <200ºC to ~300ºC, which may have been a result of shock processing. So the important conclusion of this section on twins is that shock pressures came after crystallization of rimmed calcite grains and the LON 94101 vein.

7.2.6 Dolomite, breunnerite and Ca-poor dolomite crystallization

7.2.6.1 Dolomite crystallization

Dolomite is more common in CI chondrites than other carbonate minerals (Johnson and Prinz, 1993), and Endress and Bischoff (1996) have reported that the CI chondrites Orgueil and Ivuna contain an abundance of dolomite. De Leuw et al. (2010) found that dolomite is absent in the most highly altered CM chondrites (CM2.0), but present in QUE 93005 CM2.1. This study shows that dolomite grains are rarely present (only two grains) in the less altered lithology of Nogoya (CM2.3), a few grains of dolomite replacing calcite also being observed in LAP 031166 (CM2.1/CM2.0). Dolomite is found mainly in the highly altered CM chondrites, including QUE 93005 (CM2.1) (0.7 vol%) and SCO 06043 (CM2.0) (0.79 vol%). Calcite intergrown with dolomite is also present in QUE 93005 (1.9 vol%) and SCO 06043. However, dolomite was not recognised in highly altered ALH 88045 (CM2.0).

The findings of this study are consistent with the suggestion by De Leuw et al. (2010) that dissolution of Mg-rich olivine was the source of Mg needed for dolomite formation. As discussed in Chapter 3, the degree of hydration of Mg-rich olivine increases in CM chondrites as a result of aqueous alteration, so in later stages of aqueous alteration fluids were probably richer in Mg. The results of SEM point counting also showed that Mg-rich serpentine is more abundant than Fe-rich serpentine in the CM2.1/CM2.0 chondrites (e.g. Table 3.23). Furthermore, increasing Mg concentrations in solutions during the late stages of aqueous alteration, which produced dolomite, would be consistent with the idea that calcite grains (not calcite replacing dolomite) formed prior to dolomite in CM chondrites (e.g. Riciputi et al., 1994; De Leuw et al., 2010).

The absence of dolomite in the highly altered chondrites (i.e. MET 01070) has been previously suggested as a consequence of dedolomitisation (De Leuw et al., 2010). The term ‘dedolomitisation’ is used for dolomite replaced by calcite, or ‘calcitisation’ if dolomite is dissolved and the pore later cemented by calcite (Lee and Harwood, 1989; Adams and Mackenzie, 1998; Nader et al., 2008). Evidence for dedolomitisation was also found in SCO 06043 (CM2.0) (Lindgren et al., 2012). This study shows that dolomite inclusions occur in calcite grains in QUE 93005 (CM2.1) (e.g. Figure 5.26) and SCO 06043 (CM2.0) (e.g. Figure 6.7), indicating that this dolomite is likely to have been replaced by calcite. It is therefore likely that the absence of dolomite in the most altered CM2.0 chondrite studied here (ALH 88045) was also due to the replacement of dolomite

by calcite. In the case of dedolomitisation, solutions become supersaturated with respect to calcite (Pacheco and Szocs, 2006) and De Leuw et al. (2010) suggested that increasing Ca relative to Mg in fluids caused the replacement. They argued that fluids acquired Ca from the hydration of glassy chondrule mesotasis, but this is inconsistent with suggestions by Rubin et el. (2007) that chondrule glass is absent in the least altered QUE 97990 (CM2.6), due to alteration that took place during the very early stages of aqueous processing. As discussed in Section 7.2.2.3, Howard et al. (2011) also suggested that glassy mesostasis altered to saponite in the early stages, and McSween (1987) found that chondrule glasses in carbonaceous chondrites (CM and CI) were simultaneously altered, probably during the early stages of aqueous alteration. Thus, during late stages of aqueous alteration, chondrule mesostasis was not the source of Ca needed for the replacement of dolomite by calcite. Alternatively, the dissolution of calcite grains formed earlier could have provided sufficient Ca for dedolomitisation. The transformation of carbonate (both dolomite and calcite) to Mg-rich serpentine in SCO 06043 may be another source of Ca for this process. The evidence of replacement of dolomite by phyllosilicate comes from TEM (Figure 5.9).

The presence of veins made of calcite and/or dolomite in QUE 93005 and SCO 06043 (highly altered chondrites) is an indicator of local water flow in the parent body of CM chondrites, but the scale of this water flow was probably limited in the less altered CM chondrites, and some of the moderately altered chondrites. The dolomite vein in SCO 06043 is different in chemical composition to the dolomite grains in the matrix of the same meteorite. It has very low concentrations of Fe and Mn in comparison with dolomite grains (see Table 6.4). This may suggest that dissolution of some dolomite grains took place, and eventually reprecipitated as dolomite veins. It also indicates that fluids in the final stages of aqueous alteration were rich in Mg, and Fe-poor (see Figure 7.11). Riciputi et al. (1994) suggested that the formation of a carbonate vein is an indicator of the final stage of aqueous alteration of carbonaceous chondrites. This observation is consistent with discussion above, that the calcite vein in LON 94011 formed during late stages of aqueous alteration also has low concentrations of Fe in comparison to calcite grains in the meteorite.

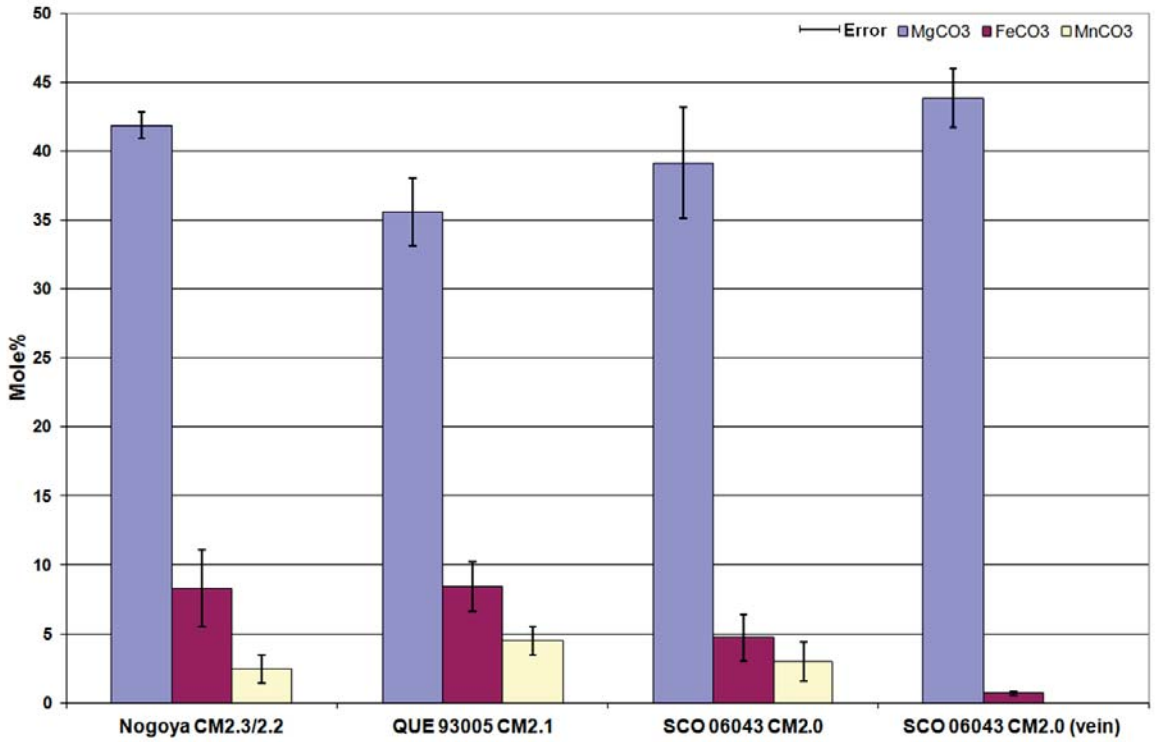

Figure 7.11- Histogram of Fe, Mg and Mn contents in dolomite grains of the CM chondrites studied. Note Fe and Mn in QUE 93005 and SCO 06043 decrease as alteration progress, but the Mg content increases with increasing of alteration degree from CM2.1 to CM2.0.

7.2.6.2 Crystallization of breunnerite, Ca-poor dolomite and calcite cement in QUE 93005

The highly altered QUE 93005 contains complex carbonate minerals that have different contents of Ca, Mg, Fe and Mn to other carbonates (Rubin et al., 2007). Complex Ca-Mg-Fe-Mn-Ni bearing carbonates are also found in CM1 EET 83334 (Zolensky et al., 1997), and this study shows that complex carbonate minerals are more abundant in QUE 93005 than SCO 06043. As discussed in Chapter 5, QUE 93005 contains breunnerite dolomite-breunnerite grains and aggregates of breunnerite-(Ca-poor dolomite)-calcite cement. The presence of these minerals only in QUE 93005, and in discrete areas of the thin section (see Figure 5.22), is consistent with the possibility that the conditions of aqueous alteration differ from area to area of the parent body/ies (e.g. Johnson and Prinz, 1993; Riciputi et al., 1994). CL images of some dolomite grains in QUE 93005 show zonation (e.g. Figure 5.33), which reveals changes in the chemical composition of fluids during growth. However, the majority of CL images of dolomite grains (mainly from SCO 06043) show a very low SEM-CL intensity, which implies the fluids from which dolomite grains in SCO 06043 precipitated were more stable or contain too much iron. BSE and CL images of dolomite-breunnerite grains reveal that dolomite is most likely to have crystallized first

within the pore space, to be followed by breunnerite. These images (Figure 5.29 and Figure 5.33 c and d) show that some of the breunnerite has grown around the dolomite. It seems that breunnerite filled some pore space that remained after the crystallization of dolomite and also some open pores in other areas within the fine grained (<1μm) matrix. BSE images and EDS X-ray maps of polymineralic grains (breunnerite-(Ca-poor dolomite)-calcite) (see Figures 5.30, Figure 5.34 and Figure 5.35) show that the breunnerite initially formed at the margins of pore spaces; subsequently Ca-poor dolomite and then calcite cement filled them. The calcite cement exhibits variations in SEM-CL intensity (e.g. Figure 5.31), which also reflects changes of fluid composition during the crystal growth. As shown in Figure 5.30, Ca-poor dolomite occurs in some cases as inclusions within the breunnerite, indicating that breunnerite was etched before filling the etch pores by Ca-poor dolomite. BSE images of polymineralic grains (e.g. Figure 5.30) also show etching at the margins of Ca-poor dolomite to the calcite interface, which is most likely to have formed as the result of partial dissolution of Ca-poor dolomite prior to the crystallization of the calcite cement, hence giving the possibility that the mineralization sequence was in the order of dolomite – breunnerite - (Ca-poor dolomite) - calcite cement.

As discussed in Section 5.4, dolomite, breunnerite and Ca-poor dolomite in QUE 93005 contain inclusions of phyllosilicates in the form of acicular crystals. These crystals occur in outer parts of the carbonate grains (e.g. Figure 5.23 a, Figure 5.27a) and it is clear that this phyllosilicate is replacing carbonate. Phyllosilicate sheets are much more common in breunnerite and Ca-poor dolomite than dolomite grains, which can be related to the high concentration of Fe and Mg in breunnerite and Ca-poor dolomite that encourage the replacement by phyllosilicate in these minerals. It was found by TEM that dolomite in Nogoya was also partially replaced by phyllosilicates (see Figure 5.9 c).

The only carbonate grains in QUE 93005 that are surrounded by rims of sulphide are dolomite grains (Section 5.4.2.2). These rims have been described as postdate dolomite (Lee et al., 2012; De Leuw et al., 2010), and so the fluids from which dolomite crystallized subsequently produced iron sulphide. The presence of these rims around dolomite, and also the complex intergrowths of carbonate minerals in QUE 93005, makes the meteorite unique in comparison to the other CM chondrites studied.

The fluids from which Ca-poor dolomite and breunnerite precipitated were probably formed briefly and locally in the parent body of QUE 93005. Endress and Bischoff (1996) related the variation in chemical composition of dolomite in CI chondrites to local changes

(on the scale of micrometres to millimetres) in the chemical composition of fluids on the parent body. Chemical analyses and X-ray maps of polymineralic grains in QUE 93005 (Table 5.10, Figure 5.34 and Figure 5.35) show significant differences in regard to chemical composition. It is clear from these observations that the formation of sequences such as breunnerite-(Ca-poor dolomite)-calcite cement and breunnerite-dolomite were controlled by variation over time in concentrations of ions including Ca, Mg, Fe, and Mn in the aqueous fluids. It is very difficult to identify the source of Ca that was used to form the calcite cement that filled the interior of polymineralic grains. One is that solutions were increasingly circulated via fractures on the parent body of the highly altered CM chondrite (see Lee, 1993; Endress and Bischoff, 1996) and most probably during the late stages of aqueous alteration.

7.2.6.3 The origins of carbonate veins in CM chondrites

The possible origins of veins (e.g. carbonates, Ca-sulphate) in carbonaceous chondrites are a subject of debate. For example, sulphate veins in the CI chondrites have been shown to be the result of terrestrial weathering, where sulphates that originally occur in the chondrites were dissolved and remobilized as a result of their reaction with atmospheric water (Gounelle and Zolensky, 2001). Richardson (1978) reported that the formation of veins (carbonate, Ca-sulphate, Mg-sulphate) in CI chondrites occurred within an extended episode of impact between brecciation and leaching events on the parent body. He suggested that the extent of multiple brecciation in CI carbonaceous chondrites were sourced from areas close to the surface of the parent body, and that the impact melt was water, which caused the remobilization of sulphates, carrying and redepositing them within pore spaces between breccias fragments. New clasts were created by further brecciation, some of these containing fragments of earlier veins (Richardson, 1978). Riciputi et al. (1994) also reported that the impact regolith has disrupted most carbonate veins in CI chondrites.

Results of this study (dissolution of calcite and dolomite grains repreciptated as veins in the parent body/ies of CM chondrites) are consistent with findings by Lee (1993) that the source of Ca-sulphate veins in Cold Bokkeveld was dissolution of calcite and metal sulphides that reprecipitated as gypsum within fractures that cross-cut the fine-grained matrix. Fracturing within the parent body/ies of carbonaceous chondrites occurred when gas pressures of fluid as well as lithostatic pressure exceeded the total tensile strength of the rock, then water vented within these fractures (Grimm and McSween, 1989). Rubin

(2012) concluded that fractures and petrofabrics in some regions of CM chondrites are a consequence of randomly spaced collisions taking place at the surface of their parent body, followed by impact mobilization of water that produced secondary minerals (e.g. carbonate and phyllosilicates) in the more fractured areas, whereas the less fractured regions were subjected to lower degrees of aqueous alteration. Melting of ice in the parent body was a result of internal heating provided by ^{26}Al decay (e.g. Grimm and McSween, 1989; Palguta et al. 2010), while impact-induced water could also be released from phyllosilicates (e.g. Lange et al., 1985). Movement of water in the parent body could have been driven by gas pressure originating from internal areas in the parent body (e.g. Grimm and McSween, 1989; Young et al., 1999) or by hydrothermal convection, as suggested by Palguta et al. (2010). Endress and Bischoff (1996) concluded that the hydration of Fe,Mg silicates during the early stages of aqueous alteration occurred by water circulating on the parent body through fractures, from its internal part to the outer part. Therefore, the formation of veins (e.g. calcite and dolomite) in the parent body of CM chondrites is most likely to have been formed after fracturing, and dissolution of carbonate grains that had previously formed in the parent body.

7.3 Summary

7.3.1 Aragonite formation

This section summarises the main findings on the crystallization and post crystallization deformation of aragonite in the CM chondrites studied.

Aragonite grains record a period relatively early in the aqueous alteration history of the parent body/ies of CM chondrites. This study suggests that in the early stages of aqueous alteration, aragonite was probably present in all CM chondrites, but was dissolved or replaced by calcite in some moderately and highly altered CM chondrites as aqueous alteration progressed. The formation of aragonite started when a few isolated pockets of relatively magnesium-rich water were available in the parent body/ies. Generally, aragonite in CM2.5-CM2.4 crystallized from fluids that have higher concentrations of Fe than those from which the aragonite grains in the CM2.3 crystallized. This initial water produced aragonite with high oxygen isotope values, these values falling as the water obtained further oxygen from anhydrous silicates (olivine/pyroxene). The majority of aragonite grains in the samples studied show homogeneous SEM-CL characteristics, which also indicates that the aragonite precipitated from chemically stable fluids. The majority of

these grains in CM chondrites have a preferred orientation, that is most likely to be the result of compression in the parent body/ies during crystallization.

7.3.2 Calcite formation

This section summarises the main findings on the crystallization and post crystallization deformation of calcite in the CM chondrites. Calcite has a variety of petrographic relationships, namely calcite free of rims and inclusions, calcite rimmed with tochilinite and/or Fe-sulphide, calcite replacing olivine, and calcite veins.

Calcite free of rims and inclusions is less abundant than calcite rimmed with tochilinite and calcite replacing olivine, in grains which are in direct contact with the fine grained (<1μm) matrix. The most remarkable feature is that the majority of calcite grains in EET 96029 (CM2.3) are free of rims and inclusions. This calcite is comparable in texture and appearance to most aragonite grains, but exhibits more complex CL patterns, indicating that these calcite grains precipitated from fluids that were less compositionally stable. The similarity in traits between aragonite and calcite free of rims and inclusions is used in this study to argue that some of the aragonite grains were probably replaced by calcite free of rims and inclusions (mainly in EET 96029). In common with other calcite types, calcite free of rims and inclusions precipitated from fluids that had a lower Mg/Ca ratio than those from which aragonite precipitated. Calcite free of rims and inclusions and aragonite either crystallized at a different time relative to tochilinite (probably before), or crystallized from isolated fluids that were supersaturated with only Ca^{2+} and CO_3^{2-}, and lacked sulphur.

Calcite grains rimmed with tochilinite and/or Fe-sulphide were present in all samples studied, but they differ in abundance from meteorite to meteorite. They are more abundant than aragonite and calcite free of rims and inclusions. These grains are uncommon in QUE 93005 and EET 96029, but more common in Pollen, LON 94101, Cold Bokkeveld and LAP 031166. This calcite has been partly or totally replaced by Mg-rich serpentine. SEM-CL characteristics of rimmed calcite are more complex than those of other carbonate minerals in CM chondrites. However, the most complicated SEM-CL characteristics have been found in grains from less altered CM chondrites (CM2.5-CM2.4), and SEM-CL characteristics gradually become simpler towards the highly altered CM chondrites (CM2.2-CM2.0). SEM-CL characteristics of calcite rimmed with tochilinite provide good evidence that this calcite was precipitated from small pockets of water by nucleation of a seed crystal within one part of a void, growing to fill the pore until the space or solution

was used up. The presence of a variety of CL patterns in calcite grains in less altered CM chondrites reveals fluctuating fluid chemistry, but fluids were more stable over the time span of calcite crystal growth during formation of grains in highly altered CMs chondrite. Chemical analyses also show that the Fe content of calcite in highly altered CM2.1/2.0 to CM2.0 chondrites falls as aqueous alteration progresses. The Mg content in calcite does not follow the pattern of overall fluid evolution of CM chondrites (i.e. increasing of Mg in the matrix with progressive alteration), but corresponds well with increasing of alteration degree in highly altered CM2.2 to CM2.0 chondrites. Calcite grains rimmed with tochilinite in LON 94101 have lower $\delta^{18}O$ values than aragonite grains, so this calcite probably formed later.

Petrographic observations of calcite replacing original anhydrous minerals (i.e. pyroxene and Mg-rich olivine) show that calcite after pyroxene is free of inclusions and cryptocrystalline, whereas calcite replacing olivine often contains inclusions of sulphide, and is composed of numerous sub-crystals. Calcite after pyroxene is rarely present in CM chondrites. Calcite replacing Mg-rich olivine is found in all the studied CM chondrites, but varies in abundance from meteorite to meteorite. It is more abundant and coarser grained with increasing degree of alteration overall. Oxygen isotope analyses (Tyra et al., 2012) reveal that calcite after olivine formed after other matrix calcite grains. Chemical analyses of calcite replacing olivine shows high concentrations of Fe, which is probably related to the Fe-sulphide inclusions. Thus, the Fe content of calcite replacing olivine cannot be used as a tool to explore fluid evolution within the studied CM chondrites.

Pseudomorphs of calcite grains (calcite rimmed with tochilinite and/or Fe-sulphide) made of Mg-rich serpentine, or Mg-rich serpentine intergrown with tochilinite, are present mainly in the moderately and highly altered CM chondrites. However, some Mg-rich serpentine pseudomorphs after calcite occur in Murchison (CM2.5), and they are also common in Pollen (CM2.4). Mg-rich serpentine after calcite is more abundant than tochilinite-serpentine pseudomorphs in the studied CM chondrites. Based on the chemical composition of the product, Mg-rich serpentine pseudomorphs (mainly present in the highly altered CM chondrites) formed from fluids that were richer in Mg than Fe, whereas tochilinite-serpentine pseudomorphs (present only in moderately CM chondrites) are likely to have crystallized from solutions that contained high concentrations of Fe, S and Ni. This is consistent with hypotheses (e.g. McSween, 1979) that solutions at later stages in the alteration sequence were dominated by Mg, a result of the dissolution of Mg-rich silicates; consequently new minerals rich in Mg were formed.

This study suggests that calcite after Mg-rich olivine, and Mg-rich serpentine or serpentine-tochilinite intergrowth after calcite, probably formed at the same time or immediately after each other. Elements including Fe, Mg and Si were released from Mg-rich olivine, and have been used for the replacement of calcite by Mg-rich serpentine. The Ca and CO_3 released from calcite may then have contributed to the replacement of Mg-rich olivine by calcite. In this case, it is most likely that calcite replaced olivine after the Mg-serpentine had replaced tochilinite-rimmed calcite.

Another finding of this work is that some of the Ca that remained in solutions after replacement of calcite by Mg-rich serpentine and was consumed by formation of calcite veins. BSE images of the calcite vein in LON 94101 shows that the calcite overgrows calcite rimmed with tochilinite, suggesting that the calcite vein formed later. Oxygen isotope analyses indicate that the calcite vein formed after calcite grains and aragonite, and may have been sourced from dissolution of earlier Ca-carbonate grains. Petrographic observations show that shock came after crystallization of rimmed calcite grains and the LON 94101 vein. The calcite vein in LON 94101 has low concentrations of Fe in comparison with other calcite and aragonite grains, which also suggests that the calcite vein originated from solutions different to those that formed the calcite and aragonite grains. Thus, this work suggests that the calcite vein in LON 94101 was formed by water flow within the parent body.

7.3.3 Formation of dolomite, breunnerite, Ca-poor dolomite and calcite cement

This section summarises the main findings about crystallization and post crystallization deformation of dolomite, breunnerite, Ca-poor dolomite and calcite cement in the CM chondrites studied.

This study shows that dolomite grains are rarely present (only two grains) in the less altered lithology of Nogoya (CM2.3), and a few grains of dolomite replacing calcite were also observed in LAP 031166 (CM2.1/CM2.0). Dolomite is found mainly in the highly altered CM chondrites, including QUE 93005 (CM2.1) and SCO 06043 (CM2.0). Calcite intergrown with dolomite is also present in QUE 93005 and SCO 06043. However, dolomite was not recognised in highly altered ALH 88045 (CM2.0). As hydration of Mg-rich olivine increases in CM chondrites as a result of aqueous alteration, later stages of aqueous alteration fluids would have been richer in Mg, encouraging dolomite formation. Increasing Mg concentrations in solutions during late stages of aqueous alteration, which

produced dolomite, would also be consistent with the idea that calcite grains (not calcite replacing dolomite) formed prior to dolomite in CM chondrites. These results are in agreement with previous work (De Leuw et al., 2010) which concluded that the absence of dolomite in the highly altered chondrites was probably a consequence of dedolomitisation, evidence for dedolomitisation being found in SCO 06043 (CM2.0) (inclusion of dolomite in calcite grains). Dissolution of earlier formed calcite grains could have provided sufficient Ca for dedolomitisation. Transformation of carbonate (both dolomite and calcite) to Mg-rich serpentine in SCO 06043 may be another source of Ca for this process. The presence of veins made of calcite and/or dolomite in QUE 93005 and SCO 06043 (highly altered chondrites) is an indicator of water flow in the parent body of CM chondrites. In common with the calcite vein in LON 94101, the dolomite veins in SCO 06043 are different in chemical composition to the matrix dolomite grains, and are a record of the final stage of aqueous alteration. They have very low concentrations of Fe and Mn in comparison with dolomite grains. The majority of CL images of dolomite grains in SCO 06043 show a very low intensity, which implies that the fluids from which dolomite grains in SCO 06043 precipitated were more stable, whereas CL images of some dolomite grains in QUE 93005 show zonation in single dolomite grains, which reveals changes in the chemical composition of fluids during their formation.

This study shows that chemically complex carbonate minerals occur mainly in QUE 93005 (dolomite-breunnerite grains and aggregates of breunnerite-(Ca-poor dolomite)-calcite cement). These minerals suggest that conditions of aqueous alteration differ from area to area of the parent body/ies. BSE and CL images of dolomite-breunnerite grains reveal that dolomite is most likely to have crystallized first within the pore space to be followed by breunnerite. BSE images and EDS X-ray maps of polymineralic grains breunnerite - (Ca-poor dolomite)-calcite cement show that the breunnerite initially formed at the margins of pore spaces; subsequently Ca-poor dolomite, and then calcite cement filled the pore space. The formation of these complex minerals was most likely controlled by fluctuating concentrations of ions including Ca, Mg, Fe, and Mn in the aqueous fluids, again suggestive of some solution movement by flow.

8

Conclusion and further work

8.1 Conclusion

As part of the overall goal of defining the environmental conditions accompanying the formation of carbonates in parent bodies, this discussion will use the results of this study and previous work (i.e. Palguta et al., 2010; Bland et al., 2009a) to develop a model of water flow in the parent body/ies of CM chondrites. Specifically, results from this study are used in this section to test predictions and assumptions of numerical models designed to simulate the evolution of icy planetesimals.

Based on meteorite petrography, oxygen isotope data, quantifying porosity and grain size distribution in primitive chondritic materials, Bland et al. (2009a) estimated the permeability in the parent bodies of carbonaceous chondrites. A small number of permeability measurements of meteorites have been previously carried out (e.g. Sugiura et al. 1984; Corrigan et al. 1997) with results ranging from 10^{-15} m^2 to < 10^{-21} m^2, which are less than values previously used in numerical modeling. Bland et al. (2009a) estimated the range of permeabilities for chondritic primitive material to be 10^{-19} -10^{-17} m^2. They suggested that spacing and fractures in carbonaceous chondrites show limitation of fracture interconnections in the scales from 1's-μm to 10's-cm. Their model suggests that water flow in the parent body is very limited in all areas, even in high porosity regions, suggesting a closed fluid system at a scale of 100's μm. The suggestion of the limitation of water flow in the parent body/ies is consistent with the notion that aqueous alteration has been isochemical on the meteorite (i.e. meter) scale (e.g. Rubin et al., 2007), which is most easily explanied by minimal water flow. The variation of lithologies in CI chondrites has also been interpreted as the result of a closed system alteration (Morlok et al, 2006). Using

petrographic data from meteorites, Bland et al. (2009a) also argued that the fractionation of soluble elements takes place by solution, then the elements also mobilised and reprecipitated, but not by more than 100's μm. They also reported that permeability is required for water movement through a rock, but a rock can be permeable if it contains fractures, or has permeability along its grain boundary, or contains both. The important thing is that in the Bland et al. model (2009a), each different type of meteorite probably needs to come from a different parent body.

Palguta et al. (2010) undertook a study to understand the nature of water/rock interactions in the parent bodies of carbonaceous chondrites, and to provide a model of fluid flow that is contrary to the closed system model. Their numerical model of hydrothermal circulation provides information about heat, water movement, geochemical reactions and the exchange of isotopes. The parent body in their model is assumed to initially be made of anhydrous minerals (mainly olivine) and water ice that was homogenously mixed and heated by ^{26}Al decay; this initial homogenous model of the parent body of carbonaceous chondrites was also proposed by Grimm and McSween (1989). The values that were used by Palguta et al. (2010) for porosity, permeability, weight fraction of ^{26}Al, and ice density are 38%, 10^{-11} m^2, 4.5 x 10^{-8}, 917 kg m^{-3} respectively. They also used 170K for initial body temperature, and assumed the water to have $\delta^{18}O$ of 20.7‰ and $\delta^{17}O$ of 14.1‰, and the rock $\delta^{18}O$ of -3.0‰ and $\delta^{17}O$ of -7.0‰. The radius of the parent body was assumed to be 50km.

The main events during the evolution of the parent body as outlined in the model of Palguta et al. (2010) can be summarised as follows: melting of ice started about 4.5 x 10^5 years after accretion, when temperatures were sufficiently warm, but water flow did not start at that time. The temperature of the interior of the parent body eventually reached about 85°C, but the temperature in the outer part fell rapidly. The temperature in the surface (4-6 km) did not exceed freezing. The transfer of heat (hydrothermal convection) began shortly after 1.2 x 10^6 years after accretion, and gradually reached the highest level by 1.4 x 10^6 years after accretion. The interior of the parent body (i.e. areas between ~ 15 and 40 km from the centre) had a temperature range from ~50 °C (alongside downwellings) to ~ 100 °C (alongside upwellings). The source of heating was diminishing by 2.2 x 10^6 after accretion causing the upwelling to spread out, and a small number of broad plumes to be formed.

Palguta et al. (2010) suggested that reactions between water and rock started in the centre of the parent body, where water ice was first melted. Prior to the convective phase, rocks in

these areas were more exposed to water than those in the external layers. The alteration structure was one of concentric layers. The alteration progressed close to the centre and along upwellings, as they are warmer and contained water at the highest pressure. The parent body contained several different layers about 2 million years after accretion: (i) the internal part characterised by extensive transformation of anhydrous silicates to hydrous minerals, about > 10% of primitive anhydrous minerals are left in areas between the centre of the parent body and radius of ~ 20km, (ii) areas between the centre of the parent body and radius of ~ 14 km are characterized by the presence of a little primary material that remained unaltered, the highly altered materials are mainly present in the interior of the parent body. Palguta et al. (2010) concluded that CM-like materials and CI-like materials were produced from the same parent body, but from different regions (see Figure 8.1). They suggested a range of temperatures from ~ 110-130 °C for regions where CI chondrites formed, and from 50 to 70 °C where CM chondrites formed. Their model also provides regions for anomalous chondrites that are not easily classified as CI or CM chondrites. The regions of anomalous chondrites lie between CI and CM chondrites.

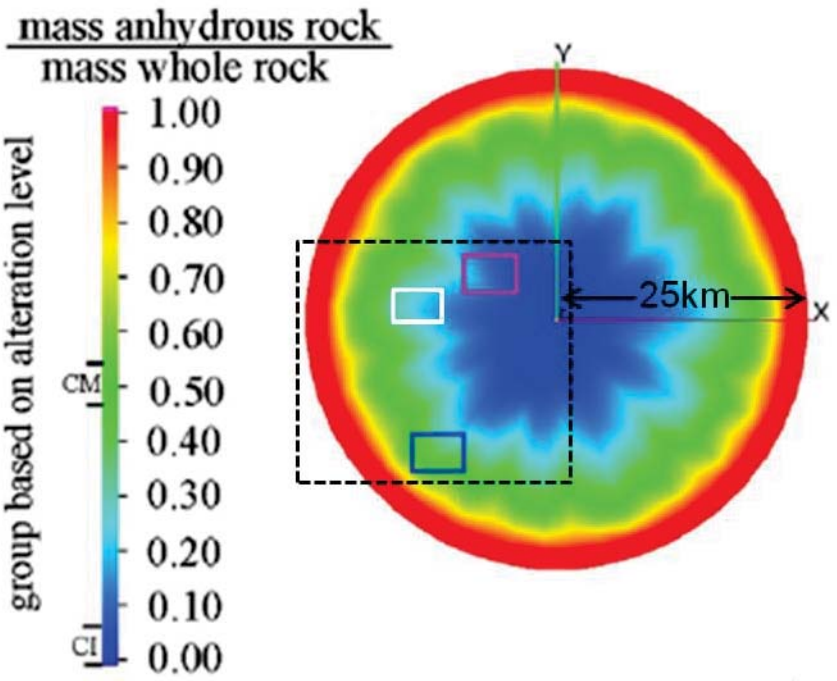

Figure 8.1- Schematic diagram showing locations in the parent body from where the CI and CM were derived.
These variations in temperatures and alteration minerals are discussed above. These variations took place at 2.2 x 10^6 after accretion. Examples of the location alterations of CI and CM chondrites are marked in red box and blue box respectively. The white box is used here to refer to the location of anomalous chondrites. Region within the black box is used in Figure 8.3 to determine possible locations of the sample stuied in the parent body. The radius of the parent body is 50 km. Modified after Palguta et al. (2010).

Alternatively, Young et al. (2003) presented a new critical Rayleigh number (Rayleigh number of fluid is defined as dimensionless no. combined with buoyancy driven flow) for water convection inside the void space of the spherical parent body that is permeable and heated inside. Their calculations suggested three models for water-rock interaction in the parent body of carbonaceous chondrites that are heated inside (by 26 Al decay) and comprised of rock and water. The first model (Figure 8.2a) shows interaction between water and rock with an absence of water movement in the parent body. The parent body was described as an unconsolidated regolith and bounded by an impermeable surface. Young et al. (2003) suggested that volumetric porosities of 0.38 to 0.55 are required in the static model for water-rock oxygen exchange. These minimum values were estimated on the assumption the rock was involved in reactions with every molecule of water that occurred in pore spaces. Their calculations showed that the first model (fluid occupying voids with a permeability of about 10^{-11} m^2) could only have motionless fluid if the radius of the body was less than 40 km. However, this model also characterizes the consolidated body that contains lower permeability than an unconsolidated regolith (~10^{-12} m^2), but the parent body accommodates large porosity (0.05-0.29) and its diameter is ~80 km. The second model (Figure 8.2b) (water exhalation) shows water-rock interaction across the parent body due to water movement from higher (at internal areas) to lower temperatures in frozen areas at the surface. Eventually, the water either refreezes within voids close to the cold surface, or blows out from the parent body into space through a permeable crust. As mentioned above, the migration of water within the parent body could have been driven by gas pressure originated from the internal areas in the parent body (e.g. Grimm and McSween, 1989; Young et al., 1999) or by hydrothermal convection as suggested by Palguta et al. (2010). The third model (Figure 8.2c) was designed for the parent body (> ~120 km in diameter) that its water-rock interaction is convection and enclosed with an impermeable zone, and the water fluid occupying pore spaces was defined as not to have been static. The water flow in this parent body was due to gravitational instability.

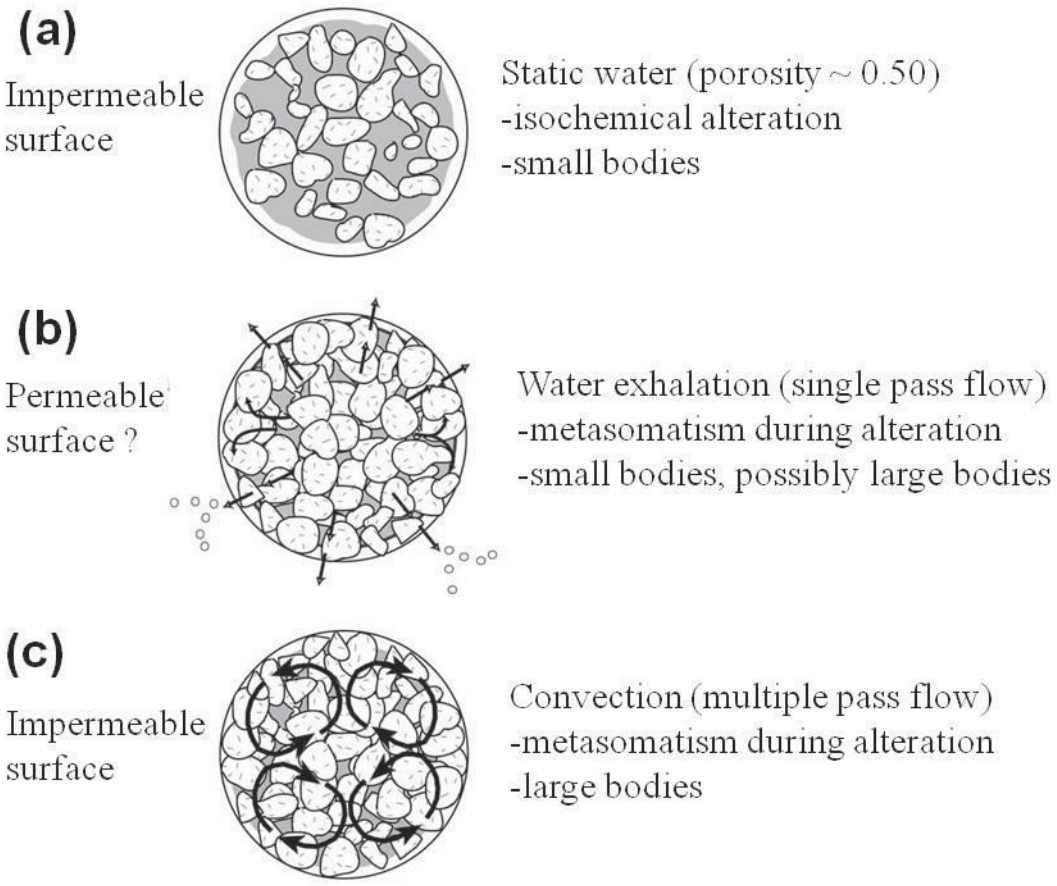

Figure 8.2- Schematic diagram showing three models of water-rock interaction within carbonaceous chondrite bodies.
(a) Schematic illustration shows interaction between water and rock with absence of water movement in the parent body. (b) Schematic illustration shows water-rock interaction across the parent body due to the water movement from higher (at internal areas) to lower temperatures in frozen areas at the surface (water exhalation). (c) Schematic illustration shows the third model of water-rock interaction that is convection and enclosed with an impermeable surface. Frozen water is indicated by white, liquid water is indicated by gray and black represents pore space. Hash pattern and arrows represent rock and the patterns of pore water flow respectively. Modified after Young et al. (2003).

A qualitative model (Figure 8.3b) for aqueous alteration of CM chondrites can be developed using the models discussed above of Bland et al. (2009a) (closed system) and Palguta et al. (2010) (fluid flow), and the results of this study as outlined in previous chapters. The closed system model is not favoured for moderately, highly and the most altered CM chondrites as some of these meteorites contain carbonate veins that are path ways for water movement within the parent body. Thus, hydrothermal circulation is more appropriate for aqueous alteration of moderately, highly and the most altered CM chondrites. The hydrothermal circulation in the parent regions, from which moderately to the most altered chondrites derived is most likely to have been occurred through fractures. The formation of the fractures was probably due to random collision on the parent body (Rubin, 2012). Lenses that are enriched with PCP, and contain Ni-bearing sulphide and Ca

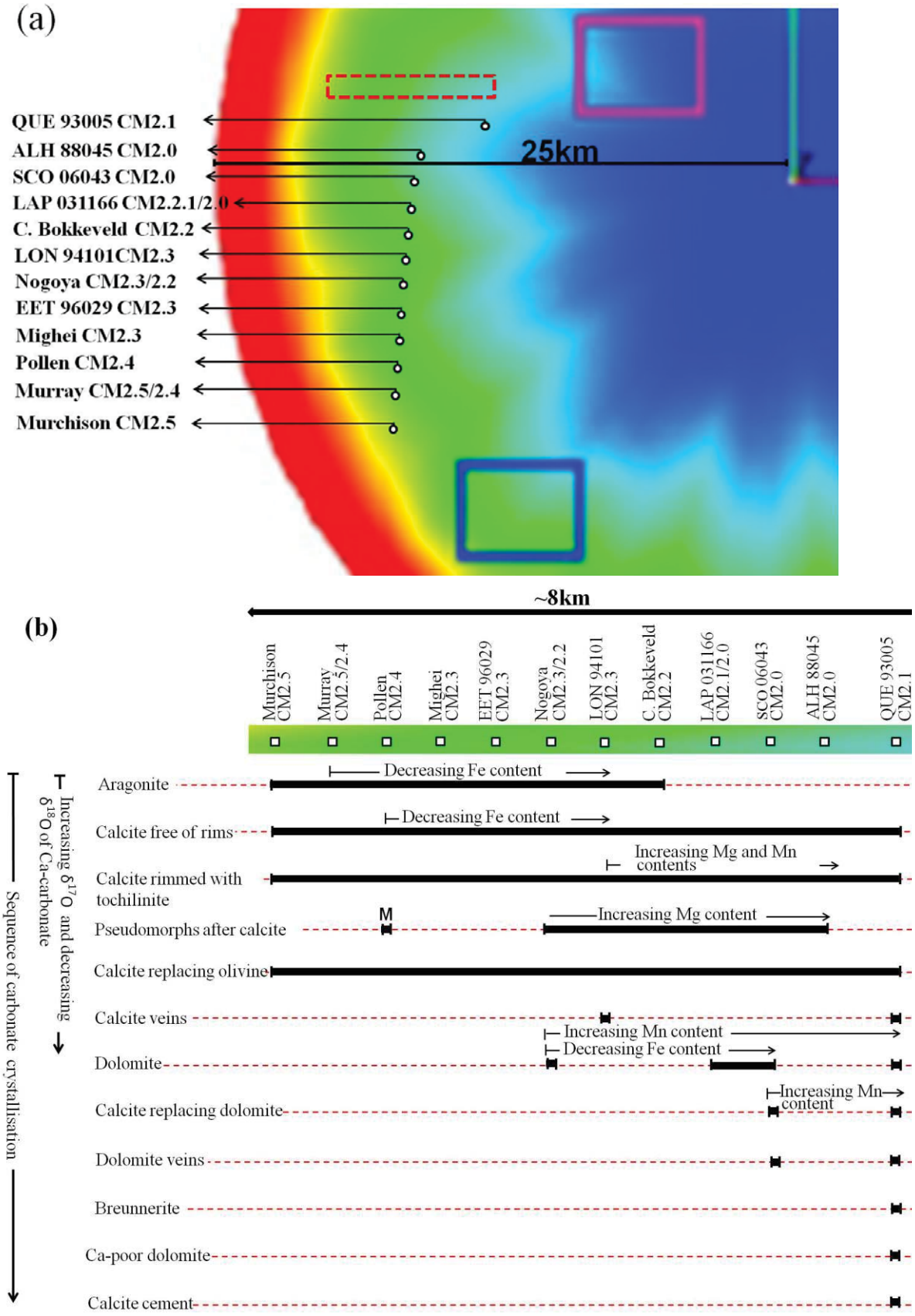
(a)
QUE 93005 CM2.1
ALH 88045 CM2.0
SCO 06043 CM2.0
LAP 031166 CM2.2.1/2.0
C. Bokkeveld CM2.2
LON 94101CM2.3
Nogoya CM2.3/2.2
EET 96029 CM2.3
Mighei CM2.3
Pollen CM2.4
Murray CM2.5/2.4
Murchison CM2.5
25km
(b)
~8km
Murchison CM2.5
Murray CM2.5/2.4
Pollen CM2.4
Mighei CM2.3
EET 96029 CM2.3
Nogoya CM2.3/2.2
LON 94101 CM2.3
C. Bokkeveld CM2.2
LAP 031166 CM2.1/2.0
SCO 06043 CM2.0
ALH 88045 CM2.0
QUE 93005 CM2.1
Sequence of carbonate crystallisation
T
Increasing δ17O and decreasing δ18O of Ca-carbonate
Aragonite
Decreasing Fe content
Calcite free of rims
Decreasing Fe content
Calcite rimmed with tochilinite
Increasing Mg and Mn contents
Pseudomorphs after calcite
M
Increasing Mg content
Calcite replacing olivine
Calcite veins
Dolomite
Increasing Mn content
Decreasing Fe content
Calcite replacing dolomite
Increasing Mn content
Dolomite veins
Breunnerite
Ca-poor dolomite
Calcite cement

Figure 8.3- A qualitative model for aqueous alteration of CM chondrites.
This model has been developed by combining the closed system (Bland et al., 2009a) and fluid low (Palguta et al., 2010) models, with the results of this study. (a) The area within the black box in Figure 8.1 has been enlarged to show possible locations in the parent body of the sample studied. (b) Paragenetic carbonate phases within the boxed region (red box) of (a) from where the studied samples were possibably derived. It also shows the sequence of the crystallisation of carbonate that differs within region. Note the absence of aragonite towards the highly altered areas where carbonate veins, dolomite and breunnerite are present. Generally, Fe content of carbonate minerals decreases towards the internal areas of this region where the contents of Mg and Mn decrease. M is Mg rich serpentine.

phosphate are suggested to have formed within fractures as a consequence of dissolution of anhydrous matrix and water flow (Lee, 1993; Rubin, 2012). Movement of water in the parent body could have been driven by gas pressure originated from the internal areas in the parent body (e.g. Grimm and McSween, 1989; Young et al., 1999) or by hydrothermal convection as suggested by Palguta et al. (2010).

As shown in Figure 8.1 and Figure 8.3a, zones in the parent body that are close to the exterior are the appropriate regions from which the less altered CM chondrites (e.g. Murchison, Murray, pollen) and a few moderately altered CM chondrites (e.g EET 96029 and Mighei) could have been derived. These regions are free of carbonate veins, and contain carbonate grains that precipitated in small isolated areas of high porosity and permeability in the matrix (e.g. Figure 4.1). In some cases, the carbonate grains that formed close to each other are similar in chemical composition. This is probably a consequence of low water flow velocities causing the chemical composition of water to be controlled by the dissolution of adjacent anhydrous minerals.

Results of this study show that QUE 93005 (CM2.1) is the only CM chondrite that contains breunnerite, and this trait can be used to classify QUE 93005 as an anomalous CM chondrite that was probably derived from regions that lie between the CI and CM chondrites (see Figure 8.1). Breunnerite is one of another four carbonate minerals (calcite, dolomite and siderite) that are found in CI chondrites (Endress and Bischoff, 1996).

In summary, the results of this study suggest that CM chondrites were probably derived from the same parent body, but from three distinct regions (example of the location first and second regions is labelled in blue box in Figure 8.1 and an example of the third region is shown by the black box). The content of ice, porosity and source of heating (^{26}Al) differ in these regions. The first region which was host to the less altered CM chondrites (e.g. Murchison, Murray, and Pollen) and some of moderately altered CM chondrites (e.g. Mighei, EET 96029, and the less highly altered lithology of Nogoya), is characterised by

an absence of water flow on a large scale, but small isolated areas (a few hundred microns) of high porosity and permeability in the matrix of this region was present. These characteristics are inferred from the occurrence of Ca-carbonate minerals (aragonite and calcite) in small isolated areas, and also in some cases in small discontinuous veins; all fractures that are found in these CM chondrites are free of carbonate minerals. The second region was host to some moderately altered CM chondrites (e.g. LON 94101), highly altered CM chondrites (e.g. highly altered lithology of Nogoya, Cold Bokkeveld, LAP 031166), and the most altered CM chondrites (SCO 06043 and ALH 88045). This region was characterised by precipitation of carbonate minerals within some fractures that occur in the matrix, and also a gradual increase of Mg-rich carbonate towards the interior of the parent body. The carbonate grains in this region are coarser and more homogenously distributed than those in the first region. The third region in which the anomalous CM chondrites formed (e.g. QUE 93005) occurs between region of CM chondrites (first and second region) and the region of CI chondrites (see Figure 8.1). This third region is characterised by an increasing abundance of carbonate veins and the occurrence of large carbonate grains (several hundred microns, e.g. Figure 5.34). The most remarkable feature is the presence of breunnerite in this region that also characterizes the region from where the CI chondrites derived (see Figure 8.1). The boundaries between these regions are most likely to be sharp, which distinguishes between two different degrees of aqueous alteration (see Figures 3.35, 3.36, 3.38).

8.2 Further work

There are a number of suggested developments to follow on from this study. The most important, as previously outlined, is to extend this study on CM chondrites by further applying petrographic study, chemical analyses and oxygen isotope analyses to carbonates in other types of carbonaceous chondrites, including CR and CI chondrites to clarify any evolutionary links between CR, CM and CI chondrites. There are other aspects of this study that could be examined in more detail. This study focused on CM chondrites which contain five phases of carbonates; namely aragonite, breunnerite, calcite, Ca-poor-dolomite and dolomite. To enhance the conclusions gained from this study, oxygen isotope compositions of breunnerite, Ca-poor-dolomite and dolomite could be carried out. The nature of such isotopic zoning (e.g. breunnerite-(Ca-poor-dolomite)-dolomite) may provide further insights into the evolution of pore fluid chemistry. In addition, this study shows that fluid inclusions are found in calcite grains of Murchison, Mighie and Nogoya. These fluid inclusions represent samples of fluids attendant on asteroidal aqueous alteration; therefore

detailed study of fluid inclusions in carbonaceous chondrites would hopefully produce more accurate and reliable results, reflecting the nature of asteroidal fluid.

Further studies on the chronology of the formation of carbonate and Mg-rich serpentine pseudomorphs after calcite are essential to clarify the timing and duration of aqueous alteration. It would also be helpful to carry out TEM studies on carbonates intergrowth such as breunnerite-(Ca-poor-dolomite)-dolomite, breunnerite-dolomite, and calcite-dolomite. This would add more insight into the sequence events of the early stages of the solar system.

Furthermore, it would be of great interest to gain a set of samples from organic-rich carbonaceous asteroids (Near-Earth Asteroid, i.e. 1999 RQ36); a sample will be collected by the OSIRIS-REx spacecraft. The mission is organised by Goddard Space Flight Center, Locheed Martin, and The University of Arizona in an effort to provide answers to origins, life and impacts. Another sample surface will be collected from primitive bodies or Near-Earth Objects (NEOs) by the JAXA Space Exploration Center (JSPEC) using the Hayabusa-2 spacecraft, which aims to explore the 1999JU3 asteroid (a C-type asteroid), with its orbit like the orbit of ltokawa (S-type asteroid). The 1999JU3 is enriched in hydrated minerals and organic matter, so study of these pristine materials will provide important information that is needed to understand the conditions for planet formation. These materials can also be used to answer how life evolves in the solar system.

List of references

ADAMS, A. E. & MACKENZIE, W. S. 1998. A colour atlas of Carbonate sediments and rocks under the Microscope, London, *Manson publishing Ltd*, 180 p.

AGNOR, C. B., CANUP, R. M. & LEVISON, H. F. 1999. On the character and consequences of large impacts in the late stage of terrestrial planet formation. *Icarus*, 142, 219-237.

ALLÉGRE, C. J., MANHÉS, G. & GÖPEL, C. 1995. The age of the Earth. *Geochimica et Cosmochimica Acta*, 59, 1445–1456.

AMELIN, Y., KROT, A. N., HUTCHEON, I. D. & ULYANOV, A. A. 2002. Lead isotopic ages of chondrules and calcium–aluminium-rich inclusions. *Science*, 297, 1678-1683.

AMELIN, Y., WADHWA, M. & LUGMAIR, G. 2006. Pb-Isotopic Dating of Meteorites Using 202Pb-205Pb Double-Spike: Comparison with Other High-Resolution Chronometers. *37th Annual Lunar and Planetary Science Conference,* abstract no.1970.

ANDREANI, M., LUQUOT, L., GOUZE, P., GODARD, M., HOISÉ, E. & GIBERT, B. 2009. Experimental Study of Carbon Sequestration Reactions Controlled by the Percolation of CO_2-Rich Brine through Peridotites. *Environ. Sci. Technol.,* 43**,** 1226–1231.

Antarctic Meteorite Newsletters, 18 (2), 1995. JSC, Houston.

Antarctic Meteorite Newsletter, 21 (1) (1998), JSC, Houston.

Antarctic Meteorite Newsletter, 29 (2) 2006. JSC, Houston

Antarctic Meteorite Newsletter, 31 (1) 2008. JSC, Houston.

ARMSTRONG, J. T., MEEKER, G. P., HUNEKE, J. C. & WASSERBURG, G. J. 1982. The Blue Angel: I - The mineralogy and petrogenesis of a hibonite inclusion from the Murchison meteorite. *Geochimica et Cosmochimica Acta*, 46, 575-595.

ARRHENIUS, G. & ALFVÉN, H. 1971. Fractionation and condensation in space. *Earth and Planetary Science Letters*, 10, 253-267.

BAKER, J., BIZZARRO, M., WITTIG, N., CONNELLY, J. & HAACK, H. 2005. Early planetesimal melting from an age of 4.5662 Gyr for differentiated meteorites. *Nature*, 436, 1127-1131.

BARBER, D. J. 1981. Matrix phyllosilicates and associated minerals in C2M carbonaceous chondrites. *Geochimica et Cosmochimica Acta*, 45, 945-970.

BARBER, D. J. & WENK, H. R. 1979. Deformation twinning in calcite, dolomite, and other rhombohedral carbonates. *Physics and Chemistry of Minerals*, 5, 141-165.

BELL, J. F., DAVIS, D. R., HARTMANN, W. K. & GAFFEY, M. J. 1989. Asteroids - The big picture. In: Binzel RP, Gehrels R & Matthews MS (eds.), Asteroids II. Tucson, *University of Arizona Press,* p. 921-945.

BENEDIX, G. K., LESHIN, L. A., FARQUHAR, J., JACKSON, T. & THIEMENS, M. H. 2003. Carbonates in CM2 chondrites: Constraints on alteration conditions from oxygen isotopic compositions and petrographic observations. *Geochimica et Cosmochimica Acta*, 67, 1577-1588.

BINZEL, R. P. & XU, S. 1993. Chips off of asteroid-4 Vesta - evidence for the parent body of basaltic achondrite meteorites. *Science*, 260, 186-191.

BISCHOFF, A. 1998. Aqueous alteration of carbonaceous chondrites: Evidence for preaccretionary alteration - A review. *Meteoritics & Planetary Science*, 33, 1113-1122.

BISCHOFF, A. 2001. Meteorite classification and the definition of new chondrite classes as a result of successful meteorite search in hot and cold deserts. *Planetary and Space Science*, 49, 769-776.

BIZZARRO, M., BAKER, J. A., HAACK, H. & LUNDGAARD, K. L. 2005. Rapid timescales for accretion and melting of differentiated planetesimals inferred from Al-26-Mg-26 chronometry. *Astrophysical Journal*, 632, L41-L44.

BLAND, P., JACKSON, M., COKERC, R., COHEN, B., WEBBERE, J., LEE, M., DUFFY, C., CHATER, R., ARDAKANI, M., MCPHAIL, D. & BENEDIX, G. 2009a. Why aqueous alteration in asteroids was isochemical: High porosity ≠ high permeability. *Earth and Planetary Science Letters,* 287, 559-568.

BLAND, P. A., SPURNY, P., TOWNER, M. C., BEVAN, A. W. R., SINGLETON, A. T., BOTTKE, W. F., JR., GREENWOOD, R. C., CHESLEY, S. R., SHRBENY, L., BOROVICKA, J., CEPLECHA, Z., MCCLAFFERTY, T. P., VAUGHAN, D., BENEDIX, G. K., DEACON, G., HOWARD, K. T., FRANCHI, I. A. & HOUGH, R. M. 2009b. An anomalous basaltic meteorite from the innermost main belt. *Science*, 325, 1525-1527.

BOSS, A. P. 1995. Collapse and fragmentation of molecular cloud cores. 2: Collapse induced by stellar shock waves. *Astrophysical*, 439, 224-236.

BOSS, A. P. 2007. The Solar Nebula. *Treatise on Geochemistry* 1, 1-23.

BOUVIER, A., BLICHERT-TOFT, J., MOYNIER, F., VERVOORT, J. D. & ALBARÈDEA, F. 2007. Pb–Pb dating constraints on the accretion and cooling history of chondrites. *Geochimica et Cosmochimica Acta,* 71, 1583-1604.

BOUVIER, A. & WADHWA, M. 2010. The age of the solar system redefined by the oldest Pb-Pb age of a meteoritic inclusion. *Nature Geosciences*, 3, 637-641.

BREARLEY, A. J. 1998. Carbonates in CM carbonaceous chondrites: complex zoning revealed by high resolution cathodoluminescence studies, *29th Lunar and Planetary Sciences Conference.* (Abstract#1246).

BREARLEY, A. J. 2003. Nebular versus Parent-body Processing. *Treatise on Geochemistry*, 1, 247-268

BREARLEY, A. J. 2006. The action of water. In: Dante Lauretta, H.Y. McSween Jr and L. Leshin (eds.), Meteorites and the early solar system II, Tucson, *Arizona University Press*, P. 587-622.

BREARLEY, A. J. & HUTCHEON, I. D. 2002. Carbonates in the Y791198 CM2 chondrite: zoning and Mn-Cr systematics. *Meteoritics& Planetary Science*, Abstracts of the 65th Annual Meeting, A23.

BREARLEY, A. J., HUTCHEON, I. D. & BROWNING, L. 2001. Compositional Zoning and Mn-Cr Systematics in Carbonates from the Y791198 CM2 Carbonaceous Chondrite. *32nd Annual Lunar and Planetary Science Conference*, (Abstract#1458).

BREARLEY, A. J. & JONES, R. H. 1998. Chondritic meteorites. In: PAPIKE, J. (ed.) Planetary Materials Mineralogical, *Mineralogical Society of America*, 36, p. 3-398.

BREARLEY, A. J., SAXTON, J. M., LYON, I. C. & TURNER, G. 1999. Carbonates in the Murchison CM chondrite: Cl characteristics and oxygen isotopic compositions. *30th Annual Lunar and Planetary Science Conference*. (Abstract#1301).

BREARLEY, A. J. & HUTCHEON, I. D. 2000. Carbonates in the CM1 chondrite ALH84034: mineral chemistry, zoning and Mn-Cr systematics. *31st Lunar and Planetary Science Conference (XXXI),* (Abstract#1407).

BROWNING, B. & KEIL, K. 1997. Were CM chondrites aqueously altered in the quiescent interior of their parent body? *28th Annual Lunar and Planetary Science Conference*, (Abstract#1276).

BROWNING, L. B., MCSWEEN, H. Y. & ZOLENSKY, M. E. 1996. Correlated alteration effects in CM carbonaceous chondrites. *Geochimica et Cosmochimica Acta,* 60, 2621-2633.

BULLOCK, E. S., MCKEEGAN, K. D., GOUNELLE, M., GRADY, M. M. & RUSSELL, S. S. 2010. Sulfur isotopic composition of Fe-Ni sulfide grains in CI and CM carbonaceous chondrites. *Meteoritics & Planetary Science*, 45, 885-898.

BUNCH, T. E. & CHANG, S. 1978. Carbonaceous Chondrite (CM) Phyllosilicates: Condensation or Alteration Origin? *Lunar and Planetary Science IX*, Abstract. TKO., 134-136.

BUNCH, T. E. & CHANG, S. 1980. Carbonaceous chondrites—II. Carbonaceous chondrite phyllosilicates and light element geochemistry as indicators of parent body processes and surface conditions. *Geochimica et Cosmochimica Acta*, 44, 1543-1577.

BURGESS, R., WRIGHT, I. P. & PILLINGER, C. T. 1991. Determination of sulphur-bearing components in C1 and C2 carbonaceous chondrites by stepped combustion. *Meteoritics & Planetary Science*, 26, 55-64.

BURKHARD, M. 1993. Calcite twins, their geometry, appearance and significance as stress-strain markers and indicators of tectonic regime - a review. *Journal of Structural Geology,* 15, 351-368.

BURTON, E. A. & WALTER, L. M. 1991. The effects of PCO_2 and temperature on magnesium incorporation in calcite in seawater and $MgCl_2$-$CaCl_2$ solutions. *Geochimica et Cosmochimica Acta,* 55, 777-785.

CALDERÓN, T., AGUILAR, M., JAQUE, F. & COY-Y11, R. 1984. Thermoluminescence from natural calcites. *J. Phys. C: Solid State Phys.,* 17**,** 2077-2038.

CAMERON, A. G. W. & TRURAN, J. W. 1977. The supernova trigger for formation of the solar system. *Icarus,* 30, 447-461.

CAMPBELL, A. J., ZANDA, B., PERRON, C., MEIBOM, A. & PETAEV, M. 2005. Origin and thermal history of Fe-Ni metal in primitive chondrites. *The Astronomical Society of the Pacific Conference Series,* 341, p. 407-431.

CHAMBERS, J. E. 2001. Making More Terrestrial Planets. *Icarus,* 152, 205-224.

CHAMBERS, J. E. 2004. Planetary accretion in the inner solar system. *Earth and Planetary Science Letters,* 223 241–252.

CHAMBERS, J. E. 2007. Planet Formation. *Treatise On Geochemistry*, 1, 1-17.

CHAMBERS, J. E. & WETHERILL, G. W. 1998. Making the terrestrial planets: N-body integrations of planetary embryos in three dimensions. *Icarus,* 136, 304-327.

CHAMPNESS, P. E. 1977. Transmission Electron Microscopy in Earth Science. *Annual Review of 842 Earth and Planetary Sciences,* 5, 203-226.

CHEN, J. H. & WASSERBURG, G. J. 1981. The isotopic composition of uranium and lead in Allende inclusions and meteoritic phosphates. *Earth and Planetary Science Letters,* 52, 1-15.

CHOUDENS-SÁNCHEZ, V. & GONZÁLEZ, L. 2009. Calcite and aragonite precipitation under controlled instantaneous super saturation: elucidating the role of $CaCO_3$ saturation state and Mg/Ca ratio on calcium carbonate polymorphism. *Journal of Sedimentary Petrology,* 79, 363-376.

CIESLA, F. J., LAURETTA, D. S., COHEN, B. A. & HOOD, L. L. 2003. A nebular origin for chondritic fine-grained phyllosilicates. *Science,* 299, 549-552.

CLAYTON, R. N. 1993. Oxygen isotopes in meteorites. *Annual Review of Earth and Planetary Sciences,* 21, 115-149.

CLAYTON, R. N. 2003. Oxygen Isotopes in Meteorites. *Treatise on Geochemistry*, 1, P129-142.

CLAYTON, R. N. & MAYEDA, T. K. 1984. The oxygen isotope record in Murchison and other carbonaceous chondrites. *Earth and planetary science letters,* 67, 151-161.

CLAYTON, R. N. & MAYEDA, T. K. 1999. Oxygen isotope studies of carbonaceous chondrites. *Geochimica et Cosmochimica Acta,* 63, 2089–2104.

CLAYTON, R. N., ONUMA, N., GROSSMAN, L. & MAYEDA, T. K. 1977. Distribution of the pre-solar component in Allende and other carbonaceous chondrites. *Earth and Planetary Science Letters,* 34, 209-224.

CORNELIS, K. & CORNELIUS, H. 1999. Manual of mineralogy, after Dana, J., New York, *Jhon Wiley & Sons, INC*, 681 p.

CORRIGAN, C. M., ZOLENSKY, M. E., DAHL, J., LONG, M., WEIR, J., SAPP, C. & BURKETT, P. J. 1997. The porosity and permeability of chondritic meteorites and interplanetary dust particles. *Meteoritics & Planetary Science,* 32, 509-515.

CUZZI, J. N. 2004. Blowing in the wind: III. Accretion of dust rims by chondrule-sized particles in a turbulent protoplanetary nebula. *Icarus,* 168, 484-497.

DAVIS, K. J., DOVE, P. M. & DE YOREO, J. J. 2000. The role of Mg^{2+} as an impurity in calcite growth. *Science,* 290, 1134-1137.

DE CHOUDENS-SÁNCHEZ, V. & GONZÁLEZ, L. 2009. Calcite and aragonite precipitation under controlled instantaneous super saturation: elucidating the role of $CaCO_3$ saturation state and Mg/Ca ratio on calcium carbonate polymorphism. *Journal of Sedimentary Petrology,* 79, 363-376.

DE LEUW, S., RUBIN, A. E., SCHMITT, A. K. & WASSON, J. T. 2009. ^{53}Mn--^{53}Cr systematics of carbonates in CM chondrites: Implications for the timing and duration of aqueous alteration. *Geochimica et Cosmochimica Acta,* 73, 7433-7442.

DE LEUW, S., RUBIN, A. E. & WASSON, J. T. 2006. Manganese-rich phases in CM chondrites: Mn-Cr systematics of carbonates and silicates. *Meteoritics & Planetary Science,* 41, A46.

DE LEUW, S., RUBIN, A. E. & WASSON, J. T. 2010. Carbonates in CM chondrites: Complex formational histories and comparison to carbonates in CI chondrites. *Meteoritics & Planetary Science,* 45, 513-530.

DELVIGNE, J., BISDOM, E. B., SLEEMAN, J. & STOOPS, G. 1979. Olivines, Their pseudomorphism and secondary products. *Pédologie,* 29, 247-309.

DINGLEY, D. 2000. The Development of Automated Diffraction in Scanning and Transmission Electron Microscopy. In: SCHWARTZ, A., KUMAR, M. & ADAMS, B. (eds.) Electron Bacscatter Diffraction in materials science. New York: *Kluwer Academic/ Plenum Publishers.* p. 1-30.

DRAKE, M. J. & RIGHTER, K. 2002. Determining the composition of the Earth. *Nature,* 419, 39-44.

EDWARDS, P. R. & MARTIN, R. W. 2011. Cathodoluminescence nano-characterization of semiconductors. *Semiconductor Science and Technology,* 26, no. 6.

EGERTON, R. 2005. Physical Principles of Electron Microscopy An Introduction to TEM, SEM, and AEM, New York, *Springer Science+Business Media, Inc.* 202 p.

ENDRESS, M. & BISCHOFF, A. 1996. Carbonates in CI chondrites: Clues to parent body evolution. *Geochimica et Cosmochimica Acta,* 60, 489-507.

ENDRESS, M., ZINNER, E. & BISCHOFF, A. 1996. Early aqueous activity on primitive meteorite parent bodies. *Nature,* 379, 701-703.

FERNANDEZ-DIAZ, L., PUTNIS, A., PRIETO, M. & PUTNIS, C. V. 1996. The role of magnesium in the crystallization of calcite and aragonite in a porous medium. *Journal of Sedimentary Research,* 66, 482-491.

FERRILL, D. A. 1991. Calcite twin widths and intensities as metamorphic indicators in natural low-temperature deformation of limestone. *Journal of Structural Geology,* 13, 667-675.

FERRILL, D. A., MORRIS, A. P., EVANS, M. A., BURKHARD, M., GROSHONG, R. H. & ONASCH, C. M. 2004. Calcite twin morphology: a low-temperature deformation geothermometer. *Journal of Structural Geology,* 26, 1521-1529.

FOLK, R. L. 1974. The natural history of crystalline calcium carbonate; effect of magnesium content and salinity. *Journal of Sedimentary Petrology,* 44, 40-53

FUCHS, L. H., OLSEN, E. & JENSEN, K. J. 1973. Mineralogy, Mineral-Chemistry, and Composition of the Murchison (C2) Meteorite. *Smithsonian Contributions to the Earth Sciences,* 10, 399.

FUJIYA, W., SUGIURA, N., HOTTA, H., ICHIMURA, K. & SANO, Y. 2012. Evidence for the late formation of hydrous asteroids from young meteoritic carbonates. *Nature Communications,* 3, 627.

FUJIYA, W., SUGIURA, N., ICHIMURA, K., TAKAHATA, N. & Y., S. 2010. Mn-Cr ages of carbonates in Murchison and ALH 83100 CM chondrites. *41st Lunar and Planetary Science Conference,* (abstract#1644).

GAETANI, G. A. & COHEN, A. L. 2006. Element partitioning during precipitation of aragonite from seawater: A framework for understanding paleoproxies. *Geochimica et Cosmochimica Acta,* 70, 4617–4634.

GOLDSTEIN, J., NEWBURY, D., JOY, D., LYMAN, C., ECHLIN, P., LIFSHIN, E., SAWYER, L. & MICHAEL, J. 2003. Scanning electron microscopy and X-Ray microanalysis. USA, *Springer Science plus business Media, Inc.* 689p.

GONZÁLEZ-CASADOA, J. M. & GARĆIA-CUEVASB, C. 1999. Calcite twins from micro veins as indicators of deformation history. *Journal of Structural Geology,* 21, 875–889.

GOPEL, C., MANHES, G. & ALLEGRE, C. J. 1994. U-Pb systematics of phosphates from equilibrated ordinary chondrites. *Earth and Planetary Science Letters,* 121, 153-171.

GOTZE, J. 2002. Potential of cathodoluminescence (CL) microscopy and spectroscopy for the analysis of minerals and materials. *Analytical and Bioanalytical Chemistry,* 374, 703-708.

GOUNELLE, M. & ZOLENSKY, M. E. 2001. A terrestrial origin for sulfate veins in CI1 chondrites. *Meteoritics & Planetary Science,* 36, 1321-1329.

GRADY, M. M., WRIGHT, I. P., SWART, P. K. & PILLINGER, C. T. 1988. The carbon and oxygen isotopic composition of meteoritic carbonates. *Geochimica et Cosmochimica Acta,* 52, Pages 2855–2866.

GRAHAM, A. L., BEVAN, A. W. & HUTCHISON, R. 1985. Catalogue of Meteorites, London, Arizona. , *British Museum (Natural History).*460 p.

GREENBERG, R. & CHAPMAN, C. R. 1983. Asteroids and meteorites: Parent bodies and delivered samples. *Icarus,* 55, Pages 455–481.

GREENWOOD, R. C., LEE, M. R., HUTCHISON, R. & BARBER, D. J. 1994. Formation and alteration of CAIs in Cold Bokkeveld (CM2). *Geochimica et Cosmochimica Acta,* 58, 1913-1935.

GRIMM, R. E. & MCSWEEN, H. Y. 1989. Water and the thermal evolution of carbonaceous chondrite parent bodies. *Meteoritics,* 24, 273-274.

GROSSMAN, J. N., ALEXANDER, C. M. O., WANG, J. H. & BREARLEY, A. J. 2000. Bleached chondrules: Evidence for widespread aqueous processes on the parent asteroids of ordinary chondrites. *Meteoritics & Planetary Science,* 35, 467-486.

GROSSMAN, J. N. & SCORE, R. 1996. Recently classified specimens in the United States Antarctic Meteorite Collection (1994-1996). *Meteoritics & Planetary Science,* 31, A161-A174.

GROSSMAN, L. & LARIMER, J. W. 1974. Early chemical history of the solar system. *Reviews of Geophysics*, 12, 71-101.

GROSSMAN, L. & STEELE, I. M. 1976. Amoeboid olivine aggregates in the Allende meteorite. *Geochimica et Cosmochimica Acta*, 40, 149–155.

GUO, W. & EILER, J. M. 2007. Temperatures of aqueous alteration and evidence for methane generation on the parent bodies of the CM chondrites. Geochimica *et Cosmochimica Acta,* 71, 5565-5575.

HABERMANN, D., NEUSER, R. D. & RICHTER, D. K. 1998. Low limit of Mn^{2+} - activated cathodoluminescence of calcite: state of the art. *Sedimentary Geology*, 116, 13-24.

HANOWSKI, N. P. & BREARLEY, A. J. 2000. Iron-rich aureoles in the CM carbonaceous chondrites, Murray, Murchison and ALH 81002: Evidence for in situ aqueous alteration. *Meteoritics&Planetary Science,* 35, 1291-1308.

HANOWSKI, N. P. & BREARLEY, A. J. 2001. Aqueous alteration of chondrules in the CM carbonaceous chondrite, Allan Hills 81002: Implications for parent body alteration. *Geochimica et Cosmochimica Acta,* 65, 495-518.

HAYASHI, C., NAKAZAMA, K. & NAKAGAWA, Y. 1985. Formation of the solar system. In: BLACK, D. C. & MATTHEWS, M. S. (eds.), Protostars and Planets II, Tucson, *University of Arizona Press,* 1100–1153.

HEANEY, P. J., VICENZI, E. P., GIANNUZZI, L. A. & LIVI, K. J. T. 2001. Focused ion beam milling: A method of site-specific sample extraction for microanalysis of Earth and planetary materials. *American Mineralogist,* 86, 1094-1099.

HÖVELMANN, J., AUSTRHEIM, H., BEINLICH, A. & MUNZ, I. 2011. Experimental study of the carbonation of partially serpentinized and weathered peridotites. *Geochimica et Cosmochimica Acta,* 75, 6760–6779.

HOWARD, K. T., BENEDIX, G. K., BLAND, P. A. & CRESSEY, G. 2009. Modal mineralogy of CM2 chondrites by X-ray diffraction (PSD-XRD). Part 1: Total phyllosilicate abundance and the degree of aqueous alteration. *Geochimica et Cosmochimica Acta,* 73, 4576-4589.

HOWARD, K. T., BENEDIX, G. K., BLAND, P. A. & CRESSEY, G. 2011. Modal mineralogy of CM chondrites by X-ray diffraction (PSD-XRD): Part 2. Degree, nature and settings of aqueous alteration. *Geochimica et Cosmochimica Acta,* 75, 2735-2751.

HUA, X., WANG, J. H., LI, J. & BUSECK, P. R. 1999. Evidence for both pre- and post-accretionary alteration in LEW90500. *30th Annual Lunar and Planetary Science Conference,* 1161.

HUTCHEON, I. D. & PHINNEY, D. L. 1996. Radiogenic 53Cr* in Orgueil carbonates: chronology of aqueous activity on the CI parent body. *Lunar and Planetary Science (XXVII),* 27, 577.

HUTCHEON, I. D., WEISBERG, M. K., PHINNEY, D. L., ZOLENSKY, M. E., PRINZ, M. & IVANOV, A. V. 1999. Radiogenic 53Cr in Kaidun Carbonates: Evidence for Very Early Aqueous Activity. *30th Annual Lunar and Planetary Science Conference,* abstract no. 1722.

HUTCHISON, R. 2004. Meteorites, New York, *Cambridge University Press*. 506 p.

IVANOV, B. & DEUTSCH, A. 2002. The phase diagram of CaCO3 in relation to shock compression and decomposition. *Physics of the Earth and Planetary Interiors*, 129, 131–143.

JOHNSON, C. A. & PRINZ, M. 1993. Carbonate compositions in CM and CI chondrites, and implications for aqueous alteration. *Geochimica et Cosmochimica Acta,* 57, 2843-2852.

JONES, C. E., BASU, S. & DUBINSKI, J. 2001. Intrinsic shapes of molecular cloud cores. *The Astrophysical Journal,* 551, 387-393.

JONES, R. H., LEE, T., CONNOLLY, J. H. C., LOVE, S. G. & SHANG, H. 2000. In: Mannings, V., Boss, A.P., Russell, S. S. (eds.), Formation of chondrules and CAIs: Theory VS. Observation. protostars and planets IV, Tucson*: University of Arizona Press*, p. 927.

JULL, A. J. T., CHENG, S., GOODING, J. L. & VELBEL, M. A. 1988. Rapid growth of magnesium-carbonate weathering products in a stony meteorite from Antarctica. *Science* 242, 417-419.

KASIOPTAS, A., PERDIKOURI, C., PUTNIS, C. V. & PUTNIS, A. 2008. Pseudomorphic replacement of single calcium carbonate crystals by polycrystalline apatite. *Mineralogical Magazine,* 72, 77-80.

KERRIDGE, J. F. & BUNCH, T. E. 1979. Aqueous activity on asteroids: Evidence from carbonaceous chondrites. In: Gehrels, T. (ed.), Asteroids. *Tucson, University of Arizona Press,* p745–764.

KIMURA, M., GROSSMAN, J. & WEISBERG, M. K. 2011. Fe-Ni metal and sulfide minerals in CM chondrites: An indicator for thermal history. *Mataoritics& Planetary Science 46*, 431-442.

KOJIMA, K. & YANAI, K. 1993. Evolution and alteration process of the CM carbonaceous chondrites. In: Oya, H. (ed.). Primitive solar nebula and origin of planets, Tokyo: Terra Scientific Publishing Company, 465-477.

KOKUBO, E. & IDA, S. 1996. On runaway growth of protoplanetesimals. *Icarus,* 123, 180-191.

KOKUBO, E. & IDA, S. 2000. Formation of protoplanets from planetesimals in the solar nebula. *Icarus,* 143, 15–27.

KRINSLEY, D., PYE, K., BOGGS, S. & TOVEY, N. K. 1998. Backscattered Scanning electron microscopy and image analysis of sediments and sedimentary rocks. Cambridge, New York, Melbourne, *Cambridge University Press*, 193P.

KROT, A., KEVIN, D., MCKEEGAN, L. A., LESHIN, L. A., MACPHERSON, G. J. & SCOTT, E. R. 2002. Existence of an ^{16}O-Rich Gaseous Reservoir in the Solar Nebula. *Science,* 295, 1051-1054.

KROT, A., PETAEVB, M., RUSSELL, S., ITOHC, S., FAGAND, T., YURIMOTO, H., CHIZMADIA, L., WEISBERG, M., KOMATSU, M., ULYANOV, A. & KEIL, K. 2004. Amoeboid olivine aggregates and related objects in carbonaceous chondrites: records of nebular and asteroid processes. *Chemie der Erde - Geochemistry*, 64, Pages 185–239.

KROT, A. N., AMELIN, Y., CASSEN, P. & MEIBOM, A. 2005. Young chondrules in CB chondrites from a giant impact in the early solar system. *Nature,* 436, 989-992.

KROT, A. N., KEIL, K., GOODRICH, C. A., SCOTT, E. R. & WEISBERG, M. K. 2007. Classification of meteorites. In: Meteorites, Comets and Planets, Chapter 1.05. *Treatise On Geochemistry,* 1-52.

KROT, A., BREARLEY, A. J., PETAEV, M., KALLEMEYN, G., SEARS, D. W., BENOIT, P., HUTCHEON, L., ZOLENSKY, M. & K EIL, K. 2000. Evidence for low-temperature growth of fayalite and hedenbergite in MacAlpine Hills 88107, an ungrouped carbonaceous chondrite related to the CM-CO clan. *Meteoritics & PIanetary Science,* 35, 1365-1386.

LANGE, M. A., LAMBERT, P. & AHRENS, T. J. 1985. SHOCK EFFECTS ON HYDROUS MINERALS AND IMPLICATIONS FOR CARBONACEOUS METEORITES. *Geochimica Et Cosmochimica Acta,* 49, 1715-1726.

LEE, M. R., BLAND, P. A. & GRAHAM, G. 2003. Preparation of TEM samples by focused ion beam (FIB) techniques: applications to the study of clays and phyllosilicates in meteorites. *Mineralogical Magazine,* 67, 581-592.

LEE, M., LINDGREN, P., SOFE, M., ALEXANDER, C. & WANG, J. 2012. Extended chronologies of aqueous alteration in the CM2 carbonaceous chondrites: evidence from carbonates in Queen Alexandra Range 93005. *Geochimica et Cosmochimica Acta,* 92**,** 148-169.

LEE**,** M. R. 2000. Imaging of calcite by optical and SEM cathodoluminescence: Microscopy and Analysis 70**,** 15-16.

LEE, M. R. 2010. Transmission electron microscopy (TEM) of earth and planetary materials: a review. *Mineralogical Magazine,* 74 (1), 1-27.

LEE, M. R. & ELLEN, R. 2008. Aragonite in the Murray (CM2) carbonaceous chondrite: Implications for parent body compaction and aqueous alteration. *Meteoritics&Planetary Science,* 43**,** 1219-1231.

LEE, M. R., SOFE, M. & LINDGREN, P. 2011. Evolution of Carbonate Mineralization in the CM2 Carbonaceous Chondrites. *42nd Lunar and Planetary Science Conference***,** 1710.

LEE, M. R. 1993. The petrography, mineralogy and origins of calcium-sulfate within the Cold Bokkeveld cm carbonaceous chondrite. *Meteoritics,* 28**,** 53-62.

LEE, M. R. & BLAND, P. A. 2004. Mechanisms of weathering of meteorites recovered from hot and cold deserts and the formation of phyllosilicates. *Geochimica et Cosmochimica Acta,* 68**,** 893-916.

LEE, M., R., BROWN, D. J., SMITH, C. L., HODSON, M. E., MACKENZIE, M. & HELLMANN, R. 2007. Characterization of mineral surfaces using FIB and TEM: A case study of naturally weathered alkali feldspars. *American Mineralogist,* 92**,** 1383-1394.

LEE, M. R. & HARWOOD, G. M. 1989. Dolomite calcitization and cement zonation related to uplift of the Raisby formation (Zechstein carbonate), Northeast England. *Sedimentary Geology,* 65**,** 285-305.

LEE, M. R., MARTIN, R. W., TRAGER-COWAN, C. & EDWARDS, P. R. 2005. Imaging of cathodoluminescence zoning in calcite by scanning electron microscopy and hyperspectral mapping. *Journal of Sedimentary Research,* 75**,** 313-322.

LENART, A., JERŠEK, M.,MIRTIC, B. & ŠTURM, S. 2010. Meteorite Jesenice: Mineral and chemical composition of the fusion crust of ordinary chondrite. *GEOLOGIJA,* 53/2, 139-146.

LEVISON, H. F., DUNCAN, M. J., ZAHNLE, K., HOLMAN, M. & DONES, L. 2000. Planetary impact rates from ecliptic comets. *Icarus,* 143**,** 415-420.

LINDGREN, P., LEE, M. R. & SOFE, M. 2012. Evidence for multiple fluid pulses in the CM1 carbonaceous chondrite parent body. *43rd Lunar and Planetary Science Conference,* (1949).

LINDGREN, P., LEE, M. R., SOFE, M. & BURCHELL, M. 2010. Microstructures of a calcite vein in LON 94101: Evidence for asteroidal fluid flow? *Meteoritics & Planetary Science,* 45**,** A119.

LINDGREN, P., LEE, M. R., SOFE, M. & BURCHELL, M. J. 2011a. Microstructure of calcite in the CM2 carbonaceous chondrite LON 94101: Implications for deformation history during and/or after aqueous alteration. *Earth and Planetary Science Letters,* 306**,** 289-298.

LINDGREN, P., LEE, M. R., SOFE, M. & ZOLENSKY, M. E. 2011b. Xenoliths in the CM2 carbonaceous chondrite LON 94101: implications for complex mixing on the asteroidal parent body. *42nd Lunar and Planetary Science Conference*, 1608, p.1349.

LIPSCHUTZ, M. E., GAFFEY, M. J. & PELLAS, P. 1989. Meteoritc Parent bodies, nature, number, size and relation to present-day asteroids In: Binzel R.P., Gehrels R. & Matthews M.S. (eds.), Asteroids II. Tucson: *University of Arizona Press,* p. 740-777.

LUGMAIR, G. W. & GALER, S. J. G. 1992. Age and isotopic relationships among the angrites Lewis Cliff-86010 and Angra-dos-Reis. *Geochimica et Cosmochimica Acta,* 56**,** 1673-1694.

MACDOUGALL, J. D., LUGMAIR, G. W. & KERRIDGE, J. F. 1984. Early solar-system aqueous activity - SR isotope evidence from the Orgueil CI meteorite. *Nature,* 307, 249-251.

MACKINNON, I. D. R. & ZOLENSKY, M. E. 1984. Proposed structures for poorly characterized phases in C2M carbonaceous chondrite meteorites. *Nature*, 309, 240-242.

MACPHERSON, G. J. 2007. Calcium–Aluminum-Rich Inclusions in Chondritic Meteorites. In: Meteorites, Comets and Planets, Chapter 1.08, *Treatise on Geochemistry*, 1, p. 1–47.

MACPHERSON, G. J., WARK, D. A. & ARMSTRONG, J. T. 1988. Primitive material surviving in chondrites - Refractory inclusions. In: IN: Kerridge, J. & Matthews, M. (eds.), Meteorites and the early solar system. Tucson, *University of Arizona Press,* p. 746-807.

MAITLAND, T. & SITZMAN, S. 2006. Electron Backscatter Diffraction (EBSD) Technique and Materials Characterization Examples In: ZHOU, W. & WANG., Z. L. (eds.) Scanning Microscopy for Nanotechnology: Techniques and Applications. New York, *Springer science plus Business media, LLC*, p. 41-75.

MALIVA, R. G. & SIEVER, R. 1988. Diagenetic replacement controlled by force of crystallization. *Geology,* 16, 688-691.

MARSHALL, D. J. 1988. Cathodoluminescence of Geological Materials. Boston: *Unwin Hyman,* p76-146.

MCGEE, J. J. & KEIL, K. 2001. Application of electron probe microanalysis to the study of geological and planetary materials. *Microscopy and Microanalysis,* 7, 200-210.

MCKEEGAN, K. D. & DAVIS, A. M. 2007. Early Solar System Chronology. *Treatise on Geochemistry,* 1, 1-38.

MCSWEEN, H. 1987. Aqueous alteration in carbonaceous chondrites: Mass balance constraints on matrix mineralogy. *Geochimica et Cosmochimica Acta,* 51, 2469-2477.

MCSWEEN, H. Y. 1979. Alteration in CM carbonaceous chondrites inferred from modal and chemical variations in matrix. *Geochimica et Cosmochimica Acta,* 43, 1761-1765, 1767-1770

MCSWEEN, H. Y. 1999. Meteorites and Their Parent Planets, New York, *Cambridge University press,* 310 p.

MCSWEEN, H. Y. & RICHARDSON, S. M. 1977. Composition of carbonaceous chondrite matrix. *Geochimica et Cosmochimica Acta,* 41, 1145-1161.

METZLER, K., BISCHOFF, A. & STÖFFLER, D. 1992. Accretionary dust mantles in CM chondrites: evidence for solar nebula processes. *Geochimica et Cosmochimica Acta,* 56, 2873-2897.

MILLER, M. F., FRANCHI, I. A., THIEMENS, M. H., JACKSON, T. L., BRACK, A., KURAT, G. & PILLINGER, C. T. 2002. Mass-independent fractionation of oxygen isotopes during thermal decomposition of carbonates. *Proceedings of the National Academy of Sciences of the United States of America,* 99, 10988-10993.

MORFILL, G. E., DURISEN, R. H. & TURNER, G. W. 1998. An accretion rim constraint on chondrule formation theories. *Icarus,* 134, 180-184.

MORLOK, A., BISCHOFF, A., STEPHAN, T., FLOSS, C., ZINNER, E. & JESSBERGER, E. 2006. Brecciation and chemical heterogeneities of CI chondrites. *Geochimica et Cosmochimica Acta,* 70, 5371–5394.

MORSE, J. W., WANG, Q. & TSIO, M. Y. 1997. Influences of temperature and Mg:Ca ratio on $CaCO_3$ precipitates from seawater. *Geology,* 25, 85-87.

MÜLLER, W. F., KURAT, G. & KRACHER, A. 1979. Chemical and crystallographic study of cronstedtite in the matrix of the Cochabamba (CM2) carbonaceous chondrite. *Mineralogy and Petrology,* 26, 293-304.

NADER, F. H., SWENNEN, R. & KEPPENS, E. 2008. Calcitization/dedolomitization of Jurassic dolostones (Lebanon): Results from petrographic and sequential geochemical analyses. *Sedimentology,* 55, 1467-1485.

NAGY, B., HENNESSY, D. J. & MEINSCHEIN, W. G. 1963. Aqueous, low temperature environment of Orgueil meteorite parent body. *Annals of the New York Academy of Sciences,* 108, 534-552.

NAIK, S. S. & NAIDU, P. D. 2008. Possible factors that control calcite dissolution in the western tropical Indian Ocean. *Current Science,* 95, 22-23.

NAKAMURA, T., NOGUCHI, T., ZOLENSKY, M. E. & TANAKA, M. 2003. Mineralogy and noble-gas signatures of the carbonate-rich lithology of the Tagish Lake carbonaceous chondrite: evidence for an accretionary breccia. *Earth and planetary science letters,* 207, 83-101.

NISHIMURA, Y., HIRAWAKA, A. & TSUBOI, M. 1995. Resonance Raman spectroscopy of nucleic acids. Adv. Infrared Raman Spectroscopy. In: POTTS, P. J.,

BOWLES, W., REED, B. & CAVE, R. (eds.) Microprobe techniques in the Earth Sciences. London, *Chapman & Hall.*

NORTON, O. R. 2002. Meteorites. Cambridge, *Cambridge University Press,* 354 p.

PACHECO, F. A. L. & SZOCS, F. 2006. ‘‘Dedolomitization reactions’’ driven by anthropogenic activity on loessy sediments, SW Hungary. *Applied Geochemistry,* 21. 614–631.

PALGUTA, J., SCHUBERT, G. & TRAVIS, B. J. 2010. Fluid flow and chemical alteration in carbonaceous chondrite parent bodies. *Earth and Planetary Science Letters*, 296, 235-243.

PRIOR, G. T. 1916. On the genetic relationship and classification of meteorites. *The mineralogical Magazine,* 18, 26-44.

PUTNIS, A. 2002. Mineral replacement reactions: from macroscopic observations to microscopic mechanisms. *Mineralogical Magazine,* 66, 689-708.

PUTNIS, C. V., TSUKAMOTO, K. & NISHIMURA, Y. 2005. Direct observations of pseudomorphism: compositional and textural evolution at a fluid-solid interface. *American Mineralogist,* 90, 1909-1912.

RAMAN, C. V. & KRISHNAN, K. S. 1928. A new type of secondary radiation. *Nature,* 121, 501-502.

RAYMOND, S. N. 2010. Formation of Terrestrial Planets. In: Barnes R. (ed.), Formation and Evolution of Exoplanets, *Wiley-VCH Verlag GmbH & Co. KGaA*, Weinheim, Germany. On line: 10.1002/9783527629763.ch6

RAYMOND, S. N., QUINN, T. & LUNINE, J. I. 2006. High-resolution simulations of the final assembly of Earth-like planets I. Terrestrial accretion and dynamics. *Icarus,* 183, 265-282.

REED, S. J. 2005. Electron Microprobe Analysis and Scanning Electron Microscopy in Geology, New York, *Cambridge University Press,* 189p.

REIMOLD, W. U., BUCHANAN, P. C., AMBROSE, D., KOEBERL, C., FRANCHI, I., LALKHAN, C., SCHULTZ, L., FRANKE, L. & HEUSSER, G. 2004. Thuathe, a new H4/5 chondrite from Lesotho: History of the fall, petrography, and geochemistry. *Meteoritics & Planetary Science,* 39, 1321-1341.

RENISHAW, P. 2006. *Raman user's Manual* UK.

RICHARDSON, S. M. 1978. VEIN FORMATION IN THE C1 CARBONACEOUS CHONDRITES. *Meteoritics & Planetary Science,* 13, 141-159.

RICIPUTI, L. R., MCSWEEN, H. Y., JOHNSON, C. A. & PRINZ, M. 1994. Minor and trace-element concentrations in carbonates of carbonaceous chondrites, and implications for the compositions of coexisting fluids. *Geochimica et Cosmochimica Acta,* 58, 1343-1351.ROBERTS, S. & BEATTIE, I. 1995. Micro-Raman spectroscopy in the Earth Sciences. In: POTTS, P. J., BOWLES, W., REED, B. & CAVE, R. (eds.) Microprobe techniques in the Earth Sciences. London, *Chapman&Hall*, p. 386.

ROWE, K. J. & RUTTER, E. H. 1990. Palaeostress estimation using calcite twinning: experimental calibration and application to nature. *Structural Geology,* 12, 1–17.

ROWE, M. W., CLAYTON, R. N. & MAYEDA, T. K. 1994. Oxygen isotopes in separated components of CI and CM meteorites. *Geochimica et Cosmochimica Acta,* 58, 5341-5347.

RUBIN, A. E. 2012. Collisional facilitation of aqueous alteration of CM and CV carbonaceous chondrites. *Geochimica et Cosmochimica Acta,* 90, 181-194.

RUBIN, A. E., TRIGO-RODRIGUEZ, J. M., HUBER, H. & WASSON, J. T. 2007. Progressive aqueous alteration of CM carbonaceous chondrites. *Geochimica et Cosmochimica Acta,* 71, 2361-2382.

SAYLOR, J., ZOLENSKY, M., BODNAR, R., LE, L. & SCHWANDT, C. 2001. Fluid Inclusions in Carbonaceous Chondrites. *32nd Annual Lunar and Planetary Science Conference,* (abstract 1875).

SCOTT, E. R. D., BARBER, D. J., ALEXANDER, C. M., HUTCHINSON, R. & PECK, J. A. 1988. Primitive material surviving in chondrites - Matrix. In: Meteorites and the early solar system. Tucson, *University of Arizona Press,* 1988, p. 718-745.

SCOTT, E. R. D. & KROT., A. N. 2007. Chondrites and Their Components. In: Meteorites, Comets and Planets, *Treatise on Geochemistry*, Chapter 1.07, 1, 1-72.

SHEARER, C. K., PAPIKE, J. J. & RIETMEIJER, F. J. 1998. The Planetary Sample Suite and environment of origin. In: PAPIKE, J. (ed.) Planetary Materials, *Mineralogical Society of America*, 36, p. 1-24.

SJÖBERG, E. L. & RICKARD, D. T. 1984. Calcite dissolution kinetics: Surface speciation and the origin of the variable pH dependence. *Chemical Geology*, 42, 136-119.

SMITH, J. W. & KAPLAN, I. R. 1970. Endogenous carbon in carbonaceous meteorites. *Science,* 167, 1367-1370.

SMITH, W. E. & DENT, G. 2005. Modern Raman Spectroscopy – A practical approach. *John Wiley & Sons, Ltd*. Online: http://pirg.ch.pw.edu.pl/instrukcje/raman_ftir2-instr.pdf

SOFE, M., LEE, M. R., LINDGREN, P. & SMITH, C. L. 2011a. CL zoning of calcite in CM carbonaceous chondrites and its relationship to degree of aqueous alteration. *Meteoritics & Planetary Science*, 46, A218.

SOFE, M., LINDGREN, P. & LEE, M. 2010a. Do calcite veins in Antarctic CM2 carbonaceous chondrites indicate asteroidal fluid flow?, *Abstract IMA 2010 Conference, Budapest*.

SOFE, M. R., LEE, M. R. & LINDGREN, P. 2011b. Aragonite in the CM carbonaceous chondrites: a proxy for the magnitude of aqueous alteration. *Meteoritics & Planetary Science,* 46, A217.

SOFE, M. R., LEE, M. R. & SMITH, C. L. 2010b. Mg-phyllosilicate pseudomorphs after calcite in the Pollen (CM2) carbonaceous chondrite: new insights into aqueous alteration. *Meteoritics & Planetary Science,* 45, A193.

SPURNÝ, P., OBERST, J. & HEINLEIN, D. 2003. Photographic observations of Neuschwanstein, a second meteorite from the orbit of the Príbram chondrite. *Nature,* 423, 151-153

STADERMANN, F. J., WALKER, R. M. & ZINNER, E. 1999. Nanosims: The next generation ion probe for the microanalysis of extraterrestrial material. *Meteoritics & Planetary Science,* 34, A111-A112.

SUGIURA, N., BRAR, N. S., STRANGWAY, D. W. & MATSUI, T. 1984. Degassing of meteorite parent bodies. *Journal of Geophysical Research*, 89, B641–B644.

TAO, X. & EADES, A. 2002. Alternatives to Image Quality (IQ) Mapping in EBSD. *Microscopy and Microanalysis,* 8, 692-693.

THIEL, B. L., TOTH, M. & CRAVEN, J. P. 2004. Charging processes in low vacuum Scanning Electron Microscopy. *Microscopy and Microanalysis,* 10, 711-720.

THOMSON, G. P. 1927 Diffraction of cathode rays by thin films of platinum. *Nature,* 120, 802-802

TOMEOKA, K. & BUSECK, P. R. 1985. Indicators of aqueous alteration in CM carbonaceous chondrites - microtextures of a layered mineral containing Fe, S, O and Ni. *Geochimica et Cosmochimica Acta*, 49, 2149-2163.

TOMEOKA, K., MCSWEEN, H. Y. & BUSEC, P. R. 1989. Mineralogical alteration of CM chondrites: *A review. Thirteenth Symposium on Antarctic Meteorites*, 2, 221-234.

TOMEOKA, K. & TANIMURA, I. 2000. Phyllosilicate-rich chondrule rims in the vigarano CV3 chondrite: evidence for parent-body processes. *Geochimica et Cosmochimica Acta,* 64, 1971–1988.

TRIGO-RODRIGUEZ, J. M., RUBIN, A. & WASSON, J. T. 2006. Non-nebular origin of dark mantles around chondrules and inclusions in CM chondrites. *Geochimica Et Cosmochimica Acta,* 70, 1271-1290.

TYRA, M. A., BREARLEY, A. J., HUTCHEON, I. D., RAMON, E., MATZEL, J. & WEBER, P. 2009. Carbonate Formation Timescales Vary Between CM1 Chondrites

ALH84051 and ALH84034. *40th Lunar and Planetary Science Conference,* (Lunar and Planetary Science XL). Abstract: 2474.

TYRA, M. A., FARQUHAR, J., WING, B. A., BENEDIX, G. K., JULL, A. J. T., JACKSON, T. & THIEMENS, M. H. 2007. Terrestrial alteration of carbonate in a suite of Antarctic CM chondrites: Evidence from oxygen and carbon isotopes. *Geochimica Et Cosmochimica Acta,* 71, 782-795.

TYRA, M. A., FARQUHAR, J., GUANC, Y. & LESHIND, L. A. 2012. An oxygen isotope dichotomy in CM2 chondritic carbonates—A SIMS approach. *Geochimica et Cosmochimica Acta,* 77, Pages 383–395.

VAN SCHMUS, W. R. & WOOD, J. A. 1967. A chemicaletrologic classification for the chondritic meteorites. *Geochimica et Cosmochimica Acta,* 31, 747–754.

VDOVYKIN, G. P. 1973. The Mighei meteorite. *Space Science Reviews*, 14, 832-879

VELBEL, M. A., TONUI, E. K. & ZOLENSKY, M. E. 2012. Replacement of olivine by serpentine in the carbonaceous chondrite Nogoya (CM2). *Geochimica et Cosmochimica Acta,* 87, 117-135.

VELBEL, M. A., TONUI, E. K. & ZOLENSKY, M. E. 2005. Aqueous Alteration in QUE 93005 (CM2): Different Alteration Scales For Antarctic and Non-Antarctic CM Chondrites?, *68th Annual Meteoritical Society Meeting,* 5191.

VENABLES, J. A. & HARLAND, C. J. 1973. Electron back-scattering patterns - a new technique for obtaining crystallographic information in the scanning electron microscope. *Philosophical Magazine,* 27, 1193-1200.

VICENZI, E. P. & HEANEY, J. 1999. Examining Martian alteration products using In Situ TEM Sectioning: A Novel Application of the Focused Ion Beam (FIB) for the Study of Extraterrestrial Materials. *30th Lunar and Planetary Science Conference.* 2005.

VOUTOU, B. & STEFANAKI, E. 2008. Electron Microscopy: The Basics. www.mansic.eu/documents/PAM1/Giannakopoulos1.pdf [Accessed 2012].

WADHWA, M. & RUSSELL, S. S. 2000. Timescales of accretion and differentiation in the early solar system: the meteoritic evidence. In Protostars and Planets IV, Tucson: *University of Arizona Press,* P. 995.

WALKER, T. R. 1957. Frosting of quartz grains by carbonate replacement. *Geological Society of America Bulletin,* 68, 267-268

WASSON, J. T. & RUBIN, A. E. 2009. Composition of matrix in the CR chondrite LAP 02342. *Geochimica et Cosmochimica Acta,* 73, 1436-1460.

WASYLENKI, L. E., DOVE, P. M. & DE YOREO, J. J. 2005. Effects of temperature and transport conditions on calcite growth in the presence of Mg^{2+}: Implications for paleothermometry. Geochimica et Cosmochimica Acta, 69, 4227-4236.

WEIDENSCHILLING, S. J. 1977. The distribution of mass in the planetary system and Solar Nebula. *Astrophysics and Space Science,* 51, p. 153-158.

WEISBERG, M. K., MCCOY, T. J. & KROT, A. N. 2006. Systematics and evaluation of meteorite classification. Tucson: *University of Arizona Press,* 943 pp., p.19-52.

WETHERILL, G. W. 1996. The formation and habitability of extra-solar planets. *Icarus,* 119, 219-238.

WHITE, S. N. 2009. Laser Raman spectroscopy as a technique for identification of seafloor hydrothermal and cold seep minerals. *Chemical Geology,* 259, 240-252.

WICKS, F. J. & WHITTAKER, E. J. W. 1977. Serpentine textures and serpentinization. *The Canadian Mineralogist,* 15, 459-488.

WIIK, H. B. 1956. The chemical composition of some stony meteorites. *Geochimica et Cosmochimica Acta* 9, 279– 289.

WIJNGAARDEN, J. V. 2005. Cathodoluminescence Imaging Spectroscopy on Plasmonic Structures, Research project for the Masters degree in Experimental Physics, *Utrecht University Issue.* 47p.

WILLIAMS, C. & CARTER, B. 2009. Transmission electron microscopy: a textbook for materials science, New York, *Springer Science plus business Media, Inc.* part I, 191 p.

WLOTZKA, F. 1990. Meteoritical Bulletin. *Meteoritics,* 25, 237-239.

WLOTZKA, F. 1993. A weathering scale for the Ordinary chondrites. *Meteoritics,* 28, 460.

WLOTZKA, F., SPETTEL, B., PALME, H. & SCHULTZ, L. 1989 Two new CM chondrites from Antarctica: Different mineralogy, but same chemistry. *Meteoritics,* 24 341-342.

WOGELIUS, R. A. & WALTHER, J. V. 1991. Olivine dissolution at 25°C: effects of pH, CO_2, and organic acids. *Geochimica et Cosmochimica Acta,* 55, 943–954.

WOLFF, F. C. 1963. THE POLLEN METEORITE, A Norwegian carbonaceous chondrite. *Geochimica et Cosmochimica Acta,* 27, 979-979.

WOOD, J. A. 1967. Olivine and pyroxene compositions in type II carbonaceous chondrites. Geochimica et Cosmochimica Acta, vol. 31, pp.2095-2108.

WOOD, J. A. 2004. Formation of chondritic refractory inclusions: The astrophysical setting. *Geochimica et Cosmochimica Acta,* 68, Pages 4007–4021

XIA, F., BRUGGER, J., CHEN, G. R., NGOTHAI, Y., O'NEILL, B., PUTNIS, A. & PRING, A. 2009. Mechanism and kinetics of pseudomorphic mineral replacement reactions: A case study of the replacement of pentlandite by violarite. *Geochimica et Cosmochimica Acta,* 73, 1945-1969.

YOSHIOKA, S., OHDE, S., KITANO, Y. & KANAMORI, N. 1986. Behavior of magnesium and strontium during the transformation of coral aragonite to calcite in aquatic environments. *Marine Chemistry,* 18, 35-48.

YOUNG, E. D. 2001. The hydrology of carbonaceous chondrite parent bodies and the evolution of planet progenitors. *Philosophical Transactions of the Royal Society of London Series a-Mathematical Physical and Engineering Sciences,* 359, 2095-2109.

YOUNG, E. D., ASH, R. D., ENGLAND, P. & RUMBLE, D. 1999. Fluid flow in chondritic parent bodies: Deciphering the compositions of planetesimals. *Science,* 286, 1331-1335.

YOUNG, E. D. & RUSSELL, S. S. 1998. Oxygen reservoirs in the early solar nebula inferred from an Allende CAI. *Science,* 282, 452-455.

YOUNG, E. D., ZHANG, K. K. & SCHUBERT, G. 2003. Conditions for pore water convection within carbonaceous chondrite parent bodies - implications for planetesimal size and heat production. *Earth and Planetary Science Letters,* 213, 249-259.

ZEGA, T. J. & BUSECK, P. R. 2003. Fine-grained-rim mineralogy of the Cold Bokkeveld CM chondrite. *Geochimica et Cosmochimica Acta,* 67, 1711-1721.

ZOLENSKY, M., BARRETT, R. & BROWNING, L. 1993. Mineralogy and composition of matrix and chondrule rims in carbonaceous chondrites. *Geochimica et Cosmochimica Acta,* 57, 3123-3148.

ZOLENSKY, M. & BODNAR, R. J. 1982. Identification of fluid inclusion daughter minerals using Gandolfi X-ray techniques. *American Mineralogist,* 67, 37-141.

ZOLENSKY, M. & MCSWEEN, H. Y. 1988. Aqueous Alteration. In: J. F. Kerridge and M. S. Matthews (ed.), Meteorites and the early solar system. Tucson, *University of Arizona Press,* 114-143

ZOLENSKY, M. E., BODNAR, R. J., GIBSON, E. K., NYQUIST, L. E., REESE, Y., SHIH, C. Y. & WIESMANN, H. 1999. Asteroidal water within fluid inclusion-bearing halite in an H5 chondrite, Monahans (1998). *Science,* 285, 1377-1379.

ZOLENSKY, M. E., BOURCIER, W. L. & GOODING, J. L. 1989. Aqueous alteration on the hydrous asteroids - results of EQ3/6 computer-simulations. *Icarus,* 78, 411-425.

ZOLENSKY, M. E., MITTLEFEHLDT, D. W., LIPSCHUTZ, M. E., WANG, M. S., CLAYTON, R. N., MAYEDA, T. K., GRADY, M. M., PILLINGER, C. & BARBER, D. 1997. CM chondrites exhibit the complete petrologic range from type 2 to 1. *Geochimica et Cosmochimica Acta,* 61, 5099-5115.

ZOLENSKY, M. E. & THOMAS, K. L. 1995. Iron and iron-nickel sulfides in chondritic interplanetary dust particles. *Geochimica et Cosmochimica Acta,* 59, 4707-4712.

On line sources:

DANILEWSKY, A. Analytics with Scanning Electron Microscopy [Online]. http://www.krist.uni-freiburg.de/studium/Praktikum/EDX_EBSD_MSc_engl.pdf. [Accessed 2012].

Historic Meteorites.com, Image of Murray fragment [Online]. www.historicmeteorites.com/HistoricMeteorites/M-Murray.html [Accessed 2012].

HORIBA scientific [Online]. http://www.horiba.com/fr/scientific/products/raman-spectroscopy/tutorial-faqs/raman-faqs/what-is-raman-spectroscopy/ [Accessed 2012].

JAC C:\IP\DOC\SIMS4.DOC [Online]. www.geos.ed.ac.uk/facilities/ionprobe/SIMS4.pdf [Accessed 2012].

The Laboratory of Meteoritics, Image of Mighei fragment [Online]. www.meteorites.ru/menu/description-e/mighei-e.html [Accessed 2012].

Meteoritical Bulletin Database, Image of EET 96029 fragment [Online].www.lpi.usra.edu/meteor/metbull.php?code=9623 [Accessed 2012].

Meteoritical Bulletin database, Image of Cold Bokkeveld fragment [Online]. http://www.lpi.usra.edu/meteor/metbull.php?code=5397 [Accessed 2012].

Meteoritical Bulletin database, Image of LAP 031166 fragment [Online]. http://www.lpi.usra.edu/meteor/metbull.php?code=35812 [Accessed 2012].

Meteoritical Bulletin Database, Image of LON 94101 fragment [Online]. http://curator.jsc.nasa.gov/antmet/amn/amnaug95/petdes.htm [Accessed 2012].

Meteoritical Bulletin database, Queen Alexandra Range 93005 [Online]. http://www.lpi.usra.edu/meteor/metbull.php?code=19094 [Accessed 2012].

Meteoritical Bulletin database, Image of SCO 06043 fragment [Online]. http://www.lpi.usra.edu/meteor/metbull.php?code=46404 [Accessed 2012].

Appendices

Appendix A

A.1 List of chemical analyses of the Murray matrix

Sigma: chondrule rims	Na_2O	MgO	Al_2O_3	SiO_2	P_2O_5	SO_2	K_2O	CaO	TiO_2	Cr_2O_3	MnO	FeO	NiO	Total
1	0.31	13.12	2.58	25.24	0.69	3.74	0.08	1.04	0.05	0.42	0.33	28.70	2.82	79.11
2	0.36	11.74	2.84	23.00	0.52	2.90	0.04	0.98	0.14	0.30	0.22	35.70	1.68	80.44
3	0.24	12.49	3.62	24.51	0.92	6.50	0.08	1.55	0.02	0.28	0.25	32.57	2.30	85.32
4	0.22	13.50	3.03	23.95	0.41	4.55	0.07	0.75	0.16	0.32	0.23	31.89	2.21	81.30
5	0.30	11.67	3.79	23.74	0.20	2.91	0.03	0.38	0.03	0.52	0.12	38.27	1.80	83.74
6	0.36	9.99	2.88	21.30	0.16	5.43	0.01	0.54	0.02	0.60	0.34	41.27	2.28	85.17
7	0.27	14.54	2.21	27.16	0.25	3.28	0.03	0.58	0.09	1.06	0.24	24.88	2.63	77.21
8	0.35	13.62	2.57	26.40	0.21	1.69	0.00	0.44	0.08	0.41	0.11	34.38	1.72	81.98
9	0.12	12.21	2.99	22.71	0.27	4.20	0.11	0.60	0.10	0.38	0.27	33.98	2.61	80.55
10	0.13	12.21	2.47	22.59	0.26	4.59	0.10	0.48	0.05	0.40	0.19	32.41	2.31	78.18
11	0.13	12.57	2.61	22.75	0.23	4.25	0.05	0.47	0.09	0.40	0.11	24.05	2.85	70.57
12	0.18	13.95	2.83	26.11	0.16	4.31	0.08	0.57	0.04	0.53	0.16	24.47	2.69	76.07
13	0.08	11.02	2.22	22.83	0.09	4.73	0.06	0.59	0.18	0.37	0.14	26.12	2.81	71.24
14	0.09	14.86	3.22	26.31	0.21	4.52	0.06	0.57	0.00	0.47	0.24	25.77	2.70	78.96
15	0.34	10.31	2.58	23.42	0.18	0.59	0.03	0.27	0.03	0.35	0.20	40.81	1.31	80.41
16	0.19	12.97	2.54	24.81	0.31	1.62	0.07	0.47	0.12	0.44	0.29	28.56	1.78	74.17
17	0.27	9.56	2.17	21.21	0.25	0.97	0.02	0.49	0.00	0.38	0.21	41.53	1.40	78.45
18	0.22	12.36	2.45	24.49	0.34	1.52	0.09	0.49	0.04	0.48	0.22	32.06	2.12	76.88
19	0.26	12.01	3.01	23.90	0.40	2.85	0.05	0.57	0.16	0.46	0.17	32.47	2.49	78.80
20	0.32	12.57	2.73	23.90	0.32	5.16	0.10	0.86	0.07	1.08	0.22	32.34	2.44	82.12
21	0.31	12.40	2.93	21.54	0.52	4.91	0.06	1.23	0.05	0.34	0.32	27.08	1.89	73.58
22	0.20	12.22	2.59	22.43	0.24	5.12	0.03	0.54	0.08	0.42	0.23	27.44	2.20	73.75
23	0.37	15.44	2.65	25.21	1.83	6.10	0.06	2.53	0.07	0.42	0.17	27.20	2.17	84.22

24	0.21	8.54	2.81	17.96	0.13	6.89	0.09	0.67	0.06	0.33	0.17	41.62	1.86	81.33
25	0.31	12.61	2.79	24.08	0.09	2.82	0.05	0.35	0.09	0.38	0.23	34.82	1.45	80.05
26	0.24	12.80	2.81	23.84	0.16	2.34	0.00	0.36	0.10	0.44	0.23	32.31	1.40	77.01
27	0.39	10.45	5.60	27.44	0.02	0.50	0.04	2.51	0.23	0.34	0.38	39.01	0.16	87.07
28	0.28	12.49	2.93	23.48	0.21	2.55	0.07	0.30	0.04	0.40	0.14	33.59	1.60	78.08
29	0.29	8.22	5.82	24.12	0.05	0.33	0.06	0.91	0.11	0.19	0.26	42.34	0.10	82.80
30	0.31	12.09	2.84	23.97	0.14	1.67	0.04	0.42	0.08	0.52	0.27	32.25	1.76	76.37
Average	0.25	12.15	2.97	23.81	0.33	3.45	0.05	0.75	0.08	0.45	0.22	32.66	1.98	--
Standard deviation	0.09	1.68	0.83	1.94	0.34	1.83	0.03	0.56	0.06	0.19	0.07	5.57	0.69	--
Sigma: Fine-grained matrix	**Na_2O**	**MgO**	**Al_2O_3**	**SiO_2**	**P_2O_5**	**SO_2**	**K_2O**	**CaO**	**TiO_2**	**Cr_2O_3**	**MnO**	**FeO**	**NiO**	**Total**
1	0.15	13.74	2.23	25.40	0.56	0.98	0.02	0.65	0.08	0.41	0.13	32.22	0.85	77.42
2	0.35	13.52	2.71	25.54	0.25	1.39	0.11	0.74	0.10	0.26	0.25	35.20	1.07	81.48
3	0.33	13.75	2.30	25.70	0.31	3.46	0.08	0.51	0.06	0.42	0.20	28.33	2.28	77.73
4	0.37	11.03	3.92	21.15	0.20	9.06	0.13	0.56	0.02	0.33	0.10	37.29	2.38	86.53
5	0.26	13.39	2.65	24.97	0.15	2.21	0.01	0.50	0.07	0.29	0.20	32.13	1.71	78.53
6	0.23	10.14	2.75	21.43	0.40	3.42	0.07	0.90	0.09	0.43	0.09	36.14	1.77	77.83
7	0.34	14.90	3.12	26.04	0.25	6.16	0.11	0.58	0.00	0.37	0.20	29.38	2.20	83.62
8	0.34	12.26	4.39	23.57	0.16	6.42	0.18	0.60	0.09	0.18	0.17	32.88	2.17	83.40
9	0.28	11.88	2.91	22.72	0.99	3.19	0.06	1.40	0.13	0.35	0.20	31.18	1.97	77.26
10	0.23	13.82	2.73	24.32	0.18	3.60	0.00	0.43	0.08	0.35	0.17	29.14	1.66	76.71
Average	0.29	12.84	2.97	24.08	0.34	3.99	0.08	0.69	0.07	0.34	0.17	32.39	1.81	--
Standard deviation	0.07	1.47	0.69	1.79	0.26	2.51	0.06	0.28	0.04	0.08	0.05	3.05	0.51	--
EPMA: Fine grained- matrix	**Na_2O**	**MgO**	**Al_2O_3**	**SiO_2**	**P_2O_5**	**SO_2**	**K_2O**	**CaO**	**TiO_2**	**Cr_2O_3**	**MnO**	**FeO**	**NiO**	**Total**
1	0.26	11.57	2.08	26.01	0.21	0.42	0.04	1.41	0.08	0.45	0.16	33.07	2.10	77.88
2	0.14	12.69	2.27	24.93	0.06	0.52	0.06	0.46	0.08	0.41	0.22	32.65	2.03	76.50
Average	0.20	12.13	2.18	25.47	0.13	0.47	0.05	0.94	0.08	0.43	0.19	32.86	2.06	
Standard deviation	0.08	0.79	0.13	0.77	0.11	0.07	0.01	0.67	0.00	0.03	0.04	0.30	0.05	--
Sigma: CI-like clasts	**Na_2O**	**MgO**	**Al_2O_3**	**SiO_2**	**P_2O_5**	**SO_2**	**K_2O**	**CaO**	**TiO_2**	**Cr_2O3**	**MnO**	**FeO**	**NiO**	**Total**
1	0.25	16.21	3.04	29.40	0.22	5.30	0.08	0.50	0.00	0.48	0.29	27.84	2.08	85.68
2	0.19	19.13	3.05	30.52	0.16	5.34	0.08	0.42	0.03	0.48	0.36	22.35	2.42	84.54

Average	0.22	17.67	3.05	29.96	0.19	5.32	0.08	0.46	0.01	0.48	0.32	25.10	2.25	--
Standard deviation	0.04	2.07	0.01	0.79	0.04	0.03	0.00	0.06	0.02	0.00	0.05	3.88	0.24	--

A.2 List of chemical analyses of the Pollen matrix

Sigma: chondrule rims and fine grained matrix phase I	**Na_2O**	**MgO**	**Al_2O_3**	**SiO_2**	**SO_2**	**K_2O**	**CaO**	**TiO_2**	**Cr_2O_3**	**MnO**	**FeO**	**NiO**	**Total**
1	0.42	19.85	2.23	32.98	3.09	0.15	0.48	0.03	0.46	0.29	18.18	1.48	79.83
2	0.41	18.15	2.19	29.99	3.96	0.09	1.20	0.08	0.31	0.33	20.01	1.77	78.76
3	0.26	18.51	2.44	31.49	3.72	0.16	0.76	0.14	0.37	0.25	20.38	1.69	80.46
4	0.40	18.57	2.64	30.88	3.49	0.08	0.50	0.10	0.42	0.29	22.23	1.46	81.25
5	0.53	18.92	1.99	30.21	4.41	0.08	1.30	0.13	0.53	0.25	17.54	1.88	77.98
6	0.58	18.41	2.16	29.83	4.22	0.10	0.40	0.12	0.52	0.36	21.40	1.72	80.01
7	0.61	18.67	1.99	29.92	4.21	0.09	0.37	0.05	0.53	0.19	18.49	1.83	77.15
8	0.60	17.47	2.33	29.30	5.60	0.13	0.43	0.08	0.53	0.27	18.60	2.00	77.65
9	0.35	19.29	2.14	32.01	3.16	0.05	0.82	0.09	0.31	0.28	19.90	1.83	80.34
10	0.20	18.24	1.81	29.82	3.68	0.06	0.65	0.08	0.38	0.20	18.88	1.60	75.88
11	0.39	16.64	2.65	29.54	4.87	0.05	0.40	0.05	0.37	0.32	20.25	1.99	77.81
12	0.31	17.94	1.94	30.19	3.36	0.06	0.88	0.07	0.42	0.25	19.24	1.73	76.69
13	0.64	18.69	2.10	29.66	5.21	0.09	0.58	0.15	0.41	0.28	17.74	1.94	77.77
14	0.54	18.28	1.81	28.85	4.97	0.08	1.44	0.05	0.48	0.30	17.66	1.93	76.41
16	0.41	18.54	1.87	29.77	5.50	0.12	0.61	0.09	0.59	0.27	19.12	2.31	79.43
17	0.35	19.45	1.92	30.77	6.53	0.09	2.02	0.09	0.52	0.16	17.14	3.58	82.97
18	0.28	18.97	2.42	30.86	6.20	0.14	0.42	0.07	0.67	0.28	21.82	1.37	83.66
19	0.31	17.63	2.16	30.03	3.83	0.06	0.41	0.04	0.37	0.18	19.78	1.94	77.02
20	0.73	18.21	1.97	29.36	5.62	0.11	1.20	0.11	0.54	0.26	17.95	1.93	78.38
21	0.74	17.96	1.91	29.35	6.98	0.11	0.69	0.11	0.46	0.17	18.30	2.44	79.31
22	0.62	19.49	2.31	32.26	3.52	0.06	0.82	0.20	0.68	0.26	17.80	1.02	79.27
23	0.44	17.54	2.34	29.27	6.82	0.10	0.71	0.11	0.55	0.23	19.28	1.75	79.35
24	0.49	17.93	2.02	30.17	4.27	0.07	1.39	0.14	0.53	0.20	20.07	1.92	79.43
25	0.53	18.75	2.09	30.74	5.19	0.15	0.82	0.02	0.52	0.34	17.66	1.81	78.66
26	0.34	17.84	2.13	29.48	5.02	0.10	1.21	0.09	0.69	0.19	19.47	2.32	79.29
27	0.45	18.55	2.27	30.94	3.63	0.00	0.28	0.09	0.51	0.34	19.89	1.74	78.98
28	0.41	18.23	2.19	28.60	7.65	0.13	0.71	0.07	0.49	0.30	23.53	2.28	84.97

29	0.45	19.38	2.19	31.39	4.23	0.10	0.53	0.09	0.62	0.23	20.57	1.76	81.84
30	0.24	18.56	1.90	31.09	5.27	0.08	1.28	0.09	0.52	0.30	18.27	2.38	80.18
31	0.31	20.10	2.11	32.46	4.87	0.09	0.57	0.09	0.51	0.23	18.84	2.02	82.43
32	0.38	16.50	2.30	28.78	3.83	0.07	0.47	0.04	0.47	0.33	22.15	1.89	77.51
33	0.37	18.09	2.18	30.10	7.09	0.20	0.47	0.08	0.62	0.19	17.97	3.18	80.96
34	0.25	17.72	2.19	29.25	5.08	0.08	0.66	0.18	0.51	0.33	18.49	2.20	77.20
35	0.42	18.38	2.22	30.80	4.44	0.03	0.76	0.11	0.42	0.23	20.52	1.88	80.49
36	0.37	18.61	2.48	31.13	5.13	0.05	0.47	0.05	0.46	0.24	20.85	1.85	81.92
37	0.31	19.40	2.08	31.65	4.84	0.06	0.72	0.03	0.43	0.30	19.36	2.06	81.65
38	0.33	18.50	2.09	30.86	4.54	0.06	0.76	0.20	0.67	0.14	21.30	2.10	81.86
39	0.29	20.87	4.24	33.00	4.03	0.08	1.62	0.12	0.29	0.11	19.31	1.67	86.00
40	0.26	18.68	1.78	30.09	5.69	0.01	0.49	0.12	0.43	0.28	16.89	2.42	77.43
41	0.56	17.74	2.09	28.89	4.70	0.07	0.48	0.08	0.71	0.23	18.26	1.99	75.94
42	0.45	18.32	2.16	31.03	3.09	0.06	0.31	0.14	0.60	0.17	22.14	1.54	80.34
43	0.47	17.91	2.06	29.29	3.66	0.06	0.64	0.05	0.63	0.27	17.83	1.73	74.78
44	0.44	17.94	1.96	28.89	4.37	0.11	0.92	0.05	0.51	0.36	18.30	1.77	75.86
45	0.37	18.58	2.16	30.61	5.08	0.10	0.36	0.07	0.58	0.25	22.61	1.49	82.60
46	0.55	18.17	1.92	29.31	4.79	0.09	0.51	0.05	0.52	0.18	21.75	1.79	79.93
47	0.53	18.73	2.37	31.34	3.73	0.09	0.38	0.10	0.68	0.15	22.03	1.32	81.73
48	0.50	19.33	2.04	30.40	4.44	0.09	0.90	0.06	0.53	0.34	18.45	1.94	79.32
49	0.59	19.22	1.84	30.81	4.36	0.11	0.84	0.00	0.53	0.21	18.67	1.97	79.35
50	0.46	17.57	2.09	29.37	3.83	0.09	0.54	0.09	0.41	0.19	19.77	1.90	76.56
51	0.41	18.23	1.79	29.20	3.18	0.08	1.19	0.09	0.41	0.12	18.20	1.67	74.78
52	0.77	18.67	1.62	29.59	6.95	0.21	0.35	0.13	0.65	0.26	15.36	2.82	77.76
53	0.85	17.86	2.03	29.35	5.27	0.16	0.46	0.05	0.45	0.21	17.26	2.16	76.30
54	0.24	24.82	1.64	34.47	2.04	0.04	0.16	0.03	0.43	0.27	13.92	0.40	78.52
55	0.31	25.62	1.48	34.99	1.90	0.00	0.12	0.14	0.41	0.19	11.98	0.62	77.84
Average	0.44	18.71	2.13	30.45	4.61	0.09	0.71	0.09	0.50	0.25	19.14	1.89	--
STDEV	0.15	1.50	0.37	1.36	1.22	0.04	0.39	0.04	0.10	0.06	2.09	0.50	
Sigma: fine grained matrix phase II	**Na_2O**	**MgO**	**Al_2O_3**	**SiO_2**	**SO_2**	**K_2O**	**CaO**	**TiO_2**	**Cr_2O_3**	**MnO**	**FeO**	**NiO**	**Total**
1	0.63	18.68	1.77	29.46	6.16	0.11	0.40	0.19	0.37	0.22	18.24	2.10	78.67
2	0.35	13.18	2.68	21.37	12.92	0.00	0.20	0.00	0.22	0.28	37.96	1.68	91.25

3	0.30	14.15	2.72	26.49	5.23	0.07	0.32	0.00	0.22	0.29	33.99	1.23	85.26
4	0.27	17.01	2.58	26.99	4.90	0.08	0.24	0.13	0.37	0.31	33.60	0.80	87.36
5	0.21	16.39	2.46	24.87	9.86	0.03	0.93	0.05	0.13	0.18	32.41	1.21	88.89
6	0.31	19.71	2.42	33.33	3.81	0.08	0.95	0.10	0.44	0.25	18.74	1.73	82.10
7	0.37	16.33	2.58	29.13	3.95	0.05	0.39	0.02	0.15	0.19	28.81	1.92	84.26
8	0.15	13.81	2.71	27.30	3.37	0.10	0.27	0.12	0.19	0.26	34.56	0.92	84.23
9	0.21	14.87	2.72	27.46	5.63	0.09	0.42	0.00	0.29	0.29	30.76	1.42	84.49
Average	0.31	16.01	2.51	27.38	6.20	0.07	0.46	0.07	0.26	0.25	29.90	1.45	--
Standard deviation	0.14	2.23	0.30	3.28	3.17	0.03	0.28	0.08	0.11	0.04	6.94	0.45	--
Sigma: CI-like-clast	**Na_2O**	**MgO**	**Al_2O_3**	**SiO_2**	**SO_2**	**K_2O**	**CaO**	**TiO_2**	**Cr_2O_3**	**MnO**	**FeO**	**NiO**	**Total**
1	0.48	21.58	2.85	34.87	4.02	0.23	0.18	0.01	0.44	0.24	15.71	1.49	82.28
2	0.48	22.59	3.10	36.10	3.38	0.21	0.22	0.07	0.38	0.22	15.74	1.21	83.81
3	0.53	19.25	1.81	30.80	4.37	0.07	0.58	0.10	0.33	0.33	17.44	2.00	77.95
Average	0.50	21.14	2.59	33.92	3.93	0.17	0.33	0.06	0.38	0.26	16.30	1.57	--
Standard deviation	0.03	1.72	0.68	2.78	0.50	0.09	0.22	0.05	0.05	0.06	0.99	0.40	--
EPMA: fine grained matrix phase II	**Na_2O**	**MgO**	**Al_2O_3**	**SiO_2**	**SO_2**	**K_2O**	**CaO**	**TiO_2**	**Cr_2O_3**	**MnO**	**FeO**	**NiO**	**Total**
1	0.17	12.40	2.36	25.33	0.55	0.05	0.27	0.09	0.22	0.24	37.14	0.76	79.47
EPMA: chondrule rims and fine grained matrix phase I	**Na_2O**	**MgO**	**Al_2O_3**	**SiO_2**	**SO_2**	**K_2O**	**CaO**	**TiO_2**	**Cr_2O_3**	**MnO**	**FeO**	**NiO**	**Total**
1	0.36	19.32	1.90	31.67	0.91	0.09	0.45	0.09	0.47	0.21	19.78	2.20	77.32
2	0.44	18.23	1.84	29.93	0.76	0.09	0.32	0.10	0.54	0.20	19.20	1.86	73.37
3	0.33	19.52	2.67	33.09	0.24	0.08	0.65	0.09	0.46	0.25	23.51	0.62	81.46
4	0.29	20.82	2.22	34.36	0.27	0.06	0.62	0.11	0.44	0.29	20.06	0.64	80.15
Average	0.35	19.47	2.16	32.26	0.54	0.08	0.51	0.10	0.48	0.24	20.64	1.33	--
Standard deviation	0.06	1.06	0.38	1.90	0.34	0.01	0.15	0.01	0.04	0.04	1.95	0.82	--

A.3 List of chemical analyses of CI-like clasts in LON 94101

EPMA: CI-like clasts	**Na_2O**	**MgO**	**Al_2O_3**	**SiO_2**	**P_2O_5**	**SO_2**	**K_2O**	**CaO**	**TiO_2**	**Cr_2O_3**	**MnO**	**FeO**	**NiO**	**Total**
1	0.47	22.89	2.60	34.82	0.26	3.10	0.17	0.37	0.09	0.26	0.18	17.00	1.17	83.39
2	0.41	25.98	2.80	36.84	0.10	2.18	0.16	0.10	0.08	0.29	0.23	15.11	0.71	85.00
3	0.58	19.67	1.50	29.93	0.07	5.77	0.10	0.16	0.08	0.37	0.16	13.77	2.81	74.98

Average	0.48	22.85	2.30	33.87	0.15	3.68	0.14	0.21	0.09	0.31	0.19	15.29	1.56	--
Standard deviation	0.09	3.16	0.70	3.55	0.10	1.87	0.04	0.14	0.00	0.06	0.04	1.62	1.10	--

A.4 List of chemical analyses of the LAP 031166 matrix

EPMA: matrix bright phase	**Na_2O**	**MgO**	**Al_2O_3**	**SiO_2**	**P_2O_5**	**SO_2**	**K_2O**	**CaO**	**TiO_2**	**Cr_2O_3**	**MnO**	**FeO**	**NiO**	**Total**
1	0.27	11.81	2.95	25.19	0.09	4.18	0.06	0.18	0.48	0.25	0.24	42.42	0.93	88.77
2	0.19	10.33	3.00	22.68	0.30	4.94	0.03	0.40	0.07	0.25	0.11	44.11	0.62	86.86
3	0.24	11.19	3.36	25.27	0.07	3.37	0.01	0.06	0.09	0.30	0.28	43.32	0.60	87.93
4	0.25	10.61	3.00	24.46	0.03	3.81	0.03	0.04	0.13	0.30	0.13	43.63	0.59	86.76
Average	0.24	10.98	3.08	24.40	0.12	4.08	0.03	0.17	0.19	0.27	0.19	43.37	0.69	--
Standard deviation	0.033	0.66	0.19	1.20	0.12	0.66	0.02	0.16	0.19	0.03	0.08	0.71	0.16	--
EPMA: matrix dark phase	**Na_2O**	**MgO**	**Al_2O_3**	**SiO_2**	**P_2O_5**	**SO_2**	**K_2O**	**CaO**	**TiO_2**	**Cr_2O_3**	**MnO**	**FeO**	**NiO**	**Total**
1	0.08	26.49	1.55	37.37	0.00	0.28	0.01	0.07	0.09	0.04	0.28	18.12	0.20	84.57
2	0.10	25.72	1.94	38.18	0.04	0.44	0.01	0.14	0.06	0.09	0.20	18.79	0.21	85.92
Average	0.09	26.11	1.75	37.77	0.02	0.36	0.01	0.10	0.08	0.07	0.24	18.45	0.20	--
Standard deviation	0.012	0.54	0.27	0.58	0.02	0.11	0.00	0.05	0.02	0.04	0.06	0.48	0.01	--

A.5 List of chemical analyses of the SCO 06043 matrix

EPMA: matrix bright phase	**Na_2O**	**MgO**	**Al_2O_3**	**SiO_2**	**P_2O_5**	**SO_2**	**K_2O**	**CaO**	**TiO_2**	**Cr_2O_3**	**MnO**	**FeO**	**NiO**	**Total**
1	0.26	14.88	2.47	27.24	0.12	4.25	0.05	0.31	0.11	0.31	0.25	37.10	1.32	88.67
2	0.21	14.96	2.54	27.44	0.03	4.43	0.07	0.05	0.11	0.29	0.16	38.05	0.61	88.95
3	0.55	14.66	2.19	22.62	0.67	2.94	0.10	0.71	0.14	0.29	0.02	36.45	0.94	82.29
4	0.37	16.14	2.82	27.16	0.04	3.72	0.07	0.05	0.09	0.38	0.14	36.95	0.82	88.76
Average	0.35	15.16	2.50	26.12	0.22	3.84	0.07	0.28	0.11	0.32	0.14	37.14	0.92	--
Standard deviation	0.15	0.67	0.26	2.33	0.30	0.67	0.02	0.31	0.02	0.05	0.10	0.67	0.30	--
EPMA: matrix dark phase	**Na_2O**	**MgO**	**Al_2O_3**	**SiO_2**	**P_2O_5**	**SO_2**	**K_2O**	**CaO**	**TiO_2**	**Cr_2O_3**	**MnO**	**FeO**	**NiO**	**Total**
1	0.15	26.31	2.57	37.71	0.05	0.48	0.07	0.03	0.07	0.57	0.21	16.15	0.80	85.16
2	0.09	26.16	1.69	37.22	0.03	0.31	0.02	0.01	0.08	0.33	0.20	18.22	0.60	84.97
3	0.11	27.00	2.00	38.03	0.02	0.16	0.02	0.03	0.08	0.31	0.18	17.06	0.42	85.41

Average	0.12	26.49	2.09	37.65	0.04	0.31	0.04	0.02	0.08	0.40	0.20	17.14	0.61	--
Standard deviation	0.02	0.36	0.36	0.33	0.01	0.13	0.02	0.01	0.00	0.12	0.01	0.85	0.15	--

A.6 List of chemical analyses of Mg-rich serpentine pseudomorphs after calcite in Pollen

EPMA: pseudomorphs after calcite	**Na_2O**	**MgO**	**Al_2O_3**	**SiO_2**	**P_2O_5**	**SO_2**	**K_2O**	**CaO**	**TiO_2**	**Cr_2O_3**	**MnO**	**FeO**	**NiO**	**Total**
1	0.2	28.36	1.21	38.6	0.01	0.25	0.07	0.18	0.07	0.16	0.29	10.48	0.41	80.3
2	0.27	26.71	1.29	35.88	0.02	0.40	0.08	0.24	0.06	0.20	0.29	12.76	0.61	78.79
3	0.18	28.07	1.16	38.10	0.00	0.28	0.08	0.13	0.08	0.17	0.25	10.57	0.48	79.55
4	0.12	26.69	1.43	34.2	0.03	0.43	0.06	0.2	0.07	0.3	0.24	15.17	0.89	79.82
5	0.25	27.61	1.11	37.19	0.00	0.39	0.06	0.15	0.07	0.17	0.21	10.11	0.58	77.9
6	0.32	27.52	1.33	37.28	0.01	0.27	0.11	0.19	0.08	0.26	0.23	10.42	0.48	78.49
7	0.27	27.35	1.22	36.64	0.00	0.29	0.10	0.13	0.07	0.25	0.24	10.65	0.50	77.71
8	0.17	28.01	1.23	37.99	0.00	0.27	0.09	0.15	0.08	0.27	0.29	10.49	0.56	79.59
9	0.13	28.62	1.32	40.77	0.02	0.14	0.10	0.28	0.08	0.20	0.25	10.77	0.36	83.04
10	0.16	27.89	1.30	38.55	0.00	0.12	0.09	0.21	0.09	0.15	0.29	10.59	0.38	79.83
11	0.27	26.99	1.22	34.64	0.04	0.77	0.10	0.25	0.08	0.26	0.24	14.14	0.75	79.75
12	0.21	27.30	1.27	36.39	0.00	0.22	0.08	0.21	0.07	0.33	0.28	10.35	0.36	77.08
13	0.14	27.13	1.27	36.25	0.02	0.26	0.09	0.18	0.06	0.29	0.25	10.19	0.44	76.56
14	0.25	27.66	1.29	38.3	0.00	0.22	0.08	0.18	0.05	0.25	0.23	10.33	0.40	79.25
15	0.28	26.85	1.21	36.29	0.01	0.20	0.07	0.18	0.09	0.2	0.26	10.09	0.40	76.12
16	0.27	27.60	1.40	36.66	0.00	0.31	0.07	0.16	0.07	0.23	0.31	12.06	0.47	79.62
17	0.38	27.62	1.32	36.51	0.00	0.36	0.16	0.20	0.07	0.25	0.26	10.21	0.46	77.79
18	0.64	26.66	1.46	33.29	0.01	1.71	0.08	0.12	0.07	0.21	0.26	15.05	1.17	80.73
19	0.62	28.05	1.36	35.54	0.02	0.49	0.07	0.13	0.06	0.20	0.26	11.26	0.51	78.57
20	0.33	26.39	1.19	37.42	0.01	0.23	0.09	0.14	0.07	0.26	0.28	10.25	0.30	76.98
21	0.42	28.3	1.26	38.29	0.01	0.27	0.11	0.15	0.07	0.31	0.29	10.86	0.46	80.81
22	0.24	27.59	1.16	37.16	0.00	0.28	0.09	0.23	0.08	0.18	0.23	12.27	0.50	80.02
Average	0.28	27.50	1.27	36.91	0.01	0.37	0.09	0.18	0.07	0.23	0.26	11.32	0.52	79.01

Standard deviation	0.14	0.61	0.09	1.65	0.01	0.33	0.02	0.04	0.01	0.05	0.03	1.59	0.19	--

A.7 List of chemical analyses of pseudomorphs after calcite in LON 94101

EPMA: pseudomorphs after calcite (phase 1)	**Na_2O**	**MgO**	**Al_2O_3**	**SiO_2**	**P_2O_5**	**SO_2**	**K_2O**	**CaO**	**TiO_2**	**Cr_2O_3**	**MnO**	**FeO**	**NiO**	**Total**
1	0.31	14.90	2.57	17.73	0.03	16.76	0.06	0.20	0.04	0.13	0.23	36.63	3.31	92.90
2	0.26	14.45	2.17	17.01	0.01	16.47	0.04	0.12	0.04	0.16	0.20	35.69	3.01	89.61
3	0.40	12.02	2.35	16.79	0.03	16.02	0.06	0.14	0.04	0.23	0.14	40.38	2.37	90.95
Average	0.32	13.79	2.36	17.18	0.02	16.42	0.05	0.15	0.04	0.17	0.19	37.57	2.89	91.15
Standard deviation	0.07	1.55	0.20	0.49	0.01	0.37	0.01	0.04	0.00	0.05	0.05	2.48	0.48	
EPMA: pseudomorphs after calcite (phase 2)	**Na_2O**	**MgO**	**Al_2O_3**	**SiO_2**	**P_2O_5**	**SO_2**	**K_2O**	**CaO**	**TiO_2**	**Cr_2O_3**	**MnO**	**FeO**	**NiO**	**Total**
1	0.34	24.19	1.97	30.24	0.01	6.46	0.12	0.10	0.04	0.21	0.18	21.51	1.35	86.70
2	0.23	24.08	1.65	28.62	0.02	10.97	0.08	0.13	0.05	0.28	0.24	21.96	2.06	90.35
Average	0.29	24.13	1.81	29.43	0.02	8.71	0.10	0.11	0.04	0.24	0.21	21.74	1.70	88.53
Standard deviation	0.08	0.07	0.23	1.14	0.01	3.19	0.03	0.02	0.00	0.05	0.04	0.32	0.50	
EPMA: pseudomorphs after calcite (phase 3)	**Na_2O**	**MgO**	**Al_2O_3**	**SiO_2**	**P_2O_5**	**SO_2**	**K_2O**	**CaO**	**TiO_2**	**Cr_2O_3**	**MnO**	**FeO**	**NiO**	**Total**
1	0.06	3.56	0.64	1.82	0.02	9.42	0.02	38.81	0.01	0.08	0.01	15.03	1.09	70.55
2	0.03	2.33	0.31	1.34	0.02	6.86	0.01	44.69	0.01	0.08	0.04	8.91	0.92	65.57
Average	0.04	2.94	0.48	1.58	0.02	8.14	0.01	41.75	0.01	0.08	0.03	11.97	1.00	68.06
Standard deviation	0.02	0.87	0.23	0.34	0.00	1.81	0.00	4.16	0.01	0.00	0.03	4.33	0.12	

A.8 List of chemical analyses of pseudomorphs after calcite in Cold Bokkeveld

EPMA: pseudomorphs after calcite (phase 1)	**Na_2O**	**MgO**	**Al_2O_3**	**SiO_2**	**P_2O_5**	**SO_2**	**K_2O**	**CaO**	**TiO_2**	**Cr_2O_3**	**MnO**	**FeO**	**NiO**	**Total**
1	0.09	14.88	1.71	17.35	0.07	15.22	0.09	0.21	0.02	0.41	0.18	36.67	2.91	89.83
2	0.13	15.66	2.04	17.62	0.02	19.18	0.04	0.11	0.05	0.14	0.12	37.05	2.58	94.74
Average	0.11	15.27	1.88	17.49	0.05	17.20	0.07	0.16	0.04	0.28	0.15	36.86	2.75	92.29
Standard deviation	0.03	0.55	0.23	0.19	0.04	2.80	0.04	0.07	0.03	0.19	0.04	0.27	0.24	--
EPMA: pseudomorphs	**Na_2O**	**MgO**	**Al_2O_3**	**SiO_2**	**P_2O_5**	**SO_2**	**K_2O**	**CaO**	**TiO_2**	**Cr_2O_3**	**MnO**	**FeO**	**NiO**	Total

after calcite (phase 2)														
1	0.10	22.20	2.00	28.75	0.06	7.21	0.08	0.22	0.06	0.05	0.21	24.76	1.53	87.23
2	0.08	20.77	1.93	25.23	0.02	12.28	0.06	0.55	0.05	0.11	0.05	28.17	1.90	91.22
3	0.11	21.59	1.72	26.81	0.12	6.87	0.08	0.30	0.05	0.11	0.29	24.36	2.24	84.65
4	0.05	24.41	1.63	34.12	0.08	6.15	0.07	0.26	0.05	0.03	0.23	19.61	1.71	88.40
5	0.09	23.65	1.62	28.01	0.04	7.93	0.10	0.26	0.07	0.13	0.18	21.61	1.97	85.67
Average	0.08	22.53	1.78	28.58	0.06	8.09	0.08	0.32	0.06	0.09	0.19	23.70	1.87	87.43
Standard deviation	0.03	1.49	0.18	3.37	0.04	2.43	0.01	0.13	0.01	0.04	0.09	3.27	0.27	--
EPMA: pseudomorphs after calcite (phase 3)	**Na_2O**	**MgO**	**Al_2O_3**	**SiO_2**	**P_2O_5**	**SO_2**	**K_2O**	**CaO**	**TiO_2**	**Cr_2O_3**	**MnO**	**FeO**	**NiO**	**Total**
1	0.08	29.19	1.60	39.22	0.05	1.12	0.07	0.17	0.11	0.07	0.28	11.73	0.75	84.44
2	0.05	29.53	1.32	36.55	0.05	3.25	0.05	0.18	0.07	0.03	0.24	13.73	1.04	86.10
3	0.05	27.72	1.33	33.62	0.04	3.99	0.04	0.16	0.07	0.09	0.15	17.90	0.88	86.02
4	0.06	29.31	1.78	35.20	0.04	5.11	0.05	0.21	0.07	0.16	0.27	14.39	1.53	88.16
Average	0.06	28.94	1.51	36.15	0.04	3.37	0.05	0.18	0.08	0.09	0.23	14.44	1.05	86.18
Standard deviation	0.01	0.83	0.23	2.37	0.01	1.68	0.01	0.02	0.02	0.05	0.06	2.57	0.34	--

A.9 List of chemical analyses of pseudomorphs after calcite in LAP 031166

EPMA: pseudomorphs after calcite	Na_2O	MgO	Al_2O_3	SiO_2	P_2O_5	SO_2	K_2O	CaO	TiO_2	Cr_2O_3	MnO	FeO	NiO	Total
1	0.15	28.56	2.37	39.37	0.01	1.18	0.11	0.11	0.08	0.31	0.22	13.75	0.20	86.41
2	0.27	28.49	2.40	39.13	0.00	1.25	0.12	0.11	0.07	0.32	0.10	14.18	0.19	86.63
3	0.21	28.08	2.36	40.10	0.01	1.19	0.12	0.09	0.08	0.27	0.22	13.88	0.27	86.90
4	0.07	28.01	2.46	40.20	0.03	1.54	0.09	0.09	0.08	0.27	0.15	13.75	0.34	87.09
5	0.18	26.50	2.38	40.85	0.03	2.09	0.07	0.00	0.08	0.28	0.22	14.20	0.79	87.66
6	0.22	27.69	2.41	39.05	0.02	1.43	0.11	0.03	0.09	0.38	0.20	13.68	0.43	85.73
7	0.16	26.10	2.39	37.62	0.00	5.57	0.07	0.06	0.08	0.31	0.26	15.35	1.24	89.20
8	0.12	26.76	2.49	39.68	0.11	1.99	0.06	0.02	0.07	0.29	0.17	13.51	0.93	86.19

9	0.07	27.40	2.18	40.03	0.02	1.16	0.22	0.07	0.07	0.32	0.29	13.31	0.31	85.45
10	0.11	27.34	2.26	40.43	0.00	1.11	0.13	0.07	0.07	0.28	0.29	14.45	0.26	86.79
11	0.14	24.90	2.15	35.47	0.01	8.75	0.12	0.13	0.07	0.37	0.22	18.55	1.42	92.31
Average	0.15	27.26	2.35	39.27	0.02	2.48	0.11	0.07	0.08	0.31	0.21	14.42	0.58	87.30
Standard deviation	0.06	1.11	0.11	1.53	0.03	2.44	0.04	0.04	0.01	0.04	0.06	1.48	0.44	--

A.10 List of chemical analyses of pseudomorphs after calcite in SCO 06043

EPMA: pseudomorphs after calcite	Na_2O	MgO	Al_2O_3	SiO_2	P_2O_5	SO_2	K_2O	CaO	TiO_2	Cr_2O_3	MnO	FeO	NiO	Total
1	0.24	26.17	2.87	33.59	0.03	2.94	0.07	0.03	0.06	0.47	0.15	20.86	0.56	88.04
2	0.18	26.14	2.48	32.27	0.00	4.50	0.13	0.05	0.09	0.44	0.15	20.71	0.53	87.67
3	0.18	25.60	3.31	29.42	0.01	6.72	0.05	0.03	0.03	0.21	0.15	24.28	0.14	90.13
4	0.24	26.99	2.43	37.64	0.01	0.13	0.02	0.05	0.06	0.17	0.13	19.71	0.10	87.69
5	0.26	24.72	2.55	29.49	0.02	8.03	0.08	0.08	0.05	0.56	0.09	24.56	0.31	90.81
6	0.21	25.27	3.10	30.95	0.01	6.93	0.05	0.06	0.04	0.30	0.09	24.16	0.17	91.34
7	0.21	26.04	2.80	35.79	0.00	0.10	0.03	0.03	0.05	0.36	0.13	20.03	0.19	85.74
8	0.19	28.21	1.96	37.52	0.01	0.10	0.01	0.02	0.09	0.09	0.10	17.90	0.05	86.24
9	0.11	26.39	2.30	36.52	0.00	0.32	0.01	0.04	0.07	0.20	0.15	19.69	0.18	85.98
11	0.15	27.10	2.05	36.07	0.05	0.42	0.05	0.07	0.09	0.44	0.15	18.02	0.45	85.12
12	0.19	26.80	1.94	34.31	0.00	0.17	0.01	0.03	0.08	0.09	0.08	17.76	0.25	81.70
13	0.25	24.28	2.66	29.83	0.04	8.25	0.15	0.04	0.05	0.70	0.14	24.67	0.48	91.55
14	0.19	24.80	1.83	35.68	0.03	1.77	0.06	0.02	0.09	0.26	0.13	21.45	0.65	86.95
Average	0.20	26.04	2.48	33.77	0.01	3.11	0.05	0.04	0.07	0.33	0.13	21.06	0.31	87.61
Standard deviation	0.04	1.10	0.46	3.07	0.02	3.33	0.04	0.02	0.02	0.19	0.03	2.59	0.20	--

Appendix B

B.1 List of chemical analyses in mol% of Ca-carbonate in Murchison

EPMA: calcite	CaCO3	MgCO3	SrCO3	FeCO3	MnCO3	Total
Calcite 1	99.43	0.03	0.00	0.54	0.00	100
Calcite 2	99.67	0.03	0.00	0.31	0.00	100
Calcite 3	99.40	0.04	0.00	0.57	0.00	100
Calcite 4	98.63	0.29	0.00	1.08	0.00	100
Calcite 5	99.30	0.03	0.00	0.68	0.00	100
Calcite 6	97.85	0.18	0.00	1.67	0.29	100
Calcite 7	95.85	0.90	0.00	3.25	0.00	100
Calcite 8	99.33	0.03	0.00	0.64	0.00	100
Calcite 9	98.77	0.05	0.00	1.18	0.00	100
Calcite 10	98.78	0.28	0.00	0.94	0.00	100
Calcite 11	99.17	0.07	0.00	0.76	0.00	100
Calcite 12	98.70	0.57	0.00	0.73	0.00	100
Calcite 13	99.19	0.05	0.00	0.76	0.00	100
Calcite 14	99.29	0.04	0.00	0.68	0.00	100
Average	98.81	0.18	0.00	0.98	0.02	100
Standard deviation	0.97	0.26	0.00	0.73	0.08	100
EPMA: aragonite	**CaCO3**	**MgCO3**	**SrCO3**	**FeCO3**	**MnCO3**	**Total**
Aragonite 1	98.55	0.24	0.05	1.16	0.00	100
Aragonite 2	98.44	0.33	0.07	1.16	0.00	100
Aragonite 3	98.45	0.27	0.00	1.28	0.00	100
Average	98.48	0.28	0.04	1.20	0.00	--
Standard deviation	0.06	0.05	0.04	0.07	0.00	--

B.2 List of chemical analyses in mol% of Ca-carbonate in Murray

EPMA: calcite	CaCO3	MgCO3	SrCO3	FeCO3	MnCO3	Total
Calcite 1	98.53	0.00	0.00	1.47	0.00	100.00
Calcite 2	98.56	0.00	0.00	1.44	0.00	100.00
Calcite 3	98.31	0.05	0.00	1.64	0.00	100.00
Calcite 4	98.27	0.06	0.00	1.67	0.00	100.00
Calcite 5	97.81	0.26	0.00	1.94	0.00	100.00
Calcite 6	98.56	0.00	0.00	1.44	0.00	100.00
Calcite 7	98.18	0.34	0.00	1.49	0.00	100.00
Calcite 8	98.12	0.22	0.00	1.66	0.00	100.00
Calcite 9	97.59	0.37	0.00	2.04	0.00	100.00
Calcite 10	98.87	0.00	0.00	1.13	0.00	100.00
Calcite 11	98.83	0.00	0.00	1.17	0.00	100.00
Calcite 12	98.44	0.00	0.00	1.56	0.00	100.00
Calcite 13	98.22	0.00	0.00	1.78	0.00	100.00
Calcite 14	98.86	0.00	0.00	1.14	0.00	100.00
Calcite 15	98.45	0.00	0.00	1.55	0.00	100.00
Calcite 16	97.90	0.23	0.00	1.87	0.00	100.00
Calcite 17	98.26	0.01	0.00	1.73	0.00	100.00
Calcite 18	97.95	0.22	0.00	1.83	0.00	100.00
Calcite 19	98.41	0.13	0.00	1.46	0.00	100.00
Calcite 20	98.88	0.00	0.00	1.12	0.00	100.00
Calcite 21	98.63	0.08	0.00	1.29	0.00	100.00
Calcite 22	98.63	0.05	0.00	1.32	0.00	100.00
Calcite 23	97.80	0.27	0.00	1.93	0.00	100.00
Calcite 24	97.56	0.53	0.00	1.91	0.00	100.00

Calcite 25	98.09	0.13	0.00	1.78	0.00	100.00
Calcite 26	98.44	0.04	0.00	1.52	0.00	100.00
Calcite 27	97.70	0.27	0.00	1.51	0.52	100.00
Calcite 28	98.38	0.11	0.00	1.33	0.18	100.00
Calcite 29	96.47	0.71	0.00	1.63	1.19	100.00
Calcite 30	98.04	0.23	0.00	1.38	0.35	100.00
Calcite 31	97.70	0.26	0.00	1.55	0.49	100.00
Calcite 32	98.96	0.00	0.00	1.04	0.00	100.00
Average	98.23	0.14	0.00	1.54	0.09	--
Standard deviation	0.51	0.17	0.00	0.27	0.25	--

B.3 List of chemical analyses in mol% of Ca-carbonate in Pollen

Note that type 1 is calcite completely rimmed with tochilinite, type 2 is calcite replacing olivine, and type 3 is calcite free of rims and inclusions. The analyses were determined by EPMA.

No.	Calcite type	$CaCO_3$	$MgCO_3$	$SrCO_3$	$FeCO_3$	$MnCO_3$	Total
1	Type 1	98.01	0.81	0.00	1.19	0.00	100.00
2	Type 1	98.98	0.20	0.00	0.82	0.00	100.00
3	Type 1	99.51	0.00	0.00	0.49	0.00	100.00
4	Type 1	99.54	0.00	0.00	0.46	0.00	100.00
5	Type 1	96.74	0.35	0.00	2.90	0.00	100.00
6	Type 1	98.38	0.32	0.00	1.30	0.00	100.00
7	Type 1	98.69	0.16	0.00	1.15	0.00	100.00
8	Type 1	94.59	0.80	0.00	4.61	0.00	100.00
9	Type 1	98.70	0.14	0.00	1.16	0.00	100.00
10	Type 1	97.70	0.78	0.00	1.51	0.00	100.00
11	Type 1	95.42	0.89	0.00	3.68	0.00	100.00
12	Type 1	98.92	0.09	0.00	0.99	0.00	100.00
13	Type 1	99.51	0.00	0.00	0.49	0.00	100.00
14	Type 1	99.48	0.00	0.00	0.52	0.00	100.00
15	Type 1	98.59	0.14	0.00	1.26	0.00	100.00
16	Type 1	98.83	0.13	0.00	0.92	0.12	100.00
17	Type 1	98.58	0.26	0.00	1.15	0.00	100.00
18	Type 1	99.44	0.00	0.00	0.56	0.00	100.00
19	Type 1	98.96	0.12	0.00	0.78	0.14	100.00
20	Type 1	95.24	0.95	0.00	3.81	0.00	100.00
21	Type 1	98.72	0.16	0.00	0.91	0.21	100.00
22	Type 1	98.03	0.58	0.00	1.38	0.00	100.00
23	Type 1	99.01	0.11	0.00	0.76	0.12	100.00
24	Type 1	98.86	0.12	0.00	1.02	0.00	100.00
25	Type 1	99.58	0.00	0.00	0.42	0.00	100.00
26	Type 1	99.57	0.00	0.00	0.43	0.00	100.00
27	Type 1	99.44	0.00	0.00	0.56	0.00	100.00
28	Type 1	99.46	0.00	0.00	0.54	0.00	100.00
29	Type 1	99.06	0.14	0.00	0.80	0.00	100.00
30	Type 1	94.84	1.34	0.00	3.82	0.00	100.00
31	Type 1	99.74	0.00	0.00	0.26	0.00	100.00
32	Type 1	99.72	0.00	0.00	0.28	0.00	100.00
33	Type 1	99.69	0.00	0.00	0.31	0.00	100.00
34	Type 1	99.57	0.00	0.00	0.43	0.00	100.00
35	Type 1	99.49	0.00	0.00	0.51	0.00	100.00
36	Type 1	98.18	0.17	0.00	1.65	0.00	100.00

37	Type 1	99.41	0.00	0.00	0.59	0.00	100.00
38	Type 1	99.41	0.00	0.00	0.59	0.00	100.00
39	Type 1	93.45	2.74	0.00	3.62	0.19	100.00
40	Type 1	95.42	0.89	0.00	3.68	0.00	100.00
1	Type 2	98.77	0.16	0.00	1.07	0.00	100.00
2	Type 2	97.91	0.00	0.00	2.09	0.00	100.00
3	Type 2	97.43	0.38	0.00	2.19	0.00	100.00
4	Type 2	96.57	0.00	0.00	3.43	0.00	100.00
5	Type 2	97.76	0.40	0.00	1.65	0.19	100.00
6	Type 2	97.26	0.13	0.00	2.61	0.00	100.00
7	Type 2	96.68	0.17	0.00	3.15	0.00	100.00
8	Type 2	98.63	0.17	0.00	1.20	0.00	100.00
9	Type 2	99.27	0.25	0.00	0.48	0.00	100.00
10	Type 2	98.52	0.10	0.00	1.38	0.00	100.00
11	Type 2	98.38	0.54	0.00	1.08	0.00	100.00
12	Type 2	99.03	0.09	0.00	0.89	0.00	100.00
13	Type 2	99.51	0.08	0.00	0.40	0.00	100.00
14	Type 2	98.39	0.11	0.00	1.51	0.00	100.00
1	Type 3	97.11	0.83	0.00	2.05	0.00	100.00
2	Type 3	97.07	1.17	0.00	1.63	0.12	100.00
3	Type 3	98.77	0.11	0.00	1.12	0.00	100.00
4	Type 3	98.47	0.40	0.00	0.97	0.17	100.00
5	Type 3	97.34	1.02	0.00	1.47	0.16	100.00
6	Type 3	99.47	0.10	0.00	0.44	0.00	100.00
7	Type 3	99.14	0.15	0.00	0.71	0.00	100.00
8	Type 3	99.26	0.12	0.00	0.63	0.00	100.00
9	Type 3	98.95	0.07	0.00	0.98	0.00	100.00
10	Type 3	97.19	0.36	0.00	2.45	0.00	100.00
11	Type 3	99.32	0.11	0.05	0.52	0.00	100.00
12	Type 3	94.51	3.12	0.11	2.27	0.00	100.00
Average		98.26	0.34	0.00	1.37	0.02	--
Standard deviation		1.48	0.57	0.01	1.07	0.06	--

B.4 List of chemical analyses in mol% of Ca-carbonate in Mighei

EPMA: aragonite	**$CaCO_3$**	**$MgCO_3$**	**$SrCO_3$**	**$FeCO_3$**	**$MnCO_3$**	**Total**
Aragonite 1	99.02	0.01	0.04	0.93	0.00	100.00
Aragonite 2	98.82	0.17	0.06	0.95	0.00	100.00
Aragonite 3	98.86	0.03	0.00	1.11	0.00	100.00
Aragonite 4	98.99	0.01	0.04	0.96	0.00	100.00
Aragonite 5	99.38	0.01	0.00	0.61	0.00	100.00
Aragonite 6	98.87	0.03	0.07	1.03	0.00	100.00
Aragonite 7	98.86	0.04	0.04	1.06	0.00	100.00
Aragonite 8	98.75	0.02	0.05	1.18	0.00	100.00
Aragonite 9	98.78	0.03	0.12	1.07	0.00	100.00
Aragonite 10	99.04	0.05	0.06	0.84	0.00	100.00
Aragonite 11	99.08	0.00	0.05	0.86	0.00	100.00
Aragonite 12	98.86	0.03	0.15	0.97	0.00	100.00
Aragonite 13	99.00	0.00	0.06	0.94	0.00	100.00
Aragonite 14	99.13	0.01	0.00	0.86	0.00	100.00
Aragonite 15	99.08	0.02	0.07	0.84	0.00	100.00
Average	98.97	0.03	0.05	0.95	0.00	--
Standard deviation	0.17	0.04	0.04	0.14	0.00	
Analyses number of calcite A (calcite rimmed)	**$CaCO_3$**	**$MgCO_3$**	**$SrCO_3$**	**$FeCO_3$**	**$MnCO_3$**	**Total**

Calcite 1	97.76	0.30	0.00	1.81	0.13	100.00
Calcite 2	97.54	0.34	0.00	2.11	0.00	100.00
Calcite 3	98.49	0.07	0.01	1.35	0.09	100.00
Calcite 4	97.64	0.37	0.00	1.99	0.00	100.00
Calcite 5	98.67	0.07	0.00	1.18	0.09	100.00
Calcite 6	98.93	0.01	0.00	1.06	0.00	100.00
Calcite 7	98.40	0.11	0.00	1.37	0.12	100.00
Calcite 8	98.58	0.06	0.00	1.26	0.10	100.00
Calcite 9	97.71	0.59	0.00	1.60	0.10	100.00
Calcite 10	94.88	1.43	0.00	3.69	0.00	100.00
Calcite 11	97.69	0.42	0.00	1.89	0.00	100.00
Calcite 12	99.12	0.00	0.00	0.89	0.00	100.00
Calcite 13	96.83	0.77	0.00	2.19	0.21	100.00
Calcite 14	99.10	0.01	0.00	0.89	0.00	100.00
Calcite 15	98.77	0.08	0.00	1.15	0.00	100.00
Calcite 16	98.61	0.03	0.00	1.36	0.00	100.00
Calcite 17	98.35	0.09	0.00	1.45	0.11	100.00
Calcite 18	98.96	0.06	0.00	0.98	0.00	100.00
Calcite 19	98.88	0.04	0.00	1.08	0.00	100.00
Calcite 20	98.60	0.06	0.00	1.34	0.00	100.00
Calcite 21	98.74	0.11	0.00	1.04	0.11	100.00
Calcite 22	98.79	0.01	0.00	1.20	0.00	100.00
Calcite 23	97.13	0.71	0.00	1.52	0.64	100.00
Calcite 24	98.73	0.17	0.00	0.88	0.22	100.00
Calcite 25	99.39	0.07	0.00	0.54	0.00	100.00
Calcite 26	98.85	0.12	0.04	0.99	0.00	100.00
Calcite 27	98.69	0.14	0.00	1.09	0.09	100.00
Calcite 28	97.90	0.21	0.00	1.89	0.00	100.00
Calcite 29	98.89	0.09	0.00	0.91	0.11	100.00
Calcite 30	95.57	0.60	0.00	3.64	0.19	100.00
Calcite 31	98.42	0.40	0.00	0.92	0.26	100.00
Calcite 32	98.68	0.03	0.00	1.29	0.00	100.00
Average	98.23	0.24	0.00	1.45	0.08	--
Standard deviation	0.99	0.31	0.01	0.70	0.13	--
EPMA: calcite B (calcite replacing olivine)	**$CaCO_3$**	**$MgCO_3$**	**$SrCO_3$**	**$FeCO_3$**	**$MnCO_3$**	**Total**
Calcite 1	94.52	2.36	0.00	3.13	0.00	100.00
Calcite 2	96.92	0.51	0.00	2.58	0.00	100.00
Average	95.72	1.43	0.00	2.85	0.00	--
Standard deviation	1.70	1.31	0.00	0.39	0.00	--

B.5 List of chemical analyses in mol% of calcite grains in EET 96029

EPMA: calcite	**$CaCO_3$**	**$MgCO_3$**	**$SrCO_3$**	**$FeCO_3$**	**$MnCO_3$**	**Total**
Calcite 1	99.26	0.03	0.00	0.70	0.00	100.00
Calcite 2	99.25	0.02	0.00	0.74	0.00	100.00
Calcite 3	99.03	0.03	0.00	0.94	0.00	100.00
Calcite 4	98.78	0.04	0.00	1.18	0.00	100.00
Calcite 5	99.08	0.04	0.00	0.87	0.01	100.00
Calcite 6	99.04	0.03	0.00	0.93	0.00	100.00
Calcite 7	98.75	0.06	0.00	1.08	0.11	100.00
Calcite 8	98.82	0.04	0.00	1.14	0.00	100.00
Calcite 9	97.00	0.38	0.00	2.15	0.48	100.00
Calcite 10	98.78	0.12	0.00	1.10	0.00	100.00

Calcite 11	98.91	0.03	0.00	1.06	0.00	100.00
Calcite 12	99.30	0.02	0.00	0.68	0.00	100.00
Calcite 13	99.32	0.03	0.00	0.65	0.00	100.00
Calcite 14	98.57	0.09	0.00	1.17	0.17	100.00
Calcite 15	98.97	0.04	0.00	0.98	0.00	100.00
Calcite 16	98.69	0.07	0.00	1.24	0.00	100.00
Calcite 17	98.86	0.04	0.00	1.10	0.00	100.00
Calcite 18	95.46	0.70	0.00	2.24	1.60	100.00
Calcite 19	98.91	0.07	0.04	0.98	0.00	100.00
Calcite 20	94.60	1.26	0.00	2.43	1.71	100.00
Calcite 21	93.57	1.33	0.01	2.63	2.47	100.00
Calcite 22	99.04	0.05	0.00	0.91	0.00	100.00
Calcite 23	98.84	0.04	0.00	1.12	0.00	100.00
Calcite 24	98.50	0.24	0.00	1.26	0.01	100.00
Calcite 25	98.81	0.03	0.00	1.16	0.00	100.00
Calcite 26	98.80	0.10	0.00	0.93	0.17	100.00
Calcite 27	98.73	0.03	0.00	1.24	0.00	100.00
Calcite 28	99.06	0.04	0.00	0.90	0.00	100.00
Calcite 29	99.07	0.03	0.00	0.89	0.01	100.00
Average	98.44	0.17	0.00	1.17	0.22	--
Standard deviation	1.42	0.34	0.01	0.51	0.61	--

B.6 List of chemical analyses in mol% of Ca-carbonate in LON 94101

EPMA: aragonite	**$CaCO_3$**	**$MgCO_3$**	**$SrCO_3$**	**$FeCO_3$**	**$MnCO_3$**	**Total**
Aragonite 1	99.39	0.00	0.05	0.56	0.00	100.00
Aragonite 2	99.10	0.03	0.09	0.78	0.00	100.00
Aragonite 3	99.15	0.04	0.08	0.73	0.00	100.00
Aragonite 4	98.55	0.38	0.09	0.98	0.00	100.00
Aragonite 5	98.76	0.17	0.07	1.01	0.00	100.00
Aragonite 6	99.17	0.00	0.06	0.77	0.00	100.00
Aragonite 7	98.72	0.23	0.05	1.00	0.00	100.00
Aragonite 8	98.34	0.60	0.05	1.01	0.00	100.00
Aragonite 9	99.13	0.03	0.05	0.79	0.00	100.00
Aragonite 10	99.14	0.04	0.09	0.73	0.00	100.00
Aragonite 11	99.07	0.07	0.07	0.78	0.00	100.00
Aragonite 12	99.24	0.09	0.07	0.60	0.00	100.00
Aragonite 13	99.31	0.08	0.06	0.54	0.00	100.00
Average	99.01	0.14	0.07	0.79	0.00	--
Standard deviation	0.31	0.18	0.02	0.17	0.00	--
EPMA: calcite vein	**$CaCO_3$**	**$MgCO_3$**	**$SrCO_3$**	**$FeCO_3$**	**$MnCO_3$**	**Total**
Calcite vein 1	99.65	0.13	0.00	0.22	0.00	100.00
Calcite vein 2	99.69	0.11	0.00	0.21	0.00	100.00
Calcite vein 3	99.60	0.14	0.00	0.26	0.00	100.00
Average	99.65	0.12	0.00	0.23	0.00	--
Standard deviation	0.04	0.02	0.00	0.03	0.00	--
EPMA: calcite free	**$CaCO_3$**	**$MgCO_3$**	**$SrCO_3$**	**$FeCO_3$**	**$MnCO_3$**	**Total**
Calcite 1	99.19	0.12	0.00	0.70	0.00	100.00
Calcite 2	99.45	0.06	0.00	0.49	0.00	100.00
Calcite 3	98.19	0.71	0.00	1.10	0.00	100.00
Average	98.94	0.29	0.00	0.76	0.00	--
Standard deviation	0.66	0.36	0.00	0.31	0.00	0.00
EPMA; complete rimmed calcite	**$CaCO_3$**	**$MgCO_3$**	**$SrCO_3$**	**$FeCO_3$**	**$MnCO_3$**	**Total**
Calcite 1	99.48	0.00	0.00	0.52	0.00	100.00

Calcite 2	99.35	0.00	0.00	0.65	0.00	100.00
Calcite 3	99.34	0.00	0.00	0.66	0.00	100.00
Calcite 4	99.29	0.00	0.00	0.71	0.00	100.00
Calcite 5	99.33	0.00	0.00	0.67	0.00	100.00
Calcite 6	99.23	0.00	0.00	0.77	0.00	100.00
Calcite 7	99.24	0.00	0.00	0.76	0.00	100.00
Calcite 8	99.28	0.00	0.00	0.72	0.00	100.00
Average	99.32	0.00	0.00	0.68	0.00	--
Standard deviation	0.08	0.00	0.00	0.08	0.00	--
EPMA;: calcite replacing olivine	**$CaCO_3$**	**$MgCO_3$**	**$SrCO_3$**	**$FeCO_3$**	**$MnCO_3$**	**Total**
Calcite 1	99.50	0.00	0.00	0.50	0.00	100.00
Calcite 2	96.81	0.22	0.00	2.96	0.00	100.00
Calcite 3	97.40	0.28	0.00	2.32	0.00	100.00
Average	97.90	0.17	0.00	1.93	0.00	--
Standard deviation	1.410	0.149	0.000	1.275	0.000	--

B.7 List of chemical analyses in mol% of carbonate grains in Nogoya

EPMA: Ca-carbonate	**$CaCO_3$**	**$MgCO_3$**	**$SrCO_3$**	**$FeCO_3$**	**$MnCO_3$**	**Total**
Aragonite 1	99.26	0.12	0.14	0.47	0.00	100.00
Calcite 1	99.66	0.03	0.00	0.31	0.00	100.00
Calcite 2	99.61	0.03	0.00	0.35	0.00	100.00
Calcite 3	99.23	0.07	0.00	0.70	0.00	100.00
Calcite 4	98.74	0.19	0.00	1.07	0.00	100.00
Calcite 5	99.47	0.21	0.00	0.33	0.00	100.00
Calcite 6	96.21	2.18	0.00	1.61	0.00	100.00
Calcite 7	96.68	1.29	0.00	2.02	0.01	100.00
Calcite 8	99.28	0.17	0.00	0.55	0.00	100.00
Calcite 9	98.68	0.12	0.00	1.20	0.00	100.00
Calcite 10	99.26	0.05	0.00	0.69	0.00	100.00
Calcite 11	99.62	0.05	0.00	0.33	0.00	100.00
Calcite 12	98.72	0.77	0.00	0.51	0.00	100.00
Calcite 13	99.17	0.10	0.00	0.73	0.00	100.00
Calcite 14	98.10	0.55	0.00	1.35	0.00	100.00
Calcite 15	99.56	0.04	0.00	0.40	0.00	100.00
Calcite 16	97.71	0.62	0.00	1.67	0.00	100.00
Calcite 17	99.67	0.01	0.00	0.32	0.00	100.00
Average (calcite)	98.79	0.38	0.00	0.83	0.00	--
S. deviation (calcite)	1.05	0.58	0.00	0.55	0.00	
EPMA: dolomite	**$CaCO_3$**	**$MgCO_3$**	**$SrCO_3$**	**$FeCO_3$**	**$MnCO_3$**	**Total**
Dolomite 1	46.18	40.75	0.00	10.56	2.51	100
Dolomite 2	42.87	42.39	0.00	10.82	3.92	100
Dolomite 3	51.41	41.37	0.00	5.64	1.58	100
Dolomite 4	49.21	42.83	0.00	6.16	1.80	100
Average	47.42	41.84	0.00	8.29	2.45	--
Standard deviation	3.71	0.95	0.00	2.78	1.05	

B.8 List of chemical analyses in mole% of Ca-carbonate grains in Cold Bokkeveld

EPMA; calcite rimmed	**$CaCO_3$**	**$MgCO_3$**	**$SrCO_3$**	**$FeCO_3$**	**$MnCO_3$**	**Total**
Calcite rimmed 1	98.86	0.02	0.01	1.11	0.00	100.00
Calcite rimmed 2	99.09	0.02	0.00	0.90	0.00	100.00
Calcite rimmed 3	99.00	0.01	0.00	0.99	0.00	100.00
Calcite rimmed 4	99.06	0.01	0.00	0.93	0.00	100.00
Calcite rimmed 5	99.08	0.03	0.00	0.89	0.00	100.00

Calcite rimmed 6	99.47	0.05	0.00	0.48	0.00	100.00
Calcite rimmed 7	99.36	0.04	0.00	0.60	0.00	100.00
Calcite rimmed 8	99.23	0.03	0.00	0.71	0.03	100.00
Calcite rimmed 9	98.76	0.06	0.00	1.18	0.00	100.00
Calcite rimmed 10	99.20	0.00	0.00	0.79	0.00	100.00
Calcite rimmed 11	99.05	0.04	0.00	0.91	0.00	100.00
Calcite rimmed 12	98.61	0.03	0.00	1.37	0.00	100.00
Calcite rimmed 13	98.87	0.01	0.00	1.12	0.00	100.00
Calcite rimmed 14	99.03	0.00	0.00	0.97	0.00	100.00
Calcite rimmed 15	99.05	0.00	0.00	0.95	0.00	100.00
Calcite rimmed 16	99.03	0.04	0.00	0.93	0.00	100.00
Average	99.05	0.02	0.00	0.93	0.00	--
Standard deviation	0.21	0.02	0.00	0.22	0.01	0.00
EPMA: aragonite	**$CaCO_3$**	**$MgCO_3$**	**$SrCO_3$**	**$FeCO_3$**	**$MnCO_3$**	**Total**
Aragonite 1	99.07	0.08	0.06	0.79	0.00	100.00
Aragonite 2	99.23	0.01	0.09	0.66	0.00	100.00
Aragonite 3	98.97	0.11	0.09	0.83	0.00	100.00
Aragonite 4	98.62	0.27	0.10	1.01	0.00	100.00
Aragonite 5	98.58	0.06	0.06	1.30	0.00	100.00
Average	98.90	0.11	0.08	0.92	0.00	--
Standard deviation	0.28	0.10	0.02	0.25	0.00	0.00
EPMA: calcite rims-free	**$CaCO_3$**	**$MgCO_3$**	**$SrCO_3$**	**$FeCO_3$**	**$MnCO_3$**	**Total**
Calcite rims-free 1	99.08	0.02	0.00	0.90	0.00	100.00
Calcite rims-free 2	98.70	0.05	0.00	1.25	0.00	100.00
Calcite rims-free 3	98.82	0.04	0.00	1.14	0.00	100.00
Calcite rims-free 4	98.89	0.03	0.00	1.08	0.00	100.00
Average	98.87	0.04	0.00	1.09	0.00	--
Standard deviation	0.16	0.01	0.00	0.15	0.00	0.00
EPMA: calcite replacing olivine	**$CaCO_3$**	**$MgCO_3$**	**$SrCO_3$**	**$FeCO_3$**	**$MnCO_3$**	**Total**
Calcite replacing olivine 1	98.42	0.05	0.00	1.53	0.00	100.00

B.9 List of chemical analyses in mole% of carbonate grains in QUE 93005

EDX: breunnerite	**$CaCO_3$**	**$MgCO_3$**	**$SrCO_3$**	**$FeCO_3$**	**$MnCO_3$**	**$CaCO_3$**	**SiO2**
Breunnerite 1	2.82	53.20	0.00	40.30	3.68	0.00	0.81
Breunnerite 2	3.53	59.51	0.00	34.72	2.24	0.00	1.39
Breunnerite 3	1.71	63.17	0.00	34.45	0.67	0.00	1.48
Breunnerite 4	3.90	62.91	0.00	31.63	1.56	0.00	1.51
Breunnerite 5	3.30	50.83	0.00	40.02	5.85	0.00	1.54
Breunnerite 6	3.68	57.46	0.00	35.95	2.91	0.00	1.65
Breunnerite 7	4.09	61.74	0.22	31.26	2.69	0.00	1.66
Breunnerite 8	5.65	47.68	0.33	43.38	2.96	0.00	1.71
Breunnerite 9	2.72	64.31	0.00	31.65	1.33	0.00	1.82
Breunnerite 10	4.04	55.09	0.00	37.33	3.54	0.00	1.95
Breunnerite 11	4.48	61.90	0.00	30.83	2.79	0.00	1.99
Breunnerite 12	1.25	66.08	0.00	31.65	1.03	0.00	2.04
Breunnerite 13	4.91	57.69	0.00	33.58	3.82	0.00	2.41
Breunnerite 14	1.88	65.32	0.00	31.90	0.90	0.00	2.46
Breunnerite 15	4.60	55.12	0.00	35.18	5.10	0.00	2.51
Breunnerite 16	4.31	53.12	0.00	36.54	6.02	0.00	2.68
Breunnerite 17	3.58	57.15	0.00	35.09	4.19	0.00	2.75

Breunnerite 18	5.17	60.45	0.00	31.28	3.10	0.01	2.79
Breunnerite 19	2.11	66.38	0.24	29.96	1.31	0.00	2.98
Breunnerite 20	5.06	61.14	0.00	30.39	3.41	0.00	3.16
Breunnerite 21	1.90	65.46	0.00	31.43	1.21	0.00	3.66
Breunnerite 22	1.46	66.33	0.00	31.20	1.02	0.00	3.72
Breunnerite 23	5.22	57.16	0.00	31.86	5.76	0.00	3.83
Breunnerite 24	5.03	62.34	0.23	29.20	3.20	0.00	4.09
Breunnerite 25	2.11	66.54	0.00	30.26	1.09	0.00	4.97
Average	3.54	59.92	0.04	33.64	2.86	0.00	2.46
Standard deviation	1.35	5.30	0.10	3.63	1.64	0.00	--
EPMA: breunnerite	**$CaCO_3$**	**$MgCO_3$**	**$SrCO_3$**	**$FeCO_3$**	**$MnCO_3$**	**NiCO3**	**Total**
Breunnerite 1	2.71	57.96	0.00	36.05	3.28	0.00	100.00
Breunnerite 2	1.07	65.91	0.00	32.24	0.71	0.07	100.00
Average	1.90	61.90	0.00	34.10	2.00	0.03	--
Standard deviation	1.16	5.63	0.00	2.70	1.81	0.05	--
EDX: Ca-poor dolomite	**$CaCO_3$**	**$MgCO_3$**	**$SrCO_3$**	**$FeCO_3$**	**$MnCO_3$**	**NiCO3**	**SiO2**
Ca-poor dolomite 1	43.07	41.12	0.00	13.92	1.89	0.00	1.16
Ca-poor dolomite 2	43.90	45.37	0.00	10.09	0.64	0.00	1.75
Ca-poor dolomite 3	42.49	45.55	0.00	10.63	1.33	0.00	2.30
Ca-poor dolomite 4	42.54	45.03	0.00	11.17	1.25	0.00	2.42
Ca-poor dolomite 5	42.56	45.53	0.00	10.92	0.99	0.00	2.57
Ca-poor dolomite 6	42.47	44.45	0.00	11.71	1.36	0.00	2.75
Ca-poor dolomite 7	41.54	45.90	0.00	11.13	1.43	0.00	3.08
Ca-poor dolomite 8	39.48	45.65	0.00	13.39	1.48	0.00	3.13
Ca-poor dolomite 9	41.77	45.58	0.00	11.20	1.44	0.00	3.38
Ca-poor dolomite 10	39.17	43.21	0.00	13.05	4.58	0.00	3.70
Ca-poor dolomite 11	42.43	40.27	0.00	15.66	1.64	0.00	3.81
Ca-poor dolomite 12	40.62	43.40	0.00	14.64	1.33	0.00	3.94
Ca-poor dolomite 13	41.31	44.59	0.00	12.58	1.52	0.00	4.21
Ca-poor dolomite 14	40.34	45.33	0.21	12.65	1.46	0.00	4.73
Ca-poor dolomite 15	41.00	44.91	0.00	13.03	1.06	0.00	4.74
Ca-poor dolomite 16	40.02	46.85	0.00	11.70	1.43	0.00	4.76
Ca-poor dolomite 17	40.39	46.92	0.00	11.18	1.51	0.00	4.95
Ca-poor dolomite 18	37.85	48.36	0.00	12.33	1.46	0.00	6.30
Ca-poor dolomite 19	37.52	48.75	0.00	12.77	0.96	0.00	6.85
Ca-poor dolomite 20	34.01	46.56	0.23	14.90	4.30	0.00	7.79
Average	40.72	45.17	0.02	12.43	1.65	0.00	3.92
Standard deviation	2.32	2.06	0.07	1.52	0.99	0.00	1.69
EPMA: Ca-poor dolomite	**$CaCO_3$**	**$MgCO_3$**	**$SrCO_3$**	**$FeCO_3$**	**$MnCO_3$**	**$NiCO_3$**	**SiO_2**
Ca-poor dolomite 1	43.12	44.50	0.04	10.52	1.77	0.05	0.76
EDX: dolomite	**$CaCO_3$**	**$MgCO_3$**	**$SrCO_3$**	**$FeCO_3$**	**$MnCO_3$**	**$NiCO_3$**	**Total**
Dolomite 1	49.86	33.72	0.00	11.42	5.01	0.00	100.00
Dolomite 2	49.86	34.14	0.00	10.66	5.34	0.00	100.00
Dolomite 3	49.99	39.66	0.00	6.03	4.32	0.00	100.00
Dolomite 4	51.29	36.37	0.00	8.23	4.11	0.00	100.00
Dolomite 5	51.34	37.83	0.00	7.28	3.55	0.00	100.00

Dolomite 6	51.50	37.69	0.00	6.57	4.24	0.00	100.00
Dolomite 7	51.63	34.92	0.00	8.46	4.99	0.00	100.00
Dolomite 8	51.90	33.32	0.00	9.67	5.11	0.00	100.00
Dolomite 9	51.99	35.67	0.00	8.45	3.89	0.00	100.00
Dolomite 10	52.49	32.91	0.00	8.23	6.37	0.00	100.00
Dolomite 11	53.65	35.80	0.00	6.47	4.08	0.00	100.00
Dolomite 12	53.77	37.93	0.00	4.86	3.44	0.00	100.00
Dolomite 13	53.98	31.93	0.00	8.05	6.03	0.00	100.00
Dolomite 14	54.07	36.32	0.00	5.88	3.72	0.00	100.00
Dolomite 15	54.43	37.05	0.00	4.91	3.61	0.00	100.00
Dolomite 16	54.43	37.04	0.00	5.08	3.45	0.00	100.00
Dolomite 17	55.20	33.28	0.00	6.41	5.11	0.00	100.00
Dolomite 18	55.63	31.64	0.00	6.98	5.76	0.00	100.00
Average	52.61	35.40	0.00	7.42	4.56	0.00	--
Standard deviation	1.84	2.29	0.00	1.89	0.93	0.00	--
EPMA: dolomite	**$CaCO_3$**	**$MgCO_3$**	**$SrCO_3$**	**$FeCO_3$**	**$MnCO_3$**	**$NiCO_3$**	**Total**
Dolomite 1	49.67	37.37	0.00	9.48	3.42	0.06	100.00
Dolomite 2	50.45	36.12	0.00	8.83	4.53	0.07	100.00
Dolomite 3	50.79	33.67	0.00	9.92	5.49	0.13	100.00
Dolomite 4	50.83	32.87	0.00	11.09	5.15	0.05	100.00
Dolomite 5	51.22	36.37	0.00	8.99	3.37	0.05	100.00
Dolomite 6	52.40	32.74	0.00	7.88	6.91	0.07	100.00
Dolomite 7	52.41	32.76	0.00	9.82	4.96	0.06	100.00
Dolomite 8	50.60	40.38	0.00	4.85	4.17	0.00	100.00
Dolomite 9	51.33	34.20	0.00	9.52	4.94	0.00	100.00
Dolomite 10	52.04	38.58	0.05	5.93	3.36	0.05	100.00
Dolomite 11	52.54	35.39	0.00	7.91	4.16	0.00	100.00
Dolomite 12	52.70	36.59	0.00	6.86	3.78	0.07	100.00
Average	51.42	35.59	0.00	8.42	4.52	0.05	--
Standard deviation	0.99	2.45	0.01	1.81	1.05	0.04	--
EDX: calcite	**$CaCO_3$**	**$MgCO_3$**	**$SrCO_3$**	**$FeCO_3$**	**$MnCO_3$**	**$NiCO_3$**	**Total**
Calcite 1	98.96	0.39	0.00	0.65	0.00	0.00	100.00
Calcite 2	98.78	0.26	0.00	0.57	0.39	0.00	100.00
Calcite 3	99.77	0.23	0.00	0.00	0.00	0.00	100.00
Calcite 4	98.42	0.74	0.00	0.84	0.00	0.00	100.00
Calcite 5	99.76	0.24	0.00	0.00	0.00	0.00	100.00
Calcite 6	99.11	0.19	0.00	0.69	0.00	0.00	100.00
Calcite 7	99.12	0.00	0.00	0.88	0.00	0.00	100.00
Calcite 8	100.00	0.00	0.00	0.00	0.00	0.00	100.00
Calcite 9	99.36	0.00	0.00	0.64	0.00	0.00	100.00
Calcite 10	100.00	0.00	0.00	0.00	0.00	0.00	100.00
Calcite 11	99.80	0.20	0.00	0.00	0.00	0.00	100.00
Calcite 12	99.45	0.00	0.00	0.55	0.00	0.00	100.00
Calcite 13	99.77	0.23	0.00	0.00	0.00	0.00	100.00
Calcite 14	99.36	0.00	0.00	0.64	0.00	0.00	100.00
Calcite 15	99.52	0.00	0.00	0.48	0.00	0.00	100.00
Calcite 16	99.80	0.20	0.00	0.00	0.00	0.00	100.00

Calcite 17	100.00	0.00	0.00	0.00	0.00	0.00	100.00
Calcite 18	99.57	0.43	0.00	0.00	0.00	0.00	100.00
Average	99.47	0.17	0.00	0.33	0.02	0.00	--
Standard deviation	0.45	0.20	0.00	0.35	0.09	0.00	--
EBMA: calcite	**$CaCO_3$**	**$MgCO_3$**	**$SrCO_3$**	**$FeCO_3$**	**$MnCO_3$**	**$NiCO_3$**	**Total**
Calcite 1	99.60	0.00	0.11	0.29	0.00	0.00	100.00
Calcite 2	99.44	0.00	0.00	0.37	0.15	0.04	100.00
Calcite 3	99.09	0.16	0.00	0.64	0.10	0.00	100.00
Calcite 4	98.31	0.30	0.00	0.66	0.67	0.06	100.00
Calcite 5	99.62	0.00	0.08	0.30	0.00	0.00	100.00
Calcite 6	99.45	0.00	0.07	0.40	0.02	0.05	100.00
Calcite 7	99.50	0.09	0.06	0.31	0.04	0.00	100.00
Calcite 8	99.59	0.00	0.06	0.32	0.02	0.00	100.00
Calcite 9	99.78	0.00	0.00	0.19	0.03	0.00	100.00
Average	99.38	0.06	0.04	0.39	0.11	0.02	--
Standard deviation	0.44	0.12	0.04	0.16	0.21	0.03	--

B.10 List of chemical analyses in mole% of calcite grains in LAP 031166

EPMA: calcite	**$CaCO_3$**	**$MgCO_3$**	**$SrCO_3$**	**$FeCO_3$**	**$MnCO_3$**	**Total**
Calcite 1	97.94	0.31	0.00	1.76	0.00	100.00
Calcite 2	98.40	0.23	0.00	1.37	0.00	100.00
Calcite 3	98.77	0.04	0.00	1.19	0.00	100.00
Calcite 4	99.03	0.05	0.00	0.92	0.00	100.00
Calcite 5	98.56	0.13	0.00	1.31	0.00	100.00
Calcite 6	98.24	0.54	0.00	1.22	0.00	100.00
Calcite 7	97.15	0.81	0.00	2.05	0.00	100.00
Calcite 8	98.90	0.04	0.00	1.06	0.00	100.00
Calcite 9	97.13	0.81	0.00	2.06	0.00	100.00
Calcite 10	98.83	0.05	0.00	1.12	0.00	100.00
Calcite 11	99.19	0.03	0.00	0.78	0.00	100.00
Calcite 12	98.79	0.13	0.00	1.08	0.00	100.00
Calcite 13	98.90	0.04	0.00	1.06	0.00	100.00
Calcite 14	98.91	0.07	0.00	1.03	0.00	100.00
Calcite 15	97.95	0.20	0.00	1.84	0.00	100.00
Calcite 16	99.13	0.03	0.00	0.83	0.00	100.00
Calcite 17	97.49	1.20	0.00	1.31	0.00	100.00
Calcite 18	99.08	0.03	0.00	0.89	0.00	100.00
Calcite 19	98.46	0.40	0.00	1.14	0.00	100.00
Calcite 20	99.17	0.08	0.00	0.76	0.00	100.00
Calcite 21	98.97	0.20	0.00	0.82	0.00	100.00
Average	98.52	0.26	0.00	1.22	0.00	--
Standard deviation	0.65	0.32	0.00	0.40	0.00	0.00

B.11 List of chemical analyses in mole% of carbonate grains in SCO 06043

EPMA: calcite grains	**$CaCO_3$**	**$MgCO_3$**	**$SrCO_3$**	**$FeCO_3$**	**$MnCO_3$**	**Total**
Calcite 1	98.64	0.27	0.00	0.72	0.37	100.00

Calcite 2	98.92	0.14	0.04	0.90	0.00	100.00
Calcite 3	98.68	0.25	0.00	0.83	0.24	100.00
Calcite 4	98.24	0.35	0.00	1.04	0.36	100.00
Calcite 5	97.60	0.50	0.00	1.61	0.29	100.00
Calcite 6	98.87	0.29	0.07	0.77	0.00	100.00
Calcite 7	96.85	0.83	0.00	1.99	0.34	100.00
Calcite 8	97.08	0.96	0.05	1.64	0.27	100.00
Calcite 9	98.22	0.51	0.00	0.99	0.28	100.00
Calcite 10	99.26	0.15	0.00	0.59	0.00	100.00
Calcite 11	98.53	0.78	0.00	0.69	0.00	100.00
Calcite 12	99.76	0.09	0.00	0.15	0.00	100.00
Calcite 13	98.89	0.35	0.00	0.76	0.00	100.00
Calcite 14	98.94	0.26	0.06	0.74	0.00	100.00
Calcite 15	99.08	0.16	0.00	0.76	0.00	100.00
Calcite 16	98.61	0.33	0.00	1.06	0.00	100.00
Calcite 17	98.94	0.20	0.00	0.48	0.38	100.00
Calcite 18	99.25	0.23	0.00	0.52	0.00	100.00
Average	98.58	0.37	0.01	0.90	0.14	--
Standard deviation	0.75	0.25	0.02	0.45	0.16	--
EPMA: calcite in dolomite	**$CaCO_3$**	**$MgCO_3$**	**$SrCO_3$**	**$FeCO_3$**	**$MnCO_3$**	**Total**
Calcite 1	99.1	0.32	0.00	0.56	0.00	100.0
Calcite 2	99.2	0.36	0.00	0.47	0.00	100.0
Calcite 3	98.5	0.74	0.00	0.79	0.00	100.0
Calcite 4	93.2	5.01	0.00	1.02	0.79	100.0
Calcite 5	99.3	0.13	0.00	0.55	0.00	100.0
Calcite 6	94.8	2.76	0.00	1.20	1.28	100.0
Average	97.34	1.55	0.00	0.76	0.35	--
Standard deviation	2.67	1.95	0.00	0.29	0.56	--
EPMA: dolomite grain	**$CaCO_3$**	**$MgCO_3$**	**$SrCO_3$**	**$FeCO_3$**	**$MnCO_3$**	**Total**
Dolomite 1	55.92	39.82	0.00	4.25	0.00	100.00
Dolomite 2	48.03	36.28	0.00	7.89	7.81	100.00
Dolomite 3	53.27	40.10	0.00	4.01	2.61	100.00
Dolomite 4	54.21	40.12	0.00	3.38	2.30	100.00
Dolomite 5	53.56	35.96	0.00	6.69	3.79	100.00
Dolomite 6	53.54	35.04	0.00	7.23	4.20	100.00
Dolomite 7	56.10	35.95	0.00	5.08	2.86	100.00
Dolomite 8	47.77	40.11	0.00	10.17	1.95	100.00
Dolomite 9	51.37	39.81	0.00	4.36	4.47	100.00
Dolomite 10	61.46	31.92	0.00	4.41	2.21	100.00
Dolomite 11	53.99	39.87	0.00	3.68	2.46	100.00
Dolomite 12	53.00	41.10	0.00	2.55	3.35	100.00
Dolomite 13	50.95	38.67	0.00	5.55	4.83	100.00
Dolomite 14	52.18	41.86	0.00	4.08	1.87	100.00
Dolomite 15	50.79	38.17	0.00	7.12	3.93	100.00
Dolomite 16	52.11	43.19	0.00	2.61	2.09	100.00
Dolomite 17	52.20	41.85	0.00	3.23	2.71	100.00

Dolomite 18	53.64	39.76	0.00	4.26	2.34	100.00
Dolomite 19	52.45	41.51	0.00	4.30	1.74	100.00
Dolomite 20	53.29	39.51	0.00	4.86	2.35	100.00
Dolomite 21	52.32	42.09	0.00	3.23	2.37	100.00
Dolomite 22	46.28	39.72	0.00	7.26	6.74	100.00
Dolomite 23	51.79	42.84	0.00	3.24	2.12	100.00
Dolomite 24	51.42	41.21	0.00	5.30	2.07	100.00
Dolomite 25	51.98	43.09	0.00	2.68	2.26	100.00
Dolomite 26	52.67	39.03	0.00	6.02	2.27	100.00
Dolomite 27	52.87	41.64	0.00	3.50	1.98	100.00
Dolomite 28	50.28	41.88	0.00	4.84	3.00	100.00
Dolomite 29	67.70	22.84	0.00	5.70	3.76	100.00
Dolomite 30	50.91	41.00	0.00	5.75	2.34	100.00
Dolomite 31	51.76	41.79	0.00	3.32	3.12	100.00
Dolomite 32	52.12	41.61	0.00	2.65	3.62	100.00
Dolomite 33	51.82	40.19	0.00	5.09	2.90	100.00
Dolomite 34	51.96	42.50	0.00	2.67	2.87	100.00
Dolomite 35	48.16	39.87	0.00	5.56	6.41	100.00
Dolomite 36	51.81	40.46	0.00	5.07	2.66	100.00
Dolomite 37	54.64	39.66	0.00	3.46	2.24	100.00
Dolomite 38	51.95	41.21	0.00	4.64	2.20	100.00
Dolomite 39	63.23	31.38	0.00	3.32	2.08	100.00
Dolomite 40	59.72	31.15	0.00	6.11	3.02	100.00
Average	53.13	39.14	0.00	4.73	3.00	--
Standard deviation	3.99	4.01	0.00	1.68	1.44	--
EPMA: dolomite vein	**$CaCO_3$**	**$MgCO_3$**	**$SrCO_3$**	**$FeCO_3$**	**$MnCO_3$**	**Total**
Dolomite 1	53.86	45.35	0.00	0.79	0.00	100.00
Dolomite 2	57.08	42.32	0.00	0.60	0.00	100.00
Average	55.47	43.83	0.00	0.69	0.00	--
Standard deviation	2.28	2.15	0.00	0.13	0.00	--

B.12 List of chemical analyses in mole% of calcite grains in ALH 88045

EPMA: calcite grains	CaCO3	MgCO3	SrCO3	FeCO3	MnCO3	Total
Calcite 1	98.83	0.24	0.00	0.66	0.27	100.00
Calcite 2	97.31	1.28	0.00	1.00	0.41	100.00
Calcite 3	97.58	0.64	0.00	0.70	1.08	100.00
Calcite 4	97.42	0.67	0.00	0.78	1.12	100.00
Calcite 5	98.99	0.20	0.00	0.81	0.00	100.00
Calcite 6	99.08	0.09	0.00	0.50	0.33	100.00
Calcite 7	97.07	1.07	0.00	1.05	0.81	100.00
Calcite 8	98.17	0.30	0.00	1.01	0.51	100.00
Calcite 9	98.97	0.19	0.00	0.84	0.00	100.00
Average	98.16	0.52	0.00	0.82	0.50	--
Standard deviation	0.82	0.42	0.00	0.18	0.42	

Appendix C

C.1. CL spectroscopy results of the zoned calcite grains in Murray

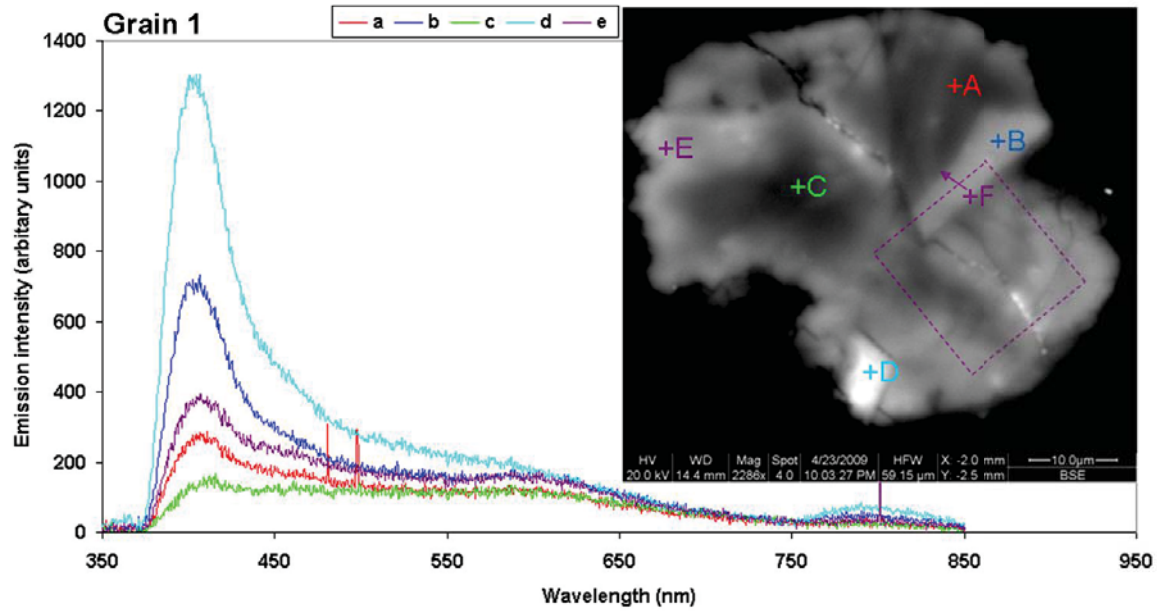

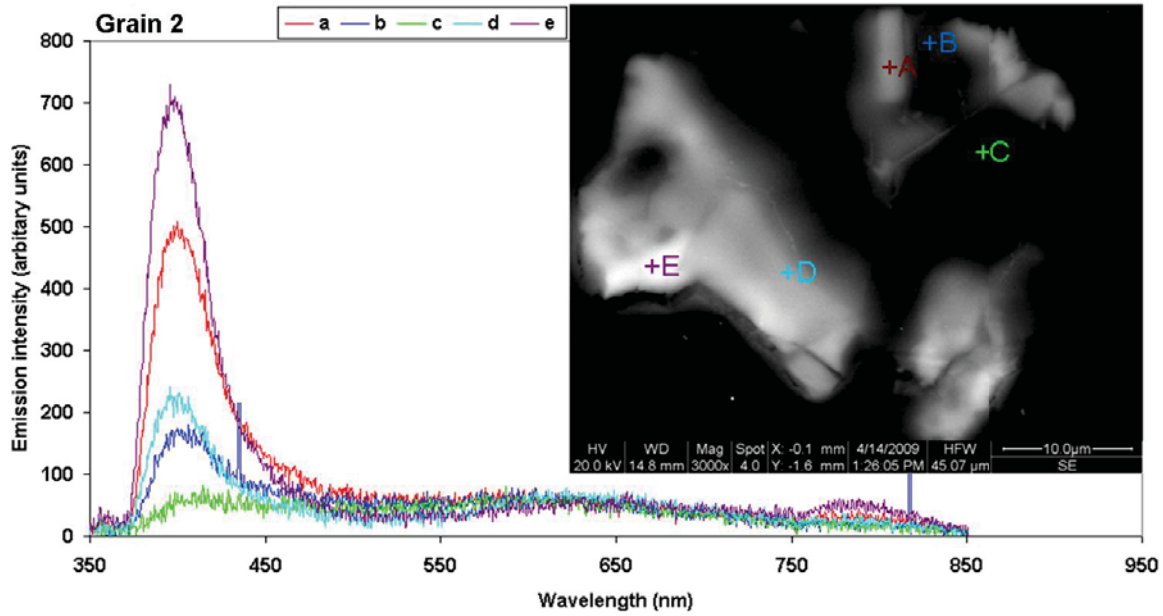

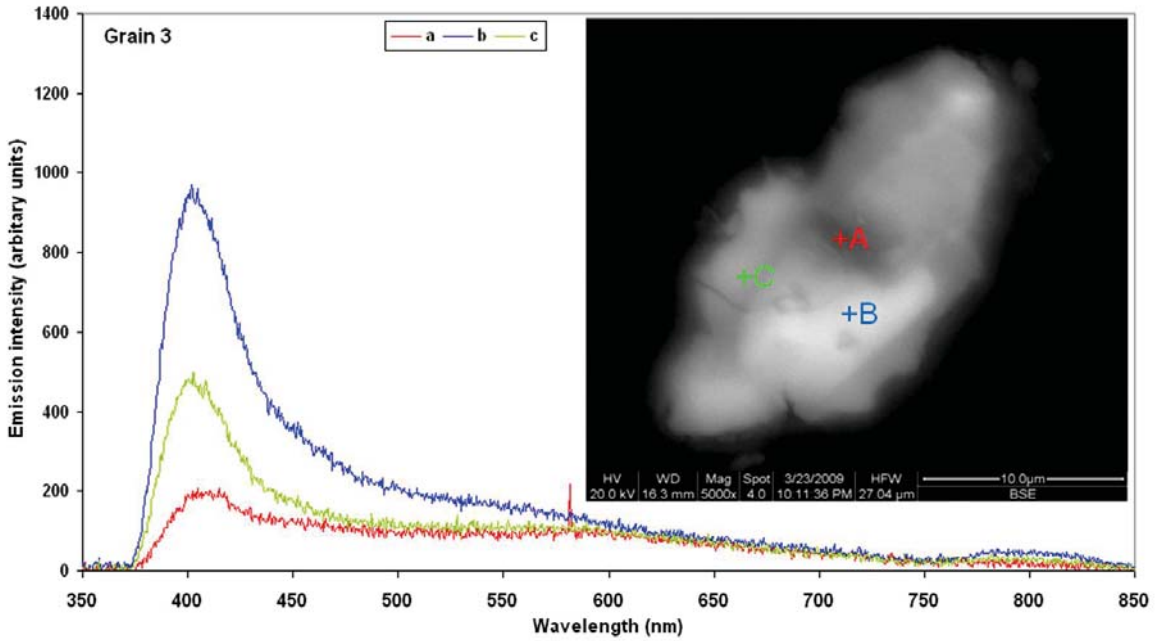
Grain 3
a
b
c
Emission intensity (arbitary units)
Wavelength (nm)
+A
+C
+B
HV 20.0 kV
WD 16.3 mm
Mag 5000x
Spot 4.0
3/23/2009 10:11:36 PM
HFW 27.04 µm
10.0µm
BSE

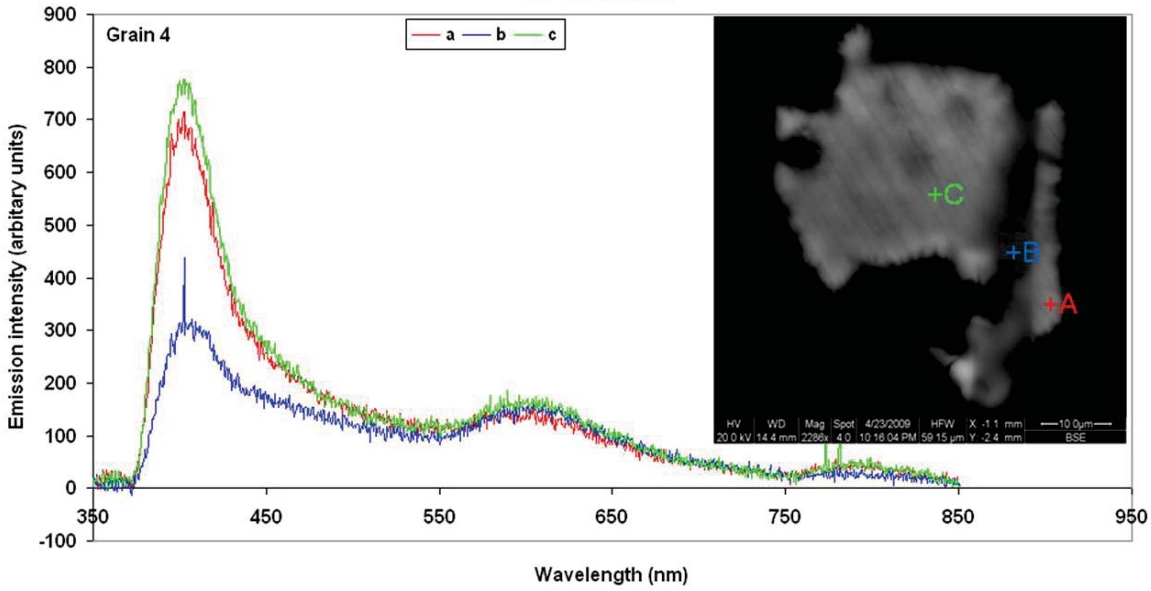
Grain 4
a
b
c
Emission intensity (arbitary units)
Wavelength (nm)
+C
+B
+A
HV 20.0 kV
WD 14.4 mm
Mag 2288x
Spot 4.0
4/23/2009 10:16:04 PM
HFW 59.15 µm
X -1.1 mm
Y -2.4 mm
10.0µm
BSE

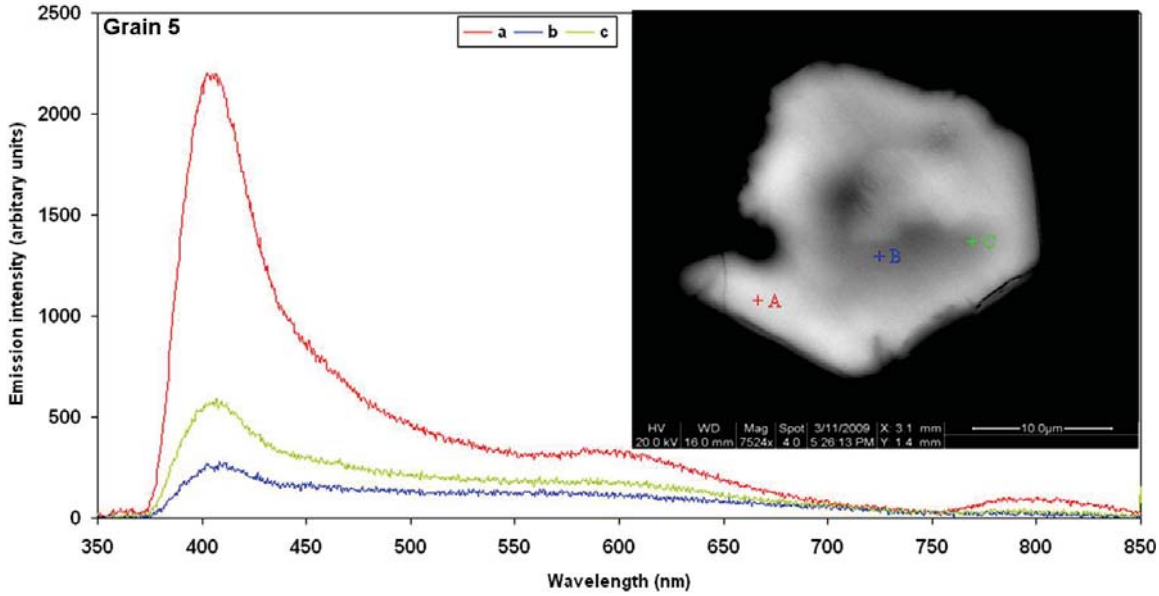
Grain 5
a
b
c
Emission intensity (arbitary units)
Wavelength (nm)
+B
+C
+A
HV 20.0 kV
WD 16.0 mm
Mag 7524x
Spot 4.0
3/11/2009 5:26:13 PM
X 3.1 mm
Y 1.4 mm
10.0µm

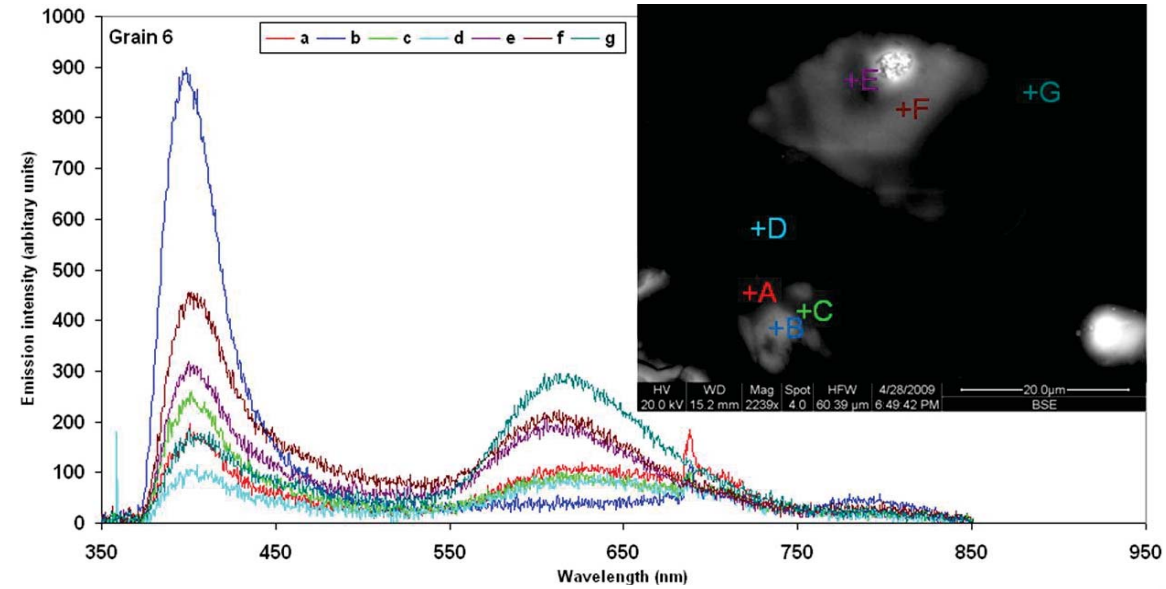
Grain 6
a b c d e f g
Emission intensity (arbitary units)
Wavelength (nm)
+E
+F
+G
+D
+A
+C
+B
HV 20.0 kV
WD 15.2 mm
Mag 2239x
Spot 4.0
HFW 60.39 µm
4/28/2009 6:49:42 PM
20.0µm
BSE

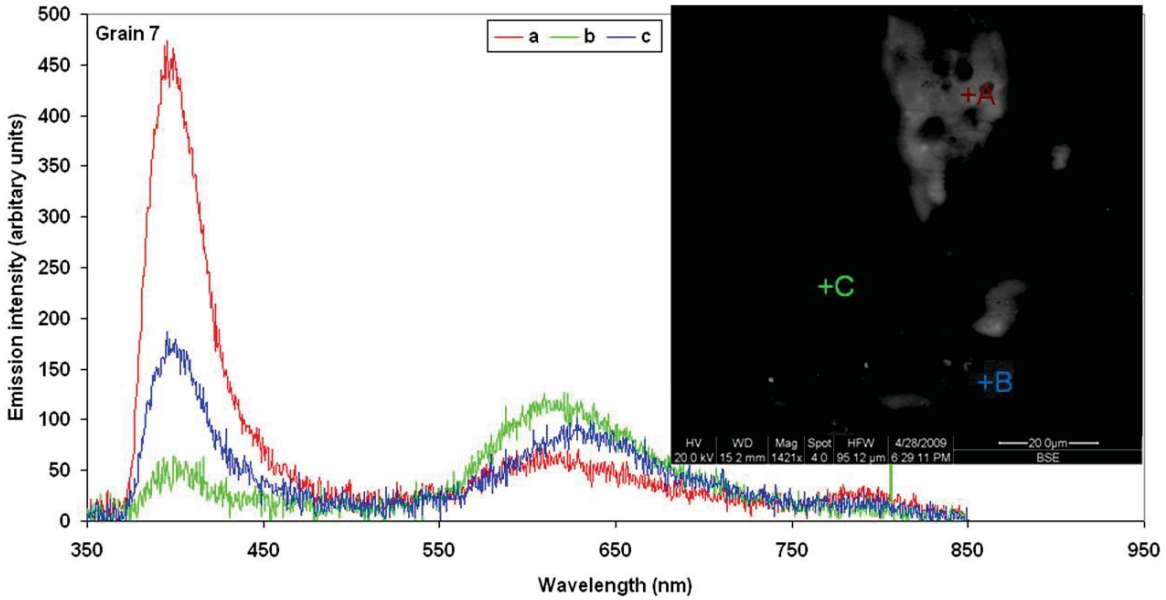
Grain 7
a b c
Emission intensity (arbitary units)
Wavelength (nm)
+A
+C
+B
HV 20.0 kV
WD 15.2 mm
Mag 1421x
Spot 4.0
HFW 95.12 µm
4/28/2009 6:29:11 PM
20.0µm
BSE

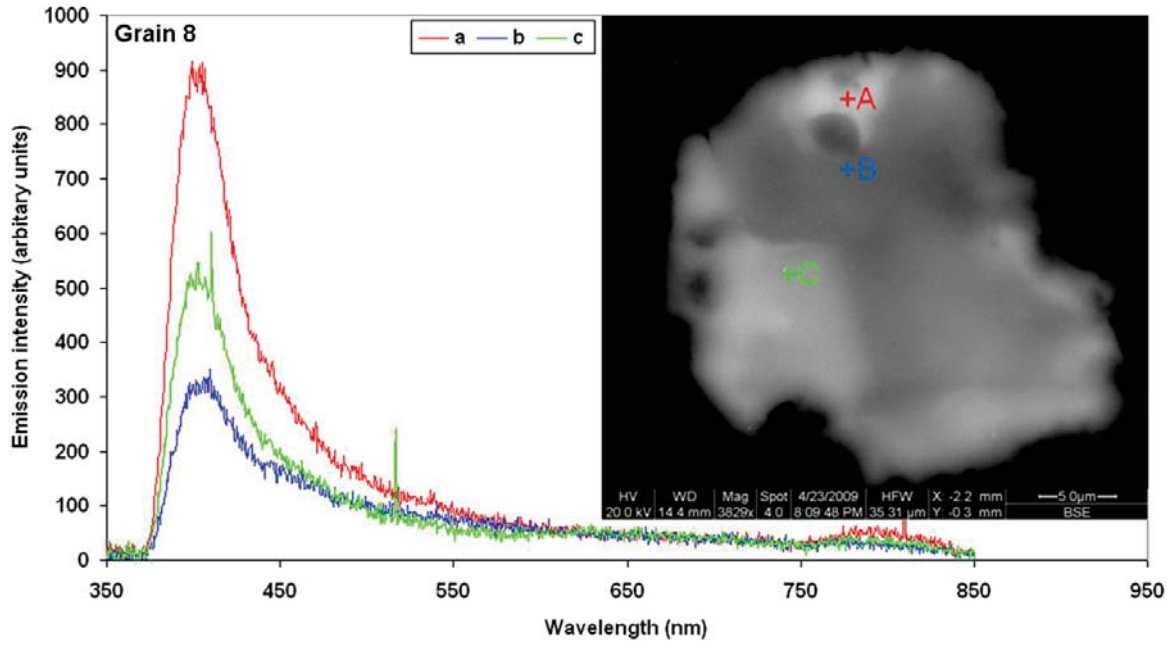
Grain 8
a b c
Emission intensity (arbitary units)
Wavelength (nm)
+A
+B
+C
HV 20.0 kV
WD 14.4 mm
Mag 3829x
Spot 4.0
4/23/2009 8:09:48 PM
HFW 35.31 µm
X -2.2 mm
Y -0.3 mm
5.0µm
BSE

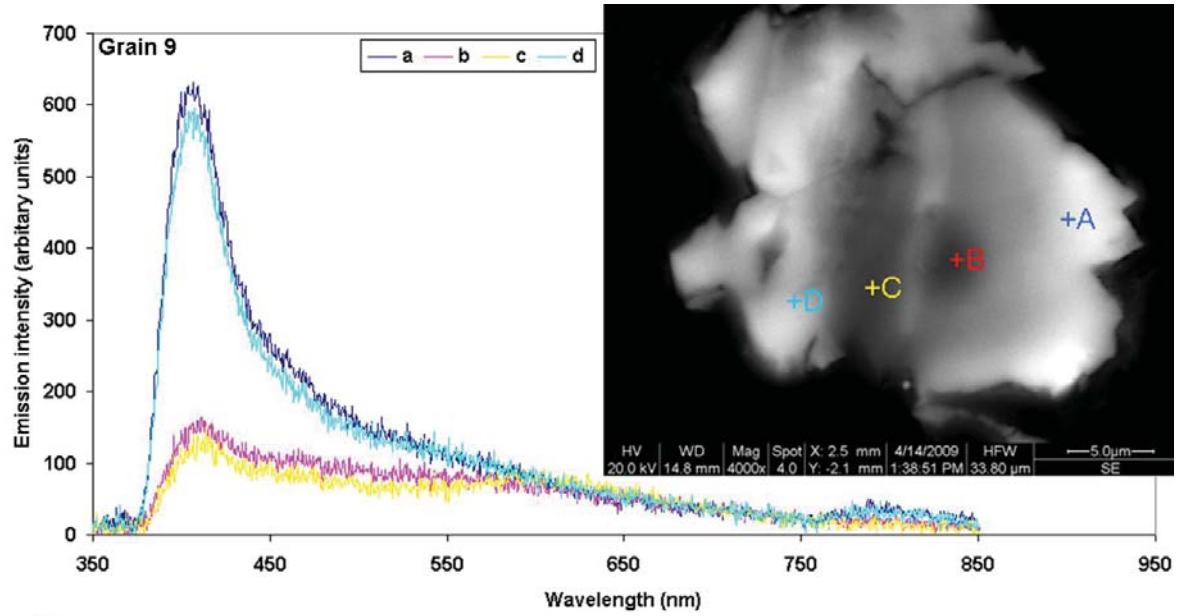
Grain 9
a b c d
Emission intensity (arbitary units)
Wavelength (nm)
+A
+B
+C
+D
HV 20.0 kV | WD 14.8 mm | Mag 4000x | Spot 4.0 | X: 2.5 mm Y: -2.1 mm | 4/14/2009 1:38:51 PM | HFW 33.80 µm | 5.0µm SE

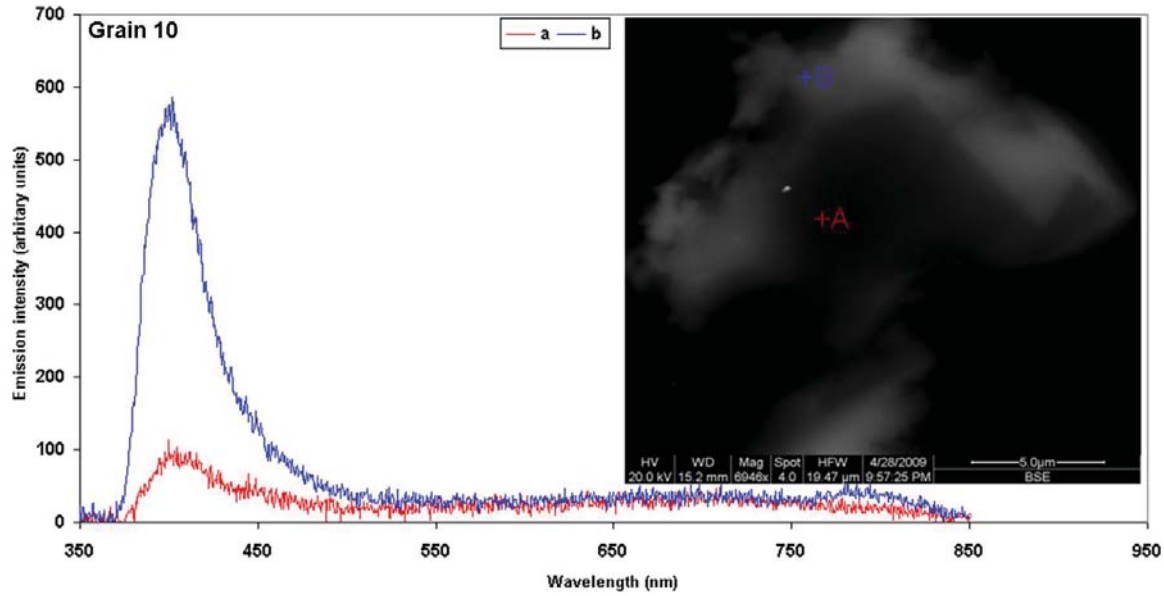
Grain 10
a b
Emission intensity (arbitary units)
Wavelength (nm)
+A
+B
HV 20.0 kV | WD 15.2 mm | Mag 6946x | Spot 4.0 | HFW 19.47 µm | 4/28/2009 9:57:25 PM | 5.0µm BSE

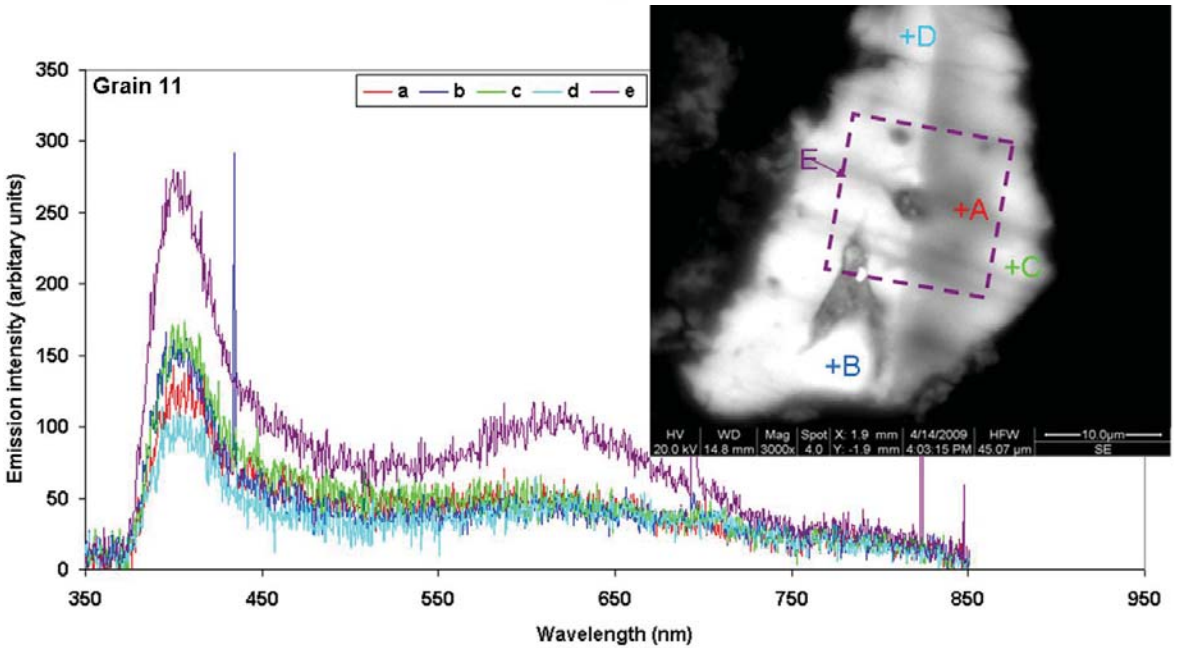
Grain 11
a b c d e
Emission intensity (arbitary units)
Wavelength (nm)
+A
+B
+C
+D
E
HV 20.0 kV | WD 14.8 mm | Mag 3000x | Spot 4.0 | X: 1.9 mm Y: -1.9 mm | 4/14/2009 4:03:15 PM | HFW 45.07 µm | 10.0µm SE

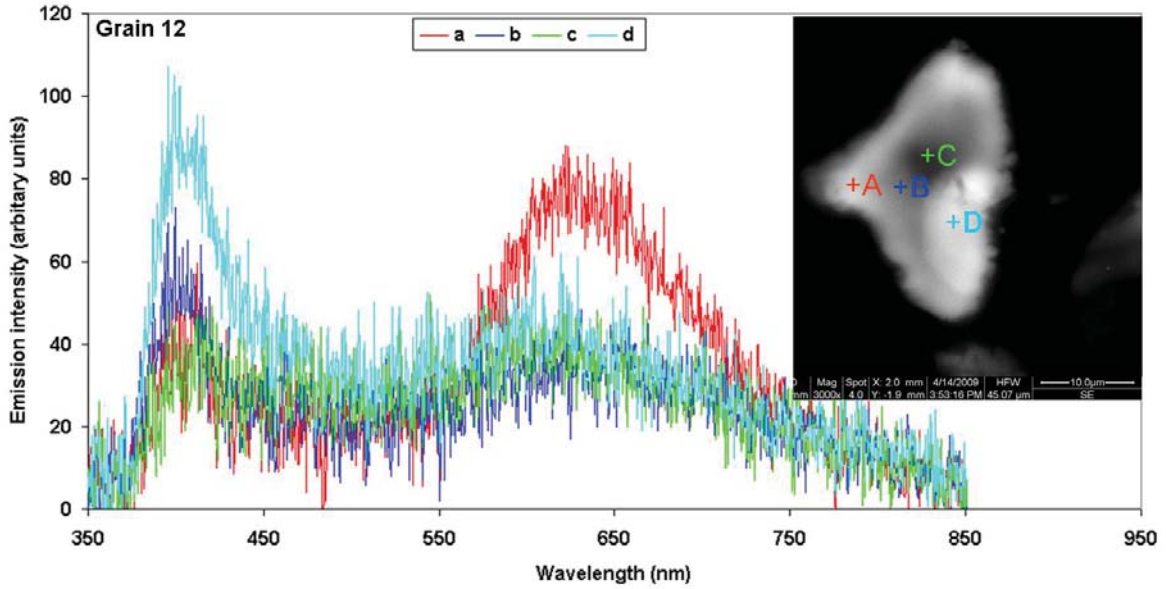
Grain 12
a
b
c
d
Emission intensity (arbitary units)
Wavelength (nm)
+A
+B
+C
+D

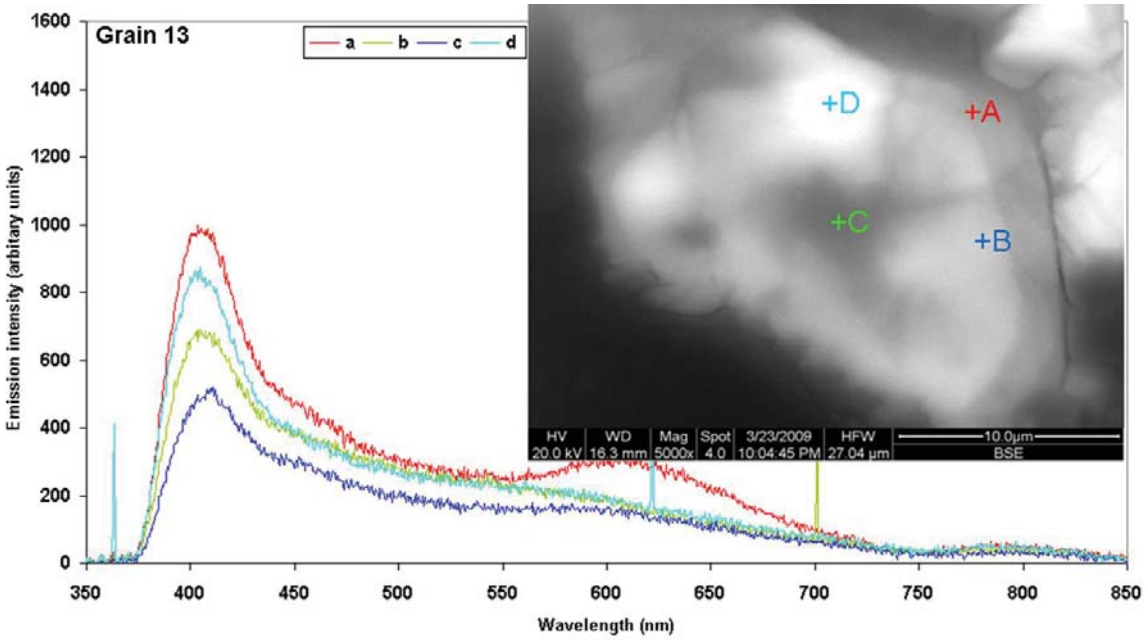
Grain 13
a
b
c
d
Emission intensity (arbitary units)
Wavelength (nm)
+A
+B
+C
+D

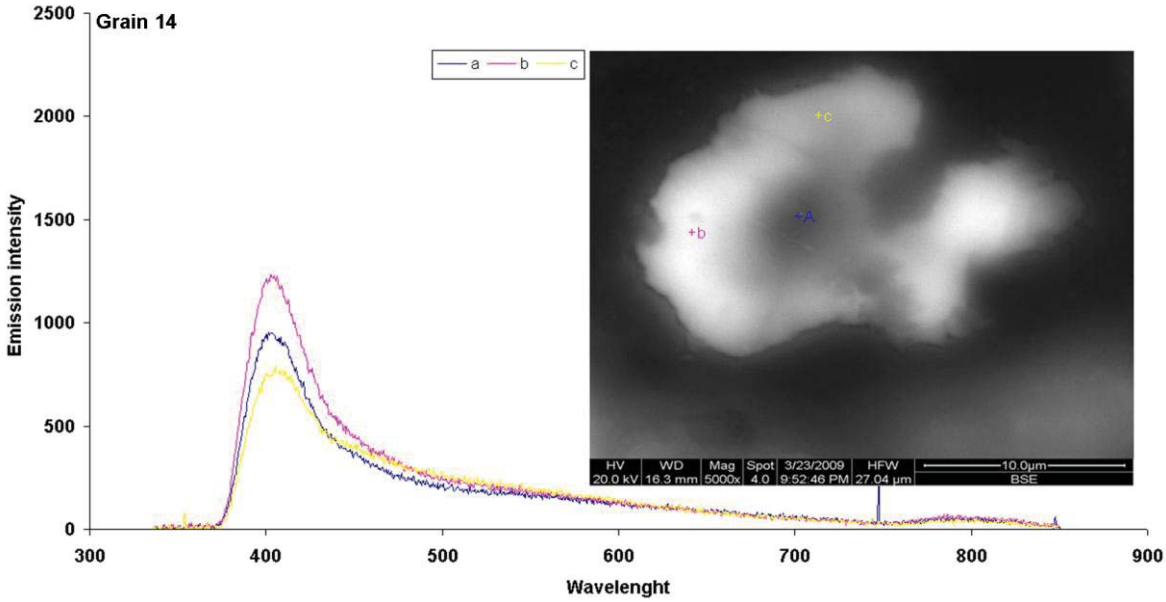
Grain 14
a
b
c
Emission intensity
Wavelenght
+A
+b
+c

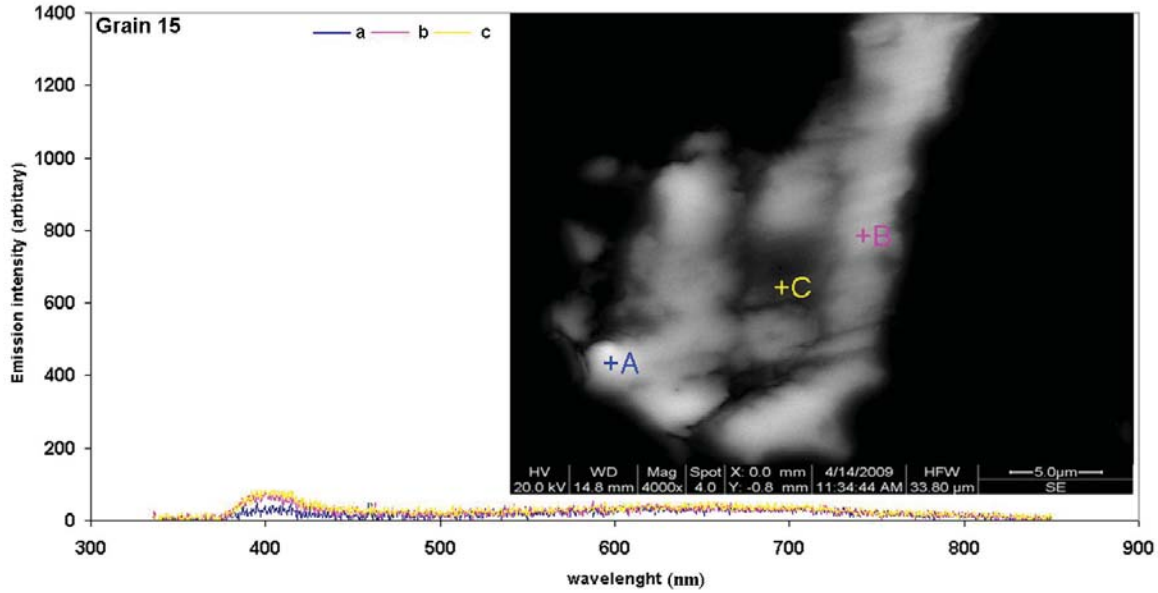

C.2. CL spectroscopy results of the zoned calcite grains in Pollen

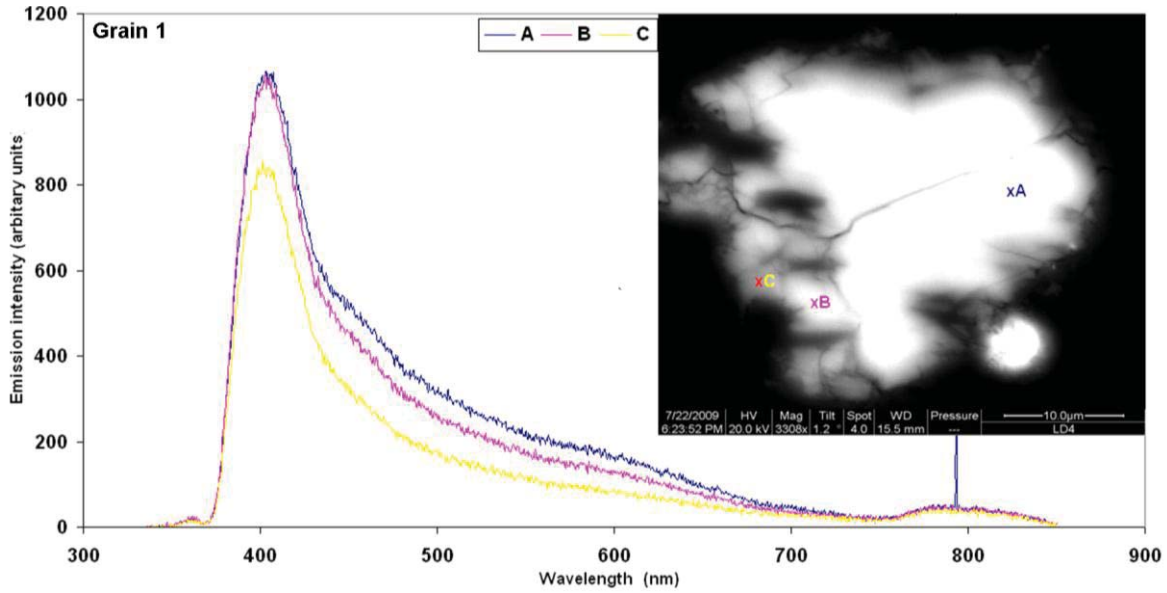

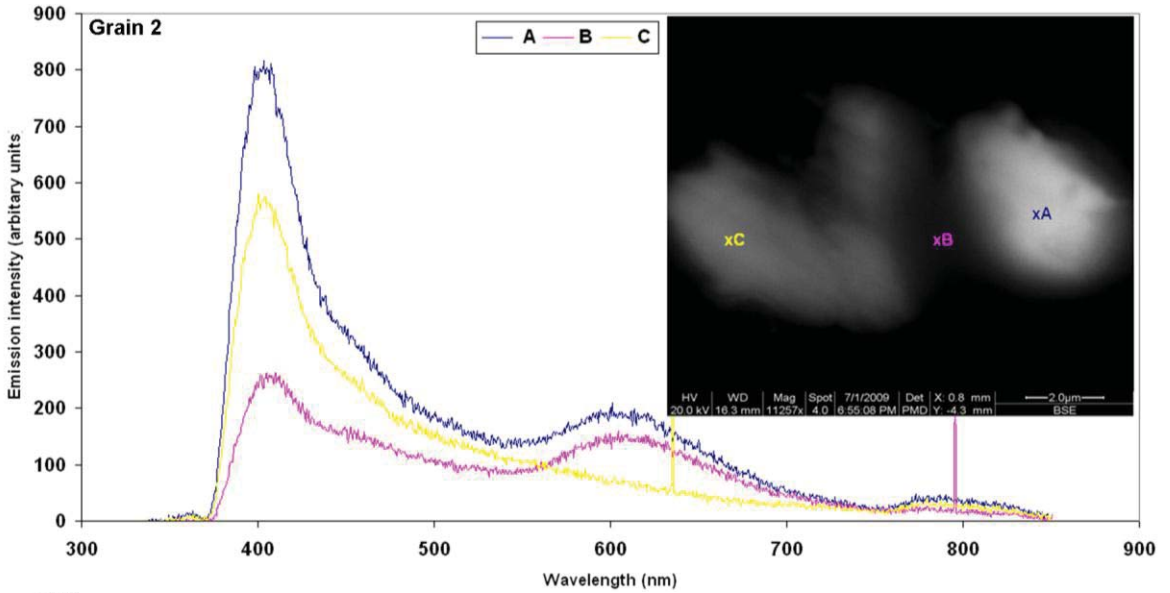
Grain 2
A
B
C
Emission intensity (arbitary units
Wavelength (nm)
xA
xB
xC
HV 20.0 kV | WD 16.3 mm | Mag 11257x | Spot 4.0 | 7/1/2009 6:55:08 PM | Det PMD | X: 0.8 mm Y: -4.3 mm | 2.0µm | BSE

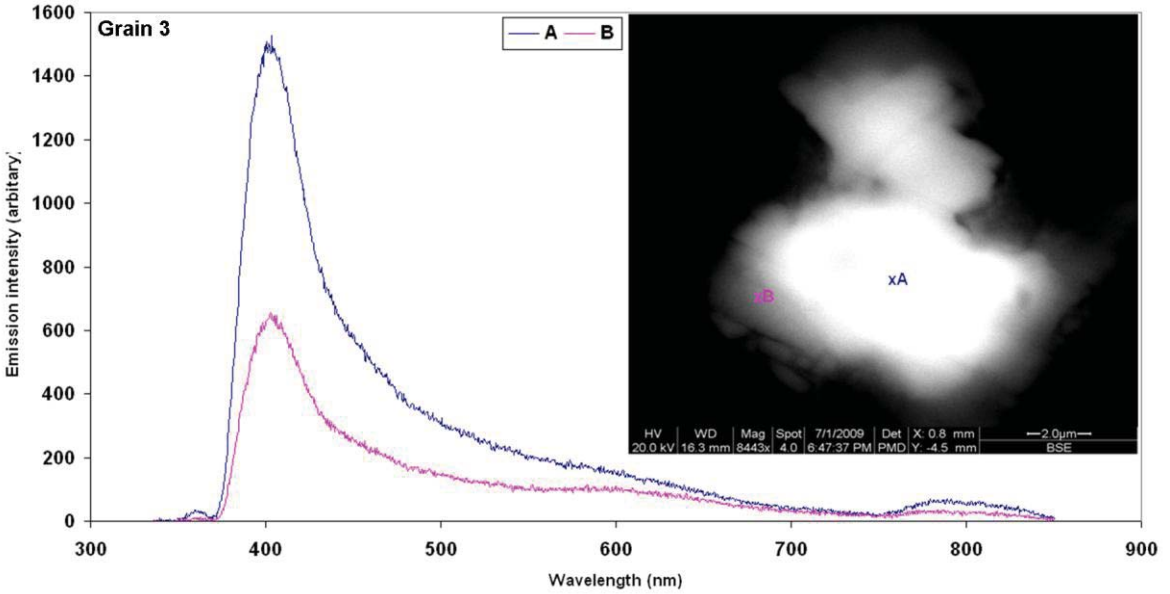
Grain 3
A
B
Emission intensity (arbitary
Wavelength (nm)
xA
xB
HV 20.0 kV | WD 16.3 mm | Mag 8443x | Spot 4.0 | 7/1/2009 6:47:37 PM | Det PMD | X: 0.8 mm Y: -4.5 mm | 2.0µm | BSE

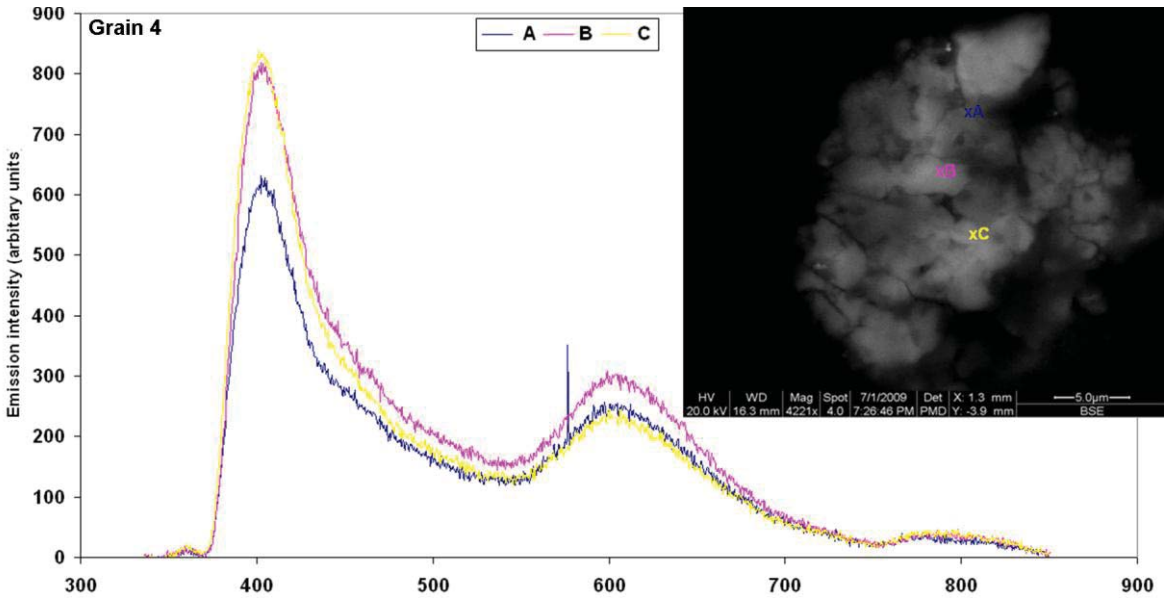
Grain 4
A
B
C
Emission intensity (arbitary units
xA
xB
xC
HV 20.0 kV | WD 16.3 mm | Mag 4221x | Spot 4.0 | 7/1/2009 7:26:46 PM | Det PMD | X: 1.3 mm Y: -3.9 mm | 5.0µm | BSE

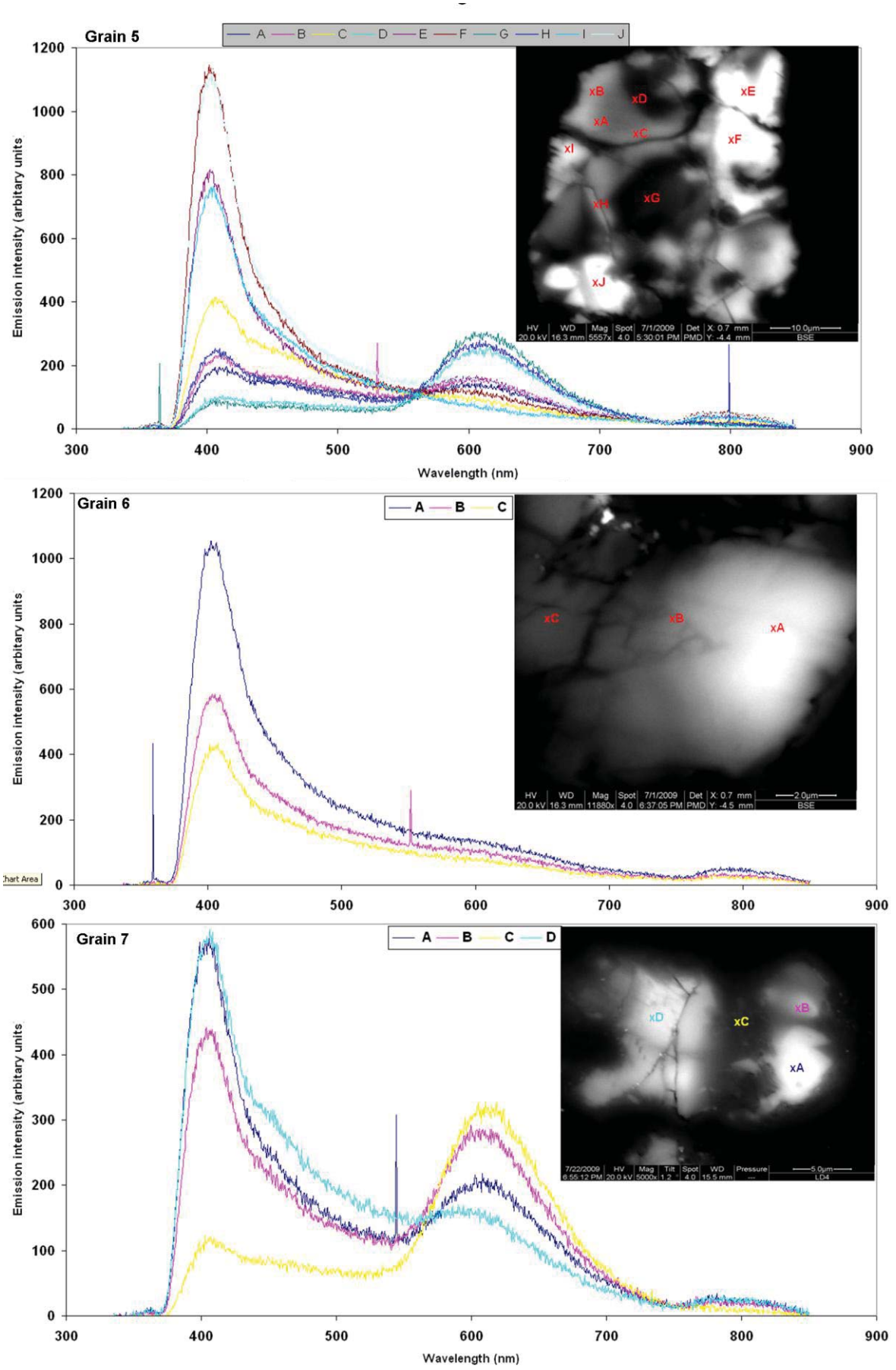
Grain 5
A B C D E F G H I J
Emission intensity (arbitary units)
Wavelength (nm)
xB
xD
xE
xA
xC
xF
xI
xG
xH
xJ
Grain 6
A B C
xC
xB
xA
Grain 7
A B C D
xD
xC
xB
xA

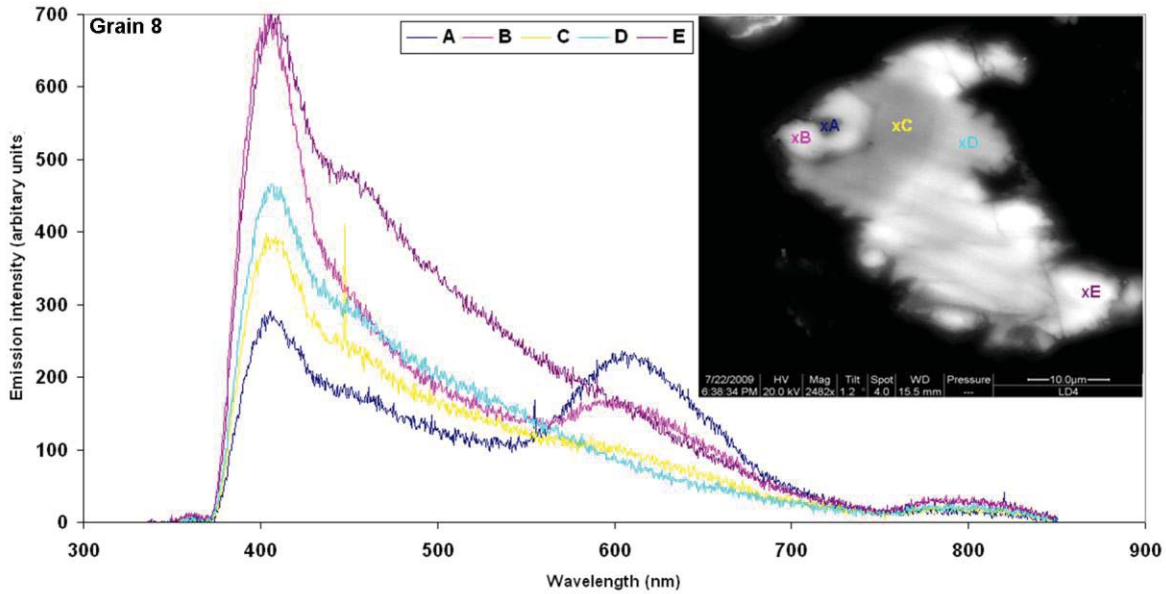
Grain 8
A
B
C
D
E
xA
xB
xC
xD
xE
Emission intensity (arbitary units
Wavelength (nm)

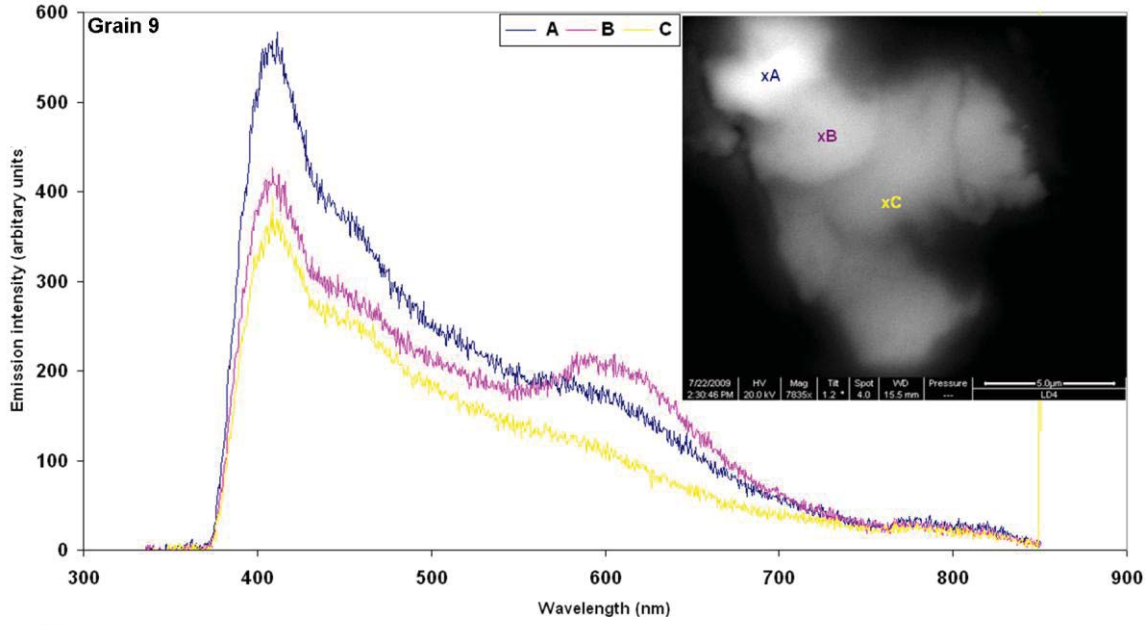
Grain 9
A
B
C
xA
xB
xC
Emission intensity (arbitary units
Wavelength (nm)

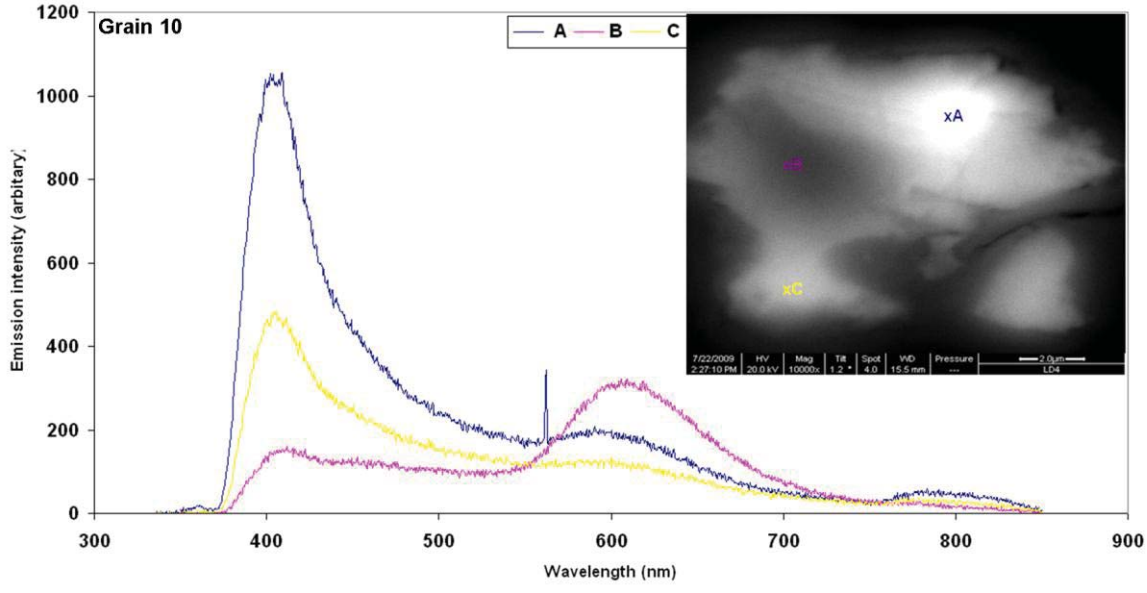
Grain 10
A
B
C
xA
xB
xC
Emission intensity (arbitary
Wavelength (nm)

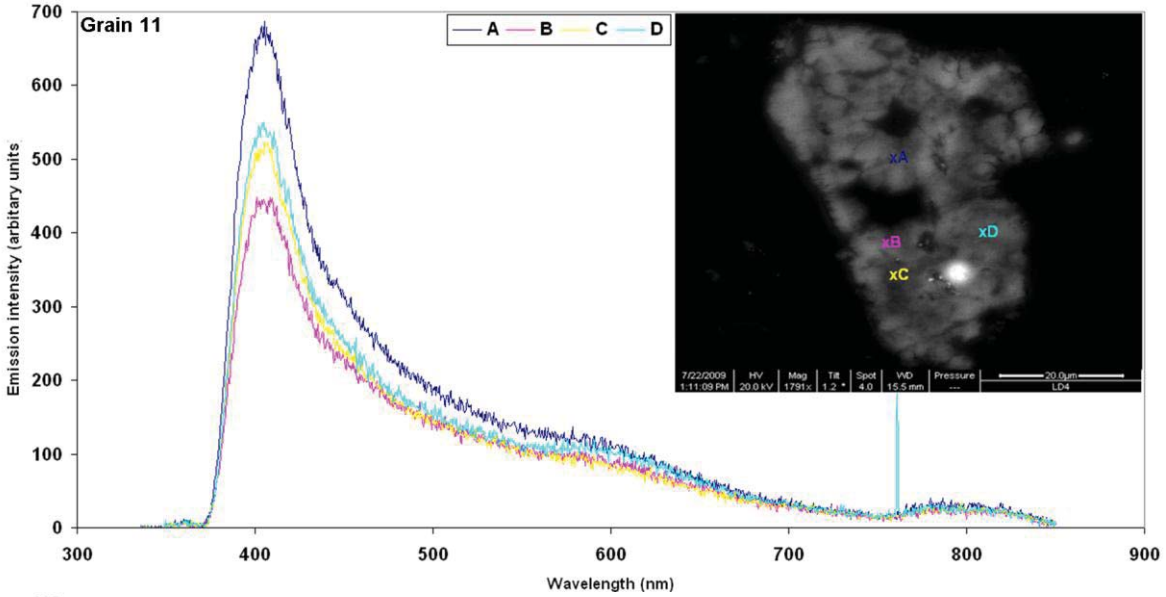
Grain 11
A
B
C
D
Emission intensity (arbitary units
Wavelength (nm)
xA
xB
xC
xD

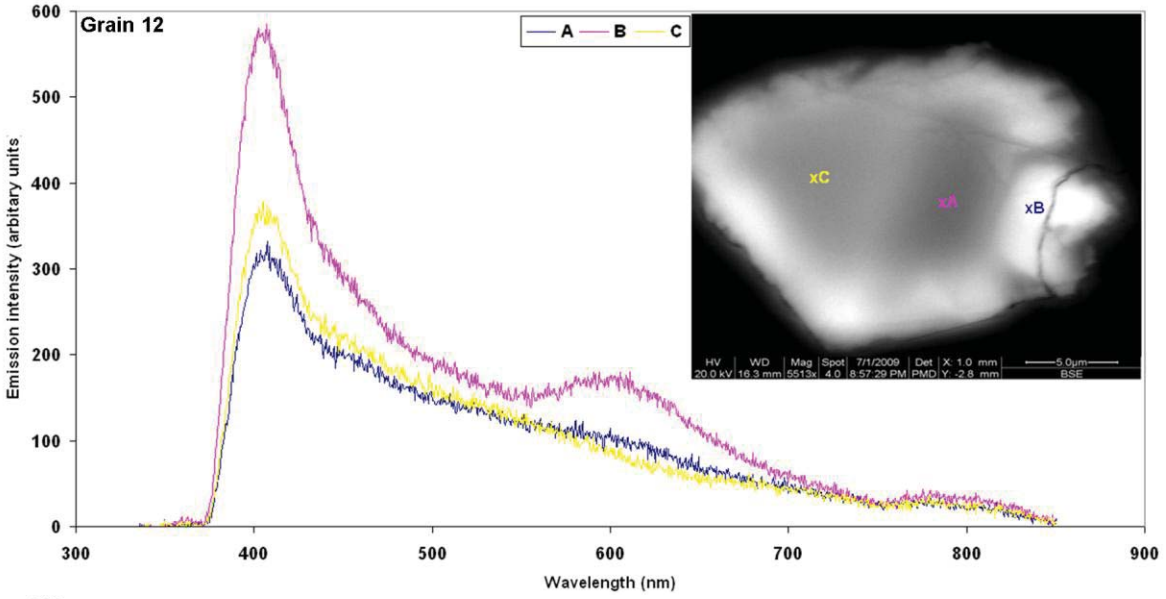
Grain 12
A
B
C
Emission intensity (arbitary units
Wavelength (nm)
xC
xA
xB

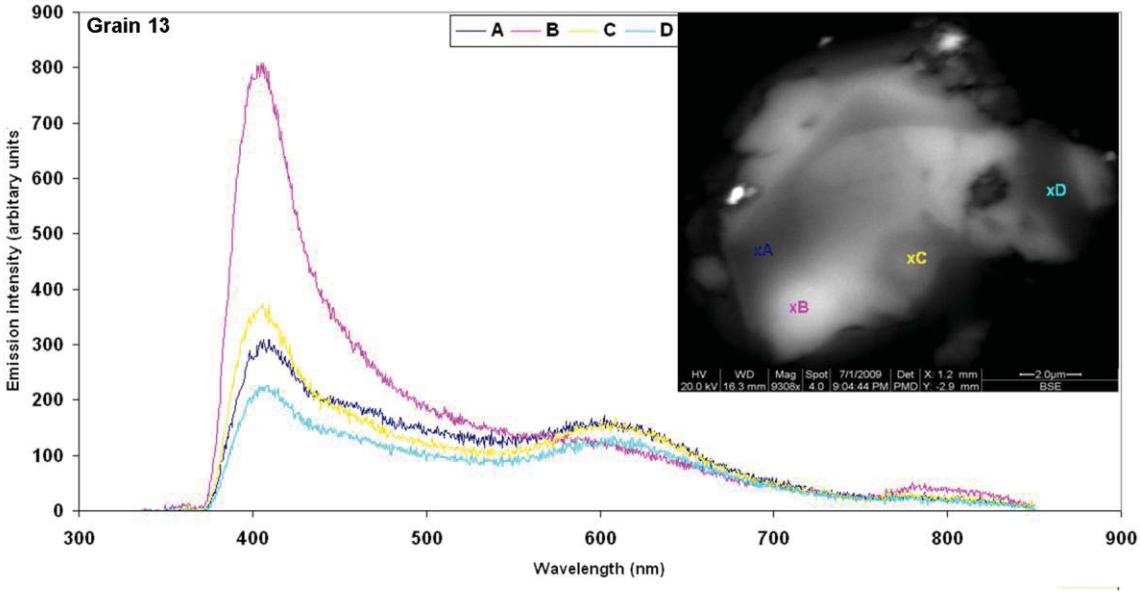
Grain 13
A
B
C
D
Emission intensity (arbitary units
Wavelength (nm)
xD
xA
xC
xB

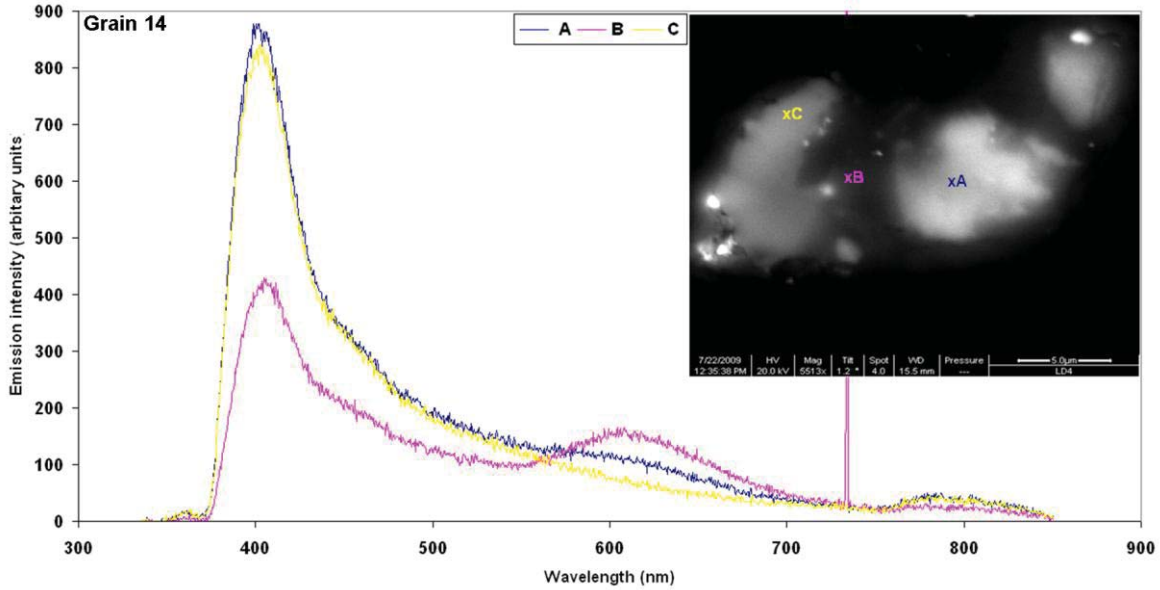
Grain 14
A
B
C
xC
xB
xA
Emission intensity (arbitary units
Wavelength (nm)

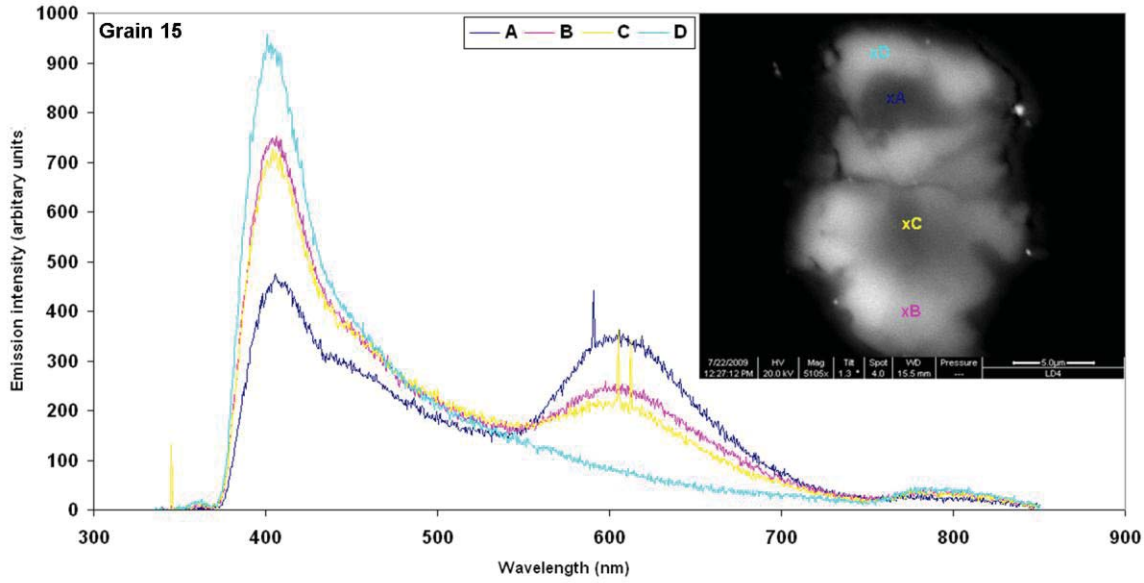
Grain 15
A
B
C
D
xD
xA
xC
xB
Emission intensity (arbitary units
Wavelength (nm)

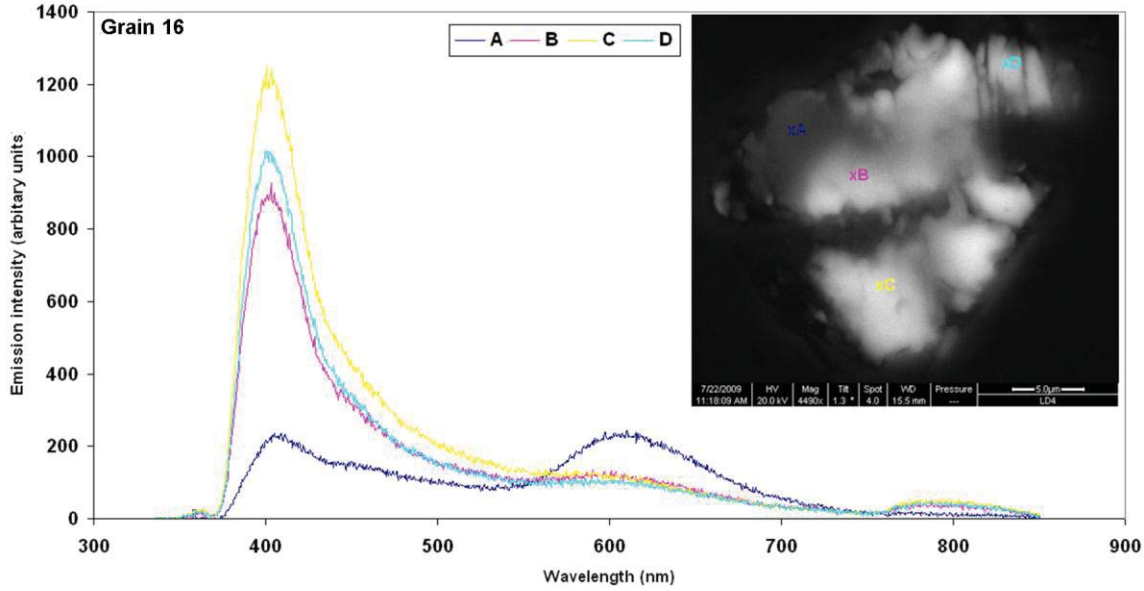
Grain 16
A
B
C
D
xD
xA
xB
xC
Emission intensity (arbitary units
Wavelength (nm)

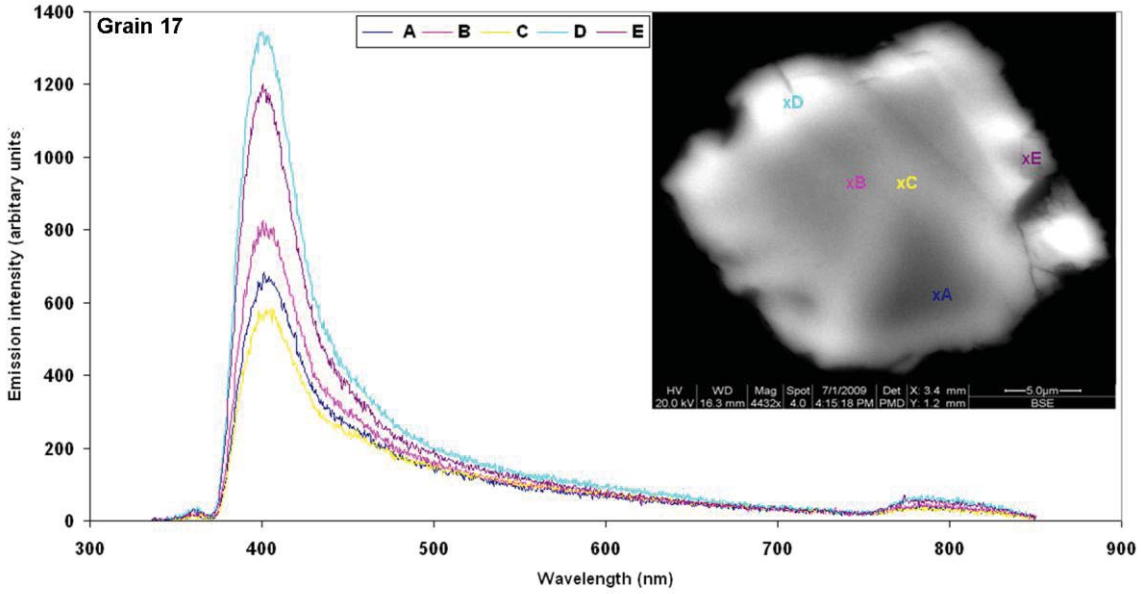
Grain 17
A B C D E
Emission intensity (arbitary units
Wavelength (nm)
xD
xE
xB
xC
xA

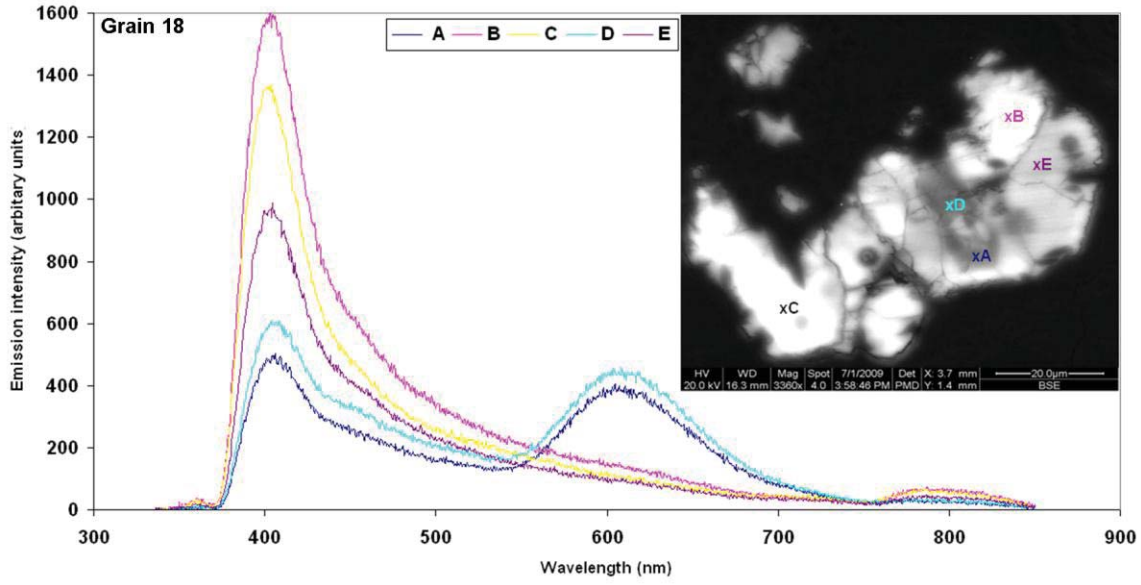
Grain 18
A B C D E
Emission intensity (arbitary units
Wavelength (nm)
xB
xE
xD
xA
xC

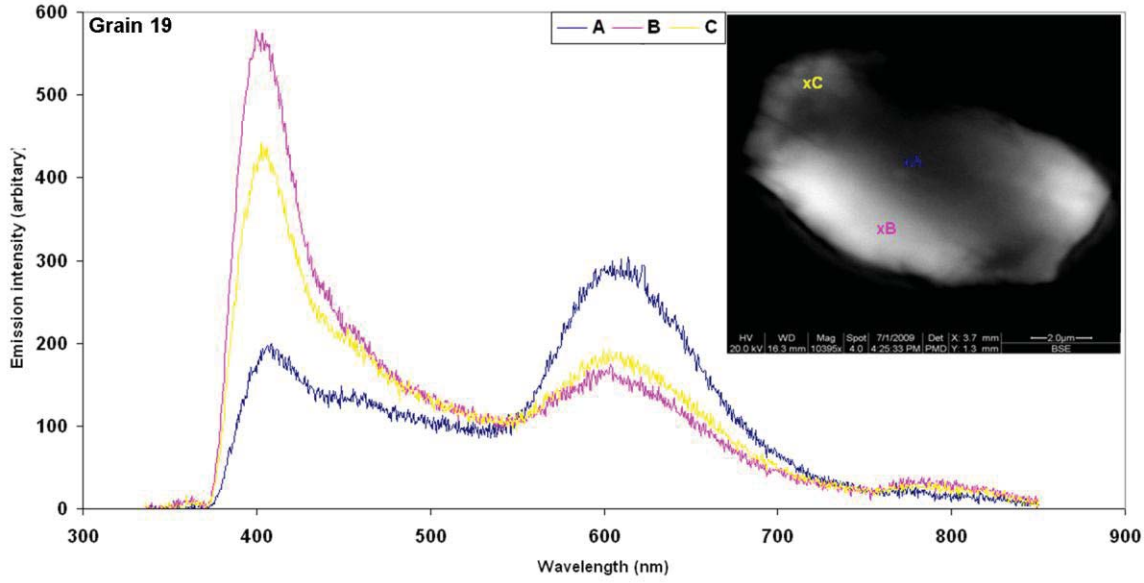
Grain 19
A B C
Emission intensity (arbitary
Wavelength (nm)
xC
xA
xB

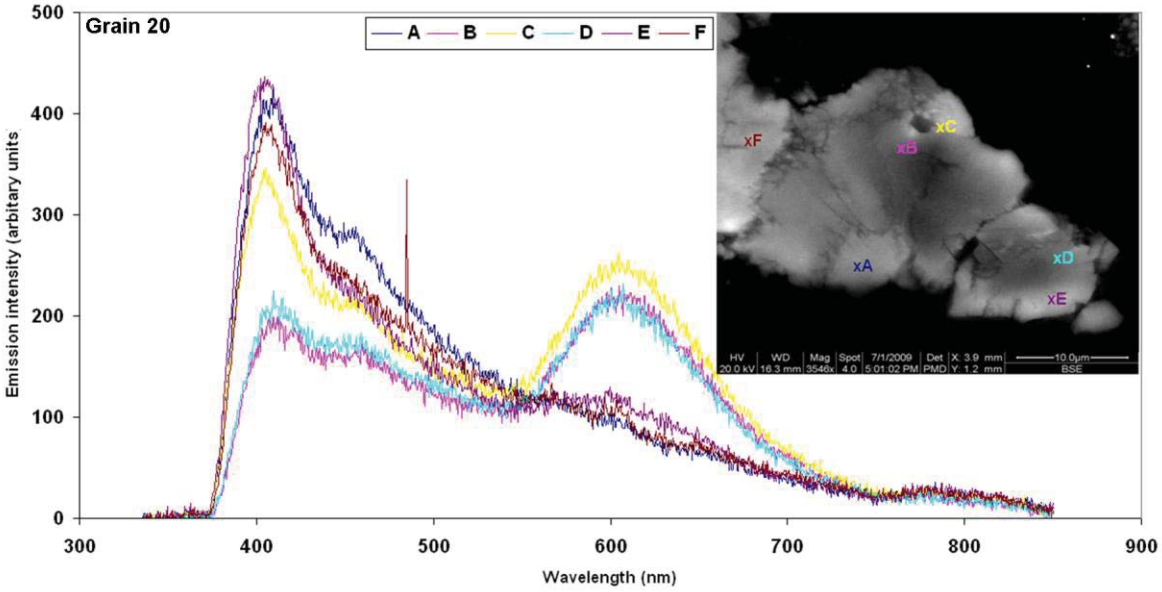
Grain 20
A B C D E F
Emission intensity (arbitary units)
Wavelength (nm)
xF
xC
xB
xA
xD
xE

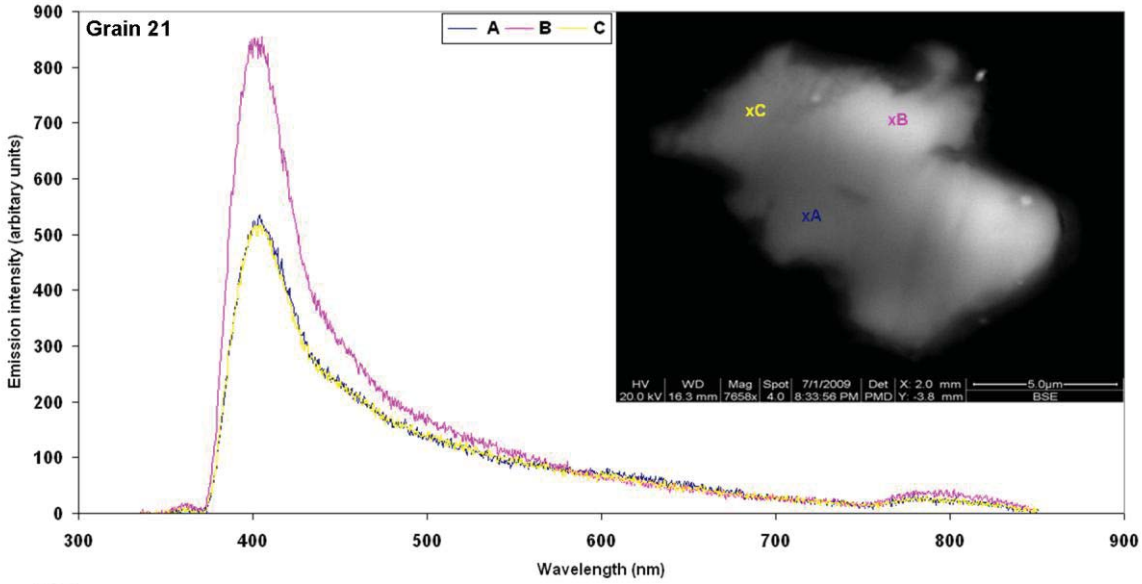
Grain 21
A B C
Emission intensity (arbitary units)
Wavelength (nm)
xC
xB
xA

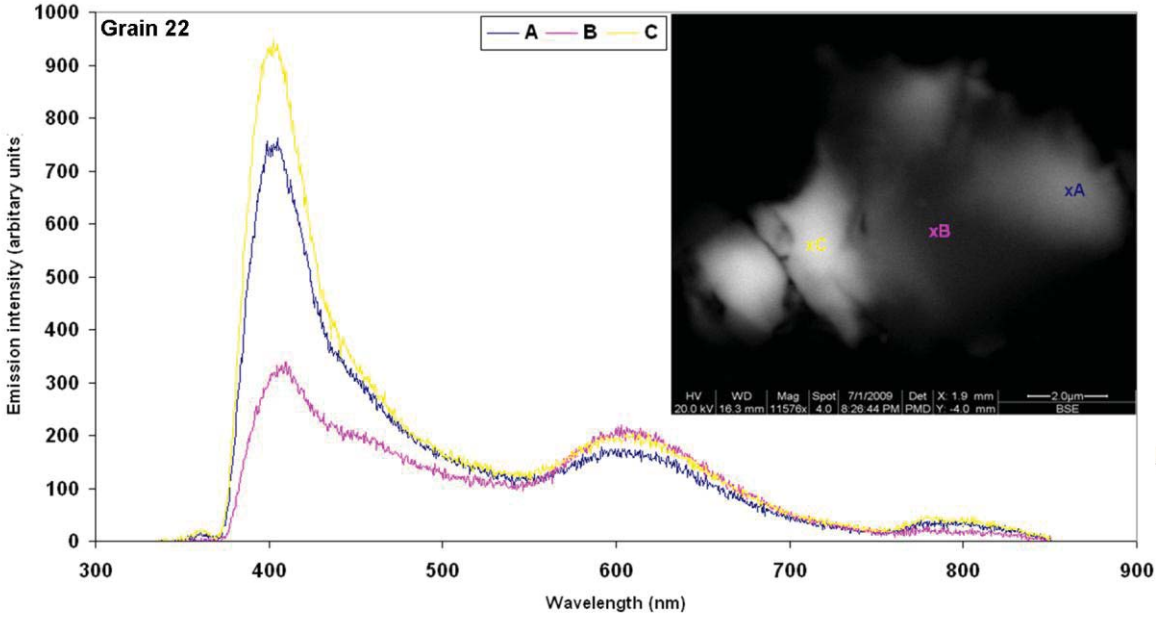
Grain 22
A B C
Emission intensity (arbitary units)
Wavelength (nm)
xA
xB
xC

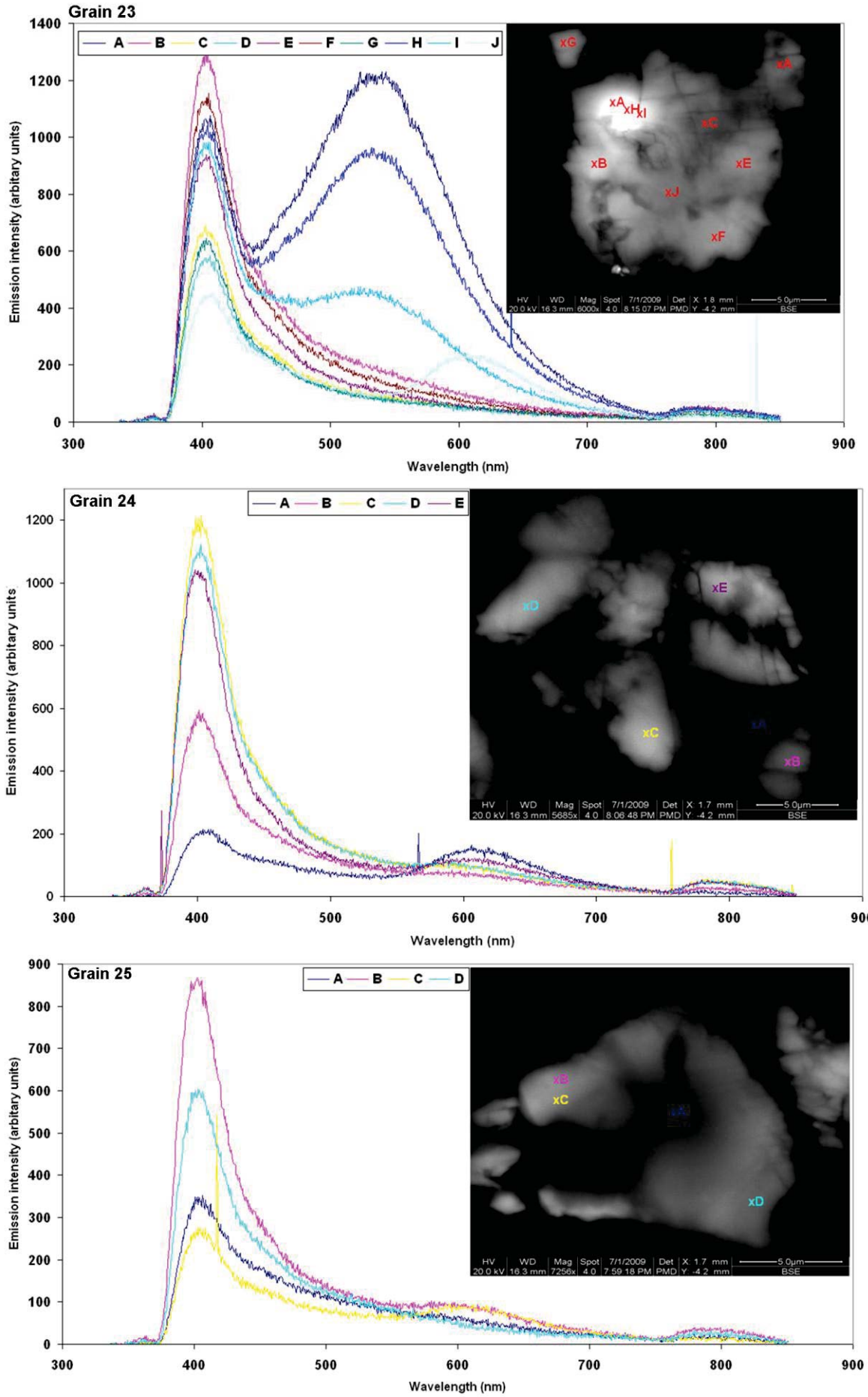
Grain 23
A B C D E F G H I J
Emission intensity (arbitary units)
Wavelength (nm)
xG
xA
xA xH xI
xC
xB
xE
xJ
xF
Grain 24
A B C D E
Emission intensity (arbitary units)
Wavelength (nm)
xE
xD
xC
xB
Grain 25
A B C D
Emission intensity (arbitary units)
Wavelength (nm)
xB
xC
xD

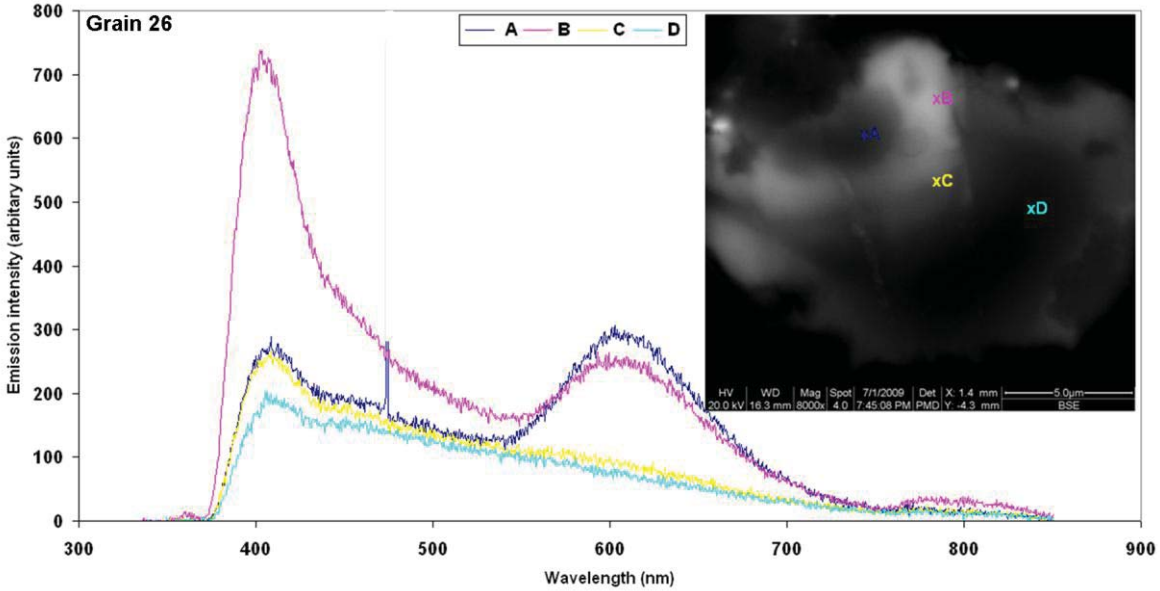
Grain 26
A
B
C
D
Emission intensity (arbitary units)
Wavelength (nm)
xB
xA
xC
xD
HV 20.0 kV
WD 16.3 mm
Mag 8000x
Spot 4.0
7/1/2009 7:45:08 PM
Det PMD
X: 1.4 mm
Y: -4.3 mm
5.0µm
BSE

Appendix D

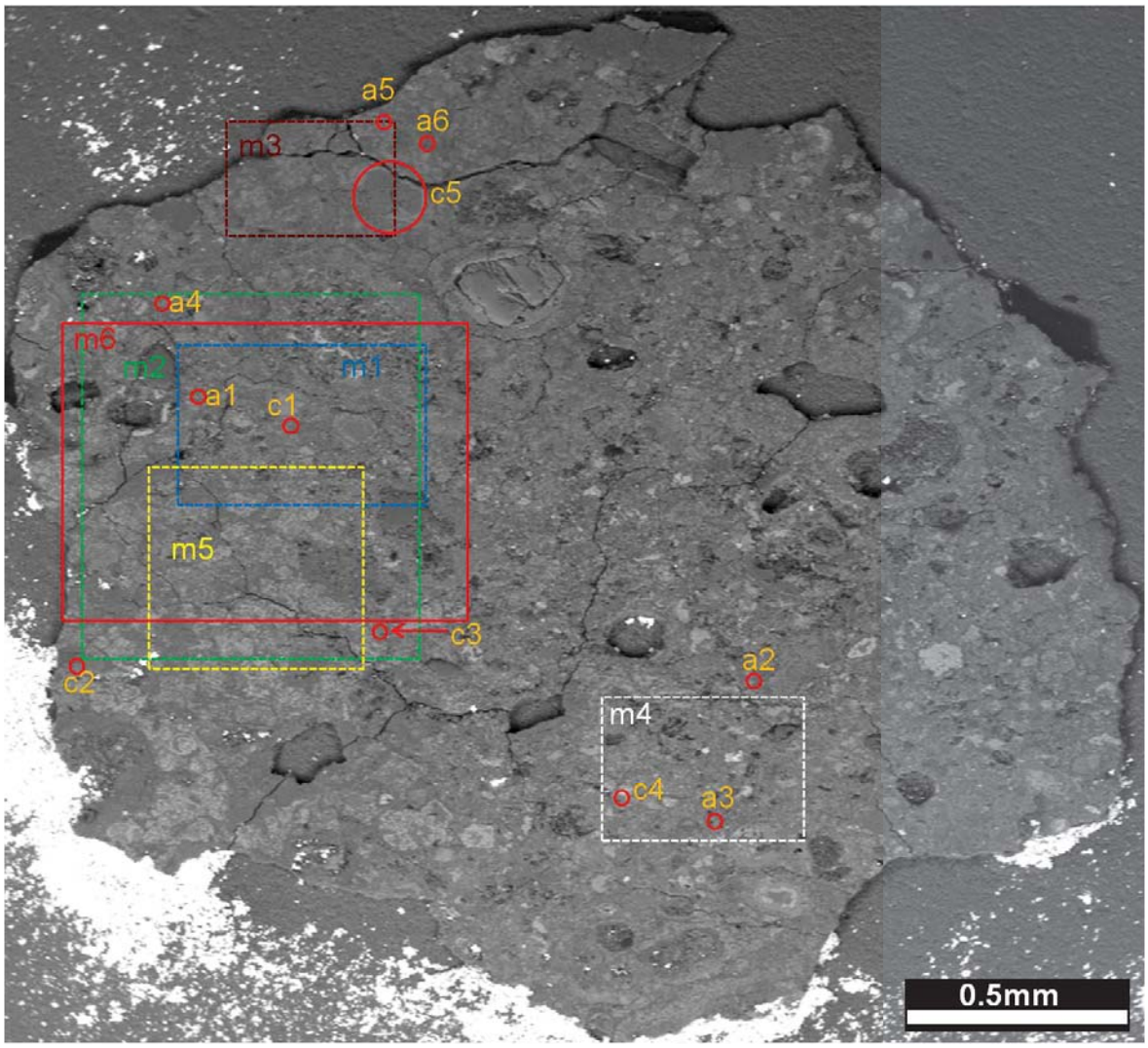

D.1. BSE image of Murchicson CM2.5 showing the locations of the detailed images and maps, boxed areas are the location of maps (m) and red circles the location of grains (a= aragonite, c= calcite). a1 is aragonite in Figure 4.3b, a2 is aragonite in figure 4.5, a3 is aragonite-calcite intergrowth grain in Figure 4.6, a4 is aragonite-calcite intergrowth in Figure 4.7, a5 is aragonite in Figure 4.13 and Figure 4.18a, a6 is aragonite in Figure 4.14, c1 is calcite in Figure 4.3a, c2 is calcite in Figure 4.4, c3 is calcite Figure 4.18b, c4 is calcite Figure 4.18c, c5 is calcite Figure 4.18d, m1 is map in Figure 3.3, m2 is map in Figure 3.5, m3 is map in Figure 4.8, m4 is map in Figure 4.9, m5 is map in Figure 4.10, m6 is map in Figure 4.19.

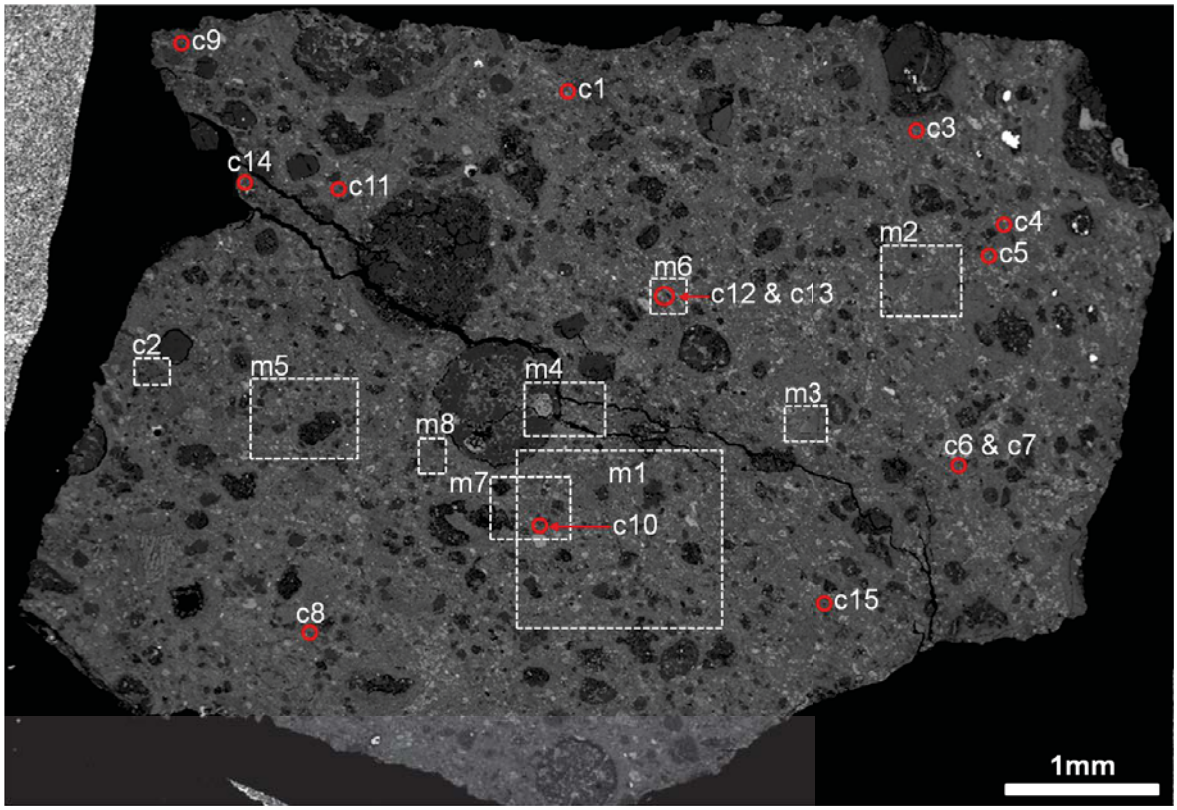

D.2. BSE image of Murray CM2.5/2.4 showing the locations of the detailed images and maps, boxed areas are the location of maps (m) and red circles the location of grains (c= calcite). c1 is calcite in Figure 4.24a, c2 is calcite in Figure 4.24b, c3 is calcite in Figure 4.25a, c4 is calcite in Figure 4.25b, c5 is calcite in Figure 4.26a, c6 is calcite in Figure 4.26b, c7 is calcite in Figure 4.34, c8 is calcite in Figure 4.36a, c9 is calcite in Figure 4.36b, c10 is calcite in Figure 4.32 and Figure 4.31e, c11 is calcite in Figure 4.33, c12 and c13 are calcite grains in Figure 4.31a and Figure 4.31b, c14 is calcite in Figure 4.31f, c15 is calcite in Figure 4.31d. m1 is map in Figure 3.7, m2 is map in Figure 3.8, m3 is map in Figure 3.9a, m4 is map in Figure 3.9b, m5 is map in Figure 3.10, m6 is map in Figure 4.27, m7 is map in Figure 4.28, m8 is map in Figure 4.29,

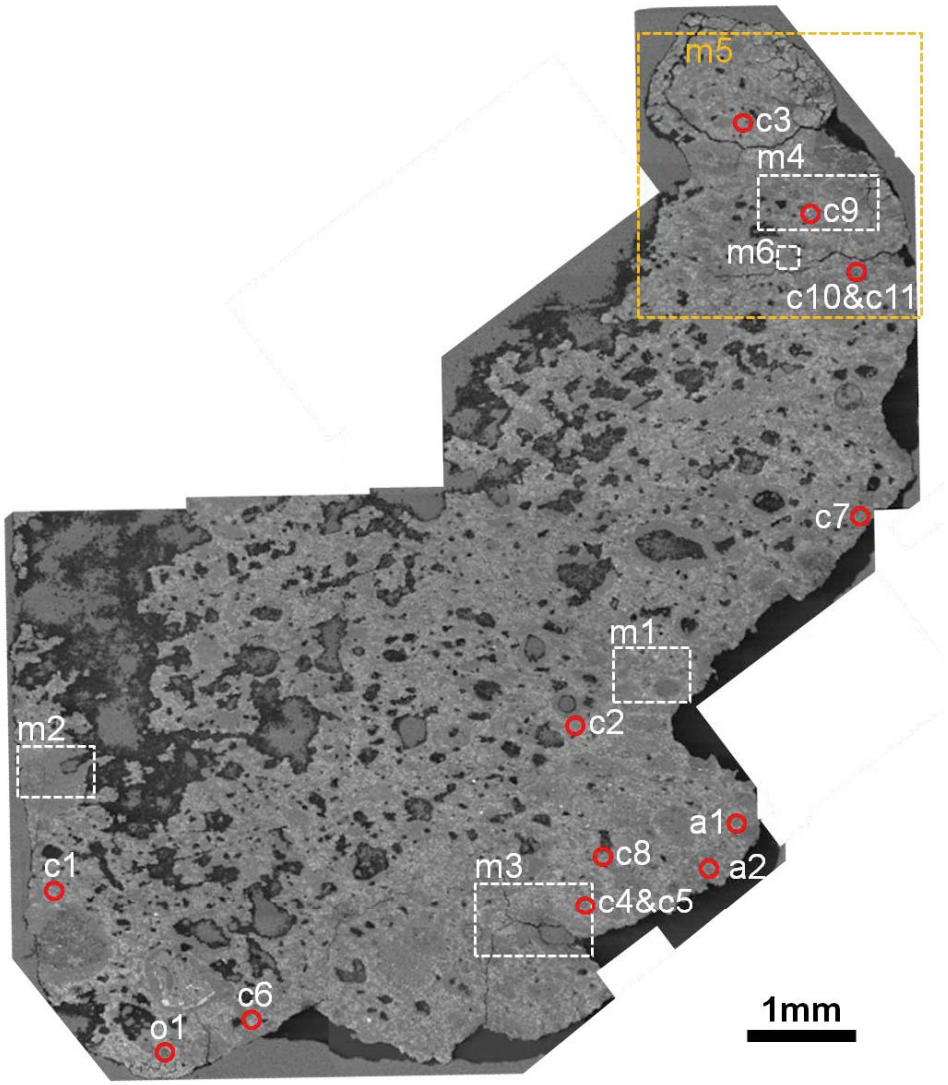

D.3. BSE image of Pollen CM2.4 showing the locations of the detailed images and maps, boxed areas are the location of maps (m) and red circles the location of grains (a= aragonite, c= calcite, o= olivine). a1 is aragonite in Figure 4.38d, a2 is aragonite-calcite intergrowth grain in Figure 4.43. c1 is calcite in Figure 4.38a, c2 is calcite in Figures 4.38b, 4.41a, 4.48a and 4.52a, c3 is calcite in Figure 4.38c, c4 is calcite in Figure 4.39, c5 is calcite in figure 4.45, c6 is calcite in Figure 4.46, c7 is calcite in Figure 4.47a, c8 is calcite in Figure 4.47b, c9 is calcite in Figure 4.47d, c10 is calcite in Figure 4.49, c11 is calcite in Figure 4.50. o1 is olivine in Figure 3.14. m1 is map in Figure 3.12, m2 is map in Figure 3.13, m3 is map in Figure 3.15, m4 is map in Figure 3.16, m5 is map in Figure 4.37, m6 is map in Figure 4.44.

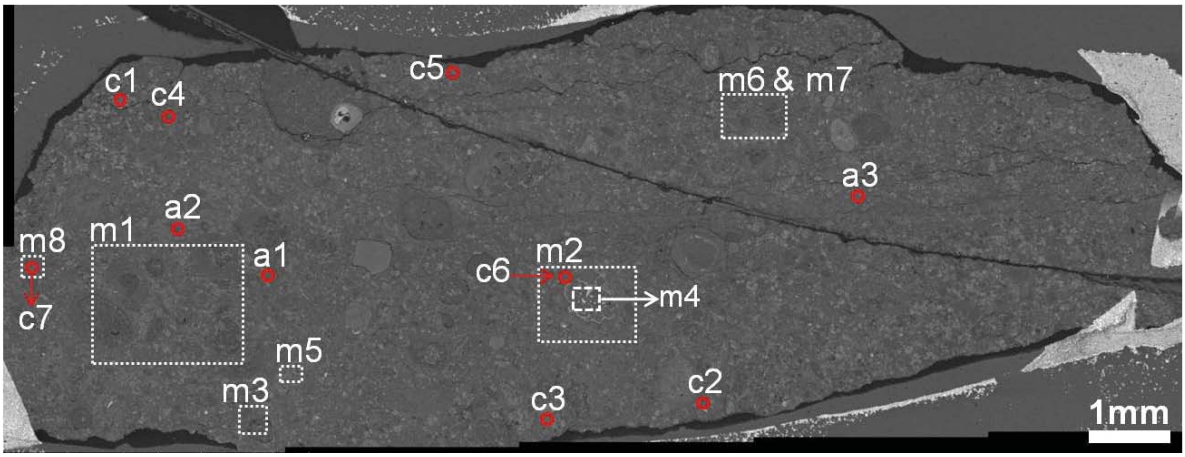

D.4. BSE image of Mighei CM2.3 showing the locations of the detailed images and maps, boxed areas are the location of maps (m) and red circles the location of grains (a= aragonite, c= calcite). a1 is aragonite in Figure 4.59, a2 is aragonite in Figure 4.60, a3 is aragonite in Figure 4.62b. c1 is calcite in Figure 4.55, c2 is calcite in Figures 4.56a, c3 is calcite in Figure 4.56b, c4 is calcite in Figure 4.57, c5 is calcite in Figure 4.62a, c6 is calcite in Figure 4.62c, c7 is calcite in Figure 4.62d. m1 is map in Figure 3.19, m2 map in Figure 3.20a, m3 map in Figure 3.20b, m4 is map in Figure 3.21a, m5 is map in Figure 3.21b, m6 is map in Figure 3.23, m7 is map in Figure 4.54, m8 is map in Figure 4.63.

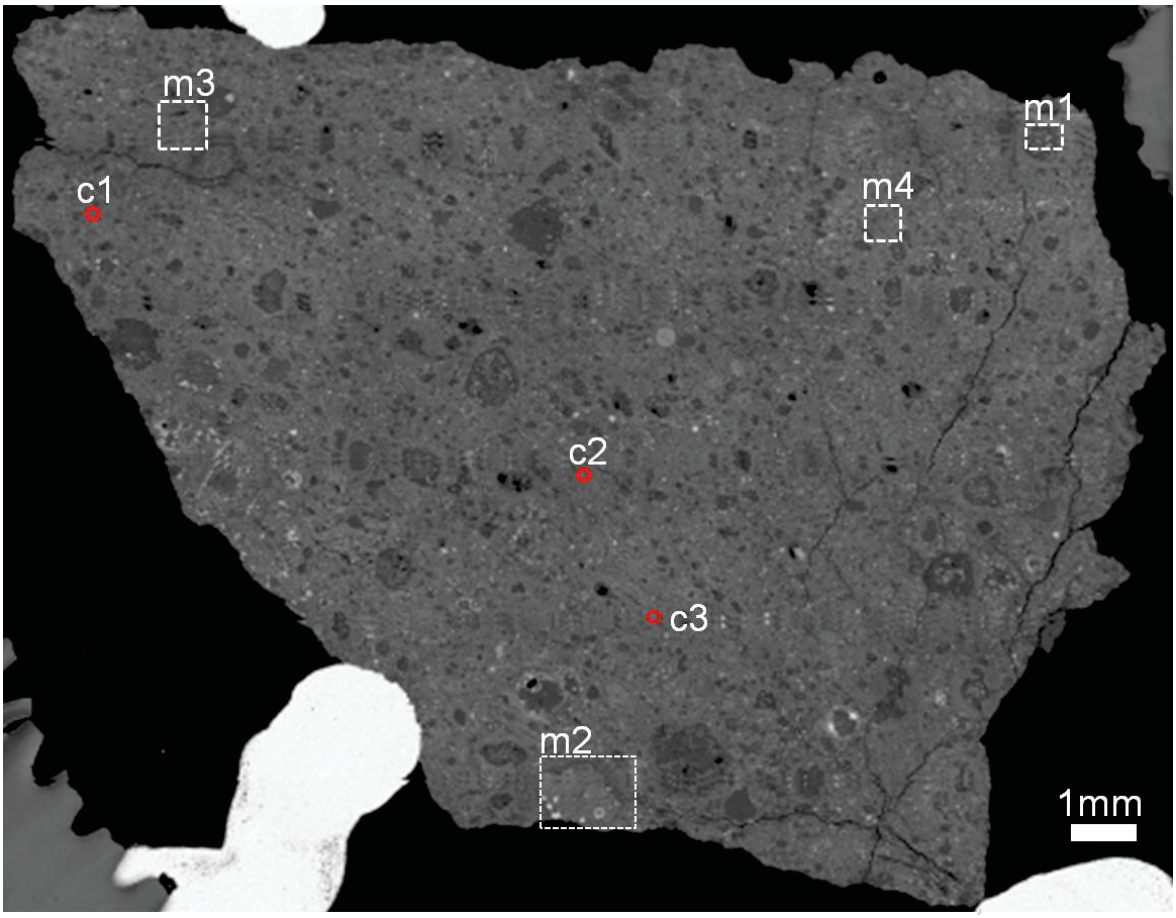

D.5. BSE image of EET 96029 CM2.3 showing the locations of the detailed images and maps, boxed areas are the location of maps (m) and red circles the location of grains (c= calcite). c1 is calcite in Figure 4.66a, c2 is calcite in Figures 4.66b, c3 is calcite in Figures 4.68. m1 is map in Figure 3.25, m2 is map in Figure 3.26, m3 is map in Figure 3.27, m4 is map in Figure 4.67.

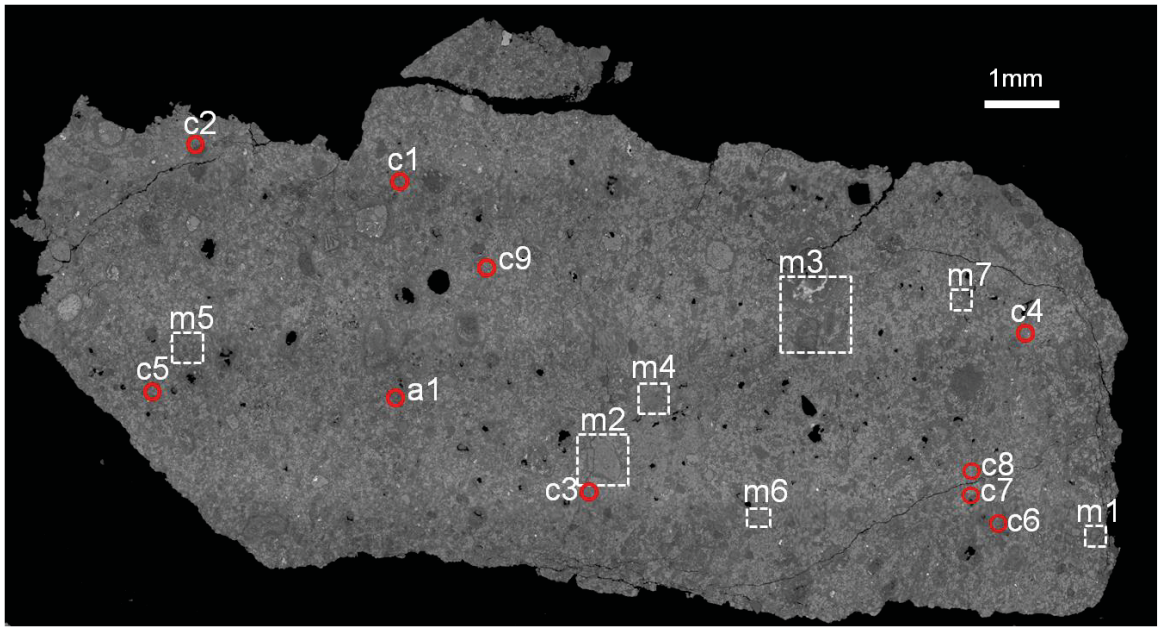

D.6. BSE image of LON 94101 CM2.3 showing the locations of the detailed images and maps, boxed areas are the location of maps (m) and red circles the location of grains (a= aragonite, c= calcite). a1 is aragonite in Figure 4.76a. c1 is calcite in Figure 4.69a, c2 is calcite in Figures 4.69b, c3 is calcite in Figure 4.69c, c4 is calcite in Figure 4.71b, c5 is calcite in Figure 4.77a, c6 is calcite in Figure 4.78a, c7 is calcite in Figure 4.78b, c8 is calcite in Figure 4.478c and 4.78d, c9 is calcite in Figure 4.76b m1 is map in Figure 3.30, m2 is map in Figure 3.31, m3 is map in Figure 3.32, m4 is map in Figure 4.69d, Figure 4.71a, and Figure 4.75a. m5 is map in Figure 4.73, m6 is map in Figure 4.79, m7 is map in Figure 3.1b.

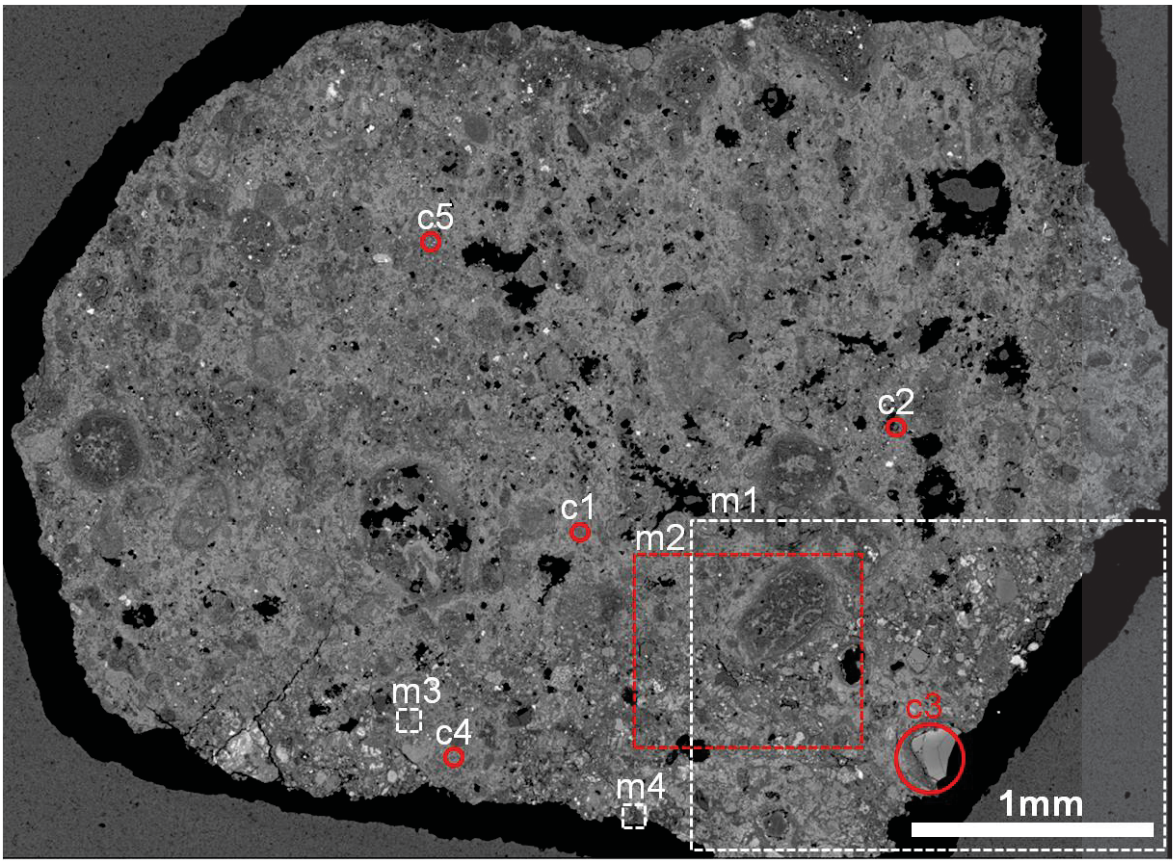

D.7. BSE image of Nogoya CM2.2/2.3 showing the locations of the detailed images and maps, boxed areas are the location of maps (m) and red circles the location of grains (c= calcite). c1 is calcite in figure 5.2a, c2 is calcite in Figures 5.2b, c3 is calcite in Figure 5.3a, c4 is calcite in Figure 5.3b and Figure 5.11a, c5 is calcite in Figure 5.5, m1 is map in Figure 3.36, m2 is map in Figure 3.38, m3 is map in Figure 5.6, m4 is map in Figure 3.1a.

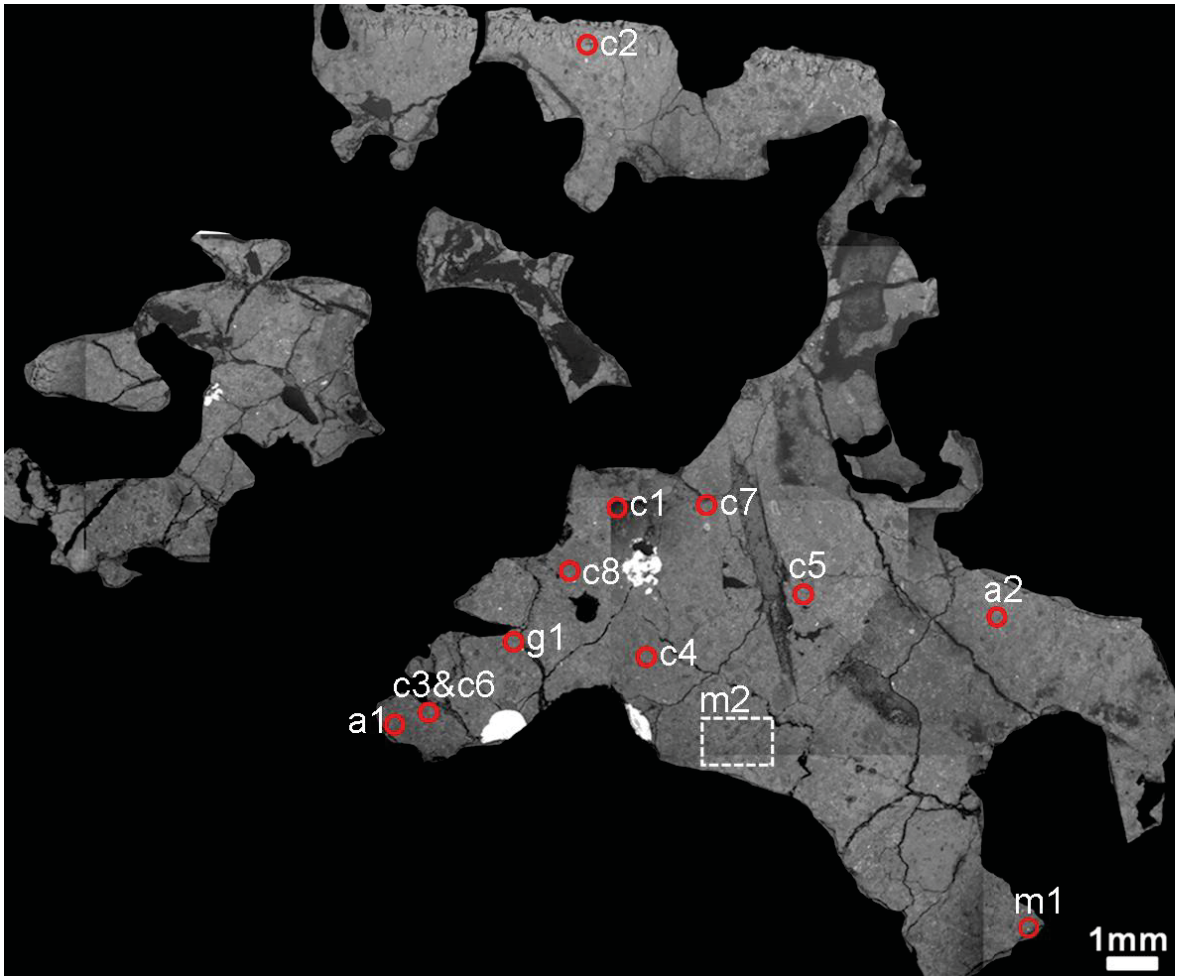

D.8. BSE image of Cold Bokkeveld CM2.2 showing the locations of the detailed images and maps, boxed areas are the location of maps (m) and red circles the location of grains (a= aragonite, c= calcite, g= calcite-spinel). a1 is aragonite in Figure 5.15, a2 is aragonite in Figure 5.16, c1 is calcite in Figure 5.14a, c2 is calcite in Figure 5.14d, c3 is calcite in Figure 5.18a, c4 is calcite in Figure 5.18b, c5 is calcite in Figure 5.19a, c6 is calcite in Figure 5.19b, c7 is calcite in Figure 5.19c, c8 is calcite in Figure 5.19d. g1 is grain in Figure 5.14b. m1 is map in Figure 3.41, m2 is map in Figure 3.42.

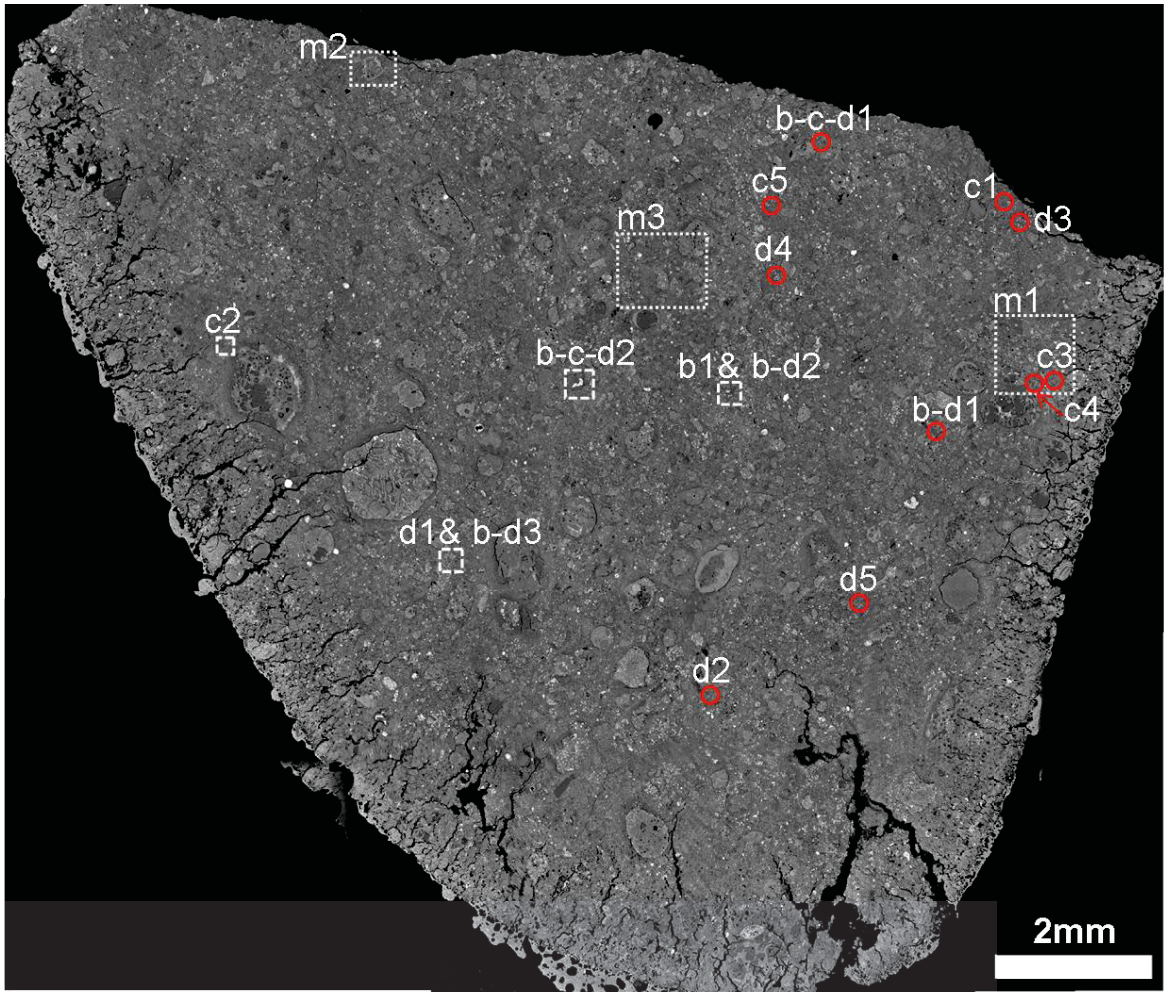

D.9. BSE image of QUE 93005 CM2.1 showing the locations of the detailed images and maps, boxed areas are the location of maps (m) and red circles the location of grains (c= calcite or calcite-dolomite, d= dolomite, b-d= breunnerite-dolomite, b-c-d= breunnerite-calcite-dolomite). b1 is breunnerite in Figure 5.27, b-d1 is breunnerite-dolomite in Figure 5.28a, b-d2 is breunnerite-dolomite in Figure 5.28b, b-d3 is breunnerite-dolomite in Figure 5.29a, c1 is calcite in Figure 5.23a, c2 is calcite in Figure 5.23b, c3 is calcite-dolomite in Figure 5.25a, c4 is calcite-dolomite in Figure 5.25b, c5 is calcite-dolomite in Figure 5.26. d1 is dolomite in Figure 5.24a, d2 is dolomite in Figure 5.24b, d3 is calcite-dolomite in Figure 5.32, d4 is dolomite in Figure 5.33a, d5 is dolomite in Figure 5.33c, b-c-d1 is breunnerite-calcite-dolomite in Figure 5.30a, b-c-d2 is breunnerite-calcite-dolomite in Figure 5.30b, Figure 5.31, Figure 5.34a and Figure 5.35a. m1 is map in Figure 3.44, m2 is map in Figure 3.45, m3 is map in Figure 3.46.

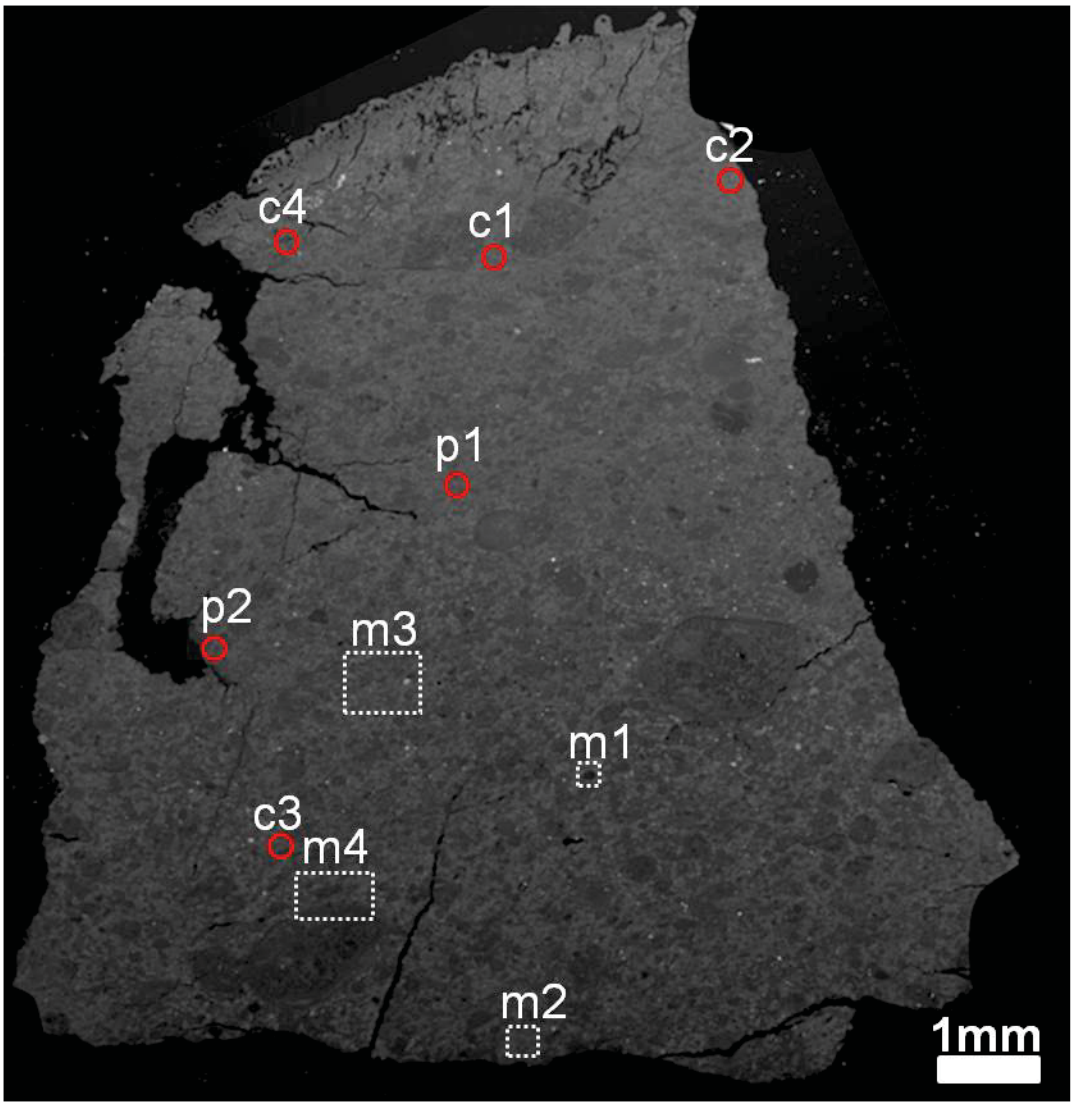

D.10. BSE image of LAP 031166 CM2.1/2.0 showing the locations of the detailed images and maps, boxed areas are the location of maps (m) and red circles the location of grains (c= calcite, p is pseudomorphs after calcite). c1 is calcite in Figure 6.2a, c2 is calcite in Figures 6.2b, c3 is calcite in Figure 6.2c, c4 is calcite in Figure 6.3, p1 is pseudomorphs in Figure 6.4a, p2 is pseudomorphs in Figure 6.4b, m1 is map in Figure 3.49, m2 is map in Figure 3.50, m3 is map in Figure 3.51, m4 is map in Figure 6.1.

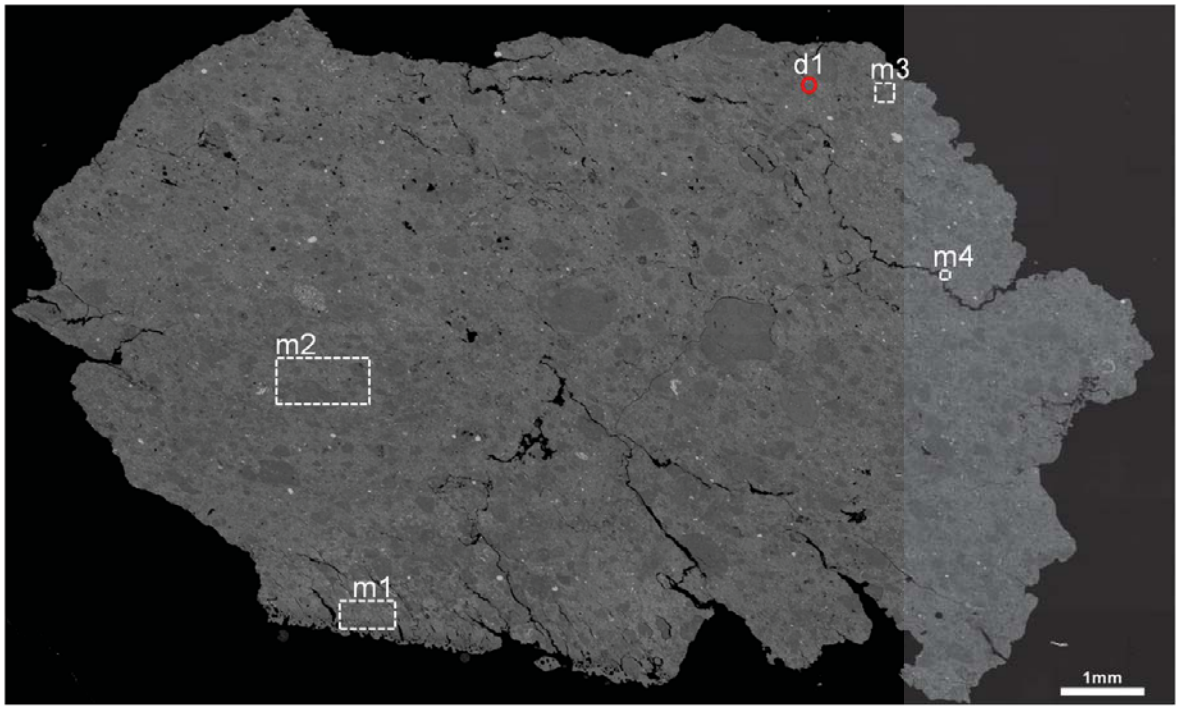

D.11. BSE image of SCO 06043 CM2.0 showing the locations of the detailed images and maps, boxed areas are the location of maps (m) and red circles the location of grains (d= dolomite). d1 is dolomite in Figure 6.6. m1 is map in Figure 3.54, m2 is map in Figure 3.55, m3 is map in Figure 6.7, m4 is map in Figure 6.8.

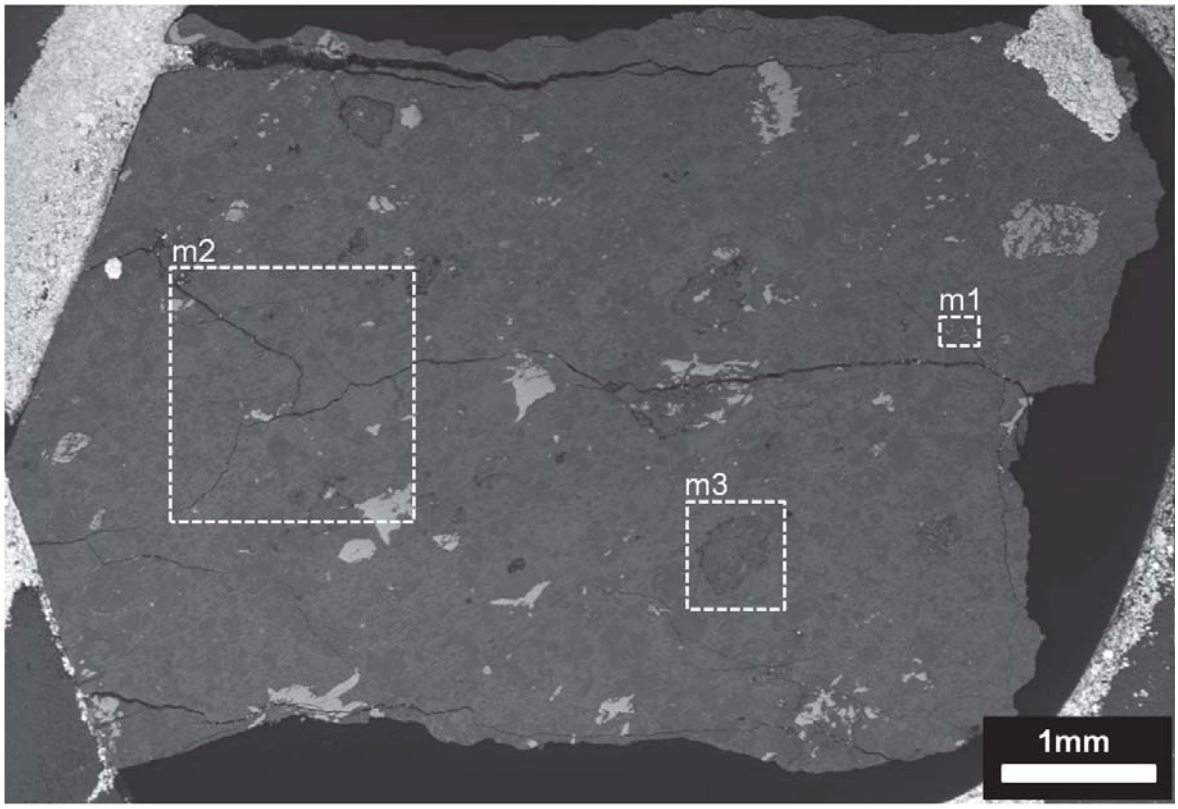

D.12. BSE image of SCO 06043 CM2.0 showing the locations of the detailed images and maps, boxed areas are the location of maps (m). m1 is map in Figure 3.57, m2 is map in Figure 3.59, m3 is map in Figure 6.10.

Peer reviewed publication from this thesis

1- LINDGREN, P., LEE, M. R., SOFE, M. & BURCHELL, M. J. 2011. Microstructure of calcite in the CM2 carbonaceous chondrite LON 94101: Implications for deformation history during and/or after aqueous alteration. *Earth and Planetary Science Letters,* 306**,** 289-298.

The author (Mahmood Sofe) contributed to this paper in the following areas: LON 94101 has been selected for this PhD study, and a sample of this meteorite has been requested from NASA by the author. The author carried out detailed petrographic description (e.g. classification of calcite generations) of the sample. He made his new observation about the presence of a large calcite vein (1.5 mm) in the sample. He also carried out analyses by Raman spectroscopy to distinguish aragonite from calcite, SEM point counting, EBSD mapping of aragonite grains and some calcite grains, CL imaging, elemental mapping using the Zeiss Sigma field-emission SEM and quantitative chemical analyses by EPMA and the Zeiss Sigma field-emission SEM. The author has also been involved in discussion and interpretation of the data used in this manuscript.

2- **LEE, M., LINDGREN, P., SOFE, M., ALEXANDER, C. & WANG, J. 2012.** Extended chronologies of aqueous alteration in the CM2 carbonaceous chondrites: evidence from carbonates in Queen Alexandra Range 93005. *Geochimica et Cosmochimica Acta,* 92**,** 148-169.

The author (Mahmood Sofe) contributed to this paper in the following areas: QUE 93005 has been selected for this PhD study and a sample of this meteorite requested from NASA by the author. The author carried out a detailed petrographic description of the sample. He made new observations about the presence of breunnerite and Ca-poor dolomite in the meteorite. He also carried out analyses by Raman spectroscopy to distinguish breunnerite from other carbonate minerals, SEM point counting, CL imaging, elemental mapping using the Zeiss Sigma field-emission SEM, and quantitative chemical analyses by EPMA using the Zeiss Sigma field-emission SEM. The author has also been involved in discussion, interpretation of the data used in this manuscript and editing some parts of it.